UNIVERSITY OF SOUTHAMPTON

FACULTY OF ENGINEERING, SCIENCE AND MATHEMATICS

School of Geography

Modelling Near-Bank Flow Hydraulics

by

Emmanouil Spyropoulos

Thesis for the degree of Doctor of Philosophy

June 2009

UNIVERSITY OF SOUTHAMPTON

ABSTRACT

FACULTY OF ENGINEERING, SCIENCE AND MATHEMATICS

SCHOOL OF GEOGRAPHY

Doctor of Philosophy

MODELLING NEAR-BANK FLOW HYDRAULICS

by Emmanouil Spyropoulos

River bank erosion models are a fundamental requirement for understanding the migration and evolution of river meanders, estimating the potential for land-loss and threat to floodplain infrastructure, and predicting the delivery of contaminated floodplain sediments to aquatic ecosystems. While progress has recently been made in understanding and modelling processes controlling large-scale mass failure, less attention has been paid to the role that fluvial erosion plays in bank retreat. This project aims to address this gap by developing a new fluvial erosion model. Recent developments in bank erosion monitoring technology, and in the quantification of the bank erodibility parameters using jet-testing devices, offer the means of determining fluvial erosion rates and bank erodibility. However, the missing link remains the need to obtain high-resolution, spatially distributed, flow data to characterize the near-bank fluid shear stresses that drive bank erosion. One possible solution is to use Computational Fluid Dynamics (CFD) models as a substitute for empirical data.

Herein I evaluate a series of three-dimensional CFD simulations for a meander loop on the River Asker at Bridport in southern England. CFD models under specific steady peak flow conditions were developed using Fluent 6.2, with peak flow discharge estimates obtained from an adjacent gauging station. All the models obtained from the three examined flow events were successfully verified and validated using clearly defined and structured procedures. The modelling results indicated that the main qualitative features of the flow remain even as flow discharge varies. However, notable differences were observed between the examined flow events, such as, a general increasing of velocity and shear stress throughout the reach as flow stage is gradually increased, a slight reduction in the size and extent of separation zones at bank full stage, a movement of impingement points further downstream, and a continuation of the secondary flow within the fast streamtube further towards the bends exits. Bed/bank shear stress is mostly seen to decrease at shallow riffles as discharge approaches bankfull, while pools experience an increase in bed/bank shear stress with increase in discharge. Zones of higher bed/bank shear stress extend and combine, while marginal recirculation zones and areas of relatively low bed/bank shear stress generally reduce in area to form discrete locations for erosion and deposition phenomena. At bank full stage, the magnitudes of velocity and simulated shear stresses within the inner bank separation zones are found to be higher than those observed under low flow conditions and they may be sufficient to result in the removal of accumulated sediments into the main downstream flow. The presence of regions of high velocity in the form of a streamtube, especially along the outer banks, creates high shear stresses within these areas. As a result, outer bank migration rates are likely to be relatively high in bends with inner bank separation zones.

TABLE OF CONTENTS

List of figures

List of tables

Declaration

I, Emmanouil Spyropoulos, declare that the thesis entitled '*Modelling Near-Bank Flow Hydraulics*' and the work presented in the thesis are both my own, and have been generated by me as the result of my own original research. I confirm that:

- this work was done wholly or mainly while in candidature for a research degree at this University;
- where any part of this thesis has previously been submitted for a degree or any other qualification at this University or any other institution, this has been clearly stated;
- where I have consulted the published work of others, this is always clearly attributed;
- where I have quoted from the work of others, the source is always given. With the exception of such quotations, this thesis is entirely my own work;
- I have acknowledged all main sources of help;
- where the thesis is based on work done by myself jointly with others, I have made clear exactly what was done by others and what I have contributed myself;
- none of this work has been published before submission

Emmanouil Spyropoulos

10th June 2009

Acknowledgements

This study was undertaken whilst in receipt of a scholarship from the Greek State Scholarships Foundation Body (ΙΔΡΥΜΑ ΚΡΑΤΙΚΩΝ ΥΠΟΤΡΟΦΙΩΝ).

I would like to acknowledge the effort of the following for helping me prepare and complete the thesis document:

Dr Steve Darby, for guiding me through the report process and giving me valuable feedback and essential encouragement that made the delivery of this work more challenging and academically enlightening.

Dr Neil Bressloff, for his support and suggestions that helped me find solutions to specific problems throughout the whole research.

Dr Andromachi Areta, my wife, for her patience, support and understanding at several junctures throughout the duration of my research.

Finally, I would like to thank my parents, Grigoris and Maria Spyropoulos, for their love, support and encouragement.

CHAPTER 1

Introduction

1.1 Introduction to the thesis

Bank erosion is recognized to be a major natural resource management problem, presenting a serious issue for river engineers, environmental managers and farmers, who are concerned that they can cause several problems relating to (*Alonso and Combs*, 1990; *Lawler et al.,* 1997; *Rinaldi and Casagli*, 1999):

- Loss of agricultural land.
- Damage to structures and roads adjacent to the river channel.
- Channel instability.
- Accumulation of sediments in downstream reaches, which can promote flooding there.
- Increase in sediment load, which can cause ecological problems due to turbidity changes.

For all these reasons, it is essential to understand the key processes and mechanisms of river bank erosion in order to diminish the undesirable effects.

River bank erosion models are used to replicate the mechanisms and processes that take place in natural channels. With these models we can estimate the potential for land loss and threat to floodplain infrastructure, as well as predict the delivery of contaminated floodplain sediments to aquatic ecosystems. Bank erosion phenomena occur through a combination of large-scale, episodic, mass failures acting in concert with the smaller-scale, but progressive, removal of sediment by the shearing action of the flow. As will be demonstrated in the following chapter, progress has recently been made regarding the processes controlling large-scale mass failures (*Osman and Thorne*, 1988; *Rinaldi and Casagli*, 1999; *Casagli et al.*, 1999; *Simon and Collison*, 2002). In contrast, less attention has been paid to the role that fluvial entrainment plays in bank erosion. This is an

important omission, not only because fluvial entrainment is a significant process in its own right, but because it often triggers mass failure. As will be shown in the following chapters, the current understanding of the process of fluvial erosion has, until now, been limited by an inability to parameterise available models of the process sufficiently accurately. Fluvial erosion models typically have the following form (*Partheniades*, 1965):

$$E = k(\tau - \tau_c)^{\alpha} \tag{1.1}$$

where E is the bank erosion rate, τ is the applied fluid shear stress, τ_c is the critical shear stress for entrainment of the bank material, k is an empirically-derived erodibility parameter, and a is an empirically-derived exponent, often assumed to be close to unity.

Application of this model requires accurate observations of near-bank applied fluid shear stresses, fluvial erosion rates and erodibility of bank sediments. Recent developments in bank erosion monitoring technology offer the means of determining fluvial erosion rates using Photo-Electronic Erosion Pin (PEEP) (*Lawler*, 1993) or Thermal Consonance Timing (TCT) (*Lawler*, 2005b) systems. These methods allow quasi-continuous erosion rate data to be collected automatically. Hence, the magnitude, timing and frequency of erosional and depositional activities can be determined with much greater precision than is available with traditional manual methods (*Lawler*, 1993). Regarding the quantification of the bank erodibility parameters k and τ_c, a non-vertical jet test device has been developed (*Hanson and Simon*, 2001; *Dapporto*, 2001). The jet-testing apparatus applies hydraulic stresses to the banks and the resulting scour due to the impinging jet is related to the excess stress parameters. This test not only gives consistent results but also it is simple, quick and relatively inexpensive to perform. Nevertheless, the problem of collecting the high-resolution spatially-distributed data needed to characterize near-bank fluid shear stresses remains. One possible solution is to use Computational Fluid Dynamics (CFD) models as a substitute for empirical data. CFD simulations potentially offer a means of acquiring near-bank, distributed, boundary shear stress data at very high spatial resolution. In contrast, empirical data sets of comparable spatial extent and

resolution are very difficult to obtain, particularly during the large flows of interest. The critical question is therefore whether CFD-derived data are sufficiently accurate for this purpose. If they are sufficiently accurate, estimates of near-bank boundary shear stress data obtained from field observations and hydraulic models could potentially be used to develop insight into the nature and effectiveness of fluvial erosion processes under varying flow conditions.

1.2 Context of the research

The research was based on a sinuous reach of River Asker, Bridport, UK. This specific site was selected as it was part of an ongoing research project, funded by the Royal Society and led by Dr Stephen Darby of the School of Geography at Southampton University, and this project involved collecting data necessary for the development of the numerical model. However, it must be emphasized that the research reported herein did not involve fieldwork, rather it relied on accessing the datasets derived from the specified project.

The selection criteria for the study site can be summarized as follows (Darby, personal communication, 2008):

- It was reasonably close to Southampton, UK; thus, promoting logistical feasibility.
- It was sited adjacent to a stream gauging station; thus, river stage and discharge data were readily available.
- It was known, based on prior field observations, that the site regularly experienced fluvial erosion bank erosion processes.
- The site experiences a very flashy hydrological regime; promoting event-based monitoring of peak flow conditions and pre versus post event bank retreat comparisons.

Data derived from the above research project, and used in the current thesis as input parameters for the numerical simulations, are as follows:

- Crest stage gauge data to define water levels;

- Bed topography surveys used in constructing model meshes;
- Erosion pin data, used to validate the results of the modelling;
- Flow velocimetry data under low flow conditions, used to validate the CFD model outputs.

Simulations were carried out on a desktop PC Linux cluster available at Computational Engineering Design Centre, University of Southampton. In addition, limited access to the Iridis computer cluster, one of the largest computational facilities in the UK, was provided.

1.3 Aims and objectives

Knowledge of the rates and controls on bank erosion is fundamental to understanding the migration and evolution of river meanders. However, detailed studies of the parameters influencing the hydraulic erosion of river banks, namely the erodibility of bank materials, and particularly the near-bank boundary shear stresses that drive the erosion process, are virtually absent from the literature. A key missing link to undertaking accurate parameterisation of fluvial erosion models, therefore remains the need to obtain high-resolution, spatially-distributed, flow data to characterize the near bank fluid shear stresses responsible for bank erosion. During high flow events it is difficult to obtain empirical data of these bank shear stresses. The key problem is that it is large flood events that typically drive bank erosion, but it is difficult to measure the applied fluid shear stresses under the hazardous circumstances associated with such events.

The main aim of this project was therefore to employ Computational Fluid Dynamics (CFD) techniques to obtain simulated near-bank boundary shear stress data as a substitute for empirical data. While the application of CFD techniques to environmental flows is still relatively unusual, an increasing number of studies are now applying such techniques to these kinds of problems (see section 2.2.5). The CFD models were built using data collected during a field monitoring phase, to ensure that the models were grounded in reality. Extraction of spatial distributions of boundary shear stresses exerted on the river banks during modelled flood flows were then undertaken as a basis for modelling fluvial

erosion. If successful, the project affords the opportunity to deliver original data sets of considerable interest to fluvial geomorphologists, while the application of CFD techniques to the problem of simulating near bank flows is itself challenging and innovative.

This thesis will attempt to address the above mentioned primary aim through several specific research objectives, which can be summarised as follows:

- Establish the frequency of occurrence of the fluvial erosion process and its subsequent importance on the river regime status.
- Quantify the three-dimensional flow structure in sinuous reaches and evaluate the ability of the numerical model to simulate observed flow structures.
- Assess the ability of various turbulence closures in modelling aspects of the near-bank flow field.
- Explore flow structures generated by different combinations of boundary conditions and flow stages, and consider the geomorphological implications of the modelling results.

The aims and objectives outlined above were tackled through a programme of research which is reported in the following sections.

1.4 Structure of thesis

When describing the interaction between water flow and sediment transport several issues associated with geomorphology, geology, physics, flow hydraulics, and hydrology are involved. This project aims to apply CFD models in order to calculate near-bank fluid shear stresses exerted by the flow. Chapter 2 gives an overview of the relevant bank erosion literature to demonstrate the importance of the fluvial erosion process. It will be shown that a key knowledge gap relates to our (in)ability to accurately estimate near-bank fluid shear stresses. It will be argued that new CFD techniques offer the potential to provide insight into the nature of these near-bank flows. Some background to hydraulic modelling in geomorphology, including a review of previous studies and definition of modelling terms and procedures, will also be presented. Chapter 3 gives specific details

of the CFD code employed, and explains how it can be used to simulate hydraulic parameters in natural channels. The development of the numerical model under low flow conditions at a specific study site, with detailed explanation of the mathematical foundations and assumptions made, is discussed. The numerical modelling of four flow events, covering a range of flow magnitudes, that occurred in the study reach is also demonstrated. In Chapter 4, the evaluation of the model is discussed, based on a comparison of model predictions and field observations under low flow conditions. Chapter 5 then focuses on simulating the fluid shear stresses exerted on the river banks from the range of high flow events. The results are synthesized in Chapter 6. A general conclusion, in which all of the findings are combined and summarized, is then presented in Chapter 7.

CHAPTER 2

Literature Review: River Bank Erosion and the Importance of Modelling Near-Bank Flows

This chapter aims to provide a context for the work that follows. In particular, this chapter starts by establishing the different bank erosion processes and mechanisms (weathering, mass-wasting, fluvial erosion) that take place in natural rivers. It will be argued that the specification of near-bank flows represents a major limitation to progress in the field, especially in the context of fluvial erosion. A key knowledge gap relates to our inability to accurately estimate near-bank fluid shear stresses. Progress can therefore only be made by improved modelling of near-bank shear stresses. Previous studies which have attempted to estimate these near-bank shear stresses will be identified and examined. In conclusion, a review of CFD models will be presented arguing that new CFD techniques offer potential to provide insight to these important near-bank flows.

2.1 Review of bank erosion processes

The processes responsible for the erosion of material from river banks, and mechanisms of failure resulting from the instability produced by those processes, are quite diverse in nature (*Thorne*, 1982). While recognising that these processes will interact to control the overall rate of bank retreat, it is nevertheless helpful to examine them separately in order to understand the way in which a river erodes its banks (*Lawler*, 1992). Hence, a subdivision of the processes and mechanisms of river bank erosion into discrete groups is adopted here.

Bank erosion processes can be divided into small-scale processes (referred to here as fluvial erosion) and large-scale processes (mass-wasting). Fluvial erosion corresponds to the detachment of grains or aggregates of grains from the bank surface and their subsequent removal by the flow (*Thorne and Osman*, 1988a), while mass-wasting is related to the collapse of river banks under the influence of gravity (*Lawler et al.*, 1997).

A further bank erosion small-scale process is sub-aerial/sub-aqueous weakening and weathering (*Thorne*, 1982).

In upstream sections where the banks are low, sub-aerial preparation processes are most effective, while in lower reaches bank heights attain critical values and mass failure can occur (*Couper and Maddock*, 2001; *Couper*, 2003). Consequently, one can expect a progression in the relative dominance of bank erosion processes as a function of the changing scale within a drainage basin, as suggested by *Lawler* (1992; Fig.2.1).

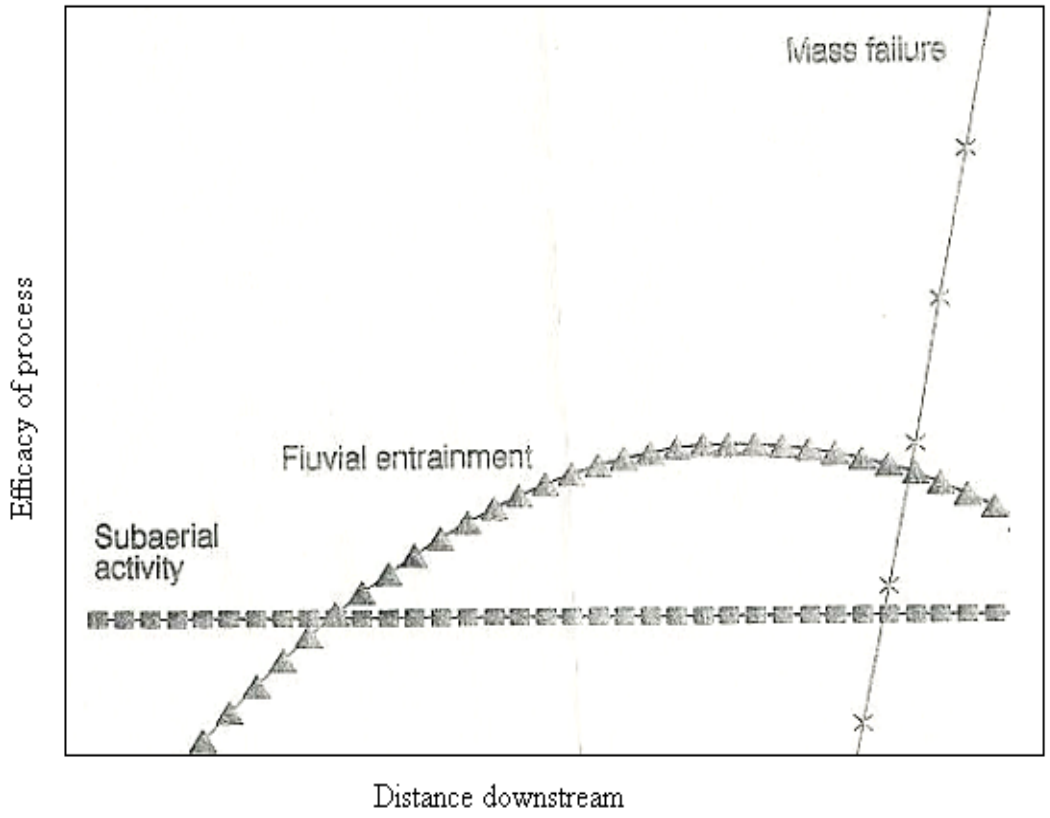

Figure 2.1: Hypothetical downstream change in dominant bank erosion processes. The system is represented as a sequence of overlapping process-intensity domains that also suggest the importance of process combinations (after *Lawler*, 1992).

2.1.1 Weakening-weathering processes

The erodibity of bank soils, whether cohesive or non-cohesive, can be increased significantly by processes of weakening and weathering (*ASCE Task Committee,* 1998a).

Climatic conditions in general, and the movement and physical state of soil moisture in particular, are the main factors that control these processes (*Thorne*, 1982), which may be classified into the following three categories (*Lawler et al.*, 1997):

- Pre-wetting
- Desiccation
- Freeze-thaw

Some of these processes operate within the bank to reduce its strength, while others act on the bank surface to directly loosen and remove particles or aggregates (*Thorne*, 1982).

2.1.1.1 Pre-wetting

The erodibility of banks tends to increase when conditions are wet. In temperate climates, banks tend to become increasingly wet during late winter flows, which are therefore more erosive compared to events earlier in the season (*Lawler et al.*, 1997). The efficiency of a given flow event in eroding the bank by weakening-weathering processes depends on the magnitude and duration of the particular event as well as on the antecedent conditions (*Langendoen*, 2000). Soil moisture conditions are therefore of great importance in bank erosion processes. The Antecedent Precipitation Index (*API*), which is defined as the cumulative precipitation during the ten days prior to the monitoring date, is a parameter that represents soil moisture content (*Weigel and Hagerty*, 1983). An equation which had been used to estimate the *API* in a case study in Devon, UK has the following form (*Hooke*, 1979; *Lawler*, 1993):

$$API_d = \left(API_{d-1} \times k_{ev}\right) + P_d \qquad (2.1)$$

where *d* and *d-1* corresponds to the calculation and previous day, respectively, *API* is the daily antecedent precipitation index (mm), *P* is the daily precipitation (mm), and k_{ev} is a constant referring to evapotranspiration losses, which varies from 0.85 to 0.98 (*Lawler*, 1993).

Wetting of the bank occurs because of three reasons (*Van De Wiel*, 2003): rise of the water table of the stream, groundwater entering the banks from valley slopes, and heavy

or prolonged precipitation. Wetting results not only in an increase of the weight of the bank, but also a build up of positive pore water pressures. Both of these factors can reduce the bank stability with respect to mass failure processes (see Section *2.1.2*) (*Darby and Thorne*, 1996a; *ASCE Task Committee,* 1998a).

The movement of pore water within the bank is a significant factor during or after a major flow event. As the water in the stream rises during a high flow, the increased hydraulic head forces seepage into the bed and banks (*ASCE Task Committee,* 1998a). In contrast, as water falls on the recession of the flood, hydraulic gradients reverse and drive seepage out from the bank into the stream. It is known that the bed shear stress represents a possible hydraulic detachment mechanism taking place longitudinally along the bed, while pore water pressure gradients and consequential seepage forces could represent a potential detachment mechanism functioning vertically upward. Both pore water pressure gradients and seepage forces are given by the following formulas (*Simon and Collison*, 2001):

$$i = (h_1 - h_2) / L \qquad (2.2)$$

$$j = i\gamma_w \qquad (2.3)$$

where i are the pore water pressure gradients, h_1 and h_2 is the hydraulic head at a higher and lower position in the bed respectively (m), L is the vertical distance between those two positions (m), j are the seepage forces (kN/m^3), and γ_w is the unit weight of the water (kN/m^3).

The seepage flow of water in the bank may lead to a process which is known as piping. Moreover, seepage from banks due to very wet conditions could cause sapping of localised areas of the bank face (*Hagerty*, 1991; *Lawler et al.*, 1997). The parameters which are most significant in controlling the amount and rate at which piping occurs are the coefficient of permeability and the variation of the capillary rise (*Ullrich et al.*, 1986). The significance of the piping process is evident from the following:

- Its widespread geographic incidence.
- Its importance in the initiation of drainage patterns on banks.

The most usually noted occurrence of piping in banks has been in alluvial soils even though it is possible to occur in many different geological settings (*Hagerty*, 1991). Piping/sapping processes remove soil grains from the exfiltration faces and transport those grains from the exfiltration zone. The major requirement for the piping process is flow concentration such that the intensity of the exfiltration, given by the exit hydraulic gradient, will be adequate to remove soil particles. The exit hydraulic gradient must produce seepage forces which are sufficient to overcome all resisting forces, such as cohesion, friction and interlocking that tend to keep the soil particles in place.

The most important source of water that helps the piping process may be the stream itself. When the stream rises, water enters into the bank soil. The volume of the water stored in the bank depends on many parameters such as:

- Hydraulic conductivity of the exfiltration zone.
- Magnitude of the recharge gradient.
- Time during which recharge occurs.

Variations in the height of the bank as well as in the height of rise can influence the amount of piping removal and the rate of removal (*Ullrich et al*., 1986). A final parameter which affects the piping mechanism can be the total duration of the flooding event.

Leaching and softening of the soil occur when water moves through the bank (*Thorne*, 1982). Leaching refers to the removal of clay particles in suspension, while softening is observed on the surfaces of soil during the movement of water through cracks and fissures. A weakening of the soil owing to a reduction in either the cohesion or the friction angle results in a decrease in the restoring forces in cohesive banks (*Thorne and Osman*, 1988b). Processes of surface erosion such as sheet erosion and gullying are also

of great importance under specific circumstances (*Thorne*, 1982). When the soil at the bank surface is saturated or when the rate of precipitation overcomes that of infiltration, surface runoff is established which may lead to surface erosion by those processes described above. Another process of weakening erosion, termed slaking, corresponds to the detachment of aggregates by positive pore water pressures owing to the compression of trapped air following a rapid immersion of a dry bank (*Van De Wiel*, 2003).

2.1.1.2 Desiccation

Both cooling in winter, and intense heating in summer, play a vital role in influencing bank surfaces, especially near the bank top, through the cycles of wetting and drying that can cause swelling and shrinkage of the soil. In turn this can significantly weaken river banks (*Bull*, 1997, *Wynn and Mostaghimi*, 2006). The latter in particular can lead to cracking and ped formation of the soil. The flow of groundwater can be influenced by cracking of the soil, leading to the formation of tension cracks, which decrease bank stability with respect to mass failure (*Ullrich et al*., 1986; *Van De Wiel*, 2003).

Desiccational activity can promote higher retreat rates owing to (*Lawler et al.*, 1997):

- Direct spalling of particle aggregates from the dryer upper bank surfaces. These aggregates accumulate at the bank foot and become available for entrainment during subsequent stage rises. Spalling, which is the peeling away of micropeds and slabs of bank material as desiccation progresses, is related to intense heating.
- Cracking up and incipient exfoliation of the bank surface, which allows flood water access around and behind unstable ped structures.

2.1.1.3 Freeze-thaw

The significance of freeze-thaw activity to bank erosion has been recognized in many studies (*Lawler*, 1986; *Lawler*, 1992; *Lawler et al.*, 1997; *Stott et al.*, 2001). Results show that almost all retreat takes place during winter months, indicating the strong seasonal influence on river bank erosion (*Lawler*, 1986). Intense frost disturbance at the bank surface occurs at some stage in the winter, preparing a layer of bank material for removal by fluvial entrainment during the next high flow event. Frost action with respect to

average and maximum bank erosion is identified as the dominant factor tending to cause bank retreat for rivers with catchment areas smaller than 85km^2 (*Lawler et al.*, 1997). In general, frost processes are effective on reaches with small catchments (*Lawler*, 1992). The dominance of frost linked variables over other factors has also been identified, using a detailed regression analysis in a river bank erosion study carried out by *Lawler* (1986).

The most important formation of freeze-thaw is known as needle-ice. This is a form of ice separation in which elongated crystals of ice grow in a direction orthogonal to the bank surface (*Stott*, 1997). This process takes place during subzero air temperature depressions. Having developed needle-ice formations the detachment of surface grains or aggregates then follows (*Lawler*, 1986; *Wynn and Mostaghimi*, 2006). For needle-ice formation to occur, air minimum temperatures must be at least as low as -0.7° C. The relationship between freezing duration and needle-ice length can be described as follows (*Lawler*, 1993):

$$L_1 = -2.79 + 0.963 D_f \qquad (2.4)$$

in which D_f is the freezing duration (h), and L_1 is the needle-ice length (mm).

Almost three hours of subzero air temperatures are required before needle-ice growth is initiated as implied by equation (*2.4*). Combinations of needle-ice action and subsequent fluvial entrainment of the weakened material seem to be an efficient mechanism for bank erosion (*Prosser et al.*, 2000). The local relation between heat and soil moisture conditions controls the occurrence of needle-ice at any given site.

2.1.2 Mass-wasting processes

Mass-wasting processes involve the destabilization and collapse of channel banks due to the force of gravity. There are many conditions under which a stable bank can be transformed into an unstable state (*Simon et al.*, 2000). These are briefly outlined as follows:

- Increase in the unit weight of the soil.

- Decrease or complete loss of negative pore water pressure (matric suction) and apparent cohesion.
- Generation of positive pore water pressures.
- Loss of hydrostatic confining pressure.
- Entrainment of intact and failed material at the bank toe, leading to deformation of the bank profile (which increases the height and steepness of the bank profile).
- Reduction in cohesion and friction angle due to weakening/weathering processes.

The interactions between the gravitational forces acting on the bank and the hydraulic forces acting at the basal area are therefore a significant control on mass-wasting processes. The basal area is defined as the part of the bed and lower bank which surrounds the toe of the bank and extends to a distance of about one or two times the bank height out from the toe (*Grissinger*, 1982).

The analysis of slope stability with respect to mass failure has been extensively examined primarily by geotechnical engineers, but also by geomorphologists and geophysicists. Engineering research has mainly focused on the development of engineering designs such as artificial slopes and embankments, so it is not clear if this work is applicable in the specific context of natural river banks (*ASCE Task Committee,* 1998a). Moreover, geotechnical analysis requires detailed site investigation in order to provide the necessary data for the geometry profile, soil properties, as well as bank stratigraphy and ground water flow. However, after high flow events it is quite difficult to collect all these data from natural eroding river banks. Despite these limitations, principles underpinning the analysis of stability of river banks with respect to mass failures are the same as those used to assess the stability of engineering designs (*Bishop*, 1955; *Morgenstern and Price*, 1965; *Spencer*, 1967; *Sarma*, 1973; *Chen and Morgenstern*, 1983; *Leshchinsky*, 1990; *Espinoza et al.*, 1992; *Michalowski*, 1995; *Kim et al.*, 2002).

The mechanisms of bank failure depend on the following characteristics (*Thorne and Osman*, 1988b; *Alonso and Combs*, 1990; *Darby et al*., 2000): size of the bank, geometry

of the bank, stratigraphy of the bank, engineering properties of the bank material, streamflow characteristics, seepage forces, climatic conditions, and vegetative protection.

Several types of river bank failure have been identified in the field. Shear failure, in which the factor of safety is calculated by assuming expressions for the forces acting on a wedge of bank material, is associated with low, near vertical steep banks and the failure surface is almost planar (*Van De Wiel*, 2003, *Duan*, 2005). In this case, a movement of a block of soil downwards and outwards by sliding before toppling forwards into the channel is commonly observed (*Thorne*, 1982). The *Culmann* method, which is based on analysis of total rather than effective stresses, and thus ignores pore water pressure phenomena, is useful in analysing this kind of failure (*Thorne*, 1982). The *Culmann* method overestimates bank stability as the bank angle, β, decreases and the bank height, H_b, increases respectively. The significance of this point is that it allows the word 'steep' to be defined quantitatively. More specifically, the method is shown to only really work when β is equal or greater than about 60° (*Thorne and Osman*, 1988b; *Darby and Thorne*, 1996b). When soil slips along a curved surface, the slide is termed rotational (*Abam*, 1997). In contrast to plane slip failures, rotational slips are observed in high, gently sloping cohesive banks. In sloping cohesive banks the orientation of the principal stresses changes with depth, whereas in nearly vertical cohesive banks there is a little change of the principal stresses with depth, so that the failure surface is almost planar (*Alonso and Combs*, 1990). The rotational slip failure can be divided into base, toe or slope failure depending on where the failure arc intersects the ground surface (*Thorne*, 1982). Rotational failures are usually analysed using the modified *Bishop's* simplified method in order to include the condition of partial submergence, which is a common feature in natural river banks.

Shear failure along a shallow, planar slip surface is very common in the case of non-cohesive materials, while in cohesive banks deep seated rotational failures are more likely (*Thorne*, 1982; *Van De Wiel*, 2003). The stability of non-cohesive banks is independent of height, while the stability of cohesive banks is dependent not only on the height but also the bank slope angle (*Alonso and Combs*, 1990).

Combinations of cohesive and non-cohesive sediments can lead to complex composite failure forms developing (*Thorne and Tovey*, 1981; *Okagbue and Abam*, 1986; *Abam*, 1997). In this case, the lower non-cohesive layers are eroded to create overhangs or cantilevers in the overlying cohesive layers (*Alonso and Combs*, 1990; *Abam*, 1997; *Lawler et al.*, 1997, *Dapporto et al.*, 2003). These cantilevers remain in the same position until a state of limiting equilibrium is reached due to erosion processes which continue to act on the lower non-cohesive part of the bank. Near vertical upper bank sections and accumulation of debris in the basal area occur when cantilevers fail (*Thorne*, 1982). The mechanisms of cantilever failure may be classified into shear, beam, and tensile failure depending on its corresponding geometry (*Thorne and Tovey*, 1981; *Alonso and Combs*, 1990).

Examples of these different types of bank failure mechanisms are depicted in Figure 2.2.

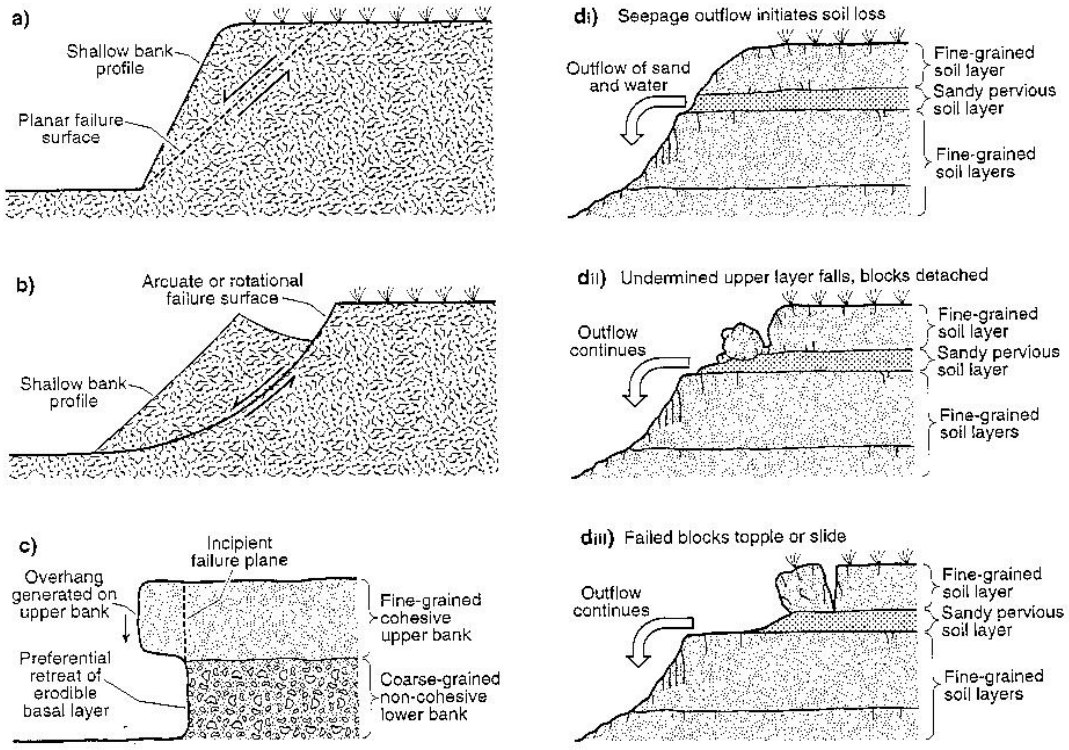

Figure 2.2: Different types of bank failure mechanisms (after *Darby*, 1998).
a) Planar failure; b) Rotational failure; c) Cantilever failure; d) Pipping/Sapping failure

2.1.2.1 Stability of cohesive banks

The effective strength and consequently the stability of poorly drained banks may be reduced by positive pore water pressures (*Simon et al*., 2000). Pore water pressure can be defined as the pressure of water filling the particles between the voids. When the voids are filled, soils are fully saturated, while partial filling of voids by water and air means the soil is unsaturated (*Casagli et al*., 1999). The shear strength of cohesive bank materials can be represented by the Mohr-Coulomb criterion (*Simon and Collison*, 2001):

$$s_r = c' + (\sigma - \mu_w)\tan\varphi' \qquad (2.5)$$

in which s_r is the shear strength (kPa), c' is the effective cohesion (kPa), σ is the total normal stress (kPa), μ_w is the pore-water pressure (kPa), and φ' is the effective friction angle (degrees). Equation (*2.5*) is valid only for saturated conditions where the effective normal stress is equal to the total normal stress minus the pore water pressure. In the case of unsaturated soils the Mohr-Coulomb criterion is modified as follows (*Fredlund et al*., 1978):

$$s_r = c' + (\sigma - \mu_\alpha)\tan\varphi' + (\mu_\alpha - \mu_w)\tan\varphi^b \qquad (2.6)$$

where $(\sigma - \mu_\alpha)$ represents the net normal stress, μ_α is the pore-air pressure (kPa), $(\mu_\alpha - \mu_w)$ corresponds to the matric suction ψ, and φ^b describes the increase in shear strength due to an increase in matric suction. Another term, called the apparent cohesion, is also introduced and is given by the following formula:

$$c_\alpha = c' + (\mu_\alpha - \mu_w)\tan\varphi^b = c' + \psi\tan\varphi^b \qquad (2.7)$$

Thus equation (*2.6*) can be written as follows (*Simon and Collison*, 2001):

$$s_r = c_\alpha + (\sigma - \mu_\alpha)\tan\varphi' \qquad (2.8)$$

Pore water pressure in the unsaturated portion of the bank above the water table is negative and relates to matric suction. The presence of matric suction in the unsaturated soils results in an increase in the shear strength of the material. During low flow periods the shear strength term owing to the matric suction, namely the apparent cohesion, allows the bank to remain stable even if it stands at steep angles (*Casagli et al*., 1999; *Rinaldi et al.*, 2004). During rainfall a reduction in matric suction and increase in the unit weight of the material can result in mass failure, without significant development of positive pore water pressures (*Rinaldi and Casagli*, 1999). During high-flow events the bank material becomes fully saturated so that the apparent cohesion disappears and positive pore water pressures build-up. Alteration between saturated and unsaturated conditions is very common due to the rising of the water table during high flow events and its subsequent falling on the recession limb of the hydrograph.

Compared to non-cohesive banks, where the stability is influenced primarily by the bank angle, the stability of cohesive banks is related to both the bank angle and height (*Thorne*, 1982). In this case failure often occurs along a deep surface within the bank, because in cohesive banks shear strength increases less quickly with depth than shear stress (*Lawler et al*., 1997). The stability of a cohesive bank may be defined through the factor of safety by considering the ratio of resisting and driving forces which act on the most critical failure surface. The resultant driving force consists of the component of the weight of the failure block plus the hydrostatic confining pressure term exerted by the water in the channel, while the resultant resisting force is a function of both the effective cohesion and internal friction angle. An increase in the driving force results from an increase in bank angle or height due to fluvial erosion. In contrast, a decrease in the resisting force results from the weakening of the soil, thereby reducing the effective cohesion or internal friction angle (*Thorne and Osman*, 1988b), while hydrostatic and pore water pressures drive changes in both. Therefore, the stability of a cohesive bank increases with an increase in c' and φ'. Conversely, an increase in bank height, H_b, and slope angle, β leads to a decrease in the stability of the bank because the driving force which originates bank failure is proportional to H_b and β (*Osman and Thorne*, 1988). The *Culmann* limit-equilibrium method is the simplest approach to bank stability of cohesive river banks, but

is only applicable for low, near vertical banks (*Thorne*, 1982). This is because two assumptions are made which are only reasonable for steep banks. Firstly, failure is assumed to take place along a planar surface and secondly the failure passes through the toe of the bank.

2.1.2.2 Stability of non-cohesive banks

The shear strength of a non-cohesive bank material is described by the Mohr-Coulomb equation as follows:

$$s_r = (\sigma - \mu_w)\tan \varphi' \qquad (2.9)$$

where the effective cohesion, c' is equal to zero. The stability of non-cohesive banks may be assessed through the use of equation (*2.9*) and by assessing the forces at static equilibrium under drained and undrained conditions. There is no influence of pore water pressure under drained conditions, except when pore pressures are negative giving an apparent cohesion, so μ_w can be neglected from equation (*2.9*). However, in natural river banks, undrained conditions are most likely and so this review focuses on these conditions.

When undrained conditions dominate, the effect of pore water pressure, μ_w, becomes significant. The limiting slope angle for an undrained non-cohesive bank is defined as follows (*Thorne*, 1982):

$$\tan \alpha_{un} = \frac{(\gamma_s z_p \cos^2 \beta - \mu_w)\tan \varphi'}{\gamma_s z_p \cos^2 \beta} \qquad (2.10)$$

where γ_s is the bulk unit weight of bank material and z_p is the vertical depth to the failure plane.

As can be observed from equation (*2.10)*, when the pore water pressure, μ_w, is positive, the limiting slope angle, α_{un}, is smaller than the effective friction angle, φ'. If the soil is partially saturated, such as above the water table, pores are filled with both air and water and negative pore pressures (matric suction) are developed. Due to those negative pore

water pressures the bank angle overcomes the effective friction angle and an apparent cohesion, c_a, is obtained for the non-cohesive material. Under these circumstances non-cohesive material can behave like a weakly cohesive soil, therefore, equations (*2.6*), (*2.7*), and (*2.8*) are valid.

In the event of instability, failure occurs by shallow slip along a plane or slightly curved surface (*Lawler et al.*, 1997). Given the fact that shear strength increases more quickly than shear stress with depth in non-cohesive banks, deep-seated failures are not usually observed. In poorly drained banks another possibility is failure due to an increase of pore water pressure (*Thorne*, 1982), while the process of piping resulting from high rates of seepage outflow could bring about failure by oversteeping the bank (*Thorne*, 1982).

2.1.3 Fluvial erosion

Fluvial entrainment occurs when the motivating forces attributable not only to the flow, but also to the downslope component of the weight of the sediment block or particle(s), exceed the forces which tend to resist movement (*Alonso and Combs*, 1990; *Lawler et al.*, 1997).When water is flowing in an alluvial channel, fluid drag and lift forces are exerted on the channel boundaries, which may result in the detachment of surface particles. Boundary sediment must provide an internally derived force to resist the erosive forces applied by the flow in order for the surface particles to remain in place (*Hasegawa*, 1989; *ASCE Task Committee,* 1998a; *Langendoen*, 2000; *Van De Wiel*, 2003). These resisting forces include the interparticle forces owing to cohesion, friction and inter-locking and any normal component of the weight of the particle(s). As long as the resisting forces are equal to or greater than the driving forces the particles will remain in place. Grain size, size distribution and the nature of electrochemical bonding that may exist between cohesive particles are, therefore, crucial factors influencing the magnitude of these resisting forces.

The nature of the grain entrainment process depends on the engineering properties of the bank material and more specifically, whether the material is non-cohesive or cohesive (*Lawler et al.*, 1997). In the case of cohesive bank materials, containing considerable

amounts of silt and clay, resistance to entrainment is generated primarily from interparticle forces due to cohesion while in the non-cohesive sediments, which comprise mainly sands and gravels, the forces resisting erosion are mainly due to the immersed weight of the particles and any particle interlocking (*ASCE Task Committee,* 1998a). Hence, fluvial entrainment processes acting on bank materials are completely different for cohesive and non-cohesive sediments. Therefore, a further classification of processes and mechanisms of fluvial entrainment for cohesive and non-cohesive bank material is adopted here.

2.1.3.1 Non-cohesive material

When banks consist of non-cohesive materials, particles are entrained by pivoting, rolling or sliding (*Thorne*, 1982; *Komar and Li*, 1986). The stability of a particle may be considered by taking into account the motivating forces tending to cause motion in relation to the resisting forces that oppose motion. The motivating forces include the fluid drag and lift forces as well as any downslope weight component of the particle. When calculating the stability of non-cohesive grains the fluid drag forces are usually determined by estimating the boundary shear stress. In the case of non-cohesive sands and gravels, the forces resisting erosion are generated mainly from the immersed weight of the particles, as previously mentioned, although close packing of grains can increase the critical boundary shear stress necessary for entrainment (*Langendoen*, 2000). Non-cohesive materials usually show close packing and, in the case of non-spherical grains, imbrication (*Lawler et al.*, 1997). The resistance of the grains to fluvial entrainment is enhanced significantly by these features, allowing such banks to stand at steep angles. Loss of both close packing and imbrication of non-cohesive grains due to weathering, therefore results in increasing susceptibility to entrainment (*Thorne,* 1982). Important to grain entrainment by a flowing fluid is the pivoting angle of the grain, Φ, about its contact point with an underlying grain. Variations of pivoting angles with grain size, shape, and imbrication are employed in an analysis of the grain entrainment threshold by *Komar and Li* (1986) in order to examine how these factors influence grain entrainment and sorting. In the case of uniform grain sizes (sand), the pivoting angle, Φ, depends on grain shape, rollability and angularity, which produces grain interlocking, while in mixed

grain sizes (gravel), the pivoting angle depends on grain shape, imbrication and size (*Komar and Li*, 1986; *Carling*, 1987).

A *Shields*-type entrainment function can be used to predict the mobility of non-cohesive bank materials, with the limitation that it must be modified to take into account the destabilizing effect of the channel side slope (*ASCE Task Committee,* 1998a). In order to identify the critical shear stress for non- cohesive materials, the *Shields* criterion, which predicts the threshold of motion, is employed (*Komar and Li*, 1986; *Ashworth and Ferguson*, 1989; *Ashworth et al.*, 1992; *Ferguson*, 1994; *Reid et al.*, 1997):

$$\theta_c = \tau_c /(\rho_s - \rho_w)gD \qquad (2.11)$$

in which θ_c and τ_c are the critical dimensionless shear stress and critical dimensional shear stress for non-cohesive materials, respectively, ρ_s is the density of sediment, ρ_w represents the density of the water, g is the acceleration due to gravity, and D is the particle diameter. This criterion is based on consideration of the balance of drag and inertia forces at the time of entrainment. The critical dimensionless shear stress can be estimated through field - or more commonly, laboratory – experiments. A constant value varying from 0.04 to 0.06 is typically assigned to the critical dimensionless shear stress (*Reid et al.*, 1997).

In turn the shear stress, τ, for steady-uniform flow conditions, is given as follows (*Ferguson*, 1994):

$$\tau = \rho_w g d S \qquad (2.12)$$

where d is the mean water depth (hydraulic radius), and S is the water surface slope.

Equation (*2.11*) can then be written in the form of critical depth for entrainment as follows:

$$d_c = \theta_c RD / S \qquad (2.13)$$

in which d_c is the critical depth for entrainment and R is the relative density of the sediment defined as:

$$R = \frac{\rho_s}{\rho_w} - 1 \qquad (2.14)$$

The critical shear stress of loose gravel on a sloping bank is defined as (*Thorne*, 1982):

$$\bar{\tau}_c = \cos\beta\sqrt{1-(\tan\beta/\tan\varphi)^2}\,\tau_c \qquad (2.15)$$

in which $\bar{\tau}_c$ is the critical shear stress on the bank, β is the side slope angle, φ is the friction angle for loose gravel, and τ_c is the critical dimensional shear stress on the bed.

Packed gravel, in contrast to loose gravel, exhibits side slope angles higher than the friction angles of the sediments. To take this into consideration, a formula proposed by *Millar and Quick* (1993) can be used, in which:

$$\bar{\tau}_c = 0.067\tan\varphi\sqrt{1-(\sin\beta/\sin\varphi)^2}\,(\gamma_s-\gamma_w)D_{50} \qquad (2.16)$$

in which $\bar{\tau}_c$ is the critical shear stress on the side slope for packed gravel, γ_s is the unit weight of the sediment, γ_w is the unit weight of the water, and D_{50} is the median particle size of the surface grain size distribution.

However, this approach to estimating the critical flow condition is limited since it is difficult to measure accurately the shear stress and mean flow depth in steep shallow rivers with rough beds and banks (*Ferguson*, 1994). Many studies (*Thorne and Furbish*, 1995; *Kean and Smith*, 2006,I; *Kean and Smith*, 2006,II) have shown that a considerable number of rivers have exactly these kind of erodible rough banks. Hence, this method is unlikely to be broadly applicable and therefore a new approach is required to address this

limitation. One possible solution undertaken in this research is to use Computational Fluid Dynamics (CFD) models as a substitute for empirical data.

An entrainment criterion, based on critical discharge rather than critical shear stress, may be better to estimating the critical flow condition. *Schoklitsch* (1962) proposed a critical discharge for entrainment in the form:

$$q_c = 0.26R^{5/3}D_{40}^{3/2} / S^{7/6} \qquad (2.17)$$

where q_c is the critical discharge per unit width, and D_{40} is the 40th percentile of the surface grain size distribution. The *Schoklitsch* (1962) equation was derived by combining the *Shields* criterion (Equation (*2.11*)) with the *Manning-Strickler* equation for flow resistance which is defined as follows:

$$u = d^{2/3}S^{1/2} / k_1 D_{50}^{1/6} \qquad (2.18)$$

in which d is the mean water depth, S is the water surface slope, and k_1 is a constant. It is known that the critical discharge per unit width is given in the following form:

$$q_c = d_c u \qquad (2.19)$$

Substitution of equations (*2.13*) and (*2.18*) into (*2.19*) gives the *Schoklitsch* type relationship for entrainment, defined previously (Equation *2.17*).

In natural non-cohesive channels a range of grain sizes is present at any one place on the bed and banks. In the case of gravel rivers there are some microforms, such as pebble clusters, which delay entrainment and transport, and increase flow resistance, while in sand rivers ripples and dunes perform the same function (*Reid et al.*, 1997). The entrainment of a coarser framework is delayed because of the different structure of sand and gravel. For sand (approximately uniform particle size) all particles tend to begin

moving at approximately the same flow condition (Equation (*2.11*)), while for gravel (non-uniform particle size) the various particle sizes may be brought into motion over a range of critical shear stresses (*Reid et al.*, 1997). For non-uniform size distributions a higher flow is required to initiate motion. The critical shear stress for entrainment of a particle of diameter D from a bed or banks with median diameter D_{50} depends not only on the absolute size D as implied in the *Shields* criterion (Equation (*2.11*)) but also on the relative size D/D_{50} of the grain relative to the matrix (*Ashworth and Ferguson*, 1989). In order to take into account the effects of the particle size distribution, several authors have followed *Andrews* (1983) in replacing Equation (*2.11*) with the following (*Reid et al*., 1997):

$$\theta_c = \theta_{c50}(D/D_{50})^{-x} \qquad (2.20)$$

where θ_{c50} is the critical dimensionless shear stress to move a particle of diameter D_{50}, D/D_{50} is the relative size of the particle, while x is a hiding factor which ranges from 0, if *Shields'* criterion applies to all sizes in a mixed bed or banks, to 1 in a state of perfect equal mobility. Equal mobility means that all sizes of the bed or banks have the same probability for entrainment regardless of their weight or size (*Ashworth et al*., 1992; *Ferguson*, 1994; *Reid et al*, 1997). In order to take into account the hiding effects, which are parameterized in equation (*2.20*), the *Schoklitsch* type relationship (Equation (*2.17*)) takes the following form:

$$q_c = D_{50}^{3/2}(D/D_{50})^{5(1-x)/3}/k_1 S^{7/6} \qquad (2.21)$$

In the cases of $x=0$ and $x=1$, equation (*2.21*) is defined as follows:

$$q_c = D_{50}^{-1/6} D^{5/3}/k_1 S^{7/6} \qquad \text{when } x=0 \qquad (2.22)$$

$$q_c = D_{50}^{3/2}/k_1 S^{7/6} \qquad \text{when } x=1 \qquad (2.23)$$

As can be seen from the previous analysis, the critical discharge criterion is based on a combination of the modified *Shields'* criterion and a flow resistance law. Sensitivity of critical discharge to grain size depends on the hiding factor, *x*, as well as the choice of the appropriate flow resistance law.

2.1.3.2 Cohesive material

The processes of fluvial erosion of cohesive bank material are much more complicated than those for non-cohesive material. In the case of cohesive materials, which contain significant amounts of silt and clay, the dominant forces resisting fluvial entrainment are interparticle forces due to cohesion rather than the immersed weight of the particles. Entrainment therefore occurs when the motivating forces applied by the flow exceed the resisting forces derived from the cohesion of the soil. However, cohesive bank material usually forms a structure of aggregates or crumbs, in the size range 1-10mm, rather than being composed of individual grains (*Thorne*, 1982). Aggregates or crumbs are particles of clay, silt and sand strongly bonded. Therefore, fluvial entrainment requires that the boundary shear stresses exceed the critical shear stress with respect to motion of the aggregates (*Langendoen*, 2000). The chemical bonding of clay particles depends on soil moisture conditions and varies with time (*ASCE Task Committee,* 1998a). Hence, the susceptibility of cohesive banks to erosion by fluvial entrainment depends strongly on their moisture content and degree of weathering. Wet banks are easily eroded, while hard, dry banks are very resistant to erosion by fluvial entrainment (*Alonso and Combs*, 1990). As previously discussed, the boundary shear stresses required to entrain cohesive materials are typically higher than those for non-cohesive materials. Consequently, rates of erosion are often lower for cohesive rather than non-cohesive banks.

As a result of these physical differences, fluvial processes are usually less effective in eroding the cohesive part of a bank, which is often located in the upper portion of the bank, than the non-cohesive materials that are typically located near the basal area. This effect is exacerbated by the more frequent occurrence of flow on the lower parts of the bank (*Rinaldi and Casagli,* 1999). Fluvial erosion of cohesive materials seems to be

associated with the biochemical-physicochemical bonding forces that form the individual particles or aggregates (*Grissinger,* 1982; *Berlamond et al.,* 1993; *Van De Wiel*, 2003).

The erodibility of cohesive materials is therefore related to many properties of the soil, which can be divided into the following groups (*Grissinger*, 1982):

- Soil properties such as the mean particle size, clay and organic matter content, type of clay, bulk density or void ratio, pH, and calcium-sodium ratio (*Lawler et al.,* 1997).
- Properties such as the temperature of the eroding water, rate of sample wetting, and bank pore water pressure (*Hanson and Simon*, 2001).
- Composite soil properties such as dielectric dispersion, permeability, and volume change characteristics (*Grissinger*, 1982).
- Hydraulic properties that can be distinguished into lift forces, turbulence, and fluid shear force, expressed as bed or bank shear stress.

The development of interparticle surface-attraction forces is defined mainly by the primary soil properties which illustrate the nature of the soil unit subjected to entrainment as well as the chemical quality of the interparticle fluid, while the rate of development of these interparticle forces is associated with the second set of properties identified above (*Grissinger,* 1982).

Cohesive soils are also often poorly drained, which can promote the generation of positive pore water pressures in the bank. Reduction of friction and apparent cohesion of the bank soil is reinforced through the development of positive pore water pressures which in extreme cases could lead to total loss of strength, namely, liquefaction (*Lawler et al.,* 1997; *Simon et al*., 2000; *Sarma*, 2005).

Given the difficulty in modelling the onset of motion for cohesive sediments, it is often necessary to search for the direct measurement of the critical shear stress and associated erodibility parameters.

Recent developments of jet-testing devices (*Hanson and Simon*, 2001; *Dapporto*, 2001) can be exploited for quantifying the critical shear stress and bank erodibility. Determination of the critical shear stress, τ_c, can be undertaken by a submerged jet-scour test, and use of the following formula (*Hanson and Cook*, 1997):

$$\tau_c = \tau_0 (\frac{H_p}{H_e})^2 \qquad (2.24)$$

in which τ_0 is the maximum applied bed shear stress within the potential core, H_p is the potential core length from the origin of the jet, and H_e (equilibrium depth) is the depth of scour at the point where the hydraulic shear is equivalent to the critical shear stress. Jet scour parameters are depicted in Figure 2.3.

In order for the equilibrium depth to be computed a hyperbolic function is developed. A logarithmic-hyperbolic function between scour and time is assumed by this method and the equilibrium depth, H_e, is then determined from the antilog of f_0:

$$f_0 = \log\left(\frac{H_e}{d_0}\right) \qquad (2.25)$$

where f_0 is the asymptotic value of the hyperbola, and d_0 is the diameter of the jet nozzle.

The potential core length, H_p, defined as the distance the centreline velocity of the jet remains equal to the velocity at the jet origin, is described as follows:

$$H_p = C_d d_0 \qquad (2.26)$$

while the maximum applied shear stress, τ_0, within the potential core is given by the following formula (*Hanson and Simon*, 2001):

$$\tau_0 = C_f \rho U_0^2 \qquad (2.27)$$

where C_d is an orifice discharge coefficient with a typical value of 0.62, C_f is the friction bed coefficient, ρ is the density of the water, and U_0 is the velocity of the jet at the origin.

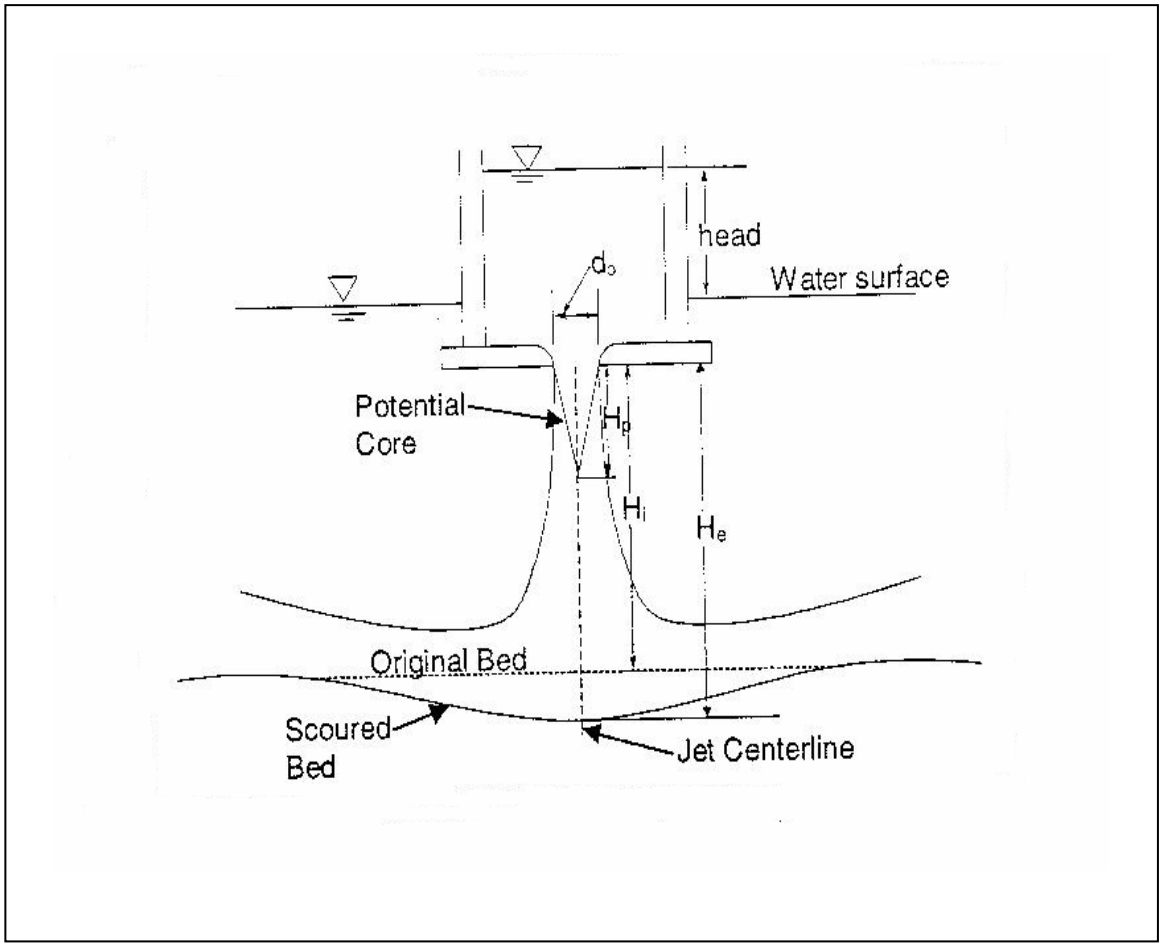

Figure 2.3: Schematic of jet scour parameters (after *Hanson and Simon*, 2001).

The erodibility coefficient, k, is determined by curve-fitting measured values of H, which is the distance from the jet nozzle to the maximum depth of scour at time t, versus t. Cohesive soils with high critical shear stress have a low erodibility coefficient and vise versa. *Hanson and Simon* (2001) found that k can be estimated as a function of τ_c:

$$k = 0.2\tau_C^{-0.5} \qquad (2.28)$$

Nevertheless, jet-testing measurements indicate a wide variation in the erosion resistance of bed and banks, spanning six orders of magnitude for τ_c and four orders of magnitude for k. *Hanson and Simon* (2001) shown that erosion resistance vary within a river, from river to river, and from region to region. Therefore, assessing both material resistance and location is crucial in estimating and modelling fluvial erosion processes.

2.1.3.3 Fluvial bank erosion rates

Published rates of fluvial bank erosion are extremely variable, both spatially and temporally (*Lawler et al.*, 1997), ranging from a few millimetres to several hundreds of metres per year (*Van De Wiel*, 2003). Moreover, fluvial bank erosion rates are influenced by the degree of seasonality so that they are higher during wet seasons. It has been found that rates of bank erosion are faster for non-cohesive than for cohesive sediments. They are also faster in concave bends than in straight reaches (*Okagbue and Abam*, 1986). The spatial and temporal variability of bank erosion rates is due to a wide range of controlling factors, as reviewed in the preceding sections, such as the engineering properties of bank material, channel geometry, hydraulic activity, geology, vegetation, and climate (*Laubel et al.*, 2003).

Several studies have been conducted to describe the rates and distribution of river bank erosion (*Ikeda et al.*, 1981; *Odgaard*, 1987; *Odgaard,* 1989a,b; *Pizzuto and Meckelnburg*, 1989; *Crossato*, 1990; *Hasegawa*, 1989). Understanding the rate of erosion is a fundamental requirement for the evaluation of the time period needed for the short-term prediction of erosion and planning of erosion control as well as for the investigation of the effects of human activities to channel processes (*Hooke*, 1980). The approach by *Ikeda et al.* (1981) was among the pioneering works addressing bank erosion when studying alluvial channel processes. In their theory of river meanders *Ikeda et al.* (1981) found that rates of bank erosion are linearly related to the excess near-bank velocities, which can be defined as the difference between near-bank depth-averaged mean velocities and reach averaged mean velocities. Therefore, their fluvial erosion model is given by the following equation:

$$E = E_0\left(u_b - U\right) \tag{2.29}$$

where E is the bank erosion rate, u_b corresponds to the near-bank depth averaged velocity, U is the reach-averaged velocity, and E_0 is a dimensionless bank erosion coefficient which accounts for variations in bend geometry and bank material properties.

The above linear bank erosion equation has subsequently been adopted in a large number of studies (e.g. *Odgaard*, 1987; *Odgaard,* 1989a,b; *Pizzuto and Meckelnburg*, 1989; *Crossato*, 1990). *Odgaard* (1987) combined the erosion model of equation (*2.29*) with a model for flow in bends with constant curvature in order to explain the patterns of bend migration along two rivers in Iowa. The developed model, which takes into account the relation between erosion velocity and channel characteristics, has the following form:

$$\frac{u_b}{U} = E\frac{b_1}{r'}(1+\frac{b_1}{2r'})^{-1}\mathrm{Z} \tag{2.30}$$

in which:

$$E = \frac{E_0}{8}\left(\frac{3\alpha_p}{2}\frac{\sqrt{\theta}}{\kappa}\frac{m_1+1}{m_1+2}F\ -1\right) \tag{2.31}$$

$$Z = 1-\exp\left[-B\frac{r'\psi_1}{b_1}(1-\frac{b_1}{\psi_1})\right] \tag{2.32}$$

$$B = \frac{2\kappa^2}{(m_1+1)^2}\frac{b_1}{d'} \tag{2.33}$$

where b_1 is the bank-full width of the channel, r' is the radius of curvature in the centreline, α_p is the ratio of projected surface area to volume for a sediment particle divided by that for a sphere of the same volume, θ is the *Shields'* parameter, κ is the *Von Karman's* constant, m_1 is a friction parameter equal to $\kappa(8/f)^{1/2}$, f is the *Darcy-Weisbach* friction factor, F is the particle *Froude* number in the centreline, ψ_1 is the bend angle, and

d' is the flow depth in the centreline. Results of the above study confirmed that the spatial patterns of bend migration were reproduced reasonably well. However, the solution was limited to steady, turbulent flow in constant radius channel segments in which the width was constant, the centreline radius of curvature was large compared to width, the depth was small compared to width, and the cross-channel velocity components were small compared to down channel components.

A near-bank flow depth rather than an excess near-bank velocity was linked to the bank erosion rate in a study employed by *Odgaard* (1989a,b). *Pizzuto and Meckelnburg* (1989) observe that for complex failure processes, simple correlations between erosion rate and near-bank velocity may not exist. The effect of both fluvial erosion and bank failure was included in the bank erosion coefficient employed by *Crossato* (1990). Equation (*2.29*), despite its simplicity, represents a sensible approach for evaluating bank erosion rates. However, several queries exist resulting in its limitation. Firstly, the near-bank velocity magnitude is inadequate to clarify the migration patterns of meanders. Moreover, it is not clear that a constant value of the bank erosion coefficient can be used for predicting accurately bend migration patterns for a specific field site (*Pizzuto and Meckelnburg*, 1989).

A study carried out by *Hasegawa* (1989) found a universal bank erosion coefficient which was related to both bank erosion rate and cross-sectional mean velocity. The latter coefficient was validated with data obtained from alluvial channels in Japan. A method for predicting bank erosion processes in meandering channels was made feasible by applying an empirical approach employed by *Hasegawa* (1981) to a computational model by *Nagata et al.* (2000). Nevertheless, the potential of the latter method was limited since the simulation of bank geotechnical failure was not included. Several authors have related the bank erosion rate to the geotechnical properties of bank material (*Hickin and Nanson*, 1984; *Osman and Thorne*, 1988; *ASCE Task Committee,* 1998a). However, the effects of hydraulic forces in the derivation of bank erosion rates were not considered.

Existing methods for calculating fluvial erosion rates are subject to serious shortcomings (*ASCE Task Committee,* 1998a,b). An analytical approach for calculating fluvial erosion rates was initiated by *Duan et al.*, (2001). This approach suggested that fluvial erosion rates depend on several factors, such as the longitudinal gradient of sediment transport, secondary flow strength, and bank eroded sediment. A method for predicting fluvial erosion rates for cohesive materials was also employed by *Duan*, (2005). This was related to the difference between sediment entrainment and deposition rather than excess shear stress (*ASCE Task Committee,* 1998b; *Darby et al*., 2002) and based on the concept that bank erosion takes place when the rate of entrainment of bank surface particles is greater than their rate of deposition.

Fluvial erosion rates can also be defined through the use of an excess shear stress model (*Darby et al*., 2002). For non-cohesive sediments, fluvial erosion rates may be found by applying a sediment transport submodel in the near-bank zone (*ASCE Task Committee,* 1998b). In contrast, applications of excess shear stress formulations for cohesive banks are unusual since the value of shear stress required for entraining surface particles varies widely and can be influenced by different processes (*Grissinger*, 1982), as discussed in Section 2.1.3.2. Nevertheless, it is believed that the fluvial erosion of cohesive materials can be determined by (*Partheniades*, 1965):

$$E = k(\tau - \tau_c) \qquad (2.34)$$

where E is the fluvial bank erosion rate, τ is the applied fluid shear stress, τ_c is the critical stress for entrainment of the bank material, and k is an empirically-derived erodibility parameter.

Equation (*2.34*) indicates that the effective shear stress must be greater than the critical shear stress to initiate motion. *Partheniades* (1965) found that erosion rates for cohesive soils were independent of the shear strength, but they depend strongly on the shear stress, increasing rapidly after a critical value of the shear stress had been reached. Application of this simple excess shear stress model requires accurate observations of applied fluid

shear stresses, fluvial erosion rates, critical shear stresses, and erodibility of bank materials. The possibilities and limitations of estimating the critical stress have been reviewed already, so I now turn to the estimation of the applied boundary shear stress.

A key missing link in the effective parameterisation of the boundary shear stresses that drive hydraulic erosion of river banks, remains the need to obtain high-resolution, spatially-distributed, flow data. Moreover, although it is large flood events that often drive hydraulic bank erosion, it is often difficult to measure the applied near-bank fluid shear stresses under the hazardous circumstances associated with these conditions. At present no simple formulas exist for estimating the distribution of those boundary fluid shear stresses (*Kean and Smith*, 2006I-II). As a result, these stresses in the near-bank zone must be estimated either by using experimental based methods (*ASCE Task Committee,* 1998a) or by various forms of modelling.

Many researchers have attempted to predict the near-bank fluid shear stresses on channels of various shapes. These studies have usually been conducted using data from laboratory studies that employ idealized rectangular, trapezoidal, or lenticular shaped cross sections (*Engelund*, 1964; *Lundgren and Jonsson*, 1964; *Knight et al.*, 1994; *Rhodes and Knight*, 1994), and only a few studies have been undertaken in the field at full scale (*Bathurst et al.*, 1979; *Dietrich and Whiting*, 1989, *Nece and Smith*, 1970). While the applicability of laboratory-based work to field situations is limited, at present no other way exists to study certain fundamental issues except under carefully controlled laboratory conditions,. Since lenticular shapes more closely approximate the shape of natural channels they have often been the focus of river studies (*Lundgren and Jonsson*, 1964; *Kovacs and Parker*, 1994). Five methods (hydraulic radius, vertical depth, normal depth, area, according to log velocity distribution) for determining the boundary shear stress were reviewed by *Lundgren and Jonsson* (1964), with the area method being found to be most suitable for general use.

For over-bank flows in straight and meandering channels, considerably less experimental data is found with regard to both velocity and especially boundary shear stress (*Knight*

and Demetriou, 1983; *Knight et al.*, 1989, 1990; *Sellin et al.*, 1993). In general terms, for straight channels with floodplains the boundary shear stresses under over-bank flows vary in a more complex way than for in-bank flows, with stresses in the main river channel decreasing because of the influence of the slower floodplain flows. On the other hand, the floodplain boundary shear stresses rise above their expected two-dimensional values because of the effect of the faster flowing, main river flow. As a result, the interaction between channel and over-bank flow events results in some localized and complex effects, which compounds the difficulty of understanding the distribution of boundary shear stresses.

A number of modelling studies have been recently carried out (*Griffin et al.*, 2005; *Kean and Smith*, 2006,I; *Kean and Smith*, 2006,II) for determining the spatial distribution of near-bank boundary fluid shear stresses.

Boundary shear stresses near banks with small scale roughness were modelled by including the effects of drag on natural topographic features such as erosional embayments (*Kean and Smith*, 2006,I). This approach was made feasible by developing a model which calculates the drag on the above features. Both a drag coefficient and an appropriate reference velocity, that includes the effects of roughness elements further upstream were used for estimating the form drag on each element. The shape geometry of these individual roughness elements was found to be well approximated by a Gaussian shaped curve, although differences not only in channel size but also in bank characteristics may exist. *Hopson's* (1999) laboratory measurements were then used to estimate the drag coefficients of these shapes. In this way, a roughness height of the bank can be determined in relation to the characteristic size, shape, and spacing of the bank topographic features. The specified bank roughness height value was then used in the flow model of *Kean and Smith* (2004) to compute the desired boundary shear stress distribution. The combined model illustrates that drag on small scale topographic features results in substantial reductions in both the near-bank velocity and boundary shear stress. However, application of this model is limited since the flow effects of irregularity in size, shape, and spacing of bank roughness elements are not included.

To address this limitation, *Kean and Smith* (2006,II) extended their method to determine the roughness properties of irregular surfaces more characteristic of natural rivers. This was achieved by distributing the resistance effects of the various bank topographic features away from the boundary by forming an outer profile capable for scaling the characteristics of each feature. Therefore, the topography of irregular surfaces can be transformed into regularly spaced, identical topographic elements. Evaluation of the importance of size, shape, and spacing of bank roughness elements is then possible. Model simulations indicate that drag on an individual topographic feature is influenced by both size and shape of the element located immediately upstream. In addition, the sequence for a given set of different sized bank roughness elements plays an important role in determining the spatial distribution of the boundary shear stresses. Our ability to calculate the near-bank boundary shear stresses responsible for fluvial bank erosion has undoubtedly been enhanced by the *Kean and Smith* (2006,II) model. Nevertheless, the three dimensionality approach associated with drag on bank topographic features is still undeveloped.

A possible alternative approach for determining the near-bank boundary shear stresses is to develop Computational Fluid Dynamics (CFD) models of competent events as a substitute for empirical data. CFD models provide a means of obtaining boundary shear stress data at very high spatial resolutions, whilst empirical data sets of equivalent spatial extent and resolution are very difficult to acquire, particularly during the hazardous competent flows of interest. Hence, a clear understanding of the potential of CFD methods and applications in respect of this requirement is needed, which is the subject of the next section.

2.2 Review of CFD Models

Until relatively recently the field of Computational Fluid Dynamics (CFD) was limited to applications in industrial fluid flow problems, and for design and development studies employed by engineers and applied mathematicians (*Bates and Lane*, 1998)**.** Since the early 1970's, CFD has subsequently been incorporated into the fields of hydrology and geomorphology and has been used to improve both the understanding and simulation of

key processes, particularly where knowledge had been limited because of a lack of empirical data from field and laboratory measurements (*Lane*, 1998). Consequently, application of CFD models to natural rivers offers the potential to develop solutions to a wide range of geomorphological and river management problems (*Nicholas*, 2001). Given that the growth of more powerful computer capacity has occurred during the last decade, simulating the interactions between river channel morphology, flow structure and sediment transport has became progressively more comprehensive, and CFD methods are increasingly being used by hydrologists and geomorphologists (*Lane et al*., 1999a). However, it should be emphasized that three-dimensional numerical models for river flows are currently in the stage of research and development, far from the mature use by engineers in industrial fluid flow applications (*Cao et al*., 2003). Application of CFD to environmental flows leads to a series of problems not encountered in industrial applications (*Bates et al.*, 2005). These problems are associated not only with greatly increased complexity resulting from the need to represent irregularly shaped boundaries, but also with variations of drag coefficients in time and space due to complex interactions between the material properties and the flow itself (*Bates et al.*, 2005).

The purpose of this section is to review the principles and applications of CFD modelling in hydrology and geomorphology, with the specific objective of evaluating whether such techniques might provide insight into the modelling strategies suitable for estimating the fluid stresses on river banks that drive the processes of fluvial bank erosion identified previously (section 2.1) as being of particular interest in this study. The use of the CFD simulations seems to be the only feasible technique of estimating the spatial distribution of boundary shear stress applied to the bank surface during large flood flows, due to the problems of being on site during, and working in, these potentially hazardous events.

2.2.1 Governing equations

Computational fluid dynamics techniques are based on an understanding of the principles of conservation of mass and momentum which govern the fluid flow processes. The conservation of mass or continuity law applied to a fluid passing through an infinitesimal, fixed control volume is represented by the following equation:

$$\frac{\partial \rho}{\partial t} + \frac{\partial (\rho u)}{\partial x} + \frac{\partial (\rho v)}{\partial y} + \frac{\partial (\rho w)}{\partial z} = 0 \qquad (2.35)$$

where u, v and w are the components of flow velocity in the x, y, and z directions respectively, ρ is the density, and t denotes time.
Equation (*2.35*) can be written in a more compact vector form as:

$$\frac{\partial \rho}{\partial t} + div(\rho u) = 0 \qquad (2.36)$$

Equation (*2.36*) is the general form of the mass conservation equation and is valid for compressible fluids. The first term on the left-hand side represents the rate of change in time of the density, namely mass per unit volume, while the second term is associated with the net flow of mass out of an elemental body of fluid and is called the convective term.

Newton's second law states that the rate of change of momentum of a fluid particle equals the sum of the forces acting on the particle. Applying this to a fluid passing through an infinitesimal, fixed control volume, yields the following equation:

$$\frac{\partial (\rho u)}{\partial t} + div(\rho u u) = -gradp + div(\tau) + \rho g + F \qquad (2.37)$$

where p is the static pressure, τ is the stress tensor, and ρg and F are the gravitational body force and external body forces, respectively.
In the i^{th} direction equation (*2.37*) is given as:

$$\frac{\partial (\rho u_i)}{\partial t} + \frac{\partial (\rho u_i u_j)}{\partial x_j} = -\frac{\partial p}{\partial x_i} + \frac{\partial \tau_{ij}}{\partial x_j} + F_i \qquad (2.38)$$

The stress tensor, τ_{ij}, is defined as follows:

$$\tau_{ij} = \mu\left(\frac{\partial u_i}{\partial x_j} + \frac{\partial u_j}{\partial x_i}\right) - \frac{2}{3}\mu div(u)\delta_{ij} \tag{2.39}$$

in which δ_{ij} represents the Kronecher delta and μ is the coefficient of viscosity for a Newtonian fluid. The first term on the right-hand side of Equation (*2.39*) includes the dynamic viscosity which relates stresses to linear deformations, while the second term is associated with the kinematic viscosity which links stresses to the volumetric deformation.

When substituting equation (*2.39*) into equation (*2.38*) the Navier-Stokes momentum equations are obtained in *x*, *y*, and *z* directions, respectively:

$$\rho\frac{du}{dt} = -\frac{\partial p}{\partial x} + \frac{\partial}{\partial x}\left(2\mu\frac{\partial u}{\partial x} + \mu div u\right) + \frac{\partial}{\partial y}\left[\mu\left(\frac{\partial u}{\partial y} + \frac{\partial v}{\partial x}\right)\right] + \frac{\partial}{\partial z}\left[\mu\left(\frac{\partial u}{\partial z} + \frac{\partial w}{\partial z}\right)\right] + F_x \tag{2.40}$$

$$\rho\frac{dv}{dt} = -\frac{\partial p}{\partial y} + \frac{\partial}{\partial x}\left[\mu\left(\frac{\partial u}{\partial y} + \frac{\partial v}{\partial x}\right)\right] + \frac{\partial}{\partial y}\left(2\mu\frac{\partial v}{\partial y} + \mu div u\right) + \frac{\partial}{\partial z}\left[\mu\left(\frac{\partial v}{\partial z} + \frac{\partial w}{\partial y}\right)\right] + F_y \tag{2.41}$$

$$\rho\frac{dw}{dt} = -\frac{\partial p}{\partial z} + \frac{\partial}{\partial x}\left[\mu\left(\frac{\partial u}{\partial z} + \frac{\partial w}{\partial x}\right)\right] + \frac{\partial}{\partial y}\left[\mu\left(\frac{\partial v}{\partial z} + \frac{\partial w}{\partial y}\right)\right] + \frac{\partial}{\partial z}\left(2\mu\frac{\partial w}{\partial z} + \mu div u\right) + F_z \tag{2.42}$$

For incompressible flows ρ is constant so it can be placed outside the derivatives in equations (*2.40*), (*2.41*), and (*2.42*) (*Lane*, 1998). These flow equations are in principle a complete description of the flow field, but there are practical problems in solving them. Thus, a range of assumptions, limitations, and ancillary models (reviewed below) are

needed to make the solution tractable. The basic assumptions can be briefly summarized as follows (*Lane et al.*, 1999a):

- If the equations are being applied in problems with spatial variation in atmospheric pressure, which implies large-scale simulations, an additional horizontal pressure gradient term has to be introduced in formulas (*2.40*), (*2.41*), and (*2.42*). In the case of geomorphological applications concerned with river channels and floodplains, this can be ignored.
- In the case of large-scale floodplain flow simulations, an additional wind stress term at the water surface must be introduced. However, following from the general concern of geomorphologists with small-scale applications to river channel systems, it is generally acceptable to ignore the terms associated with the wind stress.

A number of further limiting simplifications are introduced to make explicit the physical processes that the three-dimensional model represents and to simplify solution. These involve:

- Reynolds averaging techniques to make the equations tractable. These are reviewed in detail in the following sub-section.
- Specification of boundary conditions regarding the inlet, the outlet, and the outer limits of the flow in contact with the river bed, banks, and water surface.
- Numerical solution procedures, where the flow domain defined by the boundary conditions is discretised into cells, and the equations produced by Reynolds averaging are applied in each cell in order to identify how the cells affect one another.

2.2.2 Turbulence modelling

The analysis of turbulence is an interdisciplinary activity including a huge variety of applications. Variations in momentum exchange at an extremely fine spatial scale can be generated by fluid flow processes (*Booker*, 2000). Turbulence is an eddying, irregular, unsteady, and three-dimensional motion (*Hinze*, 1975). The basic features of turbulent flows can be summarized as follows (*Tennekes and Lumley*, 1972):

- **Irregularity**: As already mentioned, all turbulent flows are highly random. Thus, a deterministic approach is not appropriate and statistical methods are adopted instead.
- **Diffusivity**: An important characteristic of all turbulent flows corresponds to the diffusivity of turbulence. This can cause rapid mixing, and increased rates of momentum, heat, and mass transfer.
- **Three-dimensional vorticity fluctuations**: All turbulent flows are rotational, three-dimensional, and characterized by high levels of fluctuating vorticity. As a result, when describing a turbulent flow attention has to be paid to the role that vorticity plays.
- **Dissipation**: Turbulent flows are always dissipative. Deformation work, which increases the internal energy of the fluid at the expense of the kinetic energy of the turbulence, is carried out by the viscous shear stresses.
- **Continuum**: Turbulence can be described as a continuum phenomenon governed by the equations of fluid mechanics.

2.2.2.1 Averaging techniques for turbulent flows

Solving turbulent flow fields by direct numerical solution (DNS) is applicable only for very simple but fundamental flow problems, such as simple turbulent channel and pipe flows (*Ingham* and *Ma,* 2005), since the computational demands for solving complicated cases are very high. DNS solves directly for the complete set of the unsteady Navier-Stokes equations, without modelling any parameters (*Fluent Inc.*, 2006). This full discretization implies a very fine grid throughout the computational domain, in order to resolve the smallest scales of motion, and hence a very small time step both for reasons of accuracy (in order to accurately resolve all the time scales) but also in terms of stability. It is these requirements that result in the high cost of the computations.

For this reason, turbulent river flows are usually modeled by employing the Reynolds-Averaged Navier-Stokes (RANS) equations incorporating an appropriate turbulence model. This approach corresponds to the standard definition of turbulence as a time-average at a fixed point in space (*Hinze*, 1975). These equations are derived from the

usual Navier-Stokes previously introduced. The method consists of decomposing all the flow quantities into a time averaged and a fluctuating part (*Booker*, 2000) (see section 2.2.2.2). The Navier-Stokes equations can be transformed in such a way that the small scale turbulent fluctuations do not have to be directly simulated. A coarse computational grid may be employed by applying this method. Nevertheless, large scale complex three dimensional river flows, such as those with irregularly shaped bed and banks, can not be solved in all cases due to the limitations in computer power (*Lane* and *Ferguson*, 2005). Therefore, various simplifications to the governing equations have to be introduced to reduce the dimensions of the problem.

An alternative approach for modelling turbulence, known as Large Eddy Simulation (LES), is associated with all fluctuations that occur at scales smaller than those resolved by the discrete volume used in the numerical calculation and can be expressed as a space-average at a fixed point in time (*Hinze*, 1975). Large turbulent scales and eddies are computed directly by the solver, and only small turbulent scales are modeled (*Leonard*, 1974). A number of attempts have been made to investigate steady and unsteady river flows by using LES techniques (*Thomas and Williams*, 1995; *Bradbrook et al*., 2000b, *Zedler and Street*, 2001; *Keylock et al*., 2005). The latter study by *Keylock et al*. (2005) introduces the LES methodology, discusses a variety of ways for representing small-scale processes within LES (the subgrid-scale modelling problem), and provides some examples of early work into the use of LES in a fluvial context. However, the use of LES in river flow modelling is still at an early stage of development (*Ingham* and *Ma*, 2005). A number of advances in computational power and numerical methods are required before LES can be effectively applied at the river reach scale. The advantage of this approach is that it computes directly the scales of flow that contain the most mass and momentum transfer using the full Navier-Stokes equations, but parameterizes the smaller features of the flow through a sub-grid scale turbulence model. Therefore, LES is potentially more accurate than the Reynolds averaged equations but it is much more computationally expensive since fine computational grids are required especially in the case of environmental flows (*Spalart*, 2000).

In summary, it can be said that turbulent flows are characterized by velocity fields of a fluctuating nature. Transported quantities such as momentum, energy, and species concentration are mixed by these fluctuations, so those quantities are also fluctuated. Nevertheless, turbulent fluctuations may be of a small scale and a high frequency, so that direct numerical simulation of them is usually too computationally expensive. As an alternative, the exact instantaneous governing equations can be averaged in a number of ways, thereby removing finer scales and providing a set of equations that are less resource intensive to solve. However, a set of unknown variables are contained within these new equations. For determining these new variables as a function of the known quantities, turbulence models are needed (see section 4.1.4).

2.2.2.2 Reynolds averaging

The Reynolds-Averaged Navier-Stokes equations utilize mean rather than exact quantities. Hence, the computational effort is greatly reduced. The exact flow variables are decomposed into mean and fluctuating components. Having applied the above process, the velocity component can be written as:

$$u_i = \overline{u}_i + u_i' \tag{2.43}$$

where $\overline{u}_i$ and u_i' are the averaged and fluctuating parts of the velocity component, respectively. This format can be used for all other scalar quantities.

Substituting variables of this form into the continuity and momentum equations and taking a time average, yields the time averaged momentum equations which in Cartesian form are given as:

$$\frac{\partial \rho}{\partial t} + \frac{\partial}{\partial x_i}(\rho u_i) = 0 \tag{2.44}$$

$$\rho \frac{du_i}{dt} = -\frac{\partial \rho}{\partial x_i} + \frac{\partial}{\partial x_i}\left[\mu\left(\frac{\partial u_i}{\partial x_j} + \frac{\partial u_j}{\partial x_i} - \frac{2}{3}\delta_{ij}\frac{\partial u_i}{\partial x_i}\right)\right] + \frac{\partial}{\partial x_i}(-\rho\overline{u_i' u_j'}) \tag{2.45}$$

Equations (*2.44*) and (*2.45*) are the known Reynolds-Averaged Navier-Stokes equations. The only difference between the above equations and their original versions (equations (*2.35*), (*2.40*)-(*2.42*)), corresponds to the fact that the velocities and other solution variables now represent time-averaged values. This decomposition introduces additional terms, $-\rho\overline{u_i' u_j'}$, known as the Reynolds stresses, which represent the transport of momentum that can be attributed to turbulence. To obtain closure of the Reynolds-Averaged Navier-Stokes equations, a variety of turbulence models have been developed, which vary in their complexity and ability to solve the Reynolds stresses in a wide range of flow scenarios. Since information regarding the turbulent structure is unavailable, the Reynolds shear stresses have to be modeled by utilizing flow parameters (*Younis*, 1992). Because there is no direct way of estimating the Reynolds stresses, the majority of hydraulic models employ a parameter for eddy viscosity in their turbulence models based on the so-called Boussinesq approximation (*Boussinesq*, 1877), which indicates that the turbulent shear stresses are proportional to the mean velocity gradients. The method used is to model the Reynolds shear stresses as being proportional to the mean rates of strain (*Lane et al*., 1999a). For general situations the eddy viscosity concept can be defined as follows:

$$-\rho\overline{u_i' u_j'} = \mu_T\left(\frac{\partial u_i}{\partial x_j}+\frac{\partial u_j}{\partial x_i}\right)-\frac{2}{3}\left(\rho k+\mu_T\frac{\partial u_i}{\partial x_i}\right)\delta_{ij} \qquad (2.46)$$

where μ_T is the turbulent eddy viscosity, k is the kinetic energy per unit mass contained in the turbulent motion, and δ_{ij} represents the Kronecher delta.

The turbulent kinetic energy, k, is given as:

$$k = \overline{u_i' u_j'}/2 \qquad (2.47)$$

The turbulent eddy viscosity depends strongly on the state of the turbulence and may vary over the flow field. Regarding the Kronecher delta, it has been added to ensure that the contribution from the normal stresses is included.

In principal, river flows can be modeled numerically by solving the Reynolds-Averaged Navier-Stokes equations in all three directions. Necessary requirements are an appropriate turbulence model and a set of properly defined boundary conditions for the fluid flow (*Ingham* and *Ma*, 2005).

2.2.3 Boundary conditions

Given the fact that the mass and momentum equations are generally applied to the entire flow domain, at the boundary special consideration must be given to the free water surface, solid surfaces (bed and banks) as well as inflow and outflow characteristics (*Lane et al.*, 1999a). Both the inflow and outflow boundary conditions can be considered as problem-dependent (*ASCE*, 1988; *Lane et al.*, 2005) and their construction is either based on hydraulic principles, such as a fully developed flow profile (*Bradbrook et al.*, 2000a) or is obtained from experimental or field data (*Hodskinson and Ferguson*, 1998; *Bradbrook et al.*, 2001). Solid boundaries and the free water surface can be parameterized using more general rules (*ASCE*, 1988). The importance of these rules is discussed in the following sub-sections.

2.2.3.1 Free water surface

The spatial variation in water surface elevation is a key process driver (*Rhoads and Kenworthy*, 1995, 1998) for the particular interest of reach-scale river flows. Therefore, surface treatments are necessary to represent free surface effects. For steady fluid flows 'rigid lid' schemes have been used to represent the water surface (*Lane et al.*, 1999a; *Bradbrook et al*., 2000a; *Ferguson et al*., 2003). In contrast, the volume of fluid method (VOF), in which the water surface is numerically predicted at each time interval has been applied in unsteady reach-scale river flow simulations (*Ma et al*., 2002).

For steady state river flows, defining the nature of the free water surface might involve the use of a 'rigid lid' approximation where the water surface is considered as a fixed planar surface, which is used to set the value of pressure (*Ingham* and *Ma*, 2005). On this 'rigid lid', frictionless conditions are implemented which permit the water to slip, but not to pass within the free water surface. The pressure represents the variation in water depth that would occur if the surface were not fixed (*Bradbrook et al.*, 1998; *Lane et al.*, 2004). In addition, this pressure may be varied allowing the influence of local changes in water surface such as super-elevation, where the pressure is greater than zero, and depression, where pressure is less than zero, to be simulated. The mass continuity equation (*2.35*) is not influenced by this since no pressure gradient term is contained within it, but the momentum equations (*2.40*), (*2.41*) and (*2.42*) are affected. Velocity overestimation results from water super-elevation, whereas underestimation would occur due to water depression. Thus, correction of the pressure gradient has to be considered in each time step. Two water surface correction models have been developed, namely the porosity model of *Spalding* (1985) and the surface mesh deformation model (*Olsen and Kjellesvig*, 1998; *Booker*, 2003).

In *Spalding's* (1985) model, pressure correction can be achieved by adjusting the mean value of the porosity of all cells (*Lane et al*., 1999a; *Ferguson et al*., 2003). For each cell in the top layer of the fluid, porosity is specified and the mass flux along any cell is set equal to the porosity multiplied by the face area and the velocity component on it. Having calculated the porosity, the pressure correction is satisfied by the change in surface deviation (*Spalding*, 1985):

$$por. = 1 + \frac{p}{\rho g h_c} \qquad (2.48)$$

where p is the pressure surface gradient, ρ is the density of the water, g is the acceleration due to gravity, and h_c is the thickness of the surface grid cell.

In the second approach (*Olsen and Kjellesvig*, 1998; *Booker*, 2003), deformation of the mesh based on the predicted pressure at the water surface is applied by correcting the free water surface. The water surface is fixed at the downstream boundary where the pressure, p_{ref}, is taken as reference pressure. A pressure deficit at each surface cell is calculated by subtracting this reference pressure from the extrapolated pressure for each cell. This pressure defect is then used to move the water surface by a vertical height. The surface mesh deformation model is given by the following formula (*Olsen and Kjellesvig*, 1998):

$$\Delta h = \frac{l}{\rho g}(p - p_{ref}) \qquad (2.49)$$

where l is the difference in the height of water surface at p and p_{ref}.

These water surface correction models can be considered adequate in the case of moderate water surface elevations for representing the free surface in CFD simulations.

In the case of large flood events, water level changes rapidly. Thus, the water surface must be free to change instantaneously in the computational domain (*Ingham* and *Ma*, 2005). Under these unsteady flow conditions the VOF method may be employed. The position of the water surface in the computational domain can be found by applying the control volume technique described in the next chapter (4.1.1) (*Hirt and Nichols*, 1981). Thus, a water volume faction can be defined in a computational cell as follows (*Ma et al*., 2002):

$$F = \frac{\delta\Omega_{water}}{\delta\Omega_{cell}} \qquad (2.50)$$

in which $\delta\Omega_{cell}$ is the volume of the computational cell, and $\delta\Omega_{water}$ is the fraction of the volume of the cell filled with water.

According to the law of mass conservation of air and water, the volume fraction of the water satisfies the following equation:

$$\frac{\partial F}{\partial t} + u^i \frac{\partial F}{\partial x^i} = 0 \qquad (2.51)$$

Implementation of the VOF method involves a multi-flow approach where some airflow can be introduced into the computational domain above the water cells. The water surface is then transformed into an interface between the air and water. The location of the interface can be predicted by numerically solving equation (*2.51*) (*Hirt and Nichols*, 1981).

When applying the VOF technique care has to be taken near to the interface between the air and the water since numerical diffusion may occur. In addition, the use of VOF is computationally expensive. Thus, application of the 'rigid lid' schemes can be considered more appropriate (relative to VOF) for treating the water surface in most river flow simulations (*Lane* and *Ferguson*, 2005).

2.2.3.2 Wall functions and bed roughness

Water flow near to the bed and banks of a river is very complex phenomenon influencing both its mean and turbulent structure (*Ingham* and *Ma*, 2005). When water is flowing near these boundaries a reduction in velocity over a boundary layer is observed satisfying the no-slip condition. Thus, very fine grids are required in near boundary regions to simulate their effects on water flow. As an alternative, wall functions may be employed especially when features of the mean fluid flow region are regarded as the major interest. These functions require specification of the roughness height, K_s, as well as wall functions for turbulent kinetic energy and dissipation rate when using the k-ε turbulence model (*Lane et al*., 1999a). The roughness parameterization is extremely complex for three-dimensional flows because the effects of changing roughness are difficult to isolate (*Nicholas*, 2001). The law of the wall for the determination of the hydraulic variables for the cells adjacent to the channel bed and banks is often based on the following semi-

logarithmic equation, which is applicable when the major interest is in the characteristics of the mean fluid flow (*Nicholas and Sambrook Smith*, 1999; *Lane et al*., 2004):

$$u^+ = \frac{1}{\kappa}\ln(E_c z^+) - \Delta B(K_s^+) \qquad (2.52)$$

$$u^+ = \frac{u_p}{u^*}, \qquad z^+ = \frac{z}{z^*}, \qquad K_s^+ = \frac{K_s}{z^*}, \qquad z^* = \frac{\mu}{u^*}, \qquad u^* = \sqrt{\frac{\tau_w}{\rho}} \qquad (2.53)$$

where u_p is the flow magnitude in the planform direction, u^* represents the wall shear velocity, z^* corresponds to the height of zero velocity, z is the elevation above a reference plane, z^+ is a dimensionless parameter interpreted as the ratio of the elevation above a reference plane to the height of zero velocity, K_s is the wall roughness height, K_s^+ is taken to be an equivalent sand grain height, E_c is a constant equal to 9.8 (*Hodskinson*, 1996; *Fluent Inc.*, 2006), ΔB is a roughness parameter, κ is the *Von Karman's* constant, usually taking a value of 0.4187, μ is the dynamic viscosity of the fluid, and τ_w is the shear stress at the solid wall boundaries.

An appropriate selection of the roughness parameter is crucial for determining the shear stress at the boundaries. In the case of 3D models, the roughness parameter contributes directly to only the bottom grid cell (*Ingham* and *Ma*, 2005).

The roughness height can be considered as an effective roughness parameter resulting in the correct variation of vertical velocity with elevation above the bed (*Nicholas*, 2005). However, specification of an appropriate value of roughness height is based on considerable uncertainty (*Hey*, 1979; *Bray*, 1980; *Ferguson et al*., 1989). Several studies have used the following equation for roughness height (*Hodskinson*, 1996; *Hodskinson and Ferguson*, 1998; *Booker et al*., 2001):

$$K_s = 3.5D_{84} \qquad (2.54)$$

where D_{84} is the 84th percentile of the bed sediment diameter cumulative frequency distribution.

Nevertheless, this relationship is based on field investigations (*Hey*, 1979), and a wide range of spatial scales are contributed in the calculation of roughness height through equation (*2.54*) (*Clifford et al*., 1992). Separation of the spatial scales into sub-grid-scale components represented by the wall function and supra-grid-scale components corresponding to the topography of the model mesh is essential when using CFD applications. Therefore, roughness height may take a lower value as follows (*Nicholas and Sambrook Smith*, 1999):

$$K_s = D_{50} \qquad (2.55)$$

Many studies (*Lane and Richards*, 1998; *Nicholas and Sambrook Smith*, 1999; *Nicholas*, 2001; *Lane et al.*, 2002) have identified that specification of an appropriate roughness height in fact depends on mesh resolution as well as topographic representation. However, interactions between these parameters are not fully understood. In summary, it can be said that relationships between roughness parameter and roughness height play a vital role in determining the correct values of simulated bed and bank shear stresses.

2.2.3.3 Inflow characteristics

Inflow boundary conditions involve specifying the three dimensional velocity distributions on the upstream boundary of the computational domain. Velocities in all three directions and the turbulence parameters, at each grid cell, have to be specified (*Lane et al*., 1999a). Experimental or field data, such as the rate of water discharge, can be used to estimate these conditions (*Hodskinson and Ferguson*, 1998; *Bradbrook et al.*, 2001). When the upstream inlet boundary is located far from the region of major interest a uniform velocity profile may be defined allowing a fully developed flow to occur in that region (*Bradbrook et al.*, 2000a).

In principle, specifying the boundary inflow conditions requires a very large amount of data. In practice it is highly unlikely that such data exists. Fortunately, it can be shown (*Bradbrook et al.*, 2000a; *Bradbrook et al.*, 2001) that as you move away from the boundary the sensitivity of the solution to the specified boundary conditions decreases.

2.2.3.4 Outflow characteristics

The outflow boundary of the computational domain has to be selected in a straight part of the river where modifications to the fluid velocity further downstream of the outflow location are not considered significant. In such cases, the flow can be treated as being fully developed. Fluid flow conditions can then be defined through the use of a reference pressure (*Ma et al*., 2002), whereas a zero gradient may be applied to all other variables in the downstream direction of the flow. When no fully developed flow exists at the downstream boundary either a pressure condition or a fluid velocity profile taken from measured data must be defined (*Ingham* and *Ma*, 2005).

2.2.4 Grid resolution and design

It has been noted in recent studies that the use of different resolution meshes applied to complex geometry river topographies not only influences the topographic representation of the channel, but it also influences the specification of the roughness parameters (*Hankin et al*., 2001). When considering environmental flows, the spatial discretization of the governing equations also influences their numerical solution, due to both complex topographic surfaces and spatial variation in flow properties which can happen within a range of spatial scales (*Lane et al.*, 2005). Thus, spatial discretization is an important factor related to the mesh resolution selection. Grid generation is a particular concern in applications involving arbitrarily and irregularly shaped channels. When a river channel is discretized, discontinuities as well as irregularities are the main features of interest. The nature of the irregularities corresponds to the scale of the discretization, which controls model predictions. Flow can not be solved accurately in the case of coarse grid spacings. One possible solution to overcome this problem is to reduce the grid spacing until the point that flow model predictions become effectively independent of grid spacing. However, this approach requires high computational demands and introduces a further

issue concerning the relationship between grid spacing and the resolution of topographic representation. If the spacing is finer than the topographic resolution, the flow model predictions will, in part, be a product of the nature of the topographic interpolation (*Lane and Richards*, 1998). If coarser than this, the flow model predictions would be a product of the discretization process and not the input topographic information. However, when dealing with the continuous surface of a natural, irregular channel, this is problematic. The topographic information will have been sampled from the surface, by likely using structured sampling to include key topographic features. However, there will be scales of topography, such as, the bedform scale or the grain scale that will not have been included in full as the topographic sampling density will not be sufficient to map either every bedform or every grain. Making the grid resolution progressively finer should make model solution independent of coarser scales of topographic variation. However, if this is carried out until the solution is independent of even the small scale the model will be resolving flow around topography that is a product of the sampling method used to represent the surface rather than any real topographic variation (*Lane and Richards*, 1998). It is a question of reducing grid spacing so as to capture all relevant scales of boundary irregularity.

The Grid Convergence Index (GCI) concept was introduced by *Roache*, (1997, 1998). This index is used to estimate the uncertainty associated with the solution at a particular grid resolution and subsequently to report the credibility of the simulations (*Hardy et al*., 2003). The GCI can be applied for a single point on a numerical mesh, for an assembly of points, or for an entire mesh, and can be estimated for all variables of interest. Perfect mesh independence can be achieved when the GCI equals to zero. However, this is not feasible because of numerical rounding errors. *Hardy et al*. (2003) found that different variables converge at different rates depending on the processes dominating the flow, and therefore these different variables converge to different GCI values.

Some of the main principles underlying high quality grid generation are summarized below (*Lane and Richards*, 1998):

- Low element skewness (angle between intersecting lines should be between 45 and 135 degrees).
- From one cell to the next the local change in grid spacing should be no more than 30%.
- Length over width ratio of the cell should be no greater than 10.
- Grid cells should be finest in the direction of the strongest depth or velocity gradient, implying that grid spacing must be finest close to the channel edges.
- An adequate number of elements for a sensible computation to be carried out, and at the same time a small enough number of elements so that the computational time can be kept to a minimum.
- The mesh close to the wall has to satisfy the near wall treatment used by the turbulence model utilized in the solution process.

Obviously satisfying all of the above requirements is difficult. Usually, some compromises have to be made in order to obtain accurate solutions within a reasonable amount of computational time.

2.2.5 CDF models and implications

In the preceding sections of this review, the general principles of CFD modelling were outlined and issues pertaining to the parameterization of CFD models for environmental flows were also discussed. While the application of CFD techniques to environmental flows is still relatively unusual, an increasing number of studies are now applying such techniques to these problems. The range of CFD applications that have been undertaken in the literature so far are summarized in this section. In addition, issues that have yet to be adequately resolved are also illustrated.

Some studies which have been conducted in recent years and which have dealt with either two-dimensional or three-dimensional modelling are summarized below. As previously discussed, the science of computational fluid dynamics has started to be applied more widely in fluvial hydraulics in the last two decades (*Hodskinson and Ferguson*, 1998; *Lane and Richards*, 1998; *Lane et al., 1999a, 2000*; *Nicholas*, 2001; *Olsen*, 2003). A computational fluid dynamic model calculates the spatial variation of many different

parameters in a river channel, such as the velocity distribution and turbulence. Examples of these studies include predictions of meander evolution (*Demuren and Rodi*, 1986; *Olsen*, 2003; *Wilson et al*., 2003; *Rodriguez et al.*, 2004; *Duan and Julien*, 2005), and investigations of processes taking place in pool-riffle sequences (*Booker et al*., 2001; *Cao et al*., 2003). Numerical simulations of either two-dimensional or three-dimensional flows have been performed in braided river channels (*Lane and Richards*, 1998; *Nicholas and Sambrook Smith*, 1999; *Nicholas*, 2003; *Jang and Shimizu*, 2005), while three-dimensional modelling of flow at the confluences of river channels has also been examined (*Bradbrook et al*., 1998; *De Serres et al.*, 1999). Moreover, attention has been paid to channel bend flow in respect of both bend flow simulation and bed evolution, as well as flow over vegetation (*Hodskinson and Ferguson*, 1998; *Fischer-Antze et al*., 2001; *Hsieh and Yang*, 2003, *Ferguson et al.*, 2003; *Ferguson and Parsons*, 2004). Computational fluid dynamics was also applied to compute flow in rivers with complex bed topography (*Olsen and Stokseth*, 1995; *Nicholas*, 2001; *Lane et al.*, 2002; *Lane et al*., 2004), sediment transport and local scour processes (*Olsen and Kjellesvig*, 1998). Finally, studies have been conducted to model the flow in fluvial dead zones (*Hankin et al.*, 2001), to simulate the flow of water and sediment into a sand trap (*Olsen and Skoglund*, 1994), to incorporate high resolution topographic data into flood inundation models (*Bates et al.*, 2003), and to replicate the free surface in open channel flows (*Cao et al.*, 2003). Examples of fluvial geomorphological investigations that have employed CFD modelling for the simulation of hydraulics are demonstrated in Table 2.1. It can be said that none of these applications are directly related to the problem of interest in this analysis, where the aim (Chapter 3) is to address the objective of applying CFD modelling techniques to define the near-bank fluid shear stresses exerted by the flow.

When simulating environmental flows several parameters relating to the application of CFD models are not adequately comprehend. Due to the complexity of natural rivers, a range of processes including domain representation, boundary condition specifications as well as model calibration/validation require that not only the amount but also the quality of field data has to be considerably increased. Furthermore, field data sets must represent a well defined flow condition. This is a major issue since the collection of a

comprehensive set of data might take a long period during which discharge may change. Thus, there is a strong relationship between data quality and accurate model formulation. Another feature that has to be taken into consideration is the ability of a numerical model to replicate the processes of flow for a specific case, such as turbulence behaviour, boundary roughness, and water surface implications. Enhanced turbulent closures for simulating turbulence anisotropy in regions of high shear, such as shear layers at confluences (*Bradbrook et al*., 1998; *Sukhodolov and Rhoads*, 2001), and separation zones at meanders (*Hodskinson and Ferguson*, 1998) are essential. Wall functions are used in most models for replicating river bed or banks roughness. As a result, maximum turbulent kinetic energy occurs at bed and banks. Although, this assumption is valid for sand bed/bank rivers, in case of gravel composed materials having high relative roughness, empirical modifications of wall functions (*Lopez*, 1997), high resolution elevation data (*Nicholas*, 2001) or artificial porosity approaches (*Olsen and Stokseth*, 1995) have to be employed. All the above issues have to be adequately clarified so that our ability to conduct reach scale modelling can be significantly enhanced.

2.3 Summary

A detailed outline of the geomorphological context of the problem was presented in the first section (*2.1*) of this chapter. In this case a classification for the different bank erosion processes and mechanisms (weathering, mass-wasting, fluvial erosion) was introduced with the aim of identifying the importance of the fluvial erosion process, as justified by evidence from the literature. A detailed review of fluvial erosion processes and models was also provided in this first section (*2.1*) showing that the key research gap seems to be an inability to accurately determine the applied fluid shear stress that drives the process. Progress can therefore be made by improved modelling of near-bank shear stresses. Reviews of studies which have either measured or attempted to model near bank boundary shear stresses were presented together with their advantages and limitations. In principle, this section identified all the relevant literature, but established the argument that CFD might be a way forward to estimate near-bank flows. Finally, the second section (*2.2*) reviewed the likely extent to which CFD models can be used to address the problem of interest, and identified appropriate modelling approaches.

Table 2.1: Examples of previous studies that have employed CFD modelling in fluvial geomorphological investigations.

Author(s)	Title	Code employed
Lane, Richards, and Chandler (1995)	Within-reach spatial patterns of process and channel adjustment.	STREMR, 2D, depth averaged.
Lane (1998)	Hydraulic modelling in hydrology and geomorphology: a review of high resolution approaches.	None
Lane and Richards (1998)	High-resolution, two-dimensional spatial modelling of flow processes in a multi-thread channel.	STREMR
Mosselman (1998)	Numerical modelling of rivers with erodible banks.	2D, Finite difference.
Nicholas and Walling (1998)	Morphological modelling of floodplain hydraulics and suspended sediment transport and deposition.	FLUENT
Bates, Horritt, and Hervouet (1998)	Investigation of two-dimensional, finite element predictions of floodplain inundation using fractal generated topography.	TELEMAC, 2D, finite element.
Bradbrook, et al. (1998)	Investigation of controls on secondary circulation in a simple confluence geometry using a 3D numerical model.	Phoenics
Thomson, Nelson, and Wohl (1998)	Interactions between pool geometry and hydraulics.	Unspecified 2D code.
Hodskinson and Ferguson (1998)	Numerical modelling of separated flow in river bends: Model testing and experimental investigation of geometric controls on the extend of flow separation at the concave bank.	FLUENT 4.2, 3D, finite element
Carroll, et al. (2004)	Modelling erosion and overbank deposition during extreme flood conditions on the Carson river, Nevada.	RIVMOD
Rodriguez, et al. (2004)	High-resolution numerical simulation of flow through a highly sinuous river reach.	FLOW-3D
Duan and Julien (2005)	Numerical simulation of the inception of channel meandering.	Unspecified 3D code.
Jang and Shimizu (2005)	Numerical simulation of relatively wide, shallow channels with erodible banks.	Unspecified 2D code.

CHAPTER 3

Methods

This chapter aims (i) to explain the basic issues related to environmental flow modelling in general and (ii) to outline the CFD code used in the current investigation. The chapter also introduces a description of the field site employed and considers the numerical modelling set up of the various flow events examined in this study. The chapter begins by reviewing the advantages and disadvantages of the use of different numerical solvers, gridding methods and turbulence closure schemes in relation to environmental flows. Introduction of the CFD code employed in this thesis will be followed by explaining how it can be used to simulate hydraulic patterns in natural channels, based on the specific issues identified within the review process. A description of the selected field site will then be presented, followed by the development of the numerical model for a range of flow conditions observed in the study reach.

3.1 Review of CFD Implementation Strategies

The CFD approach to simulating fluid flow problems appears to have significant potential as a tool for use in fluvial geomorphology. Current application of CFD software is mainly restricted to the investigation of three-dimensional open channel flow structures (*Nicholas and Sambrook Smith*, 1999). Despite its potential, the CFD approach therefore remains relatively untested. CFD software is not fully physically based and so its performance may be affected by factors such as specification of the numerical solution, the resolution and geometric qualities of the model mesh, and the turbulence model used. All these issues are discussed in this section.

3.1.1 Numerical solvers

The solver, as the name implies, is the heart of a CFD code. Having specified both the flow domain and boundary conditions within the pre-processing stage, its main role is to provide solutions to the mathematical equations that represent the underlying physical

processes. Thus, the flow field can be resolved by applying numerical methods that form the basis of the solver. This section aims to provide an understanding on the conversion of the equations describing models of environmental systems to a form that is acceptable for solution on a computer. Mathematical equations that represent physical processes can be considered representations of reality. Simulation of real word conditions is feasible with the aid of computer models consisting of equations and algorithms that are used to simulate processes (*Booker*, 2000). Most physical models are articulated by means of differential equations, whilst their solution lies on the fundamental mathematical theories of the solution of differential equations (*Wright*, 2005). As previously defined, the basic aim is to convert the differential equations, which have defined functions as solutions, to a set of algebraic equations that connect values at various discrete points that can be operated by a computer. This process is known as discretization. The performance of numerical codes is associated with several issues, such as the accuracy of discretization (*Wallis and Manson*, 1997), the spatial discretization required for verification (*Hardy et al.*, 2003), and convergence problems related to fine grids in finite volume discretizations (*Cornelius et al.*, 1999). Thus, when applying CFD at the river reach scale attention has to be paid to the way the domain of interest will be discretized. The main three discretization options, differ in quite fundamental ways, are finite difference, finite element, and finite volume.

Finite difference schemes are based on the differential form of the mass and momentum equations, which are approximated by a system of linear algebraic equations (*Ferziger and Peric*, 1999). Therefore, the finite difference method may be considered as a method of approximation. The values of variables at the grid nodes represent the unknowns of these algebraic equations. A finite difference approximation replaces each term of the partial differential equation at a particular node. Finite differences can be estimated through three different approaches, namely backward, central, and forward. First, second, third, and higher-order terms can be obtained by using finite differences since the differential equations are defined as *Taylor* expansions (*Smith*, 1978). However, the most common approximation used is the second-order central difference, where values are calculated at the cell face using the average of the values at the two cell centres. When

diffusion dominates, the second-order central differencing scheme is applicable since the properties of the flow are equally influenced in all directions (*Parsons*, 2002). In contrast, downstream effects on the upstream values become less important in problems with convection where properties do not spread equally in all direction. As a result, in high convection problems the central differencing scheme can become unstable and false numerical diffusion can be introduced. Hence, the weakness of this scheme is its inability to identify flow direction as well as to recognize the strength of convection relative to diffusion. The central differencing scheme will be stable and accurate only if the cell *Peclet* number, a measure of the ratio of convective terms to diffusive terms, is less than 2. This condition corresponds to the requirement for positive coefficients in the particular scheme. Error representation for finite differences resulting from the approximations of the partial differential equations can be undertaken by defining the truncation error (*Smith*, 1978; *Lohner*, 2001), which is an estimate of error as a function of grid size. Thus, grid refinement is an important factor affecting finite difference schemes. Applications of finite differences to environmental flow problems with irregular geometries and non-linear equations, such as rivers are, therefore, often found to have limitations (*Wright*, 2005).

Finite element techniques, initially developed by *Zienkiewicx* and *Cheung* (1965) provide an alternative approach to numerical solution with regards to the problem of fluid dynamic simulation. With this method the equations are set up in such a way that a solution is obtained by minimizing the global error (*Lane and Ferguson*, 2005). In particular, shape or basis functions corresponding to each element are identified and used to approximate the local solution. A global function, developed on the basis functions, is then substituted into the partial differential equations. Integration of these equations with weighting functions is then followed and the resulting error is minimized to give coefficients for trial functions which can be considered as an approximate solution (*Wright*, 2005). In contrast with the finite difference approach, the finite element method is based on unstructured grids that can be easily fit to arbitrary boundaries since they consist of triangular, rather than quadrilateral, footprints. Thus, when dealing with

complex geometries, a characteristic feature of environmental river flows, the finite element schemes can be applied with more confidence (*Ferziger and Peric*, 1999).

The finite volume or control volume technique may be considered as a modified version of the finite difference approach. The difference between them, in terms of fluid dynamics simulation, is that the partial differential equations making use of a finite volume technique are created in such a way that the conservation of mass is of a great importance compared to the conservation of momentum since mass is conserved in the discrete form of the equations just as it is in the physical situation (*Booker*, 2000). The integral, rather than the differential, form of the conservation equations is utilized by the finite volume schemes. Initially, the computational domain is divided into control volumes with a node specified at each volume centre, while integrals are applied not only to the surface but also to the volume of the control. Approximation of both surface and volume integrals are essential for determining an algebraic equation in terms of values on the face of each control volume (*Ferziger and Peric*, 1999). These face values are then obtained from adjacent values by interpolation. Several methods can be utilized for the interpolation: upwind schemes which are similar to forward or backward differencing and require very fine grids, linear schemes equivalent to central differencing, and non-linear schemes. However, the most common scheme used is the upwind differencing. As previously mentioned, the definition of the flow direction is quite difficult when applying the central scheme. In contrast, the flow direction is taken into account through upwind differencing. In the latter scheme the convected value at a cell face is supposed to be equal to the value at the upstream node. When applying the upwind scheme, the coefficients of the discretized equation are constantly positives, leading to reasonable results. This scheme is very stable in flows with very high convection. Nevertheless, in regions with low convection and where flow is skewed to the grid lines problems may arise since it is only first-order accurate. Hence, attention has to be paid when designing the grid. These problems can be gradually overcome as the grid becomes finer, although it may become too computationally expensive (*Parsons*, 2002). The finite volume method can use either structured or unstructured grids. When using unstructured grids, a solution can be obtained by deforming the grid to fit the shape of the domain. However, in some

cases the grid is so deformed that solutions to the problem are difficult to attain (*Wright*, 2005).

Combination of the finite element and finite volume schemes can be considered as a significant development for complex geometries, such as rivers with irregular surfaces. This involves application of the finite volume methodology into unstructured grids of finite elements (*Schneider and Raw*, 1987). In river flow applications, both high and low convection regions exist due to the complex geometries. Thus, the hybrid differencing solution scheme was developed (*Spalding*, 1972) based on a combination of upwind and central differencing schemes. When applying the hybrid differencing, the local cell *Peclet* number has to be carefully considered. In regions with high convection (P_e>2) upwind differencing is applied. In contrast, when diffusion dominates (P_e<2) central differencing is more applicable. The combined scheme is fully conservative with always positive coefficients (*Parsons*, 2002), leading to physically realistic solutions. The hybrid differencing approach can be considered highly stable when compared to higher order schemes, while it has been widely used in natural river flow problems (*Hodskinson*, 1996; *Hodskinson and Ferguson*, 1998; *Lane et al.*, 1999a; *Nicholas and Sambrook Smith*, 1999). However, its main disadvantage lies in its first-order accuracy, although it has been demonstrated that errors owing to the interpolation scheme are not of great importance (*Waterson*, 1994). When the flow makes an angle with the grid and a higher numerical accuracy is needed, the Quadratic Upstream Interpolation for Convective Kinetics (QUICK) scheme developed by *Leonard* (1979) can be used. The calculation of face values is made by providing a blending based on local flow conditions, of second order upwind as well as central differencing. The interpolation can occupy values from two cells upstream of the face and the cell downstream. The QUICK differencing scheme defines a quadratic interpolation in which the face value is based on the adjacent nodal values and on an additional neighbour node (*Ferziger and Peric*, 1999). Although the QUICK scheme is much more accurate than the hybrid differencing, the differences are small enough (*Parsons*, 2002).

The majority of commercial 3D CFD codes such as Fluent, CFX, and Star-Cd are based on these mixed approaches, which are applicable to environmental river type flows including natural complex geometries and holds the advantage of implicit conservation of physical quantities (*Lane and Ferguson*, 2005).

Having applied one of the differencing schemes described above, the partial differential equations are converted to a set of non-linear algebraic equations. Computation of the entire flow field can be achieved by coupling the mass continuity equation with the Navier-Stokes equations and the pressure field that drives the flow (*Wright*, 2005). Local velocity components, as well as the pressure field, are the main features that have to be defined in order to determine the flow field. Both these elements are estimated from the appropriate governing equations. The velocity components can be addressed by the momentum equations using an iterative method. However, a difficulty remains in characterizing the unknown pressure field since no direct equation exists for acquiring pressure. A possible solution for overcoming this problem lies in the indirect specification of the pressure field through the continuity equation. After substituting the correct pressure field into the momentum equations, the continuity equation is satisfied by the resulting velocity field (*Newton*, 1998). Nevertheless, this method is computationally intensive, since it requires the determination of four unknowns in the case of a three-dimensional problem. As a result, an iterative solution method that works out each of the four equations sequentially has been created. In addition, a development of a procedure which permits the pressure to be updated is essential, since this is not explicitly available within the conservation equations. This particular process, termed the pressure correction technique, is based on the idea of constructing the next iteration from the results of the previous iteration, and can be related in an algorithm (*Utama*, 1999).

The first pressure correction technique widely used was the SIMPLE (Semi Implicit Method for Pressure Linked Equations) technique of *Patankar and Spalding* (1972). In this pressure-velocity coupling algorithm the convective fluxes contained at cell faces are calculated with the aid of the so-called guessed velocity components. A pressure field is initially guessed and the discretized momentum equations are solved using this guessed

pressure field. Mass continuity errors are then calculated for each cell and the pressure field and velocity are corrected for mass continuity. The velocities now satisfy mass continuity but do not necessarily conserve momentum. The momentum equations are therefore used to re-calculate the velocities with the new pressure field and this procedure continues until errors in continuity and momentum are both acceptably small. Figure 3.1 illustrates the steps that have to be performed in each iteration.

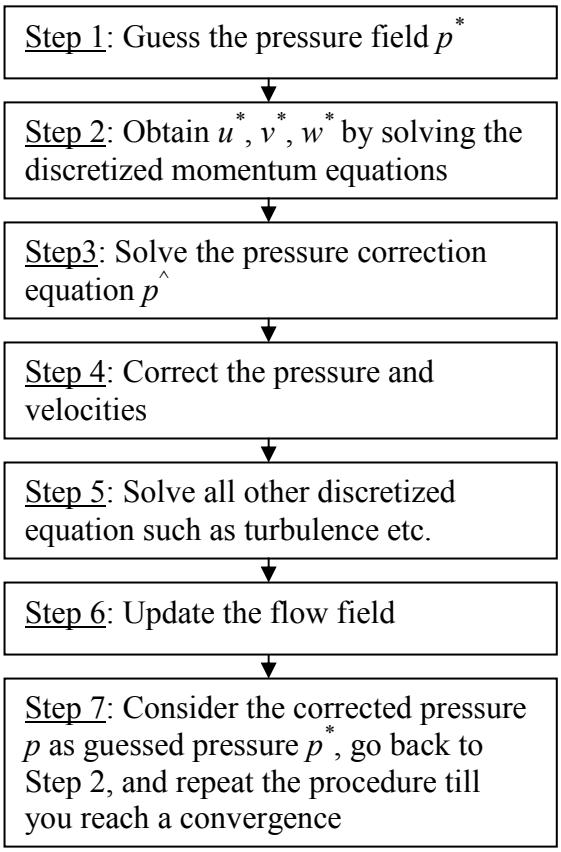

Figure 3.1: Basic functions of each iteration undertaken by SIMPLE, where u^*, v^*, w^* are the guessed components of flow velocity in the x, y, and z directions respectively.

A variety of pressure correction techniques based on the SIMPLE algorithm have subsequently been developed (SIMPLEC, *Vandoormaal and Raithby*, 1984; PISO, *Issa*, 1986). The difference between SIMPLE and SIMPLEC (SIMPLE Consistent) lies in the presence of a modified pressure correction equation. In problems where the pressure-velocity coupling is the main factor affecting the speed of reaching a solution, the modified pressure equation helps to accelerate convergence. The PISO (Pressure Implicit

with Splitting of Operators) pressure-velocity algorithm (*Issa*, 1986), although originally constructed for the non-iterative computation of unsteady incompressible flows, nowadays has been adopted for the iterative solution of steady state flows. The feature that makes PISO different from the other algorithms relates to the higher degree of the approximate relation among the corrections regarding pressure and velocity.

3.1.2 Controls on numerical solution

A simulation is said to be converging when the residuals in the equations decrease as the iterative solution proceeds (*Lane et al.,* 2005). Any numerical solution procedure can only give a solution which is converged relative to some criteria. These criteria can be summarized as follows:

- All discretized transport equations are obeyed to a specified tolerance.
- The solution no longer changes as iterations continue.

Once these criteria are met the solution is referred to as grid independent which reflects the fact that further refinement makes no difference to the solution (*Wright*, 2005). The solution is deemed to have converged when all governing equations are balanced at each point in the solution domain and all residual values are in the order of $1x10^{-3}$ for each cell.

Convergence on a solution through the iterations can be controlled by employing initial controls, value controls and relaxation methods. Initial values can be defined within the domain without affecting the final solution. Determination of realistic values can accelerate the convergence. Specification of realistic minimum and maximum values for a certain variable during simulation, associated with value controls, restricts the path taken to convergence. Relaxation is a method that may be employed to accelerate the convergence rate by slowing down the rate at which variables may alter during the iteration procedure. During the iterative solution process the dependent variables within the flow domain are iterated. From one iteration to the next each variable can fluctuate by an amount that corresponds to a relaxation factor. In most cases it is of great importance to decelerate changes in the values of the dependent variable (*Lane et al.*, 2005). In

particular, there are two common relaxation techniques, namely, linear relaxation and false time step relaxation. Linear relaxation employs a multiplier, usually between 0 and 1, by which the solution can be altered. If the linear relaxation is low, the permitted change in a value is slow. False time step relaxation can be applied when a conservation equation is being solved by adding a source term to the finite volume equation for a given conserved variable. The rate of change of the solution is slower when the false time step is large. As a result, the number of iterations required for convergence is increased. In general, under relaxation decreases the possible amount of change, while over relaxation causes the opposite result.

3.1.3 Numerical grid

Creation of a numerical grid, which refers to the subdivision of the computational domain, is a primary step in obtaining a numerical solution to the equations that describe a physical process. When attempting to generate a numerical grid three main issues have to be carefully examined: grid construction, grid resolution, and topographic representation (*Booker*, 2000). Grid construction is associated with the geometrical definition of the domain over which fluid flow is calculated. Grids can be classified into structured and unstructured types.

A structured mesh is characterized by regular connectivity that can be expressed as a two or three dimensional array. This restricts the element choices to quadrilaterals in 2D or hexahedra in 3D. The regularity of the connectivity allows us to conserve computer memory space since neighborhood relationships are defined by the storage arrangement. The mesh type can additionally be classified based upon whether the mesh is conformal or not. An unstructured mesh is characterized by irregular connectivity that is not readily expressed as a two or three dimensional array in computer memory. This allows for any possible element that a solver might be able to use. Compared to structured meshes, the storage requirements for an unstructured mesh can be substantially larger since the neighborhood connectivity must be explicitly stored (*Ferziger and Peric*, 1999).

More specifically, in structured grids cell density is the same in all directions, while in unstructured meshes the density is variable. A structured grid format is illustrated in Figure 3.2.

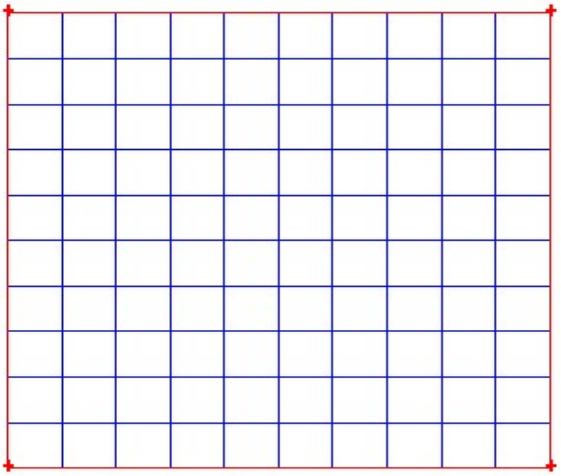

Figure 3.2: Rectangular structured grid

Each cell within a structured grid is not defined separately. The topology of the cells is indicated for the mesh as a whole and is not assumed from the nodes. The numerical solver employed by the CFD code to solve the governing equations of fluid flow is closely related to the grid determination, as the mesh states where the equations are to be applied. In a CFD model, a clear understanding of Cartesian (*x, y, z*) as well as computational space (*i, j, k*) is required (*Booker*, 2000). The difference between these domains can be found in their formation. Computational spaces are regular, whereas Cartesian spaces are both regular and irregular. A regular rectangular grid is utilized by the finite-difference technique. Cartesian grid references can be employed to describe this grid. Alteration of the grid in a simulated space is then followed as depicted in Figure 3.3.

In environmental flows, where complex geometries of natural river channels are incorporated, boundary fitted coordinates (BFC) are used since the grid cells in Cartesian space have to be distorted to fit the domain. As a result, cells that are regular in the computational domain but irregular in the Cartesian space are contained within the spatial domain (*Parsons*, 2002).

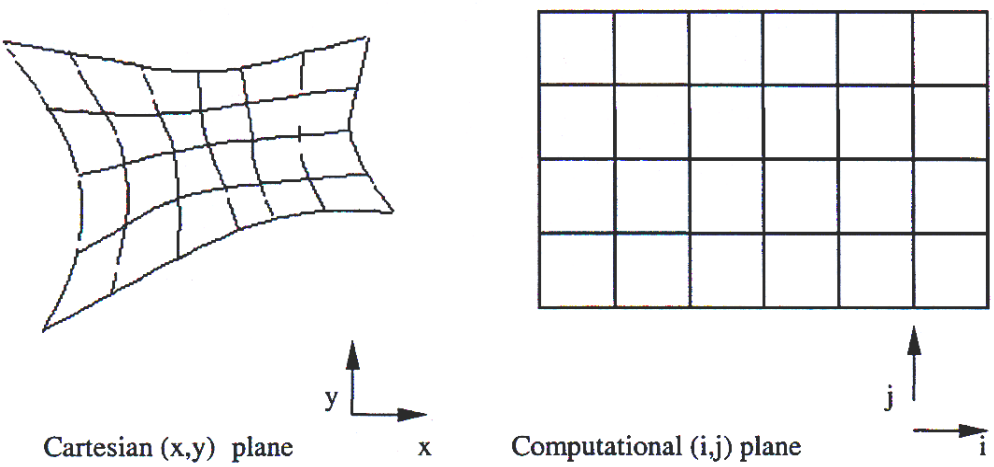

Figure 3.3: Finite-difference grid appearance in Cartesian and computational forms (after *Booker*, 2000).

Several attempts have been made to model non-uniform river reaches in three dimensions using boundary fitted coordinates (*Bradbrook et al.*, 1998, 2000a,b, 2001; *Hodskinson and Ferguson*, 1998; *Lane et al.*, 1999a; *Nicholas and Sambrook Smith*, 1999; *Nicholas*, 2001). However, fitting the computational grid to a Cartesian grid increases the probability of skewing the primary flow direction with respect to computational space. Consequently, high levels of numerical diffusion can be generated even if the grid is not considerably skewed (*Lane and Ferguson*, 2005).

As previously mentioned, attention has to be paid to the way in which the grid is generated since performance of the model can be largely affected by the discretization process (*Lane et al.*, 1999a). Spatial variations in water depth are commonly observed in natural river channels. When using structured grids this may lead to large variations in the average cell thickness (*Lane et al.*, 1999a). As a result, instability problems can be generated as the water depth becomes small close to the channel margin. Specification of a minimum water depth at the channel margin can be considered as a solution to this problem that has an insignificant effect upon model output, since the flow is generally very slow in these areas. When either the rate of change of bottom geometry is rapid or unexpected changes in the channel direction occurs, such as at tight meander bends, seriously skewed grid cells are created enhancing not only numerical diffusion, but also

leading to numerical instabilities. Guidelines for identifying mesh locations which lead to instability or high levels of numerical diffusion have been developed (*Bradbrook*, 1999). However, grid construction of complex geometries, such as natural river channels, utilizing structured approaches is an exceptionally time consuming process.

The two main alternatives that can be used for generating a grid involve using either unstructured approaches or porosity treatments. The latter method employs structured schemes and represents bed geometry by blocking out cells via a numerical porosity term (*Olsen and Stoksteth*, 1995). An improvement of model predictive ability has been reported in a number of studies when using the porosity treatment approach (*Lane et al*., 2002; *Lane et al*., 2004). However, application of the numerical porosity term at the river reach scale requires extensive computational power, especially when the spatial resolution of the domain is very fine, as is the case in this research.

For this reason, river reach scale flows are often better represented using unstructured grids (*Ferziger and Peric*, 1999). These grids use triangular, rather than quadrilateral, cell type elements which make them easier to fit an arbitrary boundary. Figure 3.4 illustrates the different cell types that can be used either in structured or unstructured approaches.

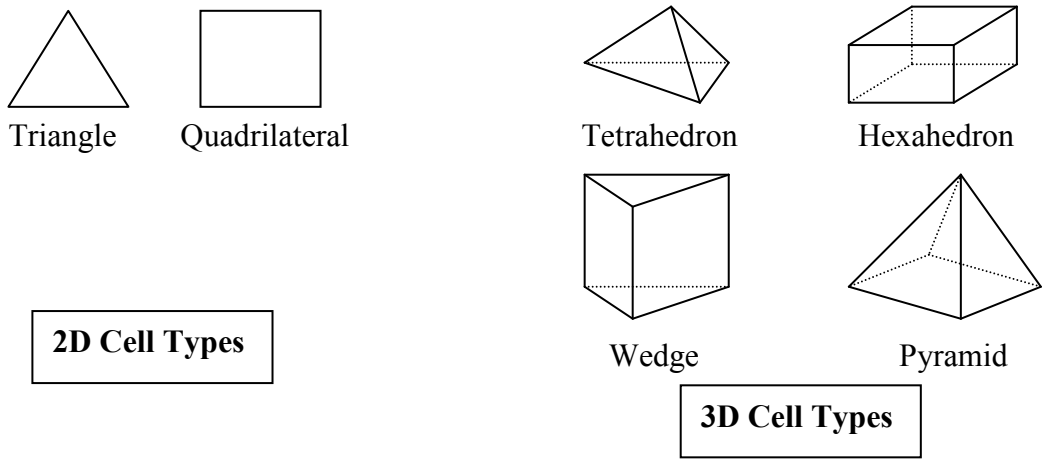

Figure 3.4: Cell Types

As previously shown, a basic feature affecting the accuracy of a numerical solution corresponds to the shape of the cell involving both its skewness and aspect ratio. The difference between the shape of an equilateral cell and the shape of an equivalent volume cell can be described as skewness, while the aspect ratio refers to the measure of the stretching of the cell. Skewness can be measured by either the equiangle skew or the equivolume skew (*Smith*, 1998).

The equiangle skew (q_{EAS}) is a normalized measure of skewness and is given by the following equation:

$$q_{EAS} = \max\left\{\frac{\theta_{\max} - \theta_{eq}}{180 - \theta_{eq}}\right\}, \left\{\frac{\theta_{eq} - \theta_{\min}}{\theta_{eq}}\right\} \qquad (3.1)$$

in which θ_{max} and θ_{min} are the maximum and minimum angles, measured in degrees, between the edges of an element, and θ_{eq} is the characteristic angle equivalent to an equilateral cell of analogous type. Table 3.1 illustrates the relation between the cell type and θ_{eq}.

Table 3.1: Optimal linking between cell type and θ_{eq}.

Cell type	**θ_{eq} (°)**
Triangular	60
Tetrahedral	60
Quadrilateral	90
Hexahedral	90

Measurement of skewness can also be achieved with the aid of the equivolume skew (q_{EVS}) which is defined as follows:

$$q_{EVS} = \frac{\left(S_{eq} - S\right)}{S_{eq}} \qquad (3.2)$$

where S is the volume of the mesh element, and S_{eq} is the maximum volume of an equilateral cell containing a radius identical to the radius of the S volume mesh element. Table 3.2 summarizes the general relationship between skew and element quality.

Table 3.2: Skew versus mesh quality (after *Fraser*, 2003).

Skew	Mesh quality
Skew = 0	Equilateral (Perfect)
0< Skew ≤ 0.25	Excellent
0.25 < Skew ≤ 0.5	Good
0.5 < Skew ≤ 0.75	Fair
0.75 < Skew ≤ 0.9	Poor
0.9 < Skew <1	Very Poor
q_{EAS} = 1	Degenerate

Unstructured grids can be defined as a connection of a fixed set of computational nodes, which are points where the grid lines of the mesh connect, developed in either homogeneous or irregular mode within the domain. When generating an unstructured mesh there is a restriction relating to the position of the nodes. This restriction implies that no triangular node can be situated along the face of another mesh element. An unstructured mesh is illustrated in Figure 3.5.

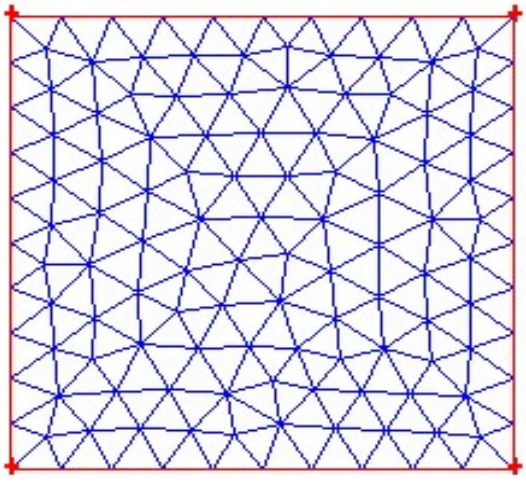

Figure 3.5: Rectangular unstructured grid

Flexibility in fitting complicated domains, quick grading from small to large elements, as well as relatively easy refinement and de-refinement are some advantages of unstructured meshes compared to regular grids. The numerical solution method plays a vital role in the selection of one of the main shapes of mesh formation. As mentioned above, a finite-difference technique employs a structured mesh. In contrast, either a finite-element or a finite-volume method makes use of an unstructured grid which is composed of a sequence of triangles. When employing a finite-element technique the size of the grid cells may be different, though the rate of change of element size must be within a certain value (*Booker*, 2000). Bearing that in mind, the use of an unstructured grid makes it feasible to describe not only complex regions in great detail, but also areas with quite uniform topography. Unstructured grids using finite volume techniques have been used in many applications to reach scale flows (*Wan et al*., 2002; *Caleffi et al*., 2003; *Apsley and Hu*, 2003; *Rameshwaran and Naden*, 2003; *Wilson et al*., 2003). Their main limitation is that they require more effort in relation to grid generation (*Lane and Ferguson*, 2005). Table 3.3 summarizes the main features of both structured and unstructured grids.

Table 3.3: Structured and unstructured grid characteristics

GRIDS	
Structured	**Unstructured**
Mainly rectangular grids	Mostly consists of triangular elements
Efficient in both computation and storage	Memory and computational cost
Operates regular, uniform geometries	Handles complex geometries
Use of finite-difference numerical solution method	Use of finite-volume or finite-element discretization
Good mesh quality status	Mesh quality becomes a concern

In order to improve numerical stability, adjustments to the grid are sometimes required, especially in the case of complex geometries, such as that of natural river channels. These modifications can contain grid line movements as well as grid line addition or deletion.

When trying to simulate fluid dynamics in river channels, creation of an unstructured mesh is more reliable than structured grid generation since the former can more easily represent the complexities of the channel. An immediate advantage of an unstructured grid is that it is able not only to conform more closely to the actual flow attributes, but also to capture flow features in more details within a river channel and this may be important with regards to river flow simulations.

The number of cells in a numerical grid is associated with the resolution of the flow details. In general, when a grid is fine the accuracy of a numerical solution reaches the desired results, although consideration has to be paid to the amount of error in the discretization process. However, in that case attention has to be paid not only to the calculation time but also to the necessary computer hardware required. Furthermore, the grid spacing must be small enough to acquire a solution that is independent of the grid being used (*Parsons*, 2002). For that reason, solutions over a range of different grid resolutions should be carried out to demonstrate grid-independent or grid convergent results.

Representation of the channel morphology is a major issue when applying CFD models to natural river flow problems. One possible solution to the latter process is to employ digital elevation models (DEM) of the channel geometry (*Lane*, 1998b). However, this can cause problems since representation of the continuous surface of a natural channel requires discrete point sampling. When modelling reach scale flows, the grid nodes and sampled points are unlikely to coincide (*Parsons*, 2002). The sampling interval in the field has to be larger than the grid size within the model in order to achieve grid independence. Hence, missing information throughout the field sampling process can be replaced by utilizing interpolation techniques. As a result, the model becomes dependent upon field sampling, point interpolation as well as grid interpolation when the grid size becomes smaller than the field data resolution.

3.1.4 Turbulence models

Environmental flows that take place in complex natural geometrical domains are turbulent and three dimensional. For such flows with complex geometry and roughness, techniques for paramerizing the impact of turbulent eddies on the large-scale flow development are required (*Bates et al*., 2005). As mentioned in Chapter 2 (section 2.2.2.1), different approaches for numerically solving the Navier-Stokes partial differential equations (*2.40*), (*2.41*), and (*2.42*) have been developed, in which different forms of these equations can be utilized for modelling the turbulent eddies (*Ingham and Ma*, 2005). These CFD techniques are defined as Direct Numerical Solution (DNS), Large Eddy Simulation (LES), and Reynolds Averaged Navier-Stokes equations (RANS). DNS can be used to model relatively simple, low Reynolds number turbulent flows. However, due to the complexity of environmental flows with high Reynolds numbers and limitation in the capabilities of present computer systems, DNS can not be considered a practical modelling approach (*Spalart*, 2000). LES is an alternative method for modelling turbulent flows. The latter method has attracted considerable attention during the past decade due to the optimum results obtained for complex flows at moderate Reynolds numbers (*Thomas and Williams*, 1995; *Bradbrook et al*., 2000b; *Zedler and Street*, 2001, *Keylock et al*., 2005). Nonetheless, in environmental flows with high Reynolds numbers LES requires very fine grid resolutions which consequently increase the demands of the computational resources (*Spalart*, 2000).

Reynolds Averaged Navier-Stokes equations (RANS) can be considered as the most practical tool for modelling the complex turbulent character of environmental flows (*Ingham and Ma*, 2005). An extensive description of this technique is given elsewhere (section 2.2.2.2). In this section, common turbulence modelling strategies for the RANS equations will be reviewed with the aim of recognizing issues and challenges that are relevant to environmental flows.

RANS equations can be closed by employing either the so-called eddy viscosity concept or the Reynolds Stress Transport (RST) models. However, RST models consist of a more physics based turbulence modelling framework compared to their eddy-viscosity

counterparts. As a result, RST models can be considered more difficult to implement numerically and they are computationally more expensive. When using the eddy-viscosity approach, reliable and efficient turbulence models are required in order to express the components of the Reynolds stress tensor in terms of the mean velocity field (*Lane et al*., 1999a). These turbulence models, known as eddy-viscosity models, can be classified either as isotropic, where the Reynolds stress tensor components vary linearly with the mean rate of strain tensor, or non-isotropic where the opposite occurs. The most widely used eddy-viscosity models are isotropic since their implementation is numerically and computationally less costly compared to their non-isotropic counterparts (*Sotiropoulos*, 2005). The turbulent eddy viscosity concept that appeared in equation (*2.46*) can be defined as follows by the isotropic turbulence models:

$$\mu_{\mathrm{T}} = l u_{\mathrm{T}} \qquad (3.3)$$

in which μ_T is the turbulent eddy viscosity, l corresponds to the turbulent length scale, and u_T represents the turbulent velocity scale.

Isotropic eddy-viscosity turbulence models are separated into three different categories based on the different approaches that are employed for calculating the length and velocity scales (*Sotiropoulos*, 2005): zero-equation or algebraic models in which both scales are specified using an explicit algebraic relation, one-equation models where the velocity scale is calculated with the aid of an additional partial differential equation and the length scale is specified through an algebraic relation, and two-equations models where both scales are solved by employing partial differential equations.

A zero-equation model can be considered as the simplest form of the *Boussinesq* (1877) approximation and has been applied in a number of open channel flow studies (*Nelson and Smith*, 1989a,b). However, problems can be created since in reality the eddy viscosity is not constant throughout the flow field and can not be measured easily (*Versteeg and Malalasekera*, 1995). Therefore, formulations have been developed for calculating the eddy-viscosity from the mean properties of the flow and consequently taking into

consideration its spatial variation. These formulations were based on *Prandtl's* (1925) famous mixing length hypothesis. By drawing an analogy with molecular viscosity, that is known to be proportional to average velocity and replacing the mean free path with characteristic turbulent velocity and length scales, the following equation was proposed by *Prandtl* (1925):

$$\mu_{\mathrm{T}} = l^2 \left(\frac{\partial \overline{u}_i'}{\partial x_i} \right) \tag{3.4}$$

Empirical formulas can then be used to specify the mixing length, l, given as follows (*Schlichting*, 1955):

$$l = \kappa z \tag{3.5}$$

in which z is the elevation above a reference plane, and κ is *Von Karman's* constant. This method has been widely used in open channel flow problems and can be considered as the basis for the law of the wall (*Lane*, 1998). However, it is valid only for very simple, 2D mean flows and is therefore limited in flows with separation and re-circulation zones (*Versteeg and Malalasekera*, 1995).

More complex one-equation models have been developed that attempt to model the transport of turbulence. This is based on *Rodi* (1980) who indicates that the eddy viscosity corresponds to the square root of turbulent kinetic energy, k, per unit mass. The square root of the kinetic energy can be considered as a velocity scale for the larger scales of turbulent motion. Thus, the eddy viscosity concept is defined as follows (*Parsons*, 2002):

$$\mu_{\mathrm{T}} = c_\mu \sqrt{kl} \tag{3.6}$$

where c_μ is an empirically derived coefficient.

The distribution of turbulent kinetic energy is acquired by solving a transport equation (*Kolmogorov*, 1942), which contains convective terms owing to the mean flow, diffusive terms due to velocity fluctuations, transfer and production terms of k from the mean flow to turbulent motion as well as transfer and dissipation terms of k through viscous processes (*Versteeg and Malalasekera*, 1995). However, the transport of the length scale can not be correctly specified by employing this approach.

The *Spalart-Allmaras* model is a well known one-equation model solving a transport equation for the kinematic viscosity, while not necessarily calculating a length scale. This turbulence model has many significant advantages such as easy implementation in unstructured grids, as well as an ability to resolve high spatial gradients of turbulent viscosity (*Spalart and Allmaras*, 1992). Furthermore, it is much less sensitive in the grid clustering near walls in resolving the boundary layer accurately, thus making it a robust model to use. This advantage, combined with the fact that it is a one-equation model usually makes it ideal for initial runs, where the desired near wall clustering can be easily quantified by providing values for the first cell centroid z^+ fairly accurately and fast. The *Spalart-Allmaras* model is related to both coarse meshes and boundary layers subjected to adverse pressure gradients, and is usually applied for Aerospace problems (*Fluent Inc.,* 2006). However, it is not viewed as applicable for environmental flows due to their geometrical complexity.

Two-equation models can be considered as the simplest complete turbulence models since prediction of a given turbulent flow is made viable without requiring prior empirical input regarding the turbulence structure (*Sotiropoulos*, 2005). They are the most widely used models in various engineering and environmental hydraulics applications due to their ease of implementation, economy in computation, as well as accuracy in their solutions within the available computer resources (*Versteeg and Malalasekera*, 1995; *Lane et al.*, 1995; *Ingham and Ma*, 2005). As previously mentioned, these models employ two additional partial differential equations for calculating both the turbulence velocity and length scales. The same transport equation for the turbulent kinetic energy is employed by most such models with the aim of quantifying a local turbulent velocity

scale. However, what differentiates the various two-equation eddy-viscosity models is the variable used to determine the actual, ε, or specific dissipation rate, $\omega = \varepsilon/k$, which are equivalent to the turbulence length scale (*Versteeg and Malalasekera*, 1995).

It is an unfortunate fact that no single two-equation turbulence closure is universally accepted as being superior for all classes of problems. The main two-equation turbulence models used are the standard k-ε model (*Launder and Spalding*, 1972), its two variants, namely Renormalization Group Theory (*RNG*) (*Yakhot and Orszag*, 1986; *Yakhot et al.*, 1992; *Choudhury*, 1993) and *Realizable* (*Shih et al.*, 1995), all of which can be coupled with a wall treatment, the *Wilcox* standard k-ω model (*Wilcox*, 1998), and the *SST* (Standard and Shear Stress Transport) k-ω model (*Menter*, 1993).

The choice of turbulence model will depend on considerations such as the physics of the flow, the established practice for a specific class of problem, the level of accuracy required, the available computational resources, and the amount of time available for the simulation. To make the most appropriate choice of model, an understanding of the capabilities and limitations of the various options is required. Consequently, the various two-equation turbulence models are briefly outlined below indicating their limitations and advantages.

Whereas both the standard and *SST* k-ω models can be used to solve the turbulent flow field all the way to the wall, the k-ε model and its variants require some kind of near wall treatment in order to model the near wall turbulence.

One technique to incorporate wall effects in the k-ε type models is based on the modification of the model's equations in such a way that wall effects are reproduced and are numerically well behaved in the vicinity of the wall (*Sotiropoulos*, 2005). These models are valid all the way to the wall and are defined as near-wall or low Reynolds number models. When applying this method, a very fine mesh in the vicinity of the wall has to be generated following an integration of the governing equations all the way to the wall, where no-slip conditions can be applied with regards to the mean velocity

components as well as the Reynolds stresses. However, these approaches are not widely used in environmental flows since their application causes not only an increase in the numerical stiffness due to the very fine grid resolution near the wall, but also a decrease in model robustness (*Patel et al*., 1984). Another limitation of such models includes the omission of wall roughness effects.

A second near-wall treatment incorporates the so-called two-layer approach, in which the flow domain is separated into two different zones, namely, the inner layer and the outer layer. The former layer consists of a sublayer, a buffer layer and a fully turbulent region while the latter one includes the remainder of the flow (*Sotiropoulos*, 2005). The equations of both turbulent kinetic energy and dissipation rate are solved within the outer layer. In contrast, only the equation corresponding to the turbulent kinetic energy can be solved within the inner layer, while an algebraic equation incorporating the turbulence length in terms of turbulent kinetic energy, the distance from the wall, and the viscosity of the fluid replaces the dissipation rate equation (*Chen and Patel*, 1988). In general, two-layer models are numerically more robust compared to their low Reynolds number counterparts. However, their application is limited in environmental flows due to the difficulty in determining the location of the interface between the inner and outer layers (*Sotiropoulos and Patel*, 1995b). Wall roughness effects are also not correctly implemented when applying this two-layer approach (*Yoon and Patel*, 1993).

The most common method for modelling the near-wall turbulence includes the use of so-called wall functions. The near-wall flow can be defined as follows according to the so-called law of the wall (*Launder and Spalding*, 1974):

$$u^+ = \frac{u_p}{u^*} = F\left(\frac{u^* z}{\mu}\right) = F\left(\frac{z}{z^*}\right) = F\left(z^+\right) \qquad (3.7)$$

where u_p is the flow magnitude in the planform direction, u^* represents the wall shear velocity, z^* corresponds to the height of zero velocity, z is the elevation above a reference

plane, z^+ is a dimensionless parameter defined as the ratio of the elevation above a reference plane to the height of zero velocity, and μ is the dynamic viscosity of the fluid.

The wall functions for all near-wall flows can be represented by a three-layer structure given as follows (*Launder and Spalding*, 1974):

$$u^+ = z^+ \quad \text{in the sublayer, } z^+<5 \tag{3.8}$$

$$u^+ = z^+ - e^{-\kappa B}\left\{e^{-\kappa u^+} - 1 - \kappa u^+ - \frac{\left(\kappa u^+\right)^2}{2} - \frac{\left(\kappa u^+\right)^3}{2}\right\} \text{ in the buffer layer, } 5< z^+<60 \tag{3.9}$$

$$u^+ = \frac{1}{\kappa}\ln(z^+) + B \text{ in the fully turbulent layer, } z^+>60 \tag{3.10}$$

where κ is the *Von Karman's* constant, and B is equal to 5.45.

The computational grid is generated in such a way that the first grid point of the wall is situated within the fully turbulent region, where $z^+>60$. Boundary conditions for both the turbulent kinetic energy and dissipation rate are then defined at this first layer of nodes off the wall by treating the mean velocity field as logarithmic (*Sotiropoulos*, 2005). These boundary conditions are acquired by assuming equilibrium between turbulence production and energy dissipation. Wall roughness effects combined with wall functions have already been reviewed elsewhere (section 2.2.3.2).

Of all the available turbulence models, the standard k-ε model (*Launder and Spalding*, 1972) is possibly the most commonly used, but it is also notorious for its known weakness. The predictive capabilities of this model together with wall functions have been demonstrated in a number of studies indicating that it performs well for moderately curved open channels of complex bathymetry (*Demuren and Rodi*, 1986; *Demuren*, 1993; *Sinha et al.*, 1998; *Meselhe and Sotiropoulos*, 2000; *Wu et al.*, 2000). However, the standard k-ε model is known to perform poorly in strong adverse pressure gradient flows,

separated flows (where the model will position the separation point downstream and under-predict the re-circulation region), skewed 3D boundary layers, regions of anisotropy, and swirl dominated flows (*Lien and Leschziner*, 1994; *Bradbrook et al*., 1998). Moreover, it was initially developed for thin shear layers, and over-predicts significantly the production and dissipation of turbulent kinetic energy (and hence turbulent viscosity as well) at the stagnation points, and it also gives a non-zero dissipation at the wall. Therefore, this model frequently produces inaccurate predictions in some turbulent fluid flows (*Mohammadi and Pironneau*, 1994; *Ingham et al*., 1997).

However, thanks to its relatively easy formulation and implementation, there have been a number of variant k-ε models developed. Of these, the two most distinguished are the *RNG* (Renormalization Group Theory) (*Yakhot and Orszag*, 1986; *Yakhot et al.*, 1992; *Choudhury*, 1993) and the *Realizable* (*Shih et al.*, 1995) k-ε models, which were developed in order to bridge some of the gaps between the standard model with the actual flow physics.

The *RNG* closure (*Yakhot and Orszag*, 1986; *Yakhot et al.*, 1992) is a significant improvement over the standard k-ε model since regions of 3D fluid flows with a large degree of strain in the fluid, such as shear layers and separation zones, as well as boundaries with large curvature can be simulated, and it has been the standard choice in recent open channel CFD applications (*Hodskinson and Ferguson*, 1998; *Bradbrook et al*., 1998; *Lane et al*., 1999b; *Nicholas and Sambrook Smith*, 1999; *Bradbrook et al*., 2000a; *Ma et al*., 2002). More specifically, it accommodates different values for the constants while an extra production term for the dissipation rate is defined. Because of these adjustments, greater dissipation of turbulence in areas of strong strain has been shown (*Bradbrook et al*., 1998). As a result, the *RNG* model not only predicts better values of turbulent eddy-viscosity than the standard k-ε model but also accommodates flows with significant swirls in them, by allowing the turbulent viscosity to be a function of the swirl level of the flow (*Choudhury*, 1993).

The *Realizable* k-ε model proposed by *Shih et al*. (1995) addresses some weaknesses of the traditional k-ε models by adopting not only a new eddy-viscosity formula but also a new model equation for dissipation based on the dynamic equation of the mean-square vorticity fluctuation. In particular, it more accurately predicts flows involving rotation, separation and recirculation. However, when the computational domain contains both rotating and stationary fluid zones non-physical turbulent eddy-viscosities are produced (*Fluent Inc.,* 2006).

Moving on to the next two-equation model, the standard k-ω model (*Wilcox*, 1998), the main principle is to avoid the numerical instabilities and overshoots that can be found in calculating the turbulent viscosity because of the temporal numerical stiffness that the coupling of the turbulent kinetic energy and the dissipation rate presents. The standard k-ω turbulence model tends to be more accurate for boundary layers flows with adverse pressure gradients, and also in transitional flows (*Wilcox*, 1988, 1998). A low Reynolds number extension for the near-wall turbulence is also incorporated within the latter model which makes it independent of wall functions. In addition, the dissipation of the turbulent kinetic energy is limited owing to a function included in the *Wilcox* k-ω model. However, problems regarding the build-up of turbulent eddy-viscosity in the vicinity of stagnation points are still present.

A known variant of the k-ω model is the *SST* (Shear Stress Transport) closure (*Menter*, 1993), which is a blend of the *Wilcox* (1988) and standard k-ε models. As its name implies, it takes into account the transport of the principal shear stress, via altering the definition of the turbulent viscosity. Moreover, enhancements are made with regards to the blending at near wall and far regions areas, as well as the inclusion of a cross-diffusion term in the ω transport equation, which is the result of transforming the k-ε model equation in terms of k and ω. However, the potential of this model for environmental flows requires further investigation.

3.2 Selection of CFD code

A significant development in tackling complex geometries has been the combination of the finite element and finite volume approaches. Researchers (*Schneider and Raw*, 1987) took the unstructured grids of finite elements, but applied the finite volume methodology. This approach now forms the basis for the main commercial 3D CFD packages. The software package used in the current analysis was Version 6.2 of *Fluent* (*Fluent Inc.*, 2006). This commercial code was utilized since it holds the advantages of ease of application to complex geometries (including natural geometries) and implicit conservation of physical quantities. *Fluent* 6.2 allows construction of model flow geometries, specification of model boundary conditions and solution of the 3D Navier-Stokes equations for calculating the flow field. Both compressible and incompressible flows can be modelled, as can turbulence with the aid of the various turbulence closures provided.

Fluent 6.2 uses a finite volume numerical technique to solve the differential equations governing fluid flow. As mentioned earlier, this powerfully built technique converts the differential equations of mass and momentum into algebraic equations that can be solved numerically through a discretization process proposed by *Patankar* (1980). The latter process engages the integration of differential conservation equations about a control volume. As a result, a sequence of finite volume equations is created that conserve each variable in a control volume basis.

Fluent 6.2 includes two solver options, namely, segregated and coupled. In the segregated approach, which is the most commonly used, the governing equations are worked out sequentially. Several iterations of the solution loop should be executed before a converged solution is achieved since the principal equations are non-linear and coupled. Each of these iterations involves the steps shown in Figure 3.6.

In contrast, the coupled algorithm solves a coupled system of equations including both the momentum and pressure equations. When employing the coupled solver the rate of convergence is much better compared to the segregated approach, since the governing

equations are solved in a coupled mode. However, use of the coupled algorithm is still limited since the memory requirement increases significantly.

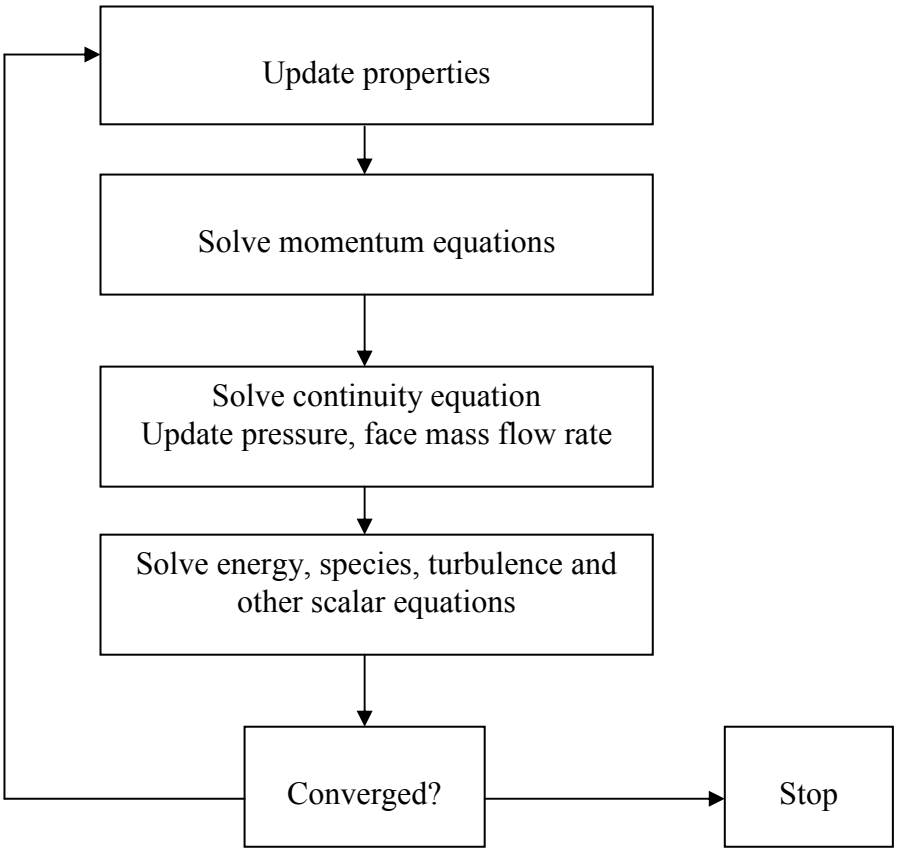

Figure 3.6: Segregated solution method (after *Fluent Inc.*, 2006).

Fluent 6.2 offers a variety of turbulence closures for simulating the turbulent nature of environmental river flows. The most commonly adopted approach used requires Reynolds averaging of the Navier-Stokes flow equations. The five different Reynolds averaging two-equation turbulence models provided by *Fluent 6.2* are the standard k-ε model used as a default, its variants, namely, *RNG* and *Realizable*, the standard k-ω, and the *SST* k-ω. Many applications of CFD codes to environmental hydraulics (*ASCE*, 1988; *Demuren*, 1993) have used the two-equation k-ε turbulence model based on the assumption of isotropic turbulence that makes it produce a large turbulent viscosity. *RNG* k-ε model was also used in a number of studies (*Hodskinson and Ferguson*, 1998; *Ma et al*., 2002) shown a greater dissipation of turbulence in areas of strong strain. However,

the choice between the different turbulence closures makes little quantitative difference to flow predictions (*Hodskinson and Ferguson*, 1998).

Boundary conditions that are commonly used in environmental river flows can be easily implemented within *Fluent 6.2*. More specifically, the latter CFD code allows the water surface to be captured by employing the frictionless rigid lid concept. In addition, it can specify bed and bank roughness by utilizing the standard wall functions described in section 2.2.3.2.

The computational grids employed in this investigation were generated using two pre-processing packages. The first package, called *Gambit 2.1* (*Fluent Inc.*, 2006), was developed by *Fluent* suppliers and was used to create the desired geometries and meshes, whereas the second one, called *Harpoon* (*Sharc Ltd*, 2006), was able to perform both the geometry and grid generation, however in the current research was used only to generate meshes. An advanced hex-dominant meshing technique is incorporated within *Harpoon* for the generation of *Fluent 6.2* meshes. The detail of the final mesh is controlled by using different size levels. Hexahedra size is decreased by a factor of two as the level increases. The imported geometry, as taken from Gambit *2.1* was placed in a large box and loaded by flood until the level at the surface is the required one. After finding the desirable surface size level, a meshing option was selected by examining both hexas and local geometry to decide whether to retain the particular structure of hexahedral or to divide it into tetrahedral, wedges, as well as pyramids. *Harpoon* was used because *Gambit 2.1* was incapable of creating the mesh in the bend between the two straight parts of the river reach (see section 3.3 for a description of the study site). Both *Gambit 2.1* and *Harpoon* deal with either structured or unstructured meshes.

An accurate physical representation of the examined river is central to capturing all relevant details of the actual flow domain. This process may take a long time in the overall modelling procedure. Flow geometries in *Gambit 2.1* are constructed by defining points in three-dimensional space that lie along the edges of the geometry, joining these points to create edge curves and then joining these curves to create the boundary surfaces.

Flow meshes in *Gambit 2.1* are created by placing nodes on the edges curves. This can be done by applying two different approaches. The first one is defined by specifying a constant interval between the nodes, which leads to a uniform mesh, while in the second case a gradually increasing or decreasing spacing is used, providing a non-uniform mesh. Once the nodes are created, the actual meshing process along the faces is ready to start.

Mesh generation of the faces can be made by selecting one of the different meshing options available within *Gambit 2.1*. These meshing options are divided into two categories. The first corresponds to the type of elements used, while the second is connected with the meshing scheme applied (*Fluent Inc.*, 2006). In the current research, the pave face meshing scheme was used corresponding to unstructured meshes. These meshes are created mainly of quadrilateral elements, whereas triangular corner elements are used at user-specified locations. As previously discussed, unstructured grids appear to be more reliable than structured meshes for simulating fluid dynamics in river channels, since they can better represent geometrical complexities. Having finished with the faces, the meshing of the volumes is then followed corresponding to a three-dimensional approach. The volumes can be meshed by choosing the appropriate meshing option available in *Gambit 2.1*. In accordance with face meshing, these meshing options are based not only on the type of elements employed but also on the meshing scheme used. In this study, the Tet/Hybrid volume meshing scheme was employed. When using this technique the volume grids are primarily generated by tetrahedral elements while hexahedral, wedge, and pyramidal elements are utilized in some cases.

3.3 Study Site Description

The River Asker (49.1 km^2) study site is located at Bridport in Dorset (Southern UK), centered on National Grid Reference SY 471 929. A location of the field site is shown in Figure 3.7.

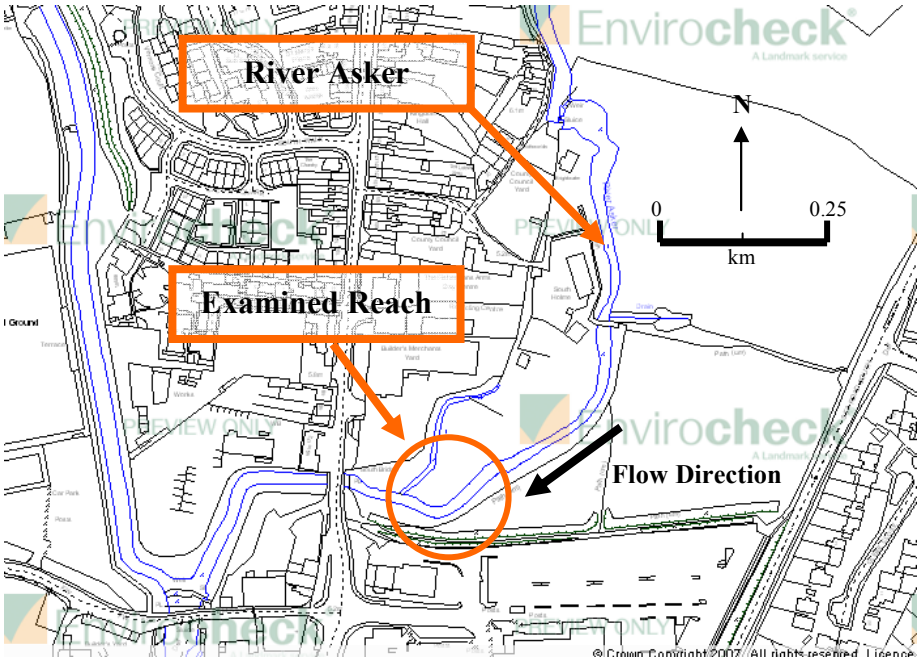

Figure 3.7: Location of the field site at Bridport, Dorset.

This specific site was selected as river stage and discharge data are readily available from a gauging station located about 150 meters downstream from the bank monitoring reach. The total length of the studied meander loop is approximately 200m, while its gradient has an average value of 0.007. The eroding bank has an average height of about 2-2.5 meters and is layered. Figure 3.8 depicts a part of the selected study reach. The stratigraphy has been characterized by grain size analysis of samples collected from two vertical sections of the bank (Table 3.4). Three different layers were identified as being composed of the following materials (from base to surface):

- Grey sand with silt (0.8-1m thick)
- Red clayey silt with sand (1m thick)
- Brown sand with silt (0.4m thick)

Figure 3.8: Part of the study reach of the River Asker.

A preliminary geotechnical characterization of these sediments was performed on the fine-grained materials. Samples were collected using a range of in-situ tests, which included seepage tests for determining the saturated hydraulic conductivity (*Amoozegar*, 1989), Borehole Shear Tests (*Lutenegger and Hallberg*, 1981), and matric suction measurements using a tensiometer. The fluvial erodibility coefficient, as well as the critical shear stress, were determined by in situ jet tests (*Hanson and Simon*, 2001) using a non-vertical jet test device recently applied specifically to river banks (*Dapporto*, 2001). A summary of the grain size analysis as well as geotechnical and erodibility data is given in Tables 3.4 and 3.5.

Data was obtained to enable specification of model boundary conditions and to establish the accuracy of model output. Peak flow discharge estimates were available from a gauging station at Bridport, Dorset, located about 150 metres downstream of the bank monitoring reach. The geometry of each model was specified using Digital Elevation Models (DEMs) of the channel created from high-resolution tacheometric surveys of the study reach. A series of features were surveyed, with concentrations of survey points in the area of high bank curvature as shown in Figure 3.9. The total number of points surveyed was 2,313 over an area of 2,512 m^2. Thus, the spatial resolution of the field

topographic data was approximately 1 m^2 (one point per square meter). The topographic survey, therefore, provided information on the geometric properties of the sinuous reach of River Asker for further analysis.

Table 3.4: River Asker grain size data (Data provided by Dr S.E. Darby, School of Geography, University of Southampton).

Materials	Grey sand with silt	Red silt with sand	Brown sand with silt
Sand (%)	59.4	41.8	57.9
Silt (%)	37.5	52.0	38.2
Clay (%)	3.1	6.2	2.7
D_{16} (mm)	0.017	0.008	0.013
D_{50} (mm)	0.073	0.050	0.064
D_{84} (mm)	0.135	0.100	0.158

Table 3.5: River Asker geotechnical properties and erodibility parameters for fine-grained layers (Data provided by Dr S.E. Darby, School of Geography, University of Southampton).

Parameter	Grey sand with silt	Red silt with sand	Brown sand with silt
Volumetric water content (%)	44.0	43.0	33.2
Bulk unit weight (kN/m^3)	18.0	17.9	18.0
Dry unit weight (kN/m^3)	13.7	13.7	14.7
Saturated permeability (m/s)	$3.5x10^{-8}$	$5.6x10^{-10}$	$4.2x10^{-6}$
Friction angle (°)	28.1	39.4	38.4
Apparent cohesion (kPa)	2.4	2.2	1.6
Erodibility coefficient (m^3/Ns)	$9.5x10^{-5}$	$5.9x10^{-6}$	-
Critical shear stress (Pa)	0.29	2.35	-

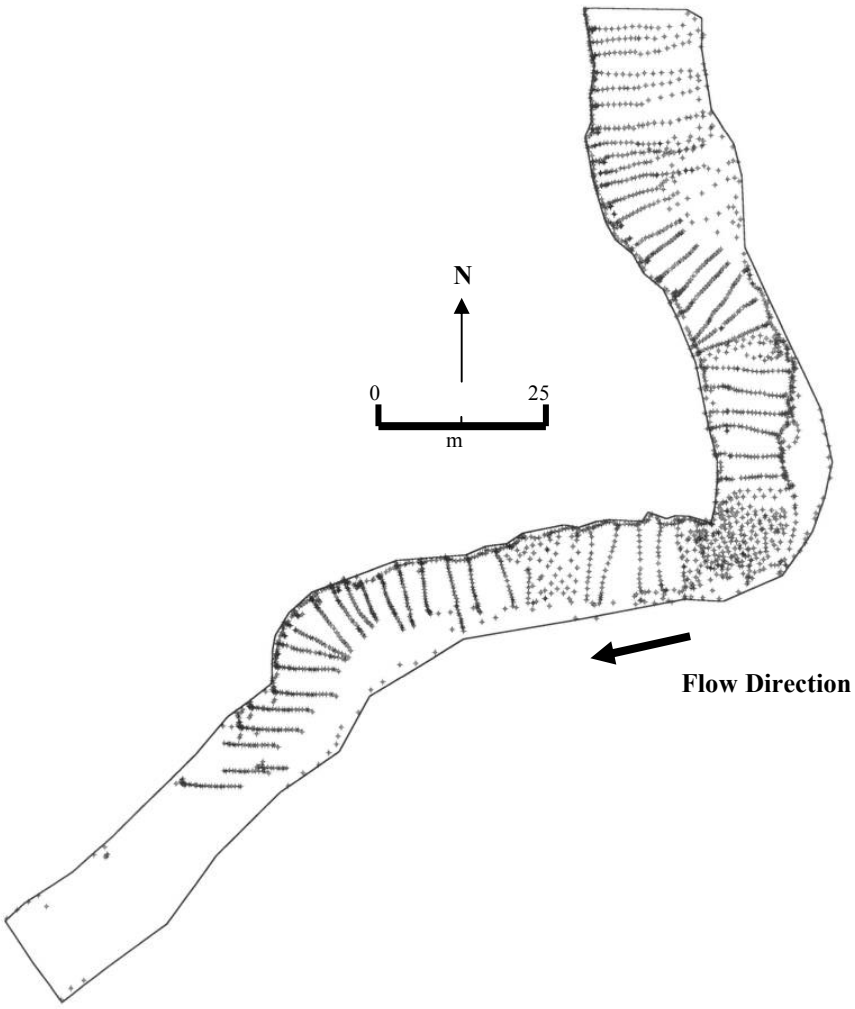

Figure 3.9: Distribution of the initial topographic data collected.

The process of obtaining field topographic data and incorporating it within a model involves filtering the topographic detail present within reality. In reach scale flow modelling, co-incidence of the grid nodes and sampled points is unlikely. For reasons of grid independence, the grid size within the model is much smaller than the sampling interval in the field. Thus, interpolation techniques are required that replace the information that is 'lost' in this field sampling process.

Water surface elevations within the reach were defined using a network of ten crest stage gauges spaced at twenty meters intervals along the reach. A crest gauge is a small diameter pipe mounted vertically in the stream, capped on the bottom, with several holes to allow water to enter. Finely ground cork is placed at the base of the pipe and a wood rod is placed on the inside of the pipe. When high water occurs, the cork floats on the water that flows into the pipe, thereby leaving a ring on the wood rod at the maximum water height. The location of the ten crest-gauges as well as the bed elevation across the monitoring reach during February 2004 can be seen in Figure 3.10.

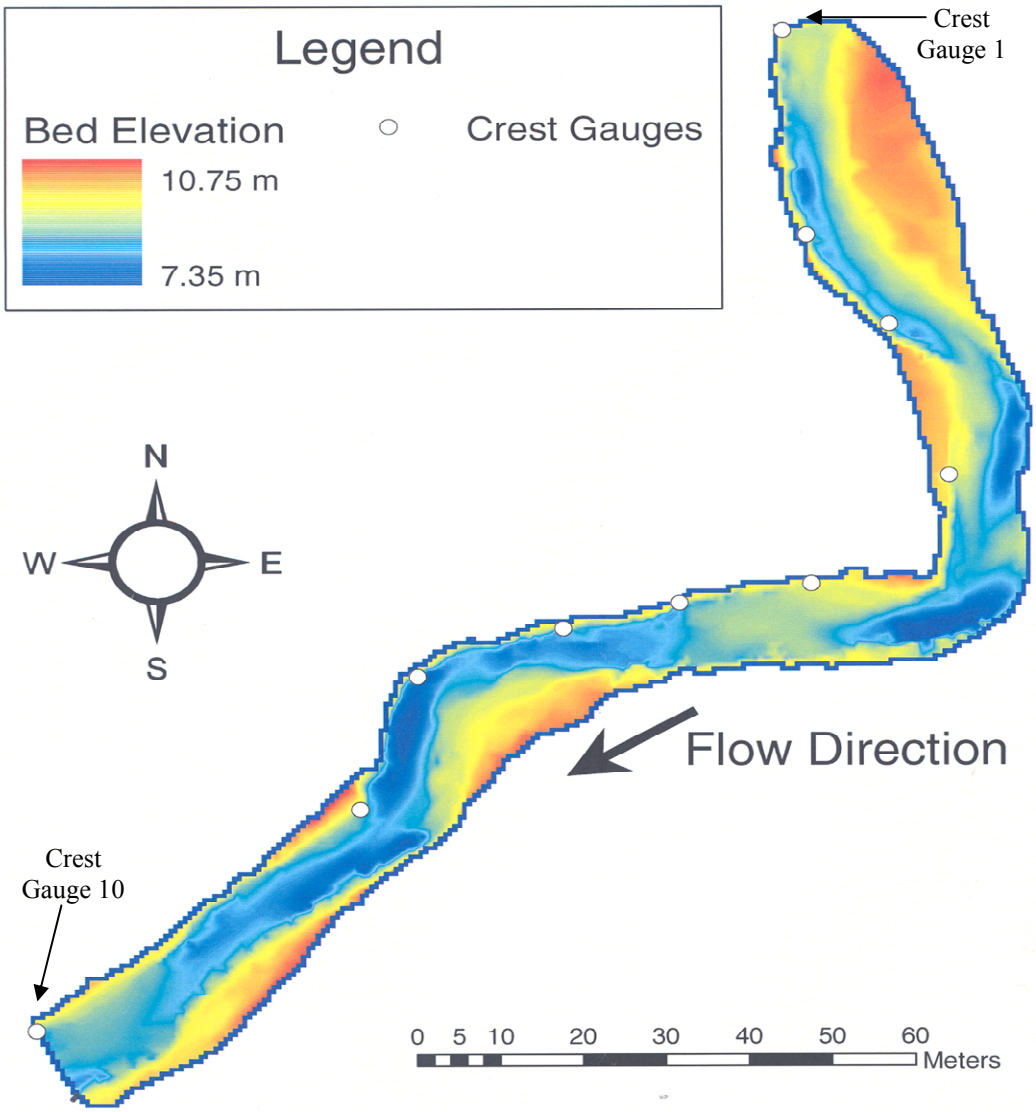

Figure 3.10: Crest-gauges locations together with the bed elevation of the examined reach during February 2004.

A range of specific flow events, with recurrence intervals ranging from approximately 1 to 10 years, were selected for further analysis, based on the data collected during the monitoring phase. The characteristics of these examined flow events are illustrated in Table 3.6, while the measured flow velocity data obtained using a two component electromagnetic current meter (ECM) in selected locations with regards to a low flow event on 5th January 2004, are given in Appendix I. These data represent the basis for comparing some measured and predicted velocity at various locations through the reach.

The individual velocity data points under low flow conditions are located at 65 field measurement positions. Each position corresponds to a vertical rod consisting of three points with the same the eastings and northings but, with a range of different elevations. Most of the field measurements were carried out, for each position, at *Z/H* values, where *Z* is the local flow depth of the measurement and *H* represents the total flow depth at that position, of 0.2, 0.6, and 0.8 with some variance for specific points. The above procedure provided a well-distributed sample of 195 points within the studied reach as illustrated in Figure 3.11.

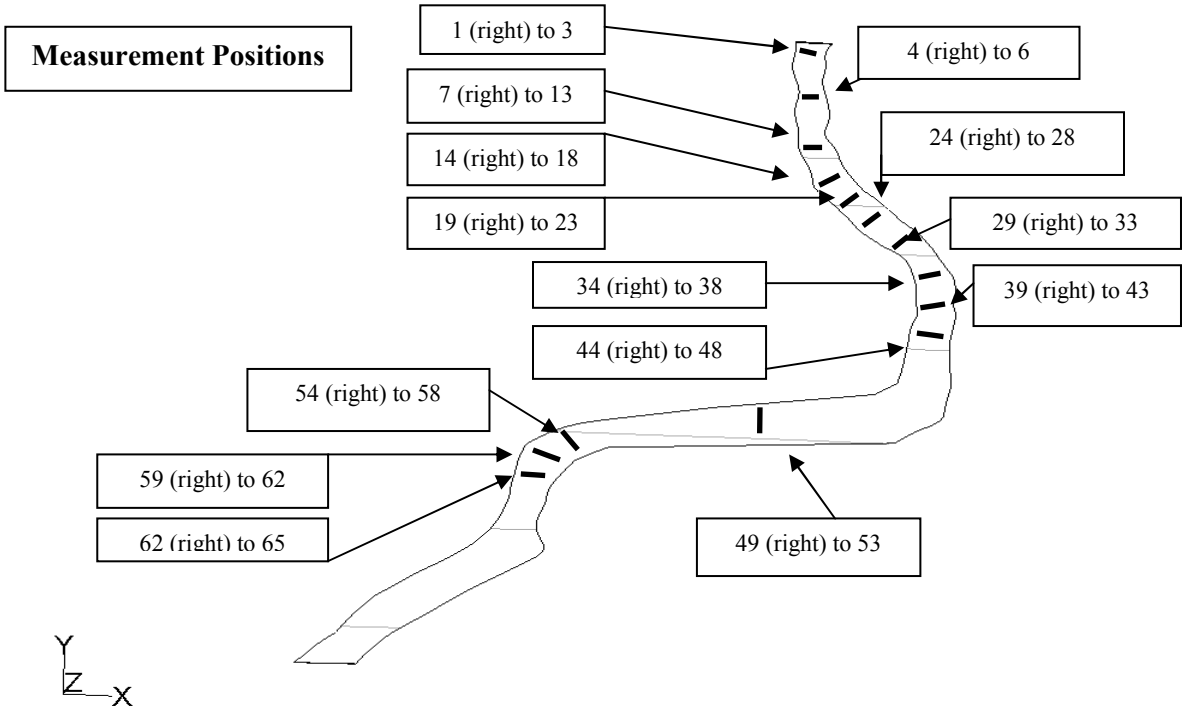

Figure 3.11: Locations of the 65 measurement positions including 195 measured velocity data points under low flow conditions.

It should be noted that all of the field data provided as input parameters to the numerical model were acquired by Dr Stephen Darby (School of Geography, University of Southampton) who made the data available to the current research.

Table 3.6: Characteristics of the examined flow events.

Flow Events	Acronyms used in Text	Date of Flow	Peak Flow Discharge (m^3/s)	Water Elevation at Upstream Boundary (m)	Average Water Surface Gradient (m/m)	Recurrence Intervals (years)
Low Flow Event	LFE	5 Jan. 2004	0.791	9.250	0.0030	-
Flow Event 1	FE1	31 Jan. 2004	6.9	9.910	0.0026	<1
Flow Event 2	FE2	26 Nov. 2003	8.2	9.960	0.0026	<1
Flow Event 3	FE3	29 Dec. 2003	10.3	10.030	0.0027	1
High Flow Event	HFE	12 Jan. 2004	18.4	10.240	0.0030	8

3.4 Implementation for Modelled Flows

This section examines the process and techniques used by the available CFD software in the creation and calculation of the computational models with regards to the different flow events studied in the examined reach of the River Asker, listed in Table 3.6. These flow events were selected because they cover a wide range of peak flow discharges (from 0.791 to 18.4m^3/s). Data collected during the monitoring phase was available only for the low flow event since monitoring of hydraulic variables is made more difficult in moderate and extreme flow conditions, which may be hazardous.

As previously mentioned, in this study the CFD code *Fluent 6.2* (*Fluent Inc.*, 2006) was utilized and is the most recent addition to the *Fluent* series of solvers, while for the

geometry and mesh generation two pre-processing programmes were employed, namely, *Gambit 2.1* (*Fluent Inc.*, 2006) and *Harpoon* (*Sharc Ltd*, 2006). Geometry creation and mesh generation for the five different flow events examined in this thesis are issues that are described in the following section.

3.4.1 Construction of the Numerical Grids

The current investigation of the studied reach of the River Asker can be divided into two different paths. The first approach corresponds to sub-reach A (SRA), while the second one contains the whole reach itself, which consists of SRA and sub-reach B (SRB) plus a bend that merges those two sub-reaches. A graphical representation of all the above is shown in Figure 3.12. The desired geometries and meshes for SRA were created using *Gambit 2.1*. As far as the whole reach is concerned, *Gambit 2.1* was used to construct the geometries while the meshes were generated with the aid of *Harpoon*. This was done because *Gambit 2.1* was incapable of creating the mesh in the bend between SRA and SRB. These two different approaches were applied to LFE. In contrast, only the whole reach models are presented with regards to the other flow events.

3.4.1.1 Geometry creation

The process of creating the geometries to represent both the reach for the various flow events and the SRA for LFE went through several stages before obtaining the desirable shapes. Initially, the topographic survey data shown in Figure 3.9 were employed to create Digital Elevation Models (DEMs) via the Arc/Info software. The DEMs were then interpolated to an IGES file format for import into *Gambit 2.1*. The IGES format file was separated into smaller files (135 for SRA, 230 for the whole reach).

The next step involved the conversion of these latter files into *Gambit 2.1* journal files. This task was carried out by employing a C code. Each one of the 135 for SRA and 230 for the whole reach journal files contains points with x, y, and z coordinates. Both the C code and an example of a journal file can be found in Appendix II. After importing the different journal files into *Gambit 2.1*, a sequence of 3,274 and 6,294 points with x, y, and

z coordinates is produced on a three dimensional space forming the geometry of both SRA and the whole reach, respectively.

i) ii)

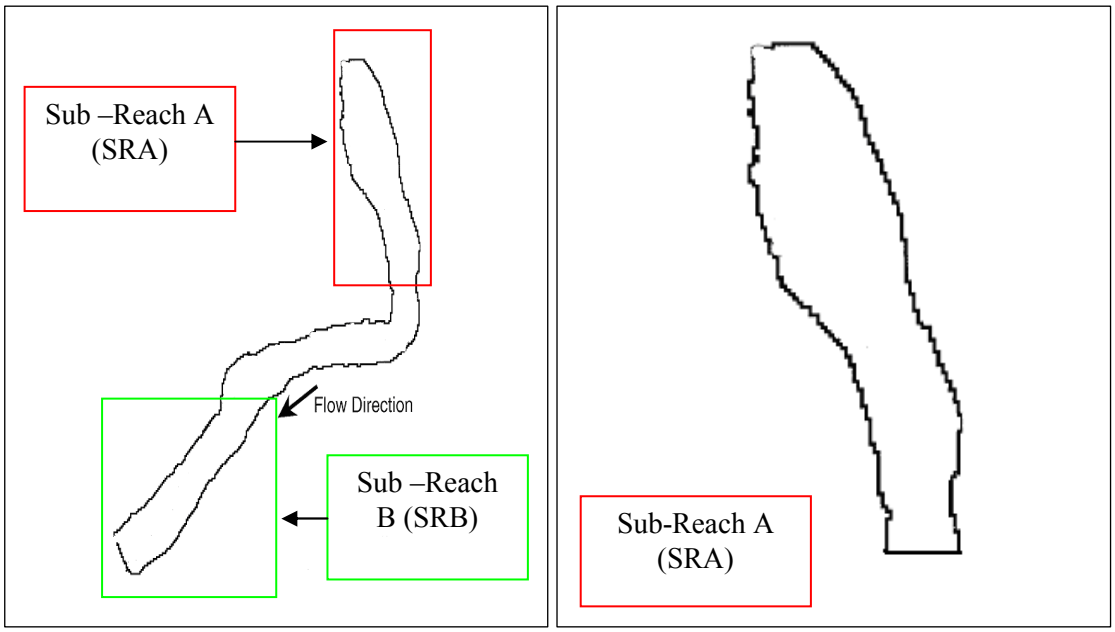

Figure 3.12: Graphical representation of the examined (i) Reach (ii) Sub-Reach A (SRA).

Due to the large amount of data, a decision was taken to decrease the number of points in order to avoid complex scenarios with regards to the geometry creation. In addition, the time framework for the particular task of creating the geometry was limited and the manual connection of all these points required a longer period. Thus, a large proportion of the interpolated topographic data was removed.

The above procedure of arbitrarily decreasing the number of points had to be done without degrading the representation of topographic variability within the examined reach. Thus, a satisfactory approach was taken by selecting arbitrarily one set of points every five. Each set of points corresponds to a single journal file which is produced from the IGES format file and is formed by a line directed east to west on a three dimensional space. Thus, the total number of journal files imported and run in *Gambit 2.1* was

reduced to 27 and 46 resulting in a subsequent decrease of points to 679 and 1,487 with regards to SRA and the whole reach, respectively.

However, this process of reducing the interpolated topographic data degrades the quality of the topographical representation since the resolution of the grid becomes five times coarser compared to the one originally surveyed. This is more critical in areas of high topographical complexity such as deep pools and shallow riffles. Investigation of the total number of topographical points collected in the field necessary to create a desirable model geometry is, however, not assessed in this study and is left as an area for further research.

After importing the revised number of journal files into *Gambit 2.1* a series of splines was created by drawing through the points, creating arbitrarily located cross-sections. The latter cross sections were oriented east-west for the whole reach which consists of sub-reach (SRA) and sub-reach B (SRB) plus a bend that merges those two sub-reaches. The predominant flow direction was north-south for SRA and SRB, while it was east-west for the intermediate bend region. Thus, the cross-sections were approximately perpendicular to the local flow direction for SRA and SRB, while they were parallel to the flow for the merging bend. The east-west rather than the north-south direction of representing the bend model geometry was chosen because of the limited number of points, approximately five, located in the north-south route for a single cross-section.

Figures 3.13 and 3.14 illustrate the topographic data points associated with the examined sub-reach A (SRA) and whole reach, respectively, based on the original interpolated data plotted on top of the data represented in the final model mesh after reduction. These figures allow the cross-sectional topography in the field and model to be compared directly with one another for cross-sections distributed throughout the study reach.

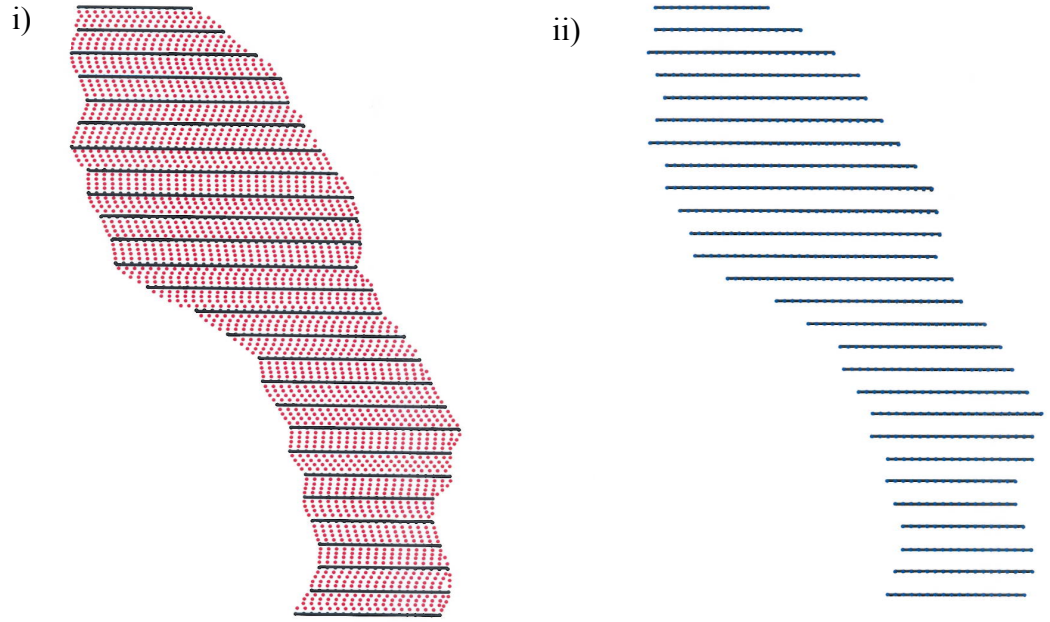

Figure 3.13: i) Initial interpolated topographic data (red points) of SRA plotted on top of final mesh topography (black points) (ii) Reduced topographic data of SRA representing the model final mesh topography.

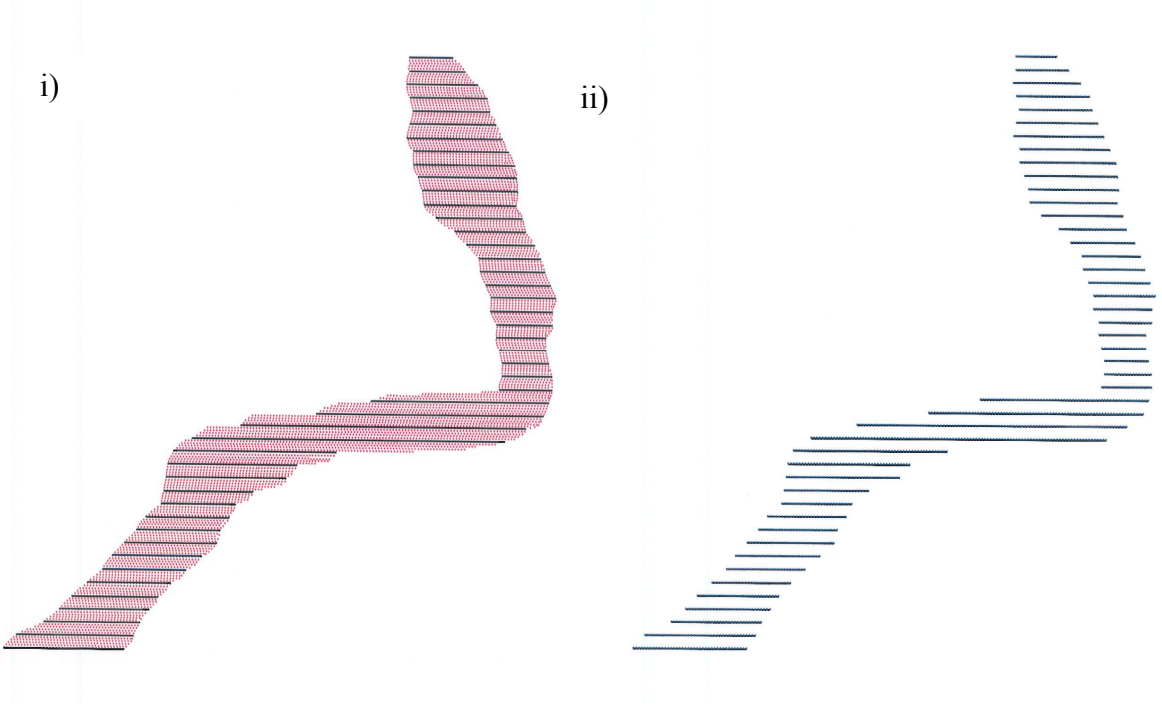

Figure 3.14: i) Initial interpolated topographic data (red points) of whole reach plotted on top of final mesh topography (black points) (ii) Reduced topographic data of whole reach representing the model final mesh topography.

The process described above provides a general topographic representation of the examined reach. However, the submerged topography of the reach varies for each of the different flow events, as the values of water elevation at each one of the cross-sections and the average water surface gradient varies with changing flow discharge. Attention therefore has to be paid to estimating the values of water elevation at each cross section in order to obtain the desirable geometries. This was done by utilizing the diagram illustrated in Figure 3.15.

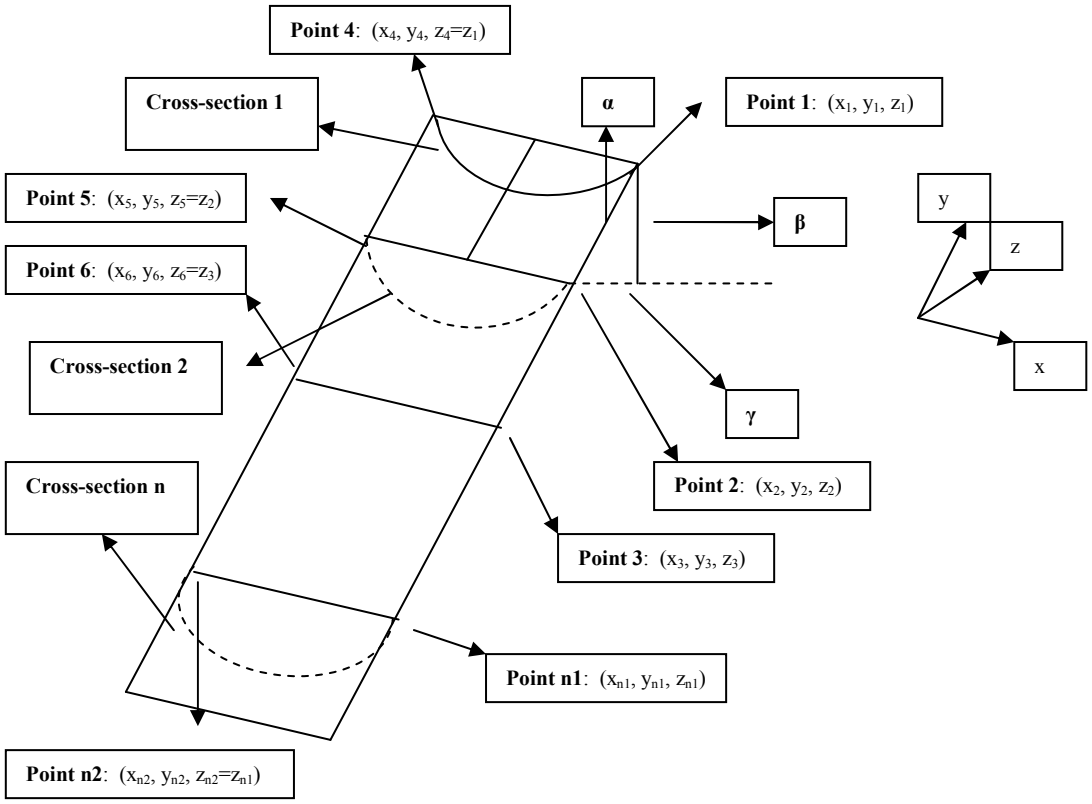

Figure 3.15: Water elevation calculation for each cross-section.

The water elevation at each cross section can then be calculated by applying the following formula:

$$WEn = WE(upstream) - (\alpha)AWSG \qquad (3.11)$$

where *WEn* represents the water elevation at cross-section *n*, *WE(upstream)* corresponds to the water elevation at the upstream boundary, *AWSG* is the average water surface gradient, and α specifies the distance between cross-sections. The values of *WE(upstream)* and *AWSG* for each of the investigated flows have already been given in Table 3.6. Hence, α is the only unknown variable in equation (*3.11*).

The water elevation at each cross section was calculated by using an average water surface gradient for each flow event. The above procedure forces a flat gradient through the central part of the reach, which may result in significant the calculated water elevations deviating from the actual values. Thus, errors in water surface elevations on the model's rigid lid are introduced. Water elevation data obtained from the ten crest gauges located within the examined reach under a range of flow events are given in Table 3.7, while the calculated surface slopes are illustrated in Table 3.8. Observed water surface profiles for the different flow events are shown in Figure 3.16. An assessment of the extent to which the observed water surface elevations and slopes deviate from the constant average slope and resulting water elevations used in model mesh construction is therefore carried out below.

Table 3.7: Water surface elevation data obtained from the ten crest gauges for the various flow events.

Crest Gauges	Observed Water Surface Elevation (m)				
	LFE	**FE1**	**FE2**	**FE3**	**HFE**
1	9.25	9.91	9.96	10.04	10.24
2	9.18	9.85	9.89	9.95	10.11
3	9.10	9.74	9.79	9.87	10.06
4	9.03	9.78	9.82	9.88	10.02
5	8.96	9.81	9.83	9.87	9.95
6	8.92	9.55	9.61	9.70	9.93
7	8.85	9.60	9.66	9.73	9.92
8	8.78	9.47	9.53	9.61	9.81
9	8.76	9.45	9.49	9.54	9.68
10	8.42	9.43	9.46	9.50	9.60

Table 3.8: Calculated gradients based on observed water surface elevation data.

Crest Gauges	Distance (m)	Increment Distance (m)	Water Surface Slope (m/m)				
			LFE	FE1	FE2	FE3	HFE
1	0	-	-	-	-	-	-
2	28.6	28.6	0.0024	0.0018	0.0023	0.0030	0.0033
3	43.5	14.9	0.0023	0.0022	0.0066	0.0056	0.0028
4	65.3	21.8	0.0026	0.0021	0.0014	0.0005	0.0018
5	87.4	22.2	0.0032	0.0011	0.0004	0.0006	0.0031
6	103.5	16.1	0.0025	0.0032	0.0137	0.0103	0.0014
7	117.9	14.4	0.0028	0.0028	0.0031	0.0021	0.0004
8	139.1	21.2	0.0027	0.0029	0.0059	0.0058	0.0034
9	156.1	17.0	0.0012	0.0015	0.0025	0.0039	0.0037
10	205.1	48.9	0.0033	0.0004	0.0006	0.0009	0.0016

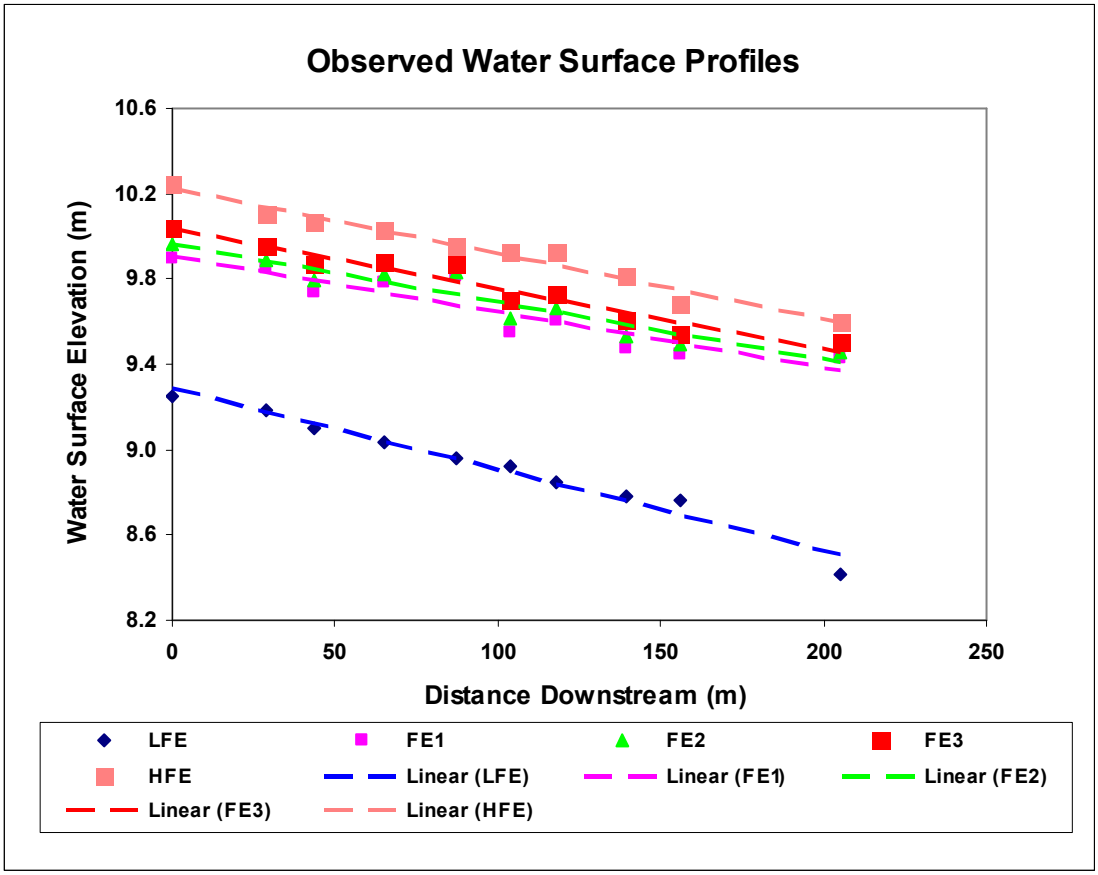

Figure 3.16: Observed water surface profiles for the different flow events.

Calculated surface slopes are based on the observed water surface elevations obtained from the crest gauges. However, as can be seen in Table 3.8, the gradients for each of the investigated flows deviate from those (given in Table 3.6) used in the model mesh construction, resulting in variations of the model water elevations.

Water elevation data are calculated for selected cross sections corresponding to the ten crest gauges located within the examined reach under a range of flow events, and their values are given in Table 3.9. These water elevations are calculated from equation (*3.11*) by using a constant water surface gradient for each of the investigated flows (see Table 3.6). Calculated water surface profiles for the different flow events are depicted in Figure 3.17.

Table 3.9: Calculated water surface elevations at the ten crest gauges by using a constant gradient for each of the various flow events.

Crest Gauges	Calculated Water Surface Elevation (m)				
	LFE	**FE1**	**FE2**	**FE3**	**HFE**
1	9.25	9.91	9.96	10.04	10.24
2	9.16	9.83	9.88	9.96	10.17
3	9.12	9.79	9.84	9.92	10.13
4	9.05	9.73	9.79	9.87	10.07
5	8.99	9.67	9.73	9.81	10.02
6	8.94	9.63	9.69	9.77	9.97
7	8.90	9.59	9.65	9.73	9.94
8	8.83	9.54	9.60	9.68	9.88
9	8.78	9.49	9.55	9.63	9.84
10	8.63	9.37	9.42	9.50	9.71

A comparison of calculated versus observed water surface elevations in the form of a scattergraph for the crest gauges positions within the River Asker reach for each of the investigated flows, was carried out in the analysis illustrated in Figure 3.18. The above process is important to provide an objective assessment of the overall ability of the model to replicate the observed water elevations by using the constant gradient assumption.

Although the calculated and observed water surface elevations do not match perfectly, the agreement is good. More specifically, there is good qualitative validation of the water elevations obtained from both field measurements and calculations for the data points corresponding to LFE, HFE, and FE3 (R^2 =0.93, R^2 =0.95, and R^2 =0.94, respectively). The same trend is observed for FE1 and FE2 but with weaker, but nonetheless good, validation (R^2 =0.86, and R^2 =0.90, respectively). Thus, water surface elevation errors on the model's rigid lid introduced by using the linear water slope assumption are not considered to be significant.

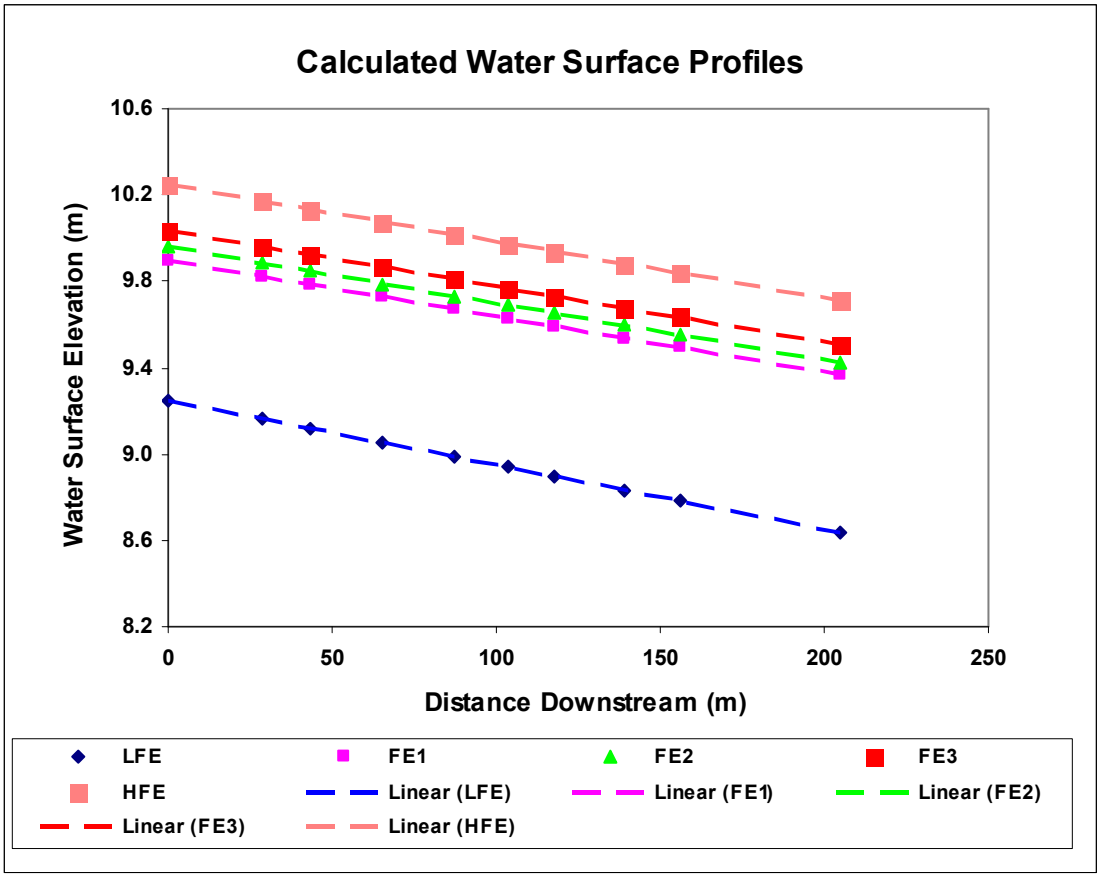

Figure 3.17: Calculated water surface profiles by using a constant gradient for each of the different flow events.

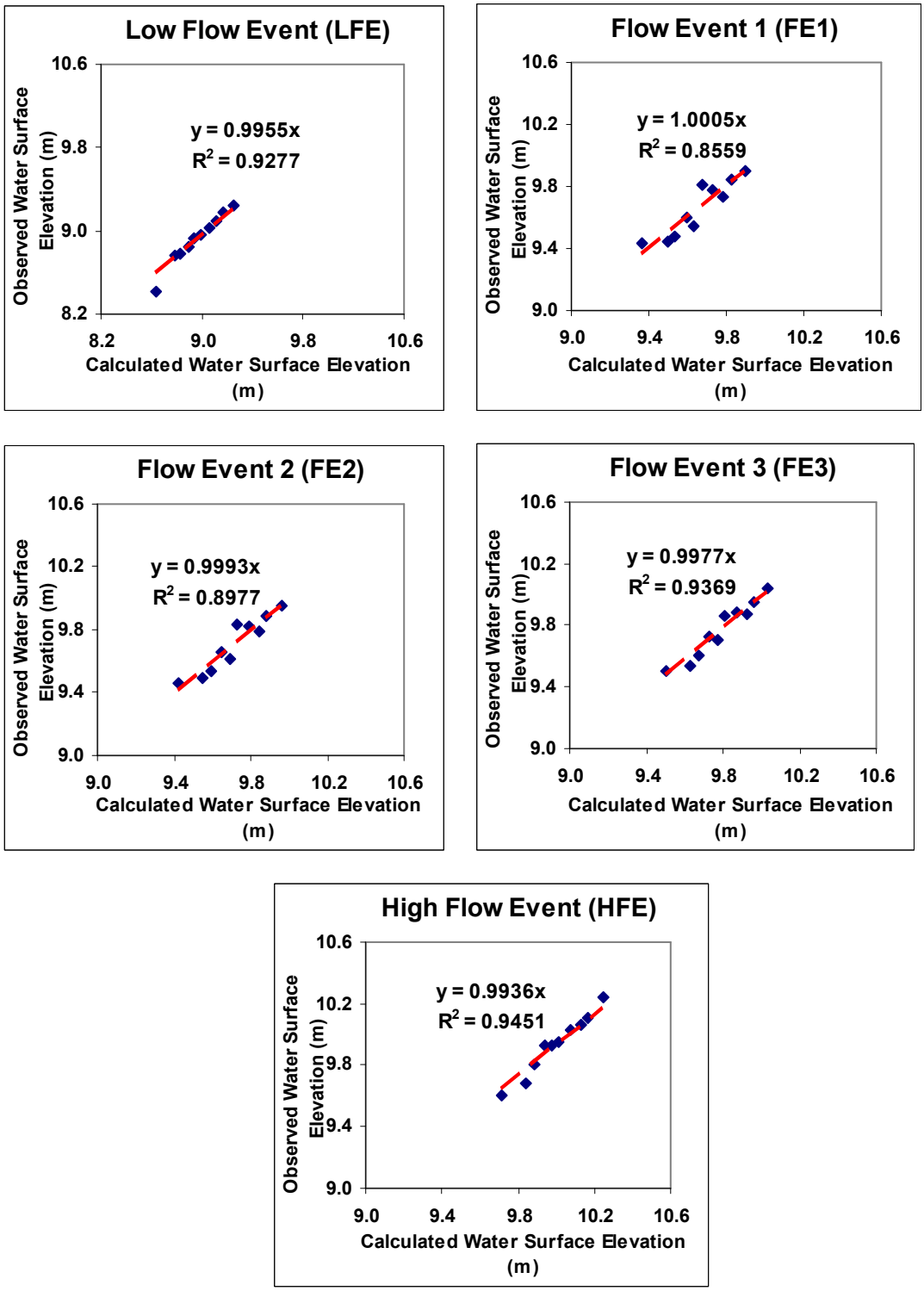

Figure 3.18: Comparison of calculated versus observed water surface elevations in the form of a scattergraph corresponding to LFE, FE1, FE2, FE3, and HFE.

Following this procedure, the vertices with *z* coordinates greater than the corresponding value of water elevation at a particular cross-section (i.e. unsubmerged vertices) were deleted. Consequently, the number of points for each flow model was significantly decreased as shown in Table 3.10.

Table 3.10: Number of points included within the different model geometries.

Flow Events	Sub-Reach A	Whole Reach				
	LFE	LFE	FE1	FE2	FE3	HFE
Number of points	390	938	1,052	1,082	1,179	1,279

A final topographic representation of the reach for each of the five different flow events and the SRA for LFE was produced in *Gambit 2.1* and depicted in Figures 3.19 to 3.24. Figures 3.19 to 3.24 indicate the topography of the examined reach based on the original interpolated data plotted on top of the topography as represented in the final mesh for each model under a range of different flow magnitudes.

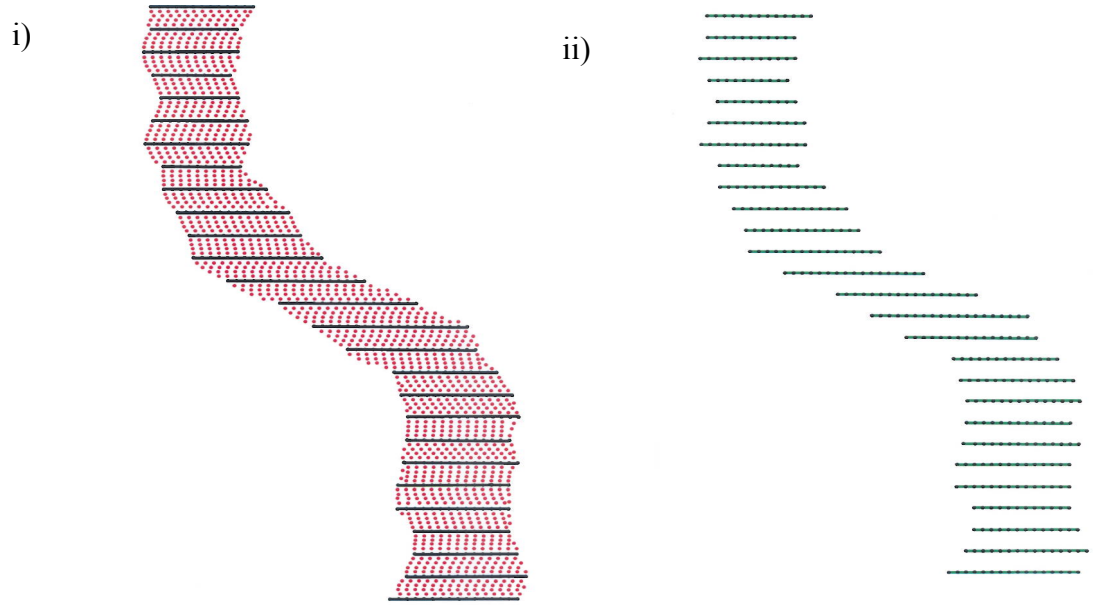

Figure 3.19: i) Initial interpolated topographic data (red points) of SRA under low flow conditions (LFE) plotted on top of final mesh topography (black points) (ii) Reduced topographic data of SRA under LFE representing the model final mesh topography.

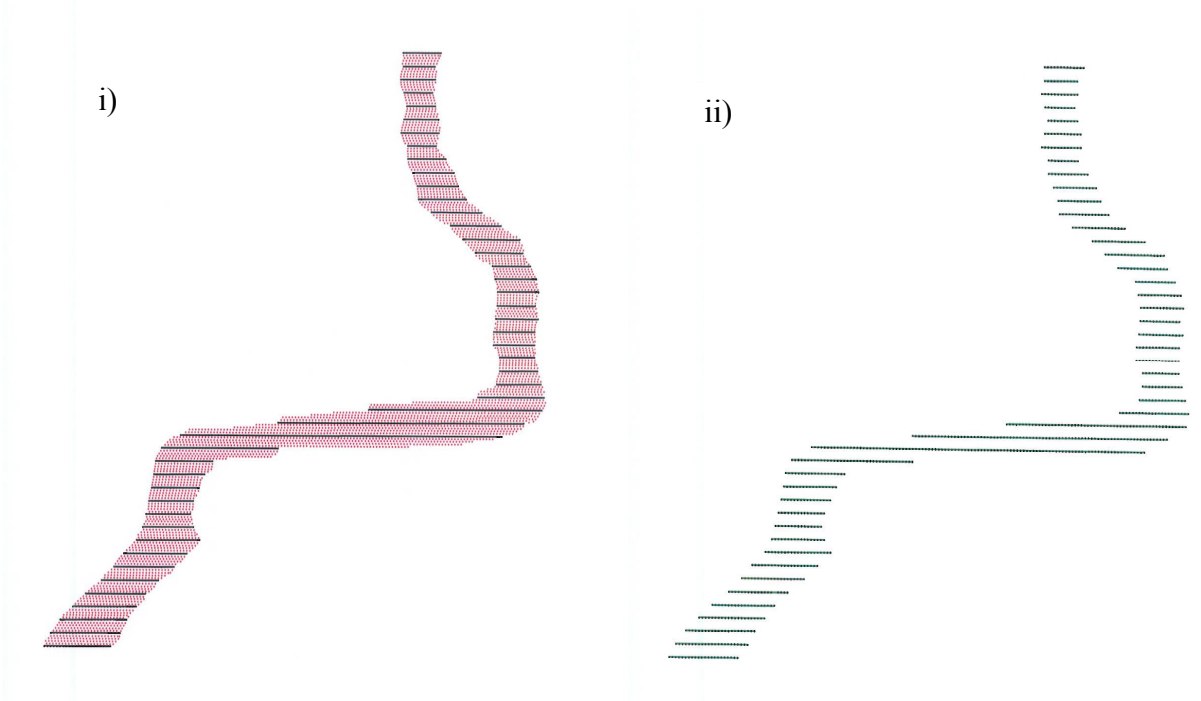

Figure 3.20: i) Initial interpolated topographic data (red points) of whole reach under low flow conditions (LFE) plotted on top of final mesh topography (black points) (ii) Reduced topographic data of whole reach under LFE representing the model final mesh topography.

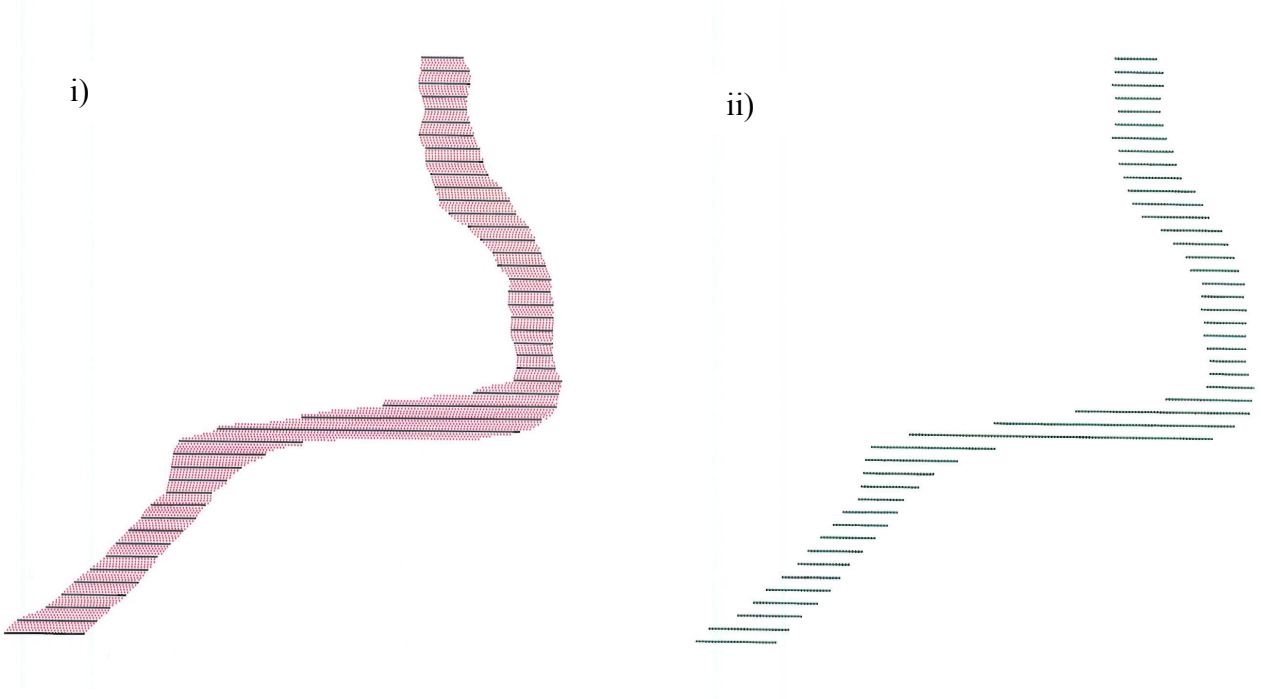

Figure 3.21: i) Initial interpolated topographic data (red points) of whole reach under flow event 1 (FE1) plotted on top of final mesh topography (black points) (ii) Reduced

topographic data of whole reach under FE1 representing the model final mesh topography.

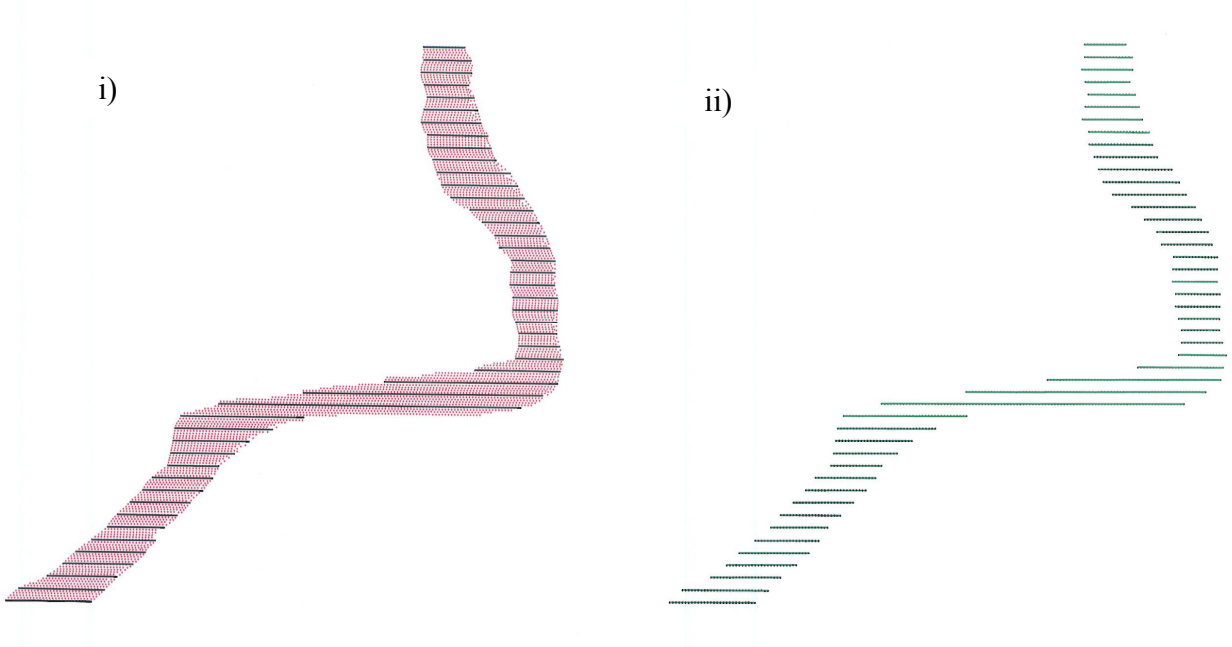

Figure 3.22: i) Initial interpolated topographic data (red points) of whole reach under flow event 2 (FE2) plotted on top of final mesh topography (black points) (ii) Reduced topographic data of whole reach under FE2 representing the model final mesh topography.

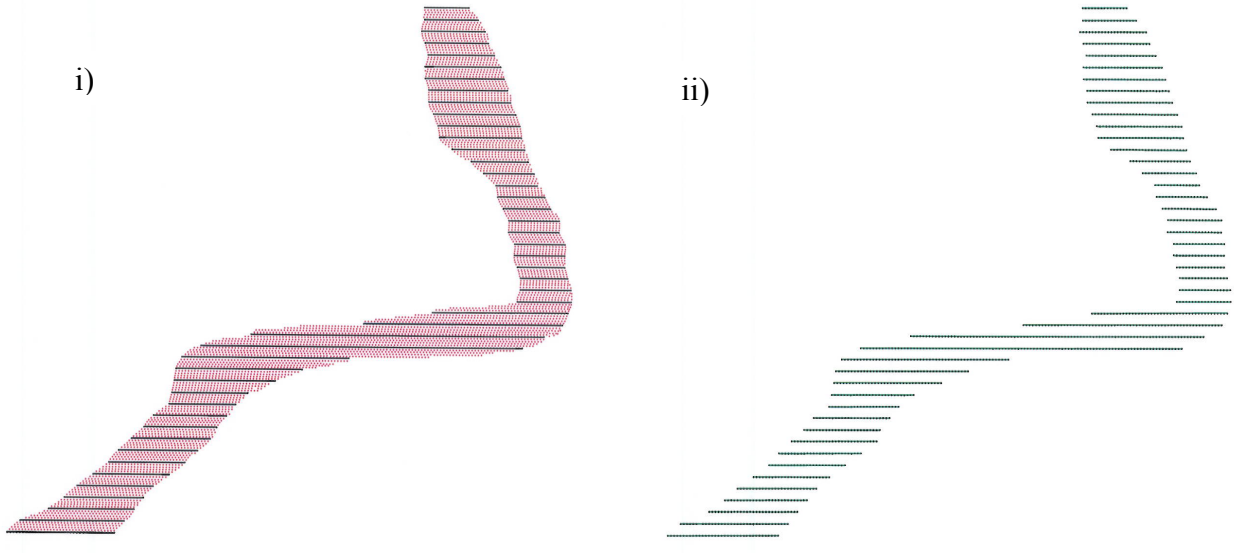

Figure 3.23: i) Initial interpolated topographic data (red points) of whole reach under flow event 3 (FE3) plotted on top of final mesh topography (black points) (ii) Reduced

topographic data of whole reach under FE3 representing the model final mesh topography.

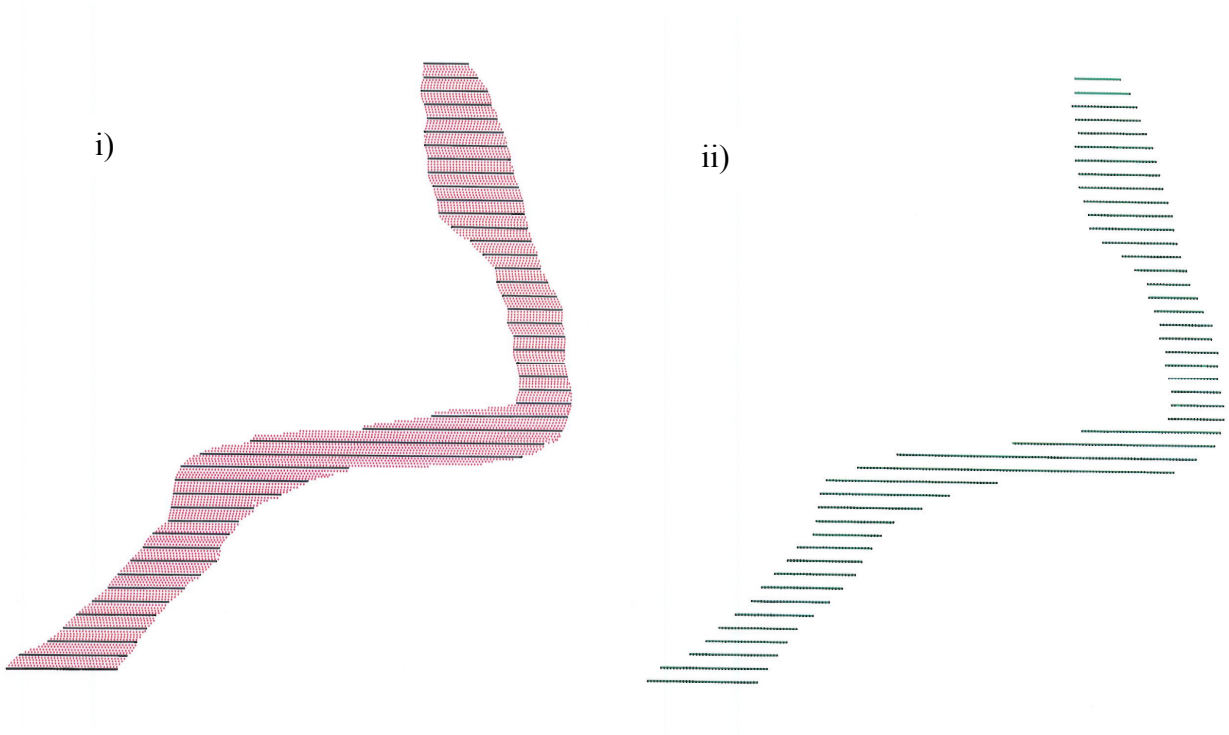

Figure 3.24: i) Initial interpolated topographic data (red points) of whole reach under high flow conditions (HFE) plotted on top of final mesh topography (black points) (ii) Reduced topographic data of whole reach under HFE representing the model final mesh topography.

Having created the topographic representation of the reach (five different flows) and SRA (LFE) the next step is to generate the mesh.

3.4.1.2 Mesh generation

As already mentioned, each cross section within the geometries of the various flow events consists of a different number of vertices. These vertices were connected to create the edges of the three-dimensional models. This connection was done by selecting the NURBS (Non-Uniform Rational B-Spline) option, which is *Gambit's 2.1* curve-fitting routine. This fits a smooth curve onto several vertices. The left and right edge points of

each cross-section were also joined with the NURBS option. Edge construction was finished by connecting the first and last points of every cross-section with a straight line. The next step in *Gambit 2.1* was to take these edges and create faces. Virtual faces were generated since the edges were irregular. Having that in mind, the bed virtual faces were merged to avoid complications with regards to the meshing of the model. As a result, four virtual faces were finally produced corresponding to the bed, water surface, inlet, and outlet. A virtual volume was then created by stitching these four virtual faces.

Before starting to set up the mesh of the three-dimensional models a boundary layer was attached to the bed virtual face. The spacing of grid node rows in regions located nearby to the edges and/or faces is defined by these boundary layers. The latter are mainly utilized to control mesh density in particular regions of interest (*Fluent Inc.*, 2006). A description of a boundary layer consists of some parameters which can be specified as follows:

- Selection of an appropriate boundary layer algorithm which decides whether the heights of all first row elements are equal to each other. In the current investigation the uniform algorithm was selected corresponding to identical heights of all first row elements.
- Specification of the height of the first row of mesh elements placed adjacent to the edge or face to which the boundary layer is attached.
- Indication of the growth factor which is specified as the ratio of the height of each row relative to that of the immediately preceding row.
- Specification of the depth of the boundary layer which can be defined by the total number of rows.
- Selection of the internal continuity characteristic which determines the manner in which *Gambit 2.1* imprints boundary layers on adjoining faces as well as the mesh pattern in regions of imprint overlap. *Gambit 2.1* modifies the mesh patterns in the overlap regions such that the imprints are joined together. In addition, the internal continuity option directly affects which types of meshing schemes are appropriate for volumes to which boundary layers have been applied.

The creation of the boundary layer employed in this analysis was made possible by selecting the values demonstrated in Table 3.11.

Table 3.11: Specification of the boundary layer attached to the bed virtual face.

Algorithm	Height of First Row	Growth Factor	Number of Rows
Uniform	0.01	1.2	4

A visual representation of the specific boundary layer can be seen in Figures 3.25 and 3.26, where three different spacings corresponding to coarse, intermediate and fine meshes were used for understanding the configuration of the cells within the boundary layer and where the boundary layer joins the rest of the mesh within those cases.

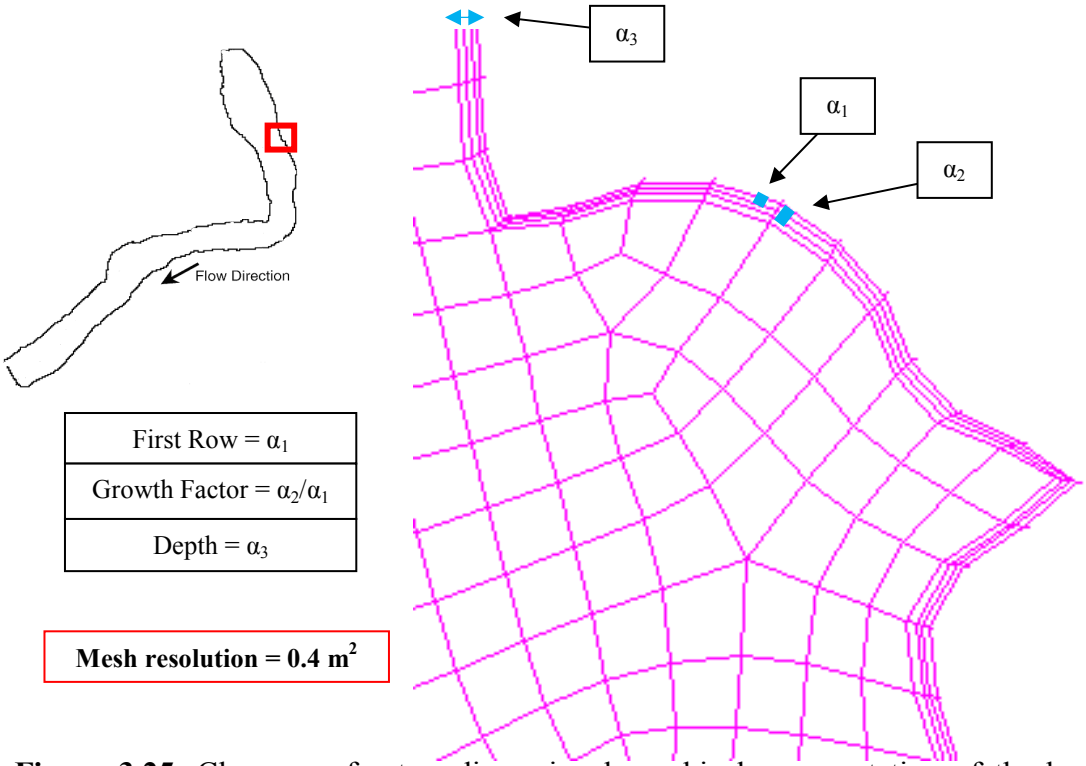

Figure 3.25: Close up of a two-dimensional graphical representation of the boundary layer attached on the left side of the examined study reach for a mesh resolution of 0.4 m^2 (2.5 cells per square meter).

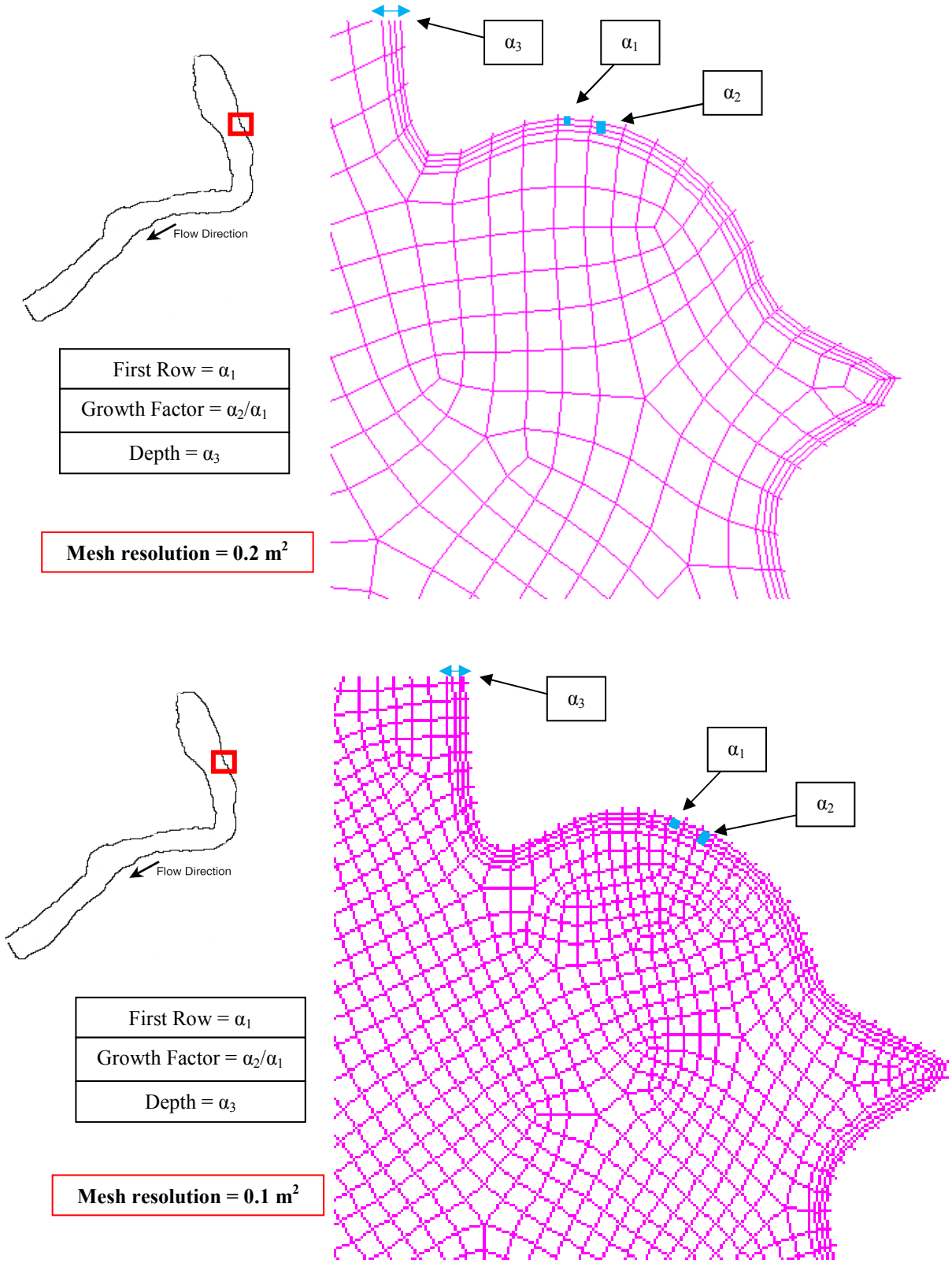

Figure 3.26: Close up of a two-dimensional graphical representation of the boundary layer attached on the left side of the examined study reach for a mesh resolution of 0.2 m^2 (5 cells per square meter) and 0.1 m^2 (10 cells per square meter), respectively.

Having attached the appropriate boundary layer to the virtual bed face, the application of three size functions is then followed. Size functions are developed to limit either the size of mesh intervals on any edge, or the mesh element size on any face or volume. Not only the way in which they are defined, but also the way in which they control the mesh, make them different from the boundary layers. Three different types of size functions are available within *Gambit 2.1*. In this study the fixed type was utilized based on the identification of the maximum mesh element edge length as a function of distance from a given source entity (*Fluent Inc.*, 2006). A fixed size function is defined by employing two entities, namely the source and the attachment. The centre of the area in which the size function is applied can be specified by the source entity. In contrast, the entity for which the mesh is to be influenced by the size function corresponds to the attachment one.

A size function is generated after estimating the following parameters:

- Start size: represents the mesh element edge length in the area placed nearby to the source entity.
- Growth rate: defined as the increase in mesh element edge length with each succeeding layer of elements.
- Size limit: corresponds to the maximum mesh element edge length allowed for the attachment entity.

Three different size functions were applied in the current investigation. The characteristics related to them can be found in Table 3.12.

The next step in *Gambit 2.1* was the meshing of the four virtual faces. As previously mentioned, due to the complex geometry an unstructured grid of mesh elements was produced for each one of the virtual faces by applying the pave face meshing scheme. This technique creates an unstructured grid mainly of quadrilateral elements, whereas triangular corner elements are used at user-specified locations.

The study was performed on three grids, coarse, intermediate and fine, to determine a minimum level of grid discretization that would enable a grid independent solution to be

obtained with the best computational efficiency. This was achieved by employing three different face interval size spacings. Table 3.13 indicates the values of the face interval size spacings used and the total number of cells generated corresponding to the coarse, intermediate, and fine grid, respectively, with regards to SRA for the LFE. Having meshed the four virtual faces a volume grid generation was then followed by using the Tet/Hybrid volume meshing scheme, while volume interval size spacing was taken equal to 1.

Table 3.12: Parameters of each applied size function.

Size Functions	Source Entity	Attachment Entity	Start Size	Growth Rate	Size Limit
1	Lower edge of Inlet Virtual Face	Inlet Virtual Face	0.01	3.5	1
2	Lower edge of Outlet Virtual Face	Outlet Virtual Face	001	3.5	1
3	Bed Virtual Face	Virtual Volume	0.01	3.5	1

Table 3.13: Different face interval size spacings applied and total number of cells created in each grid with regards to SRA for the LFE.

Grid	Coarse	Intermediate	Fine
Spacing	0.4	0.2	0.1
Total Number of Cells	76,383	295,202	1,024,570

In order to understand the difference between the coarse, intermediate, and fine grids, zoomed views in a specific area of SRA (LFE), shown in Figure 3.27, are taken and depicted in Figure 3.28.

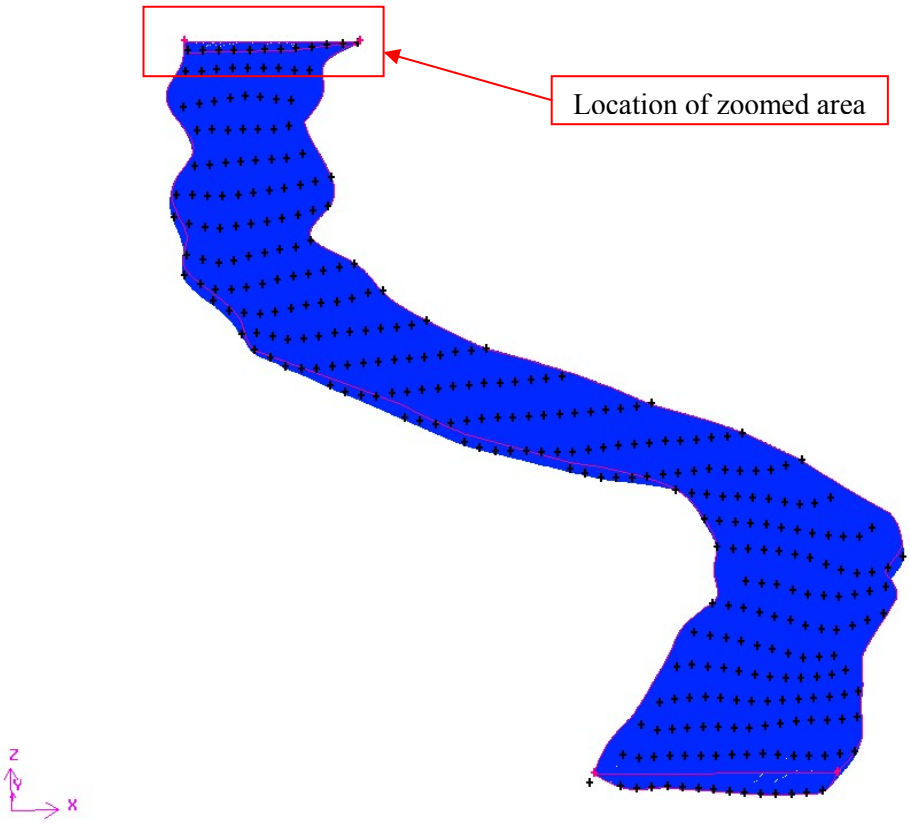

Figure 3.27: Location of selected zoomed area within SRA for LFE.

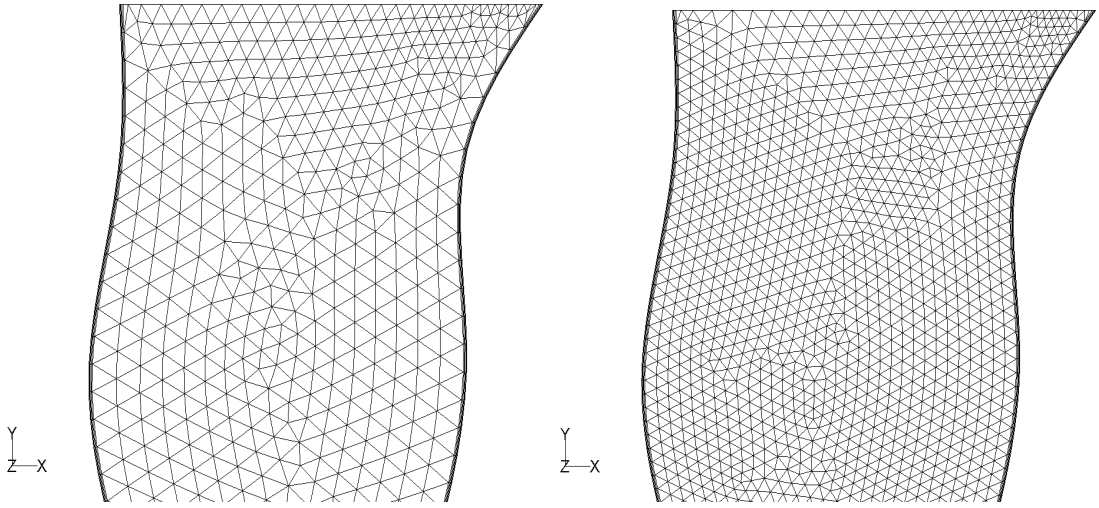

Coarse Grid **Intermediate Grid**

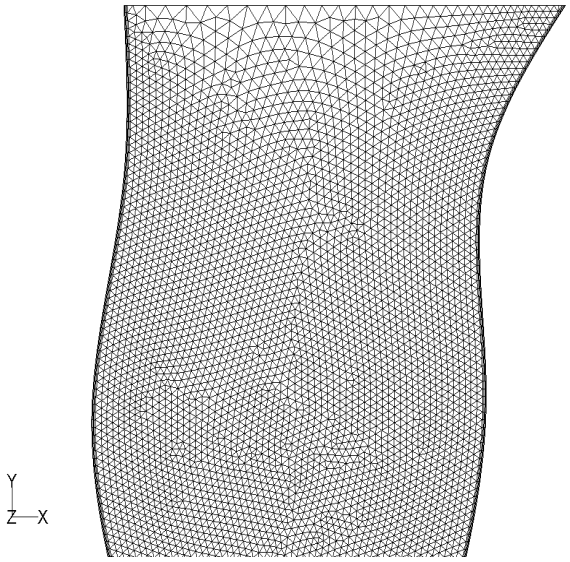

Fine Grid

Figure 3.28: Close up of coarse, intermediate, and fine grids created by using *Gambit 2.1* at the upstream area with regards to SRA for LFE.

Initially, *Gambit 2.1* was employed for meshing the whole reach three-dimensional models for the different flow events. A boundary layer was attached to the virtual bed face and three size functions were applied as described above. When attempting to mesh the whole virtual volumes problems with regards to the bend were identified. Thus, a solution was tried by separating the whole reach into three different virtual volumes that represent the upstream (SRA), downstream (SRB), as well as the mid-bend reaches. While the meshing of both the upstream and downstream reaches was performed without difficulties, the mid-bend part was again problematic since a negative volume was achieved after meshing. Hence, it was concluded that *Gambit 2.1* could not be used for meshing this particular problem. As an alternative, the *Harpoon* (*Sharc Ltd*, 2006) software meshing tool was utilized for generating the mesh of the whole reach. The five geometries as created in *Gambit 2.1* were imported into *Harpoon*. In the latter software no size functions were used. The first step taken corresponds to the creation of a boundary layer attached to the bed virtual face. The characteristics of this boundary layer, which was identical for all flow events, are specified in Table 3.14.

Table 3.14: Specification of the boundary layer attached to the bed virtual face of the whole reach by using *Harpoon*.

Initial Cell Height	Number of Layers	Expansion Rate
0.005	4	1.5

The grid independence of the solution was confirmed by creating three different meshes for each flow event. This was made feasible by employing different base levels which represent a particular cell size that may be typed to obtain the accurate size required. The base levels used in this study can be specified as 0.4, 0.2, and 0.1 corresponding to coarse, intermediate and fine meshes, respectively. The grid generation process was completed by selecting the internal meshing option. The number of cells contained within the three different grids for each one of the five flow events is demonstrated in Table 3.15.

Table 3.15: Total number of cells created in each grid by using *Harpoon* for each of the five different flow events.

Grids/ Flow Events	Coarse		Intermediate		Fine	
	Number of Cells	Time to Mesh	Number of Cells	Time to Mesh	Number of Cells	Time to Mesh
LFE	73,441	5sec	344,858	18sec	2,148,510	98sec
FE1	155,837	9sec	611,116	33sec	2,500,068	180sec
FE2	170,299	10sec	746,957	42sec	2,634,908	195sec
FE3	281,428	12sec	852,386	47sec	2,800,567	210sec
HFE	295,853	13sec	887,333	49sec	2,976,883	220sec

A better view on those grids can be obtained by performing a close up of the coarse, intermediate, and fine meshes for each flow event as depicted in Figures 3.29 through 3.34.

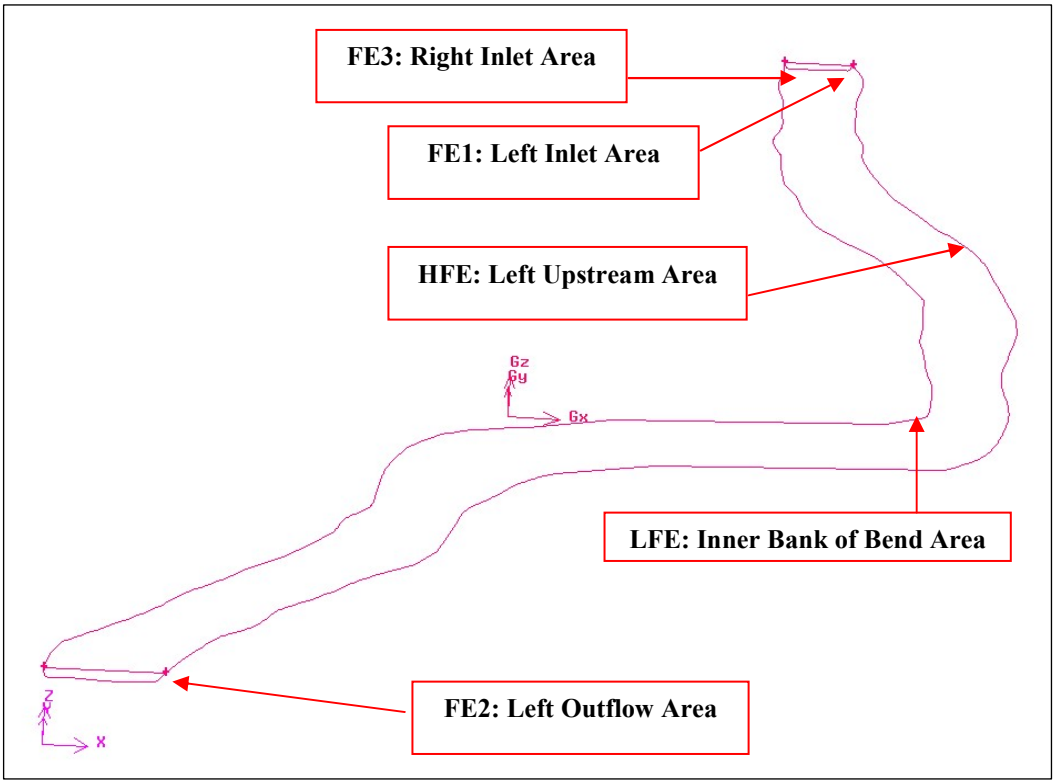

Figure 3.29: Locations of selected zoomed areas within the five different flow events.

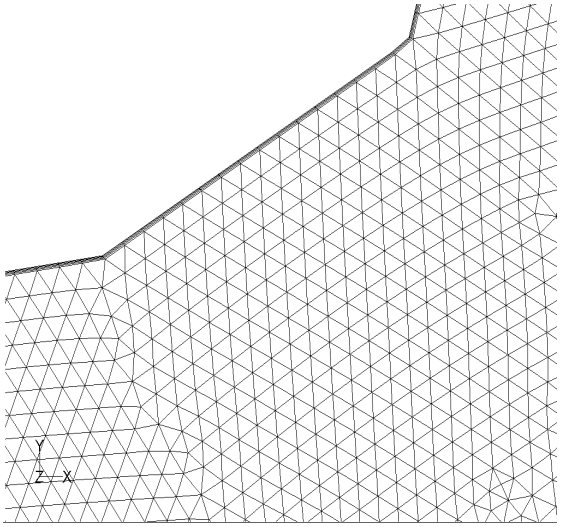

Coarse Grid

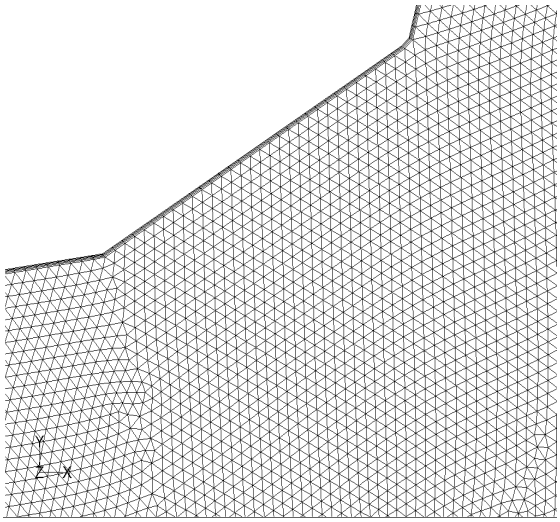

Intermediate Grid

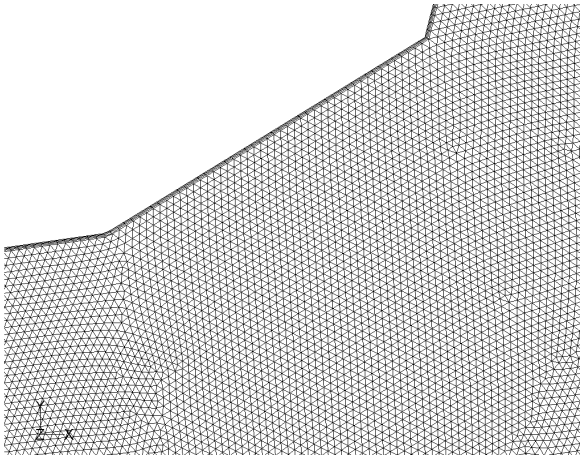

Fine Grid

Figure 3.30: Close up of coarse, intermediate, and fine grids created by using *Harpoon* at the inner bank of the large bend area with regards to LFE.

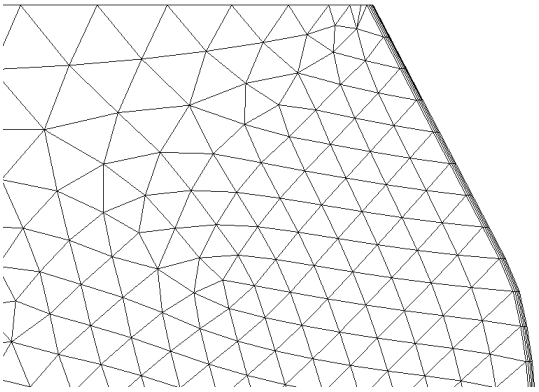

Coarse Grid

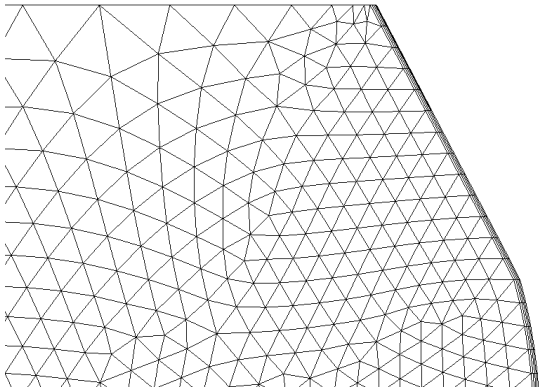

Intermediate Grid

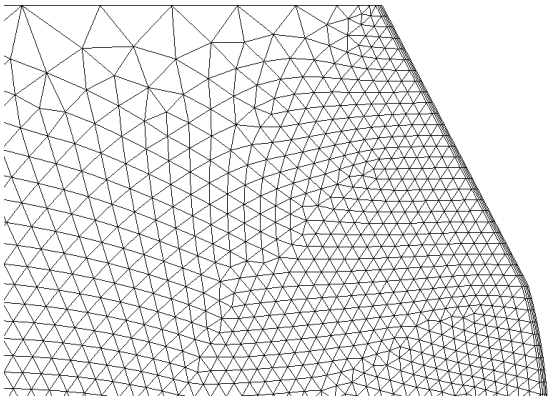

Fine Grid

Figure 3.31: Close up of coarse, intermediate, and fine grids created by using *Harpoon* at the left hand side of the inflow area with regards to FE1.

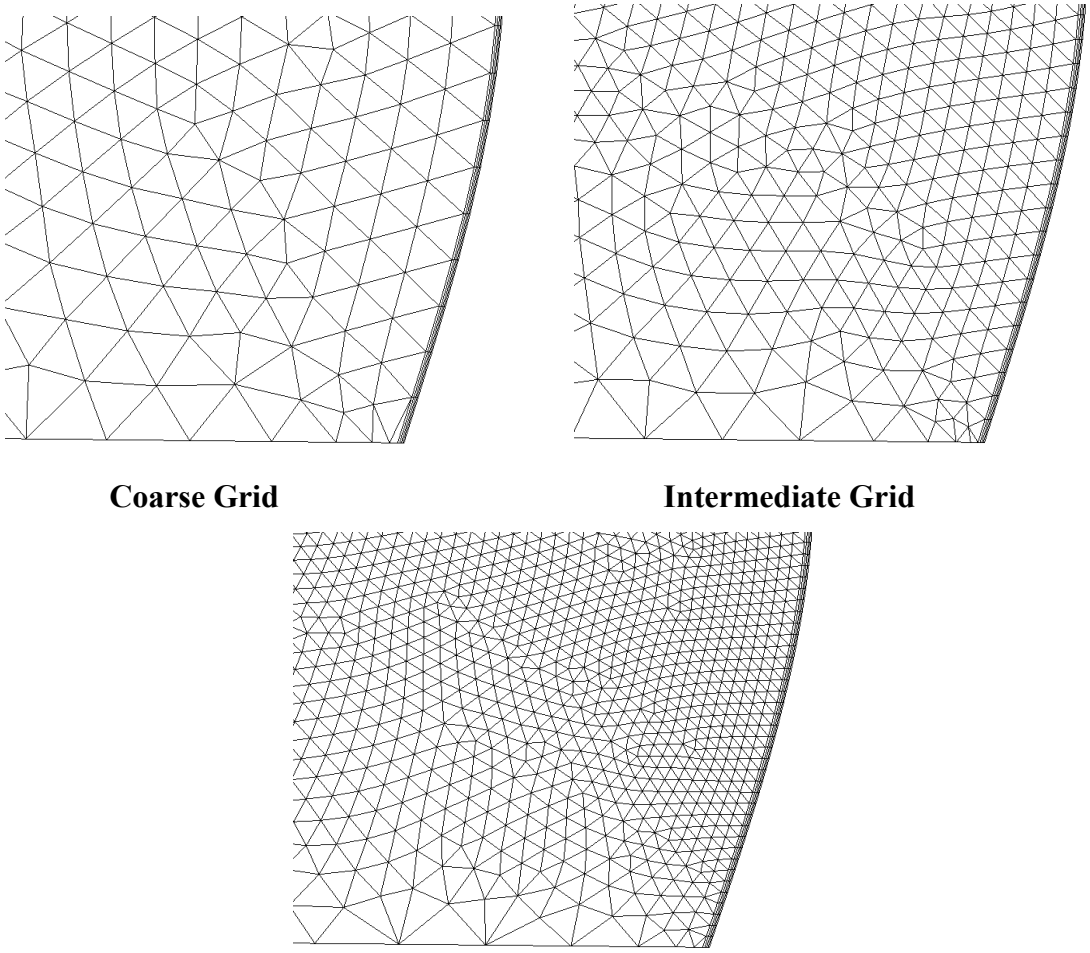

Coarse Grid **Intermediate Grid**

Fine Grid

Figure 3.32: Close up of coarse, intermediate, and fine grids created by using *Harpoon* at the left hand side of the outflow area with regards to FE2.

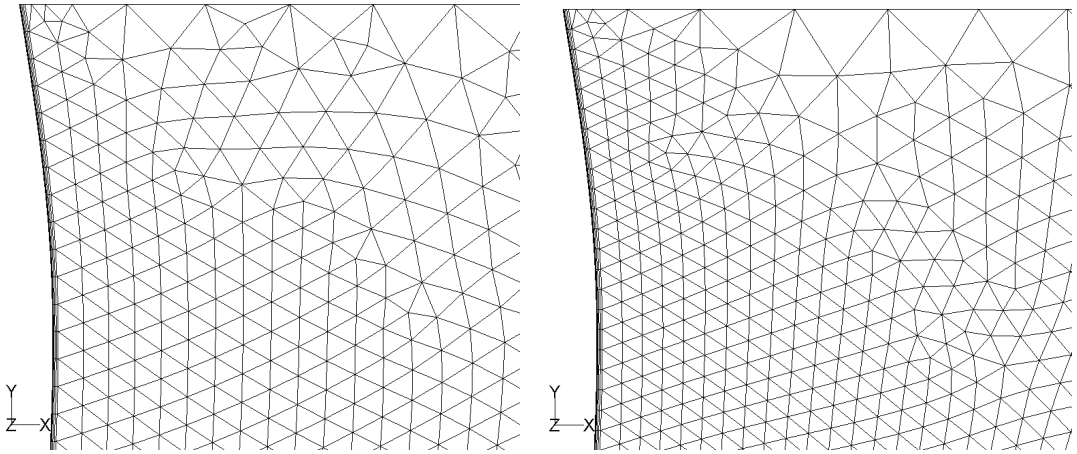

Coarse Grid **Intermediate Grid**

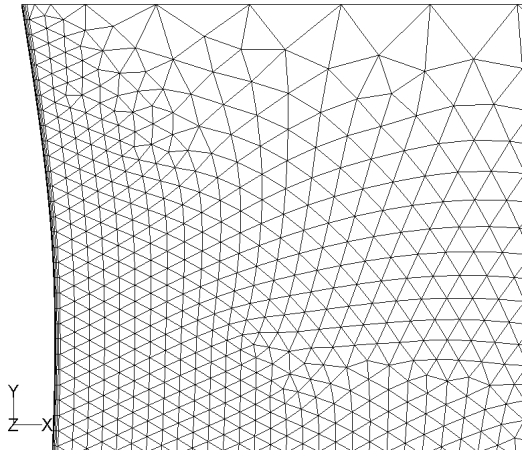

Fine Grid

Figure 3.33: Close up of coarse, intermediate, and fine grids created by using *Harpoon* at the right hand side of the inflow area with regards to FE3.

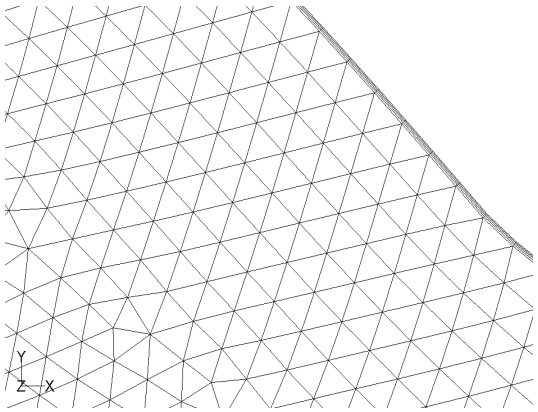

Coarse Grid

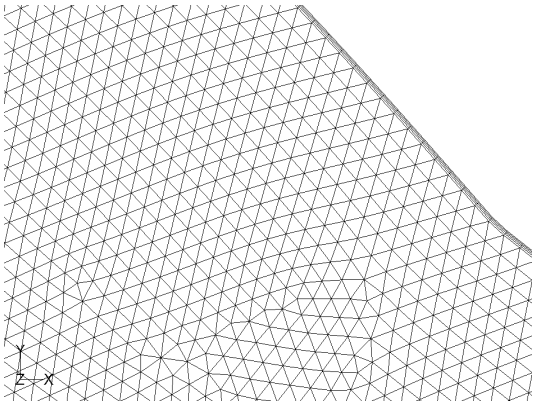

Intermediate Grid

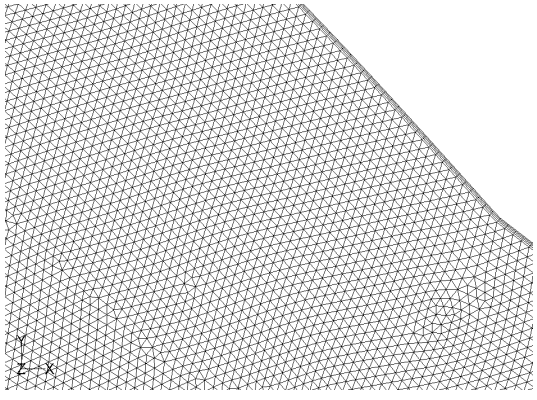

Fine Grid

Figure 3.34: Close up of coarse, intermediate, and fine grids created by using *Harpoon* at the left upstream area with regards to HFE.

Once the geometries and meshes of the computational models were constructed, the grids were then imported into *Fluent 6.2*.

3.4.2 Fluent 6.2 specifications

Following the creation of the meshes in *Gambit 2.1* and *Harpoon*, the eighteen grids (three correspond to SRA for the LFE and fifteen represent the whole reach within the five different flow events) were then converted to *Fluent* compatible grid files. These grid files could then be read into *Fluent 6.2* and converted into *Fluent* case files for solution. Errors that might have been introduced through the mesh generation process were examined by checking the grid. These errors may include incorrect model dimensions. When checking the mesh, attention also has to be paid to avoid negative volumes. If a volume is referred to as negative then there is a grid problem, since no negative volume exists. After checking the correctness and quality of mesh, the grid would be scaled in the desired units, given that *Gambit 2.1* enters the coordinates as non-dimensional numbers. Once the grid was set, the specifications of the solver were also set and the eighteen cases were run and analyzed. Specifications of the solver include the following:

- Turbulence model selection and solver parameters.
- Definition of material properties, as well as operating conditions.
- Identification of the appropriate boundary conditions.
- Selection of the differencing scheme, relaxation factors, and pressure-velocity coupling algorithm.

The *Fluent 6.2* default solver, segregated (see Figure 3.6), was employed for the model solution. This solves the governing equations of momentum, continuity, and turbulence sequentially. The segregated solver was utilized over the alternative coupled solver since it requires less memory allocation. The analysis of all cases was performed by selecting the steady, three-dimensional, options.

Before choosing the appropriate turbulence model several runs were executed, in which the use of almost all the available turbulence closures within *Fluent 6.2* were compared. More specifically, the simulations were carried out by employing four different models,

namely, the standard k-ε, the *RNG* k-ε, the standard k-ω, and the *SST* k-ω. The results were tested and used for comparison with the field data. The latter data was found to be better replicated by the results obtained using the standard k-ε turbulence model (see Chapter 4.1.2). Therefore, a decision was made to employ the relatively simple standard k-ε turbulence model throughout this study. Further mathematical formulation of the turbulent closure used in this study can be found in Appendix III.

A vital step in the set up of the modelling process corresponds to the definition of the materials and their physical properties. These properties consist of characteristics such as density, and viscosity, which were specified as constants within the current analysis. The operating conditions include pressure, gravity, and the reference pressure location. Gravity can be entered in values of m/s^2 in *x, y* and *z* components. The operating pressure was also set equal to the default value provided by *Fluent 6.2* and can be defined as a large pressure almost equal to the average absolute pressure in the flow. The reference pressure location corresponds, by default, to the cell center at or closest to (0, 0, 0) (*Fluent Inc.*, 2006). For this study, the selected reference pressure location represents a point which is located at a place close to the inlet virtual face of the reach. The operating conditions employed in this analysis are summarized in Table 3.16.

Table 3.16: Applied operating conditions.

Operating Conditions	Operating Pressure (Pascal)	Reference Pressure Location (m)	Gravity (m/s^2)
Values	101,325	X: 36 Y: 65.3 Z: 9	X: 0 Y: 0 Z: -9.81

The boundary conditions can be described as the physical properties that govern the model solution. In *Fluent 6.2*, boundary conditions must be defined at each surface created in the mesh generation process, namely the inflow, outflow, bed, and water surface virtual faces. The velocity inlet boundary condition was specified in the inflow

virtual face. A wall boundary type without a slip condition was chosen for the bed virtual face which is a single surface forming the bed and banks of the examined reach. As far as the surface virtual face is concerned, the wall boundary layer was also chosen with a slip condition applied on a solid lid.

The velocity and scalar properties of the flow at the inlet boundary were defined by applying the velocity inlet boundary condition. To provide an inflow velocity distribution for the model, the inflow characteristics in the furthest upstream reach are required. The inflow data must comprise velocity vectors in all three dimensions and the turbulence parameters k and ε, for each grid cell. Two main approaches can be applied: specifying constant values for all cells in the inflow section and allowing the flow to develop; or specifying individual values for each cell based on theoretical considerations or empirical measurements.

To avoid the extra computation of including upstream flow development, in the case of a rectangular cross section inflow, such as in a flume, a fully developed inflow can be prescribed by a separate model that calculates a fully developed flow profile (*Patankar* and *Spalding*, 1972). The model requires the dimensions of the channel and the mass-flow rate to be defined and the fully developed flow profile is derived for an infinitely long channel. However, this fully developed flow profile model is only applicable to regular channels and could not be applied for irregular inflow cross sections.

The second approach of applying the inlet boundary condition is based on the law of the wall (*Launder and Spalding*, 1974) given in equation (*3.7*). In this case, where field measurements are required, the law of the wall is fitted to each vertical profile. The values for each grid node are then estimated for the correct height in the profile. Assessments for each vertical profile of grid cells between those measured are performed using linear interpolation. This is carried out for velocities in each direction, which provided the inflow velocity distribution for the reach.

However, in modelling field reaches with only a specified discharge for the inflow, a different technique of inflow distribution is required (*Hodskinson*, 1997). This method applies the total discharge and calculates the velocity in each cell based upon the cell distance from any boundary using the law of the wall. The turbulent kinetic energy and dissipation rate of the fluid flow at the upstream boundary, which is usually not known, may be determined by specifying the turbulent intensity of the fluid flow. Uniform values of turbulent kinetic energy, k (m^2/s^2), and dissipation, ε (m^2/s^3), were calculated using:

$$k = \left(IV_{\inf low}\right)^2 \tag{3.12}$$

$$\varepsilon = 0.1643\frac{k^{\frac{3}{2}}}{l} \tag{3.13}$$

where I is the turbulent intensity, $V_{\inf low}$ (m/s) is the mean average velocity magnitude, and l (m) is a mixing length scale of the channel across the inflow section.

Nallasamy (1987) recommends using an empirical value of 5−20% of the average inflow velocity for the turbulent intensity to represent a wide variety of fluid flows that have not experienced intense interruptions to the three-dimensional flow or do not require any special treatment of the turbulence. Various values between 5% and 20% for the turbulence intensity at the upstream boundary location have been investigated (*Ma et al* 2002) and it is noted that the differences in the fluid velocities predicted are graphically indistinguishable. However, employing different values for the turbulent intensity at the upstream boundary do affect the predicted magnitude of the turbulent kinetic energy and dissipation rate of the fluid flow, but this appears to be limited to the region near the upstream boundary having little effect on the flow field in reaches downstream.

In the current analysis the velocity specification technique was set as normal to the boundary, whilst the turbulent kinetic energy and dissipation rate was selected as the turbulence specification method. At that point it should be noted that the velocity in the

inflow is not measured, so it must be guessed. Therefore, its calculation is a loose approximation and should be recognized as such. In reality the distribution of the velocity in the inflow will vary across the inlet. The method of velocity inlet distribution based on a specified discharge (*Hodskinson*, 1997) is applied in this study.

The inlet velocity magnitude was estimated by employing the following formula:

$$V_{\inf low} = \frac{Q}{A_{\inf low}} \qquad (3.14)$$

where $V_{\inf low}$ (m/s) is the mean velocity magnitude at the inflow, Q (m^3/s) corresponds to the peak flow discharge, and A_{inflow} (m^2) is defined as the total area of the inlet virtual face. The only unknown variable in the above equation is A_{inflow} which can be easily calculated through geometrical means. Velocity magnitudes for each of the five different flow events are given in Table 3.17.

An equation that describes the intensity of turbulence is given as (*Fluent Inc.*, 2006):

$$I = 0.16(R)^{-1/8} \qquad (3.15)$$

in which R represents the Reynolds number which can be estimated as follows:

$$R = \frac{\rho V_{\inf low} w}{\mu} \qquad (3.16)$$

where ρ is the density of the water equal to 998.2 kg/m^3, V_{inflow} is the mean velocity at the inlet calculated above, w (m) is the width of the inlet, and finally μ is the viscosity of the water, assumed to be equal to 0.001003 $kg/m\text{-}s$.

However, in this study a value of 10% (*Lane et al.*, 1998) is assumed for the turbulent intensity of the fluid flow at the upstream end.

Evaluation of the length scale of the turbulence was then followed by introducing the equation below:

$$l = 0.1d \qquad (3.17)$$

where d (m) is the average depth of the channel across the inflow section.

Turbulent kinetic energy, k, and dissipation rate, ε, are calculated by using equations (*3.12*) and (*3.13*). A summary of the basic features employed in the velocity inlet boundary condition is displayed in Table 3.17.

Table 3.17: Applied velocity inlet boundary condition.

Flow Events	Q (m^3/s)	V_{inflow} (m/s)	w (m)	R	I (%)	d (m)	l (m)	k (m^2/s^2)	ε (m^2/s^3)
LFE	0.791	0.387	6.7	2.58×10^6	10	0.30	0.03	1.5×10^{-3}	3.2×10^{-4}
FE1	6.9	0.95	8.4	7.94×10^6	10	0.96	0.10	0.9×10^{-2}	1.5×10^{-3}
FE2	8.2	1.2	8.8	1.05×10^7	10	1.01	0.10	1.4×10^{-2}	2.8×10^{-3}
FE3	10.3	1.0	11	1.09×10^7	10	1.05	0.11	1.0×10^{-2}	1.7×10^{-3}
HFE	18.4	1.6	11.6	1.84×10^7	10	1.29	0.13	2.6×10^{-2}	5.2×10^{-3}

The inflow boundary condition and the parameters used in each of the five different flow events are assumptions and this therefore introduces error. The effects of the error on these simulated flows must therefore be addressed. This can be done via sensitivity tests, designed to determine the downstream distance at which the simulated flows become independent of the specified boundary conditions at the inlet. Recent approaches have applied sensitivity analysis thoroughly using Monte Carlo or generalized likelihood uncertainty estimation approaches (*Beven and Binley*, 1992), where combinations of input data are varied and the sensitivity of the output is examined. However, the assessment and validation of model performance in this thesis initially considers the development and assumptions applied in each application and uses spatially distributed flow velocity data for validating model performance without carrying out any sensitivity analysis. The specified discharge method, in which a nominal value of the turbulent

intensity (*Hodskinson*, 1997; *Lane et al.*, 1998) is applied, is used in this study for determining the velocity inlet distribution. According to the latter technique, the downstream distance at which the simulated flows become independent of the specified velocity inlet is limited to the region near the upstream boundary (*Ma et al* 2002) having little effect on the flow field in reaches downstream, and therefore, sensitivity analysis is not considered to be crucial.

Flow exits are modeled by using the outflow boundary conditions provided in *Fluent 6.2*. When applying an outflow boundary, no conditions are specified since the flow velocity and pressure details are not known prior to solution of the flow problem. Hence, the only variable that needs to be defined corresponds to the flow rate weighting which indicates what section of the outflow passes through the boundary. For this study, the particular flow rate was set equal to 1, which is the default value.

The wall boundary condition was applied along the bed and water surface virtual faces. Wall boundaries can be either stationary or moving. The stationary option was chosen for both the bed and water surface virtual faces. The only difference between them relates to the shear conditions. The no-slip condition was defined with regards to the bed virtual face. The latter condition requires that the working fluid is attached to the wall and moves with the same velocity as the wall, in case that it is moving. As far as the water surface virtual face is concerned, a specified shear was selected. In this way a slip wall can be modeled by defining zero or non-zero shear. For this analysis, zero shear condition was specified in order to take into consideration the fluctuations of the top virtual face of the reach.

As previously shown (section 2.2.3.2), it is necessary and extremely important to specify the conditions at the solid boundary interface. At the solid boundary, the normal velocity components will reduce to zero. Thus, either very fine grids or wall functions are required in near boundary regions to simulate their effects on water flow. Nevertheless, in practice, the large-scale flow dynamics simulations are not considered due to the limited computational resources. Thus, a suitable empirical approximation is introduced which

models the effect of the near-wall flow on the outer flow. The law of the wall requires specification of the roughness height, K_s, which can be defined as an extremely complex parameter since roughness changes are difficult to isolate (*Nicholas*, 2001). The roughness height can be considered as an effective roughness parameter resulting in the correct variation of vertical velocity with elevation above the bed (*Nicholas*, 2005). An appropriate selection of this parameter is crucial for determining the shear stress at the boundaries. The value of the roughness height is dependent on the amount and size of bed and bank forms as well as the scales of topographic variation that is represented within the grid. *Nikuradse* (1952) specified the roughness height as a function of D_{65}, which is the size of the sixty-fifth percentile of the grain size distribution. However, this formulation was based upon sand distributions. In gravel bed rivers, the *Nikuradse* (1952) roughness height, K_s, has been found to be dominated by the larger clasts and bedforms and, K_s, has been put at 3.0 times the D_{90} or 5.2 times the D_{65} (*Bray*, 1980; *Clifford et al*., 1992). Other researchers (*Hodskinson*, 1996; *Hodskinson and Ferguson*, 1998; *Booker et al*., 2001) have linked K_s with 3.5 times the D_{84}, as shown in equation (*2.54*), for gravel bed rivers. A number of studies of three-dimensional numerical flow models have applied a constant bed and bank roughness height within the domain. Nevertheless, reach scale sorting can be significant in many cases, such as meander bends. This may results in large variations in roughness height over the bed and banks. In addition, many studies (*Lane and Richards*, 1998; *Nicholas and Sambrook Smith*, 1999; *Nicholas*, 2001; *Lane et al.*, 2002) have pointed out that roughness height has to be determined as function of both the mesh resolution and topographic representation, and therefore, it may link to a lower value of D_{50} as shown in equation (*2.55*).

In this thesis, a roughness height equal to the D_{50} of the sediment distribution was used for both solid boundaries since the bed virtual face is a single surface forming the bed and banks of the examined reach. The bed of the examined reach was found to be dominated by fine gravels, while its banks have been characterized as mostly sand and silt deposits (see Table 3.4). Thus, a representative value of D_{50} (0.065 mm) was chosen as an input roughness height for taking into account all different layers encountered and also the

reduction due to the required mesh resolution. However, the effect of a spatially variable roughness is unknown and could have a significant effect in near-bed velocity and shear stress predictions. The investigation of model sensitivity to spatially variable roughness is not assessed in this thesis and is left as an area that requires more research.

As previously mentioned, the *Fluent 6.2* solver utilizes a control volume based technique to convert the governing equations into discretized algebraic equations that can be solved numerically. The particular technique applies fluxes within the volumes faces to solve the flow field. These fluxes can be estimated by employing quantities in the neighboring cells located upstream. The above description represents an upwind scheme. In the current research, the differencing scheme used with regards to momentum, turbulence kinetic energy, as well as turbulence dissipation rate corresponds to a first order upwind. After executing 5000 iterations, a second order upwind scheme was employed to increase the accuracy of the solution, while the standard pressure interpolation numerical scheme was utilized. The SIMPLEC pressure-velocity coupling algorithm was operated since it is fully adapted for the case of steady calculations. It is also designed in such a way that it accelerates the convergence of the flow solution. Its mathematical formulation is demonstrated in Appendix IV. Finally, the values of the under relaxation factors employed in this analysis are summarized in Table 3.18.

Table 3.18: Values of the under relaxation factors utilized for this study where *TKE, TDR,* and *TV* are the turbulence kinetic energy, turbulence dissipation rate, and turbulence viscosity, respectively.

Under Relaxation Factors	Pressure	Density	Body Forces	Momentum	TKE	TDR	TV
Values	0.3	1	1	0.7	0.6	0.6	0.6

All information regarding the solver specifications for the current analysis was written in a log file and can be viewed in Appendix II (Part C). Once all the models, operating conditions, and boundary conditions were specified, the *Fluent 6.2* code can be executed.

3.5 Summary

A detailed outline of the basic issues related to environmental flow modelling in general was presented in the first section of this chapter. A review of advantages and disadvantages of the use of different numerical solvers, gridding methods and turbulence closure schemes was introduced with the aim of identifying the importance of the above features in environmental flows, fully justified by evidence from the literature. Introduction of the CFD code employed in the current investigation was followed by an explanation of the fact that its selection was based on the specific issues identified within the review process. A description of the field site employed in this thesis was introduced in the third section of this chapter, while the development of the numerical model for a range of flow conditions in the study reach was then outlined. More specifically, the final section has discussed the principles and procedures applied for modelling the various flow events that occurred in the examined reach of the River Asker. Models have been developed using *Fluent 6.2*, and its additional pre-processor *Gambit 2.1*. Having faced difficulties in meshing the mid-bend part of the reach the *Harpoon* mesh generator software was also utilized. At the end of this analysis eighteen different cases were created. Three of them correspond to SRA for the LFE, while the remaining fifteen represent the whole reach within the five different flow events. A verification of the models, as well as a validation with the field data obtained for the LFE, is now presented in Chapter 4.

CHAPTER 4

Results: Model Verification and Validation (Low Flow Conditions)

This chapter aims to examine the three-dimensional time-averaged flow structure of the studied River Asker reach under low flow conditions (Q = 0.791m/s^3) using a combination of Computational Fluid Dynamics simulations that are validated against detailed field observations, including direct velocity measurements. Results are analysed only for the whole reach and not for sub-reach A since the same flow features are identified in both cases. Flow structures in four areas of interest have been investigated. An assessment of the numerical model, including both its verification and validation, is examined (4.1), before the flow structures under low flow conditions within the four areas of interest are investigated (4.2). Finally, the chapter ends with a brief summary of the findings presented.

4.1 Model Assessment

As mentioned in Chapter 2, CFD models have been developed by applied mathematicians as well as civil, mechanical, and chemical engineers for applications to many types of flow process. Therefore, the suitability of CFD models to open channel flow processes raises a number of methodological and philosophical issues, which have to be addressed (*Lane and Richards*, 2001). The terminology applied in this process is that validation corresponds to the correct determination of variables predicted by the model and verification is associated with the correct solution of the model to produce these predictions. Hence, verification includes checking for coding errors as well as errors associated with both spatial and temporal discretisation specific to this study (*Lane and Richards*, 2001).

4.1.1 Verification

The most important activity in verification testing as implied by many engineering journals is systematically refining the grid size to estimate the discretisation error in the numerical solution. As the discretisation interval tends to zero the code should converge mathematically upon the correct solution of the continuum equations. However, as the discretisation interval reduces, computation costs increase. There is, therefore, a need to specify a grid resolution that produces a sufficiently independent solution.

The influence of grid resolution on the wall functions employed in this thesis (sections 2.2.3.2 and 3.1.4) can be investigated using the dimensionless parameter z^+ defined as the ratio of the elevation above a reference plane to the height of zero velocity. The latter recommendation for the layer of cells closest to solid boundaries does not, in itself, constitute a measure of grid independence. However, it is typically established in the process of exploring whether the grid resolution is appropriate for the wall function utilized given that a correct setup for a particular turbulence model and the associated approximations at solid boundaries have already been undertaken. Specifically, the computational grid should be generated in such a way that the first grid point of the wall is situated within the fully turbulent region, where $z^+>60$ (*Launder and Spalding*, 1974). Comparison of at least three different mesh spacings has to be carried out when checking for the effect of grid resolution on the wall functions.

In the current study, the appropriateness of the different meshes used in relation to the wall functions employed was confirmed by creating three different grids for the Low Flow Event (LFE). The first relatively coarse grid constructed for the River Asker consists of 73,441 cells using a grid spacing of approximately 0.4 m. Further refinement was undertaken to create a second grid consisting of 344,858 cells using a grid spacing of roughly 0.2 m. This represents a considerable improvement on the first grid but is still not sufficient to obtain a low z^+ value close to 60. Consequently the mesh is still too coarse to satisfy the wall functions employed. Further refinement was, therefore, carried out to generate a grid consisting of 2,148,510 cells using a grid spacing of 0.1 m.

The suitability of the wall functions to the grid resolutions applied was verified by examining the z^+ value at seven arbitrarily selected cross sections within the River Asker reach. These specific cross sections, annotated in Figure 4.1, were chosen because they cover a wide range of different regions throughout the reach representing the upstream, midstream bend, and downstream areas.

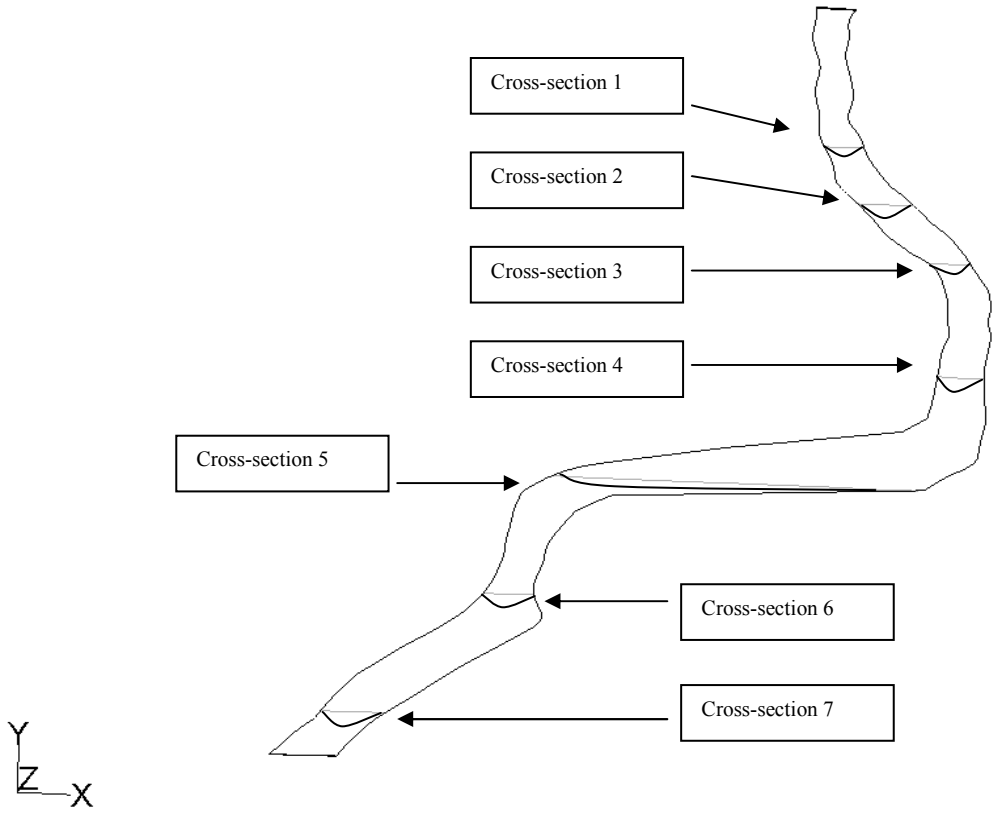

Figure 4.1: Locations of seven arbitrarily selected cross-sections.

As can been seen in Figures 4.2 through 4.4, the mesh created using a grid spacing of 0.1 m is adequate for obtaining a low z^+ close to 60 and consequently a condition satisfying the wall functions employed.

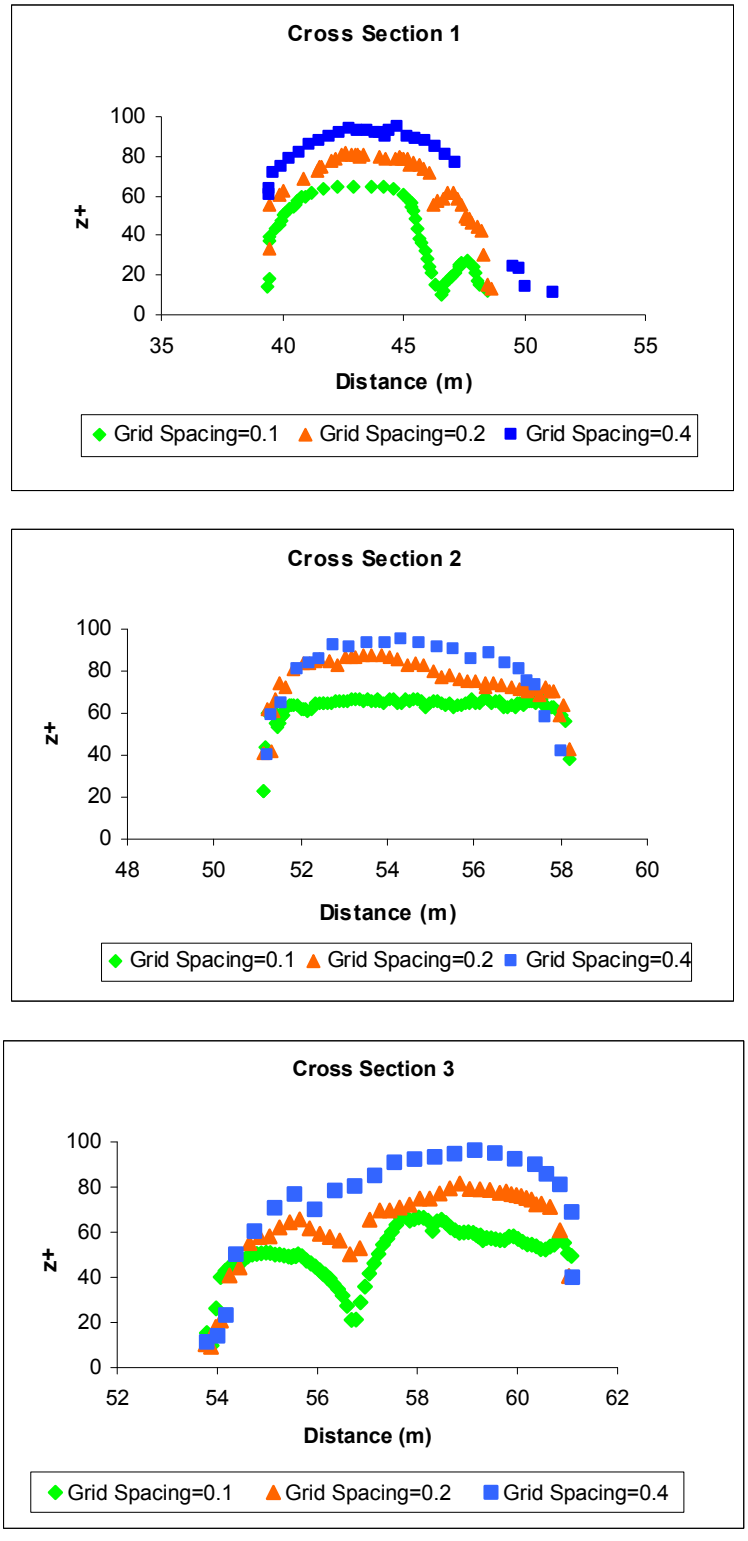

Figure 4.2: Investigation of various grid resolutions in relation to the wall functions employed, for cross-sections 1, 2, and 3.

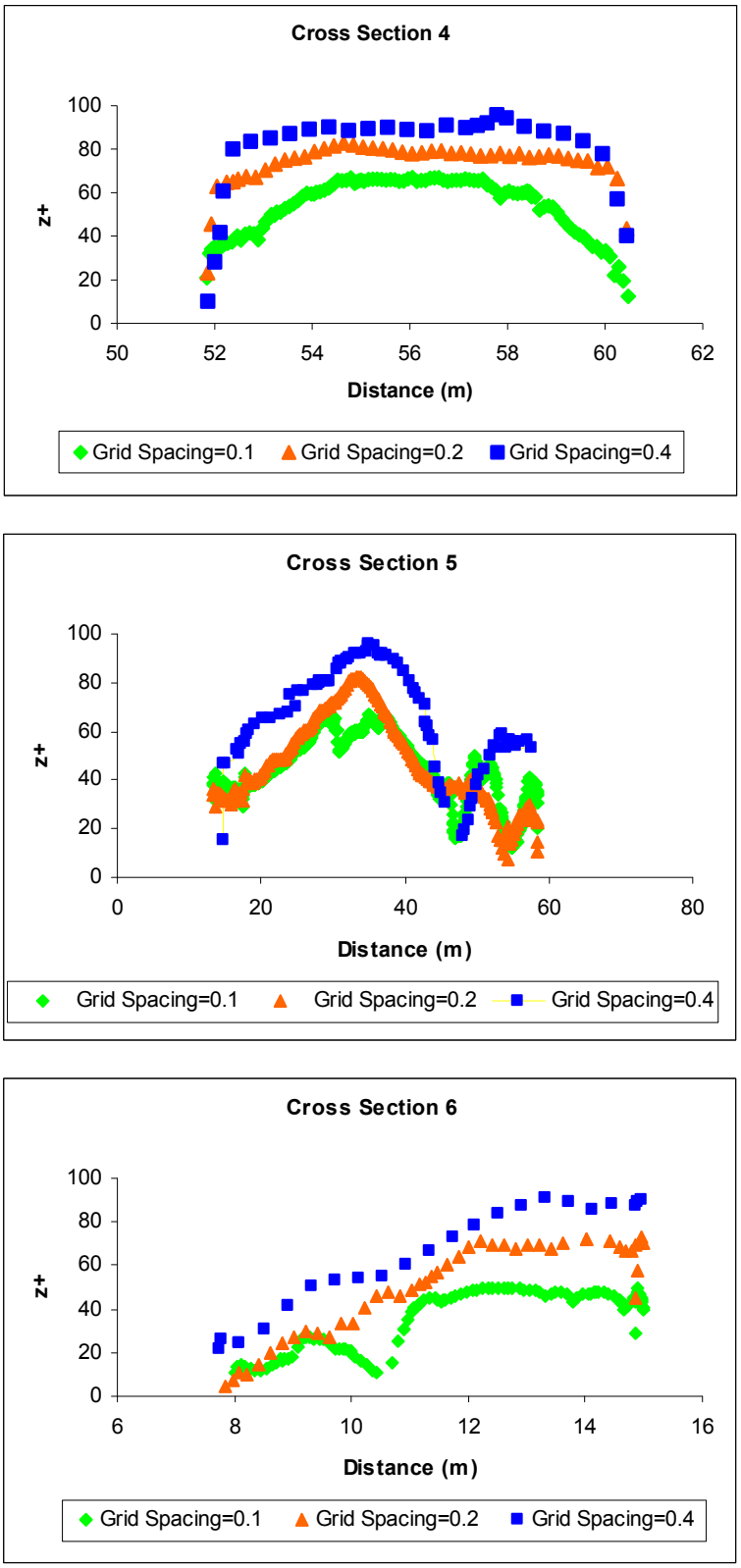

Figure 4.3: Investigation of various grid resolutions in relation to the wall functions employed, for cross-sections 4, 5, and 6.

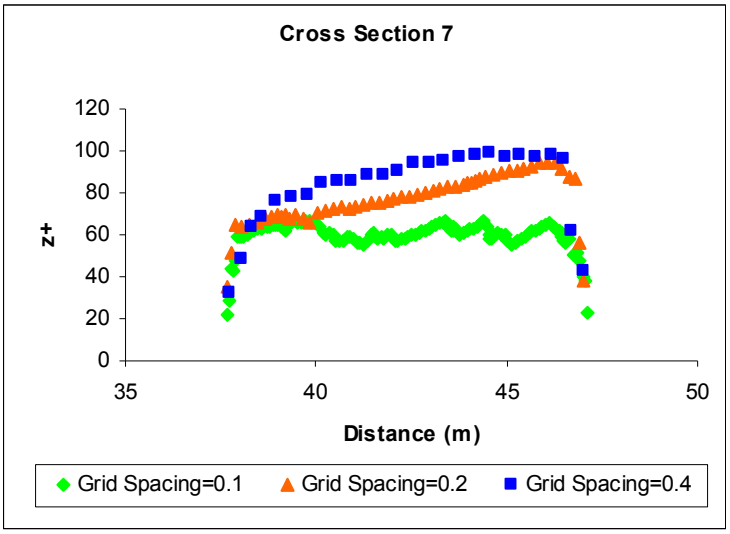

Figure 4.4: Investigation of various grid resolutions in relation to the wall functions employed, for cross-section 7.

The most important activity in verification is systematically refining the grid size and time step to a point where successive refinement ceases to influence the solution. However, for the simulation of river channel available computer hardware is often a limiting factor in determining the number of elements that can be used. Although CFD models have been applied in fluvial geomorphology, there are still few formal frameworks for the systematic verification of numerical models. In this study two approaches were employed to address the issue of grid discretisation verification. First, the simulated flow velocities obtained from the different mesh resolutions were directly compared to each other using data from selected cross-sections. Next, as a more formal metric of grid independence, the Grid Convergence Index (GCI) concept introduced by *Roache*, (1997, 1998) and mentioned in Chapter 2 was employed. The GCI technique provides an objective and reliable method for the determination of truncation error in CFD applications.

The comparison of predicted flow velocities was undertaken in the form of a scattergraph, using the three different grid spacings for the seven arbitrarily selected cross-sections (Figures 4.5 to 4.7). More specifically, model runs using grid spacings of 0.4 m, and 0.2 m were compared with calculations produced from the 0.1 m grid spacing

run. Although the simulated flow velocities using the different grid spacings do not always match perfectly, the agreement is generally good, providing some statistical support for grid independence of the results. For example, there is good qualitative correlation between velocities calculated on grids using 0.4 m, and 0.2 m versus 0.1 m resolution grids (average R^2 =0.90 for the 0.4 m versus the 0.1 m grids and average R^2 =0.89 for the 0.2 m versus the 0.1 m grids).

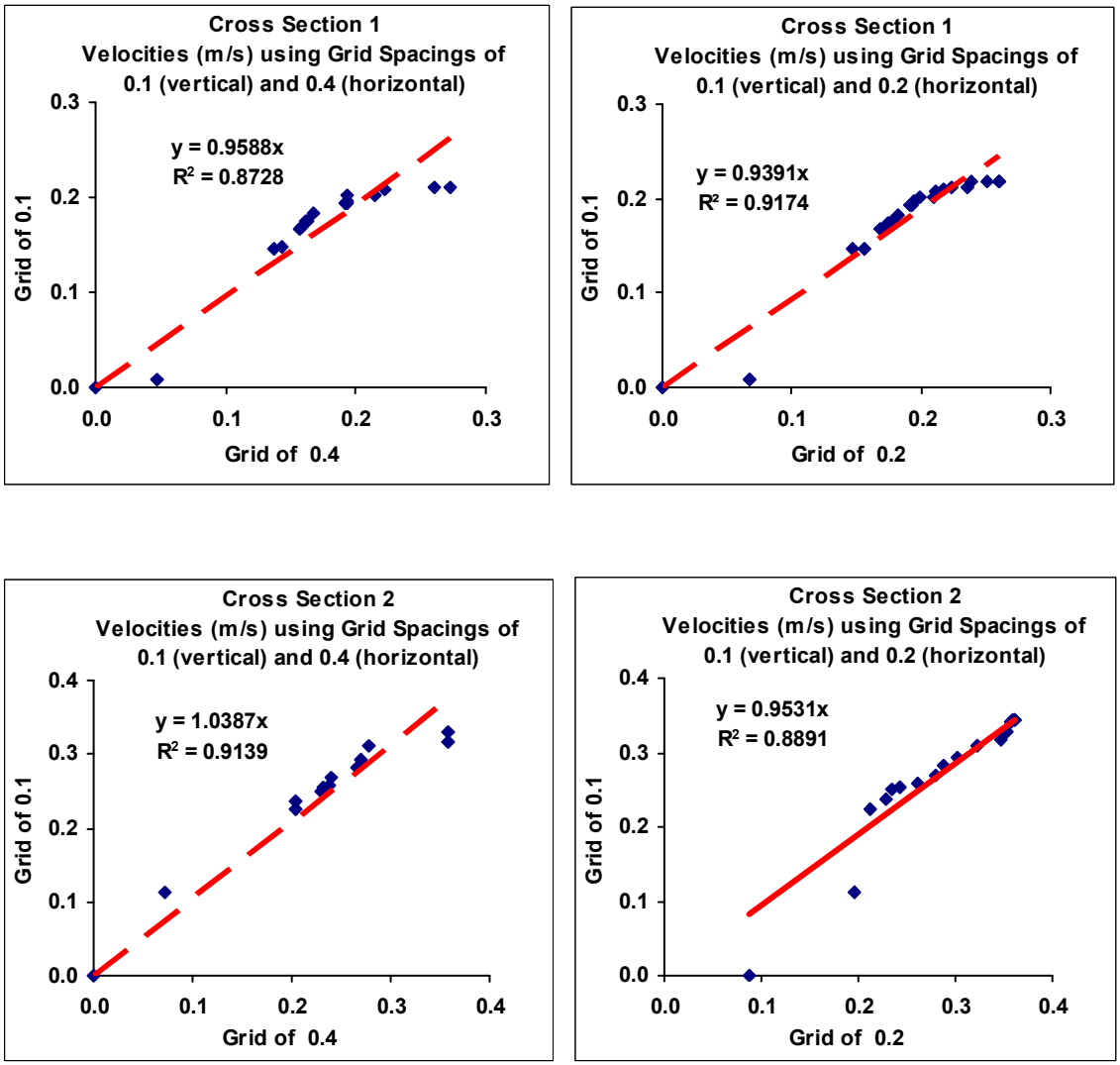

Figure 4.5: Correlation between flow velocities calculated on grids using 0.4, 0.2, and 0.1 m grid for cross-sections 1 and 2. Plots show the correlation between the first two (i.e. coarse) meshes relative to the solution calculated using the finer grid spacing of 0.1 m.

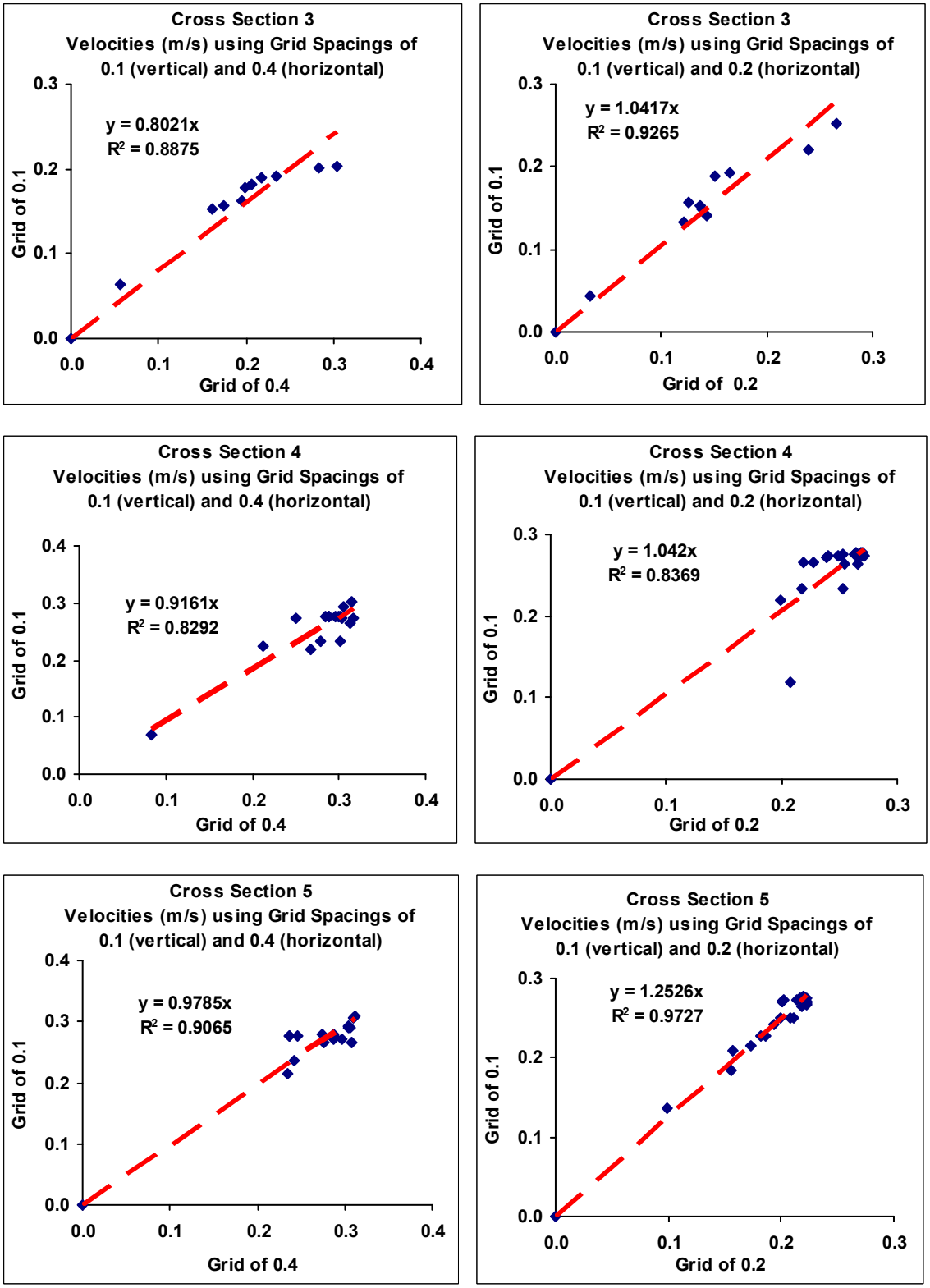

Figure 4.6: Correlation between flow velocities calculated on grids using 0.4, 0.2, and 0.1 m grid for cross-sections 3, 4, and 5. Plots show the correlation between the first two

(i.e. coarse) meshes relative to the solution calculated using the finer grid spacing of 0.1 m.

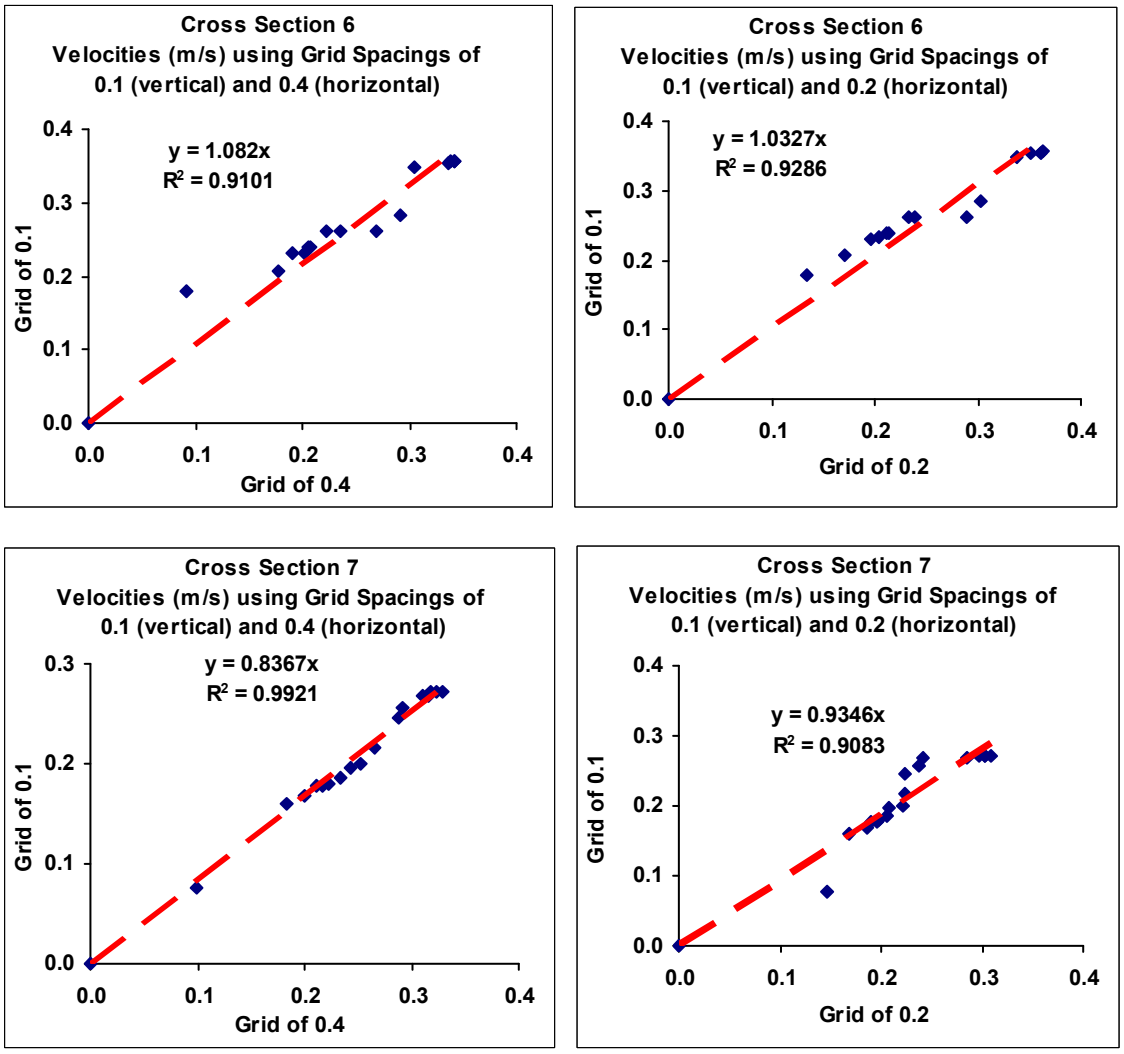

Figure 4.7: Correlation between flow velocities calculated on grids using 0.4, 0.2, and 0.1 m grid for cross-sections 6 and 7. Plots show the correlation between the first two (i.e. coarse) meshes relative to the solution calculated using the finer grid spacing of 0.1 m.

However, as will be shown below, the scattergraphs can only be used to evaluate the flow velocity outputs from the models, whereas the GCI approach provides a more comprehensive approach to grid verification. The GCI can be applied for a single point on a numerical mesh, for an assembly of points, or for an entire mesh. Moreover, it can be estimated for all variables of interest. Perfect mesh independence can be achieved

when the GCI equals to zero. However, this is not usually feasible because of numerical rounding errors.

GCI is used to estimate the uncertainty associated with the solution at a particular grid resolution and subsequently to report the credibility of the simulations (*Hardy et al*., 2003) and is based on the theory of generalized *Richardson* extrapolation. This theory assumes that, within a certain radius of convergence *r*, the discrete solution for some flow variable *f* converges monotonically at all points in the continuum as the grid spacing *h* tends to zero (*Roache*, 1997). The error is given by a power series in *h*:

$$f = f_x + g_1 h + g_2 h^2 + g_3 h^3 + \ldots \qquad (4.1)$$

where f_x denotes the exact solution and *g* is defined in the continuum which is not dependent on the discretisation.

For a solution method accurate to order *p*, equation (*4.1*) can be modified as follows:

$$f = f_x + g_p h^p + (higher - order - terms) \qquad (4.2)$$

If two such solutions exist, f_1 on a fine grid of resolution h_1 and f_2 on a coarser grid of resolution $h_2 = r\, h_1$, then equation (*4.2*) is given as:

$$f_x = f_1 + (f_1 - f_2)/(r^p - 1) \qquad (4.3)$$

Error estimates for the two solutions are acquired by the following equations when neglecting higher-order terms:

$$E_1 = f_x - f_1 = \frac{\varepsilon}{(r^p - 1)} \qquad (4.4)$$

$$E_2 = f_x - f_2 = \frac{\varepsilon r^p}{\left(r^p - 1\right)} \tag{4.5}$$

where $\varepsilon = f_1 - f_2$. Equations (*4.4*) and (*4.5*) correspond to fine and coarse grids, respectively.

When a second-order solver is employed, equations (*4.4*) and (*4.5*) are modified as follows:

$$E_1 = \frac{\varepsilon}{3} \tag{4.6}$$

$$E_2 = \frac{4\varepsilon}{3} \tag{4.7}$$

Equations (*4.6*) and (*4.7*) represent absolute errors and can be expressed as absolute percentages. GCI for a particular grid was defined by *Roache* (1997) as the error estimate multiplied by a factor of safety, F_s, and is given by the following equations:

$$GCI_{Fine} = F_s \left| E_1 \right| \tag{4.8}$$

$$GCI_{Coarse} = F_s \left| E_2 \right| \tag{4.9}$$

The factor of safety is recommended to be 3 for comparisons of two grids and 1.25 for comparisons over three or more grids. The higher factor of safety is recommended for reporting purposes and is quite conservative of the actual errors, being similar to the 99.9% statistical confidence interval. When the true solution is unknown the only way to establish that a given solution is within a radius of convergence, and to estimate the effective order of solution accuracy, is to compare it with solutions on two or more other grids and check that *E*, and consequently GCI, scales as a power function of *r*. In the case of three grids, named from 1 (finest) to 3 (coarsest), equation (*4.3*) is modified as follows:

$$\frac{\varepsilon_{23}}{\varepsilon_{12}} = \frac{r_{12}^{p}\left(r_{23}^{p} - 1\right)}{\left(r_{12}^{p} - 1\right)} \tag{4.10}$$

where $\varepsilon_{23} = f_2 - f_3$, $\varepsilon_{12} = f_1 - f_2$, $r_{23} = h_3 / h_2$, and $r_{12} = h_2 / h_1$

Equation (*4.10*) can be solved for p, either iteratively or directly as follows:

$$p = \frac{\ln\left(\frac{\varepsilon_{23}}{\varepsilon_{12}}\right)}{\ln r} \qquad \text{if } r_{12} = r_{23} = r \tag{4.11}$$

In the current study, a GCI analysis was performed to ascertain that the solution from the grid resolution was independent of the grid spacing. This was confirmed by creating three different grids for the Low Flow Event (LFE). The first relatively coarse grid constructed for the River Asker consists of 73,441 cells using a grid spacing of 0.4 m. Further refinement was undertaken to create a second grid consisting of 344,858 cells using a grid spacing of 0.2 m and a third grid consisting of 2,148,510 cells using a grid spacing of 0.1 m. The GCI analysis was performed between the coarse and intermediate resolution grids and the intermediate and fine resolution grids. The GCI values presented in Table 4.1 were obtained using a factor of safety of 1.25.

The low GCI values obtained between the fine and intermediate resolution meshes indicate that both the fine and intermediate resolution grids are suitably verified for the three components of velocity (Table 4.1). However, the convergence for the turbulence parameters is generally poor with relatively high GCI values reflecting the large amount of shear present within the reach and the fact that at the grid resolutions examined the turbulence model used (standard k-ε model) is unable to fully capture this intense shear process.

Table 4.1: GCI results in percentage terms for velocity components in *x*, *y*, and *z* directions, turbulent kinetic energy, and turbulent dissipation rate.

Variable	GCI Analysis	
	Fine Grid / Intermediate Grid	**Intermediate Grid / Coarse Grid**
X Velocity Component	4.38	14.22
Y Velocity Component	5.36	9.34
Z Velocity Component	4.84	8.14
Turbulent Kinetic Energy	22.30	35.40
Dissipation Rate	17.38	30.68

The mesh with a grid spacing of 0.1 m (fine grid) was therefore employed to generate all the results described in the following subchapters, since it produces a sufficiently independent solution.

4.1.2 Validation

The conventional approach to model validation relies upon a comparison of predictions with empirical measurements, with tests for goodness of fit, precision and accuracy (*Lane and Richards*, 2001). However, all models corresponding to open systems can be misrepresented since they require some form of closure. In addition, appreciable uncertainties in both field data and model predictions can be considered as a limiting factor when a model validation is carried out.

The boundary conditions and parameters used in a model are defined by applying theoretical reasoning, empirical measurement or informed knowledge. Each of the above approaches may include error or uncertainty. An understanding of the consequences of this uncertainty can be analysed through sensitivity analysis (*Lane et al*., 1994b) by using the Monte Carlo or generalised likelihood uncertainty estimation approaches (*Beven and Binley*, 1992), where combinations of input data are varied and sensitivity of output examined. However, the assessment and validation of model performance in this thesis initially considers the development and assumptions applied in each application and uses spatially distributed flow velocity data for validating model performance without carrying out any sensitivity analysis.

Before flow structures are analysed using CFD models it is necessary to validate the solution against measured flow properties. In the current study this is achieved by comparing measured and predicted values of the velocity magnitude calculated from two velocity components. Velocity measurements were carried out at spatially distributed locations within the River Asker reach to obtain data with which to validate the CFD model. The characteristics of these measured flow velocity data, which corresponds to the Low Flow Event happened on 5th January 2004 are given in Appendix I. The latter data represent the basis for comparing some measured and predicted velocity magnitudes at various locations through the studied reach.

The comparisons are made at 65 field measurement positions. Each position corresponds to a vertical rod consisting of three points with the same the eastings and northings but, with a range of different elevations. Velocity measurements were undertaken by fixing the Electromagnetic Current Meter (ECM) at these three separate heights along each vertical. Most of the field measurements were carried out, for each position, at *Z/H* values, where Z is the local flow depth of the measurement and H represents the total flow depth at that position, of 0.2, 0.6, and 0.8 with some variance for specific points. The above procedure provided a well-distributed sample of 195 points within the studied reach.

Before choosing the appropriate turbulence model several runs were executed, in which the use of almost all the available turbulence closures within *Fluent 6.2* were compared. This was done to define the significance of the different turbulent closures when simulating flows in rivers. More specifically, the simulations were carried out by employing four different models, namely, the standard k-ε, the *RNG* k-ε, the standard k-ω, and the *SST* k-ω. The results were compared with the field data. These comparisons, shown in Figures 4.8 to 4.11, correspond to ten measurement positions located in the upstream and midstream areas of the River Asker reach shown in Figure 4.13.

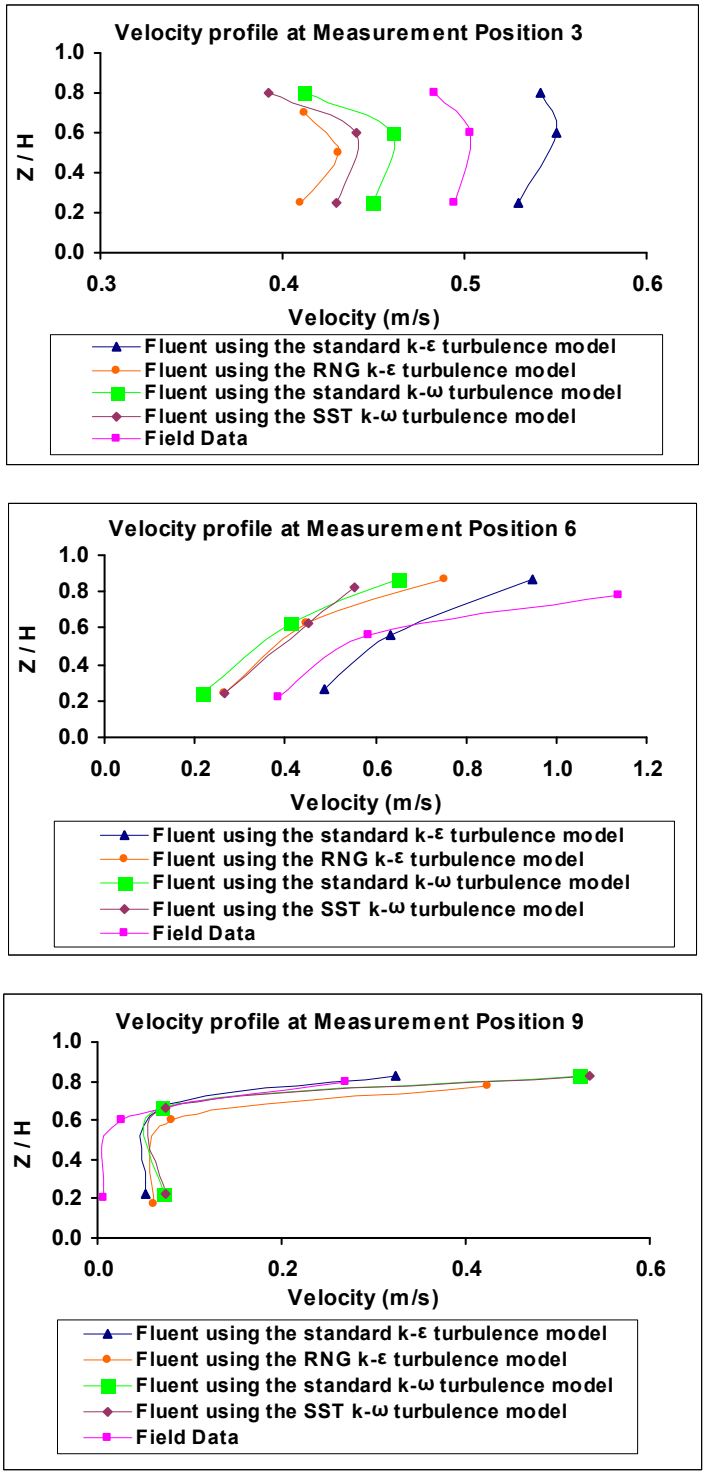

Figure 4.8: Comparison of observed versus predicted flow velocity profiles by using all the available turbulence closures within *Fluent 6.2* at measurement positions 3, 6, and 9.

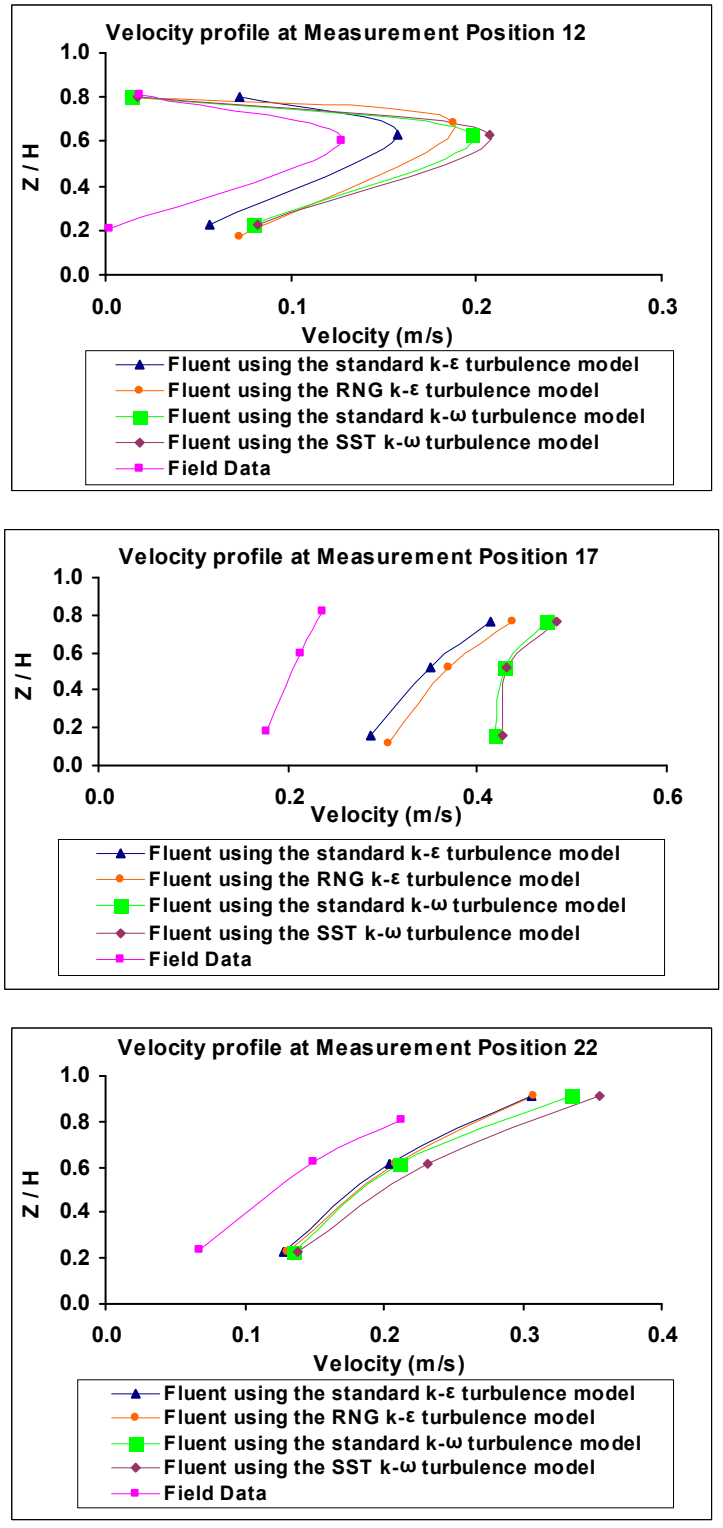

Figure 4.9: Comparison of observed versus predicted flow velocity profiles by using all the available turbulence closures within *Fluent 6.2* at measurement positions 12, 17, and 22.

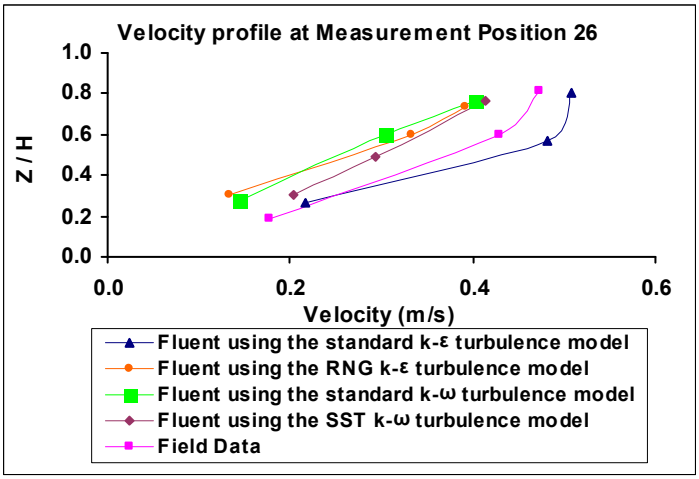

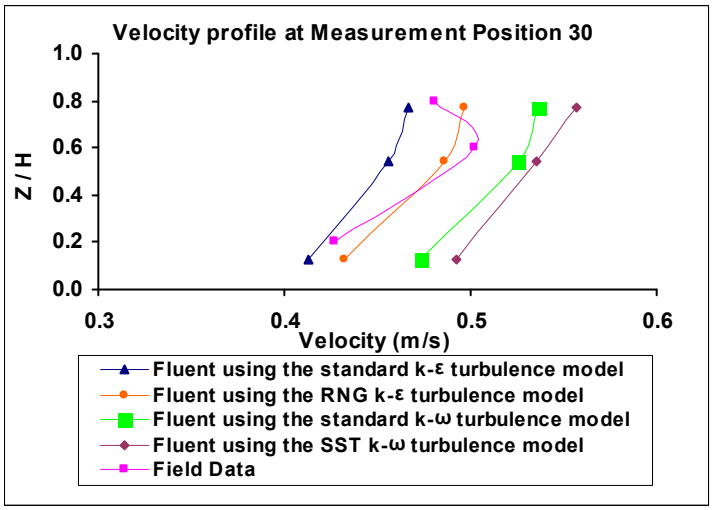

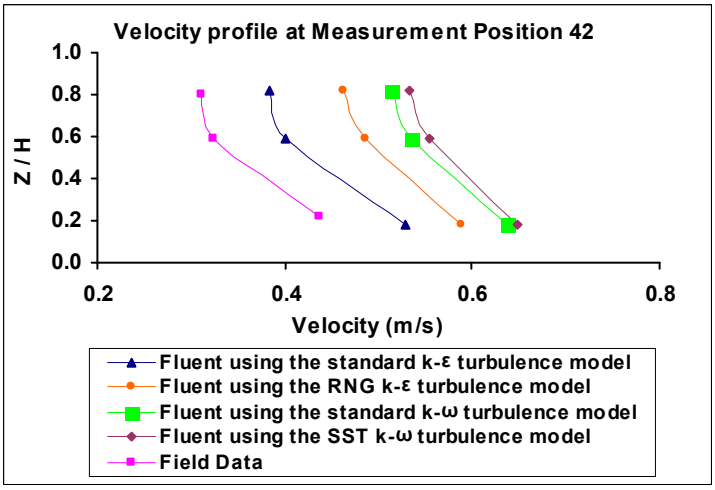

Figure 4.10: Comparison of observed versus predicted flow velocity profiles by using all the available turbulence closures within *Fluent 6.2* at measurement positions 26, 30, and 42.

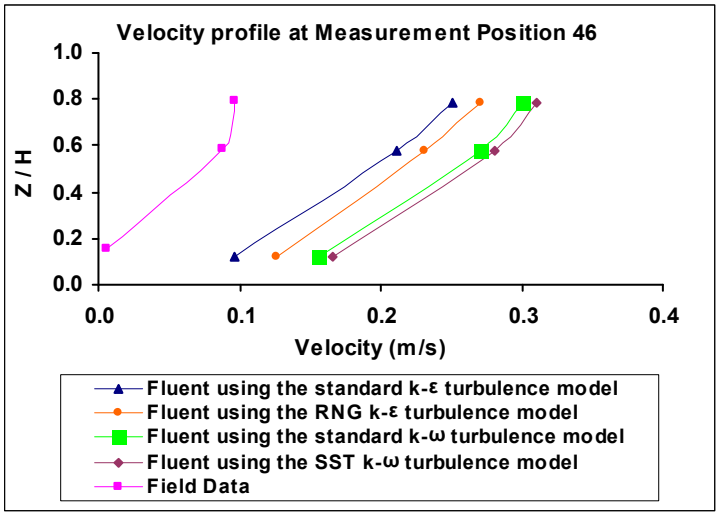

Figure 4.11: Comparison of observed versus predicted flow velocity profiles by using all the available turbulence closures within *Fluent 6.2* at measurement position 46.

In addition, a comparison of predicted versus observed velocities in the form of a scattergraph, using the four different turbulence models for all measurement positions throughout the reach, was undertaken in the global analysis shown in Figure 4.12.

The latter analysis revealed that the results obtained using the standard k-ε turbulence model give the best fit compared to the field data. In all the subsequent results presented herein turbulence was, therefore, modeled using a standard k-ε model.

The predicted versus observed flow velocity magnitude profiles at ten measurement positions, selected to cover a large area of the monitored reach in the upstream and midstream areas, are presented in Figures 4.14 through 4.17. In addition, profiles of the downstream and transverse flow velocity components at those ten measurement positions are also illustrated in Figures 4.18 to 4.21 and Figures 4.22 to 4.25, respectively. Only a limited number of flow velocity profiles are presented in the main body of the thesis for reasons of clarity. However, the whole set of velocity profiles, including those of the downstream and transverse velocity components for all measurement positions are illustrated in Appendix V, while their location is shown in Figure 4.13.

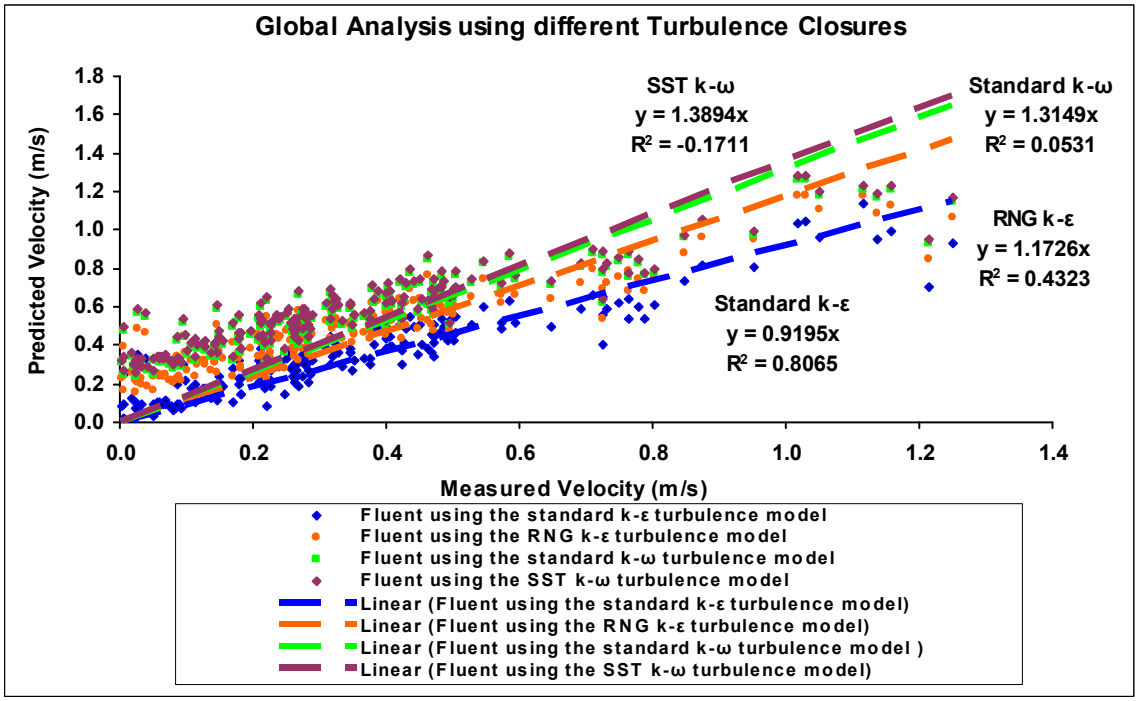

Figure 4.12: Global analysis of predicted versus observed velocities in the form of a scattergraph using the four different turbulence models for all measurement positions.

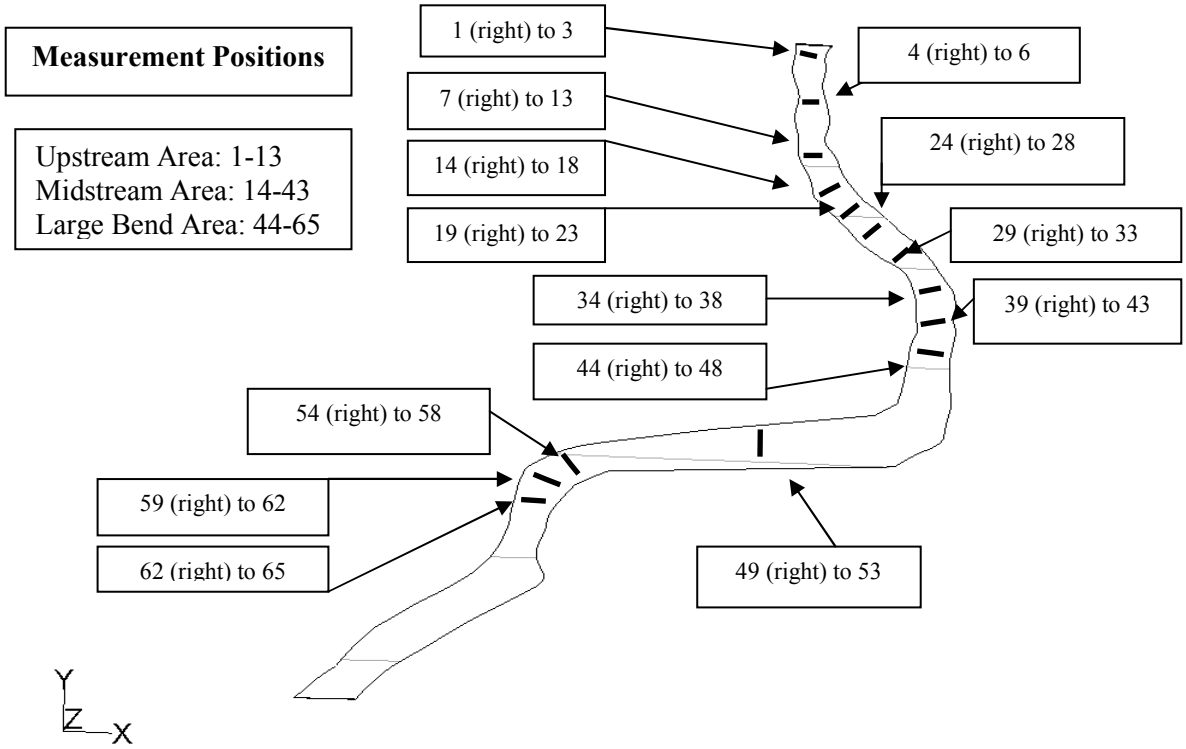

Figure 4.13: Locations of the 65 measurement positions.

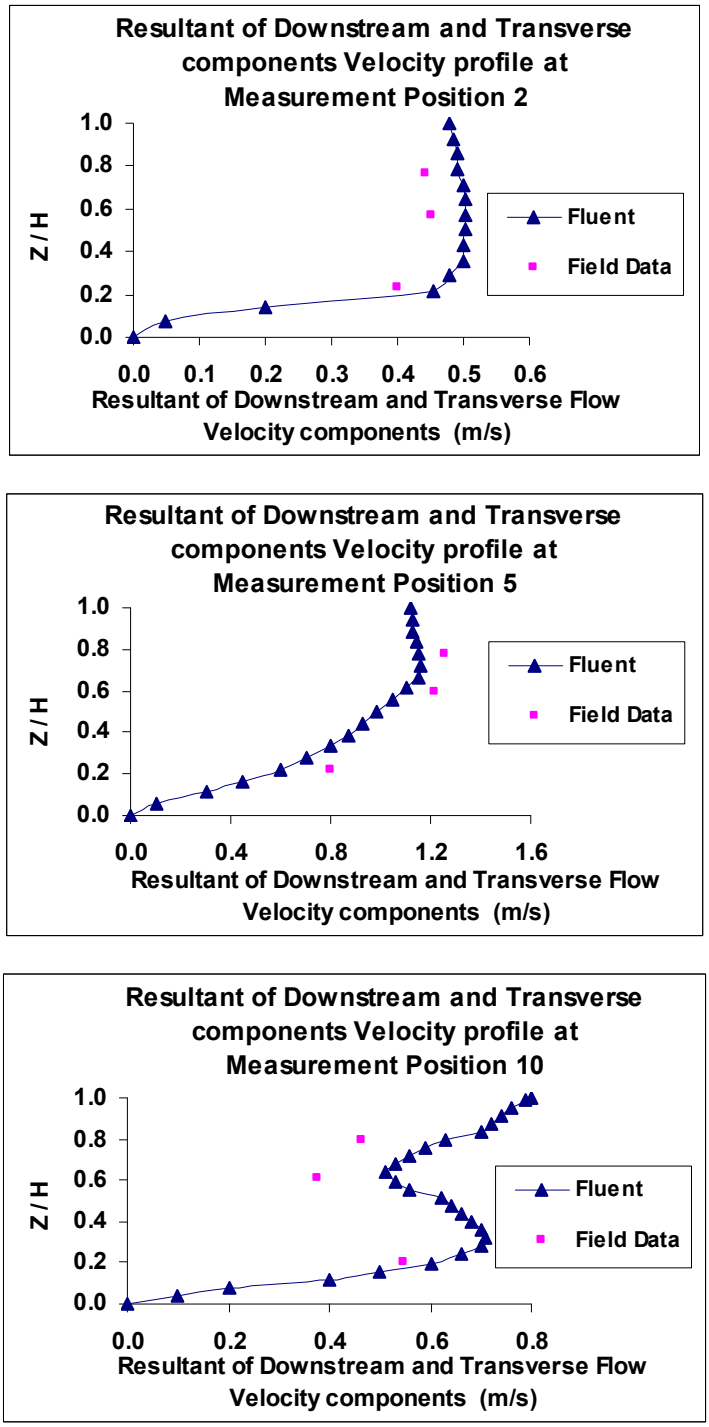

Figure 4.14: Predicted versus observed resultant of downstream and transverse flow velocity components at measurement positions 2, 5, and 10.

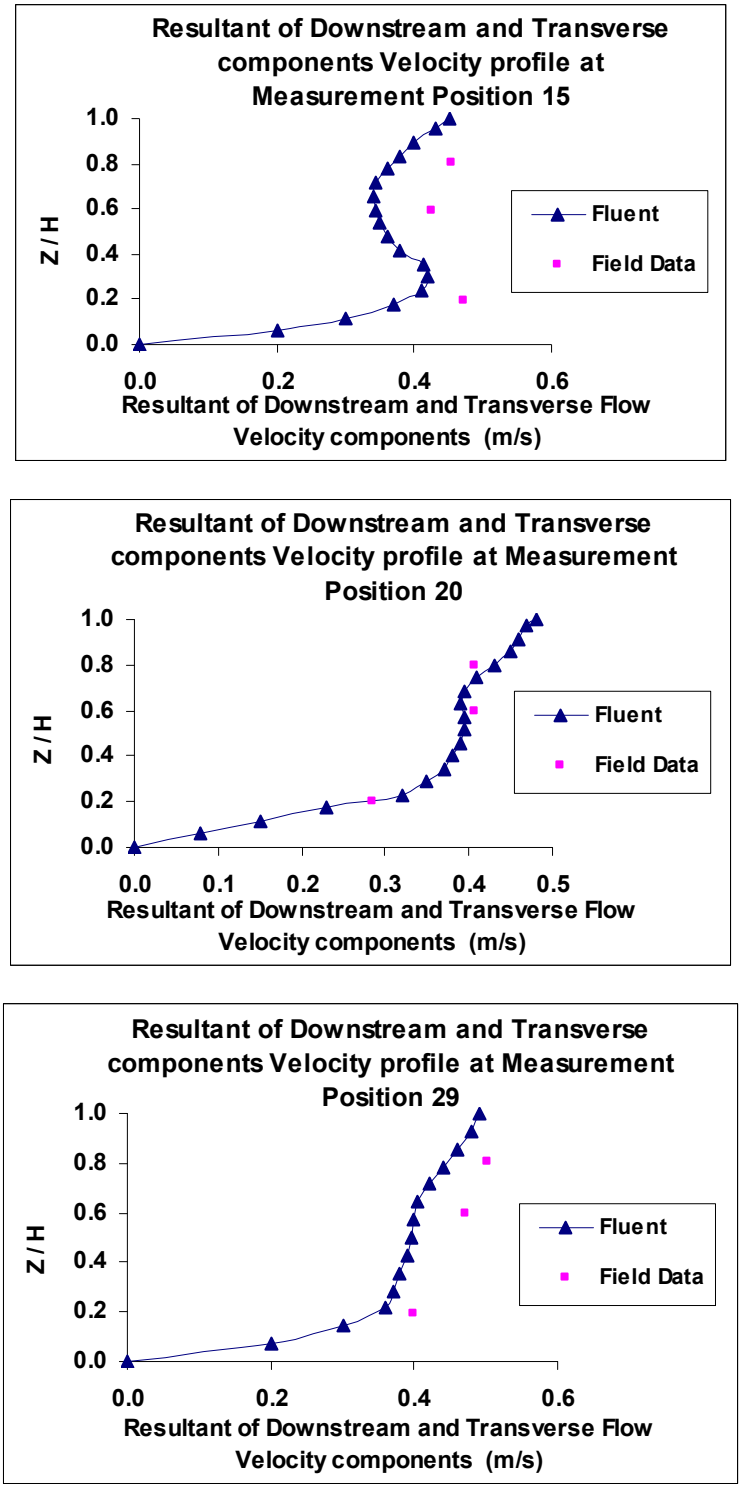

Figure 4.15: Predicted versus observed resultant of downstream and transverse flow velocity components at measurement positions 15, 20, and 29.

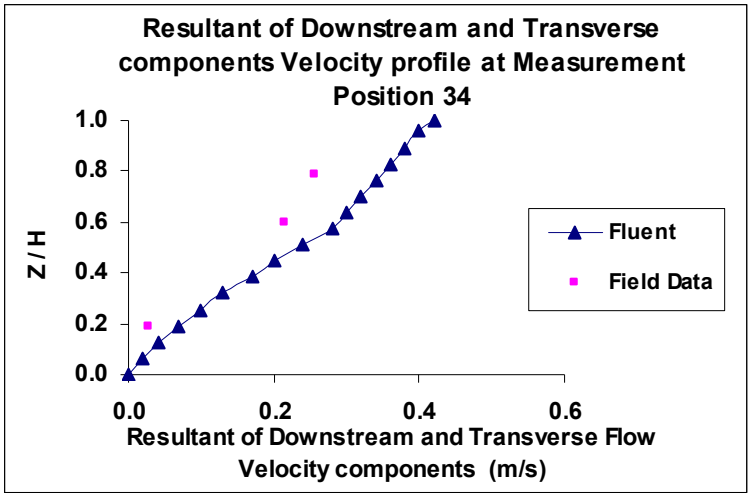

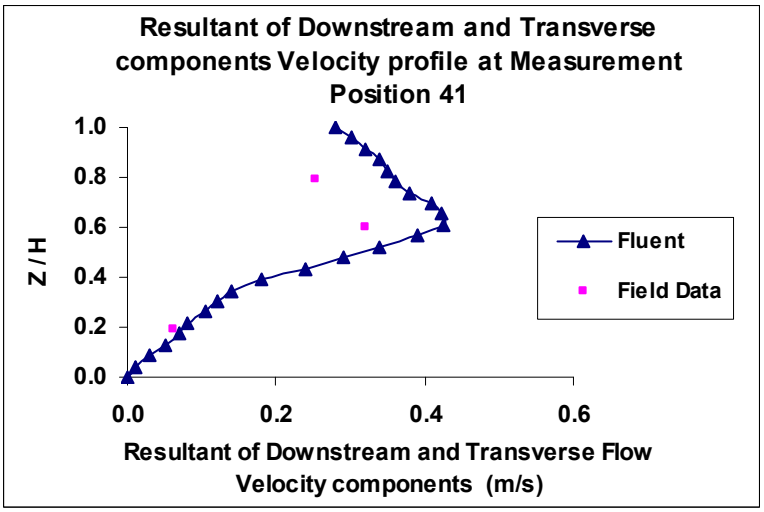

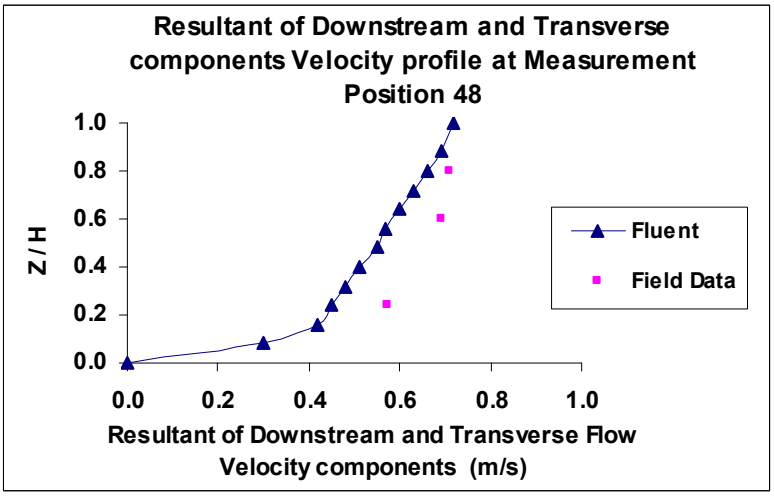

Figure 4.16: Predicted versus observed resultant of downstream and transverse flow velocity components at measurement positions 34, 41, and 48.

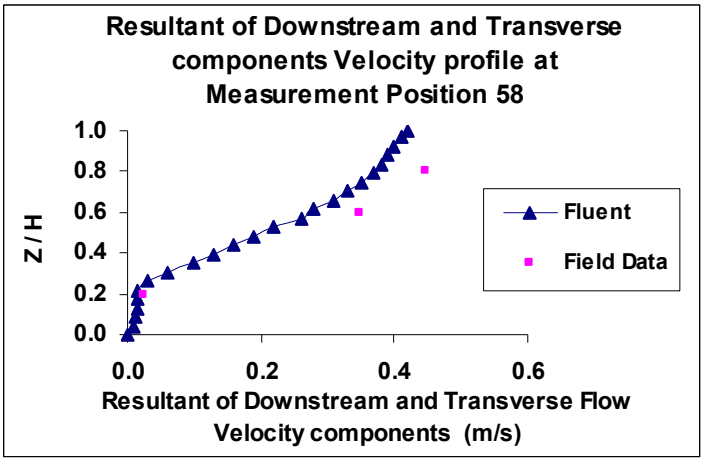

Figure 4.17: Predicted versus observed resultant of downstream and transverse flow velocity components at measurement position 58.

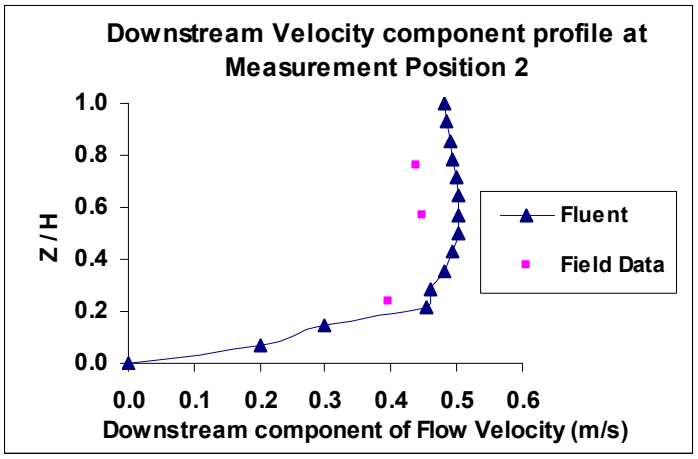

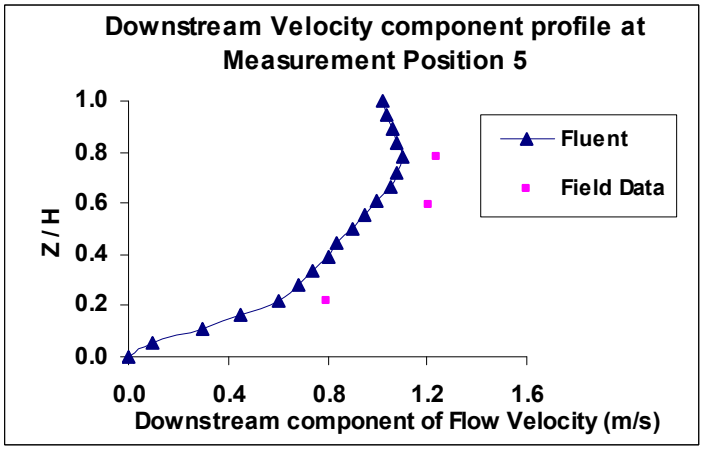

Figure 4.18: Predicted versus observed downstream flow velocity component at measurement positions 2, and 5.

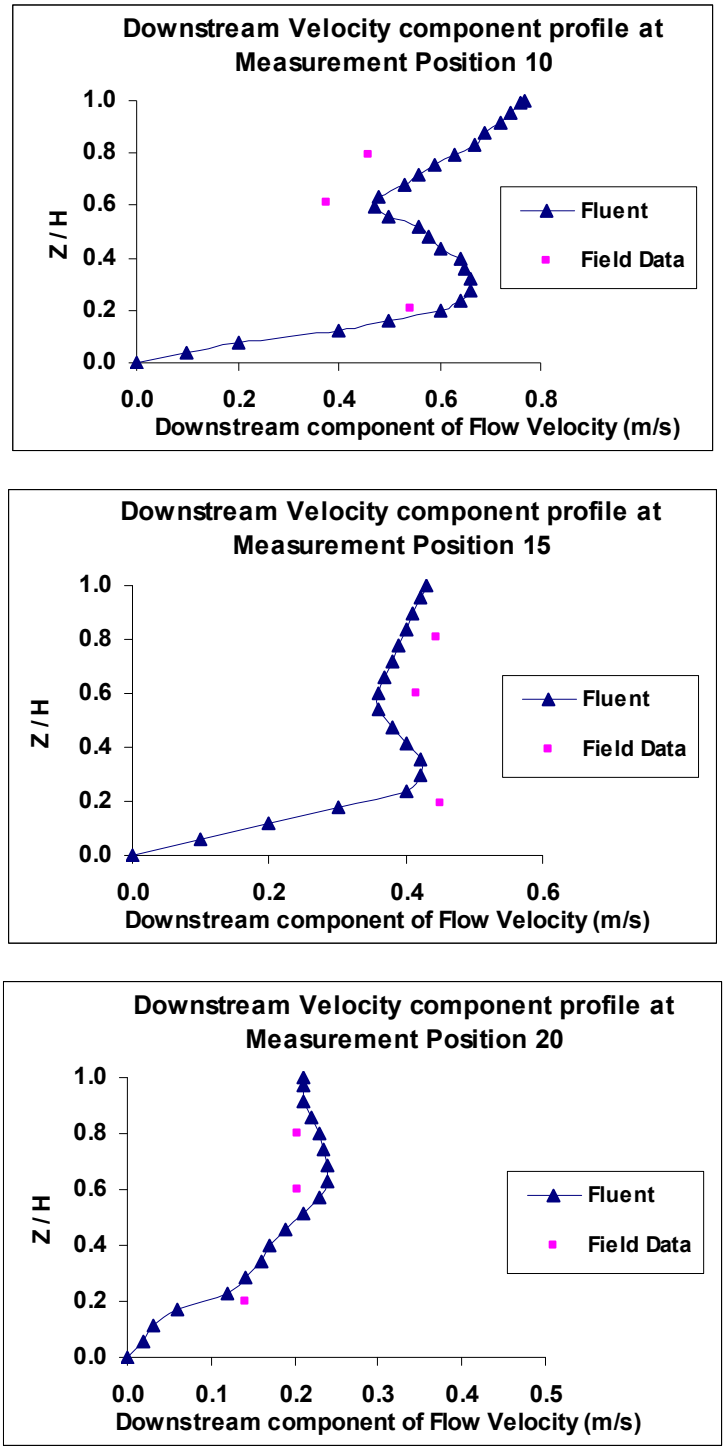

Figure 4.19: Predicted versus observed downstream flow velocity component at measurement positions 10, 15, and 20.

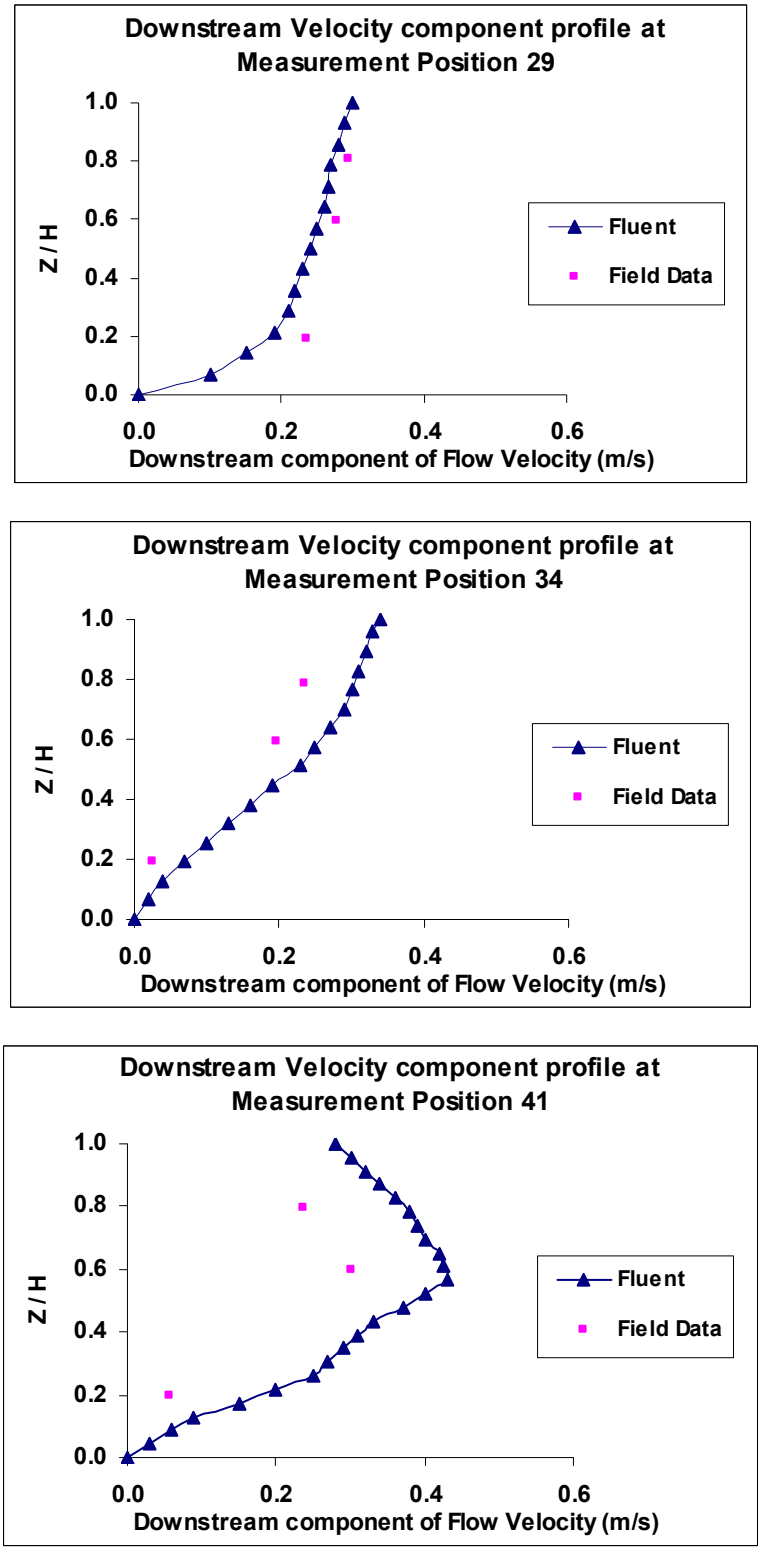

Figure 4.20: Predicted versus observed downstream flow velocity component at measurement positions 29, 34, and 41.

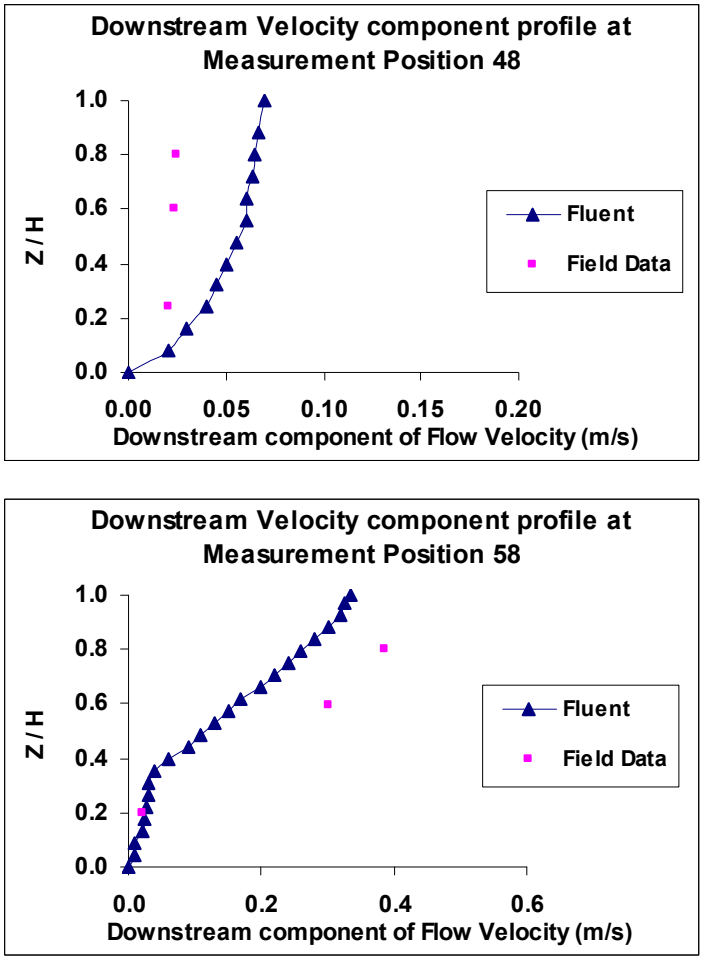

Figure 4.21: Predicted versus observed downstream flow velocity component at measurement positions 48, and 58.

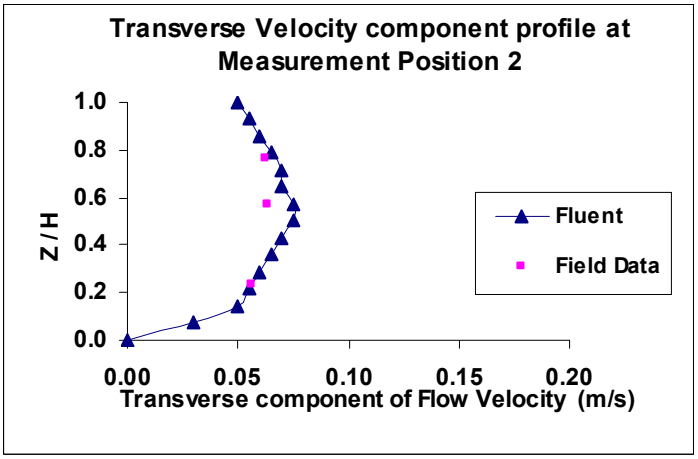

Figure 4.22: Predicted versus observed transverse flow velocity component at measurement position 2.

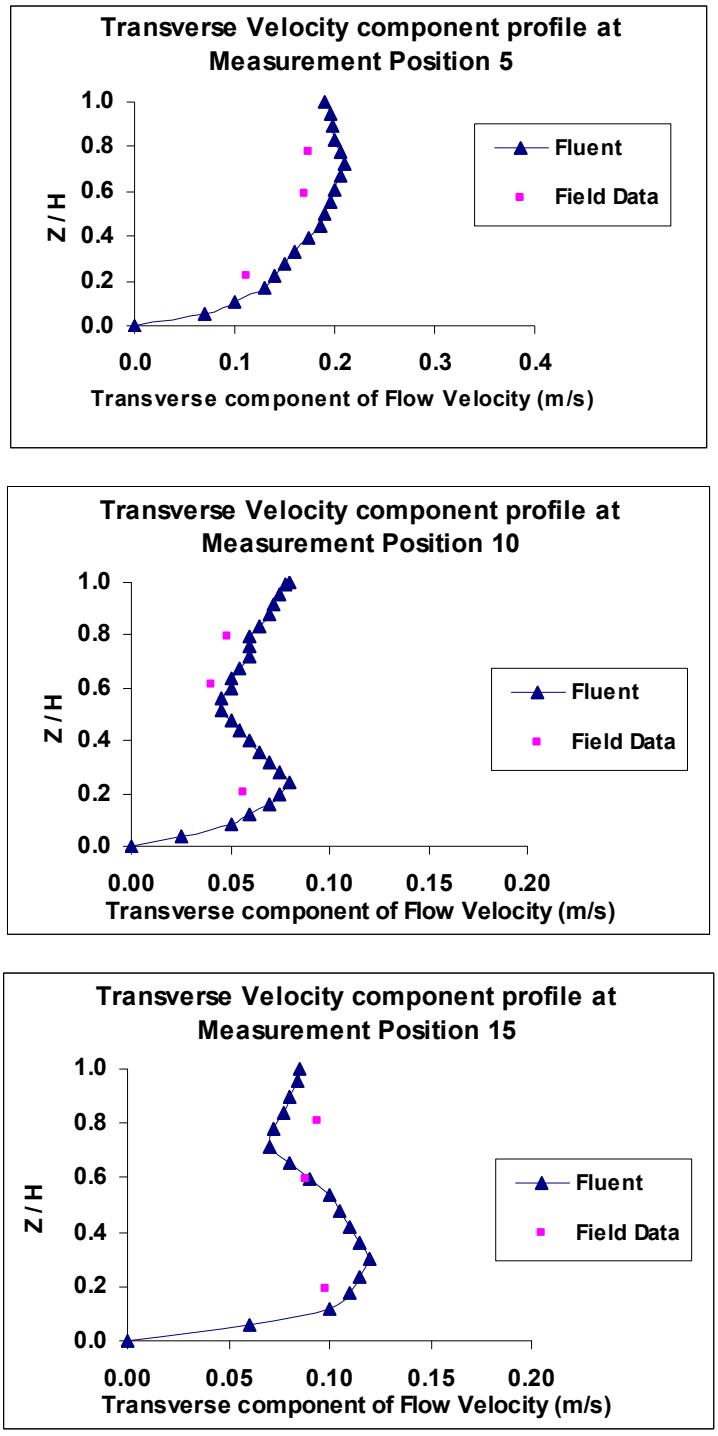

Figure 4.23: Predicted versus observed transverse flow velocity component at measurement positions 5, 10, and 15.

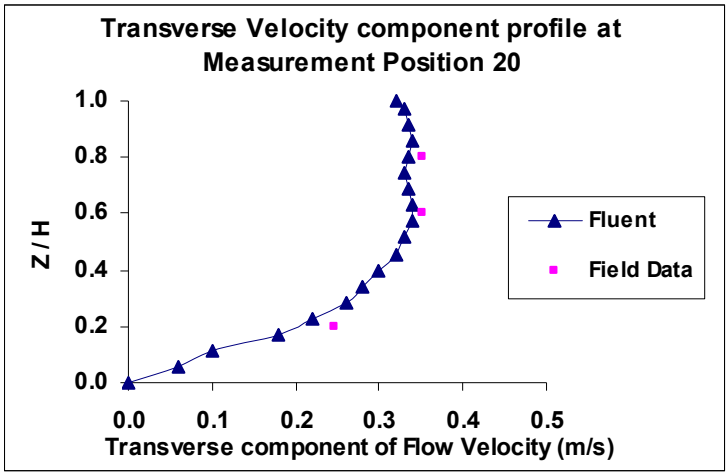

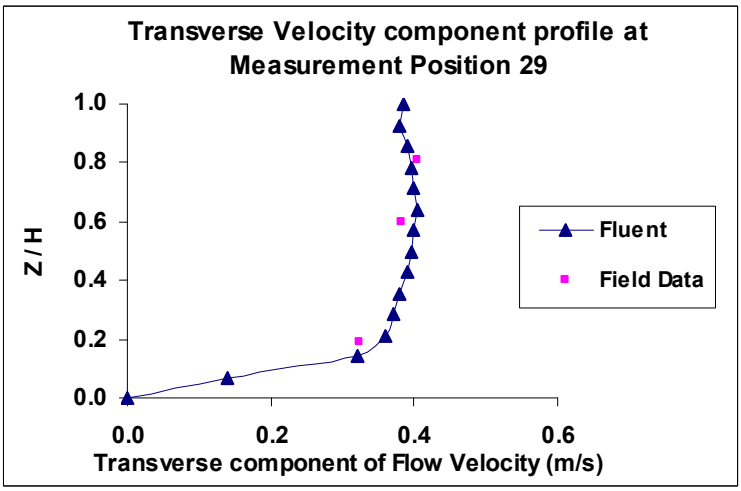

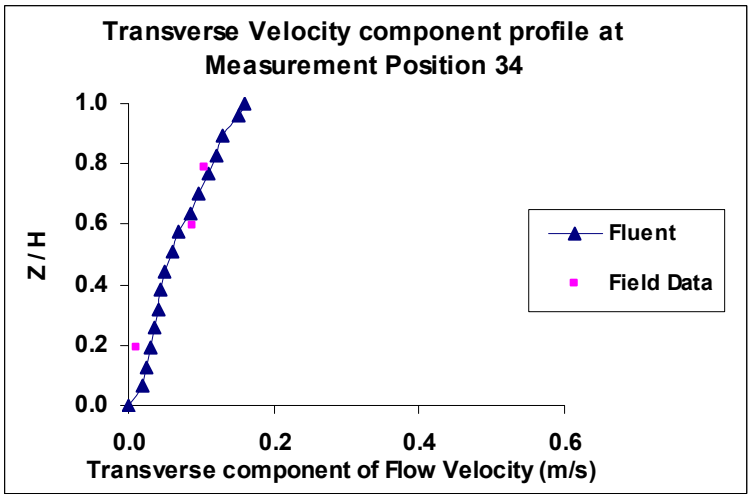

Figure 4.24: Predicted versus observed transverse flow velocity component at measurement positions 20, 29, and 34.

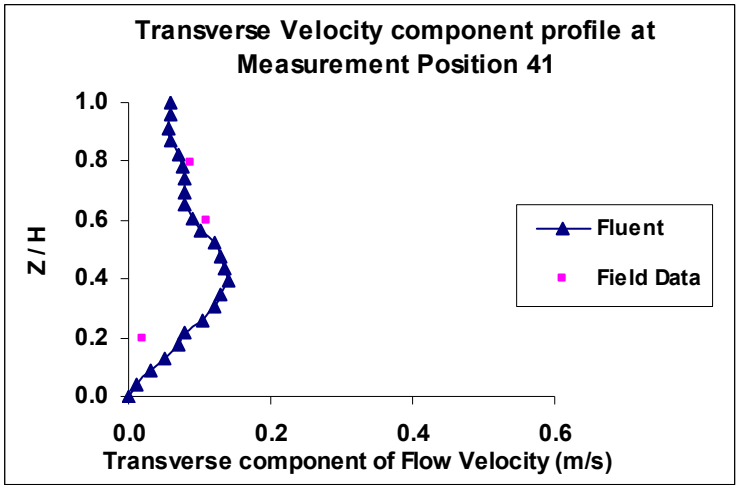

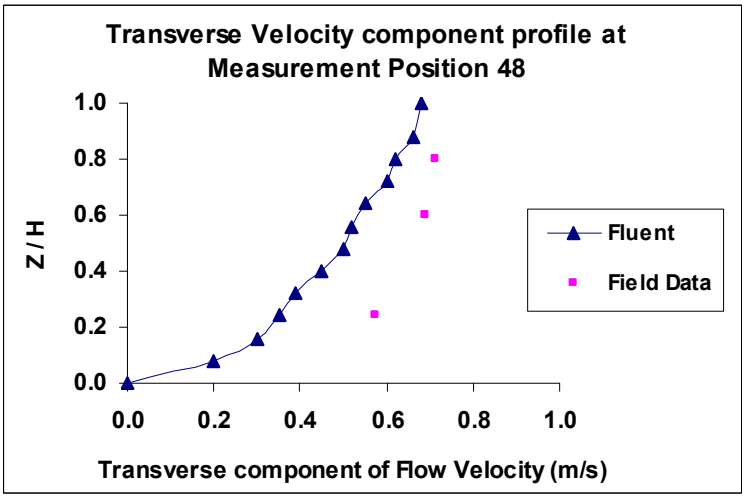

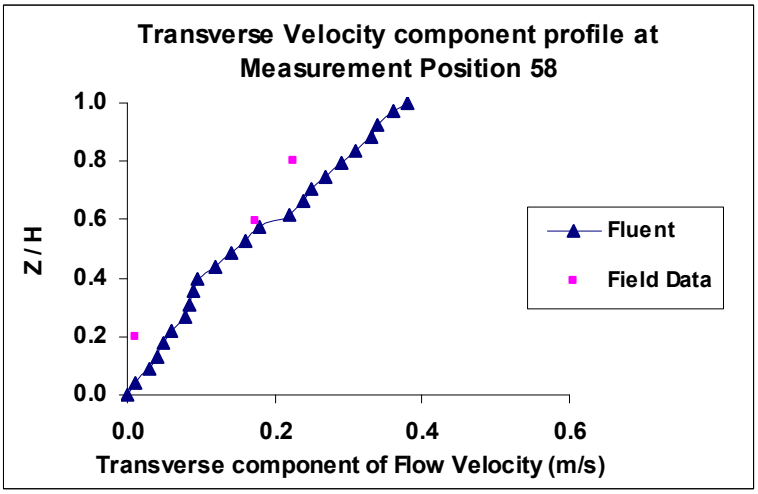

Figure 4.25: Predicted versus observed transverse flow velocity component at measurement positions 41, 48, and 58.

A comparison of predicted versus observed velocity magnitudes of the resultant of downstream and transverse components in the form of a scattergraph for all measurement positions within the study reach, was carried out in the global analysis illustrated in Figure 4.26.

A regional analysis corresponding to three different locations, namely, the upstream area, midstream area, and large bend area is then followed and shown in Figures 4.27 to 4.29. Moreover, both the global and regional analyses were undertaken evaluating the model errors in both the downstream and transverse velocity components, as shown in Figures 4.30 to 4.37. Both the global and regional analyses use three different symbols on each plot to indicate the data points that are at each of the three *Z/H* values, namely, 0.2, 0.6, and 0.8. In this way, any errors as a function of the flow depth can be identified. The above process is important to provide an objective assessment of the overall ability of the model to replicate the observed velocity fields.

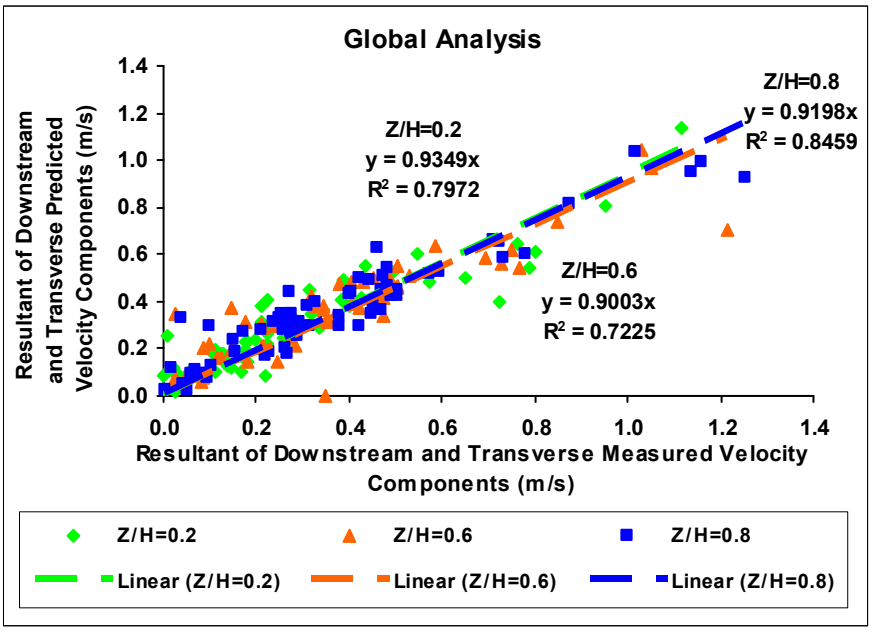

Figure 4.26: Global analysis of predicted versus observed velocity magnitudes of the resultant of downstream and transverse components in the form of a scattergraph corresponding to all measurement positions within the River Asker reach.

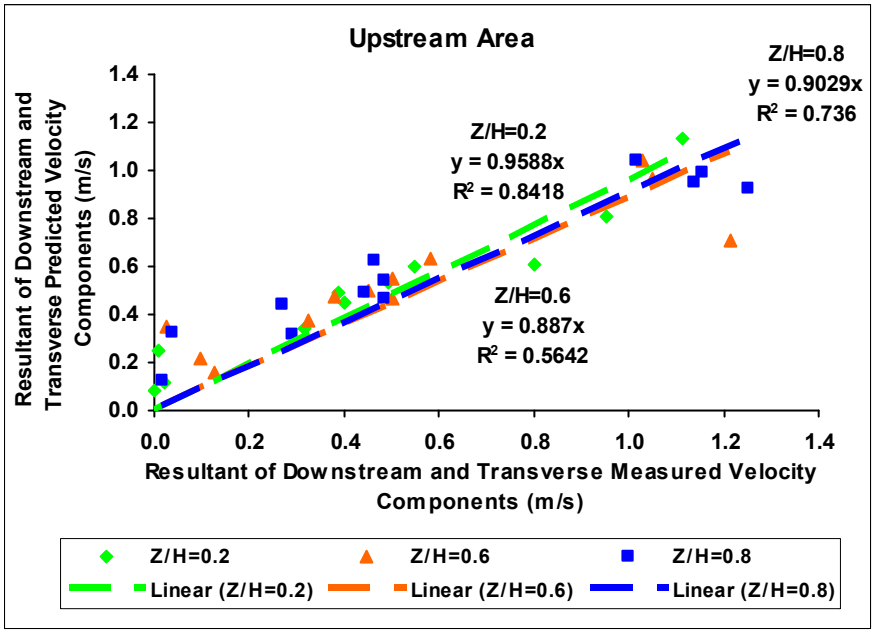

Figure 4.27: Comparison of predicted versus observed velocity magnitudes of the resultant of downstream and transverse components in the form of a scattergraph corresponding to the upstream area.

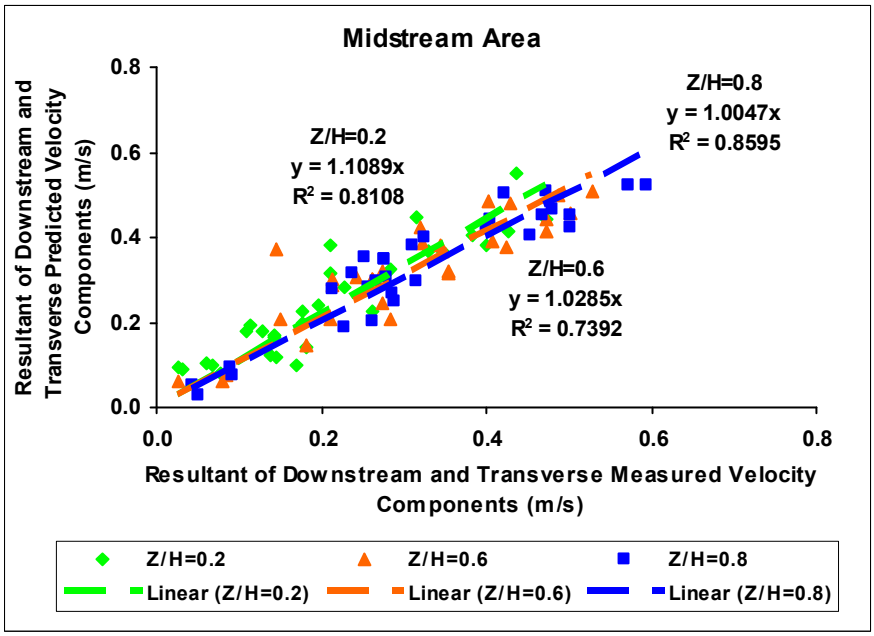

Figure 4.28: Comparison of predicted versus observed velocity magnitudes of the resultant of downstream and transverse components in the form of a scattergraph corresponding to the midstream area.

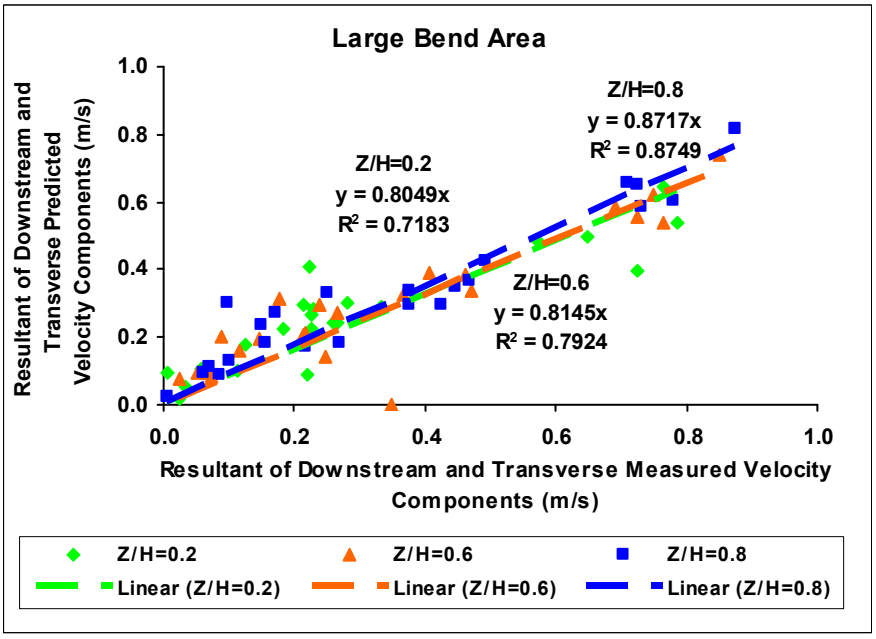

Figure 4.29: Comparison of predicted versus observed velocity magnitudes of the resultant of downstream and transverse components in the form of a scattergraph corresponding to the large bend area.

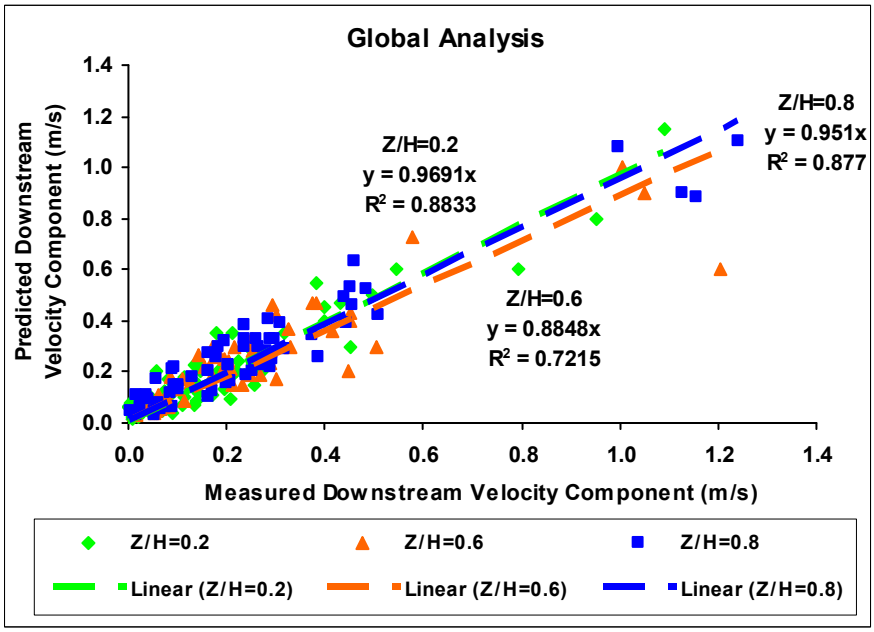

Figure 4.30: Global analysis of predicted versus observed downstream velocity components in the form of a scattergraph corresponding to all measurement positions within the River Asker reach.

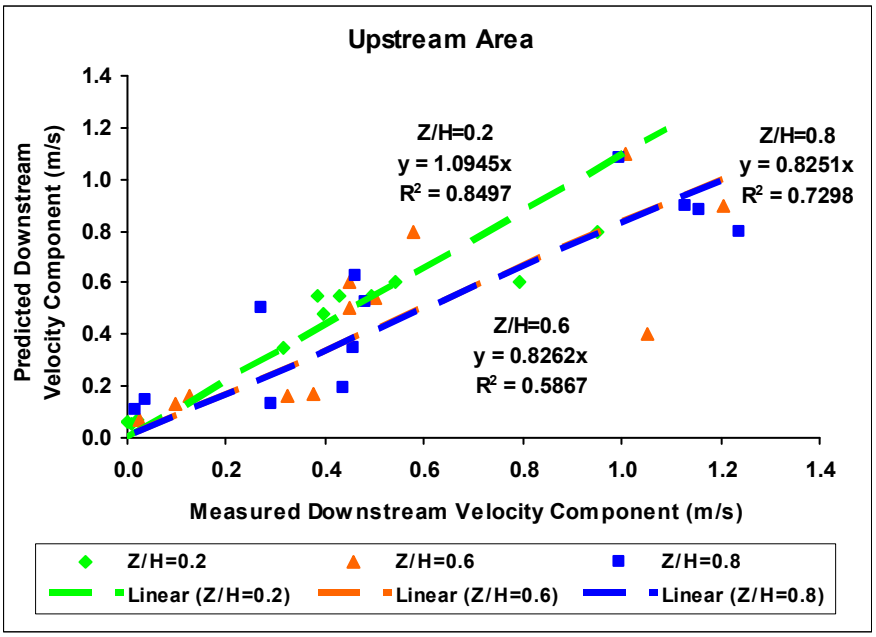

Figure 4.31: Comparison of predicted versus observed downstream velocity components in the form of a scattergraph corresponding to the upstream area.

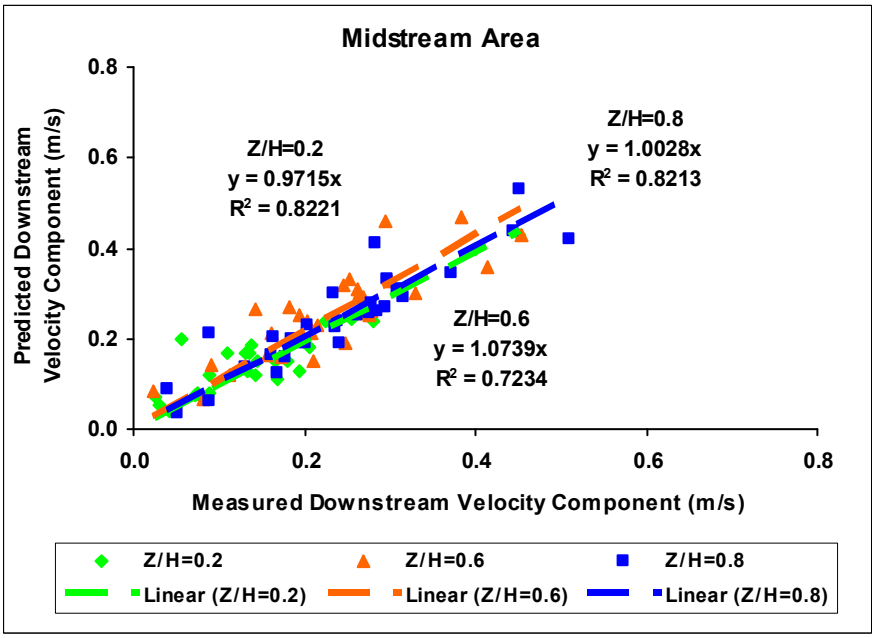

Figure 4.32: Comparison of predicted versus observed downstream velocity components in the form of a scattergraph corresponding to the midstream area.

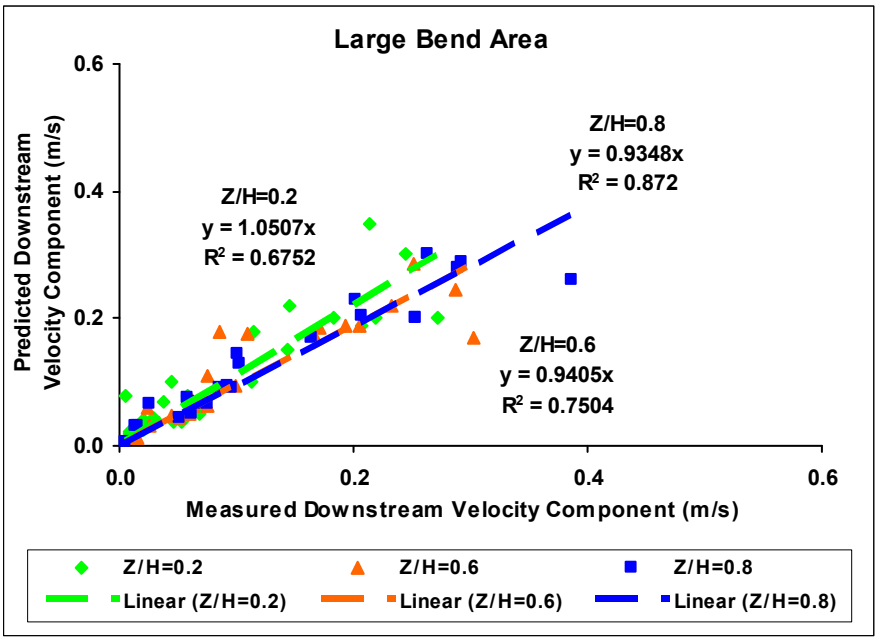

Figure 4.33: Comparison of predicted versus observed downstream velocity components in the form of a scattergraph corresponding to the large bend area.

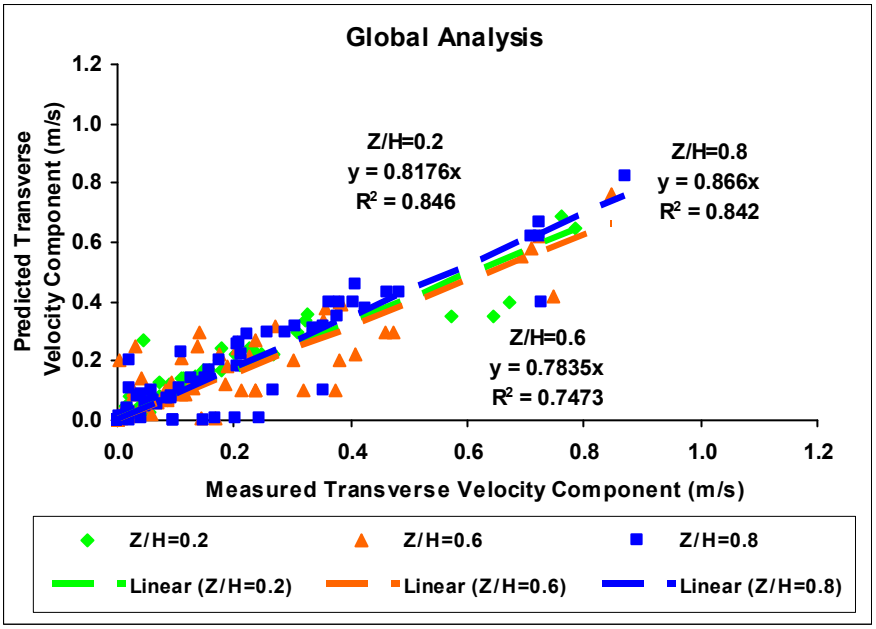

Figure 4.34: Global analysis of predicted versus observed transverse velocity components in the form of a scattergraph corresponding to all measurement positions within the River Asker reach.

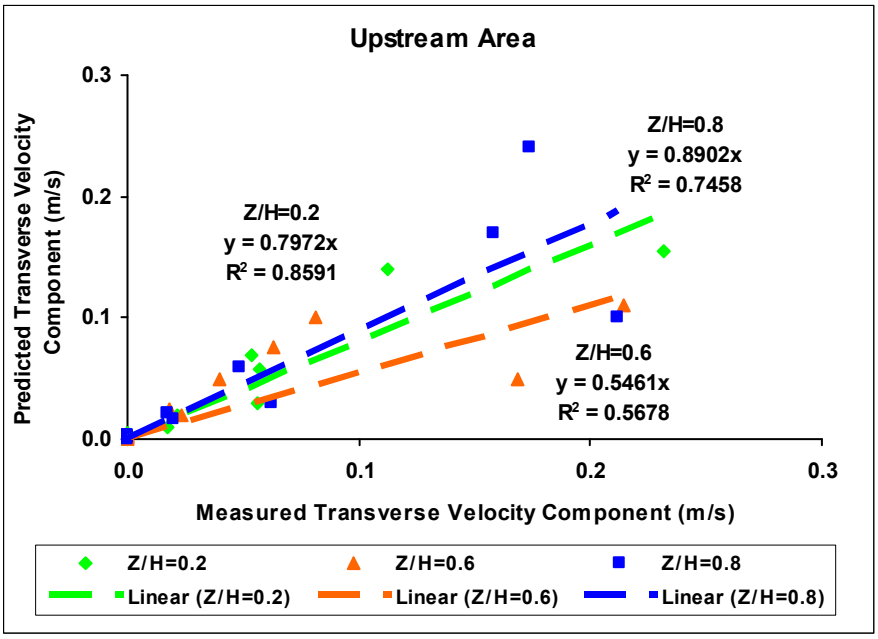

Figure 4.35: Comparison of predicted versus observed transverse velocity components in the form of a scattergraph corresponding to the upstream area.

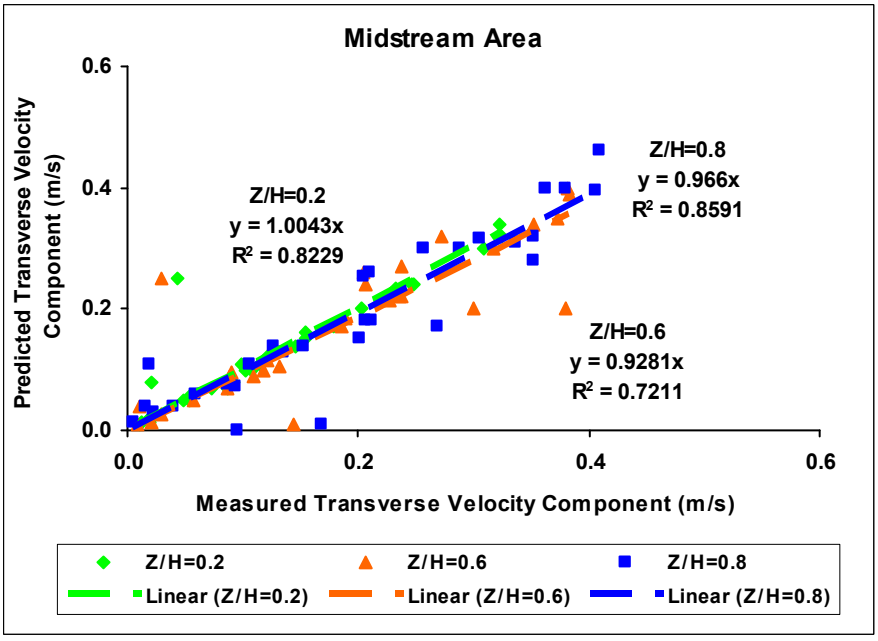

Figure 4.36: Comparison of predicted versus observed transverse velocity components in the form of a scattergraph corresponding to the midstream area.

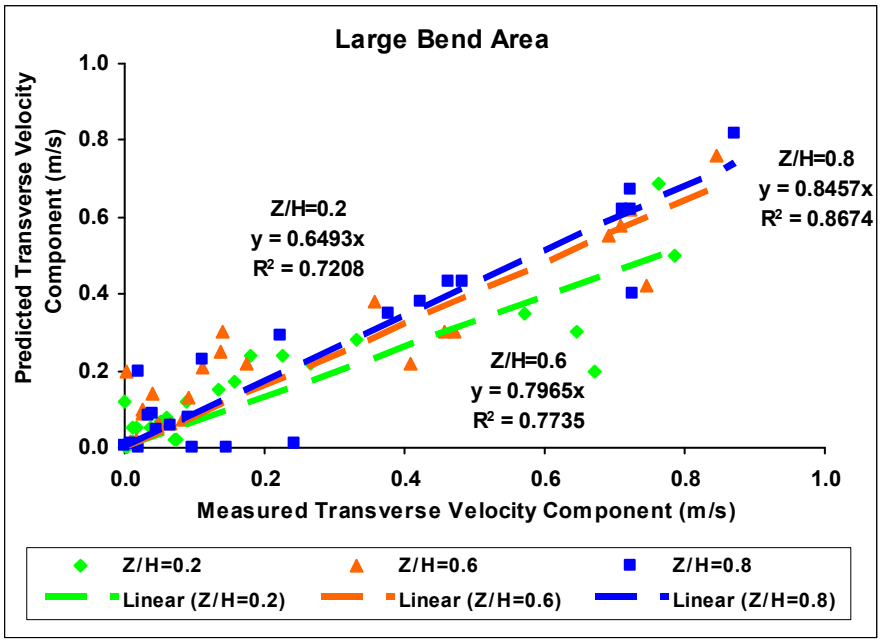

Figure 4.37: Comparison of predicted versus observed transverse velocity components in the form of a scattergraph corresponding to the large bend area.

Predicted versus observed velocity magnitudes of the resultant of downstream and transverse components

Although the CFD predictions do not always match perfectly with measured velocity values, the agreement is generally good as can be seen in Figures 4.26 to 4.29. More specifically, there is good qualitative validation of the velocity magnitude measured in the field for the data points corresponding to *Z/H* values of 0.2, and 0.8 (R^2 =0.79 and R^2 =0.85, respectively), although the model perform less well for the *Z/H* value of 0.6 (R^2 =0.72). The same trend is observed in the midstream area where at *Z/H* values of 0.2 (R^2 =0.81) and 0.8 (R^2 =0.86) the model replicates the measured field data well, but at *Z/H* value of 0.6 (R^2 =0.74) the agreement between simulated and observed data is somewhat weaker. At the upstream area the model validates well for *Z/H* value of 0.2 (R^2 =0.84), while it poorly performs for *Z/H* values of 0.6 (R^2 =0.56) and 0.8 (R^2 =0.73). Finally, in the large bend area there is good qualitative validation for *Z/H* values of 0.6 (R^2 =0.79) and 0.8 (R^2 =0.87) but the model perform less well for the *Z/H* value of 0.2 (R^2 =0.71).

Predicted versus observed downstream velocity components

As can be seen in Figures 4.30 to 4.33 there is good qualitative validation of the downstream velocity components measured in the field for the data points corresponding to *Z/H* values of 0.2, and 0.8 (R^2 =0.88 and R^2 =0.88, respectively) but the model perform less well for the *Z/H* value of 0.6 (R^2 =0.72). The same trend is observed in the midstream area where at *Z/H* values of 0.2 (R^2 =0.82) and 0.8 (R^2 =0.82) the model replicates the measured field data well, but at a *Z/H* value of 0.6 (R^2 =0.72) there is less qualitative validation. At the upstream area the model validates well for *Z/H* value of 0.2 (R^2 =0.85), while it poorly performs for *Z/H* values of 0.6 (R^2 =0.59) and 0.8 (R^2 =0.73). Finally, in the large bend area there is good qualitative validation for *Z/H* values of 0.8 (R^2 =0.87) but the model perform less well for *Z/H* values of 0.2 (R^2 =0.65) and 0.6 (R^2 =0.75).

Predicted versus observed transverse velocity components

As can be seen in Figures 4.34 to 4.37 there is also a good qualitative validation of the transverse velocity component for the data points corresponding to *Z/H* values of 0.2, and 0.8 (R^2 =0.85 and R^2 =0.84, respectively) but the model perform less well for the *Z/H* value of 0.6 (R^2 =0.75).

In conventional approaches to model validation, a fundamental assumption has been made that the validation data are better than the model predictions (*Lane and Richards*, 2001). However, error exists in both and significant errors can exist in both the empirical data used in model boundary conditions and in the validation data itself. Indeed, empirical data tend to be very poor at representing the spatio-temporal dynamics of the system and model predictions of systems can be richer in space and sometimes in time. Hence, in view of these uncertainties the model in this thesis is considered adequately validated (at least for the low flow conditions for which empirical data are available) for use in discussing the flow structures present in the River Asker reach.

4.2 Results: Low Flow Conditions

Discussions of flow structures in river channel features such as meander bends, confluences and braids, have always been based on detailed field measurements at a number of cross sections (*Dietrich and Smith*, 1984; *Ashmore et al*., 1992; *Rhoads and Sukhodolov*, 2001). Results have typically been visualised using cross-section plots with isovels of the streamwise velocity component and vectors calculated from the transverse and vertical components. These plots have been used to identify patterns of the secondary circulation (*Lane et al*., 1999b). A downstream sequence of such plots is often used to infer the nature of streamwise changes in the flow structure, although this can be considered as approximate in the absence of data between cross-sections. In contrast, some authors have presented maps with streamwise and transverse vectors, typically just for near-surface and near-bed measurements (*Ashmore et al*., 1992; *Andrle*, 1994).

CFD results are spatially much richer compared with studies based on field or laboratory measurements. Thus, a wider choice of ways for identifying and describing the various flow structures exists. In this thesis a combination of vectors showing both flow direction and velocity magnitude at constant elevations is used. Moreover, dynamic pressure and shear stress distributions are also employed, while planform maps show the spatial patterns of the velocity magnitude and orientation, again at a constant elevation. In addition, this study uses cross-section contour plots of downstream velocity magnitude, with vector plots superimposed on top showing cross stream and vertical velocity components.

To help locate particular flow events, four Areas of Interest (AOI), namely, upstream inflow area (AOI 1), midstream small bend area (AOI 2), upstream large bend area (AOI 3), and downstream large bend area (AOI 4), were identified within the River Asker reach. These four AOI illustrated in Figure 4.38 were chosen since they cover a wide range of different regions throughout the reach representing various flow structures explained below. This was sensible from the point of view of making the writing up of the results easier.

Simulated near-bed (at a constant elevation of 8.6m) and near-surface (at a constant elevation of 9.0m) flow patterns corresponding to AOI 1 are shown in Figures 4.39 and 4.40. The vectors not only demonstrate the resultant direction of the streamwise, leftwards, and rightwards components of velocity at alternate cells in each direction but also show the velocity magnitude at each one of those cells. A predicted planform map of near surface velocity magnitude (at a constant elevation of 9.0m) for AOI 1 is also shown in Figure 4.41. The velocity magnitude although calculated from all three velocity components, it is dominated by the horizontal ones.

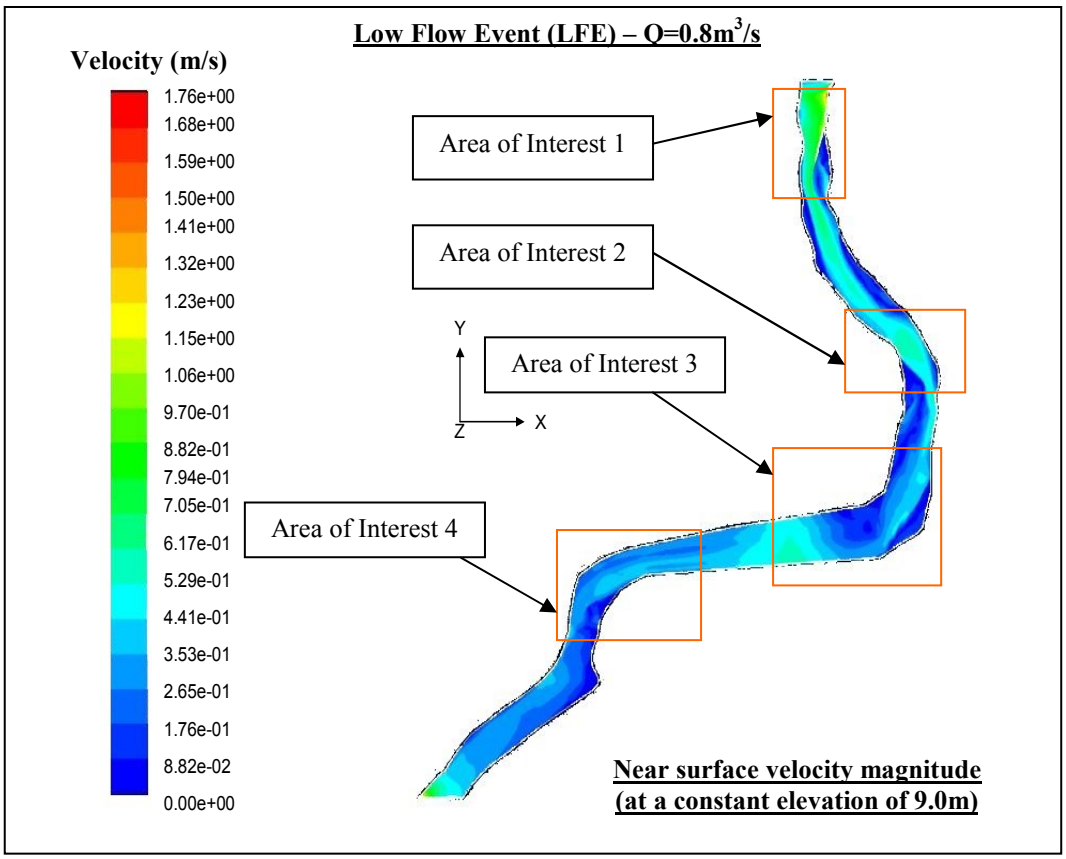

Figure 4.38: Predicted planform map of near surface velocity magnitude (at a constant elevation of 9.0m) for the River Asker reach under low flow conditions (Q = 0.8m^3/s) showing the four identified Areas of Interest (AOI).

Flow features in AOI 1 were identified by drawing three different cross sections within the upstream inflow area (Figures 4.39 and 4.40), labelled A-C in downstream order. As noted in Figures 4.39 and 4.40, there is a deceleration of the flow towards the right bank.

More specifically, between sections A and B the near bed velocity is much higher at the shallow riffle close to the left bank (~0.8 m/s) rather than at the deeper pool towards the right bank (~0.2 m/s). In contrast, the near surface flow corresponding to the above mentioned locations is shown to be decelerated from ~0.8 m/s at the shallow riffle to ~0.3 m/s only very close to the right bank.

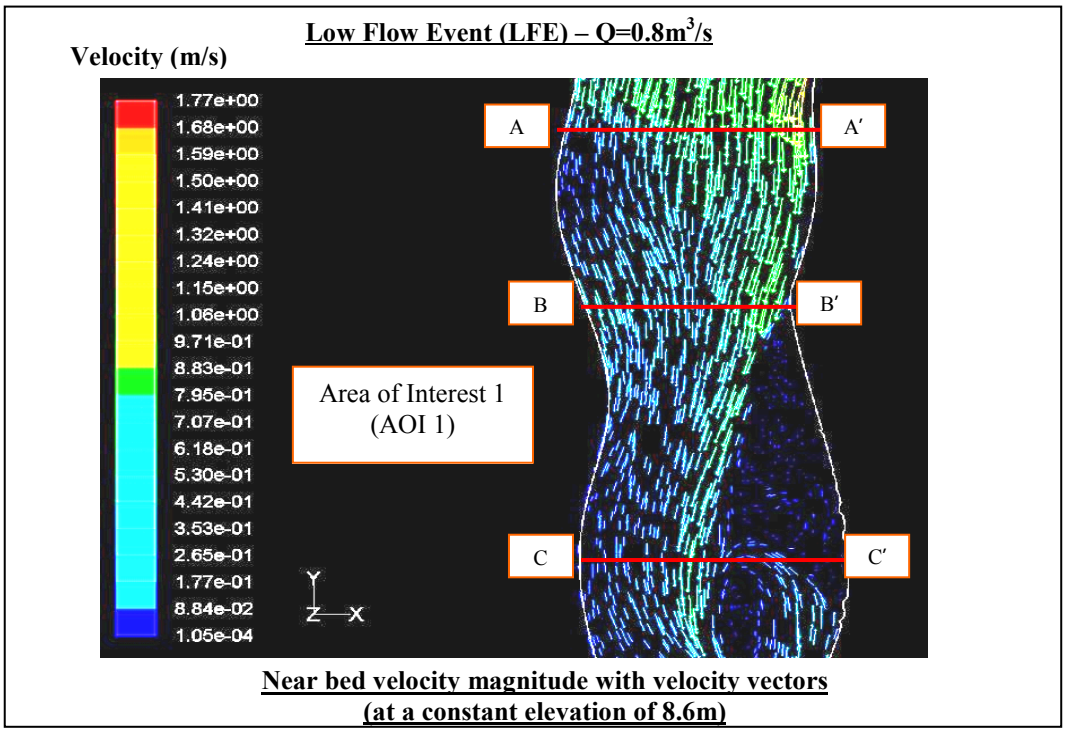

Figure 4.39: Predicted planform map of velocity magnitude with velocity vectors at AOI 1 under low flow conditions (Q = 0.8m^3/s) showing flowing direction near the bed (at a constant elevation of 8.6m).

The left side area between sections B and C is shown to be a dead zone of stagnant flow (<0.1 m/s at both surface and bed). The near bed fast flow (~0.8 m/s) is mainly concentrated into the central area in the form of a small streamtube, while the near surface flow is extended towards the right bank at almost the same intensity (~0.9 m/s). A recirculation zone comes close to the middle part of cross-section C within the dead flow zone, although the near surface and near bed isovels have different patterns leading to a helicoidal flow. The region of stagnant flow, within which a zone of flow separation occurs, is extensive. The separated zone has a clockwise circulation in plan view. Low

near surface velocities (~0.5 m/s) merged with the main flow after recirculating, while near bed flow velocities at the same location appeared to be smaller and do not return to the fast near bed streamtube.

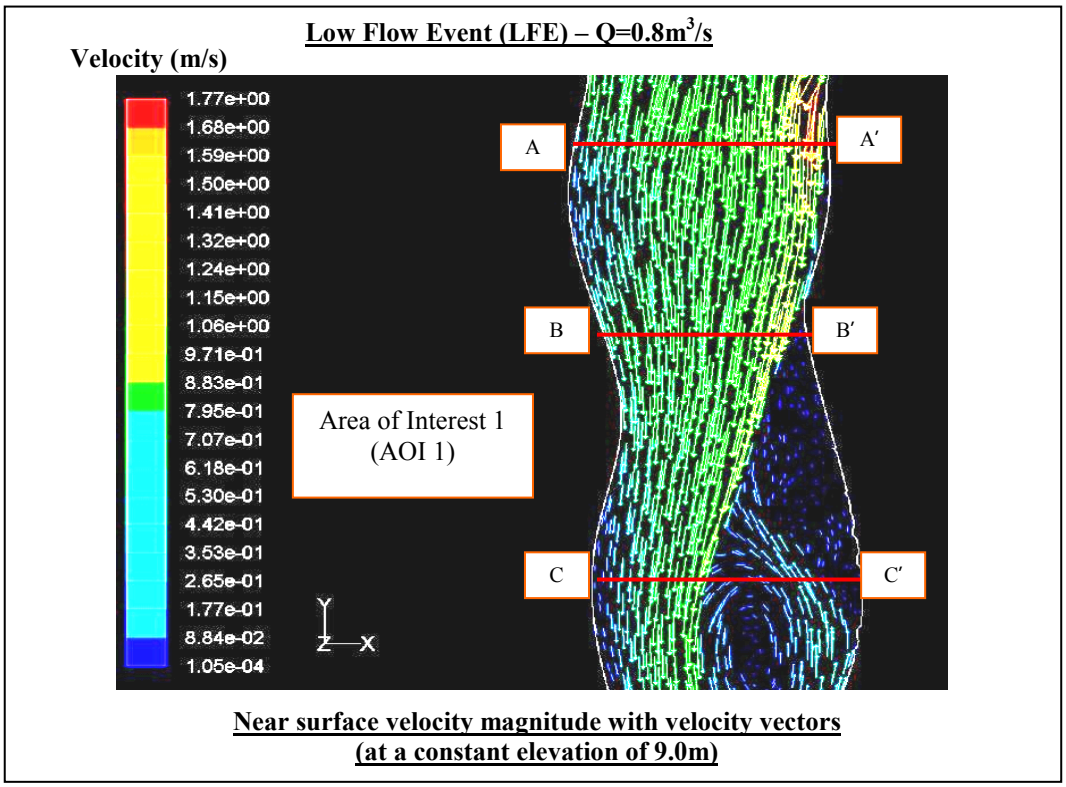

Figure 4.40: Predicted planform map of velocity magnitude with velocity vectors at AOI 1 under low flow conditions (Q = 0.8m^3/s) showing flowing direction near the surface (at a constant elevation of 9.0m).

The down channel flow between sections A and B at approximately mid way towards the right bank has also the classic characteristics of helicoidal flow, with bed vectors angled leftwards but the surface vectors remaining straight in place. The interpretation of secondary circulation is based upon the differences between the near bed and the near surface velocity magnitude and direction. In this particular case, the difference in direction is as much as 45 degrees, whereas the velocity component at the surface can exceed 0.8 m/s in a straight line but that at bed can exceed 0.4 m/s to the left. The second area of significant secondary circulation can be found in the right-hand half after section C in the downstream direction. Its characteristics are similar to those for the one

previously discussed, with magnitudes of surface velocity more than 0.8 m/s flowing forwards and magnitudes of bed velocity component at approximately 0.3 m/s to the left.

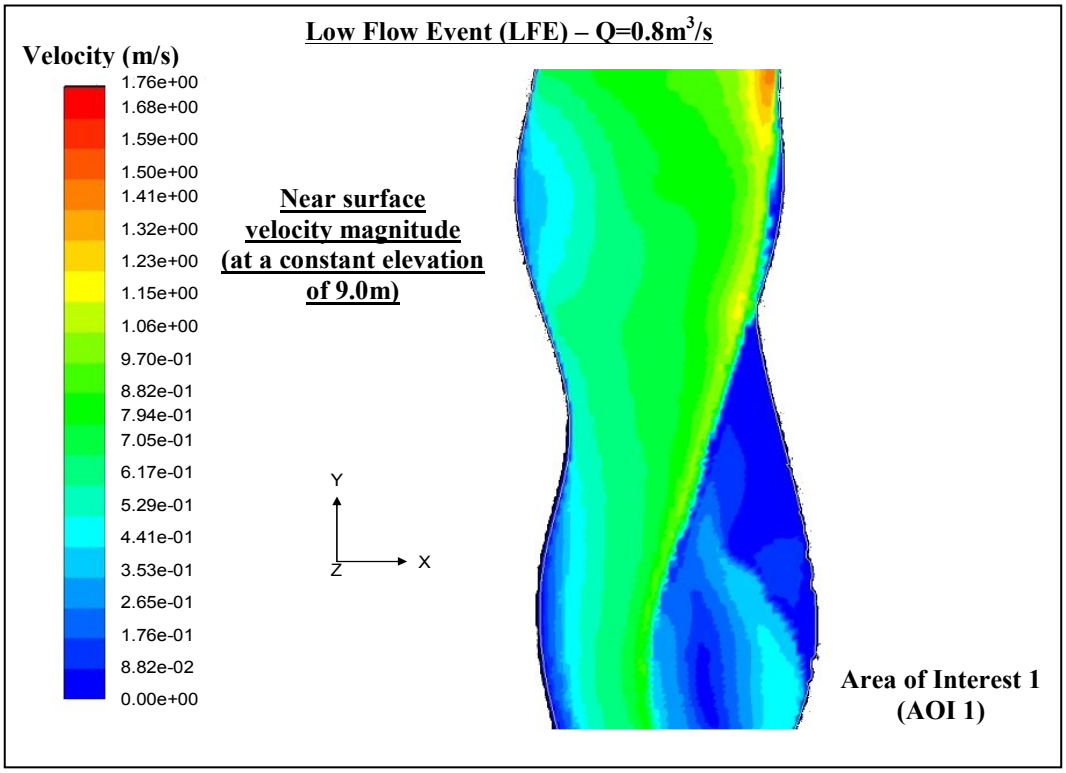

Figure 4.41: Predicted planform map of near surface velocity magnitude (at a constant elevation of 9.0m) at AOI 1 under low flow conditions (Q = 0.8m^3/s).

Simulated near-bed (at a constant elevation of 8.6m) and near-surface (at a constant elevation of 9.0m) flow patterns corresponding to AOI 2 are illustrated in Figure 4.42. The near surface velocity magnitude (at a constant elevation of 9.0m) in a planform map for AOI 2 is depicted in Figure 4.43. Three cross-sections (labelled A-C in downstream order) were drawn within the midstream small bend area (AOI 2) for defining the various flow features more easily. As can be seen in Figure 4.43, there is a general acceleration of the flow from the upstream to the shallower middle part of the reach, and some subsequent deceleration to the left-hand half of the outflow section as the reach deepens towards the exit within AOI 2. The acceleration is most prominent in the near surface

flow where the minimum velocity increases from ~0.6 m/s at the inflow just before section A to ~0.9 m/s towards the middle part of section B.

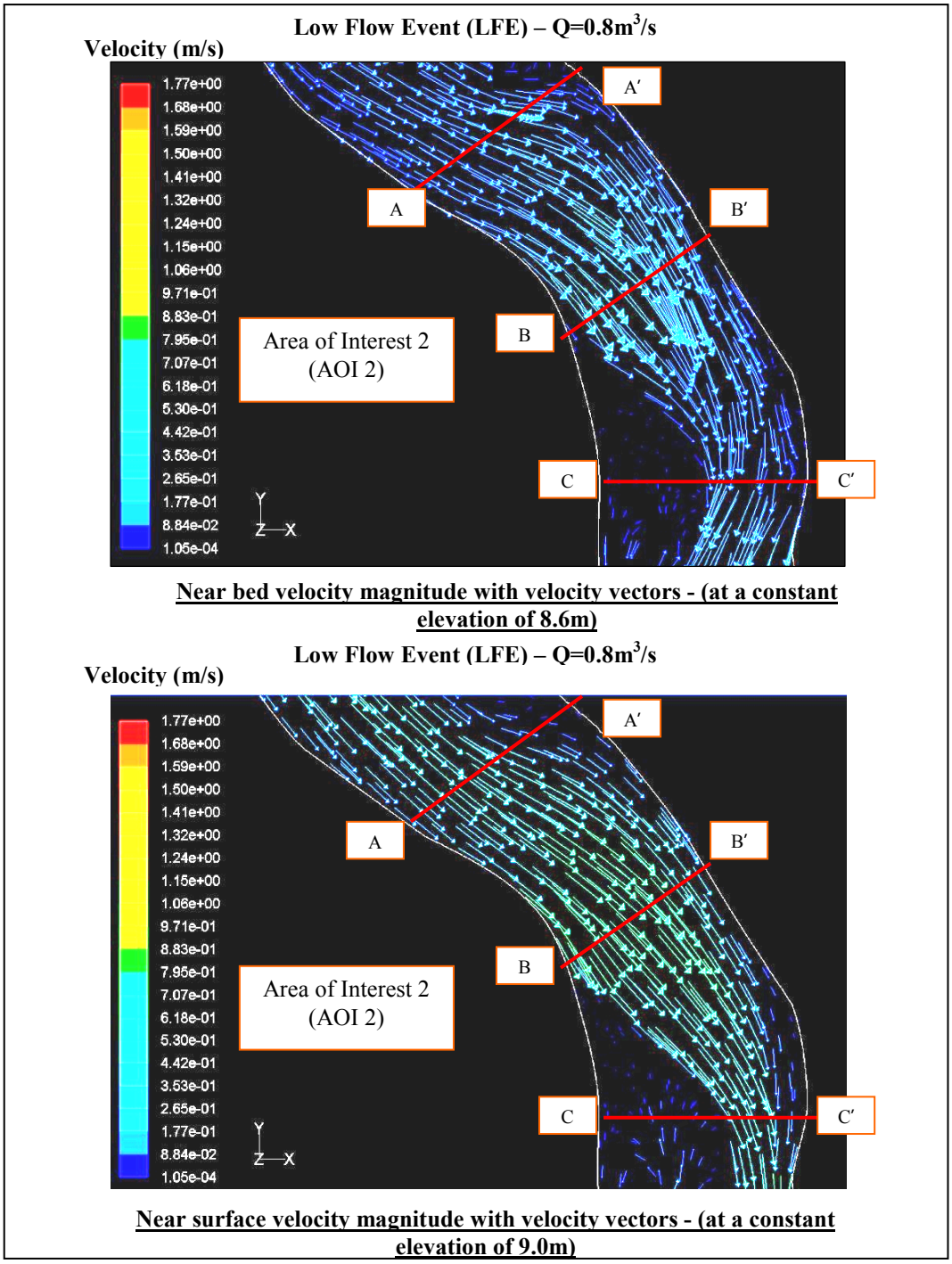

Figure 4.42: Predicted planform map of velocity magnitude with velocity vectors at AOI 2 under low flow conditions (Q = 0.8m^3/s) showing flowing direction near the bed (at a constant elevation of 8.6m) and near the surface (at a constant elevation of 9.0m).

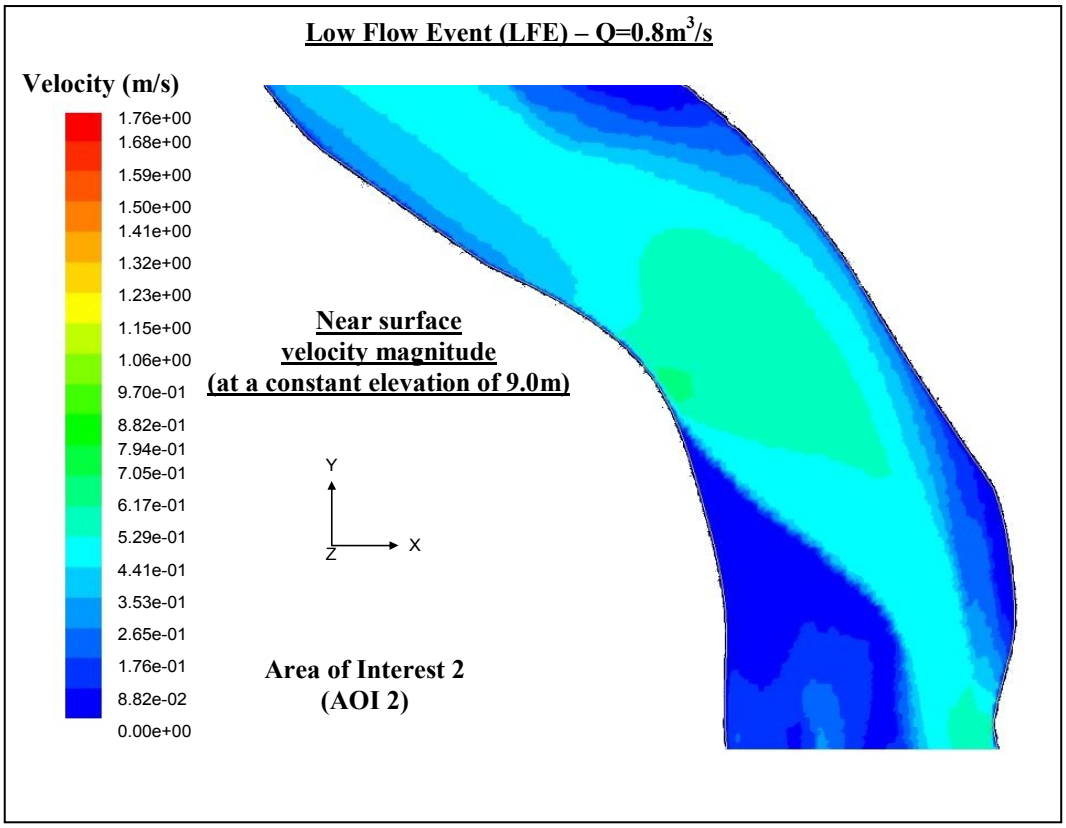

Figure 4.43: Predicted planform map of near surface velocity magnitude (at a constant elevation of 9.0m) at AOI 2 under low flow conditions (Q = 0.8m^3/s).

The fast flow is mostly concentrated towards the outer bank (mostly over 0.8 m/s at the surface, 0.5 m/s at the bed), which is in stark contrast to the extensive area of slow flow extending across the channel from the inner bank dead zone of stagnant flow after the inner apex in the downstream direction (<0.1 m/s at both surface and bed). Low velocities also extend very close to the outer bank at the start of the flow (near section A) at both bed and surface.

Two regions corresponding to the characteristic helicoidal flow are identified within the streamtube of relatively fast down channel flow. The first one is located at the left-hand half of section A, with bed vectors angled towards but surface vectors forced parallel to the outer bank. The difference in direction is as much as 45 degrees. As can be seen the velocity component at the surface can exceed 0.7 m/s flowing forwards but that at bed can exceed 0.4 m/s to the left. The second is close to the outer bank in the midstream

portion of the small bend, where the helical motion is at maximum. This strong helical circulation, looking downstream, can be seen in the left-hand half between sections B and C. This second area of significant secondary flow includes several places where surface vectors are angled towards the outer bank (~0.8 m/s to the left) and bed vectors are angled away towards the inner bank (0.4 m/s to the right).

Figure 4.44 depicts the simulated near-bed (at a constant elevation of 8.2m) and near-surface (at a constant elevation of 8.8m) flow patterns corresponding to AOI 3, while the contour of near-surface velocity magnitude is illustrated in Figure 4.45. The velocity magnitude although calculated from all three velocity components, it is dominated by the horizontal ones.

As can be noted in Figure 4.45, the inflow to the bend is dominated by high velocities (~0.4 m/s), except at the right bank where the velocity magnitudes are low (<0.1 m/s). There is a general decrease in both bed and surface velocity (<0.2 m/s) at the outer bank bend apex between sections A and B. Low velocities can also be observed after the inner bank bend apex (<0.2 m/s). Significant re-circulation zones are developed within those two areas of stagnant flow with near surface and near bed vectors having similar patterns with regards to both their flow direction and magnitude. The periphery of the inner bank re-circulation zone comes close to the outer bank at section B near the outer bend apex, while it is spreads almost up to the right-hand corners of sections A, and C. A narrow zone of fast flow is concentrated between the two re-circulation zones. Both the magnitude and the direction of the bed and surface velocities differ considerably within this fast flow zone. A zone of flow separation occurs within the outer bank stagnant flow area after the bend apex towards to section B. The surface vectors are angled towards the outer bank, while the bed vectors are angled away. This feature is produced by the contrast between outwards flow at the surface and inwards flow at the bed and is essentially the same as in the classical model of curvature-induced flow structure in bends. Flow reattachment is located between sections B and C, midway between the outer bend apex and the end of the model domain. At this stage the flow is expanded to

the whole width of the channel with varying bed (~0.3 m/s) and surface (~0.5m m/s) velocity magnitudes.

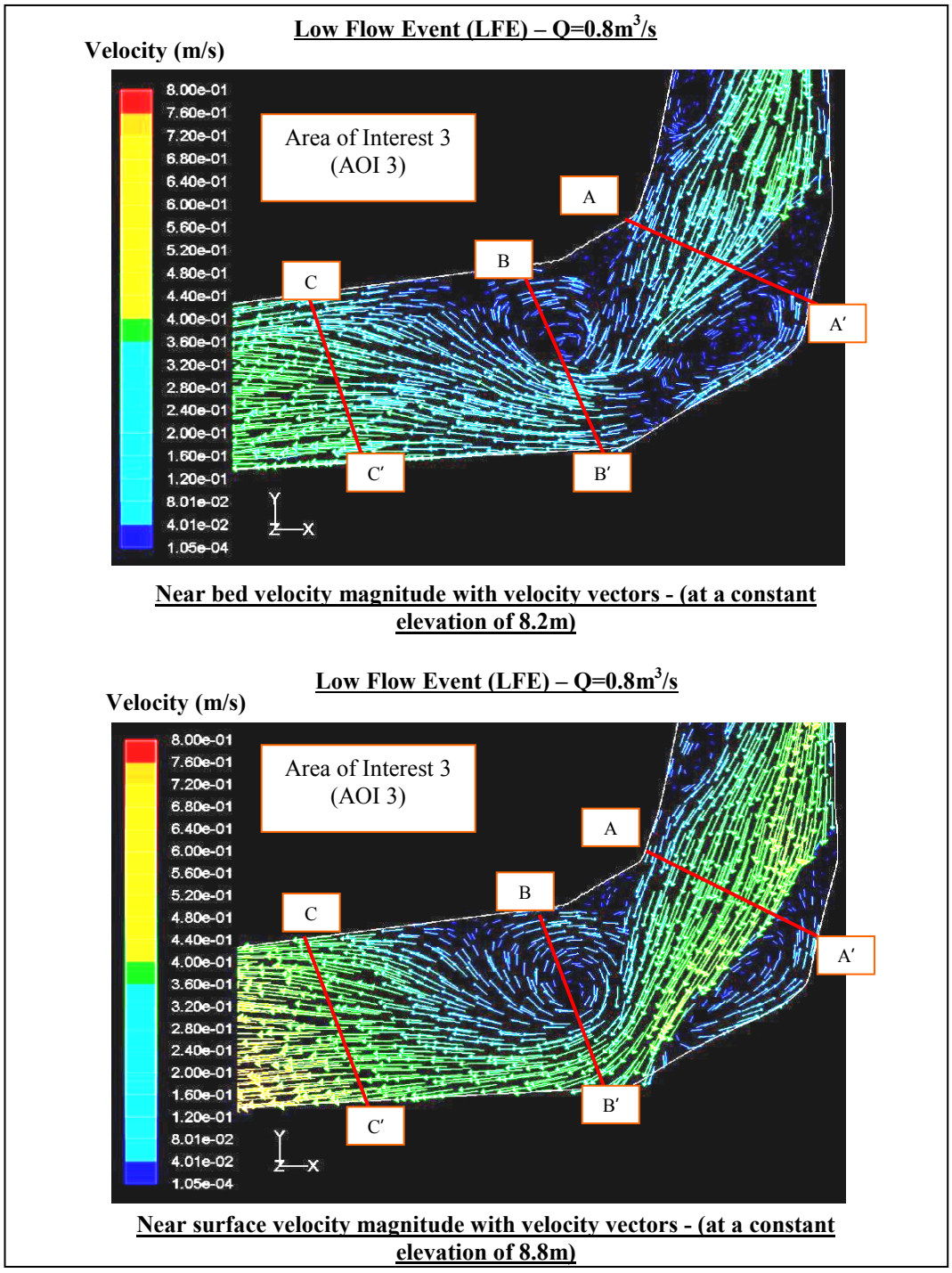

Figure 4.44: Predicted planform map of velocity magnitude with velocity vectors at AOI 3 under low flow conditions (Q = 0.8m^3/s) showing flowing direction near the bed (at a constant elevation of 8.2m) and near the surface (at a constant elevation of 8.8m).

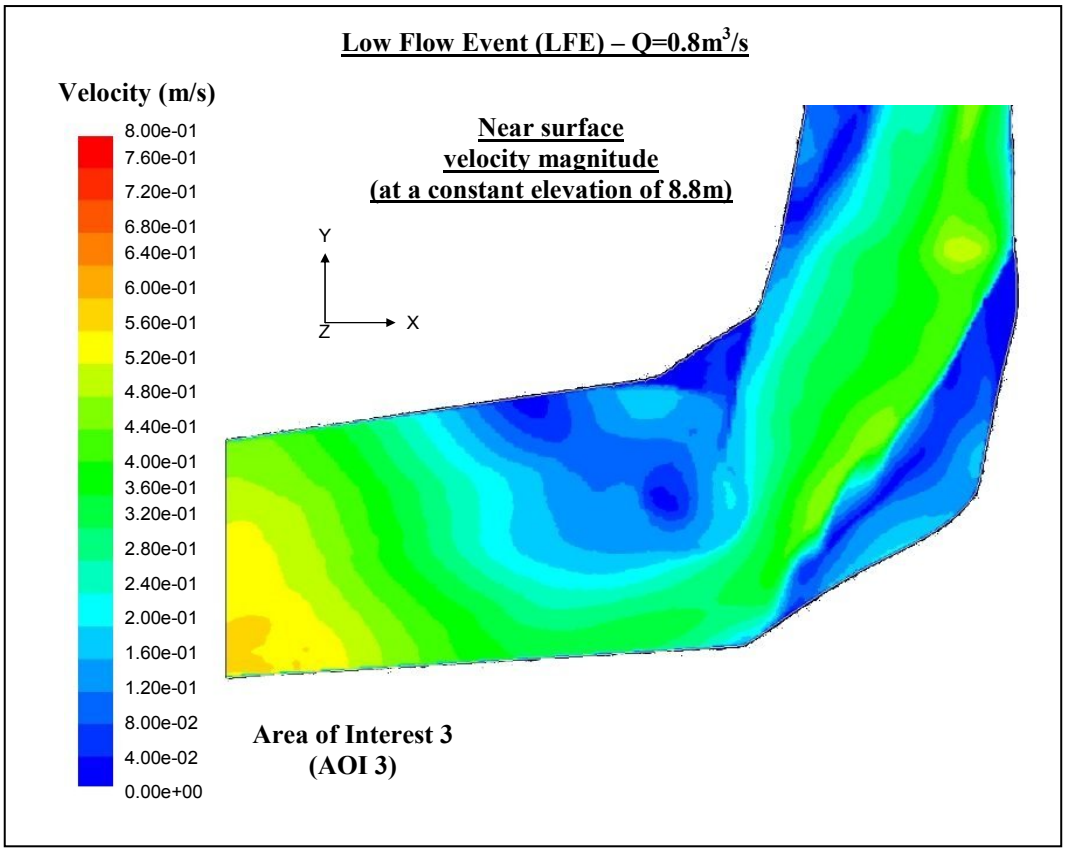

Figure 4.45: Predicted planform map of near surface velocity magnitude (at a constant elevation of 8.8m) at AOI 3 under low flow conditions (Q = 0.8m^3/s).

To help locate particular flow features within the downstream large bend area (AOI 4), three section lines are marked on the maps of velocity magnitude with velocity vectors (Figure 4.46) and labelled A-C in downstream order. Section A runs across the fast flow zone not far from the inflow, B just above the recirculation zone, and C just downstream of the flow reattachment point.

As noted in Figure 4.46, there is an acceleration of the flow towards the bend inner bank just before section A. Both the near bed (~0.2 m/s) and near surface (~0.4 m/s) velocities are higher at the inner bank as the flow enters the bend. In contrast, the flow velocities corresponding to the outer bank of the bend are low. Therefore, the fast flow zone is concentrated towards the inner bank between sections A and B. A dead zone of stagnant

flow (<0.1 m/s at both surface and bed) can be observed on the left-hand half starting after section B.

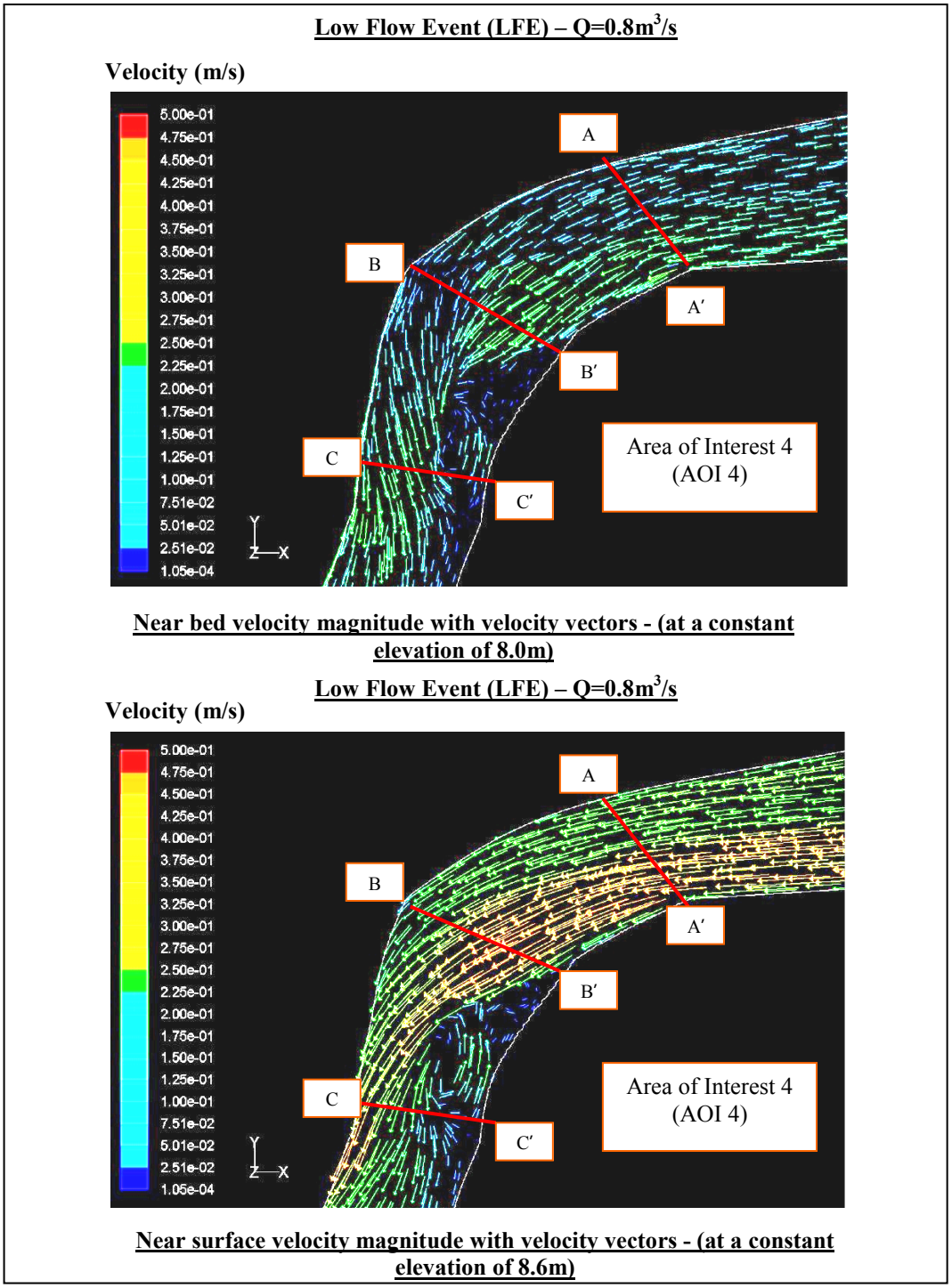

Figure 4.46: Predicted planform map of velocity magnitude with velocity vectors at AOI 4 under low flow conditions (Q = 0.8m^3/s) showing flowing direction near the bed (at a constant elevation of 8.0m) and near the surface (at a constant elevation of 8.6m).

The outer bend apex is dominated by very low near bed velocities. A recirculation zone is located at the midway between sections B and C. However, within this recirculation zone the near surface and near bed velocities exhibit similar patterns with regards to flow direction. Flow reattachment is located close to section C.

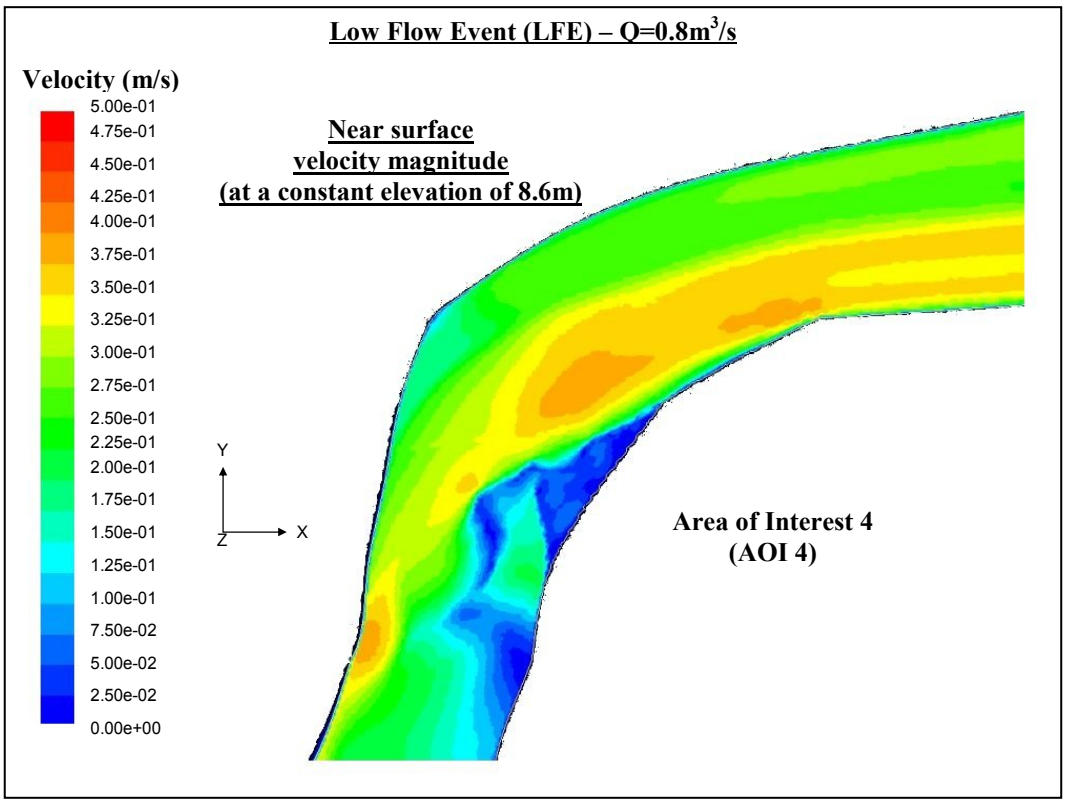

Figure 4.47: Predicted planform map of near surface velocity magnitude (at a constant elevation of 8.6m) at AOI 4 under low flow conditions (Q = 0.8m^3/s).

A large region corresponding to the characteristic helicoidal flow is identified at the right-hand half between sections B and C within the relatively fast down channel flow. The helicoidal flow also extends downstream from section C. Near bed velocity vectors are shown to be angled towards the inner (left) bend bank, while surface vectors are angled away towards the outer (right) bank. The difference in their direction is as much as 45 degrees in some places, where the velocity component at the surface can exceed 0.3 m/s to the right but that at bed can exceed 0.2 m/s to the left.

Contour plots of the magnitude of the downstream velocity, with vector plots showing the cross stream and vertical velocity components superimposed, were created at three different cross sections (Figure 4.48), labelled 1-3 in downstream order.

Low Flow Event (LFE) – Q= 0.8m^3/s

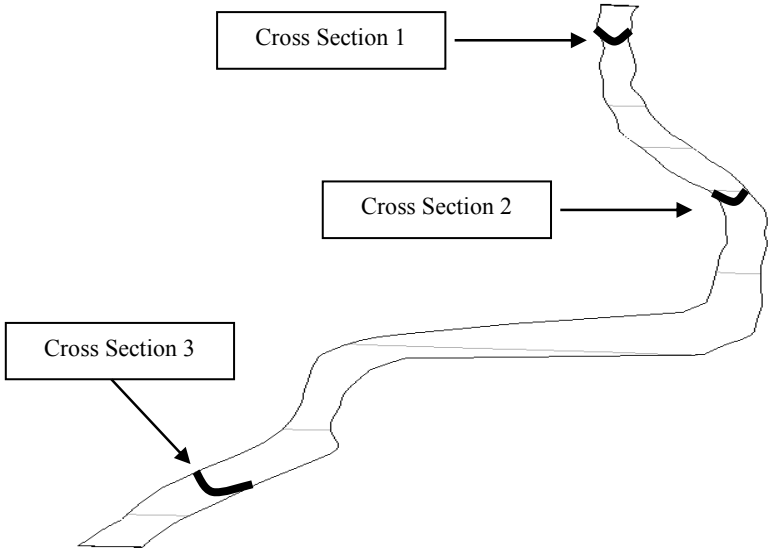

Figure 4.48: Locations of three selected cross-sections at Low Flow Event (LFE) where contour plots of downstream velocity magnitude showing cross-stream and vertical velocity components are undertaken.

These three cross-sections illustrated in Figure 4.48 were chosen since they cover a wide range of different regions throughout the reach, representing various flow structures as explained below.

Figures 4.39 and 4.40 combined with the pattern of vertical velocities revealed by Figure 4.49 indicate that an area of significant secondary flow exists mid way towards the right bank within cross-section 1, where the strength of helical motion is at a maximum.

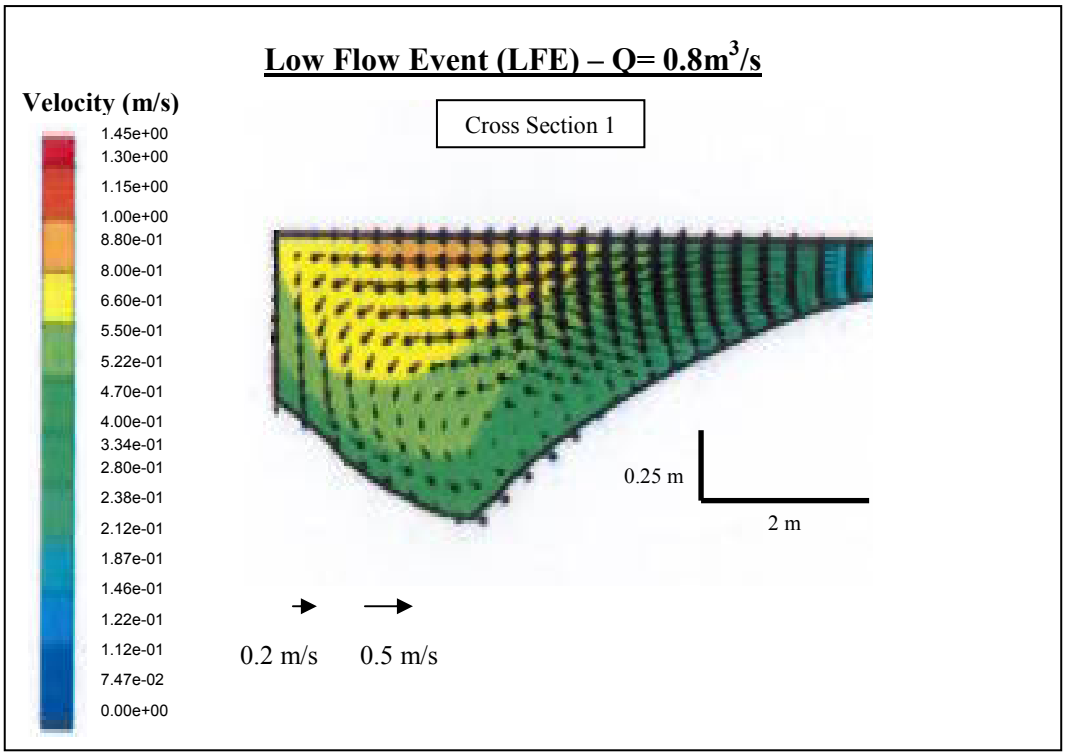

Figure 4.49: Predicted contour plots of downstream velocity magnitude showing cross-stream and vertical velocity components at cross section 1 under Low Flow Event (Q = 0.8m^3/s).

At cross-section 1, the classical helical circulation is fully developed, but is restricted to the right part of the channel, in the deepest portion of the channel. This is the classical pattern of curvature-induced circulation, although it is rapidly dissipated downstream. Contour plots of cross steam and vertical velocity components within cross-sections 2 and 3 are shown in Figures 4.50 and 4.51, respectively.

At cross-section 2 the remains of the helix can still be seen at the base of the bed mid way towards the right bank but with leftwards flow limited. The progressive movement of the locus of maximum downstream velocity down the inner bank from the surface at cross-sections 1 and 2, to the base of the right bank at cross-section 3, is clearly shown by the cross section plots in Figures 4.49 to 4.51.

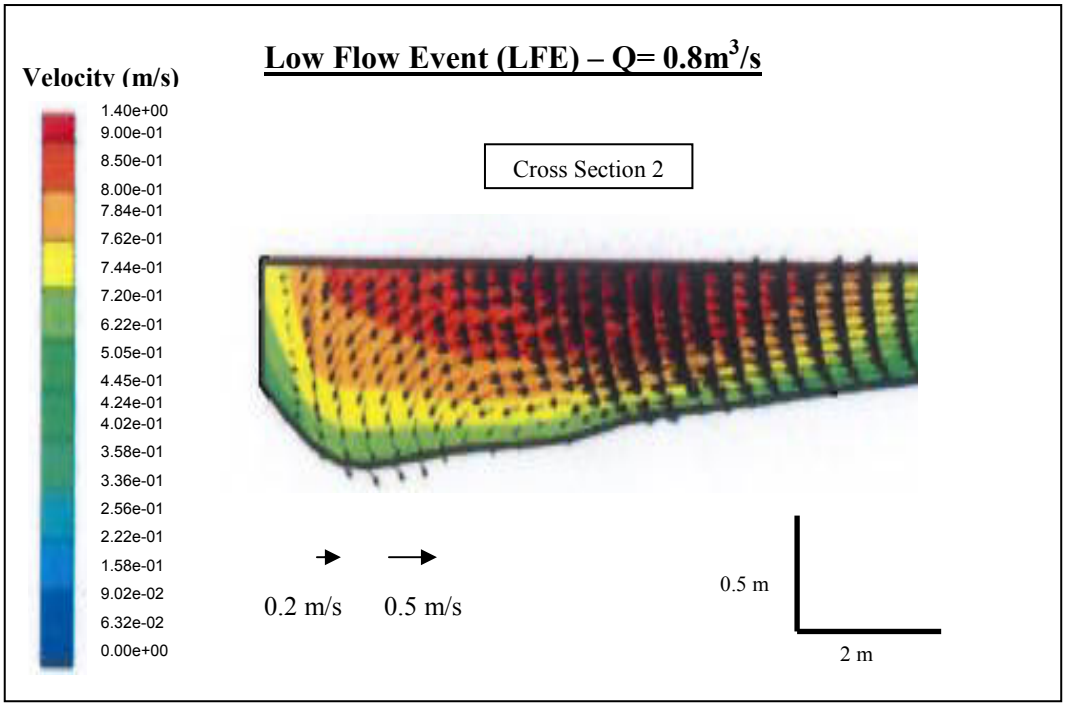

Figure 4.50: Predicted contour plots of downstream velocity magnitude showing cross-stream and vertical velocity components at cross section 2 under Low Flow Event (Q = 0.8m^3/s).

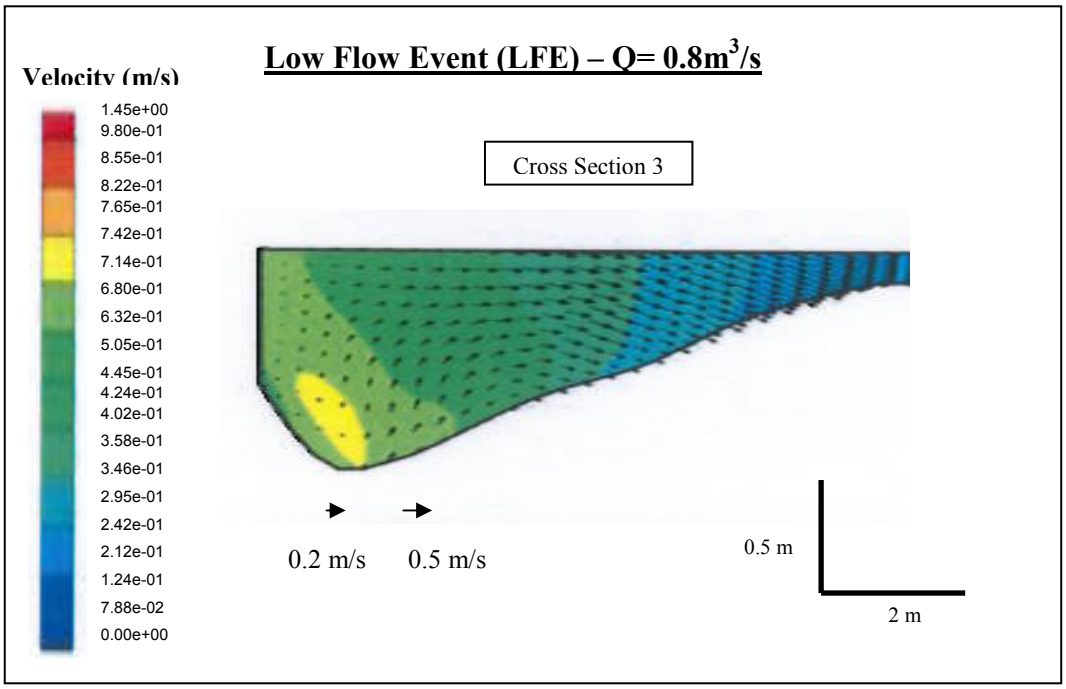

Figure 4.51: Predicted contour plots of downstream velocity magnitude showing cross-stream and vertical velocity components at cross section 3 under Low Flow Event (Q = 0.8m^3/s).

This downward plunging of fast surface water is accompanied by a large deviation in near bed and near surface flow direction close to the inner bank of the upstream large bend and downstream large bend areas (Figures 4.44 and 4.46). At cross-section 3, the inner bank helix is almost dissipated and is replaced by an upwelling and outwards movement of flow as shown in Figure 4.51, with the fast flow concentrated at the base and towards the right bank.

The results of the analysis of the three-dimensional time-averaged flow structures presented in this study reveal some similarities between the four areas of interest under low flow conditions. Dead zones of stagnant flow, as well as recirculation flow zones, were identified within all the above areas. The presence of a recirculation zone is significant in that it acts to confine the main downstream flow into a streamtube of relatively high velocity close to the outer bank. The streamtube in all cases has increased velocity near the surface (Figures 4.40, 4.42, 4.44, 4.46). In addition, flow in the streamtube has the classical helical motion with flow directed outwards at the surface but inwards at the bed. This flow pattern initially is extremely strong, but past the apex it is dissipated as the near surface and near bed velocities are in a similar direction (Figures 4.44, 4.46). Deceleration of near bed flow can result in a deviation of near bed flow towards the inner bank, while the simultaneous acceleration of near surface flow increases the outwards velocity component. However, turbulent diffusion in the shear layer between the fast flow streamtube and the adjacent recirculation zone aids the dissipation of the helical motion. The two cases corresponding to the upstream and downstream large bend area reveal that the strongest current is near the surface, close to the outer bank, with a zone of near bed stagnant flow in the centre of the channel. Nevertheless, high near surface velocities are likely to be less significant than high near bed velocities at the bank, due to the significance of fluvial basal erosion as a mechanism driving bank retreat.

Several factors, such as, streamline curvature, inflow distribution, as well as topographic forcing can be considered to control the flow structures within the above mentioned areas. Strong streamline curvature produced by the local bankline direction acts to

produce a region of high dynamic pressure against the outer bank as the inertia of the flow is too great to adjust to the imposed curvature of the channel. As an example the midstream small bend area (AOI 2) is illustrated in Figure 4.52. This impingement creates a region of high dynamic pressure some distance before the outer bank apex and results in a region of relatively low or negative dynamic pressure opposite the outer bank apex.

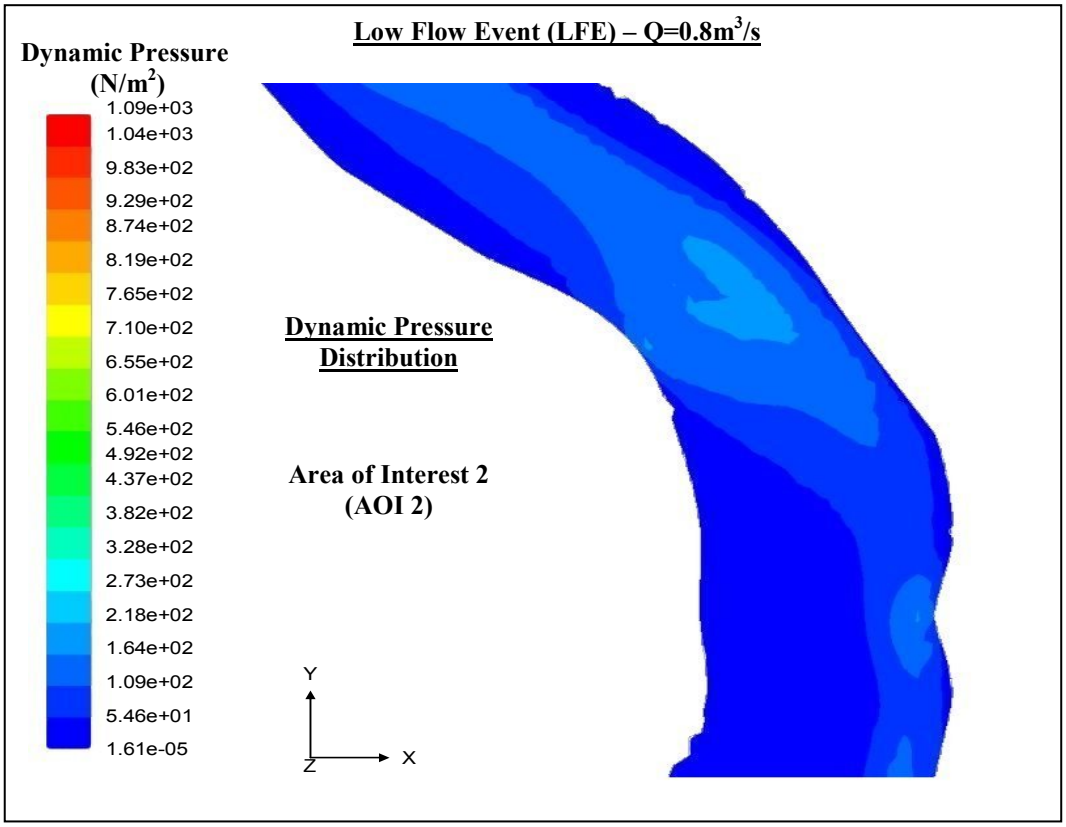

Figure 4.52: Dynamic pressure distribution in midstream small bend area (AOI 2) under low flow conditions ($Q = 0.8\text{m}^3/\text{s}$).

The general flow structure and water surface elevation are a response to the high dynamic pressure on the outer bank. The inflow distribution, which is governed by a combination of upstream planform and local topographic forcing on the upstream channel, also seems to have a pronounced effect on the flow structure observed. The inflow distribution can act to enhance or diminish the potential pressure gradients produced by streamline curvature by acting to drive flow into the outer bank at a higher or lower angle than the local bankline direction (Figures 4.42, 4.44, 4.46).

The interaction between the streamtube of relatively fast downstream velocity and the regions of slow or reverse flow within the separation zones produces intense shear along the boundaries of the channel. These flow structures will have implications for the resulting bank erosion developed within the reach, and these will be further discussed in Chapter 6.

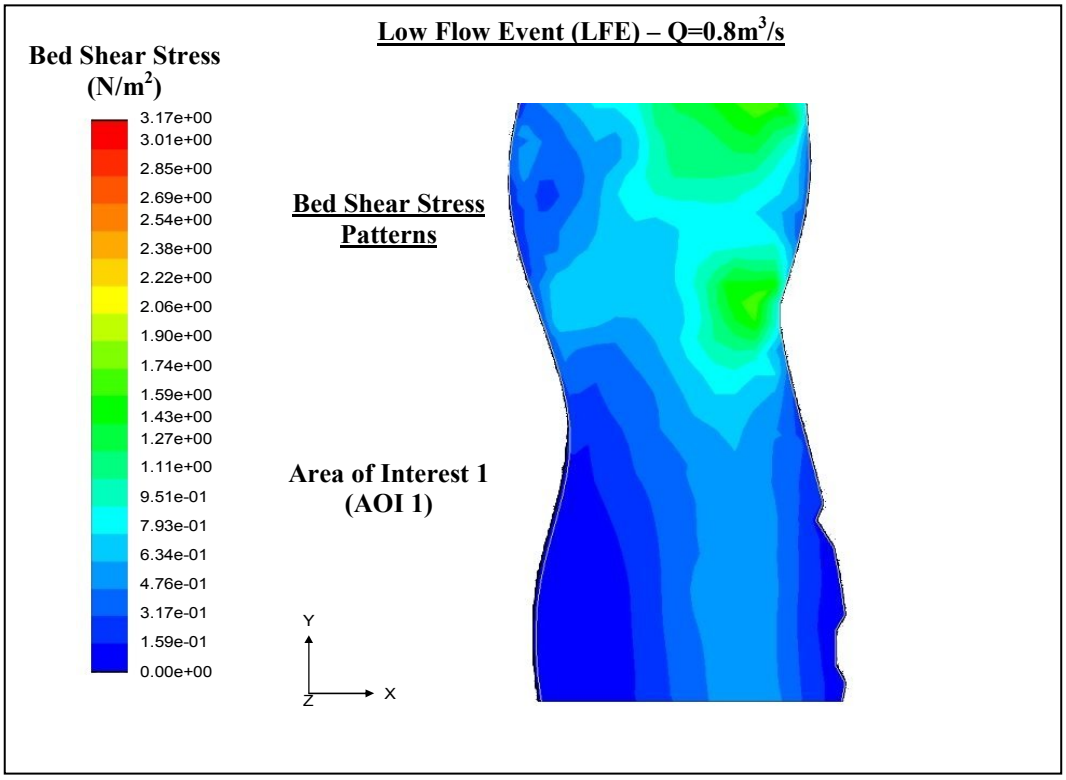

Figure 4.53: Predicted bed shear stress patterns in upstream inflow area (AOI 1) under low flow conditions ($Q = 0.8\text{m}^3/\text{s}$).

The existence of large areas of slow downstream or reverse flow in the four areas of interest within the River Asker reach has several important implications. The velocity patterns discussed above imply maximum boundary shear stress in various locations such as, the upstream left-hand half (AOI 1), the area close to the inner bank apex (AOI 2, AOI 4) as well as the downstream area in AOI 3. However, these bed shear patterns reveal significant difference from the classical model of flow through bends which indicate maximum shear stress near the outer bank downstream of the bend apex. Figures 4.53 through 4.55 demonstrate this general pattern of bed shear stress at the low flow stages examined. These patterns will also have implications for the sediment dynamics

within the reach, as well bank erosion and meander migration, and will be further examined in Chapter 6.

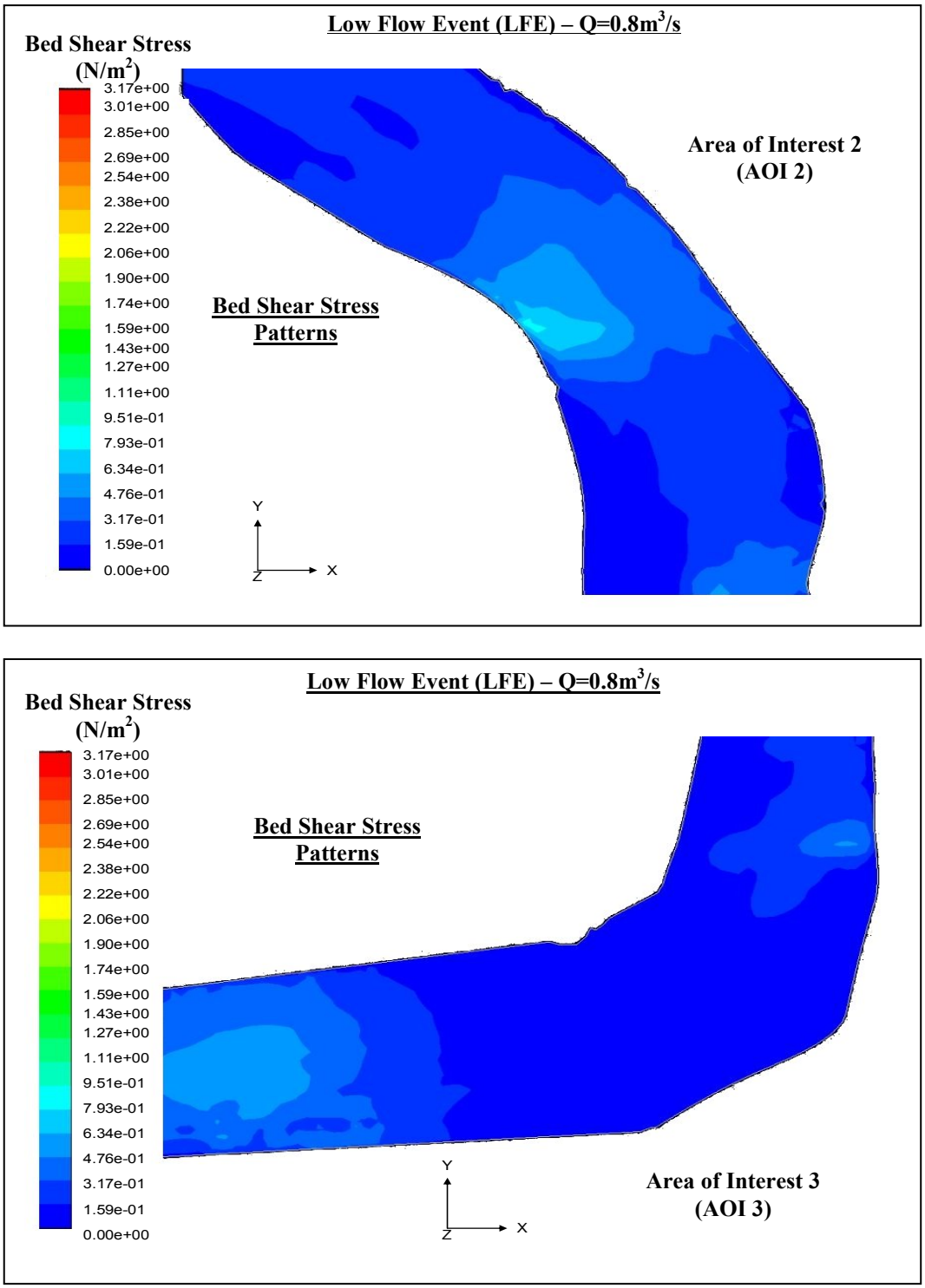

Figure 4.54: Predicted bed shear stress patterns in midstream small bend and upstream large bend areas (AOI 2 and AOI 3) under low flow conditions (Q = 0.8m^3/s).

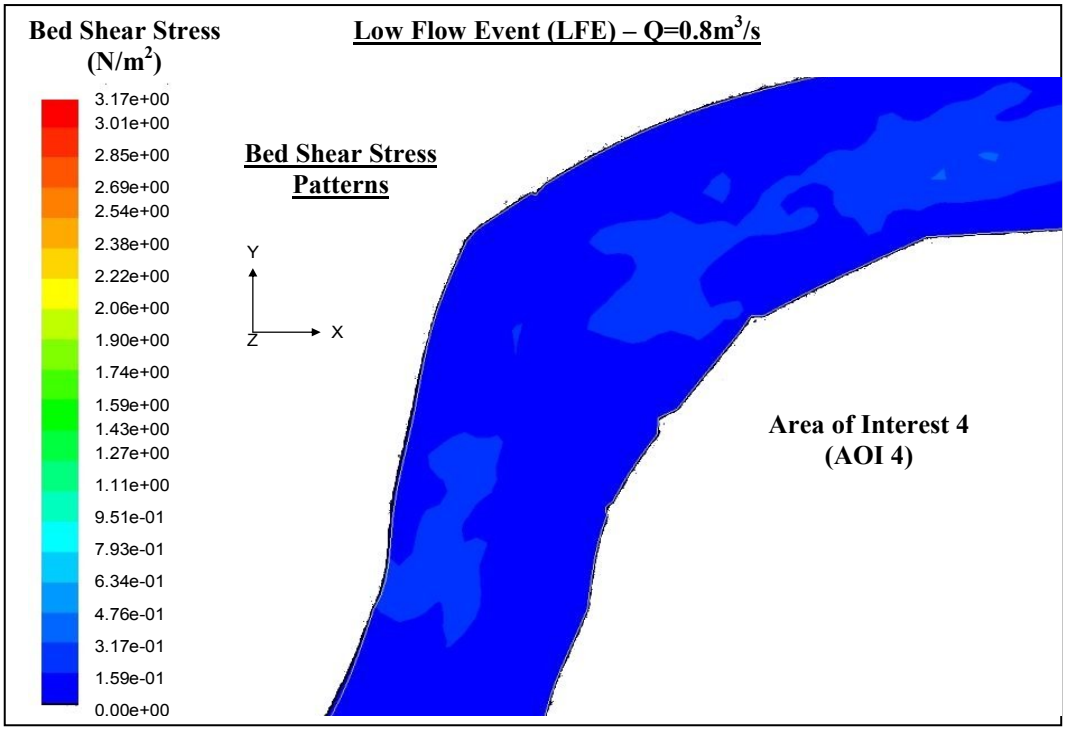

Figure 4.55: Predicted bed shear stress patterns in downstream large bend area (AOI 4) under low flow conditions (Q = 0.8m^3/s).

Boundary shear stress values derived from the model simulations can be compared to crude estimates of shear stress within the reach under low flow conditions. Estimates of shear stress at downstream intervals of several tens of meters can be determined from the average depths and water surface slopes derived from the crest gauge data. Shear stress, for steady-uniform flow conditions, is given as follows (*Ferguson*, 1994):

$$\tau = \rho_w xgxdxS \qquad (4.12)$$

where τ (N/m^2) is the bed shear stress, d (m) is the local flow depth, S (m/m) is the water surface slope, ρ_w (kg/m^3) represents the density of the water, and g (m/s^2) is the acceleration due to gravity.

Estimates of bed shear stress from Equation (4.12) were calculated along a network of the ten crest gauges spaced at twenty meters intervals along the reach, and their values are given in Table 4.2.

Table 4.2: Estimates of bed shear stress under low flow conditions (Q=0.8m^3/s).

Crest Gauge	Distance	Gradient	Water Surface Elevation	Bed Elevation	Local Flow Depth	Water Density	Gravity	Bed Shear Stress
No	m	m/m	m	m	m	kg/m^3	m/s^2	N/m^2
1	-	-	9.25	8.92	0.33	998.2	9.81	-
2	28.6	0.0024	9.18	8.34	0.84	998.2	9.81	19.7
3	43.5	0.0023	9.10	8.60	0.50	998.2	9.81	11.3
4	65.3	0.0026	9.03	8.82	0.21	998.2	9.81	5.3
5	87.4	0.0032	8.96	8.64	0.32	998.2	9.81	10.0
6	103.5	0.0025	8.92	8.40	0.52	998.2	9.81	12.7
7	117.9	0.0028	8.85	7.90	0.95	998.2	9.81	26.0
8	139.1	0.0027	8.78	7.60	1.18	998.2	9.81	31.2
9	156.1	0.0012	8.76	8.02	0.74	998.2	9.81	8.7
10	205.1	0.0033	8.42	8.08	0.34	998.2	9.81	11.0
Average Bed Shear Stress								13.6

As can be seen from the analysis undertaken, bed shear stresses derived from the model simulations are much lower than those acquired by means of estimating using average depths and water surface slopes and assuming steady, uniform, flow. This can be attributed to the roughness height chosen within this research.

The steady uniform flow model over-estimates because it does not account for the influence of form drag. The latter is parameterized in the model by meshing the grid to conform to the large scale roughness elements (e.g. bars, riffles, pools) present within the channel and by using a large value of roughness height to parameterize the sub-grid scale roughness. Thus, the true magnitude of the form roughness used in this study is more accurately accounted for within the fine mesh.

As previously mentioned the bed of the examined reach was found to dominate by very small gravels while its banks have been characterized as mostly sand and silt deposits. Thus, a representative value of D_{50} (0.065 mm) was chosen as an input roughness height to take into account all the different layers encountered and also the reduction due to the required mesh resolution. However, the effect of a spatially variable roughness is unknown and could have a significant effect on shear stress predictions as shown above. The investigation of model sensitivity to spatially variable roughness is not assessed in this thesis and is left as an area that requires more research.

4.3 Summary

This chapter has considered the verification, validation, and analysis of time-averaged flow structures under low flow conditions within the study reach of the River Asker. Results are analysed only for the whole reach and not for sub-reach A since the same flow features are identified in both cases. Flow structures in four areas of interest have been investigated. The chapter has demonstrated that numerical modelling can be applied to these areas even where highly complex grids are required. It can be concluded that the combination of fieldwork for validation of a numerical model provides an extremely powerful means of investigating flows in such complex areas where the field data cannot realistically provide adequate process representation.

In the first section of Chapter 4, an assessment of the numerical model was discussed, including both its verification and validation. A GCI analysis was performed to ascertain that the solution was independent of the grid spacing. This was confirmed by creating three different meshes for the Low Flow Event (LFE). The GCI analysis was performed between the coarse and intermediate resolution grids and the intermediate and fine resolution grids. It was found that a mesh consisting of 2,148,510 cells using a grid spacing of 0.1 m was adequate to obtain a sufficiently independent solution. Hence, this mesh was used to generate the results previously described. Validation of the model was based on comparison of model predictions under low flow conditions with field observations. Before choosing the appropriate turbulence model several runs were executed, in which almost all the available turbulence closures within *Fluent 6.2* were

compared. The latter analysis revealed that the results obtained using the standard k-ε turbulence model give the best fit compared to the field data. After validating the numerical model it was found that although the CFD predictions did not always match perfectly with measured velocity values, the agreement was generally good.

The results of the analysis of the three-dimensional time-averaged flow structures under low flow conditions, presented in the second section of this chapter demonstrated notable similarities between the four areas of interest. Dead zones of stagnant flow as well as recirculation flow zones were identified within all the above areas. A relatively high velocity flow streamtube with increased velocity near the surface was also illustrated close to the outer bank. The flow in the streamtube revealed the classical helical motion with flow directed outwards at the surface but inwards at the bed. This flow pattern initially was extremely strong, but past the apex it was dissipated as the near surface and near bed velocities were in a similar direction. Turbulent diffusion in the shear layer between the fast flow streamtube and the adjacent recirculation zone resulted in dissipating the helical motion.

In all cases, large amounts of shear exist between the slowly re-circulating flow and the fast streamtube. The existence of large areas of slow downstream flow at the inner bank apex has several important implications. The velocity patterns discussed above imply maximum boundary shear stress near the inner bank upstream of the apex. However, these bed shear patterns differ significantly from the classical model of flow through bends (*Dietrich*, 1987) which indicate maximum shear stress near the outer bank downstream of the bend apex.

There are extensive areas of low boundary shear stresses across the inner bank separation areas downstream of the apex. There are also zones of higher bed shear stresses at the toe of the outer bank along the path of the streamtube. These patterns have implications for the sediment dynamics within the bend, bank erosion and meander migration within such bends.

Bed shear stresses derived from the model simulations were much lower than those acquired by means of estimation based on average depths and water surface slopes. This can be attributed to the roughness height chosen within this research. The steady uniform flow model over-estimates because it does not account for the influence of form drag. The latter is parameterized in the model by meshing the grid to conform to the large scale roughness elements (e.g. bars, riffles, pools) present within the channel and by using a large value of roughness height to parameterize the sub-grid scale roughness. Thus, the true magnitude of the form roughness used in this study is more accurately accounted for within the fine mesh. The effect of a spatially variable roughness is unknown and could have a significant effect in shear stress predictions. The investigation of model sensitivity to spatially variable roughness is not assessed in this thesis and is left as an area that requires more research.

The production of separation within the four areas of interest was attributed to three interrelated factors: streamline curvature, inflow distribution, and topographic forcing. However, the relative importance of these factors varied among the identified areas of interest. In addition, how these factors vary through time and at different flow stages is uncertain since the presence and nature of separation zones are likely to alter with increasing flow stage as the relative influence of the controlling factors outlined above varies. For that reason, understanding how these areas of interest change requires investigation of the flow structures at higher channel formative flow stages. Therefore, Chapter 5 examines the flow structure within the four areas of interest at higher flow discharges.

CHAPTER 5

Results: High Flow Conditions

This chapter aims to examine the three-dimensional time-averaged flow structure of the River Asker study reach under high flow conditions. Results are analysed for the Flow Event 1 (FE1) as well as the High Flow Event (HFE). These flow events happened on 31st and 12th January 2004 and are associated with peak flow discharges of 6.9 m/s^3 and 18.4 m/s^3, respectively. Analysis of Flow Events 2 and 3 was omitted since their geometry and flow characteristics are similar to those observed in FE1 and HFE, respectively. Flow structures in the same four areas of interest identified within the LFE (Chapter 4), representing a wide range of different regions throughout the reach, will be investigated for FE1 and HFE. These four areas of interest were selected since the interesting flow structures identified on them within the examined higher flow events do not differ from those observed in LFE.

The next section (5.1) provides a brief background to this intensive case study research of reach scale river channel flow structures under high flow conditions. The stage dependence of the examined flow structures is analysed, permitting a discussion of the geomorphological implications of the findings (5.2).

5.1 Background and Methods

An inability to understand how flow structure changes with discharge is one of the fundamental limitations of most studies of reach scale channel flow structures. This is because the vast majority of investigations have only analysed the flow structure at one discharge (*Bathurst et al.*, 1977; *Carson* and *Lapointe*, 1983; *Ashmore et al.*, 1992; *Lane et al.*, 1995; *Hodskinson* and *Ferguson*, 1998), which is often at a low to intermediate level. This is primarily due to the low frequency and short duration of higher flows in many of the rivers investigated. However, it can also be due to logistical and safety reasons. Thus, little may be known about how flow structures change with stage and the

nature of flow structures present at higher flow discharges, which are primarily responsible for determining channel form.

Current understanding of three dimensional flow structures at high flow stage is based upon a few field studies that have examined the influence of flow stage, including *Jackson's* (1975) analysis who presented the flow field at different stages at a single cross section in a meander bend. A study of the topographic and shear stress adjustments at two flow stages in a typical meander bend, one of which was 70% of the bankfull discharge was carried out by *Dietrich* and *Smith* (1984). *Markham* and *Thorne* (1992) investigated the effect of flow stage on flow structure through a meander by undertaking detailed velocity measurements at three cross sections. Moreover, an examination of how patterns of flow alter as flow increases around and over a mid-channel bar was accomplished by both *Bridge* and *Gabel* (1992) and *Whiting* (1997). It is important to mention though that many of these investigations encountered problems concerning the gathering of the data required. More specifically, *Markham* and *Thorne* (1992) were only able to obtain measurements at three widely spaced cross sections through a bend and had difficulties in acquiring cross section velocity measurements at comparable flow discharges for both high and low flow stage conditions, due to the time taken to acquire velocity measurements at each point in the cross-section.

In the studies previously mentioned, it is assumed that the strength of the helical circulation in bends increases with streamline curvature, flow velocity as well as the degree of super-elevation, since each of those factors will increase the magnitude of the centrifugal acceleration and consequently the pressure gradient force (*Dietrich*, 1987). As a result, a feedback relationship is identified between channel form and flow processes, allowing deeper, sharper bends to have higher secondary circulation velocities. Therefore, the relationship between discharge and strength of secondary circulation is based on the variation of the factors already mentioned, specifically velocity and curvature, in individual bends (*Hooke*, 1975; *Bathurst et al.*, 1979; *Thorne*, 1992). Thus, the strength of secondary circulation has been assumed to increase to a maximum at

intermediate discharges and when stage increases, primary currents dominate and secondary circulation strength declines due to the main flow (*Dietrich* and *Smith*, 1983). Taking the relationship described above further to flow separation, it may be suggested that at higher flow stages than those observed in Chapter 4, the separation zone at the inner bank gradually disappears, whereas at the outer bank it may grow (*Hodskinson* and *Ferguson*, 1998; *Parsons,* 2002). Both the occurrence and size of flow separation is based on the way the hydraulic geometry of the channel is changed as a result of varying flow stages (*Bridge* and *Jarvis*, 1982). However, the linkage between flow separation occurrence and flow stage is still poorly understood, especially in bends. The significance of the above with respect to near bank flows is of great importance since flow separation can be considered as a key mechanism controlling the possible onset of hydraulically-driven bank erosion.

In this chapter the flow structures within the River Asker reach under two high flow conditions, one of which correspond to a near bank full flow (HFE), are examined. The characteristics of these two flow events have already been given in Table 3.6. When modelling high flow events attention has to be paid to several factors, such a, how the grid was reconstructed for the increase in the size of the channel geometry, how the bank-full discharge was computed, and how this discharge was distributed through the inflow cross section.

The peak high flow discharge estimates which were available from a gauging station 150 metres downstream of the bank monitoring reach were almost nine times (FE1) and twenty three times (HFE) the low flow stage (LFE) investigated in Chapter 4. The above estimated discharges were then used to calculate an average inflow velocity for the two examined flow events using equation (*3.14*). The geometry of each model was specified using Digital Elevation Models (DEMs) of the channel created from high-resolution tacheometric surveys of the study reach, with water surface elevations defined using a network of ten crest gauges spaced at twenty meters intervals along the reach. However, the submerged topography of the reach varies for the two different flow events, as the values of water elevation at each one of the specified cross-sections within their grids and

the average water surface gradient fluctuated with changing flow discharges. Attention therefore had to be paid to estimating the values of water elevation at each cross section in order to obtain the desirable geometries. This was done by utilizing the diagram already presented in Chapter 3 (Figure 3.15) as well as equation (*3.11*).

No high flow velocity measurements were undertaken within FE1 and HFE. Thus, to model the flow structures at those higher stages, the grids were restructured allowing the increased volume of flow to be computed. The same grid resolution used for the LFE was applied for the high flow cases, despite the grids occupying greater volumes and greater lengths in both the vertical and cross-stream directions.

The grid independence of the high-flow meshes was verified by examining GCI values to ascertain that the solution from the grid resolution was independent of the grid spacing. Initially, three different meshes were constructed for both FE1 and HFE. The relatively coarse grids (using a grid spacing of 0.4 m) constructed for the River Asker under FE1 and HFE consists of 155,837 and 295,853 cells, respectively. Further refinement was undertaken to create intermediate grids (using a grid spacing of 0.2 m) consisting of 611,116 and 887,333 cells for FE1 and HFE, respectively. Finally, the number of cells contained within the FE1 and HFE meshes corresponding to a grid spacing of 0.1 m are 2,500,068 and 2,976,883, respectively.

The GCI analysis was performed between the coarse and intermediate resolution grids and the intermediate and fine resolution grids for each flow event. The GCI values presented in Tables 5.1 and 5.2 were obtained using a factor of safety of 1.25.

The low GCI values obtained between the fine and intermediate resolution meshes for both flow events indicate that the fine and intermediate resolution grids are suitably verified for the three components of velocity (Tables 5.1 and 5.2). However, similar to the verification of the low flow grids, the convergence for the turbulence parameters is generally poor with relatively high GCI values for both the FE1 and HFE reflecting the large amount of shear present within the reach and the fact that at the grid resolutions

examined the turbulence model used (standard k-ε model) is unable to fully capture this intense shear process.

Table 5.1: GCI results in percentage terms for velocity components in x, y, and z directions, turbulent kinetic energy, and turbulent dissipation rate with regards to FE1.

Variable	GCI Analysis	
	Fine Grid / Intermediate Grid	**Intermediate Grid / Coarse Grid**
X Velocity Component	5.62	16.48
Y Velocity Component	4.42	8.56
Z Velocity Component	5.92	9.24
Turbulent Kinetic Energy	21.68	39.48
Dissipation Rate	20.22	32.54

Table 5.2: GCI results in percentage terms for velocity components in x, y, and z directions, turbulent kinetic energy, and turbulent dissipation rate with regards to HFE.

Variable	GCI Analysis	
	Fine Grid / Intermediate Grid	**Intermediate Grid / Coarse Grid**
X Velocity Component	4.88	14.58
Y Velocity Component	5.44	9.12
Z Velocity Component	5.22	8.76
Turbulent Kinetic Energy	18.48	37.62
Dissipation Rate	19.86	29.46

The meshes acquired using a grid spacing of 0.1 m (fine grids) were undertaken to generate the results described in the following subchapters, since they produce sufficiently independent solutions.

In the current study, the influence of grid resolution on the wall functions employed was confirmed by examining the z^+ value at five arbitrarily selected cross sections within the River Asker reach under both the FE1 and HFE. These specific cross sections, annotated in Figures 5.1 and 5.2, were chosen because they cover a wide range of different regions throughout the reach representing the upstream, midstream bend, and downstream areas.

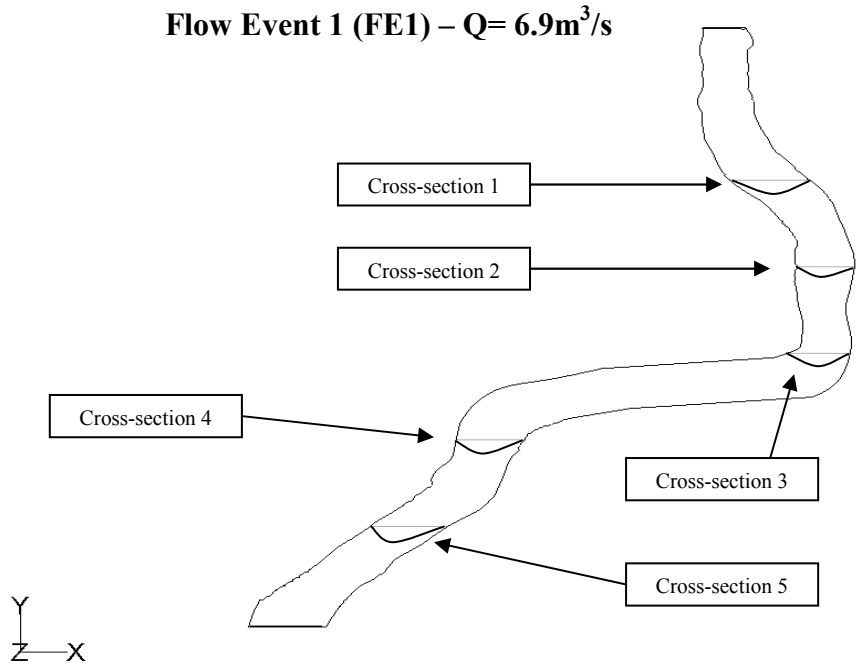

Figure 5.1: Locations of five arbitrarily selected cross-sections at Flow Event 1 (FE1).

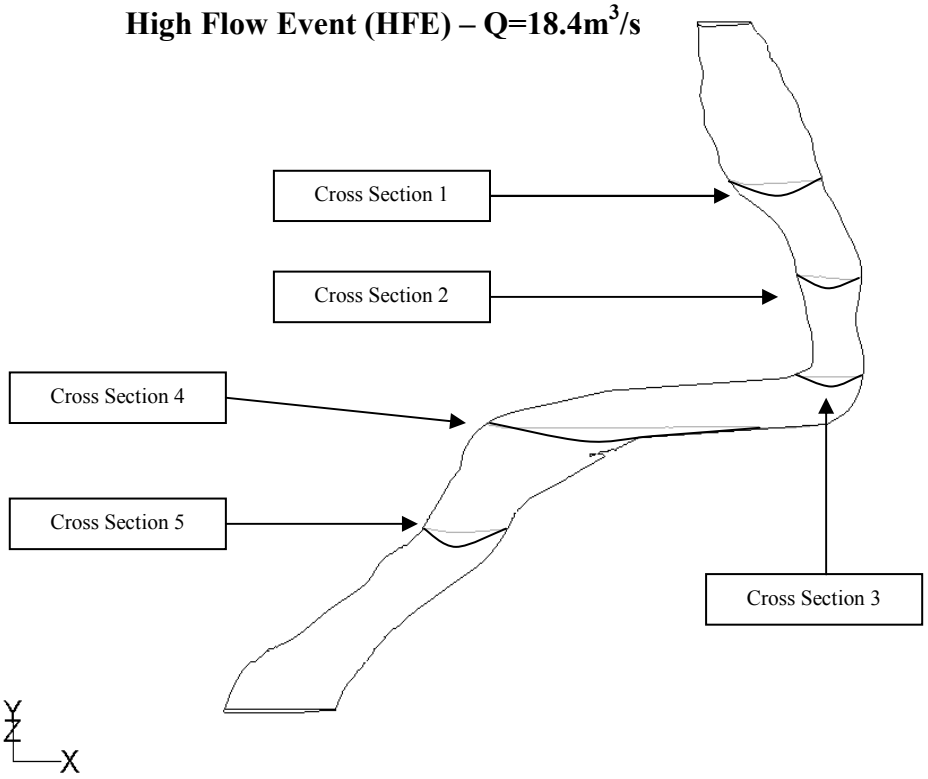

Figure 5.2: Locations of five arbitrarily selected cross-sections at High Flow Event (HFE).

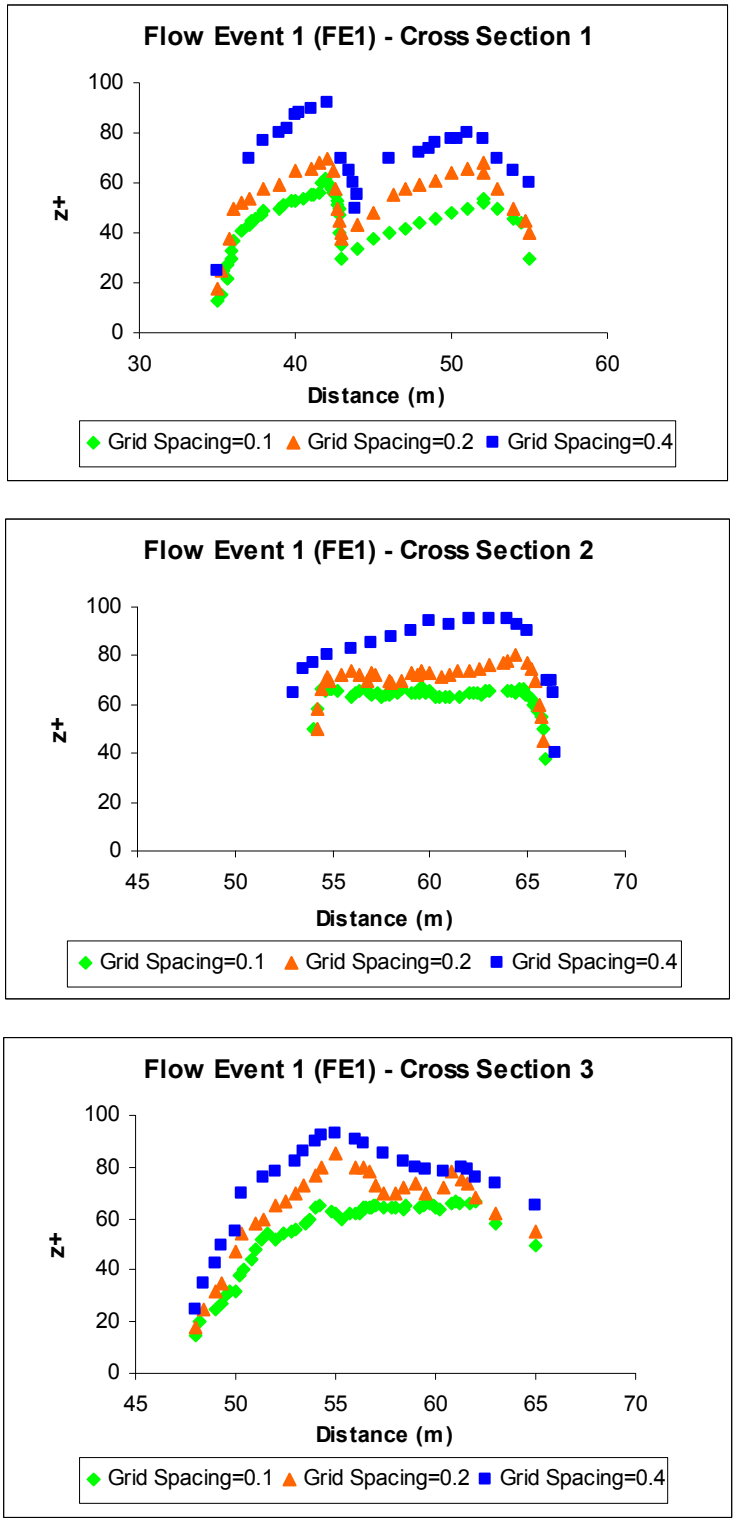

Figure 5.3: Investigation of various grid resolutions in relation to the wall functions employed, for cross-sections 1, 2, and 3 and Flow Event 1 (FE1).

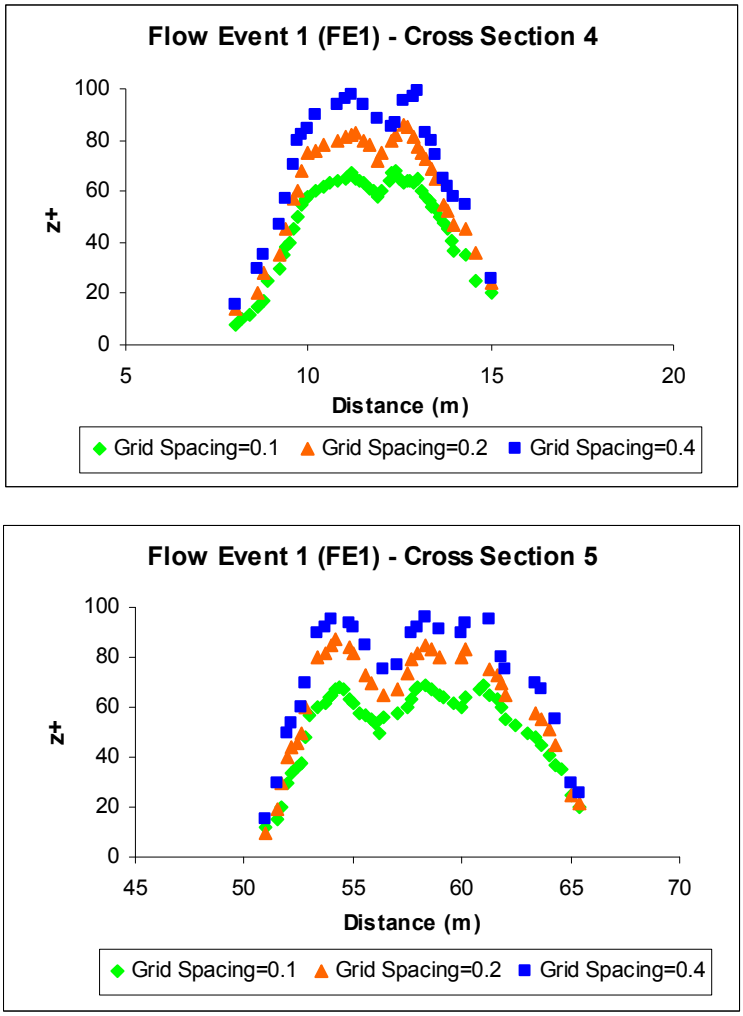

Figure 5.4: Investigation of various grid resolutions in relation to the wall functions employed, for cross-sections 4 and 5 and Flow Event 1 (FE1).

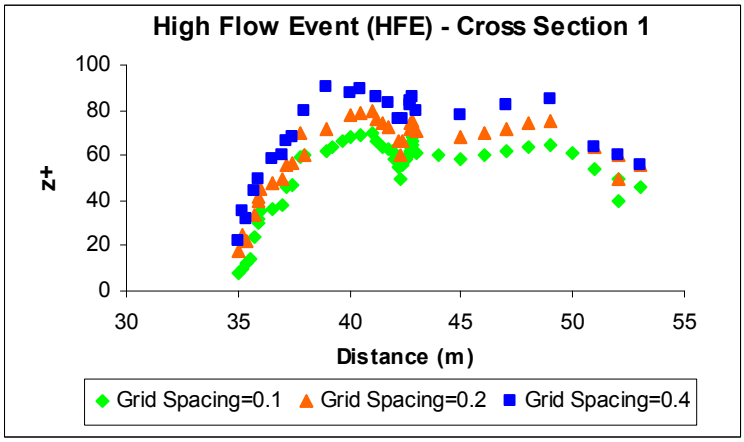

Figure 5.5: Investigation of various grid resolutions in relation to the wall functions employed for cross-section 1 and the High Flow Event (HFE).

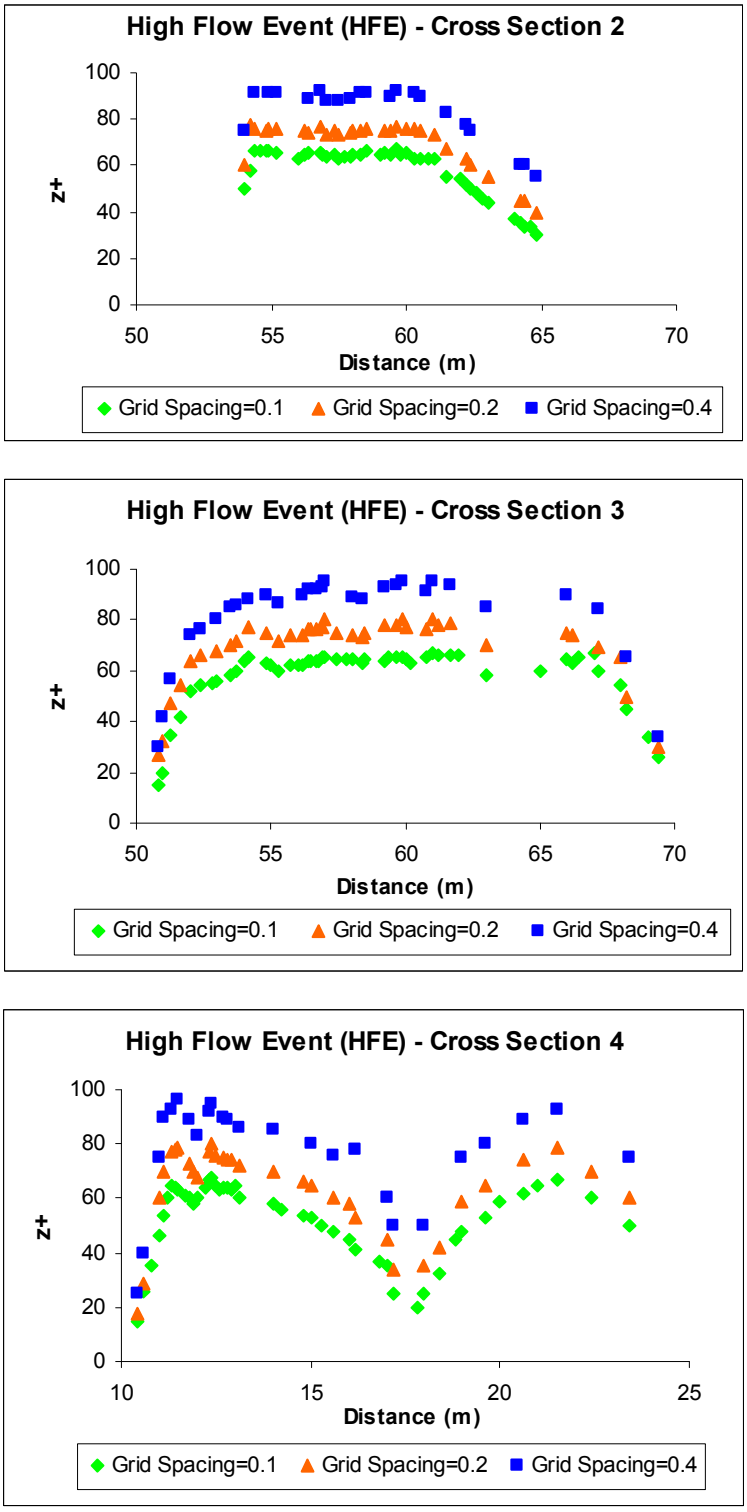

Figure 5.6: Investigation of various grid resolutions in relation to the wall functions employed for cross-sections 2, 3, and 4 and High Flow Event (HFE).

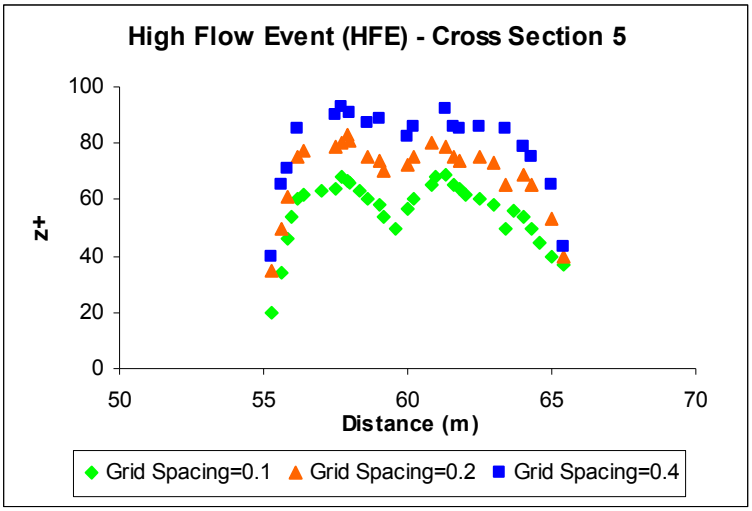

Figure 5.7: Investigation of various grid resolutions in relation to the wall functions employed for cross-section 5 under the High Flow Event (HFE).

As can been seen in Figures 5.3 through 5.7, the meshes related to the grid spacing of 0.1 m are adequate to obtain a low z^+ close to 60 and consequently a condition satisfying the wall functions employed. The number of cells contained within the FE1 and HFE meshes corresponding to the grid spacing of 0.1 m are 2,500,068 and 2,976,883, respectively.

The modelling results obtained are presented and explained in the next section. A combination of near-surface and near-bed vectors showing both flow direction and velocity magnitude at constant elevations is utilized. In addition, dynamic pressure and shear stress distributions are examined, while planform maps show the spatial patterns of the near-surface velocity magnitude and orientation. Finally, cross-section contour plots of downstream velocity magnitude, with vector plots superimposed on top showing cross steam and vertical velocity components are undertaken.

5.2 Results: High Flow Conditions

5.2.1 Flow Event 1 (FE1)

To help locate particular flow features, the same four Areas of Interest (AOI) identified at the Low Flow Event, namely, upstream inflow area (AOI 1), midstream small bend area (AOI 2), upstream large bend area (AOI 3), and downstream large bend area (AOI 4) are

investigated within Flow Event 1 (FE1). As previously mentioned, these four AOI, illustrated in Figure 5.8, were selected since the interesting flow structures identified within them at FE1 do not differ from those observed in LFE.

Simulated near-bed (at a constant elevation of 8.6m) and near-surface (at a constant elevation of 9.8m) flow patterns within AOI 1 are shown in Figure 5.9. The vectors not only demonstrate the resultant direction of the streamwise, leftwards, and rightwards components of velocity at alternate cells in each direction but also show the velocity magnitude at each one of those cells. A predicted planform map of near surface velocity magnitude (at a constant elevation of 9.8m) for AOI 1 is also shown in Figure 5.10.

The velocity magnitude, although calculated from all three velocity components, is dominated by the horizontal ones. Flow features in AOI 1 were identified by drawing three different cross sections within the upstream inflow area (Figure 5.9), labelled A-C in downstream order.

Figures 5.9 and 5.10 demonstrate that, compared to the LFE, the main features of the flow are maintained at this higher flow discharge, but several significant alterations in flow detail are also evident.

As flow stage increases, the sloping nature of the shallow riffle along the left bank, results in a general widening of the channel. The mean inflow velocity into AOI 1 is almost twice as high at FE1 (~1.0 m/s), with the main core of velocity occupying a greater width of the channel. As noted in Figure 5.10, there is a deceleration of the flow towards the right bank. More specifically, between sections A and B the near bed velocity is much higher at the shallow riffle close to the left bank (~1.2 m/s) rather than at the deeper part towards the right bank (~0.7 m/s). In contrast, the near surface flow corresponding to the above mentioned locations is shown to be decelerated from ~1.5 m/s at the shallow riffle to ~1.0 m/s towards the right bank.

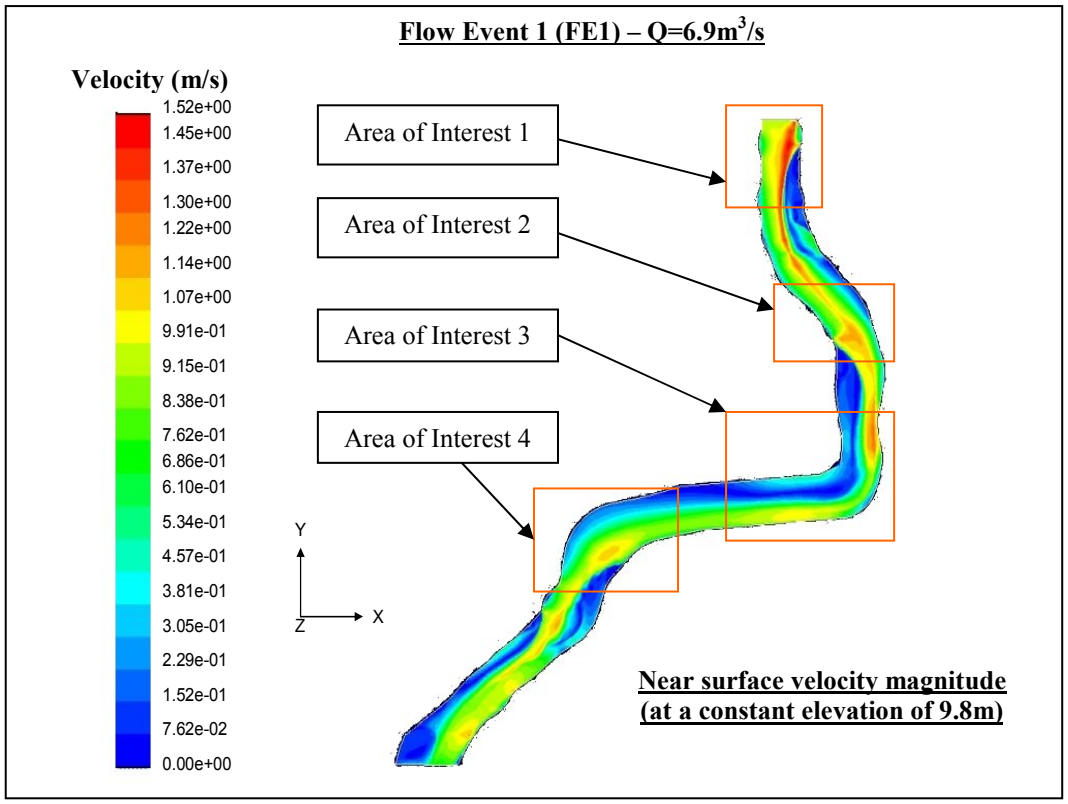

Figure 5.8: Predicted planform map of near surface velocity magnitude (at a constant elevation of 9.8m) for the River Asker reach under Flow Event 1 (Q = 6.9m^3/s) showing the four identified Areas of Interest (AOI).

The left side between sections B and C is also shown to be a dead zone of stagnant flow (<0.1 m/s at both surface and bed). The fast flow (~1.0 m/s) is mainly concentrated into the central area in the form of a small streamtube, with near bed and near surface velocities of ~1.0 m/s and ~1.5 m/s, respectively.

The recirculation zone identified close to the middle part of cross-section C within the dead flow zone at LFE is also observed at FE1. However, the region of stagnant flow is more extensive and a zone of flow separation also occurs. The velocity within this separation zone is much smaller at this higher flow stage, with the flow towards the left bank and the reverse flow at the surface both not exceeding 0.1 m/s.

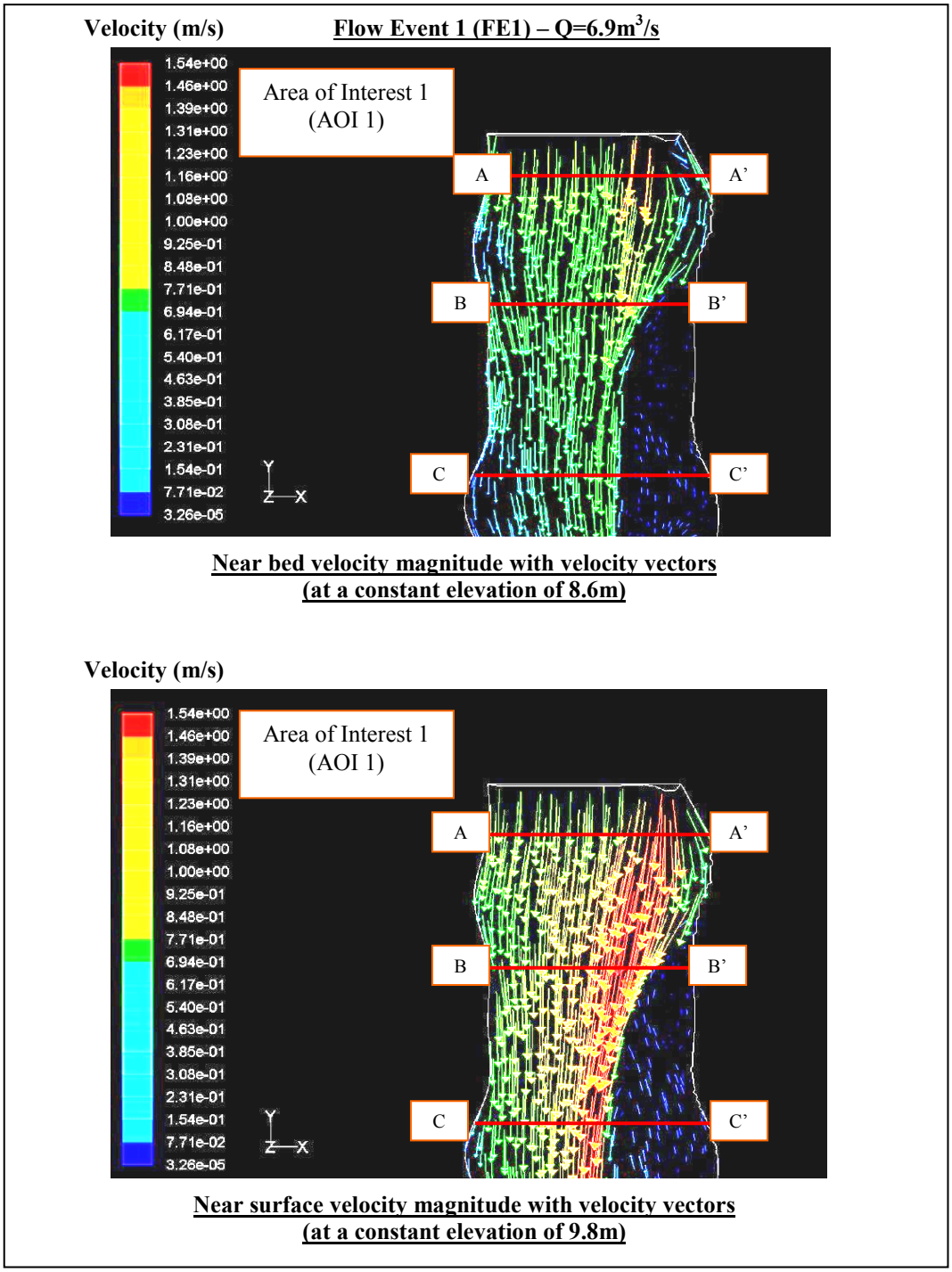

Figure 5.9: Predicted planform map of velocity magnitude with velocity vectors at AOI 1 under Flow Event 1 (Q = 6.9m^3/s) showing flowing direction near the bed (at a constant elevation of 8.6m) and near the surface (at a constant elevation of 9.8m).

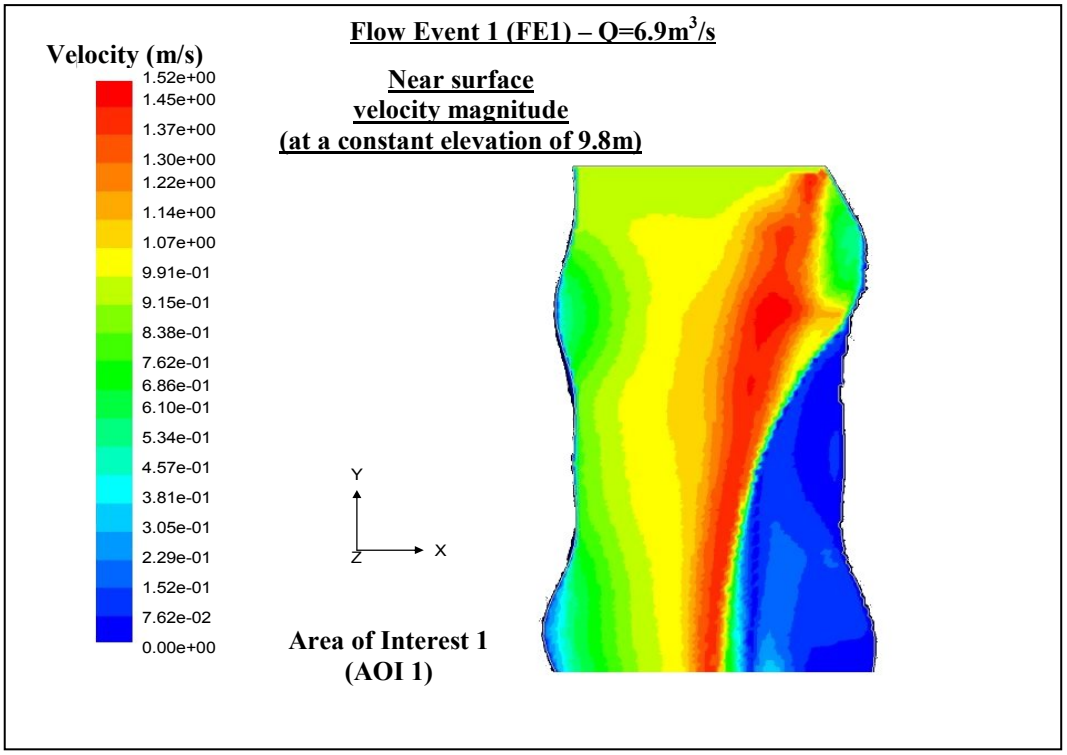

Figure 5.10: Predicted planform map of near surface velocity magnitude (at a constant elevation of 9.8m) at AOI 1 under Flow Event 1 (Q = 6.9m^3/s).

An area of weak secondary circulation with the classic characteristics of helicoidal flow can be found in the right-hand half after section C in the downstream direction. The interpretation of secondary circulation is based upon differences between the near bed and the near surface velocity magnitude and direction. The difference in direction is as much as 30 degrees. The velocity component at the surface can exceed 0.8 m/s in a straight line but that at bed can exceed 0.4 m/s to the left. Although the beginnings of such a flow pattern are present at the normal flow stage (LFE), it is not as clearly defined or developed as at FE1.

Simulated near-bed (at a constant elevation of 8.6m) and near-surface (at a constant elevation of 9.8m) flow patterns corresponding to AOI 2 are illustrated in Figure 5.11. A near-surface velocity magnitude (at a constant elevation of 9.8m) in a planform map for AOI 2 is depicted in Figure 5.12. Three cross-sections (labelled A-C in downstream

order) were also drawn within the midstream small bend area (AOI 2) to more easily define the various flow features.

A general widening of the channel, especially along the outer left bank, can be observed as flow stage increases. As can be seen in Figure 5.12, there is a general deceleration of the flow from the upstream to the middle part of the AOI 2 and some subsequent acceleration to the left-hand half of the outflow section as the reach deepens towards the exit. The deceleration is most prominent in the near surface flow where the maximum velocity decreases from ~1.5 m/s at the inflow just before section A to ~1.0 m/s towards the middle part of section B.

After section B, the fast flow is mostly concentrated towards the outer bank (with velocities over 1.3 m/s at the surface, and 0.7 m/s at the bed), which is in stark contrast to the extensive area of slow flow extending across the channel from the inner bank dead zone of stagnant flow after the inner apex in the downstream direction (<0.1 m/s at both surface and bed).

This significant difference of flow velocities within these flow structures might have implications with respect to the way the reach erodes its banks. Bank erosion seems to be more prominent after the outer bank apex since high values of flow velocity and shear stress leading to erosion phenomena and consequently changing the bankline of the channel.

The area of slow velocity very close to the outer bank at the start of the flow (near section A) also remains. Upstream of this slow flow area a recirculation zone is present. The mean inflow velocity into the small bend in some places is more than twice as high at this higher flow stage (~1.6 m/s). Impingement of this flow core on the outer bank occurs further downstream than at low flow stage, but it is still located downstream of the bend apex.

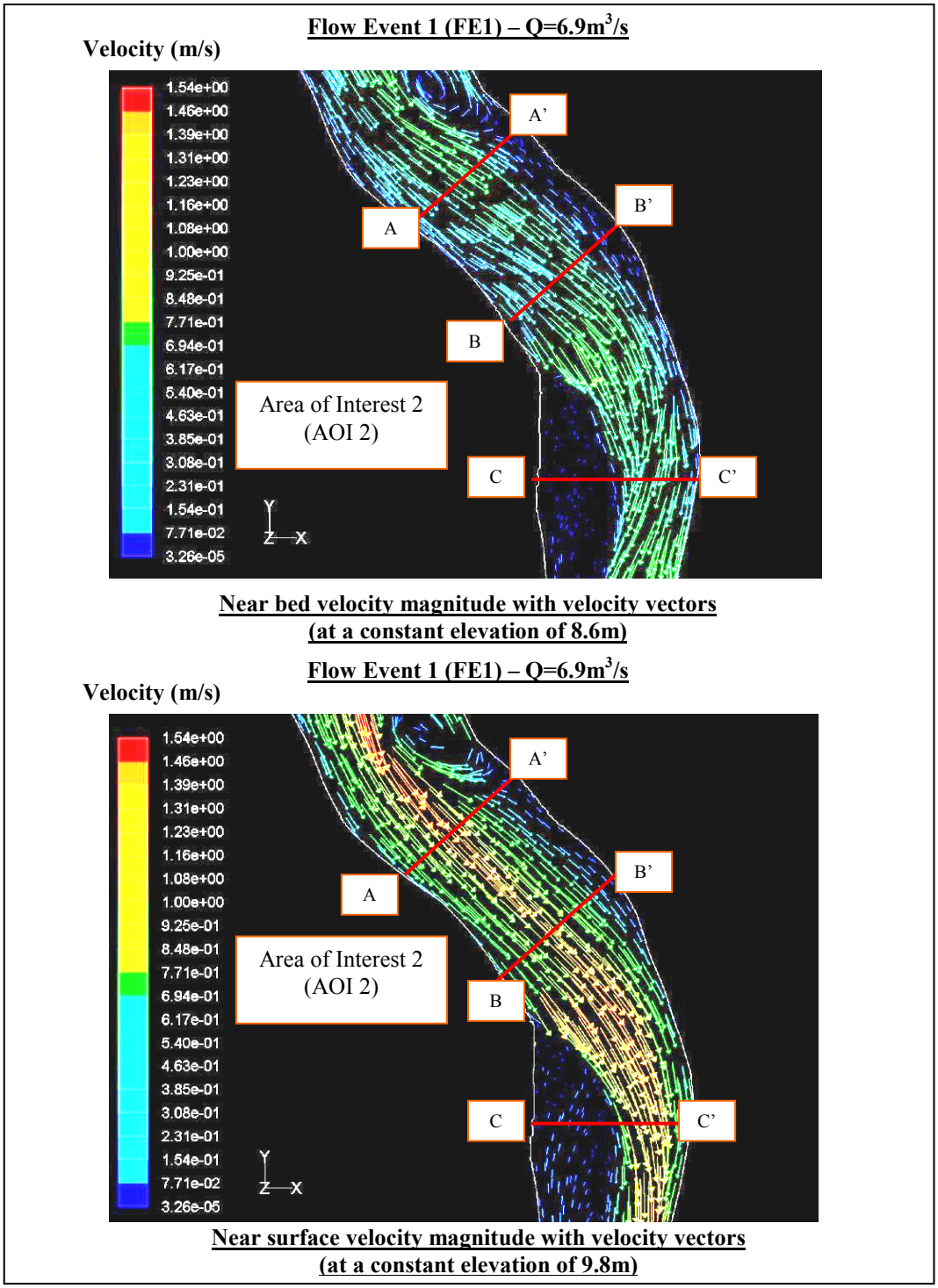

Figure 5.11: Predicted planform map of velocity magnitude with velocity vectors at AOI 2 under Flow Event 1 (Q = 6.9m^3/s) showing flowing direction near the bed (at a constant elevation of 8.6m) and near the surface (at a constant elevation of 9.8m).

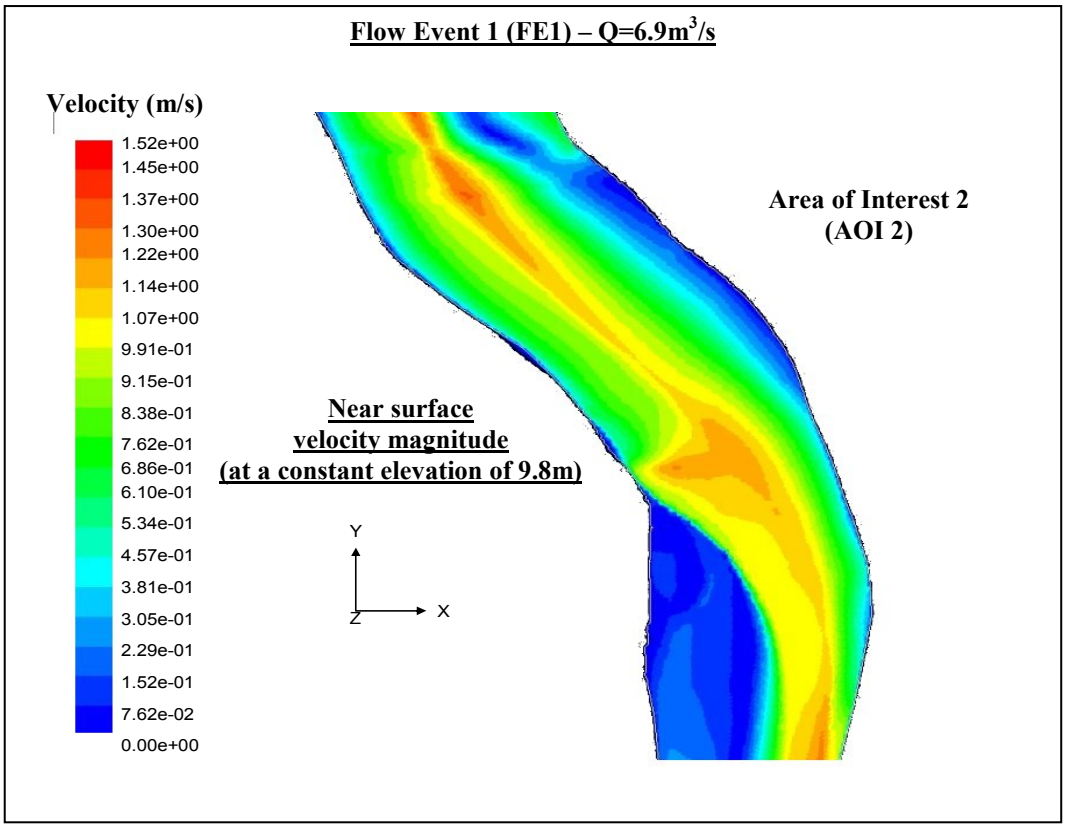

Figure 5.12: Predicted planform map of near surface velocity magnitude (at a constant elevation of 9.8m) at AOI 2 under Flow Event 1 (Q = 6.9m^3/s).

Two regions corresponding to the characteristic helicoidal flow are also identified within the streamtube of relatively fast down channel flow at FE1. The first one is located at the upstream right-hand half of section A (next to the separation zone), with bed vectors angled towards the outer bank but surface vectors angled towards the inner bank. The difference in direction is as much as 60 degrees with velocity component at the surface exceeding 1.5 m/s inwards but that at bed exceeding 0.7 m/s outwards.

The second one is close to the outer bank in the midstream portion of the small bend, where the helical motion is at a maximum. This strong helical circulation, looking downstream, can be seen in the left-hand half between sections B and C. This second area of significant secondary flow includes several places where surface vectors angled towards the outer bank (~1.5 m/s to the left) and bed vectors angled away towards the inner bank (~0.8 m/s to the right). The same flow structures have been identified within

the low flow stage with surface and bed velocity vectors of ~0.8 m/s and ~0.4 m/s, respectively.

Figure 5.13 depicts the simulated near-bed (at a constant elevation of 8.2m) and near-surface (at a constant elevation of 9.6m) flow patterns within AOI 3, while a contour of the near-surface velocity magnitude (at a constant elevation of 9.6m) is illustrated in Figure 5.14. Flow features in AOI 3 were also identified by drawing three different cross sections within the upstream large bend area (Figure 5.13), labelled A-C in downstream order. The velocity magnitude, although calculated from all three velocity components, is dominated by the horizontal ones.

As is evident in Figure 5.14, the inflow to the bend at its left-hand half is dominated by high velocities (~1.5 m/s), whereas in its right-hand half the velocity magnitudes are found to be very low (<0.3 m/s). A general deceleration in both bed and surface velocity is observed at the outer bank bend apex between sections A and B. As flow stage increases, a widening of the channel can be observed along the banks of this particular area (AOI 3). The mean inflow velocity into the bend is more than twice as high at FE1 (~1.0 m/s), with the main core of velocity occupying a greater width of the channel, especially at its outer bank.

The strong flow asymmetry through the bend continues to exist past the apex at this higher stage, with the inner bank separation remaining present and the downstream flow still confined into an outer bank streamtube. However, the very slow velocity area at the outer bank bend apex between sections A and B observed in LFE is no longer in place. Thus, as flow stage increases the area corresponding to the outer bank apex is likely to be eroded since high flow velocities and shear stresses dominate.

Although the separation zone remains at this higher flow stage, it is smaller and the flow structure within and around it is altered considerably. The upstream extent of the reverse flow is not limited as noted in LFE, where high flow velocity exists and the point of detachment is located further upstream along the inner bank.

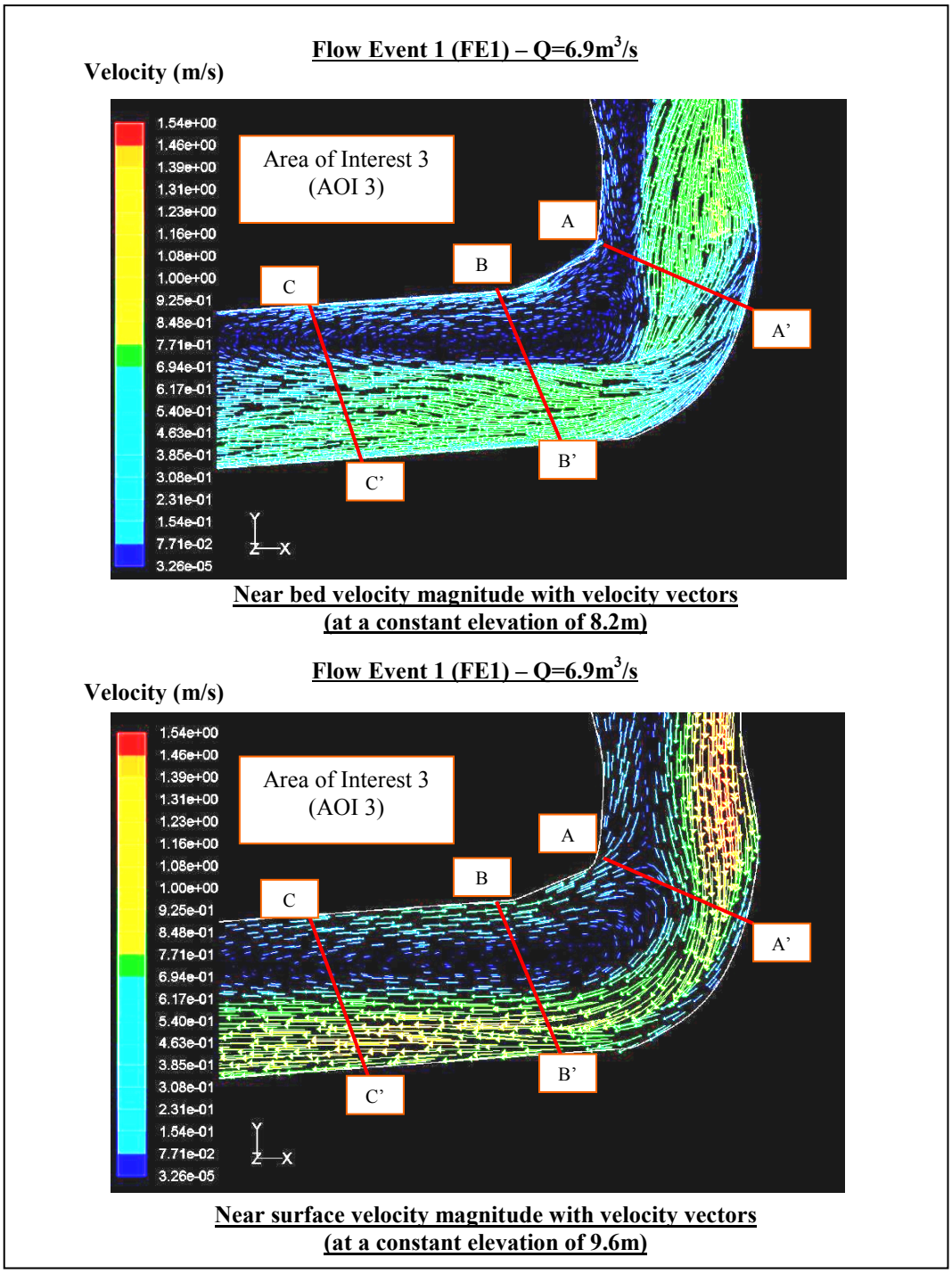

Figure 5.13: Predicted planform map of velocity magnitude with velocity vectors at AOI 3 under Flow Event 1 (Q = 6.9m^3/s) showing flowing direction near the bed (at a constant elevation of 8.2m) and near the surface (at a constant elevation of 9.6m).

The area of very slow velocity along the inner bank remains, although it is significantly greater in FE1, extending all the way downstream. The velocity within the separation zone is much lower at this higher flow stage, with the flow towards the inner bank and the reverse flow at the surface not exceeding 0.5 m/s. Therefore, bank erosion does not play a vital role across the inner bank area since flow velocities are decreased as flow stage increases.

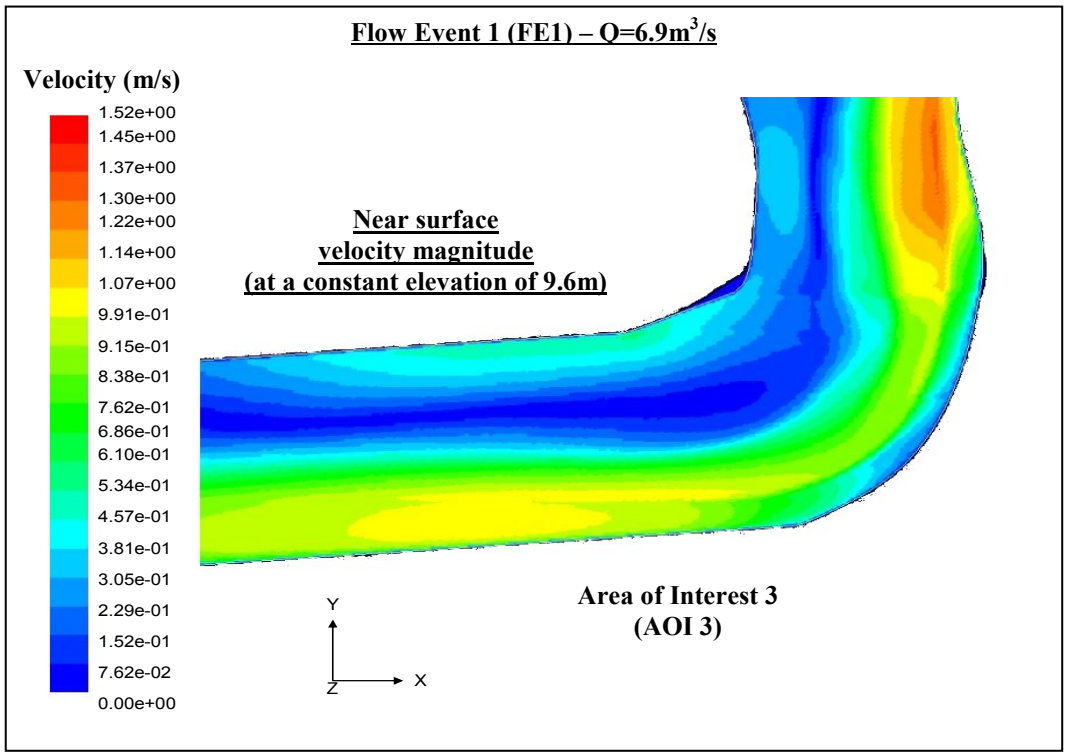

Figure 5.14: Predicted planform map of near surface velocity magnitude (at a constant elevation of 9.6m) at AOI 3 under Flow Event 1 (Q = 6.9m^3/s).

An area of secondary circulation with the classic characteristics of helicoidal flow can be observed in the left-hand half within the fast flow streamtube both upstream and downstream of section A, with bed vectors angled towards the inner bank but surface vectors angled towards the outer bank. The interpretation of secondary circulation is based upon differences between the near bed and the near surface velocity magnitude and direction. The difference in direction is as much as 60 degrees in some places, where the velocity component at the surface can exceed 1.0 m/s outwards but that at bed can exceed 0.5 m/s inwards.

To help locate particular flow features within the downstream large bend area (AOI 4), three section lines are marked on the maps of velocity magnitude with velocity vectors (Figure 5.15) and labelled A-C in downstream order. Section A runs across the fast flow zone not far from the inflow, B runs at the starting point of the separation zone, and C just downstream of the flow recirculation zone.

Figures 5.15 and 5.16 demonstrate that the main features of the flow are maintained at this higher flow discharge. A general widening of the channel along both the inner and outer banks can be observed as flow stage increases.

As noted in Figure 5.15, there is an acceleration of the flow towards the inner bank of the bend just before section A. Both the near bed (~0.5 m/s) and near surface (~1.0 m/s) velocities are higher at the inner bank as the flow enters the bend. In contrast, the flow velocities corresponding to the outer bank of the bend are shown to be low. Therefore, the fast flow zone is concentrated towards the inner bank between sections A and B.

A dead zone of stagnant flow (<0.1 m/s at both surface and bed) can be observed on the left-hand half starting after section B. The outer bend apex is also dominated by low velocity magnitudes. A recirculation zone comes on the left-hand half just before section C. Flow reattachment is located downstream after section C. Although the separation zone remains at this higher stage, it is smaller compared to the LFE and the flow structure alters considerably.

The large region corresponding to the characteristic helicoidal flow identified at LFE at the right-hand half between sections B and C within the relatively fast down channel flow remains in place. Near bed velocity vectors are angled towards the inner (left) bend bank, while the surface vectors are angled away towards the outer (right) bank. The difference in direction is as much as 45 degrees in some places, where the velocity component at the surface can exceed 1.0 m/s to the right but that at bed can exceed 0.6 m/s to the left.

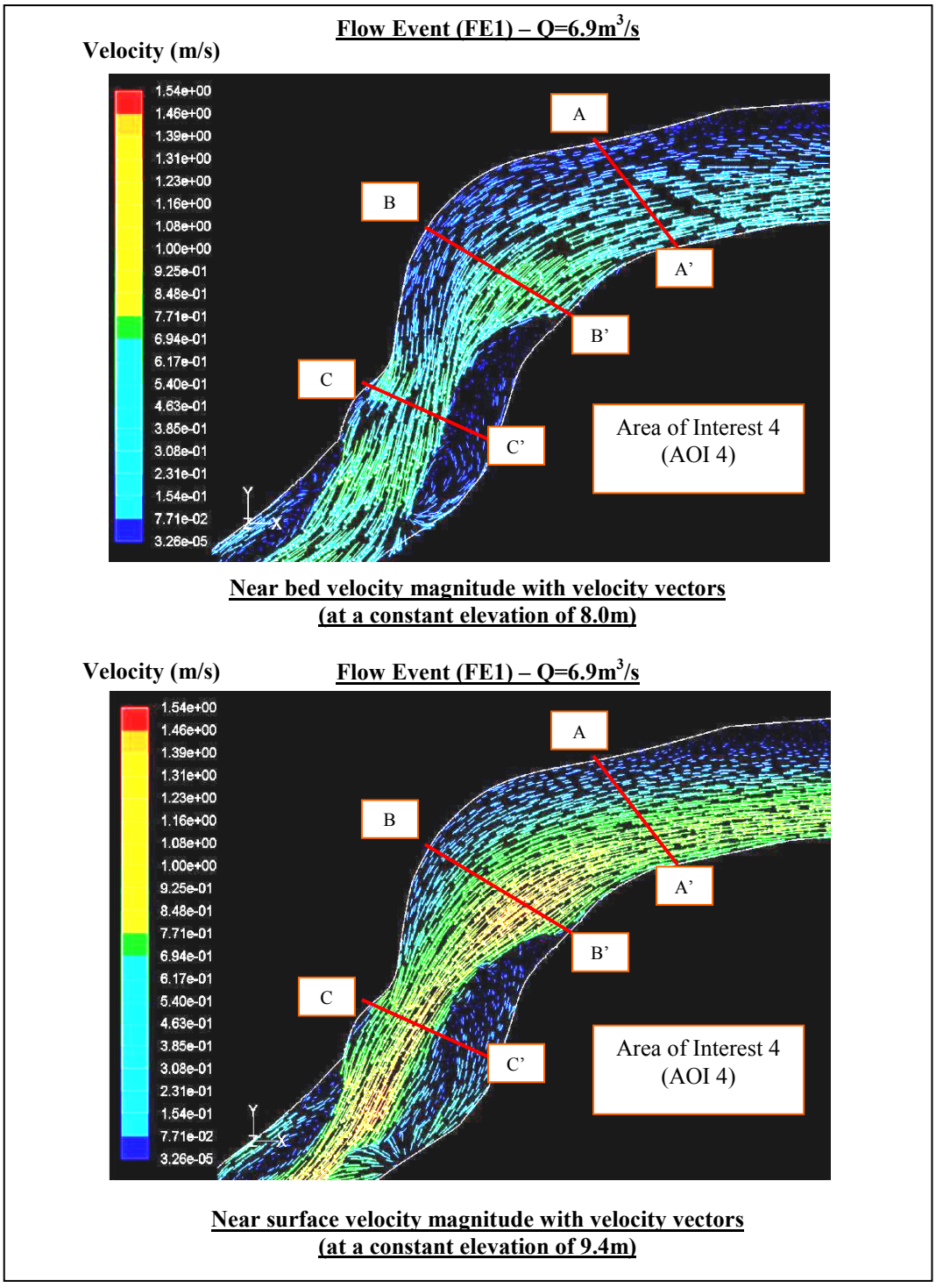

Figure 5.15: Predicted planform map of velocity magnitude with velocity vectors at AOI 4 under Flow Event 1 (Q = 6.9m^3/s) showing flowing direction near the bed (at a constant elevation of 8.0m) and near the surface (at a constant elevation of 9.4m).

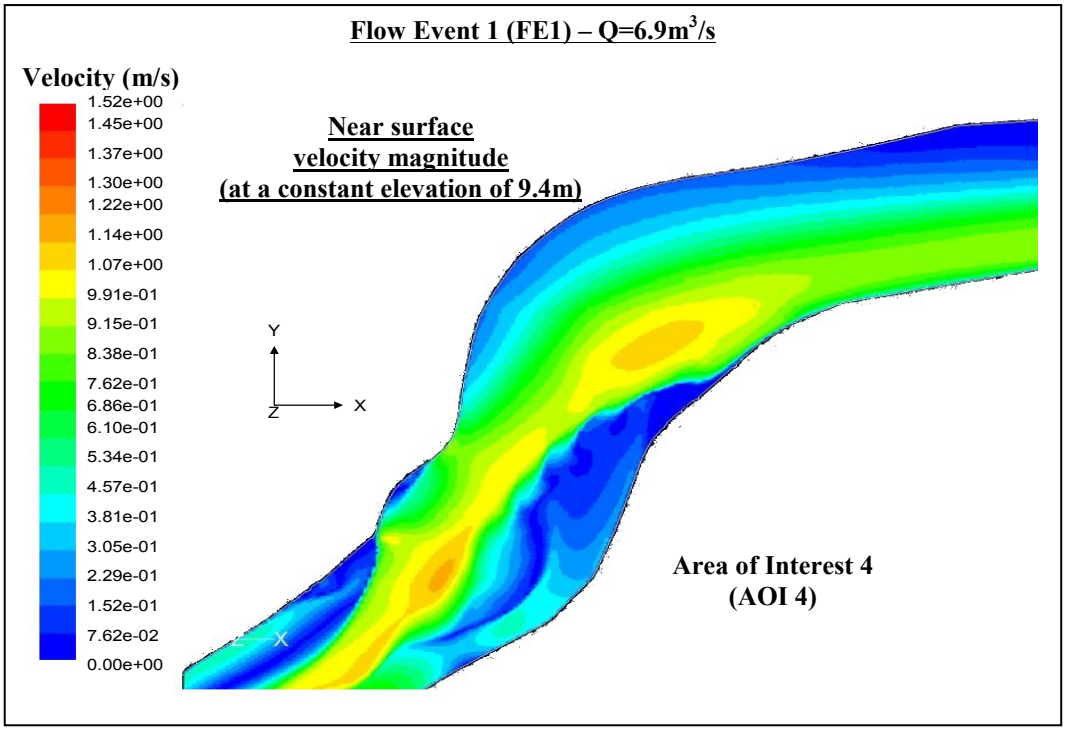

Figure 5.16: Predicted planform map of near surface velocity magnitude (at a constant elevation of 9.4m) at AOI 4 under Flow Event 1 (Q = 6.9m^3/s).

Contour plots of downstream velocity magnitude, with vector plots superimposed on top to illustrate the cross steam and vertical velocity components, were produced for Flow Event 1 by drawing three different cross sections (Figure 5.17), labelled 1-3 in downstream order. These three cross-sections, annotated in Figure 5.17, were chosen since they cover a wide range of different regions throughout the reach representing various flow structures as explained below. The contour plots of cross steam and vertical velocity components within cross-sections 1, 2 and 3 are shown in Figures 5.18, 5.19 and 5.20.

Similar to the lower discharge, at this flow stage there is a progressive movement of the locus of maximum downstream velocity down the inner bank from the surface to the base of the right bank. This movement occurs as rapidly as at low flow stage, although the areas of high downstream velocity are much larger and occupy greater portions of the bed through sections 1, 2, and 3.

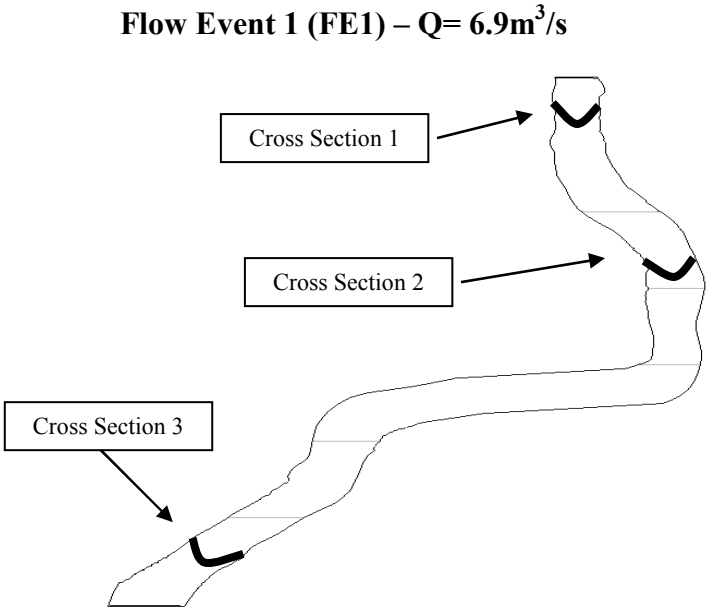

Figure 5.17: Locations of three arbitrarily selected cross-sections at Flow Event 1 (FE1) where contour plots of downstream velocity magnitude showing cross-stream and vertical velocity components are undertaken.

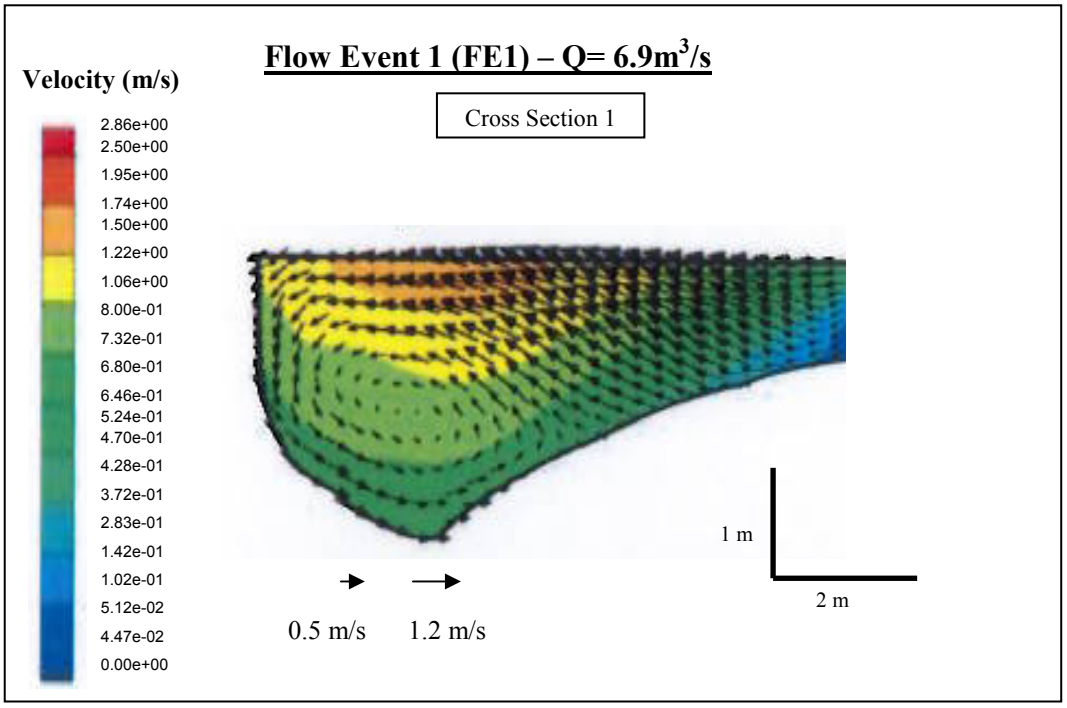

Figure 5.18: Predicted contour plots of downstream velocity magnitude showing cross-stream and vertical velocity components at cross section 1 under Flow Event 1 (Q = 6.9m^3/s).

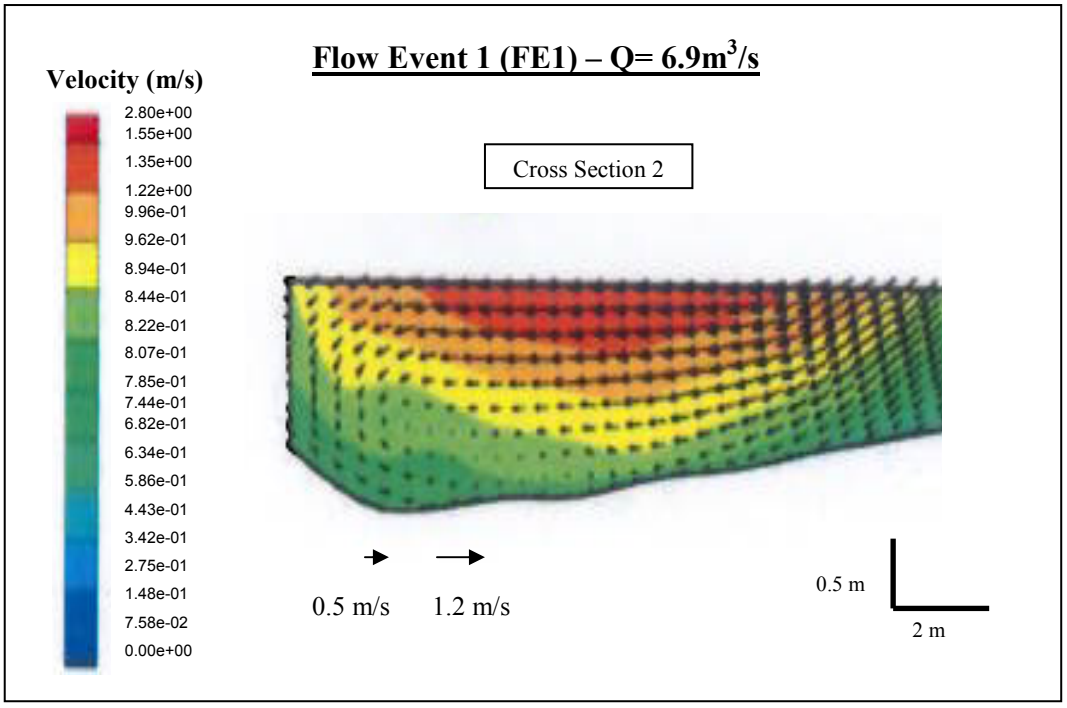

Figure 5.19: Predicted contour plots of downstream velocity magnitude showing cross-stream and vertical velocity components at cross section 2 under Flow Event 1 (Q = 6.9m^3/s).

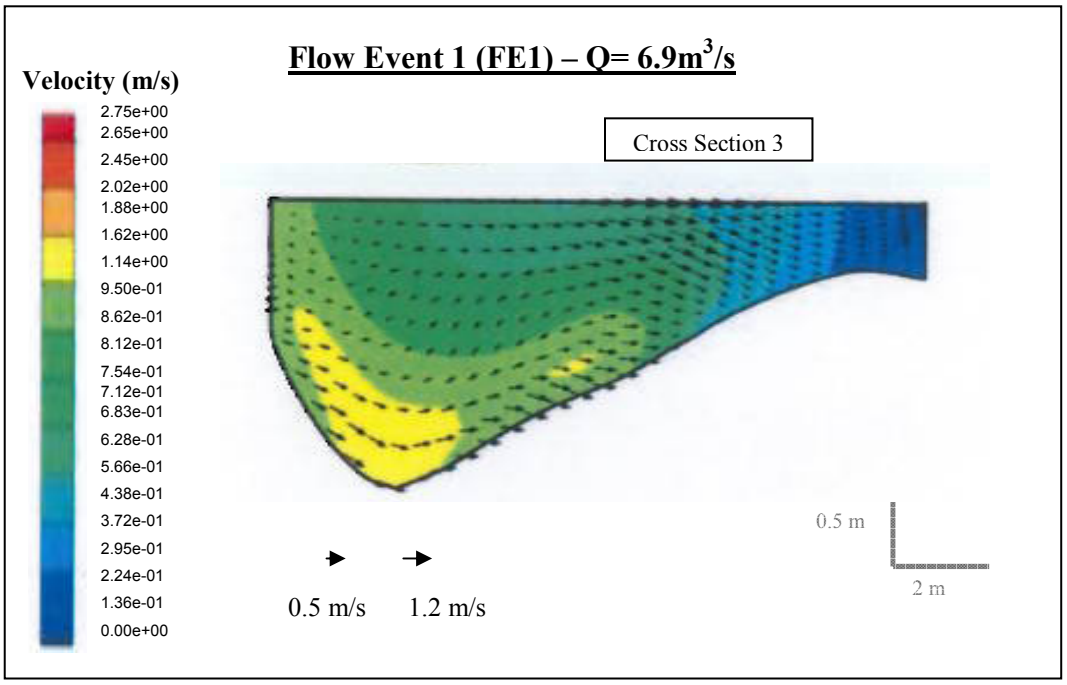

Figure 5.20: Predicted contour plots of downstream velocity magnitude showing cross-stream and vertical velocity components at cross section 3 under Flow Event 1 (Q = 6.9m^3/s).

The changing location of the high downstream velocity component through the reach as observed in cross-sections 1 to 3 is strongly related to the patterns of upwelling and downwelling.

As can be seen in Figure 5.18 the area of significant secondary flow mid way towards the right bank within cross-section 1 is still present at FE1. However, the streamtube secondary cell is more intense and much larger, occupying half the channel. Upwelling dominates the outer half of the channel, and a region of reverse flow is present below the surface at the outer bank. At low flow stage, this secondary cell is much smaller and is suppressed towards the bed. The intensity of the helical circulation at section 1 is much higher in FE1, with downwelling at the inner bank in excess of 0.6 m/s, which compares with the value of less than 0.5 m/s simulated for the low flow stage case.

At FE1, the increase in depth and width at cross-section 2, are associated with patterns of upwelling and downwelling that suggest a coherent secondary circulation cell close to the inner bank. The secondary cell observed in cross-section 3 is mainly dissipated within FE1. Although there is still a remnant of the bottom section of this cell through the base of the pool, the majority of the secondary cell is replaced by a leftwards expansion of the flow as the size of the separation zone rapidly diminishes.

Although both the width and depth, and the velocities throughout the reach all increase, the main qualitative features of the flow present at the lower discharge investigated in Chapter 4 are retained at this higher flow stage. This illustrates that inner bank separation zones do not always disappear at high flow as suggested by *Bridge* and *Jarvis* (1982) (*Hodskinson* and *Ferguson*, 1998; *Parsons,* 2002).

The flow velocities in the separation zones were found to be smaller than those observed under low flow conditions. In addition, the simulated shear stress values within these zones are also very low and are therefore likely to be unable to mobilize any sediment particles. Thus, inner bank erosion seems to be either very low or negligible within the above areas of interest as shown in Figures 5.21 to 5.23. In contrast, simulated flow

velocities and shear stresses close to the outer bank apexes were found to be higher than those identified under LFE. Therefore, outer bank erosion seems to be active on the above mentioned locations increasing in magnitude as flow stage increases.

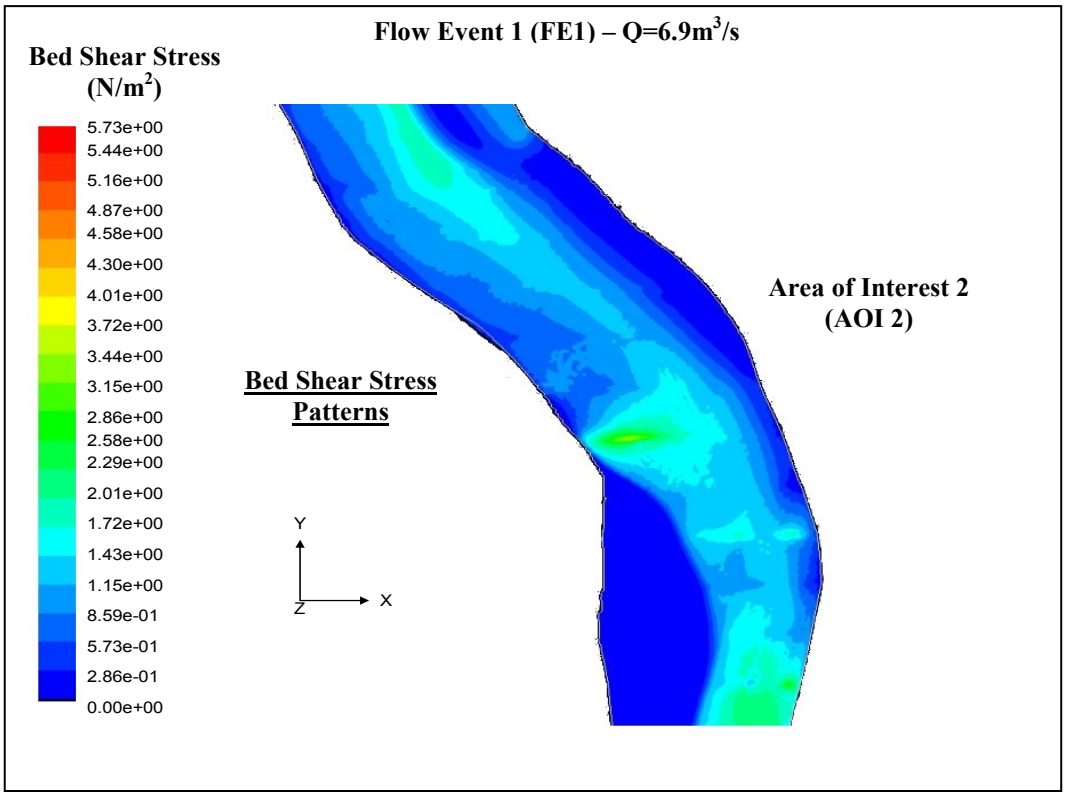

Figure 5.21: Predicted bed shear stress patterns in midstream small bend area (AOI 2) under Flow Event 1 (Q = 6.9m^3/s).

Based on these findings, the nature and type of outer bank erosion acting in bends or in areas dominated by high velocities are likely to be very different to classical models of migration patterns. The presence of regions of high velocity in the form of a streamtube, especially along the outer banks, will create high shear stresses within these areas (Figures 5.21 to 5.23). As a result, the outer bank migration rates are likely to be relatively high in bends with inner bank separation zones (*Parsons,* 2002).

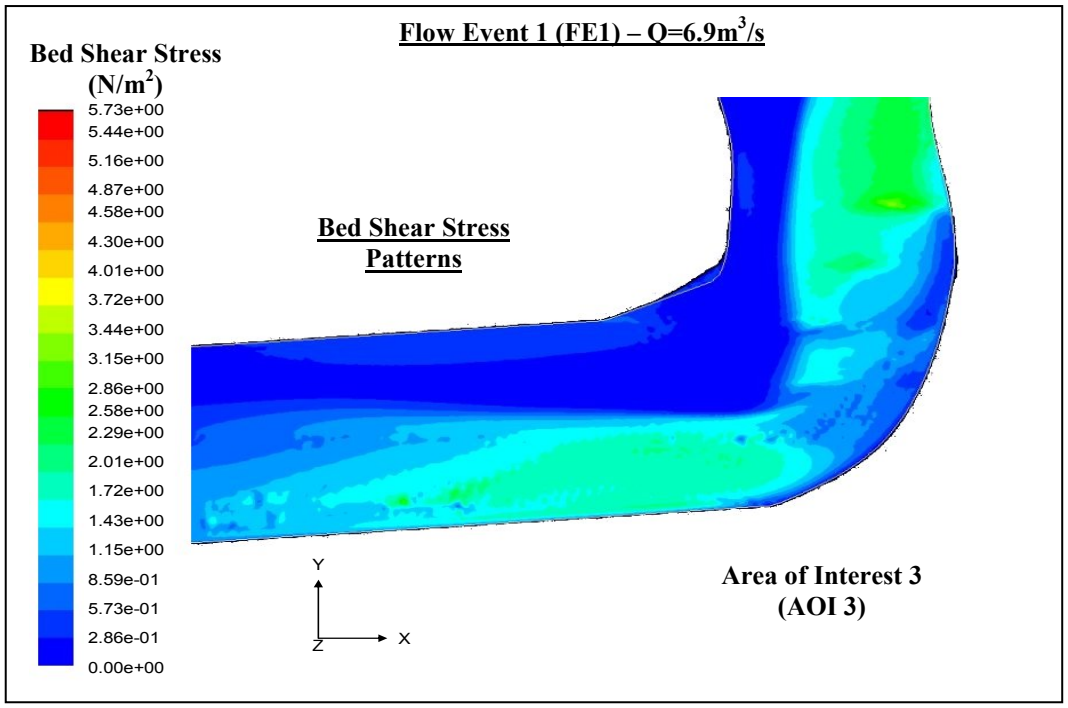

Figure 5.22: Predicted bed shear stress patterns in upstream large bend area (AOI 3) under Flow Event 1 (Q = 6.9m^3/s).

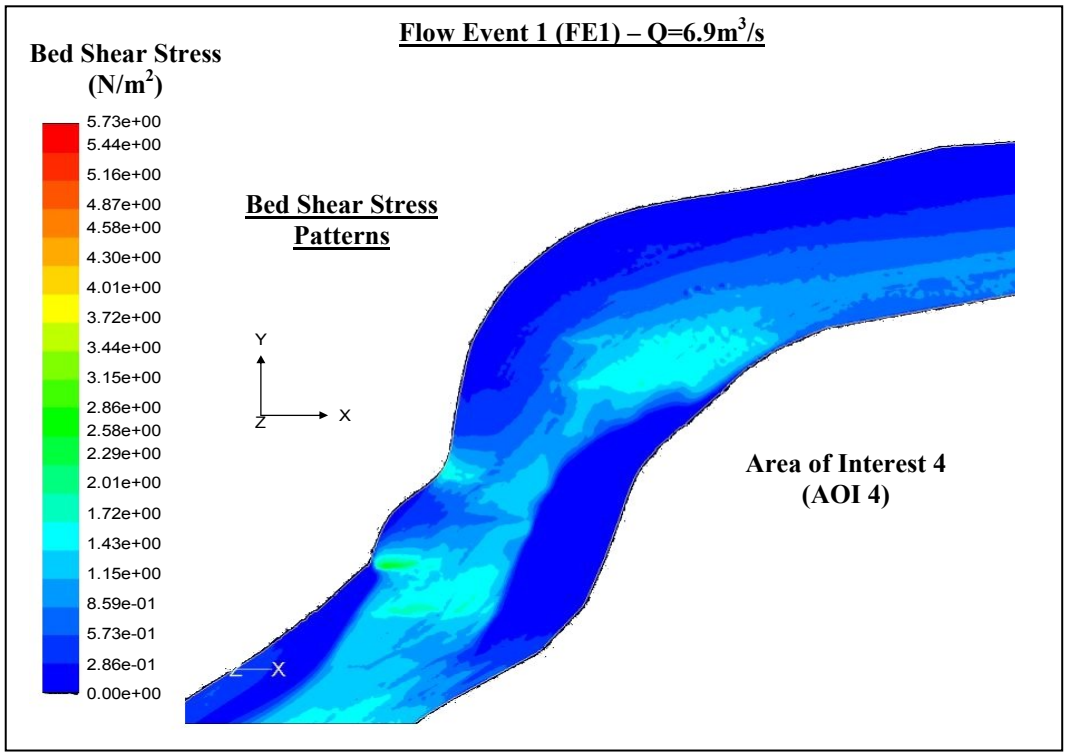

Figure 5.23: Predicted bed shear stress patterns in downstream large bend area (AOI 4) under Flow Event 1 (Q = 6.9m^3/s).

5.2.2 High Flow Event (HFE)

The same four Areas of Interest (AOI) identified for the previous flow events are investigated within High Flow Event (HFE). These four AOI with regards to HFE are depicted in Figure 5.24. To help locate particular flow features within these AOI three cross sections are marked on the maps and labelled A-C in downstream order.

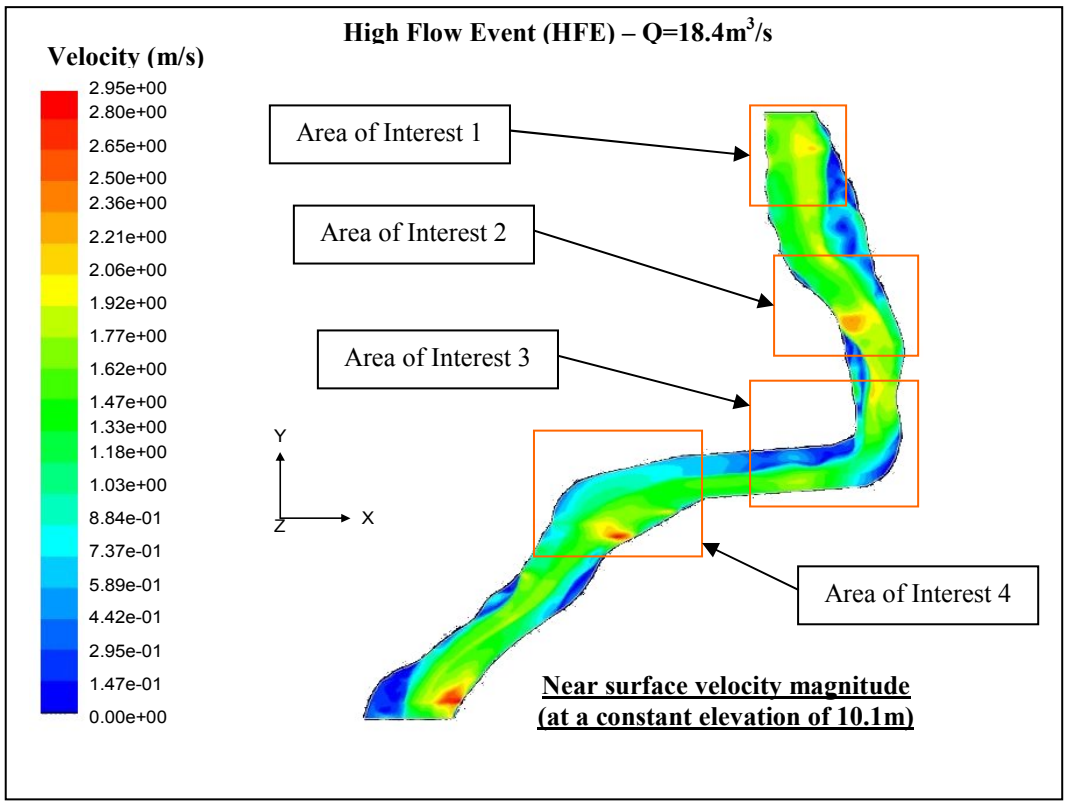

Figure 5.24: Predicted planform map of near surface velocity magnitude (at a constant elevation of 10.1m) for the River Asker reach under high flow conditions (Q = 18.4m^3/s) showing the four identified Areas of Interest (AOI).

Simulated near-bed (at a constant elevation of 8.6m) and near-surface (at a constant elevation of 10.1m) flow patterns corresponding to AOI 1 are shown in Figure 5.25, while a near-surface velocity magnitude (at a constant elevation of 10.1m) in a planform map for AOI 1 is depicted in Figure 5.26. Figures 5.25 and 5.26 demonstrate that the main features of the flow are maintained at this higher near bank full flow discharge. As flow stage increases, the sloping nature along both banks of the reach, results in a general widening of the channel. The mean inflow velocity into AOI 1 is almost twice as high at

HFE (~1.9 m/s) compared to FE1 with the main core of velocity occupying a greater width of the channel.

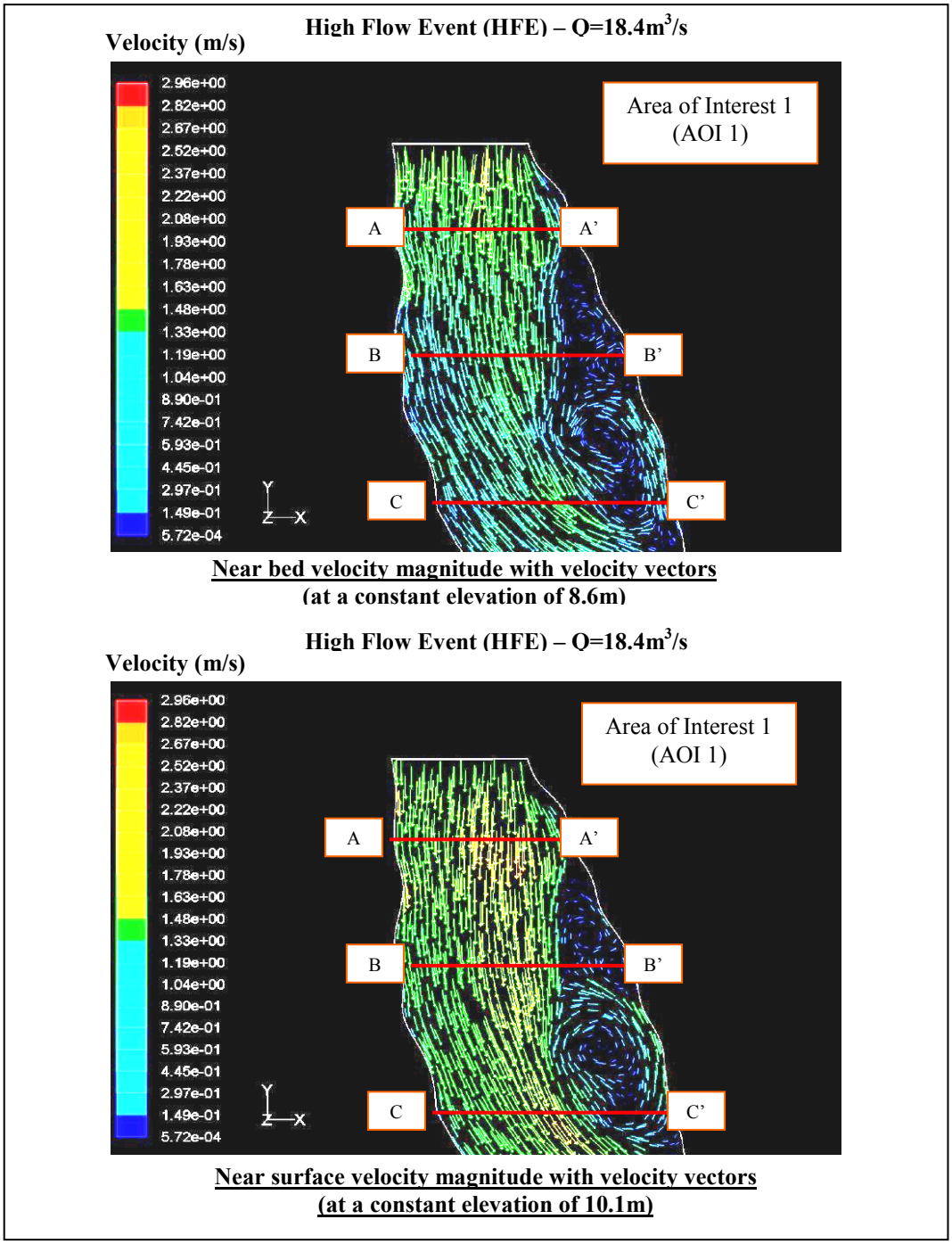

Figure 5.25: Predicted planform map of velocity magnitude with velocity vectors at AOI 1 under high flow conditions (Q = 18.4m^3/s) showing flowing direction near the bed (at a constant elevation of 8.6m) and near the surface (at a constant elevation of 10.1m).

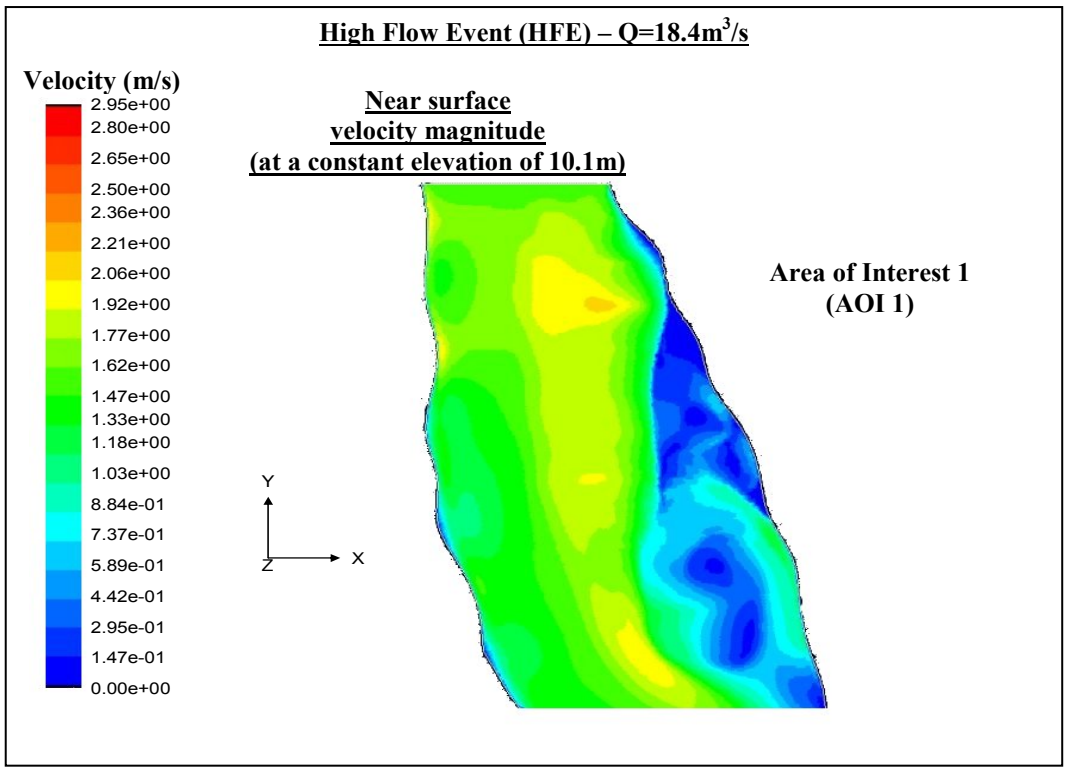

Figure 5.26: Predicted planform map of near surface velocity magnitude (at a constant elevation of 10.1m) at AOI 1 under high flow conditions (Q = 18.4m^3/s).

The same slight deceleration of the flow towards the right bank can be observed in Figure 5.25. Between sections A and B the near bed velocity is much higher over the shallow riffle close to the left bank (~1.4 m/s) rather than in the deeper part towards the right bank (~1.0 m/s), whereas the near surface flow is shown to be decelerated from ~1.9 m/s at the shallow riffle to ~1.3 m/s towards the right bank.

In addition, the left side area between sections A and B retains a dead zone of stagnant flow (<0.1 m/s at both surface and bed) within which a small zone of flow separation occurs. The fast flow (~1.7 m/s) is mainly concentrated into the central area in a form of a small streamtube, with near bed and near surface velocities of ~1.4 m/s and ~1.9 m/s, respectively. A more noteworthy recirculation zone is also observed within the dead flow zone on the left-hand half just downstream of section B. The velocity within this second separation zone is much larger at this near bank full stage, with the flow towards the left bank and the reverse flow at the surface both exceeding 0.8 m/s. The separated zone has a

clockwise circulation in plan view. Near surface velocities merge with the main flow after recirculating, while near bed flow velocities at the same location appear to be smaller and do not fully return to the fast near bed streamtube.

Simulated near-bed (at a constant elevation of 8.6m) and near-surface (at a constant elevation of 10.1m) flow patterns corresponding to AOI 2 are illustrated in Figure 5.27, while a contour of the near-surface velocity magnitude (at a constant elevation of 10.1m) is illustrated in Figure 5.28.

Compared to FE1 a general widening of the channel along both banks is observed as flow stage increases. However, the main features present in the lower of the flows are maintained at this near bank full flow discharge. As can be seen in Figure 5.28, there is a general acceleration of the flow from the upstream to the middle part, with a peak at the inner small bend apex and some subsequent deceleration to the left-hand half outflow section of the reach. The acceleration is most prominent in the near surface flow where the maximum velocity increases from ~1.5 m/s at the inflow just before section A to ~2.8 m/s towards section B, especially near to the small inner bend apex.

After section B, the fast flow is mostly concentrated towards the outer bank (mostly over 1.5 m/s at the surface, 1.0 m/s at the bed), which is in stark contrast to the extensive area of slow flow extending across the channel from the inner bank dead zone of stagnant flow after the inner apex in the downstream direction (<0.1 m/s at both surface and bed).

Upstream of section A on the left-hand half there is a recirculation zone much bigger compared to the one observed within FE1. The mean velocities within AOI 2 under the near bank full high discharge are higher than those observed within FE1 (~1.9 m/s), while impingement of the fast flow core on the outer bank occurs further downstream than at the intermediate flow stage. In addition, a second area corresponding to a separation zone can be found within the stagnant flow after section C.

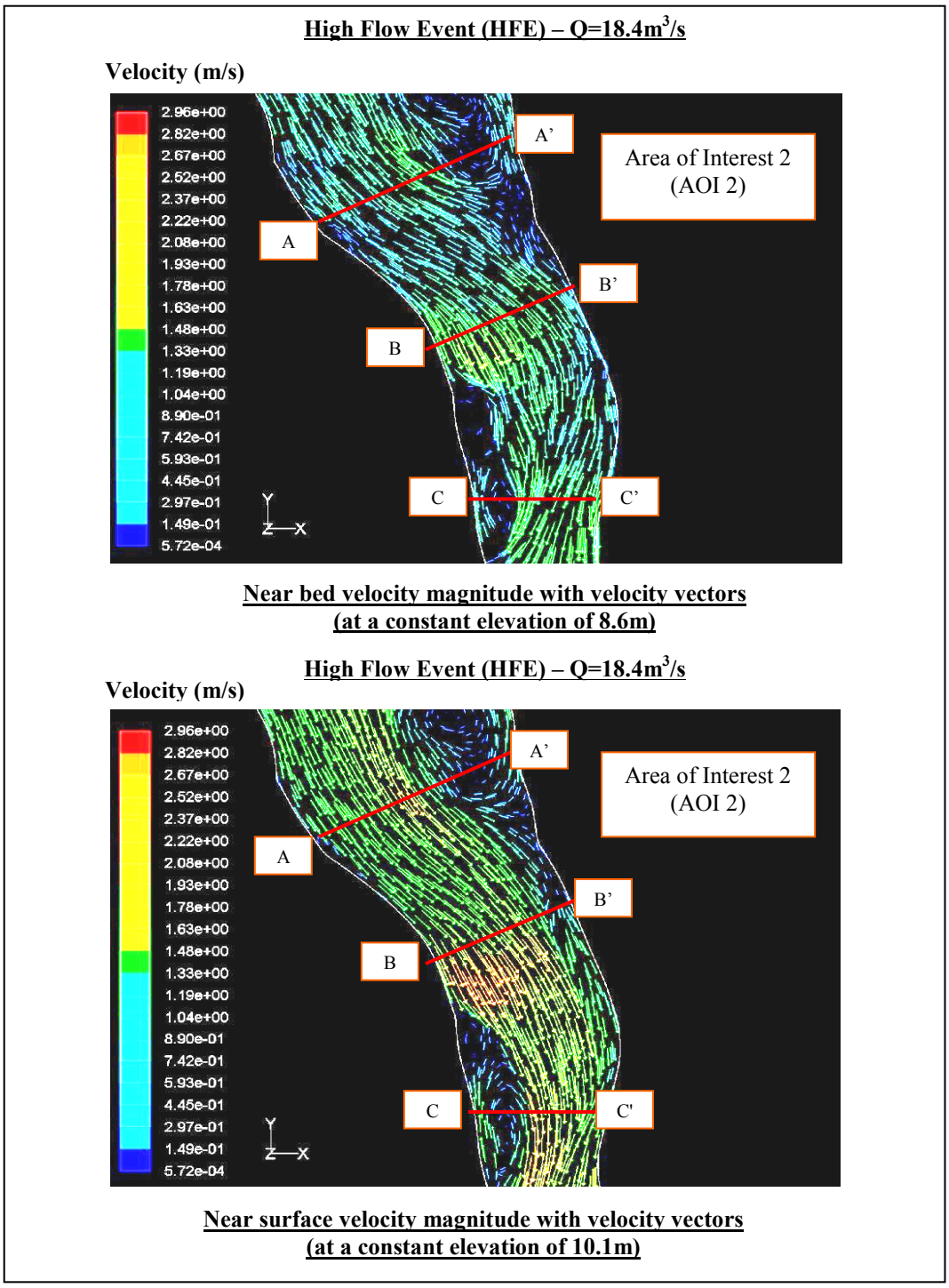

Figure 5.27: Predicted planform map of velocity magnitude with velocity vectors at AOI 2 under high flow conditions (Q = 18.4m^3/s) showing flowing direction near the bed (at a constant elevation of 8.6m) and near the surface (at a constant elevation of 10.1m).

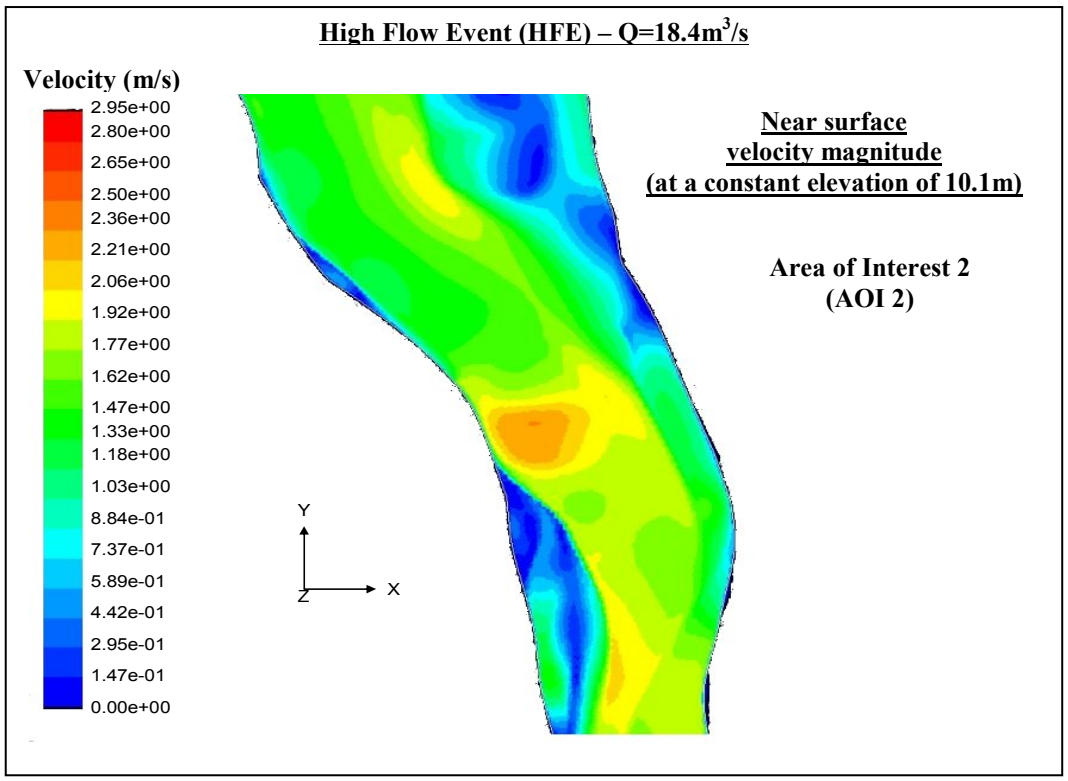

Figure 5.28: Predicted planform map of near surface velocity magnitude (at a constant elevation of 10.1m) at AOI 2 under high flow conditions (Q = 18.4m^3/s).

The same regions of the characteristic helicoidal flow identified within FE1 are also observed in this higher flow stage. The first one is located at the right-hand half of section A (next to the recirculation zone). The second one is close to the outer bank in the midstream portion of the small bend, where the helical motion is at a maximum. This strong helical circulation, looking downstream, can be seen in the left-hand half between sections B and C with bed vectors angled towards the inner bank but surface vectors angled towards the outer bank. The difference in direction is as much as 45 degrees with velocity component at the surface exceeding 1.9 m/s outwards but that at bed exceeding 1.1 m/s inwards.

Simulated near-bed (at a constant elevation of 8.2m) and near-surface (at a constant elevation of 9.9m) flow patterns within the upstream large bend area (AOI 3) are shown in Figure 5.29. A near-surface velocity magnitude (at a constant elevation of 9.9m) in a planform map for AOI 3 is also depicted in Figure 5.30.

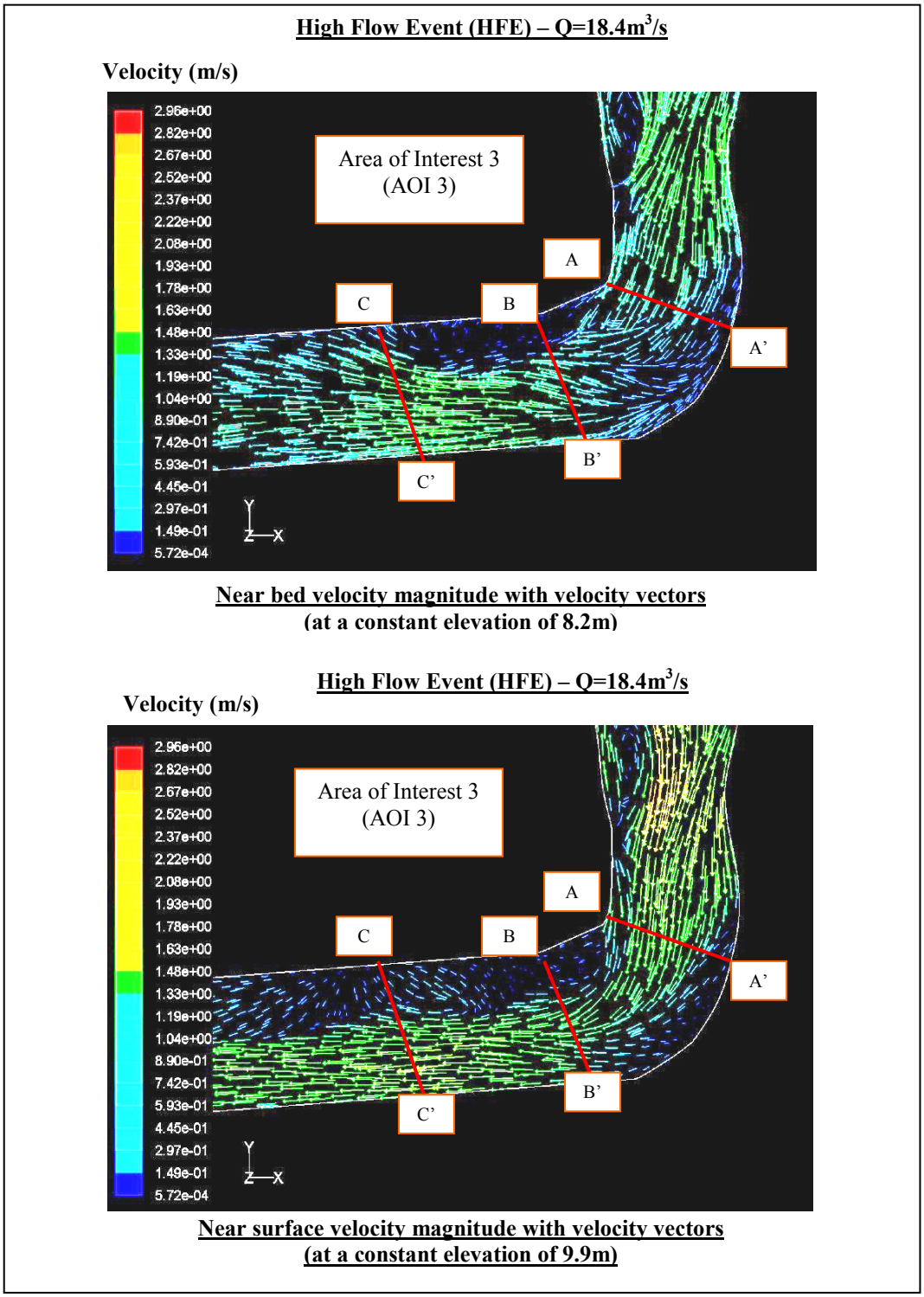

Figure 5.29: Predicted planform map of velocity magnitude with velocity vectors at AOI 3 under high flow conditions (Q = 18.4m^3/s) showing flowing direction near the bed (at a constant elevation of 8.2m) and near the surface (at a constant elevation of 9.9m).

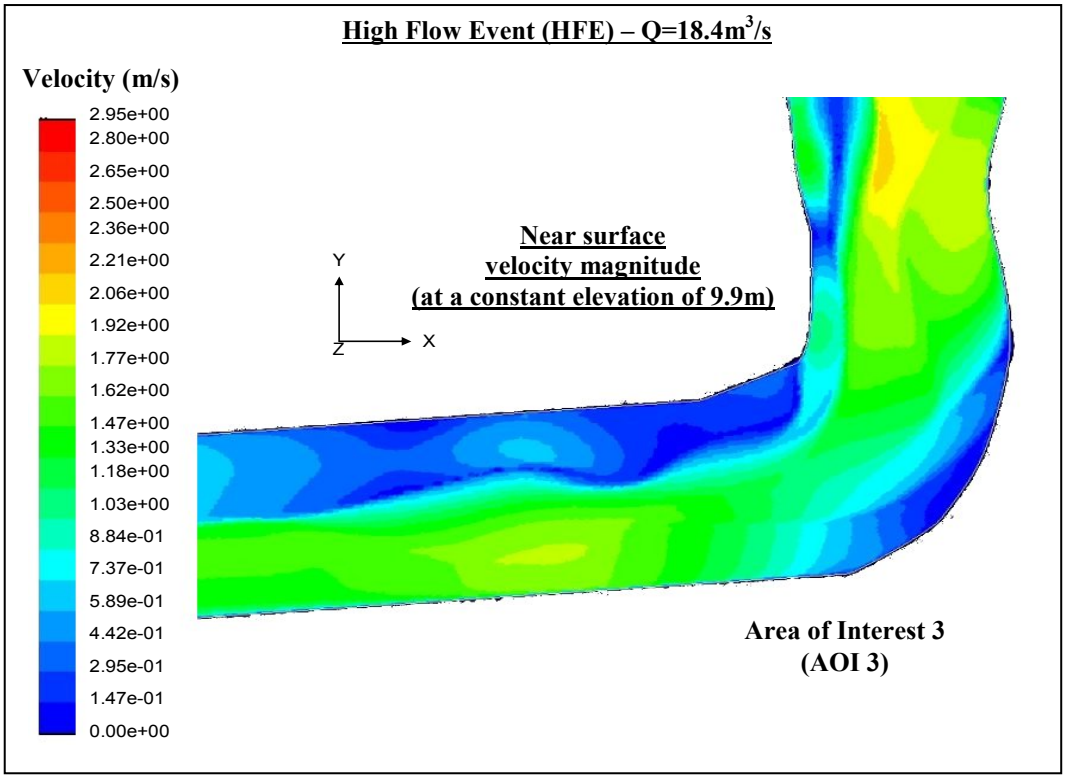

Figure 5.30: Predicted planform map of near surface velocity magnitude (at a constant elevation of 9.9m) at AOI 3 under high flow conditions (Q = 18.4m^3/s).

As can be noted in Figure 5.30, the inflow to the bend except on the right-hand close to the inner bank is dominated by high velocities (~2.0 m/s). At the inner bank the velocity magnitudes are found to be lower. A general deceleration in both bed and surface velocity is observed at the outer bank bend apex between sections A and B as can be seen in Figure 5.29. The mean inflow velocity into the bend (~ 2.0 m/s) is higher compared to the one observed at FE1 (~1.0 m/s) with the main core of velocity occupying almost the whole width of the channel, especially along the inner bank apex.

The strong flow asymmetry through the bend continues to exist past the apex at this near bank full higher stage, with the inner bank separation remaining present but smaller compared to FE1 and the downstream fast flow confined into a thin streamtube between the inner and outer bank apexes. The very slow velocity area at the outer bank bend apex between sections A and B after disappearing in FE1 is again present, as happened within LFE. In addition, the area of very slow velocity along the inner bank all the way

downstream is still in place. The velocity magnitude within the separation zone is similar to the one observed within FE1.

An area of secondary circulation with the classic characteristics of helicoidal flow can be observed in the right-hand half downstream of section C with bed vectors angled towards the inner bank but surface vectors angled towards the outer bank. The interpretation of secondary circulation is based upon differences between the near bed and the near surface velocity magnitude and direction. The difference in direction is as much as 60 degrees in some places, where the velocity component at the surface can exceed 0.2 m/s outwards but that at the bed can exceed 1.2 m/s inwards.

Simulated near-bed (at a constant elevation of 8.0m) and near-surface (at a constant elevation of 9.7m) flow patterns corresponding to the downstream large bend area (AOI 4) are illustrated in Figure 5.31, while a predicted planform map of near-surface velocity magnitude (at a constant elevation of 9.7m) is shown in Figure 5.32.

Figures 5.31 and 5.32 demonstrate that the main features of the flow are maintained at this higher flow discharge. As noted in Figure 5.32, there is an acceleration of the flow towards the bend inner bank apex. Both the near bed (~1.0 m/s) and near surface (~1.5 m/s) velocities are higher at the inner bank as the flow enters the bend. The outer bank of the bend up to the outer apex is shown to be dominated by low velocities. However, the later velocities are higher than those at FE1. In addition, the fast flow zone is gradually occupying a larger width of the channel as the flow approaches the inner bank apex.

The dead zone of stagnant flow (<0.1 m/s at both surface and bed) on the left-hand half starting after the peak high velocity downwards of section B is still in place but is smaller in extent. Although the separation zone at the left-hand half just before section C remains at this higher stage, it is smaller and the flow structure alters considerably.

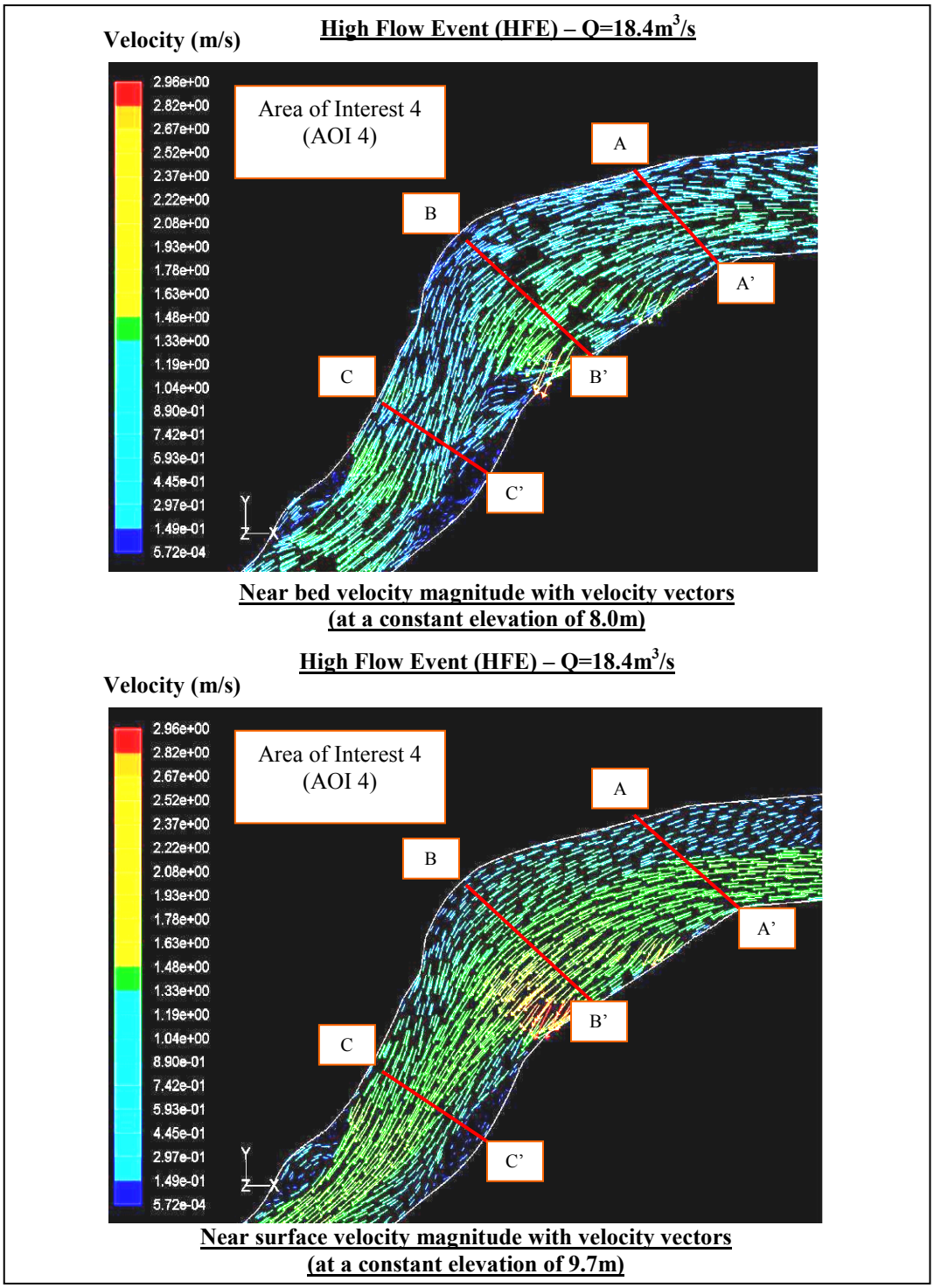

Figure 5.31: Predicted planform map of velocity magnitude with velocity vectors at AOI 4 under high flow conditions (Q = 18.4m^3/s) showing flowing direction near the bed (at a constant elevation of 8.0m) and near the surface (at a constant elevation of 9.7m).

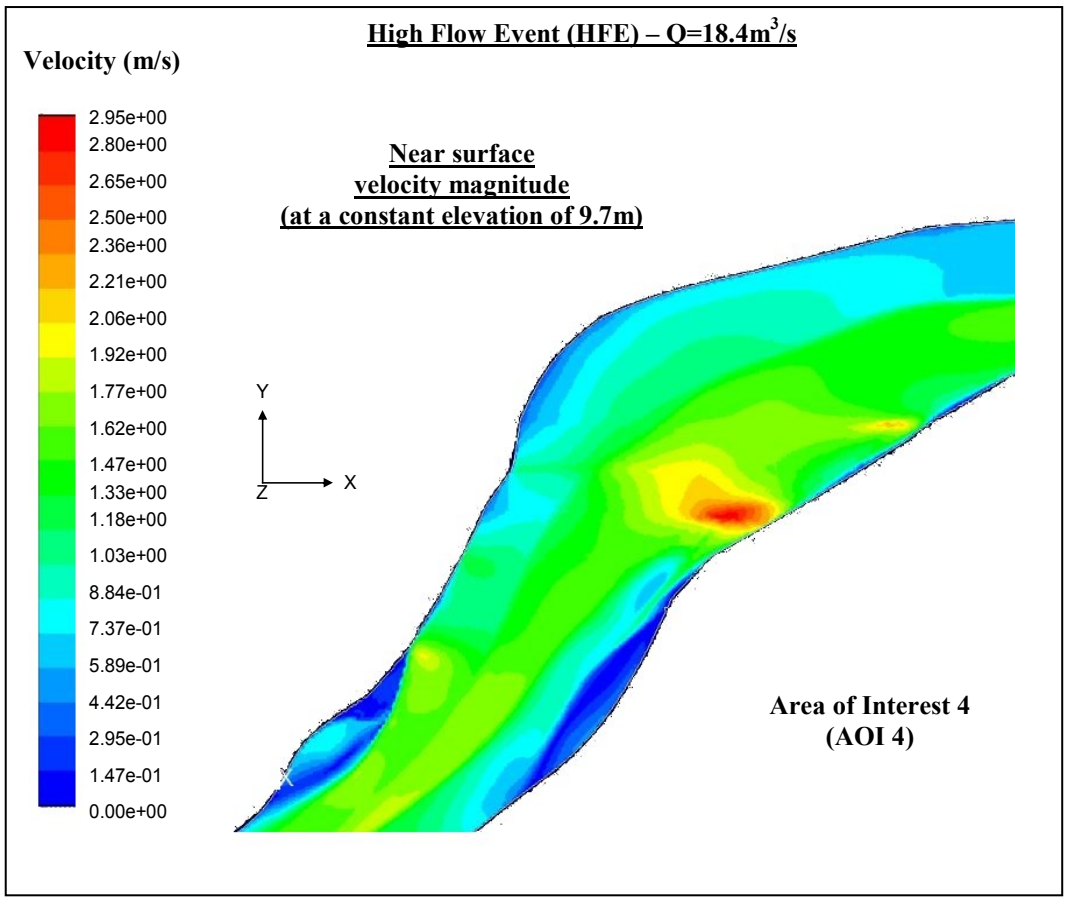

Figure 5.32: Predicted planform map of near surface velocity magnitude (at a constant elevation of 9.7m) at AOI 4 under high flow conditions (Q = 18.4m^3/s).

The large region corresponding to the characteristic helicoidal flow identified at both LFE and FE1 between sections B and C within the relatively fast down channel flow remains in place. Near bed velocity vectors are angled towards the inner (left) bend bank, while surface vectors are angled towards the outer (right) bank. The difference in direction is as much as 45 degrees in some places, where the velocity component at the surface can exceed 1.6 m/s to the right, but that at the bed can exceed 1.0 m/s to the left.

Contour plots of downstream velocity magnitude, with vector plots superimposed on top to show the cross steam and vertical velocity components, were identified within the River Asker reach under high flow conditions by drawing three different cross sections (Figure 5.33), labelled 1-3 in downstream order and shown in Figures 5.34 to 5.36.

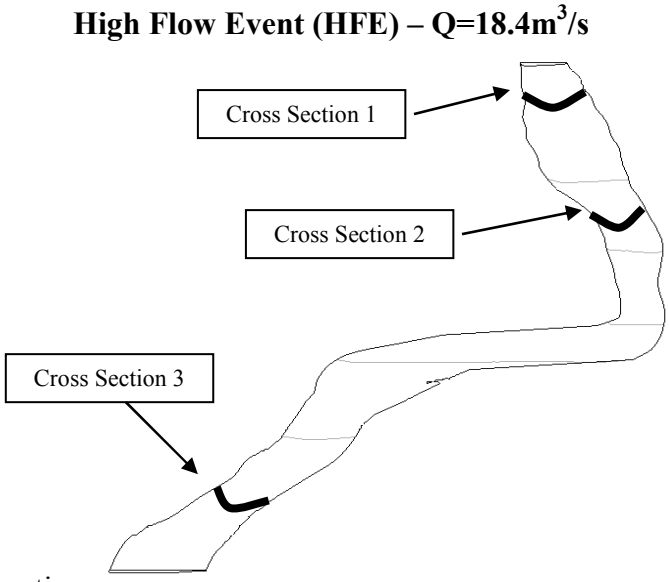

Figure 5.33: Locations of three arbitrarily selected cross-sections at High Flow Event (HFE) where contour plots of downstream velocity magnitude showing cross-stream and vertical velocity components are undertaken.

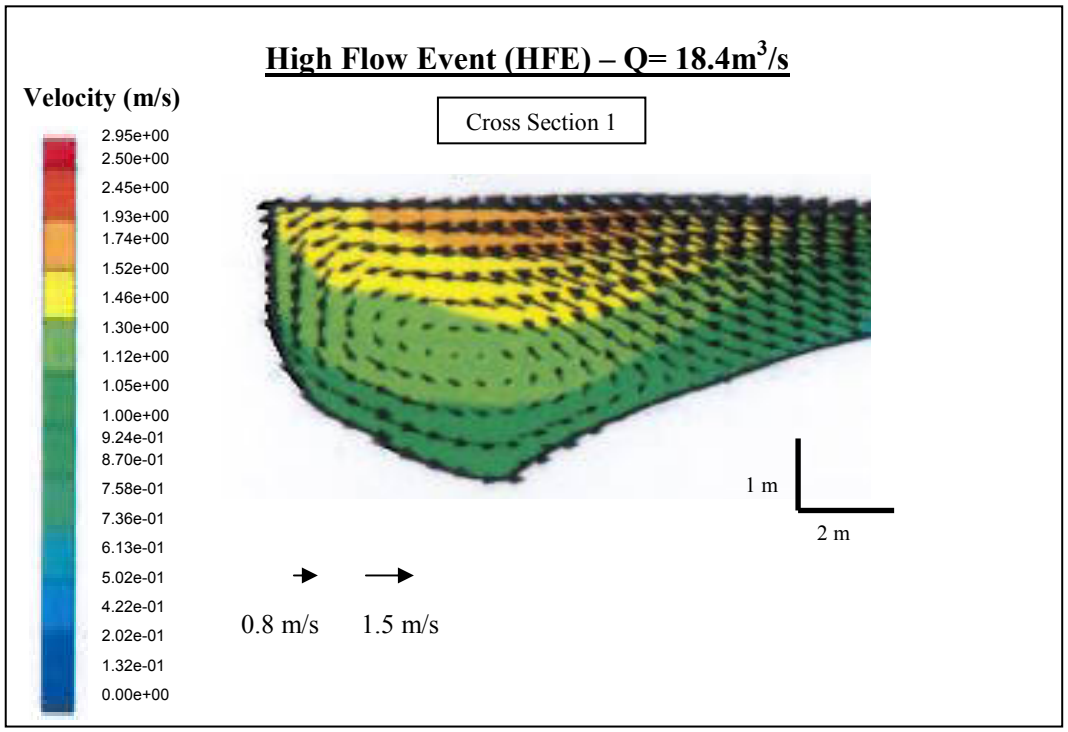

Figure 5.34: Predicted contour plots of downstream velocity magnitude showing cross-stream and vertical velocity components at cross section 1 under High Flow Event (Q = 18.4m^3/s).

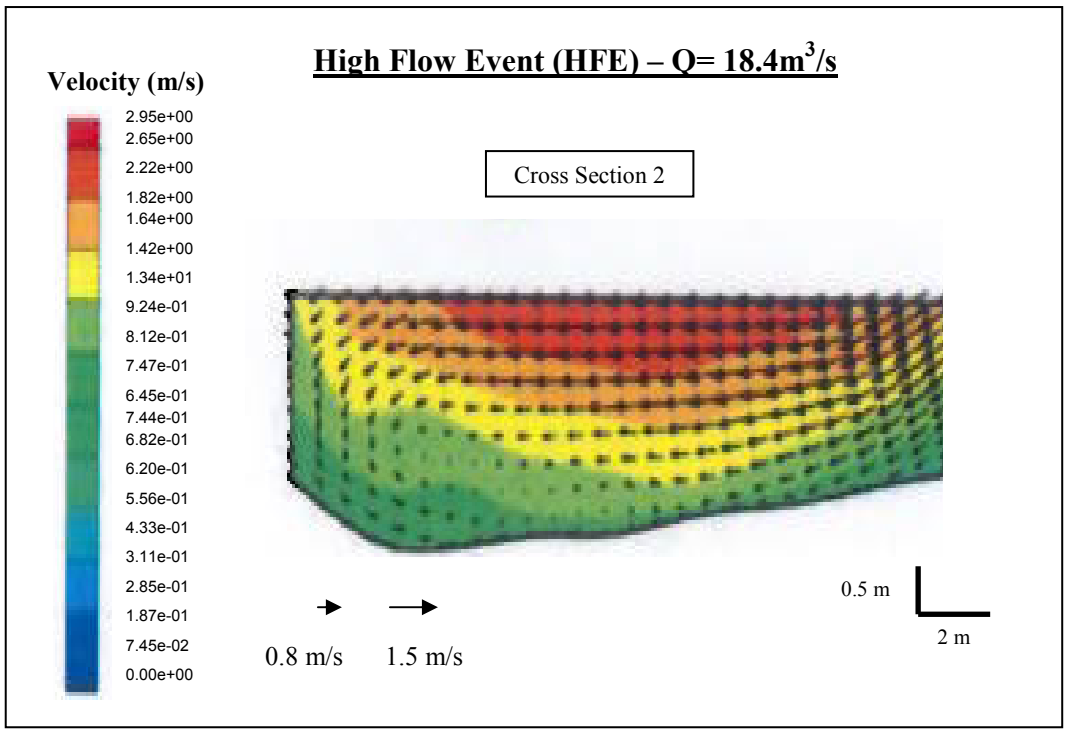

Figure 5.35: Predicted contour plots of downstream velocity magnitude showing cross-stream and vertical velocity components at cross section 2 under High Flow Event (Q = 18.4m^3/s).

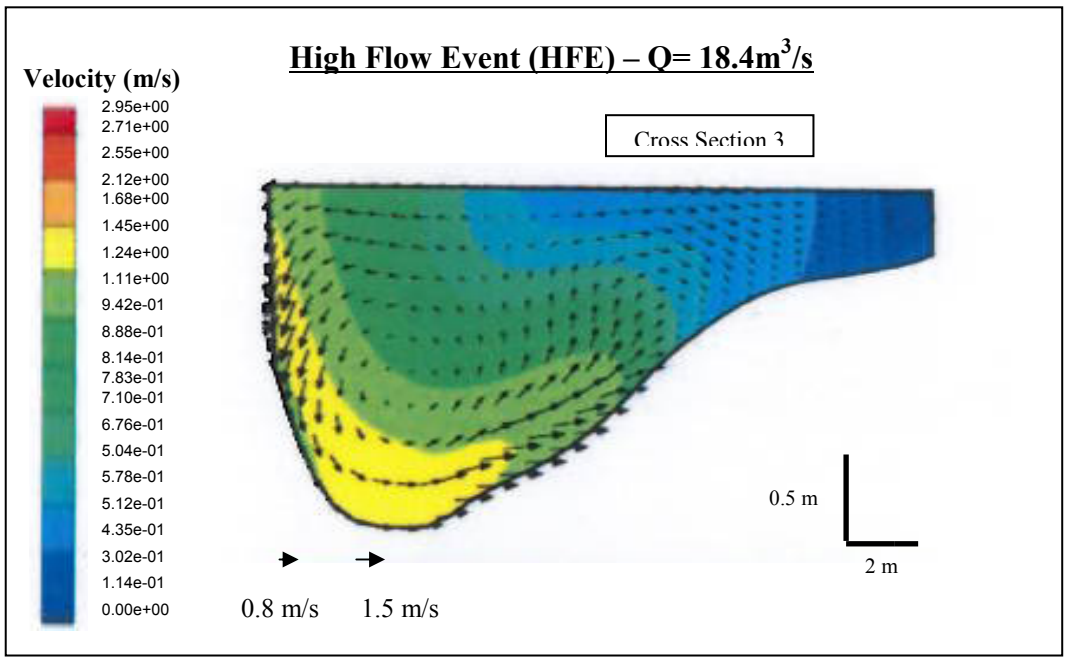

Figure 5.36: Predicted contour plots of downstream velocity magnitude showing cross-stream and vertical velocity components at cross section 3 under High Flow Event (Q = 18.4m^3/s).

Similar to the flow events already examined, at near bank full stage there is still a progressive movement of the locus of maximum downstream velocity down the inner bank. This movement occurs as rapidly as at low and mid flow stages, although the areas of high downstream velocity are much larger and occupy greater portions of the bed.

As in the lower and mid flow stage cases, the changing location of the high downstream velocity component through the reach is related to the patterns of upwelling and downwelling. At high flow stage, the increase in vertical and horizontal dimensions at cross-section 1, are associated with a more intense and larger secondary cell occupying half the channel towards the inner bank. A region of reverse flow is present below the surface at the outer bank similar to the one observed within FE1. At cross-section 2 a secondary circulation cell is also shown close to the inner bank, suggesting upwelling and downwelling flow patterns. Moreover, the secondary cell observed in cross-section 3 is mainly dissipated within high flow conditions, although there is still a relic at the bottom section of this cell through the base of the pool.

As can be seen in Figures 5.37 to 5.39 the patterns of simulated bed shear stress are not significantly changed in places but are almost twice as high as the flow stage increases. At bank full stage the flow velocities in the separation zones were found to be higher than those observed under FE1. The higher magnitudes of velocity and simulated shear stresses through the latter regions will likely result in the removal of accumulated sediments into the main downstream flow. Thus, removal of materials from within the separation zones will act to maintain the presence of the separation zones at low flow stages by permitting erosion of the inner banks.

In contrast, the nature and type of outer bank shear stresses (and thus bank erosion) acting in bends or in areas dominated by high velocities are found similar to those observed within FE1. High shear stresses are created at the regions of high velocity in a form of streamtube, especially along the outer banks. As a result, the bank erosion rates are likely to be relatively high in bends with inner bank separation zones.

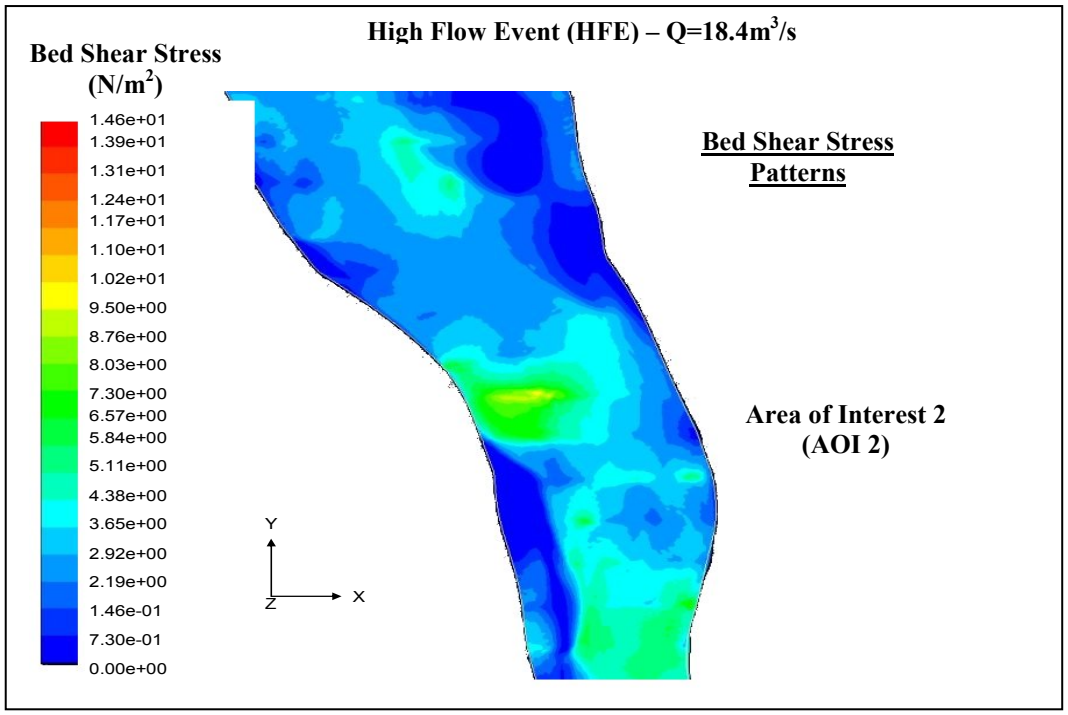

Figure 5.37: Predicted bed shear stress patterns in midstream small bend area (AOI 2) under high flow conditions (Q = 18.4m^3/s).

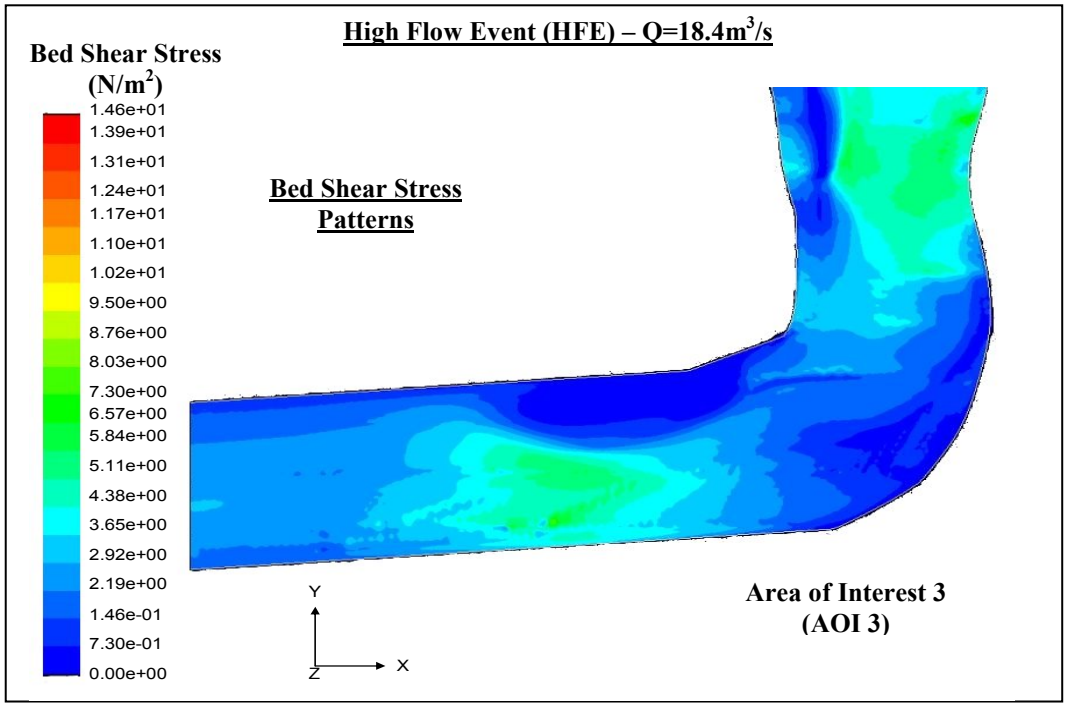

Figure 5.38: Predicted bed shear stress patterns in upstream large bend area (AOI 3) under high flow conditions (Q = 18.4m^3/s).

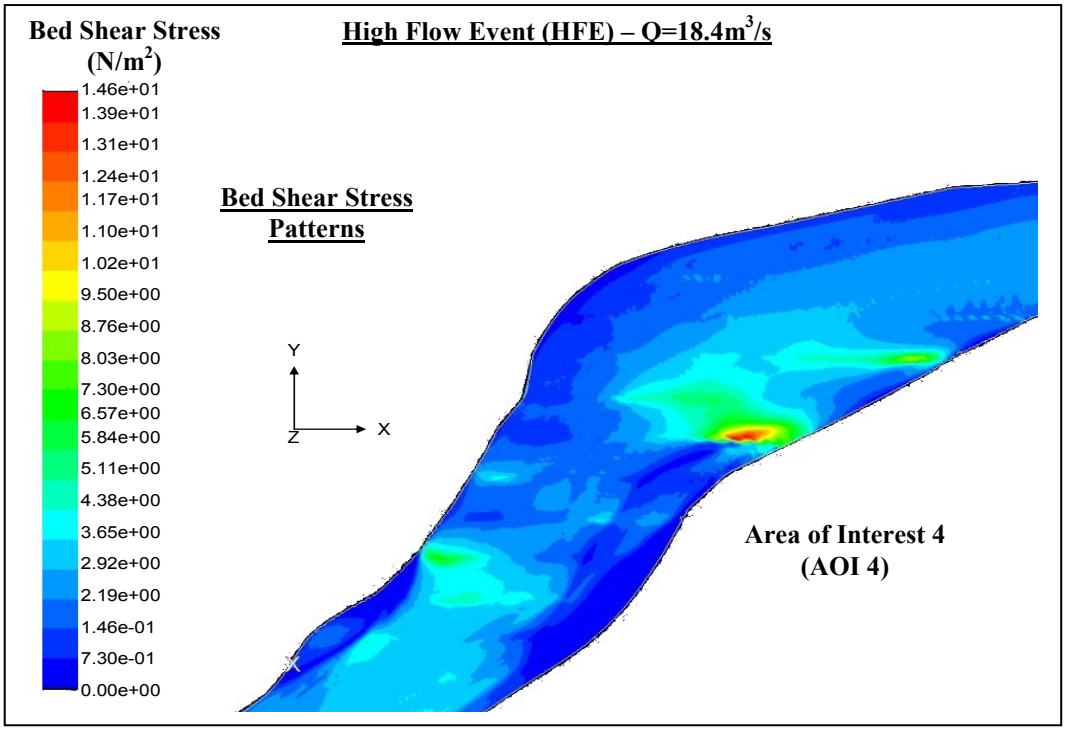

Figure 5.39: Predicted bed shear stress patterns in downstream large bend area (AOI 4) under high flow conditions (Q = 18.4m^3/s).

Having finished with the presentation and analysis of the results for all the examined flow events, a discussion of the geomorphological implications of the findings is presented at Chapter 6.

CHAPTER 6

Synthesis of the Data

6.1 Introduction

There are several potential ways in which three-dimensional Computational Fluid Dynamics output can be employed to help understanding of sediment transport and bank erosion processes. Nevertheless, due to a lack of understanding of the physics active in the boundary layer (*Carling*, 1992), and limitations in computational resources and boundary condition specification (*Lane*, 1998), there is no predefined best practice as to the best method for abstracting the most useful information from such a flow field.

Given a three-dimensional flow field captured at one moment in time the variables of interest to the geomorphologists include, near-bed and near-surface velocity, water surface elevation, and bed/bank shear stress. There are several interrelated factors influencing these variables in a CFD simulation. The latter variables are affected by the same factors as those present in the real world, such as the vertical gradient in velocity of the water flowing over the bed which, in turn, results from a particular discharge, channel shape and roughness (*Booker*, 2000). Moreover, there are some elements of the model, namely, near bed/bank cell size, roughness characterization, and method of calculation that may influence the above mentioned variables and, therefore, simulated spatial patterns of these variables. To completely understand the complex morphological changes within a reach with respect to the previously illustrated variables there is a need to investigate the flow structures at channel forming discharges.

6.2 Discussions and Implications

The results of the three-dimensional time–averaged flow structures presented in this study reveal significant differences in, but some similarities between, the flow structures associated with the various flow events examined herein. Although, the width and depth, as well as the velocities and shear stresses, throughout the River Asker reach increase as

flow discharge increases, the main structures of the flow present at the lower discharge investigated in Chapter 4 are retained at the higher flow discharges.

There are several important similarities in the results for the three examined flow events, namely, LFE, FE1, and HFE. All of them have dead zones of slow and recirculating flow close to the inner banks just past their apices. The presence of recirculation zones acts to confine the main downstream flow into streamtubes of relatively high velocity, these being displaced to a position close to the outer banks. The streamtubes therefore have the effect of increasing flow velocity near the bed and at the toe of the outer bank.

In all cases, flow in the streamtubes initially has the classical helical motion with mostly flow directed outwards at the surface but inwards at the bed, with plunging flow at the outer banks. This flow pattern is extremely strong in the first half of the bends, but past their apices it is rapidly dissipated as the near-surface and near-bed velocities are in a similar direction. This dissipation of helical motion can be attributed to a number of factors: acceleration of near-bed flow results in less deviation of near-bed flow towards the inner bank, whereas the simultaneous deceleration of near-surface flow reduces the outwards component; deceleration and asymmetric expansion where the streamtube spreads back rightwards past the end of the recirculation zone; turbulent diffusion in the shear layer between the streamtube and the adjacent recirculation zone.

6.2.1 Flow impingement

However, there are also notable differences as flow is increased, for example the location of flow impingement of the main flow against the bank tends to occur further downstream as discharge increases. In addition, this impingement is observed downstream of the bends apices, supporting the classical model of flow through bends. The impingement on the outer banks influences the size of separation at both banks and is likely to provide a clear control on where erosion and deposition occurs.

6.2.2 Flow separation - Recirculation zones

Another significant feature within all the examined flow events corresponds to inner bank flow separation. Predicted planform maps of velocity magnitude with velocity vectors showing flow directions near the bed and near the surface for all four AOI within the three examined flow events (LFE, FE1, and HFE) illustrate the presence of these zones. Inner bank flow separation is seen to exist even at the higher flow stages, although it is somewhat reduced in both size and extent as discharge increases. This change in flow structure with discharge is similar at both the surface and bed. The flow structure around the separation zones, as well as the movement of the flow into and out of them, is similar for all the flow events investigated.

As previously shown (Chapter 4), the exact causes of inner bank separation can not readily be established. Nevertheless, a number of factors such as, flow distribution at the inflows, planform curvature as well as topographic forcing, especially in deep positions, could be responsible for inner bank separation. Strong streamline curvature produced by the local bankline direction acts to produce a region of high dynamic pressure against the outer banks as the inertia of the flow is too great to adjust to the imposed curvature of the bends. This impingement creates a region of high dynamic pressure some distance before the outer bank apices, and results in a region of relatively low or negative dynamic pressure opposite the outer bank apices. The inflow distribution, which is governed by a combination of upstream planform and local topographic forcing on the upstream channels, also seems to have a pronounced effect on the flow structures observed. The inflow distribution can act to enhance or diminish the potential pressure gradients produced by streamline curvature by acting to drive flow into the outer banks at a higher or lower angle than the local bankline direction. Moreover, the interaction between the streamtube of downstream velocity and the regions of slow or reverse flow within the separation zones produces intense shear along the boundary. Numerical experiments similar to those performed for outer bank separation (*Hodskinson* and *Ferguson*, 1998) have to be undertaken in order to understand the relative contribution of each of the above factors in controlling the flow separation presence and extent at the inner banks.

The size and shape of the recirculation zones and their variations at higher flow stages are likely influenced by the position and size of the deep parts throughout the reach. The recirculation zones have the effect of increasing velocity with a resulting increase in capacity to transport materials out of the deep parts of the reach (*Booker*, 2000). Moreover, there is the possibility that the recirculation zones may become stronger when the pools experiences deposition. As a result, velocity and bed/bank shear stress would rise and enable maintenance of the overall reach morphology.

6.2.3 Secondary flows at streamtube zones

The patterns of near-surface and near-bed velocity vectors, as well as the cross-section contour plots of downstream velocity, reveal that secondary circulations in the streamtube zone of fast flow remain present even at higher flow stages. At those stages the magnitude of secondary flows either is enhanced, remaining for longer through the bends (FE1, HFE), or is dissipated before the bends exits as observed in a number of studies (*Dietrich* and *Smith*, 1983). The rapid dissipation of the secondary flow shown by the common alignment of the near-surface and near-bed vectors in the fast streamtube implies that the effect of a bend with separation would be unlikely to affect the flow distribution in downstream bends. However, some studies revealed that the secondary cells generated from upstream bends could follow on into downstream bends (*Thompson*, 1986; *Furbish*, 1991). As a result, the development of secondary circulation in downstream bends might be delayed and therefore an irregular meandering pattern, through the effect of separation in a bend upstream on the inflow to the next bend, may be more likely to develop.

Secondary circulations are formed in straight reaches as a result of pool-riffle topography and in non-straight reaches as a result of irregularities in planform such as channel constrictions or a sinuous planform. Secondary circulations in straight reaches are a possible mechanism for meander development, due to differential spatial patterns in bank erosion (*Booker*, 2000).

6.2.4 Bank erosion and shear stresses

Application of CFD modelling techniques was employed to define the near-bank fluid shear stresses exerted by the flow. As previously mentioned (Chapter 2) fluvial erosion of cohesive materials can be determined by the following equation (*Partheniades*, 1965):

$$E = k(\tau - \tau_c) \qquad (6.1)$$

where E is the fluvial bank erosion rate, τ is the applied fluid shear stress, τ_c is the critical stress for entrainment of the bank material, and k is an empirically-derived erodibility parameter. Discussion of the patterns and variations of the bed/bank shear stress, τ, at different flow structures within the examined flow events now follows.

Bed/bank shear stress is mostly seen to decrease over shallow riffles as discharge approaches bankfull. In contrast, pools experience an increase in bed/bank shear stress with increases in discharge. Figures 4.54 to 4.56, 5.21 to 5.23, and 5.37 to 5.39 illustrated simulated bed shear stresses at the midstream small bend area (AOI 2), upstream large bend area (AOI 3), and downstream large bend area (AOI 4), for the low (LFE), intermediate (FE1) and high (HFE) flows, respectively. At the higher discharges, shallow parts of the study reach experience a uniformly distributed decrease in shear stress. This is in contrast with the deeper parts of the channel, where large increases in shear stress are simulated as a function of increasing flow discharge.

Overall, as discharge approaches bankfull, the width of the zone of higher near-bed, near-surface velocity, and bed shear stress widens. As discharge rises, marginal deadwaters become activated and, in general, decrease in downstream extent, leading to a more fragmented series of low bed shear stress zones. Planform controls on secondary flow clearly affect the migration of the zone of high bed/bank shear stress. As discharge rises, the inner bank zones of low bed/bank shear stress extends upstream and widens downstream whilst it reduces at the outer bank as the high bed/bank shear stress region migrates towards the inner bank.

There is a downstream migration of the zones of faster near-bed and near-surface velocity as well as bed/bank shear stress in pools as the discharge increases. The complexity of the above mentioned hydraulic variables within the reach declines as discharge rises. The patterns of boundary shear stress acting on both bed and banks are highly complex. Zones of higher bed/bank shear stress extend and combine, while marginal recirculation zones and areas of relatively low bed/bank shear stress generally reduce in area to form; it follows that the pattern of associated erosion and deposition processes becomes more spatially coherent as flow discharge increases. The flow velocities in the inner bank separation zones were found to be smaller at FE1 than those observed under low flow conditions. As a result, the simulated shear stress values within these zones are also very low and are therefore likely to be unable to mobilize any sediment particles. Thus, inner bank erosion seems to be either very low or negligible. However, at bank full stage (HFE), the magnitudes of velocity and simulated shear stresses through the regions of inner bank separation are higher than those simulated in LFE and may be sufficient to result in the removal of accumulated sediments into the main downstream flow. This removal of materials from within the separation zones will act to maintain the presence of the separation zones at low flow stages by permitting erosion of the inner banks.

In contrast, bank erosion seems to be active on the outer banks, increasing in magnitude as flow stage increases. Based on these findings, the nature and type of outer bank erosion acting in bends or in areas dominated by high velocities are likely to be very different to classical models of migration patterns. The presence of regions of high velocity in the form of a streamtube, especially along the outer banks, will create high shear stresses within these areas. As a result, outer bank migration rates are likely to be relatively high in bends with inner bank separation zones (*Parsons,* 2002). This is in contrast with accepted theories that suggest the formation of a separation zone as a likely cause of a reduction in migration bend rates (*Hickin* and *Nanson*, 1975).

It can be concluded that the existence of large areas of slow downstream or reverse flow across the bends within the examined flow events has several important implications. The velocity patterns identified within those bends generally imply maximum boundary shear

stress near the outer banks, whereas extensive areas of low boundary shear stresses are located close to the inner bank separation zones. There are also zones of higher bed/bank shear stresses at the toe of the outer bank along the path of the streamtube. These patterns will have implications for the sediment dynamics, bank erosion and meander migration in such bends.

Boundary shear stress values derived from the model simulations were compared to coarse estimates of shear stress within the reach under low flow conditions. Estimates of shear stress at downstream interval of several tens of meters were determined from average depths and water surface slopes derived from the crest gauge data and found to be higher than those obtained from model simulations. This was may be due to the roughness height chosen within this research. The steady uniform flow model over-estimates because it does not account for the influence of form drag. The latter is parameterized in the model by meshing the grid to conform to the large scale roughness elements (e.g. bars, riffles, pools) present within the channel and by using a large value of roughness height to parameterize the sub-grid scale roughness. Thus, the true magnitude of the form roughness used in this study is more accurately accounted for within the fine mesh. However, the effect of a spatially variable roughness is unknown and could have a significant effect on shear stress predictions as shown above. The investigation of model sensitivity to spatially variable roughness is not assessed in this thesis and is left as an area that requires more research.

6.3 Summary

In summary, it can be said that notable differences are highlighted between the examined flow events. These differences include a general doubling of velocity and shear stress throughout the reach as flow stage is gradually increased, a slight reduction in the size and extent of the separation zone at bank full stage, a movement of the impingement point further downstream, and finally a continuation of the secondary flow within the fast streamtube further towards the bends exits.

CHAPTER 7

Conclusions

7.1 Conclusions

Knowledge of the rates and controls on bank erosion is fundamental to understand the migration and evolution of river meanders. However, detailed studies of the erodibility of bank materials, and of near-bank boundary shear stresses in particular, are virtually absent from the literature. A missing link in the effective parameterisation of fluvial erosion models, which is of great importance in this study, remains the need to obtain high-resolution, spatially-distributed, flow data to characterize the near bank fluid shear stresses responsible for bank erosion. However, during high flow events it is difficult to obtain empirical accurate data of the shear stresses exerted by the flow on the banks. The key problem is that it is large flood events that typically drive bank erosion, but it is difficult to measure the applied fluid shear stresses under the hazardous circumstances associated with such events.

The main aim of this project was therefore to employ Computational Fluid Dynamics (CFD) techniques to obtain simulated near-bank boundary shear stress data for different flow structures and across a range of flow events as a substitute for empirical data. The CFD models were built using high-resolution topographic information collected during prior fieldwork, with initial and boundary conditions specified using the flow velocity and water profile data also acquired during monitoring.

A combination of field case study monitoring and CFD modelling was employed to investigate the time averaged flow structures within the River Asker reach under a range of flow conditions (LFE, FE1, and HFE). To help locate particular flow events, four Areas of Interest (AOI), namely, upstream inflow area (AOI 1), midstream small bend area (AOI 2), upstream large bend area (AOI 3), and downstream large bend area (AOI

4), were identified. Channel shape, discharge, downstream water surface elevation were measured in the field and input as boundary conditions to the model.

All the models obtained from the three examined flow events were successfully verified using clearly defined and structured procedures. It was found that, with careful consideration of grid construction, the numerical modelling could be applied even where highly complex grids were required. Grid dependence experiments showed that hydraulic patterns were effectively independent of numerical grid resolution, as only slight differences in simulated flow fields were apparent when the grid resolution was increased.

The model calculations obtained from the LFE were tested against field observations. Although the CFD predictions of the velocity magnitudes of the resultant of downstream and transverse components do not always match perfectly with measured velocity values, the agreement is generally good. More specifically, there is good qualitative validation of the velocity magnitude measured in the field for the data points corresponding to *Z/H* values of 0.2, and 0.8 (R^2 =0.79 and R^2 =0.85, respectively), although the model perform less well for the *Z/H* value of 0.6 (R^2 =0.72). The same trend is observed in the downstream and transverse velocity components where at *Z/H* values of 0.2 (R^2 =0.88 and R^2 =0.85 respectively) and 0.8 (R^2 =0.88 and R^2 =0.84 respectively) the model replicates the measured field data well, but at *Z/H* value of 0.6 (R^2 =0.72 and R^2 =0.75 respectively) the agreement between simulated and observed data is somewhat weaker.

Although, the width and depth as well as the velocities and shear stresses throughout the River Asker reach increase as flow discharge increases, the main structures of the flow present at the lower discharge are retained within the higher flow discharges.

The modelling results indicate that all examined flow events (LFE, FE1, and HFE) have dead zones of slow and recirculating flow close to the inner banks just past their apices. The presence of recirculation zones acts to confine the main downstream flow into streamtubes of relatively high velocity, in locations close to the outer banks. The

streamtubes have increased velocity near the bed and at the toe of the outer bank. Moreover, the flow structures identified at the various bends within the four AOI for all examined flow events are significantly different from classical meander bends where curvature-induced helical circulation occupies most or all of the channel width. In all cases, fast downstream flow with a helical circulation was present, but it is restricted to a streamtube occupying less than half the channel width. The flow within the streamtube is characterised by an intense helical motion, but both velocity magnitude and strength of helical circulation decrease past the apices of the bends, and the secondary circulation also disappears before the exits of the bends. This is in contrast to bends that are more classical, where this helical motion usually extends beyond the bend exits.

Another significant feature within all the examined flow events corresponds to inner bank flow separation. This separation was simulated even at the higher flow stages, although it is somewhat reduced in both size and extent as discharge increases. This change in flow structure with discharge is similar at both the surface and bed. The flow structure around the separation zones, as well as the movement of the flow into and out of them, is similar for all the flow events investigated. The interaction between the streamtube of downstream velocity and the regions of slow or reverse flow within the separation zones produces intense shear along the boundary.

As discharge increases the location of flow impingement of the main flow against the bank tends to occur further downstream. The impingement on the outer banks influences the size of separation at both banks and is likely to provide a clear indication on where erosion and deposition occurs.

Bed/bank shear stress was mostly seen to decrease at shallow riffles as discharge approaches bankfull. In contrast, pools experience an increase in bed/bank shear stress with increase in discharge. An increase in discharge results in a widening of the bed shear stress zone. As discharge rises, the inner bank zones of low bed/bank shear stress extends upstream and widens downstream whilst it reduces at the outer bank as the high bed/bank shear stress region migrates towards the inner bank. Zones of higher bed/bank shear

stress extend and combine, while marginal recirculation zones and areas of relatively low bed/bank shear stress generally reduce in area to form discrete locations for erosion and deposition phenomena.

At bank full stage (HFE), the magnitudes of velocity and simulated shear stresses through the regions of inner bank separation were found to be higher than those observed in LFE and may be sufficient to result in the removal of accumulated sediments into the main downstream flow. This removal of materials from within the separation zones will act to maintain the presence of the separation zones at low flow stages by permitting erosion of the inner banks. The presence of regions of high velocity in the form of a streamtube, especially along the outer banks, will create high shear stresses within these areas. As a result, outer bank migration rates are likely to be relatively high mainly in bends with inner bank separation zones.

The velocity patterns identified within the different flow events generally imply maximum boundary shear stress near the outer banks, whereas extensive areas of low boundary shear stresses are located close to the inner bank separation zones. These patterns will have implications for the sediment dynamics, bank erosion and meander migration in such bends.

7.2 Limitations

Comparison between model results and field measurements showed that, where there is sufficient correspondence between modeled and monitored hydraulics, CFD modeling can be used to provide predictive hydraulic fields. However, a great deal of model testing was required to assess the sensitivity of model calculations to the designation of boundary conditions. In this research the assessment and validation of model performance initially considered the development and assumptions applied in each application and used spatially distributed flow velocity data for validating model performance without carrying out any sensitivity analysis. Nevertheless, sensitivity analysis was required to assess changes in model output in relation to areas of uncertainty as a result of possible measurement error, for example, sensitivity to possible errors in

discharge measurement. This is especially true where boundary conditions are poorly constrained, as is the case for the inlet boundary condition. Isolating the effects of changes in boundary conditions is particularly difficult because of the complex interactions involved in CFD modeling.

7.3 Recommendations for future research

There are many paths for further future research arising from the findings of this thesis. This section briefly describes few options for future research objectives, which are necessary for further understanding the complex flow features within this reach.

Long term monitoring of this specific reach within the River Asker is required. More particularly, there is a need to understand how this reach develops and alters over a longer period of time. Aerial photographs could be used to investigate the longer term development together with continued detailed surveying in order to produce further digital elevation models through time providing a more detailed picture of how the flow features develop and migrate within the River Asker reach system.

As previously mentioned (Chapter 3), the process of reducing the interpolated topographic data degrades the quality of the topographical representation since the resolution of the grid becomes five times coarser compared to the one originally surveyed. This is more critical in areas of high topographical complexity such as deep pools, and shallow riffles. Therefore, investigations that focus on defining the total number of topographical points collected in the field for the purpose of creating a desirable model geometry is not assessed in this study, but nevertheless presents an important area for further research.

The bed of the examined reach was found to be dominated by very small gravels while its banks have been characterized as mostly sand and silt deposits. Thus, a representative value of D_{50} (0.065 mm) was chosen as an input roughness height for taking into account all different layers encountered and also the reduction due to the required mesh resolution. However, the effect of a spatially variable roughness is unknown and could

have a significant effect in the shear stress predictions shown in Chapter 4. The investigation of model sensitivity to spatially variable roughness is not assessed in this thesis and is left as an area that requires more research.

In the work presented above, the model calculations obtained from the LFE were tested against field observations and were found to replicate measured velocity directions and magnitudes. However, CFD model testing is an area of geomorphological research that includes great uncertainty and, therefore, generalizations that can be made from this study are undetermined. An extension to the reconnaissance survey to higher flow events would provide some information with regards to validation purposes across a fuller range of discharges. Having measured and validated the various hydraulic variables under higher flow stages much more confidence would be obtained for the applicability of the current research.

Bank erosion processes are still poorly understood. A field study, combined with numerical experiments, could be used to investigate and quantify the amount, nature, and timing of the above processes. The results of this work would provide information on the importance of bank erosion and meander migration patterns on the flow structures identified within the current study.

APPENDIX I

Field flow velocity data with regards to Low Flow Event

Part 1: Field flow velocity data with regards to low flow event.

Vertical Rod	Point ID	Easting (m)	Northing (m)	Bed Elevation (m)	Flow Depth (m)	Water Surface Elev. (m)
1	4	33.80	64.33	8.91	0.27	9.18
	5	33.80	64.33	8.91	0.27	9.18
	6	33.80	64.33	8.91	0.27	9.18
2	7	34.87	64.00	9.02	0.21	9.23
	8	34.87	64.00	9.02	0.21	9.23
	9	34.87	64.00	9.02	0.21	9.23
3	10	36.28	63.78	9.02	0.20	9.22
	11	36.28	63.78	9.02	0.20	9.22
	12	36.28	63.78	9.02	0.20	9.22
4	13	37.56	63.26	9.05	0.12	9.17
	14	37.56	63.26	9.05	0.12	9.17
	15	37.56	63.26	9.05	0.12	9.17
5	22	33.92	55.80	8.80	0.27	9.07
	23	33.92	55.80	8.80	0.27	9.07
	24	33.92	55.80	8.80	0.27	9.07
6	25	34.84	55.82	8.85	0.23	9.08
	26	34.84	55.82	8.85	0.23	9.08
	27	34.84	55.82	8.85	0.23	9.08

Part 1: Field flow velocity data with regards to low flow event (continued).

Vertical Rod	Point ID	Easting (m)	Northing (m)	Bed Elevation (m)	Flow Depth (m)	Water Surface Elev. (m)
7	28	35.72	55.60	8.88	0.18	9.06
	29	35.72	55.60	8.88	0.18	9.06
	30	35.72	55.60	8.88	0.18	9.06
8	31	33.77	45.71	8.59	0.46	9.05
	32	33.77	45.71	8.59	0.46	9.05
	33	33.77	45.71	8.59	0.46	9.05
9	34	34.42	45.82	8.36	0.70	9.06
	35	34.42	45.82	8.36	0.70	9.06
	36	34.42	45.82	8.36	0.70	9.06
10	37	35.14	45.81	8.18	0.88	9.06
	38	35.14	45.81	8.18	0.88	9.06
	39	35.14	45.81	8.18	0.88	9.06
11	40	36.00	45.98	8.38	0.65	9.03
	41	36.00	45.98	8.38	0.65	9.03
	42	36.00	45.98	8.38	0.65	9.03
12	43	36.84	46.02	8.58	0.48	9.06
	44	36.84	46.02	8.58	0.48	9.06
	45	36.84	46.02	8.58	0.48	9.06
13	46	35.72	36.48	8.62	0.42	9.04
	47	35.72	36.48	8.62	0.42	9.04
	48	35.72	36.48	8.62	0.42	9.04
14	49	36.44	36.64	8.41	0.64	9.05
	50	36.44	36.64	8.41	0.64	9.05
	51	36.44	36.64	8.41	0.64	9.05

Part 1: Field flow velocity data with regards to low flow event (continued).

Vertical Rod	Point ID	Easting (m)	Northing (m)	Bed Elevation (m)	Flow Depth (m)	Water Surface Elev. (m)
15	52	37.17	37.11	8.37	0.67	9.04
	53	37.17	37.11	8.37	0.67	9.04
	54	37.17	37.11	8.37	0.67	9.04
16	55	38.22	37.53	8.60	0.45	9.05
	56	38.22	37.53	8.60	0.45	9.05
	57	38.22	37.53	8.60	0.45	9.05
17	58	39.19	38.06	8.77	0.27	9.04
	59	39.19	38.06	8.77	0.27	9.04
	60	39.19	38.06	8.77	0.27	9.04
18	61	38.84	31.32	8.58	0.47	9.05
	62	38.84	31.32	8.58	0.47	9.05
	63	38.84	31.32	8.58	0.47	9.05
19	64	39.23	31.82	8.26	0.70	8.96
	65	39.23	31.82	8.26	0.70	8.96
	66	39.23	31.82	8.26	0.70	8.96
20	67	39.94	32.47	8.36	0.70	9.06
	68	39.94	32.47	8.36	0.70	9.06
	69	39.94	32.47	8.36	0.70	9.06
21	70	40.78	32.97	8.58	0.47	9.05
	71	40.78	32.97	8.58	0.47	9.05
	72	40.78	32.97	8.58	0.47	9.05
22	73	41.82	33.83	8.84	0.21	9.05
	74	41.82	33.83	8.84	0.21	9.05
	75	41.82	33.83	8.84	0.21	9.05

Part 1: Field flow velocity data with regards to low flow event (continued).

Vertical Rod	Point ID	Easting (m)	Northing (m)	Bed Elevation (m)	Flow Depth (m)	Water Surface Elev. (m)
23	76	43.33	26.68	8.54	0.52	9.06
	77	43.33	26.68	8.54	0.52	9.06
	78	43.33	26.68	8.54	0.52	9.06
24	79	43.93	27.21	8.48	0.58	9.06
	80	43.93	27.21	8.48	0.58	9.06
	81	43.93	27.21	8.48	0.58	9.06
25	82	44.61	27.90	8.43	0.62	9.05
	83	44.61	27.90	8.43	0.62	9.05
	84	44.61	27.90	8.43	0.62	9.05
26	85	45.43	28.58	8.67	0.37	9.04
	86	45.43	28.58	8.67	0.37	9.04
	87	45.43	28.58	8.67	0.37	9.04
27	88	46.34	29.47	8.76	0.24	9.00
	89	46.34	29.47	8.76	0.24	9.00
	90	46.34	29.47	8.76	0.24	9.00
28	91	49.65	21.21	8.70	0.35	9.05
	92	49.65	21.21	8.70	0.35	9.05
	93	49.65	21.21	8.70	0.35	9.05
29	94	50.56	22.14	8.64	0.42	9.06
	95	50.56	22.14	8.64	0.42	9.06
	96	50.56	22.14	8.64	0.42	9.06
30	97	51.25	22.75	8.66	0.40	9.06
	98	51.25	22.75	8.66	0.40	9.06
	99	51.25	22.75	8.66	0.40	9.06

Part 1: Field flow velocity data with regards to low flow event (continued).

Vertical Rod	Point ID	Easting (m)	Northing (m)	Bed Elevation (m)	Flow Depth (m)	Water Surface Elev. (m)
31	100	52.18	23.61	8.71	0.35	9.06
	101	52.18	23.61	8.71	0.35	9.06
	102	52.18	23.61	8.71	0.35	9.06
32	103	53.06	24.46	8.76	0.29	9.05
	104	53.06	24.46	8.76	0.29	9.05
	105	53.06	24.46	8.76	0.29	9.05
33	106	55.03	16.10	8.82	0.22	9.04
	107	55.03	16.10	8.82	0.22	9.04
	108	55.03	16.10	8.82	0.22	9.04
34	109	56.17	16.55	8.57	0.47	9.04
	110	56.17	16.55	8.57	0.47	9.04
	111	56.17	16.55	8.57	0.47	9.04
35	112	57.29	16.81	8.44	0.62	9.06
	113	57.29	16.81	8.44	0.62	9.06
	114	57.29	16.81	8.44	0.62	9.06
36	115	58.27	17.05	8.22	0.94	9.16
	116	58.27	17.05	8.22	0.94	9.16
	117	58.27	17.05	8.22	0.94	9.16
37	118	59.21	17.39	8.34	0.69	9.03
	119	59.21	17.39	8.34	0.69	9.03
	120	59.21	17.39	8.34	0.69	9.03
38	121	56.03	9.41	8.71	0.34	9.05
	122	56.03	9.41	8.71	0.34	9.05
	123	56.03	9.41	8.71	0.34	9.05

Part 1: Field flow velocity data with regards to low flow event (continued).

Vertical Rod	Point ID	Easting (m)	Northing (m)	Bed Elevation (m)	Flow Depth (m)	Water Surface Elev. (m)
39	124	57.61	9.69	8.15	0.90	9.05
	125	57.61	9.69	8.15	0.90	9.05
	126	57.61	9.69	8.15	0.90	9.05
40	127	58.72	9.74	7.77	1.25	9.02
	128	58.72	9.74	7.77	1.25	9.02
	129	58.72	9.74	7.77	1.25	9.02
41	130	60.07	9.81	8.12	0.92	9.04
	131	60.07	9.81	8.12	0.92	9.04
	132	60.07	9.81	8.12	0.92	9.04
42	133	60.78	10.14	8.30	0.64	8.94
	134	60.78	10.14	8.30	0.64	8.94
	135	60.78	10.14	8.30	0.64	8.94
43	139	55.06	2.57	8.61	0.43	9.04
	140	55.06	2.57	8.61	0.43	9.04
	141	55.06	2.57	8.61	0.43	9.04
44	142	56.98	2.42	8.31	0.73	9.04
	143	56.98	2.42	8.31	0.73	9.04
	144	56.98	2.42	8.31	0.73	9.04
45	145	58.11	2.46	8.20	0.83	9.03
	146	58.11	2.46	8.20	0.83	9.03
	147	58.11	2.46	8.20	0.83	9.03
46	148	59.02	2.19	8.65	0.39	9.04
	149	59.02	2.19	8.65	0.39	9.04
	150	59.02	2.19	8.65	0.39	9.04

Part 1: Field flow velocity data with regards to low flow event (continued).

Vertical Rod	Point ID	Easting (m)	Northing (m)	Bed Elevation (m)	Flow Depth (m)	Water Surface Elev. (m)
47	151	34.45	-14.72	8.82	0.20	9.02
	152	34.45	-14.72	8.82	0.20	9.02
	153	34.45	-14.72	8.82	0.20	9.02
48	154	34.41	-16.34	8.79	0.25	9.04
	155	34.41	-16.34	8.79	0.25	9.04
	156	34.41	-16.34	8.79	0.25	9.04
49	157	34.48	-17.31	8.78	0.23	9.01
	158	34.48	-17.31	8.78	0.23	9.01
	159	34.48	-17.31	8.78	0.23	9.01
50	160	34.45	-18.76	8.90	0.14	9.04
	161	34.45	-18.76	8.90	0.14	9.04
	162	34.45	-18.76	8.90	0.14	9.04
51	163	34.43	-19.98	8.84	0.18	9.02
	164	34.43	-19.98	8.84	0.18	9.02
	165	34.43	-19.98	8.84	0.18	9.02
52	166	-3.75	-19.76	8.33	0.45	8.78
	167	-3.75	-19.76	8.33	0.45	8.78
	168	-3.75	-19.76	8.33	0.45	8.78
53	169	-3.43	-20.31	8.12	0.66	8.78
	170	-3.43	-20.31	8.12	0.66	8.78
	171	-3.43	-20.31	8.12	0.66	8.78
54	172	-3.30	-20.73	8.09	0.67	8.76
	173	-3.30	-20.73	8.09	0.67	8.76
	174	-3.30	-20.73	8.09	0.67	8.76

Part 1: Field flow velocity data with regards to low flow event (continued).

Vertical Rod	Point ID	Easting (m)	Northing (m)	Bed Elevation (m)	Flow Depth (m)	Water Surface Elev. (m)
55	175	-3.19	-21.44	8.16	0.68	8.84
	176	-3.19	-21.44	8.16	0.68	8.84
	177	-3.19	-21.44	8.16	0.68	8.84
56	178	-2.69	-22.29	8.31	0.48	8.79
	179	-2.69	-22.29	8.31	0.48	8.79
	180	-2.69	-22.29	8.31	0.48	8.79
57	181	-12.06	-23.17	8.02	0.72	8.74
	182	-12.06	-23.17	8.02	0.72	8.74
	183	-12.06	-23.17	8.02	0.72	8.74
58	184	-11.47	-23.78	7.74	1.02	8.76
	185	-11.47	-23.78	7.74	1.02	8.76
	186	-11.47	-23.78	7.74	1.02	8.76
59	187	-11.01	-24.18	7.76	1.02	8.78
	188	-11.01	-24.18	7.76	1.02	8.78
	189	-11.01	-24.18	7.76	1.02	8.78
60	190	-9.64	-25.08	8.39	0.39	8.78
	191	-9.64	-25.08	8.39	0.39	8.78
	192	-9.64	-25.08	8.39	0.39	8.78
61	193	-8.46	-25.69	8.67	0.11	8.78
	194	-8.46	-25.69	8.67	0.11	8.78
	195	-8.46	-25.69	8.67	0.11	8.78
62	199	-13.88	-29.21	7.57	1.20	8.77
	200	-13.88	-29.21	7.57	1.20	8.77
	201	-13.88	-29.21	7.57	1.20	8.77

Part 1: Field flow velocity data with regards to low flow event (continued).

Vertical Rod	Point ID	Easting (m)	Northing (m)	Bed Elevation (m)	Flow Depth (m)	Water Surface Elev. (m)
63	202	-12.80	-29.68	7.64	1.12	8.76
	203	-12.80	-29.68	7.64	1.12	8.76
	204	-12.80	-29.68	7.64	1.12	8.76
64	205	-11.22	-30.04	8.03	0.75	8.78
	206	-11.22	-30.04	8.03	0.75	8.78
	207	-11.22	-30.04	8.03	0.75	8.78
65	208	-10.15	-29.91	8.46	0.32	8.78
	209	-10.15	-29.91	8.46	0.32	8.78
	210	-10.15	-29.91	8.46	0.32	8.78

Part 2: Field flow velocity data with regards to low flow event.

Vertical Rod	Point ID	Inst. Depth (m)	Inst. Elev. (m)	Dim. Inst. Depth	Flow Velocity (m/s)	Orientation (degs)	X Velocity (m/s)	Y Velocity (m/s)
1	4	0.05	8.96	0.19	0.430	0	0.430	0.000
	5	0.18	9.09	0.67	0.451	0	0.451	0.000
	6	0.24	9.15	0.89	0.457	0	0.457	0.000
2	7	0.05	9.07	0.24	0.401	352	0.397	0.056
	8	0.12	9.14	0.57	0.452	352	0.448	0.063
	9	0.16	9.18	0.76	0.443	352	0.439	0.062
3	10	0.05	9.07	0.25	0.495	2	0.495	-0.017
	11	0.12	9.14	0.60	0.503	2	0.503	-0.018
	12	0.16	9.18	0.80	0.483	2	0.483	-0.017
4	13	0.05	9.10	0.42	1.115	12	1.091	-0.232
	14	0.07	9.12	0.58	1.030	12	1.007	-0.214
	15	0.09	9.14	0.75	1.018	12	0.996	-0.212
5	22	0.06	8.86	0.22	0.803	352	0.795	0.112
	23	0.16	8.96	0.59	1.216	352	1.204	0.169
	24	0.21	9.01	0.78	1.252	352	1.240	0.174
6	25	0.05	8.90	0.22	0.387	352	0.383	0.054
	26	0.13	8.98	0.57	0.584	352	0.578	0.081
	27	0.18	9.03	0.78	1.138	352	1.127	0.158
7	28	0.05	8.93	0.28	0.952	0	0.952	0.000
	29	0.10	8.98	0.56	1.050	0	1.050	0.000
	30	0.14	9.02	0.78	1.157	0	1.157	0.000
8	31	0.09	8.68	0.20	0.022	0	0.022	0.000
	32	0.27	8.86	0.59	0.099	0	0.099	0.000
	33	0.36	8.95	0.78	-0.038	0	-0.038	0.000

Part 2: Field flow velocity data with regards to low flow event (continued).

Vertical Rod	Point ID	Inst. Depth (m)	Inst. Elev. (m)	Dim. Inst. Depth	Flow Velocity (m/s)	Orientation (degs)	X Velocity (m/s)	Y Velocity (m/s)
9	34	0.14	8.50	0.20	-0.007	0	-0.007	0.000
	35	0.42	8.78	0.60	0.026	0	0.026	0.000
	36	0.56	8.92	0.80	0.270	0	0.270	0.000
10	37	0.18	8.36	0.20	0.547	354	0.544	0.057
	38	0.54	8.72	0.61	0.378	354	0.376	0.040
	39	0.70	8.88	0.80	0.463	354	0.460	0.048
11	40	0.13	8.51	0.20	0.318	356	0.317	0.022
	41	0.39	8.77	0.60	0.326	356	0.325	0.023
	42	0.52	8.90	0.80	0.291	356	0.290	0.020
12	43	0.10	8.68	0.21	-0.002	356	-0.002	0.000
	44	0.29	8.87	0.60	0.127	356	0.127	0.009
	45	0.39	8.97	0.81	0.018	356	0.018	0.001
13	46	0.08	8.70	0.19	0.138	352	0.137	0.019
	47	0.24	8.86	0.57	0.210	352	0.208	0.029
	48	0.34	8.96	0.81	0.288	352	0.285	0.040
14	49	0.13	8.54	0.20	0.262	348	0.256	0.054
	50	0.39	8.80	0.61	0.275	348	0.269	0.057
	51	0.51	8.92	0.80	0.285	348	0.279	0.059
15	52	0.13	8.50	0.19	0.472	348	0.462	0.098
	53	0.40	8.77	0.60	0.424	348	0.415	0.088
	54	0.54	8.91	0.81	0.454	348	0.444	0.094
16	55	0.09	8.69	0.20	0.143	340	0.134	0.049
	56	0.27	8.87	0.60	0.262	340	0.246	0.090
	56	0.36	8.96	0.80	0.278	340	0.261	0.095

Part 2: Field flow velocity data with regards to low flow event (continued).

Vertical Rod	Point ID	Inst. Depth (m)	Inst. Elev. (m)	Dim. Inst. Depth	Flow Velocity (m/s)	Orientation (degs)	X Velocity (m/s)	Y Velocity (m/s)
17	58	0.05	8.82	0.19	0.178	325	0.146	0.102
	59	0.16	8.93	0.59	0.213	325	0.174	0.122
	60	0.22	8.99	0.81	0.237	325	0.194	0.136
18	61	0.09	8.67	0.19	0.183	318	0.136	0.122
	62	0.28	8.86	0.60	0.283	318	0.210	0.189
	63	0.37	8.95	0.79	0.227	318	0.169	0.152
19	64	0.14	8.40	0.20	0.143	320	0.110	0.092
	65	0.42	8.68	0.60	0.353	320	0.270	0.227
	66	0.56	8.82	0.80	0.315	320	0.241	0.202
20	67	0.14	8.50	0.20	0.284	300	0.142	0.246
	68	0.42	8.78	0.60	0.407	300	0.204	0.352
	69	0.56	8.92	0.80	0.406	300	0.203	0.352
21	70	0.09	8.67	0.19	0.315	308	0.194	0.248
	71	0.28	8.86	0.60	0.403	308	0.248	0.318
	72	0.37	8.95	0.79	0.326	308	0.201	0.257
22	73	0.05	8.89	0.24	0.068	308	0.042	0.054
	74	0.13	8.97	0.62	0.150	308	0.092	0.118
	75	0.17	9.01	0.81	0.213	308	0.131	0.168
23	76	0.10	8.64	0.19	0.114	310	0.073	0.087
	77	0.31	8.85	0.60	0.243	310	0.156	0.186
	78	0.42	8.96	0.81	0.277	310	0.178	0.212
24	79	0.12	8.60	0.21	0.346	318	0.257	0.232
	80	0.35	8.83	0.60	0.355	318	0.264	0.238
	81	0.46	8.94	0.79	0.401	318	0.298	0.268

Part 2: Field flow velocity data with regards to low flow event (continued).

Vertical Rod	Point ID	Inst. Depth (m)	Inst. Elev. (m)	Dim. Inst. Depth	Flow Velocity (m/s)	Orientation (degs)	X Velocity (m/s)	Y Velocity (m/s)
25	82	0.12	8.55	0.19	0.227	317	0.166	0.155
	83	0.37	8.80	0.60	0.345	317	0.252	0.235
	84	0.50	8.93	0.81	0.422	317	0.309	0.288
26	85	0.07	8.74	0.19	0.178	300	0.089	0.154
	86	0.22	8.89	0.59	0.430	300	0.215	0.372
	87	0.30	8.97	0.81	0.472	300	0.236	0.409
27	88	0.06	8.82	0.25	0.146	308	0.090	0.115
	89	0.18	8.94	0.75	0.183	308	0.113	0.144
	90	0.23	8.99	0.96	0.263	308	0.162	0.207
28	91	0.07	8.77	0.20	0.196	312	0.131	0.146
	92	0.19	8.89	0.54	0.274	312	0.183	0.204
	93	0.28	8.98	0.80	0.276	312	0.185	0.205
29	94	0.08	8.72	0.19	0.400	306	0.235	0.324
	95	0.25	8.89	0.60	0.472	306	0.277	0.382
	96	0.34	8.98	0.81	0.502	306	0.295	0.406
30	97	0.08	8.74	0.20	0.427	311	0.280	0.322
	98	0.24	8.90	0.60	0.502	311	0.329	0.379
	99	0.32	8.98	0.80	0.481	311	0.316	0.363
31	100	0.07	8.78	0.20	0.382	306	0.225	0.309
	101	0.21	8.92	0.60	0.473	306	0.278	0.383
	102	0.28	8.99	0.80	0.469	306	0.276	0.379
32	103	0.06	8.82	0.21	0.129	308	0.079	0.102
	104	0.17	8.93	0.59	0.263	308	0.162	0.207
	105	0.23	8.99	0.79	0.267	308	0.164	0.210

Part 2: Field flow velocity data with regards to low flow event (continued).

Vertical Rod	Point ID	Inst. Depth (m)	Inst. Elev. (m)	Dim. Inst. Depth	Flow Velocity (m/s)	Orientation (degs)	X Velocity (m/s)	Y Velocity (m/s)
33	106	0.05	8.87	0.23	-0.032	338	-0.030	-0.012
	107	0.13	8.95	0.59	-0.026	338	-0.024	-0.010
	108	0.18	9.00	0.82	-0.043	338	-0.040	-0.016
34	109	0.09	8.66	0.19	0.027	336	0.025	0.011
	110	0.28	8.85	0.60	0.214	336	0.195	0.087
	111	0.37	8.94	0.79	0.257	336	0.235	0.105
35	112	0.12	8.56	0.19	0.210	329	0.180	0.108
	113	0.37	8.81	0.60	0.529	329	0.453	0.272
	114	0.49	8.93	0.79	0.595	329	0.510	0.306
36	115	0.24	8.46	0.26	0.329	322	0.259	0.203
	116	0.56	8.78	0.60	0.487	322	0.384	0.300
	117	0.75	8.97	0.80	0.572	322	0.451	0.352
37	118	0.14	8.48	0.20	-0.108	318	-0.080	-0.072
	119	0.41	8.75	0.59	0.353	318	0.262	0.236
	120	0.55	8.89	0.80	0.502	318	0.373	0.336
38	121	0.07	8.78	0.21	-0.078	346	-0.076	-0.019
	122	0.20	8.91	0.59	-0.085	346	-0.082	-0.021
	123	0.27	8.98	0.79	-0.093	346	-0.090	-0.022
39	124	0.18	8.33	0.20	0.170	354	0.169	0.018
	125	0.54	8.69	0.60	0.081	354	0.081	0.008
	126	0.72	8.87	0.80	0.052	354	0.052	0.005
40	127	0.25	8.02	0.20	0.212	348	0.207	0.044
	128	0.75	8.52	0.60	0.145	348	0.142	0.030
	129	1.00	8.77	0.80	0.090	348	0.088	0.019

Part 2: Field flow velocity data with regards to low flow event (continued).

Vertical Rod	Point ID	Inst. Depth (m)	Inst. Elev. (m)	Dim. Inst. Depth	Flow Velocity (m/s)	Orientation (degs)	X Velocity (m/s)	Y Velocity (m/s)
41	130	0.18	8.30	0.20	0.061	340	0.057	0.021
	131	0.55	8.67	0.60	0.320	340	0.301	0.109
	132	0.73	8.85	0.79	0.253	340	0.238	0.087
42	133	0.14	8.44	0.22	0.437	336	0.399	0.178
	134	0.38	8.68	0.59	0.323	336	0.295	0.131
	135	0.51	8.81	0.80	0.311	336	0.284	0.126
43	139	0.08	8.69	0.19	0.220	20	0.207	-0.075
	140	0.26	8.87	0.60	0.247	20	0.232	-0.084
	141	0.34	8.95	0.79	0.269	20	0.253	-0.092
44	142	0.14	8.45	0.19	0.229	18	0.218	-0.071
	143	0.43	8.74	0.59	0.216	18	0.205	-0.067
	144	0.58	8.89	0.79	0.218	18	0.207	-0.067
45	145	0.16	8.36	0.19	0.222	16	0.213	-0.061
	146	0.49	8.69	0.59	0.178	16	0.171	-0.049
	147	0.66	8.86	0.80	0.171	16	0.164	-0.047
46	148	0.06	8.71	0.15	0.005	12	0.005	-0.001
	149	0.23	8.88	0.59	0.088	12	0.086	-0.018
	150	0.31	8.96	0.79	0.097	12	0.095	-0.020
47	151	0.05	8.87	0.25	0.724	112	-0.271	-0.671
	152	0.12	8.94	0.60	0.765	112	-0.287	-0.709
	153	0.16	8.98	0.80	0.779	112	-0.292	-0.722
48	154	0.06	8.85	0.24	0.572	92	-0.020	-0.572
	155	0.15	8.94	0.60	0.692	92	-0.024	-0.692
	156	0.20	8.99	0.80	0.711	92	-0.025	-0.711

Part 2: Field flow velocity data with regards to low flow event (continued).

Vertical Rod	Point ID	Inst. Depth (m)	Inst. Elev. (m)	Dim. Inst. Depth	Flow Velocity (m/s)	Orientation (degs)	X Velocity (m/s)	Y Velocity (m/s)
49	157	0.06	8.84	0.26	0.649	96	-0.068	-0.645
	158	0.14	8.92	0.61	0.726	96	-0.076	-0.722
	159	0.20	8.98	0.87	0.731	96	-0.076	-0.727
50	160	0.05	8.95	0.36	0.787	86	0.055	-0.785
	161	0.08	8.98	0.57	0.748	86	0.052	-0.746
	162	0.11	9.01	0.79	0.725	86	0.051	-0.723
51	163	0.05	8.89	0.28	0.764	86	0.053	-0.762
	164	0.10	8.94	0.56	0.849	86	0.059	-0.847
	165	0.14	8.98	0.78	0.874	86	0.061	-0.872
52	166	0.09	8.42	0.20	0.266	88	0.009	-0.266
	167	0.27	8.60	0.60	0.408	88	0.014	-0.408
	168	0.36	8.69	0.80	0.377	88	0.013	-0.377
53	169	0.13	8.25	0.20	0.226	88	0.008	-0.226
	170	0.39	8.51	0.59	0.472	88	0.016	-0.472
	171	0.52	8.64	0.79	0.424	88	0.015	-0.424
54	172	0.13	8.22	0.19	0.183	78	0.038	-0.179
	173	0.39	8.48	0.58	0.366	78	0.076	-0.358
	174	0.52	8.61	0.78	0.493	78	0.103	-0.482
55	175	0.13	8.29	0.19	0.334	82	0.046	-0.331
	176	0.39	8.55	0.57	0.462	82	0.064	-0.458
	177	0.52	8.68	0.76	0.469	82	0.065	-0.464
56	178	0.10	8.41	0.21	0.213	48	0.143	-0.158
	179	0.29	8.60	0.60	0.148	48	0.099	-0.110
	180	0.39	8.70	0.81	0.150	48	0.100	-0.111

Part 2: Field flow velocity data with regards to low flow event (continued).

Vertical Rod	Point ID	Inst. Depth (m)	Inst. Elev. (m)	Dim. Inst. Depth	Flow Velocity (m/s)	Orientation (degs)	X Velocity (m/s)	Y Velocity (m/s)
57	181	0.14	8.16	0.19	-0.034	30	-0.029	0.017
	182	0.44	8.46	0.61	0.052	30	0.045	-0.026
	183	0.58	8.60	0.81	0.069	30	0.060	-0.035
58	184	0.20	7.94	0.20	0.024	30	0.021	-0.012
	185	0.61	8.35	0.60	0.349	30	0.302	-0.175
	186	0.82	8.56	0.80	0.447	30	0.387	-0.224
59	187	0.20	7.96	0.20	0.059	40	0.045	-0.038
	188	0.61	8.37	0.60	0.215	40	0.165	-0.138
	189	0.82	8.58	0.80	0.377	40	0.289	-0.242
60	190	0.08	8.47	0.21	0.155	20	0.146	-0.053
	191	0.23	8.62	0.59	0.267	20	0.251	-0.091
	192	0.31	8.70	0.79	0.281	20	0.264	-0.096
61	193	0.05	8.72	0.45	0.226	36	0.183	-0.133
	194	0.06	8.73	0.55	0.240	36	0.194	-0.141
	195	0.09	8.76	0.82	0.250	36	0.202	-0.147
62	199	0.24	7.81	0.20	0.260	20	0.244	-0.089
	200	0.72	8.29	0.60	0.116	20	0.109	-0.040
	201	0.96	8.53	0.80	0.062	20	0.058	-0.021
63	202	0.22	7.86	0.20	0.125	24	0.114	-0.051
	203	0.67	8.31	0.60	0.067	24	0.061	-0.027
	204	0.89	8.53	0.79	0.102	24	0.093	-0.041
64	205	0.15	8.18	0.20	-0.058	4	-0.058	0.004
	206	0.45	8.48	0.60	-0.025	4	-0.025	0.002
	207	0.60	8.63	0.80	-0.005	4	-0.005	0.000

Part 2: Field flow velocity data with regards to low flow event (continued).

Vertical Rod	Point ID	Inst. Depth (m)	Inst. Elev. (m)	Dim. Inst. Depth	Flow Velocity (m/s)	Orientation (degs)	X Velocity (m/s)	Y Velocity (m/s)
65	208	0.06	8.52	0.19	-0.113	354	-0.112	-0.012
	209	0.19	8.65	0.59	-0.074	354	-0.074	-0.008
	210	0.25	8.71	0.78	-0.086	354	-0.086	-0.009

APPENDIX II

A: C code

```
#include <stdio.h>
#include <stdlib.h>

int CalculateBlocks(float a[200000], int cnt);
void WriteBlocksToFiles(float a[200000], int noBlocks, int cnt);

/* Main C function which executes the program */
int main(void)
{
      /* Variables declaration --- */
    FILE *fp;
    char filename[40];
    float x =0;
    float y =0;
    float z =0;
    float array [200000];

    int counter=0;
    int array_counter=0;
    int numberOfBlocks=0;
    /* End of variables declaration */

    printf("\nEnter XYZ filename: ");
    gets(filename);

    if ((fp=fopen(filename, "r")) != NULL)
    {
        printf("\nFile opened sucessfully\n");
        while (1)
        {

            if (feof(fp))
                break;
            fscanf (fp, "%f %f %f", &x, &y, &z);
            array[array_counter]     =x;
            array[array_counter+1]   =y;
            array[array_counter+2]   =z;

            counter++;         // Counter to read number of lines in
the txt file

            //printf ("VALUES: %f %f %f   %d\n", array[array_counter],
array[array_counter+1], array[array_counter+2], counter);
            array_counter+=3;  // Counter to increment the number of
elements in the array by 3

        }
        fclose(fp);
```

```
        numberOfBlocks=CalculateBlocks(array, array_counter);
        WriteBlocksToFiles(array, numberOfBlocks, array_counter);

    }
    else
    {
        fprintf(stderr, "\nError opening file %s\n", filename);
        exit(1);
    }
    return 0;
}

int CalculateBlocks(float a[200000], int cnt)
{
    int i;
    int block_counter=1;
    float compared_value, value_now;

    compared_value=a[1];
    for (i=0; i<cnt; i+=3)
    {
        value_now=a[i+1];
        if (compared_value == value_now)
        {
            // Do nothing
        }
        else
        {
            compared_value = value_now;
            block_counter++;
        }
        //printf ("VALUES: %f %f %f   %d\n", a[i], a[i+1], a[i+2],
block_counter);
    }
    return block_counter;
}

void WriteBlocksToFiles(float a[200000], int noBlocks, int cnt)
{
    int i=0;
    int j=0;
    int tmpCntNow=0;
    int clmnCnt1=-1;
    int clmnCnt2=0;
    FILE *fp_out;
    char buffer[80];
    float compared_value, value_now;

    compared_value=a[1];

    for (i=0; i<noBlocks; i++)
    {
        sprintf(buffer, "GambitFeb%d.txt", i);
        fp_out=fopen(buffer, "w");


        //fprintf(fp_out, "vertex create PT1 coordinates\n")
```

```
        for (j=tmpCntNow; j<cnt; j+=3)
        {
            value_now=a[j+1];
            if (compared_value == value_now)
            {
                clmnCnt1+=2;
                //clmnCnt2++;
                fprintf(fp_out, "vertex create \"PT1\" coordinates ",
clmnCnt1);
                /* MONO SAVE XYZ */
                fprintf(fp_out, "%f %f %f\n",/*x*/ a[j], /*y*/a[j+1],
/*z*/a[j+2]);

            }
            else
            {
                tmpCntNow=j+3;
                compared_value = value_now;
                //clmnCnt1=-1;
                //clmnCnt2=0;
                break;
                //block_counter++;
            }
        }
        fclose(fp_out);
    }
}
```

B: Journal File example

Journal file 2 corresponding to the second cross-section:

```
vertex create "PT1" coordinates 32.044800 65.039597 8.881500
vertex create "PT1" coordinates 32.634998 65.039597 8.862800
vertex create "PT1" coordinates 33.225201 65.039597 8.856500
vertex create "PT1" coordinates 33.815399 65.039597 8.863200
vertex create "PT1" coordinates 34.405602 65.039597 8.866200
vertex create "PT1" coordinates 34.995800 65.039597 8.870800
vertex create "PT1" coordinates 35.585999 65.039597 8.896700
vertex create "PT1" coordinates 36.176201 65.039597 8.888600
vertex create "PT1" coordinates 36.766399 65.039597 8.925200
vertex create "PT1" coordinates 37.356602 65.039597 8.990900
vertex create "PT1" coordinates 37.946800 65.039597 9.060600
vertex create "PT1" coordinates 38.536999 65.039597 9.112200
vertex create "PT1" coordinates 39.127201 65.039597 9.171500
vertex create "PT1" coordinates 39.717400 65.039597 9.454000
vertex create "PT1" coordinates 40.307598 65.039597 9.754000
```

C: Fluent 6.2 log file

Low flow event log file:

```
grid/check
define/models/solver/segregated yes
define/models/viscous/ke-standard? yes
define/models/viscous/near-wall-treatment/enhanced-wall-treatment? yes
define/models/viscous/near-wall-treatment/wf-pressure-gradient-effects?
yes
define/materials/copy/fluid/water-liquid
define/materials/change-create/water-liquid/water-liquid no no no no no
no no no no no
define/operating-conditions/gravity yes 0 0 -9.81
define/operating-conditions/operating-pressure 101325
define/operating-conditions/reference-pressure-location 36 65.3 9
define/boundary-conditions/fluid/water yes water-liquid no no yes 0 0 0
0 0 1 no no
define/boundary-conditions/velocity-inlet/inflow no no yes yes no 0.387
yes no yes 2.5 0.45
define/boundary-conditions/outflow/outflow 1
define/boundary-conditions/wall/bed no no
define/boundary-conditions/wall/surface no yes shear-bc-spec-shear no 0
no 0 no 0
define/models/viscous/buoyancy-effects? yes
solve/set/equations/flow/yes
solve/set/equations/ke/yes
solve/set/discretization-scheme/pressure/10
solve/set/discretization-scheme/mom/0
solve/set/discretization-scheme/k/0
solve/set/discretization-scheme/epsilon/0
solve/set/p-v-coupling/21
solve/set/under-relaxation/pressure/0.3
solve/set/under-relaxation/density/1
solve/set/under-relaxation/body-force/1
solve/set/under-relaxation/mom/0.7
solve/set/under-relaxation/k/0.6
solve/set/under-relaxation/epsilon/0.6
solve/set/under-relaxation/turb-viscosity/0.6
```

```
solve/monitors/residual/plot/yes
solve/monitors/residual/check-convergence yes no no no no no
solve/monitors/residual/convergence-criteria 0.0000001
solve init init
```

APPENDIX III

Standard k-ε Turbulence Model

The standard k-ε turbulence model (*Launder and Spalding*, 1972) is the most commonly used turbulence closure, in which k and ε are the turbulent kinetic energy and dissipation rate, respectively. In the derivation of the k-ε model, two assumptions were made by *Launder and Spalding* (1972):

- The flow field is fully turbulent.
- The effects of viscosity are negligible.

Hence, the later turbulence closure can be applied only to fully turbulent flows. The definition of the velocity scale ∂ as well as the length scale l representative of the large scale turbulence is feasible by using k and ε as follows:

$$\partial = k^{1/2} \qquad (1)$$

$$l = \frac{k^{3/2}}{\varepsilon} \qquad (2)$$

The turbulent kinetic energy represents the energy extracted from the mean flow by motion of the turbulent eddies (*De Serres et al.*, 1999). The turbulent eddy viscosity, μ_T, is supposed to be proportional to the product of a turbulent velocity scale and a length scale. The equation which describes the above statement can be written as:

$$\mu_{\mathrm{T}} = C_{\mu} \frac{k^2}{\varepsilon} \qquad (3)$$

where C_{μ} is a constant in the k-ε model.

The turbulent kinetic energy is defined as $k = \frac{1}{2}\overline{u_i u_j}$ while its corresponding modeling is given by the following formula (*Olsen and Skoglund*, 1994):

$$\frac{\partial k}{\partial t} + U_j\left(\frac{\partial k}{\partial x_j}\right) = \frac{\partial}{\partial x_j}\left(\frac{\mu_T}{\sigma_k}\frac{\partial k}{\partial x_j}\right) + P_\kappa - \varepsilon \qquad (4)$$

where $\overline{u_i u_j}$ represent the Reynolds shear stresses, U_j is the average velocity, and P_k is the term for production of turbulence and is given by the following equation (*Fluent Inc.*, 2006):

$$P_k = \mu_T \frac{\partial U_i}{\partial x_j}\left(\frac{\partial U_j}{\partial x_i} + \frac{\partial U_i}{\partial x_j}\right) \qquad (5)$$

The dissipation rate ε in the standard k-ε turbulence model is modeled as:

$$\frac{\partial \varepsilon}{\partial t} + U_j\frac{\partial \varepsilon}{\partial x_j} = \frac{\partial}{\partial x_j}\left(\frac{\mu_T}{\sigma_\varepsilon}\frac{\partial \varepsilon}{\partial x_j}\right) + C_{\varepsilon 1}\frac{\varepsilon}{\kappa}P_k - C_{\varepsilon 2}\frac{\varepsilon^2}{k} \qquad (6)$$

The equations (*3*), (*4*) and (*6*) contain five adjustable constants, $C_{\varepsilon 1}$, $C_{\varepsilon 2}$, C_μ, σ_κ, σ_ε. Their values have been determined from experiments using air and water for fundamental shear flows including homogeneous shear flows and decaying isotropic grid turbulence and have been found to work fairly well for a wide range of wall bounded and free shear flows (*Fluent Inc.*, 2006). Their values are given as:

$C_{\varepsilon 1} = 1.44$, $C_{\varepsilon 2} = 1.92$, $C_\mu = 0.09$, $\sigma_\kappa = 1.0$, $\sigma_\varepsilon = 1.3$

Going back to the dissipation transport rate (Equation (*6*)), it is important to pay close attention to the last term of the equation:

$$C_{\varepsilon 2}\frac{\varepsilon^2}{k} \qquad (7)$$

As we approach the wall, the turbulent kinetic energy approaches zero, whereas the dissipation rate does not (within the scope of the model, because in reality it does). Hence, the term goes to infinity close to the wall, which not only is unphysical, but it also introduces numerical instabilities in the solution. This is known as the near wall singularity of the dissipation rate transport equation. Where the inflow boundary conditions are very important, and the flow is a low Reynolds number problem, thus making the situation worse, this can be a significant drawback in terms of accuracy and quality (*Launder and Spalding,* 1972).

Another important feature of the standard k-ε model, which is common with the other models, is the pressure diffusion term, which is represented as follows:

$$\mu_{\mathrm{T}} \frac{\partial U_i}{\partial x_j} \qquad (8)$$

Although the pressure diffusion term is relatively very small in most flows, it is important in re-circulation regions, and hence it can be expected that the model deficiencies will have an impact on the distribution of kinetic energy in these areas.

The simplest application of the standard k-ε model has involved a zero-equation turbulence model (*Lane*, 1998). The eddy viscosity is defined by this model using Prandtl's mixing length hypothesis, which indicates that μ_T is thought to depend upon an average fluctuating velocity and a mixing length (*Hankin et al.*, 2001). This mixing length is given as the product of water depth and Von Karman's constant κ. The latter approach of calculating the eddy viscosity parameter is likely to be the most widely tested and successfully applied in hydraulics.

APPENDIX IV

SIMPLEC pressure-velocity coupling algorithm

When solving the momentum equations with a guessed pressure field p^* the resulting face flux, J_f^*, is defined by the following equation (*Fluent Inc.*, 2006):

$$J_f^* = \hat{J}_f^* + d_f(p_{c0}^* - p_{c1}^*) \qquad (1)$$

where J_f^* corresponds to the guessed mass flux through face *f*, p_{c0}^* and p_{c1}^* are the guessed pressures within the two cells on either side of the face, $\hat{J}_f^*$ contains the influence of velocities in these cells, and d_f is a function of $\overline{\alpha}_p$, the average of the momentum equation α_p coefficients for the cells on either side of face *f*.

Unfortunately, the continuity equation is not satisfied by equation (*1*). Hence, a correction J_f' is added to the guessed face flux J_f^*. As a result, the corrected face flux, J_f, is given as:

$$J_f = J_f^* + J_f' \qquad (2)$$

Having made the above modifications equation (*2*) satisfies the continuity equation. According to SIMPLE pressure-velocity coupling algorithm J_f' can be written as:

$$J_f' = d_f(p_{c0}' - p_{c1}') \qquad (3)$$

in which p' represents the cell pressure correction.

As the later algorithm implies, a discrete equation for the pressure correction p' in the cell is acquired by substituting equations (*2*) and (*3*) into the continuity equation (*Fluent Inc.*, 2006):

$$\alpha_p p' = \sum_{nb} \alpha_{nb} p'_{nb} + b \qquad (4)$$

where *b* is the net flow rate into the cell given as:

$$b = \sum_{f}^{N_{faces}} J_f^* A_f \qquad (5)$$

The pressure correction equation (Equation (*4*)) can be solved by using the algebraic multigrid method. After obtaining a solution, both the cell pressure and the face flux are corrected through the following equations:

$$p = p^* + \alpha_p p' \qquad (6)$$

$$J_f = J_f^* + d_f (p'_{c0} - p'_{c1}) \qquad (7)$$

in which α_p is the under-relaxation factor for pressure. The corrected face flux, J_f, obtained by equation (*7*) satisfies the discrete continuity equation.

The SIMPLEC (SIMPLE-Consistent) pressure-velocity coupling algorithm, introduced by *Vandoormaal and Raithby* (1984), is similar to the SIMPLE one. The only difference can be found in the expression utilized for the face flux correction, J'_f. The correction equation developed above for the SIMPLE algorithm (Equation (*7*)) is also valid for the SIMPLEC. Nevertheless, The coefficient d_f is modified as a function of $\overline{\alpha_p - \sum_{nb} \alpha_{nb}}$. Convergence is accelerated with the usage of this modified correction equation.

With SIMPLEC, the pressure correction under-relaxation factor is usually set to 1, for accelerating the convergence. However, in some cases when the pressure correction under-relaxation is increased to 1, instabilities owing to high grid skewness may develop. Finally, for complicated flows including turbulence and physical models, SIMPLEC will improve convergence.

APPENDIX V

Predicted versus Observed Resultant of Downstream and Transverse Flow Velocity Components at all Positions

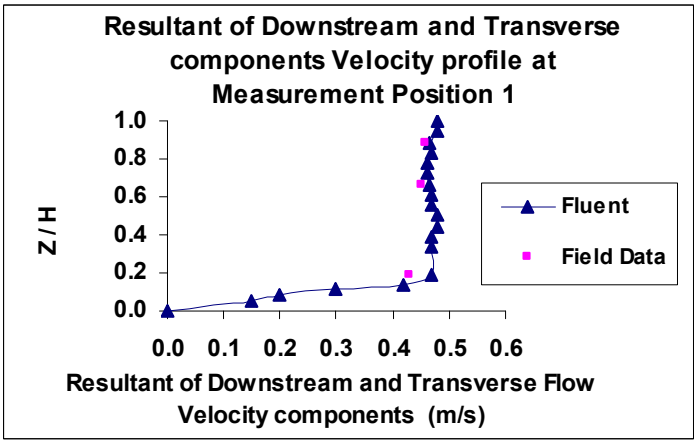

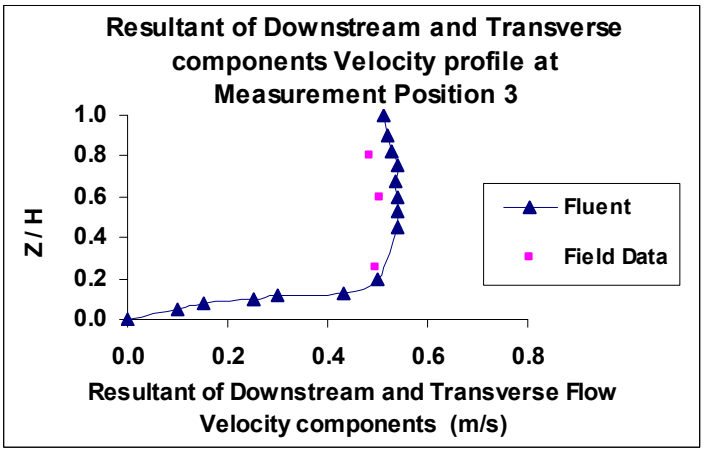

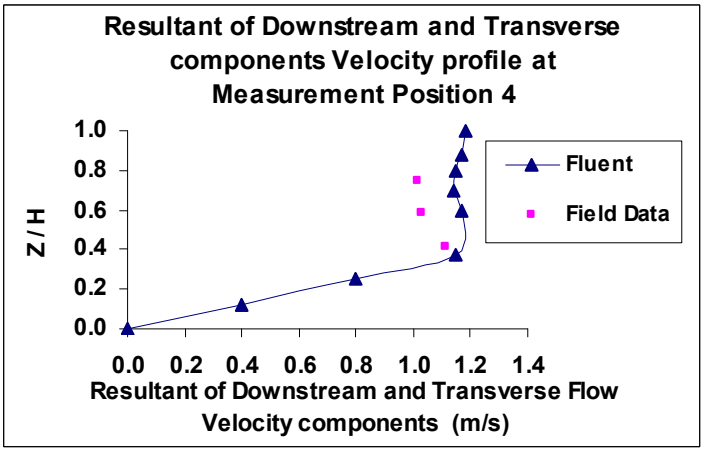

Predicted versus observed resultant of downstream and transverse flow velocity components at measurement positions 1, 3, and 4.

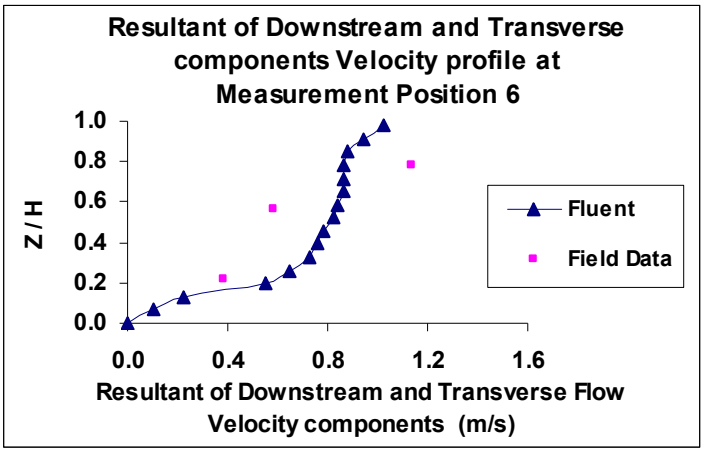

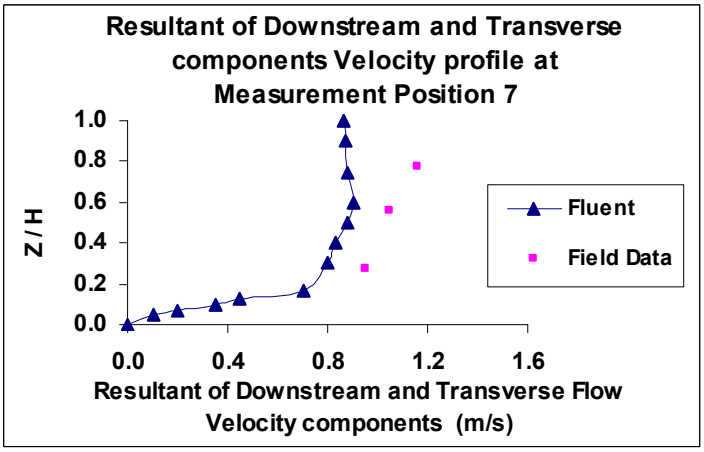

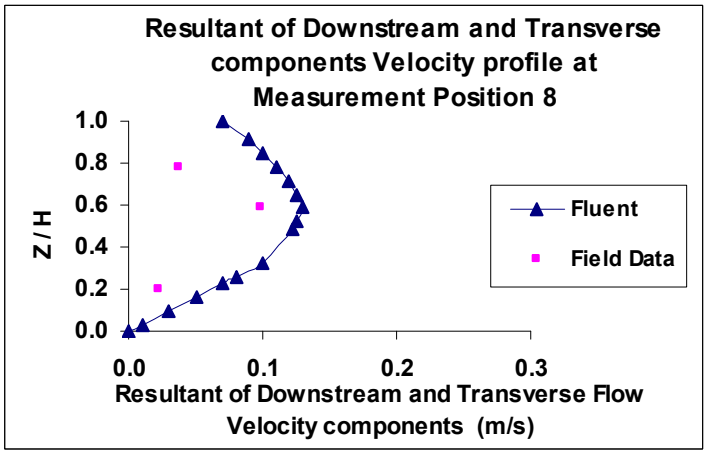

Predicted versus observed resultant of downstream and transverse flow velocity components at measurement positions 6, 7, and 8.

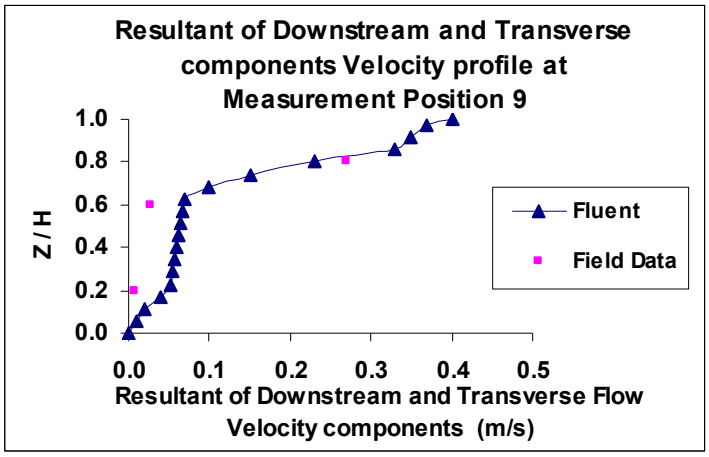

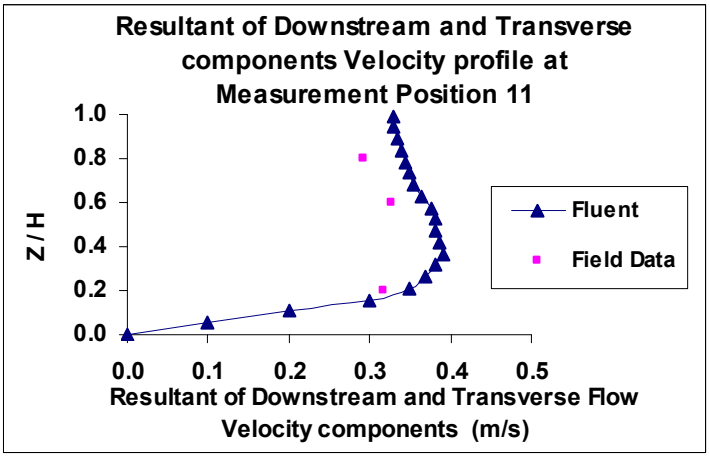

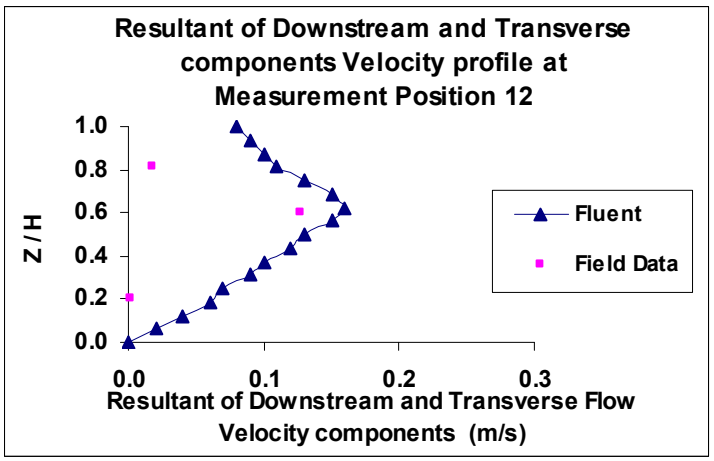

Predicted versus observed resultant of downstream and transverse flow velocity components at measurement positions 9, 11, and 12.

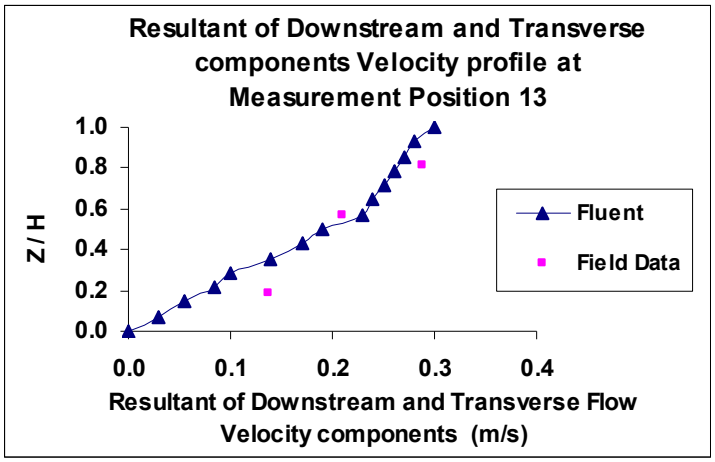

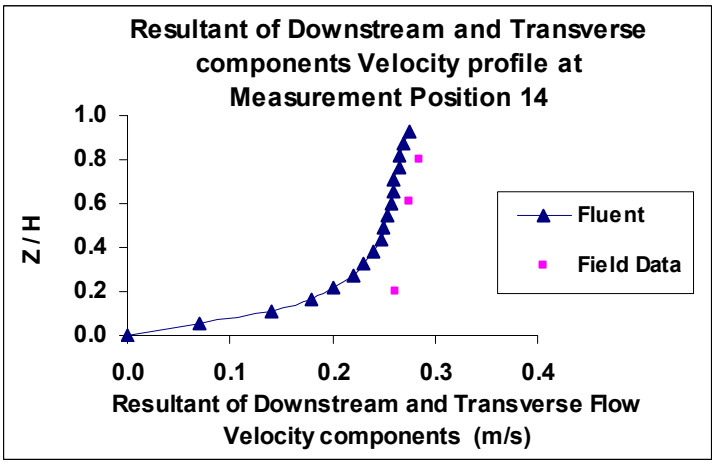

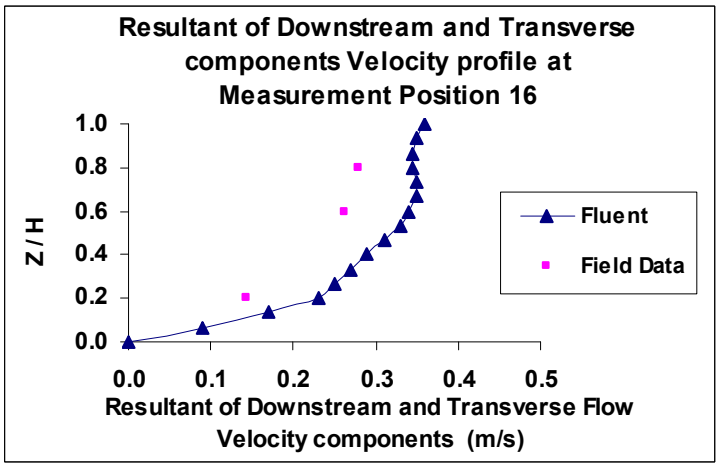

Predicted versus observed resultant of downstream and transverse flow velocity components at measurement positions 13, 14, and 16.

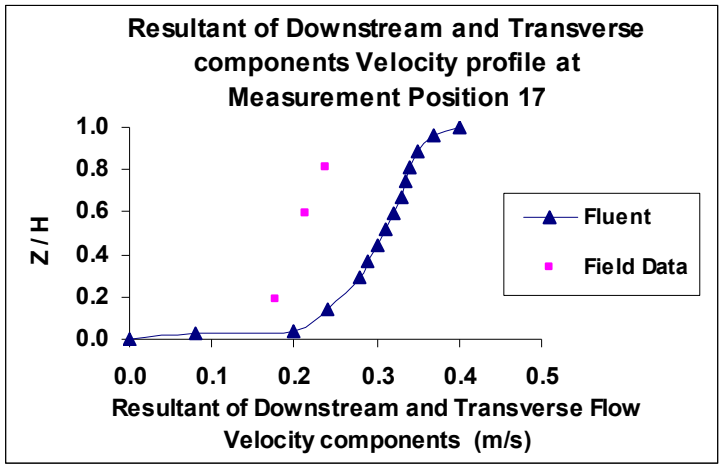

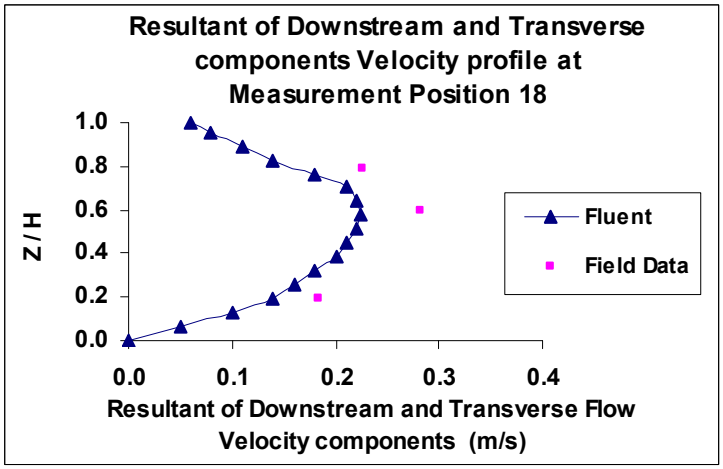

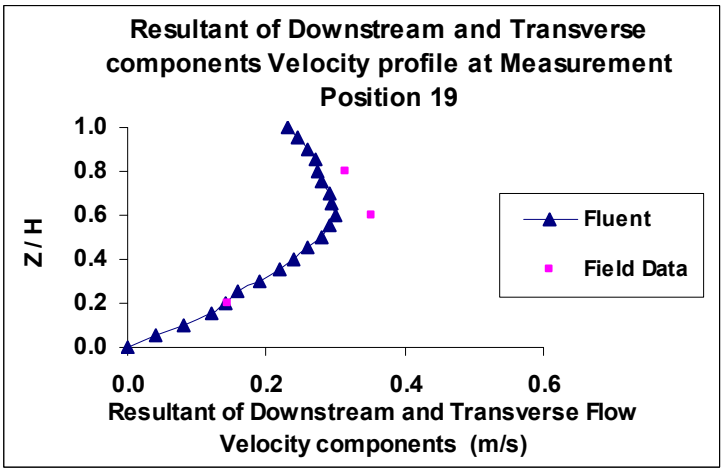

Predicted versus observed resultant of downstream and transverse flow velocity components at measurement positions 17, 18, and 19.

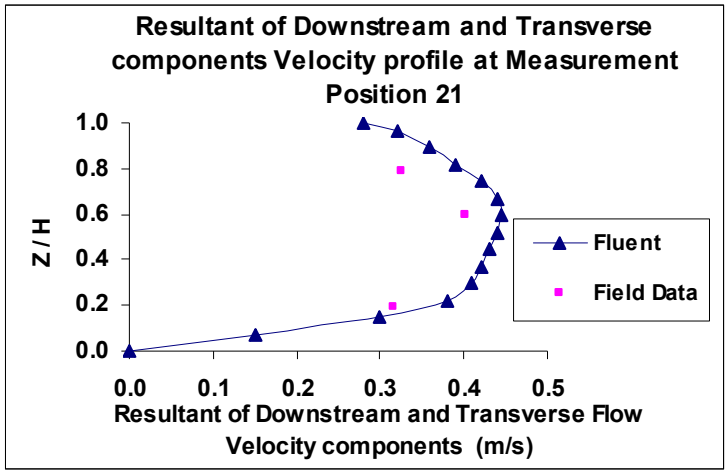

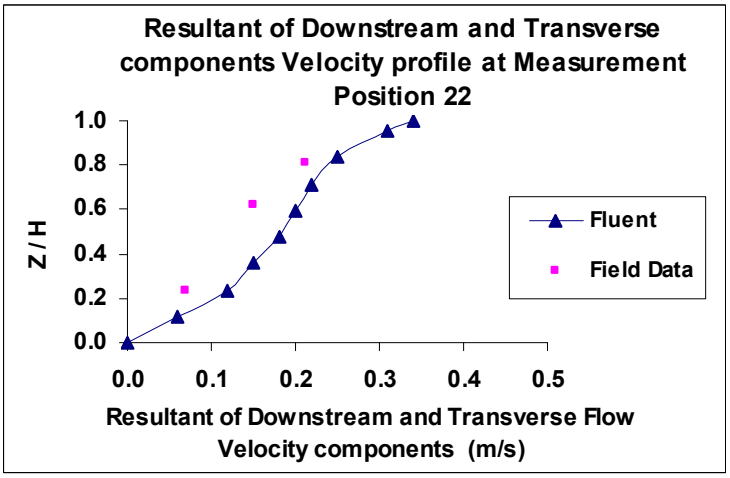

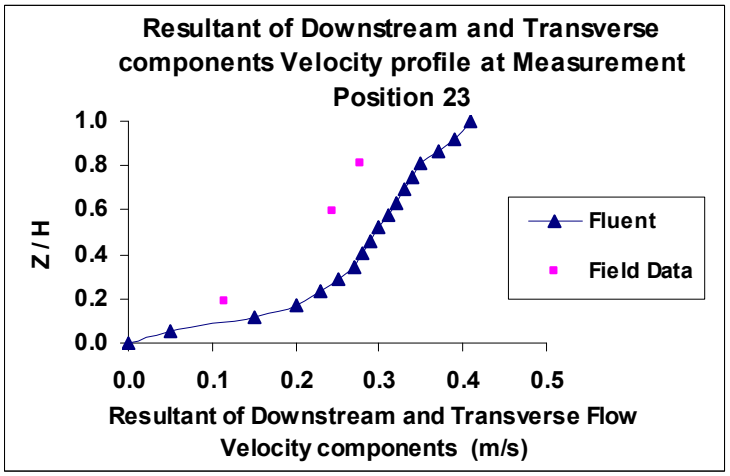

Predicted versus observed resultant of downstream and transverse flow velocity components at measurement positions 21, 22, and 23.

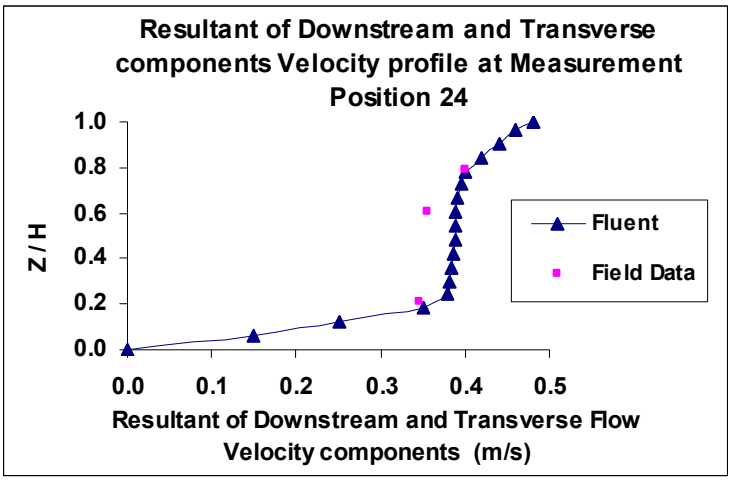

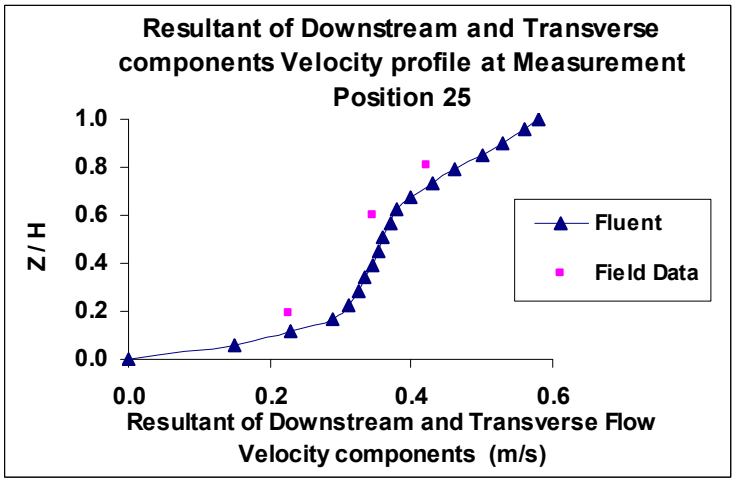

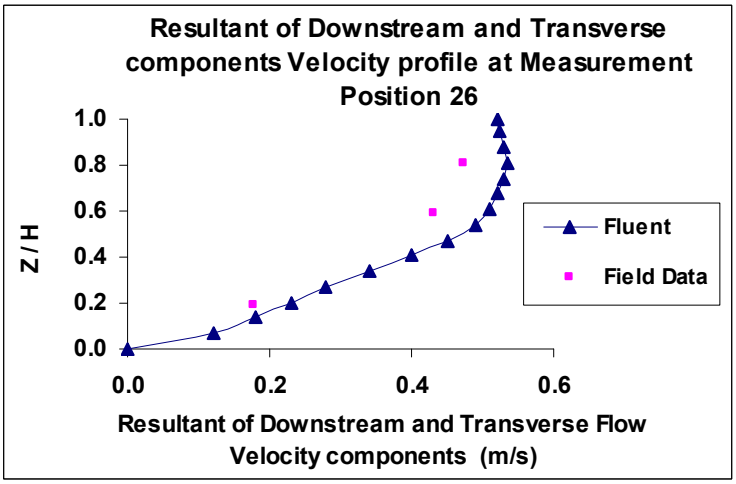

Predicted versus observed resultant of downstream and transverse flow velocity components at measurement positions 24, 25, and 26.

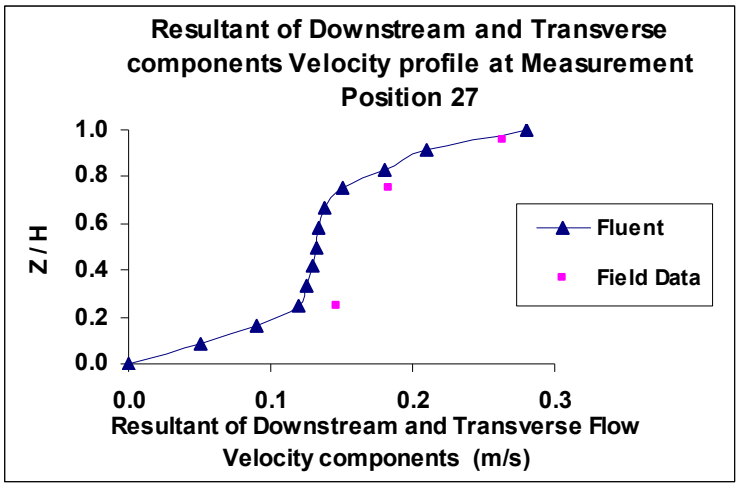

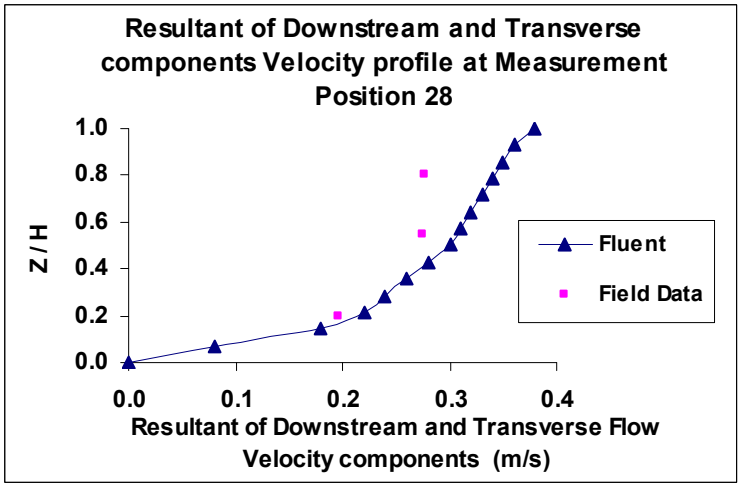

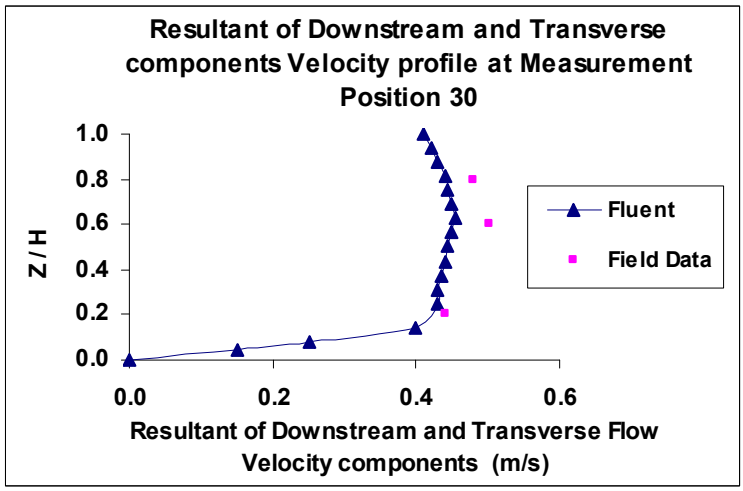

Predicted versus observed resultant of downstream and transverse flow velocity components at measurement positions 27, 28, and 30.

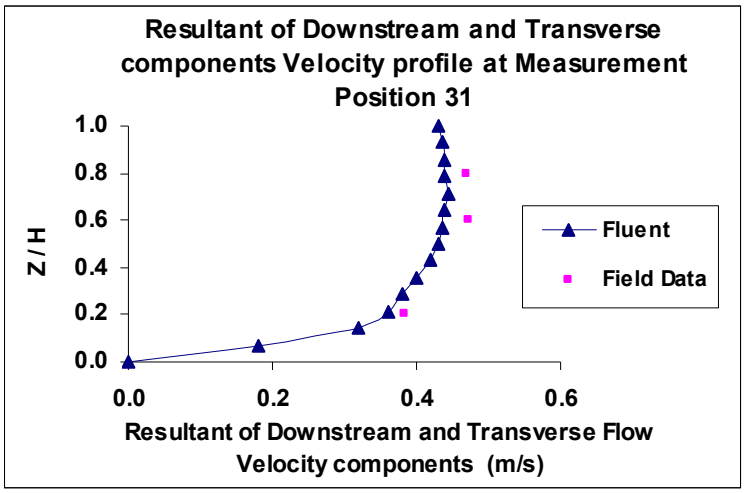

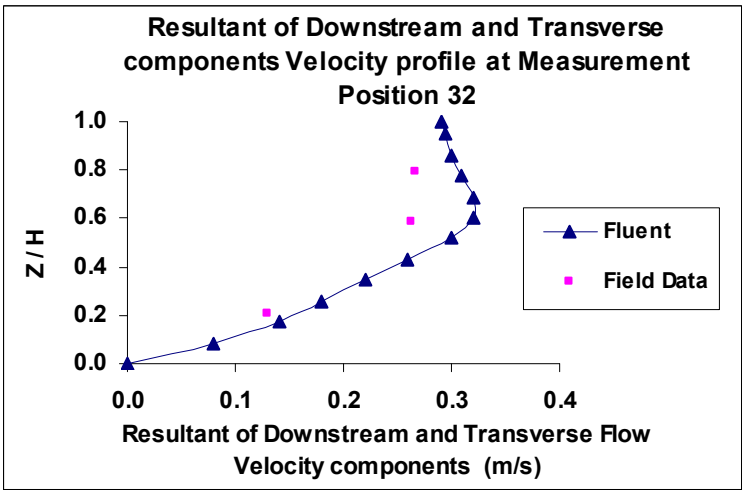

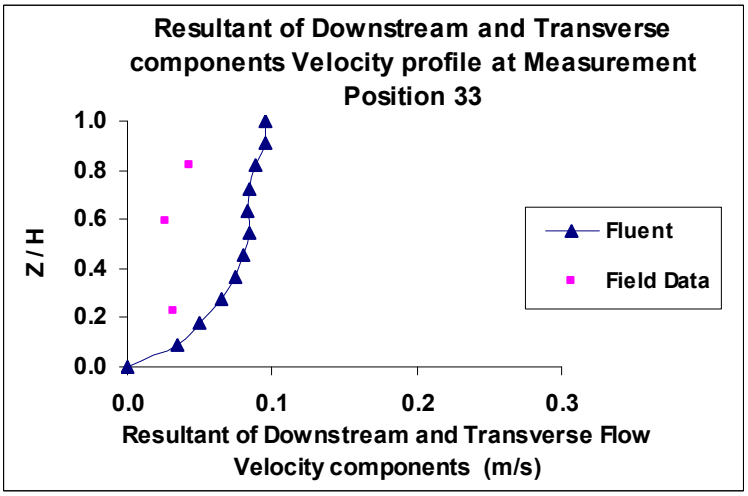

Predicted versus observed resultant of downstream and transverse flow velocity components at measurement positions 31, 32, and 33.

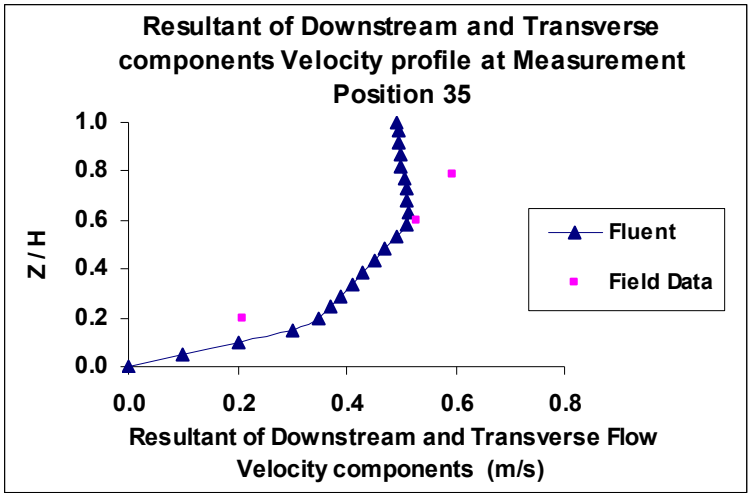

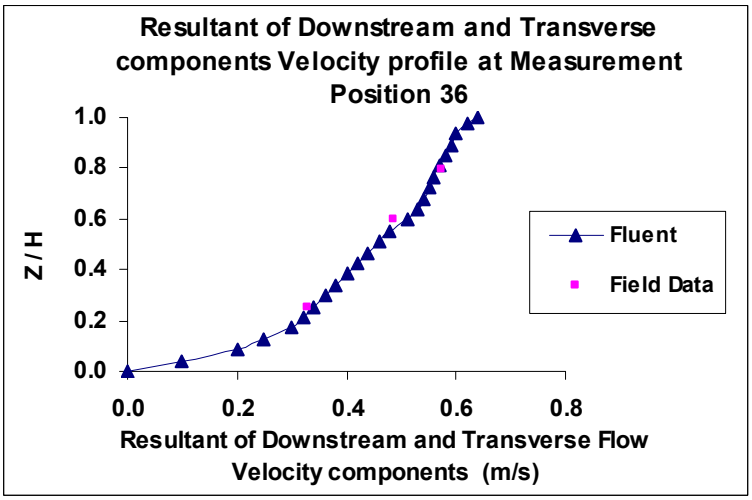

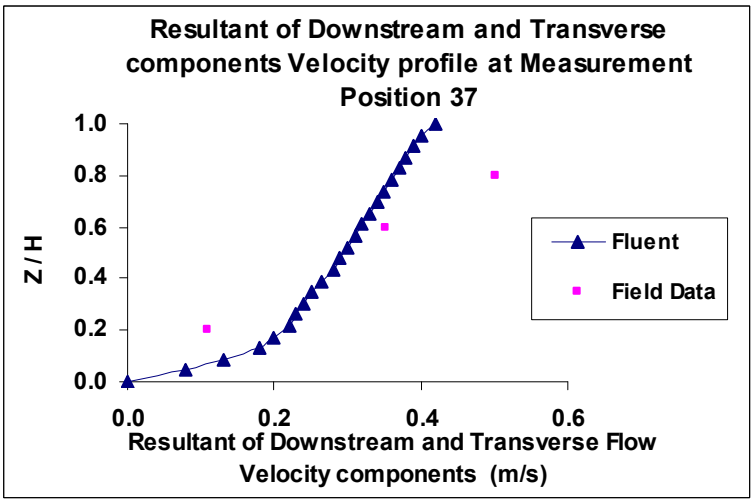

Predicted versus observed resultant of downstream and transverse flow velocity components at measurement positions 35, 36, and 37.

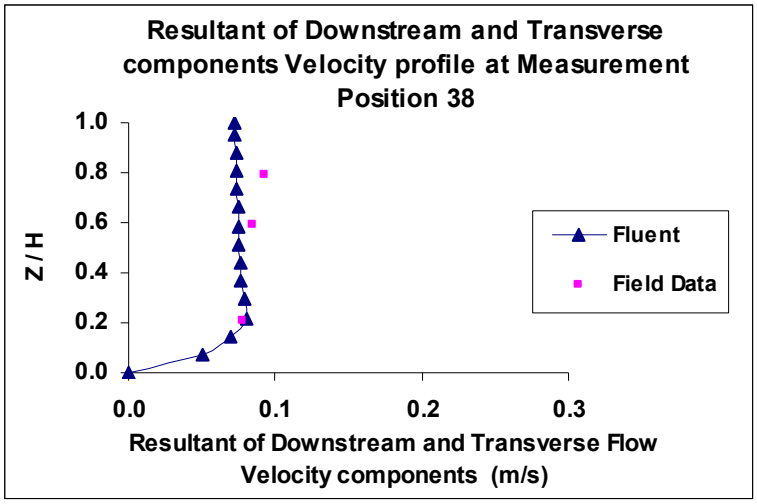

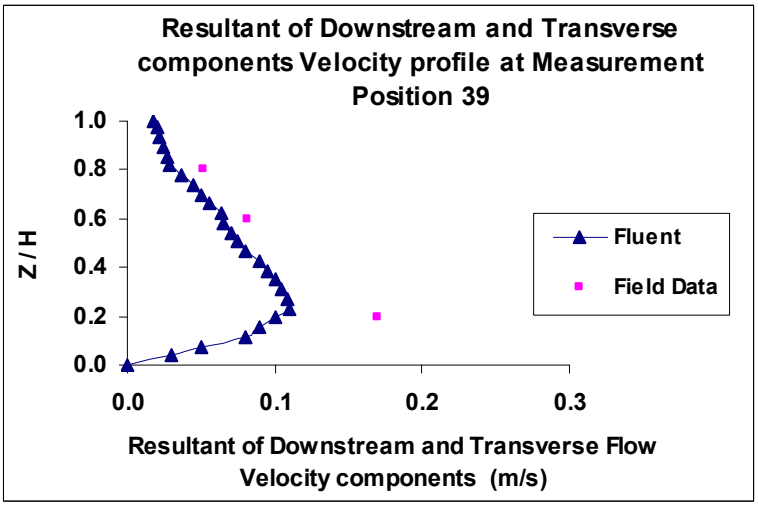

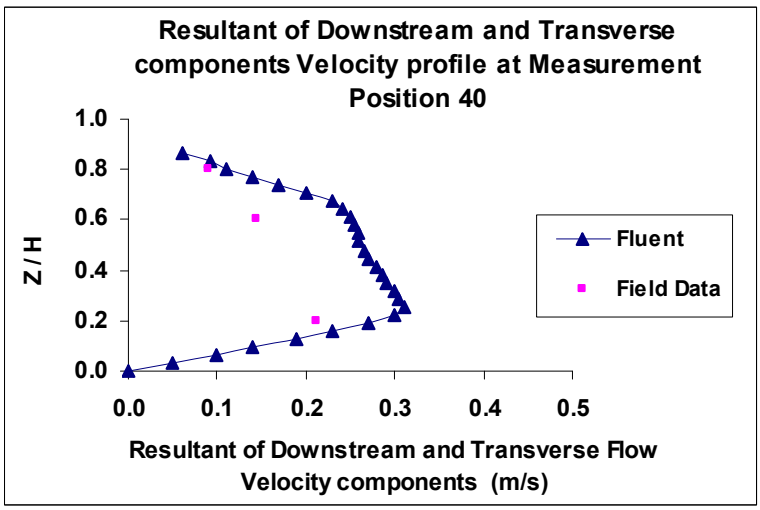

Predicted versus observed resultant of downstream and transverse flow velocity components at measurement positions 38, 39, and 40.

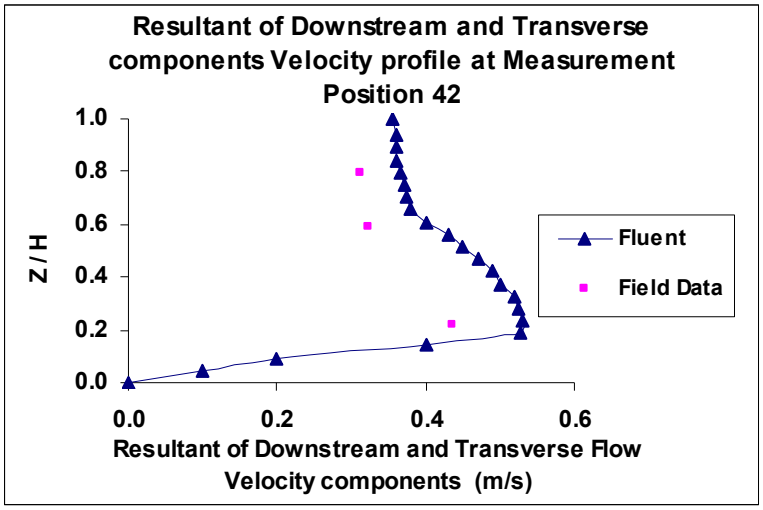

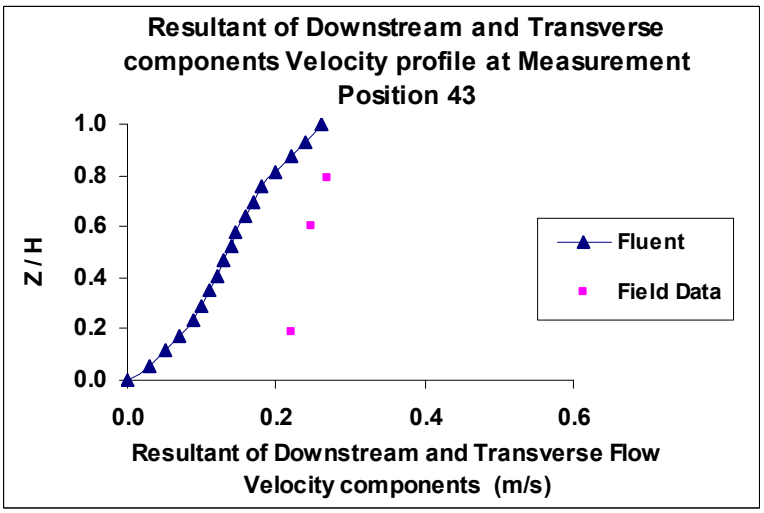

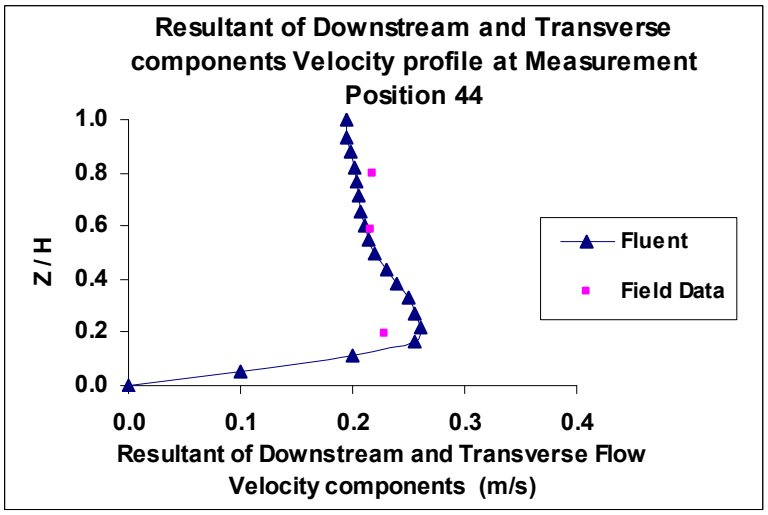

Predicted versus observed resultant of downstream and transverse flow velocity components at measurement positions 42, 43, and 44.

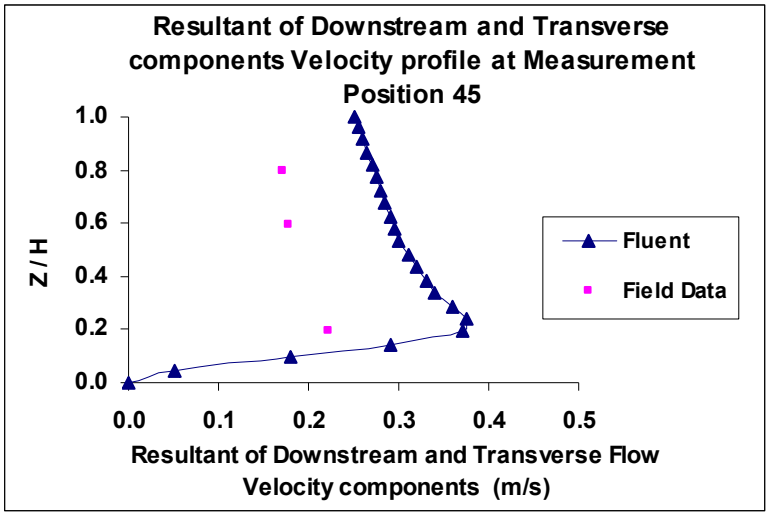

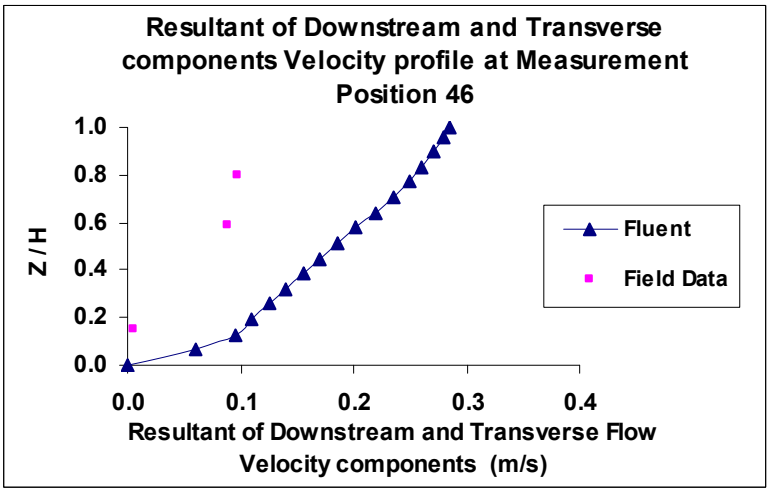

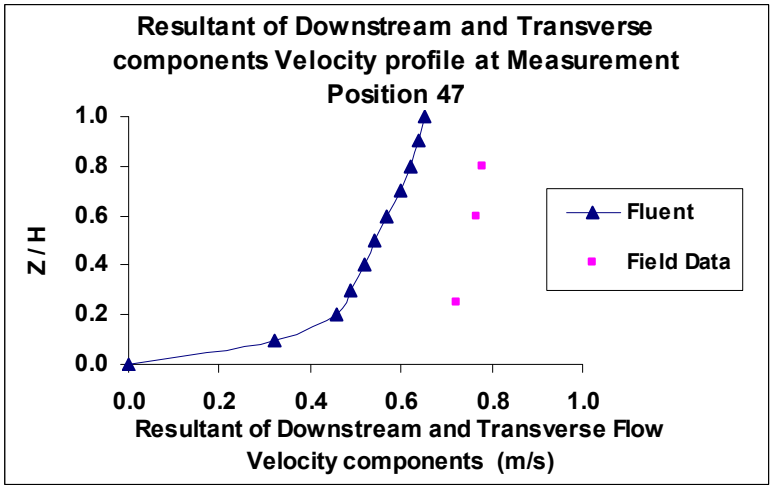

Predicted versus observed resultant of downstream and transverse flow velocity components at measurement positions 45, 46, and 47.

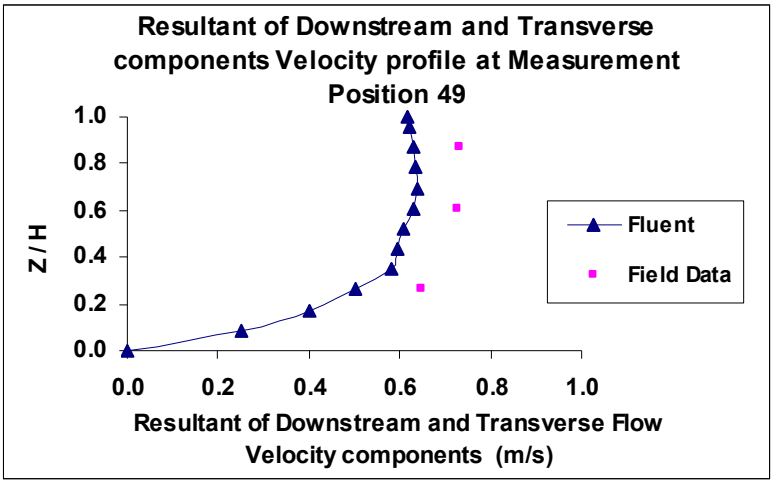

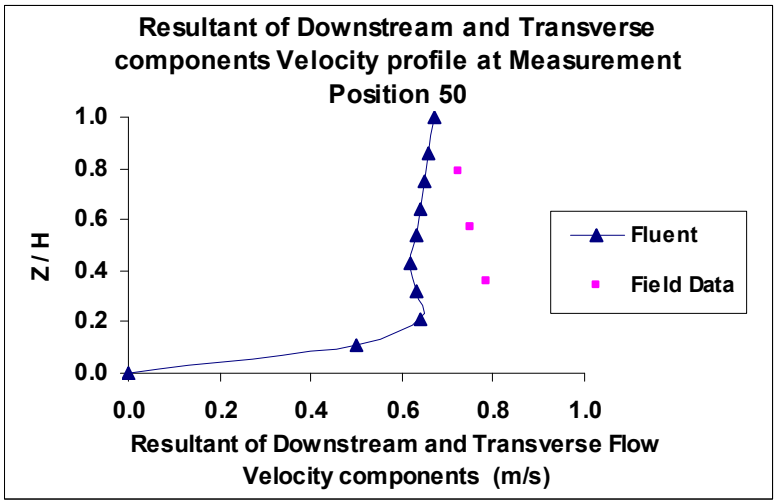

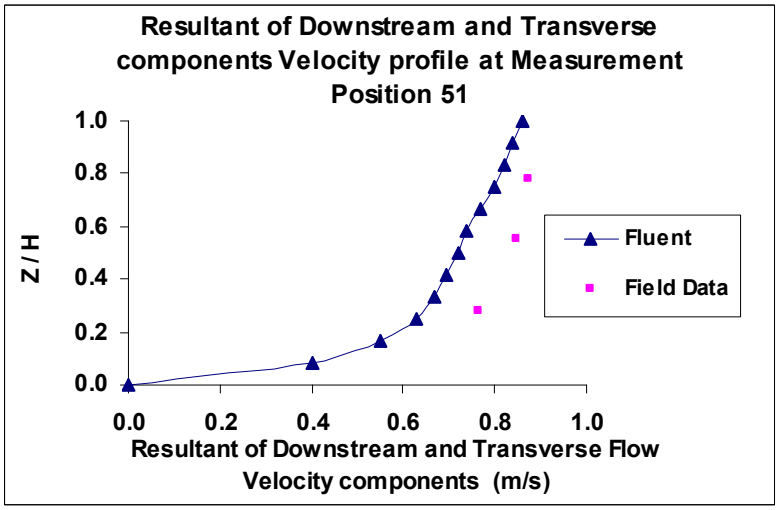

Predicted versus observed resultant of downstream and transverse flow velocity components at measurement positions 49, 50, and 51.

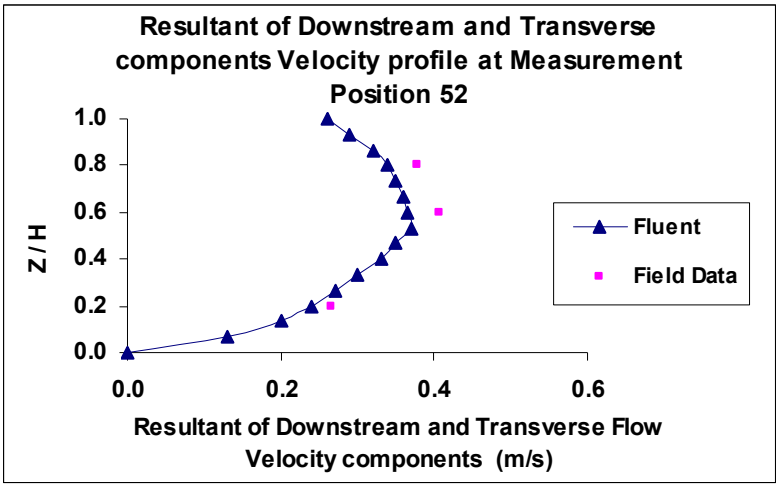

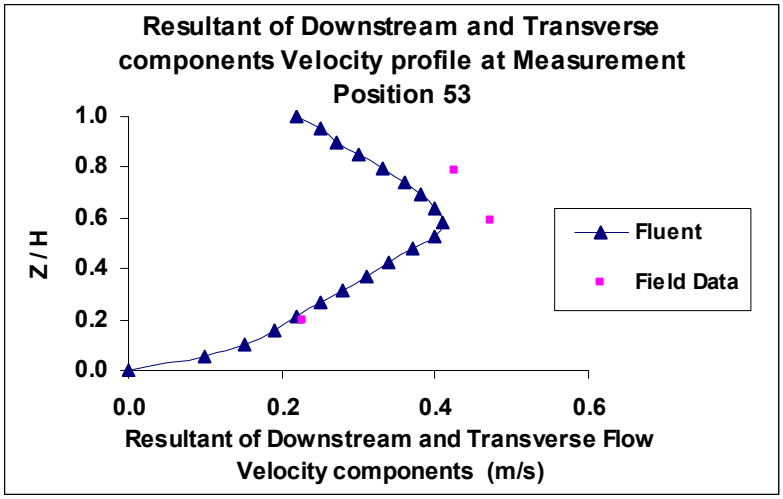

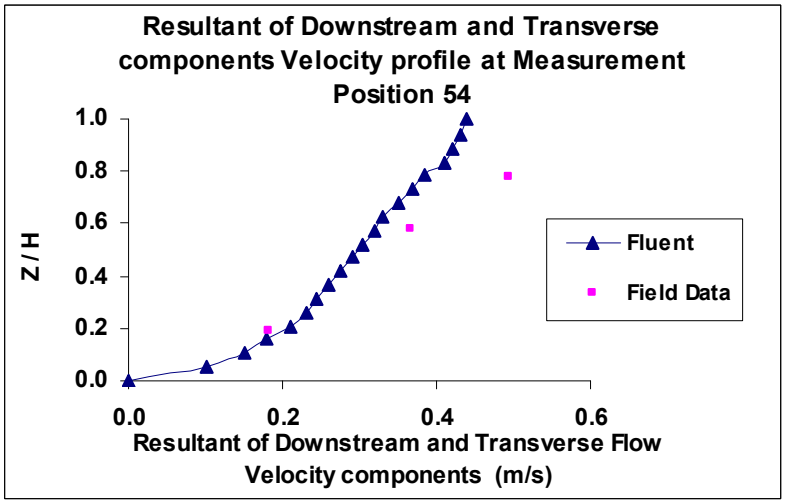

Predicted versus observed resultant of downstream and transverse flow velocity components at measurement positions 52, 53, and 54.

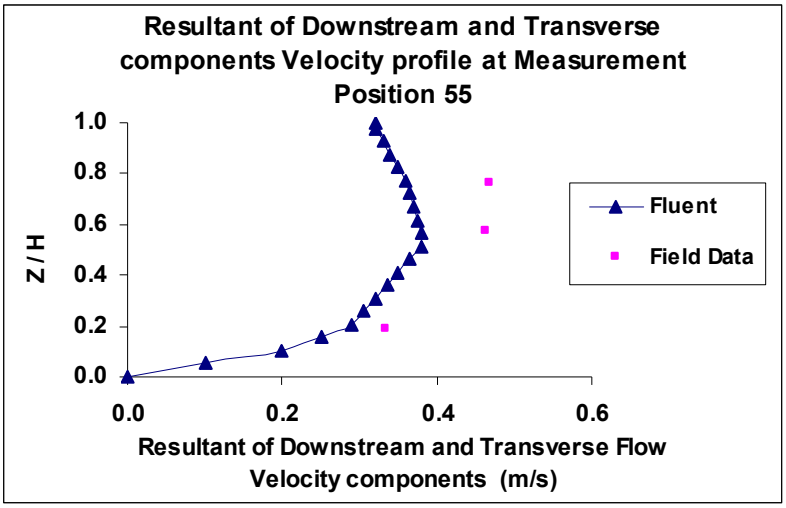

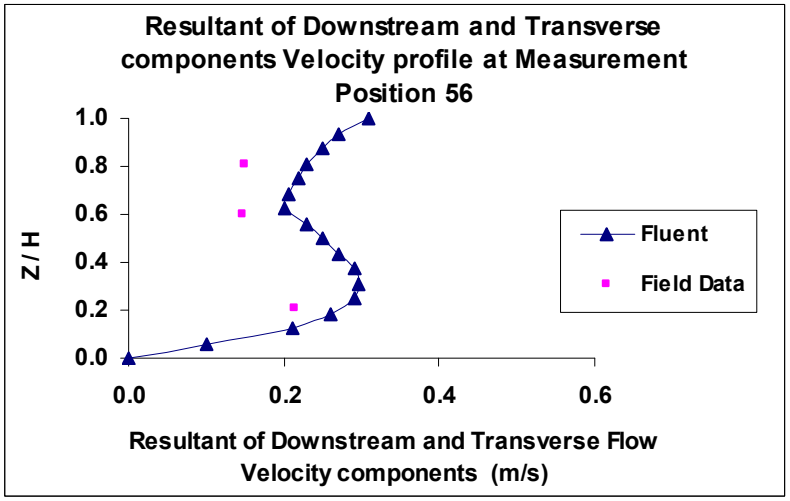

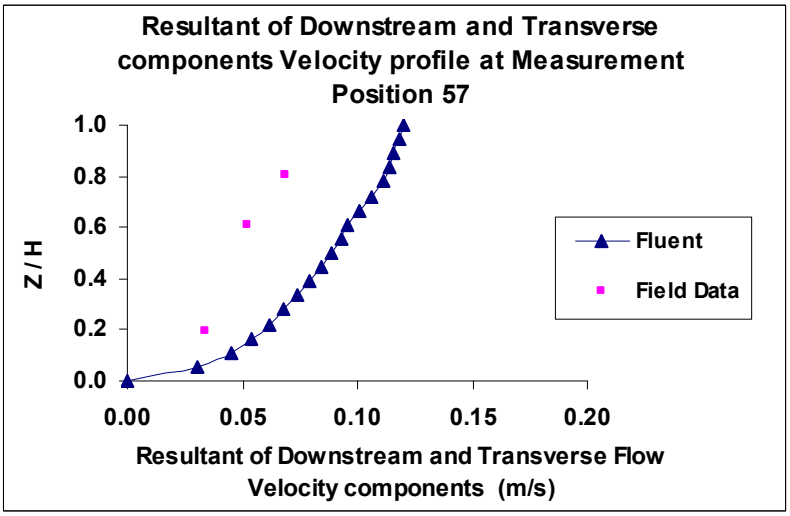

Predicted versus observed resultant of downstream and transverse flow velocity components at measurement positions 55, 56, and 57.

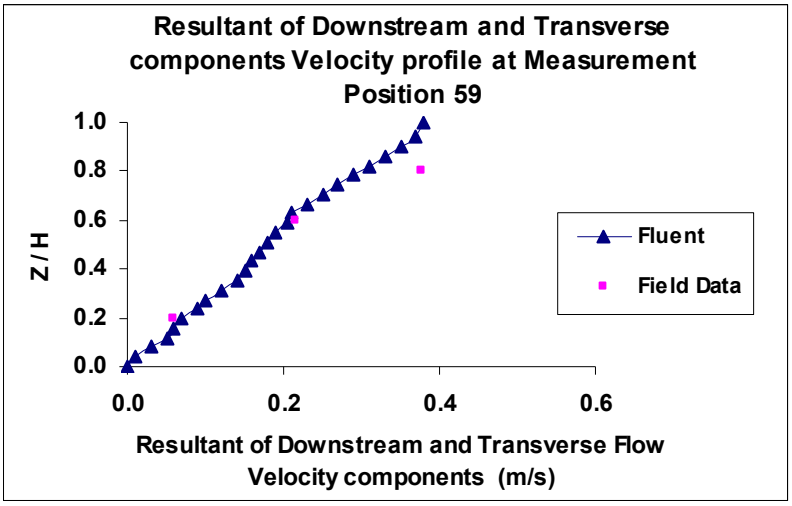

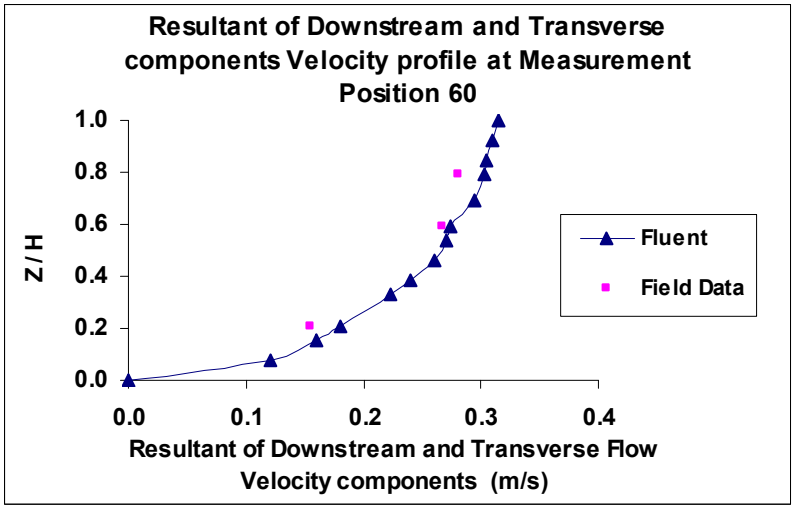

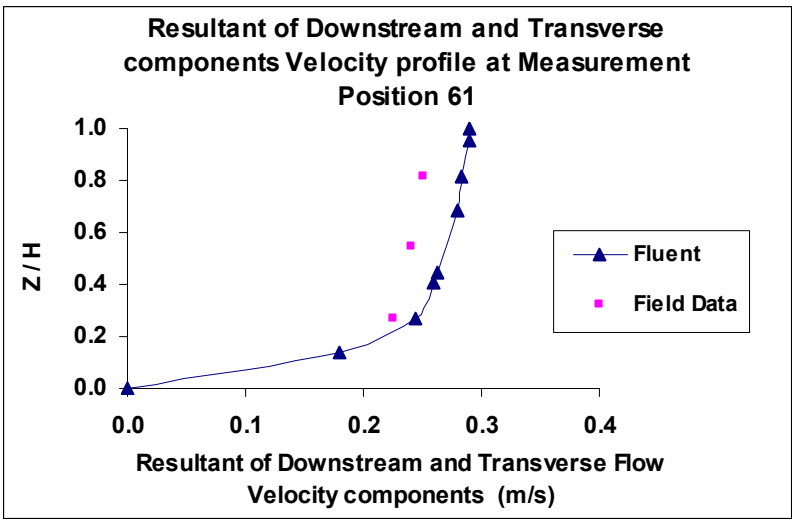

Predicted versus observed resultant of downstream and transverse flow velocity components at measurement positions 59, 60, and 61.

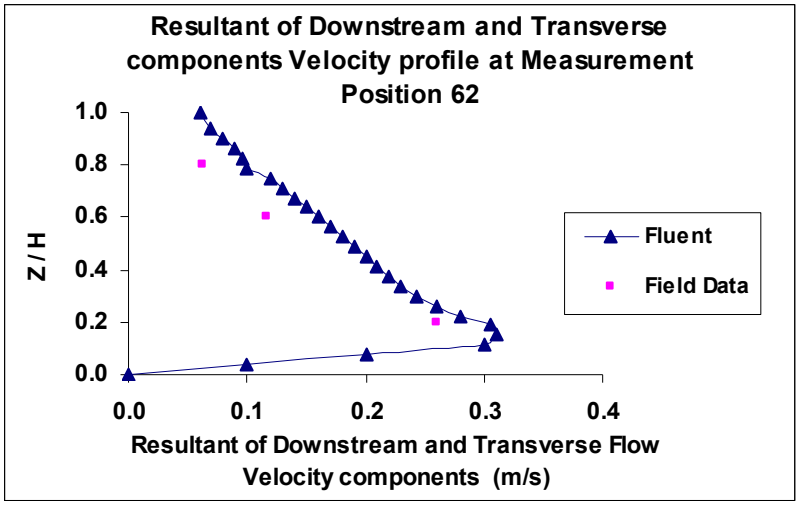

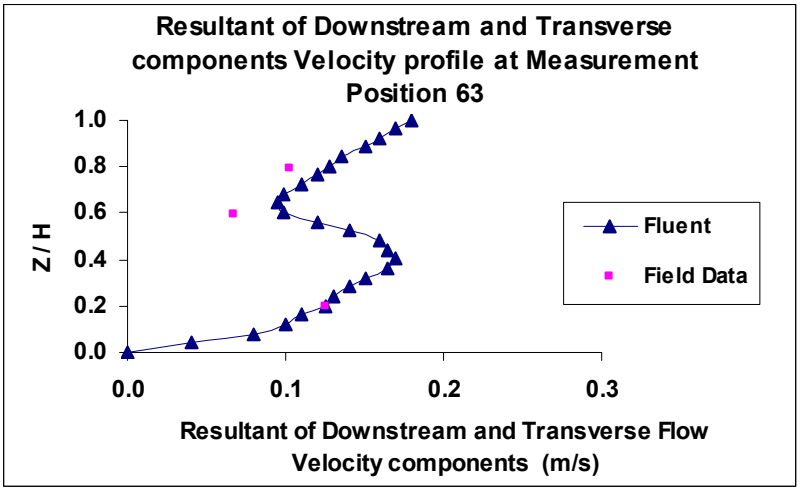

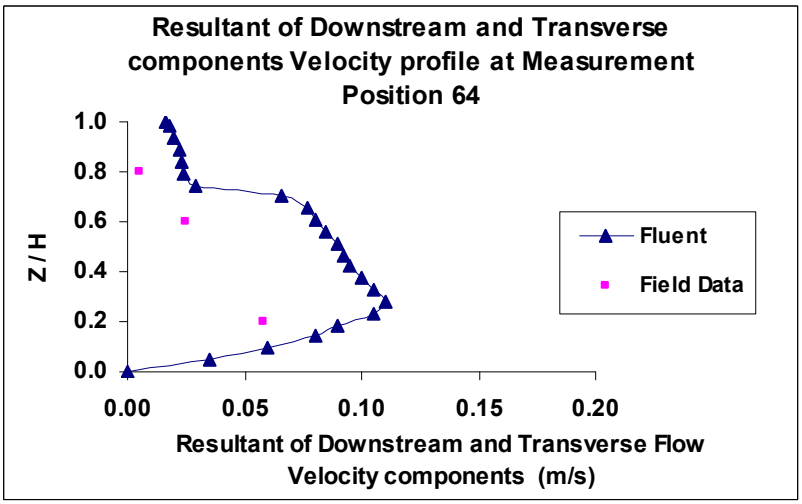

Predicted versus observed resultant of downstream and transverse flow velocity components at measurement positions 62, 63, and 64.

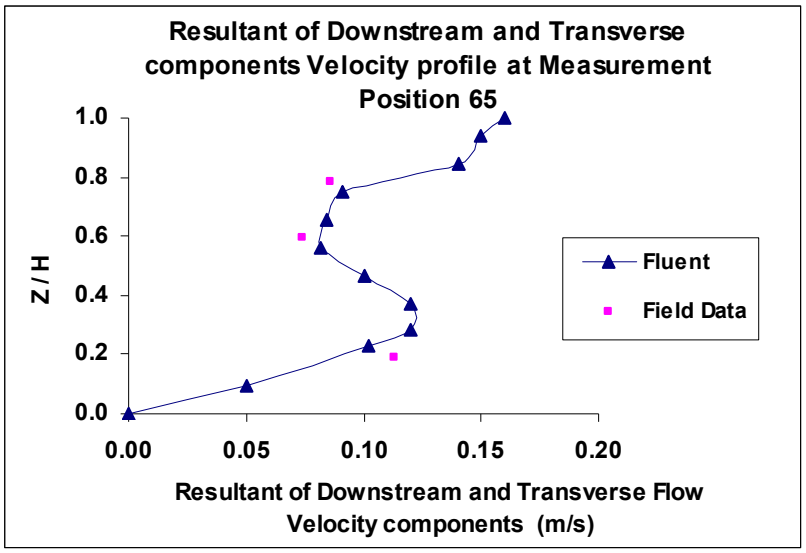

Predicted versus observed resultant of downstream and transverse flow velocity components at measurement position 65.

Predicted versus Observed Downstream Component of Flow Velocity at all Positions

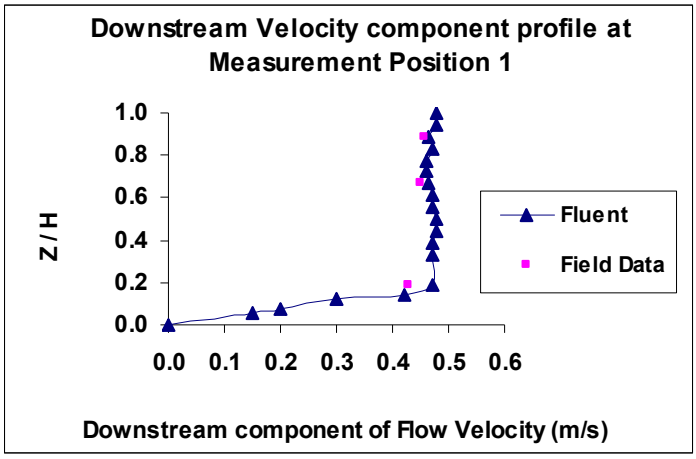

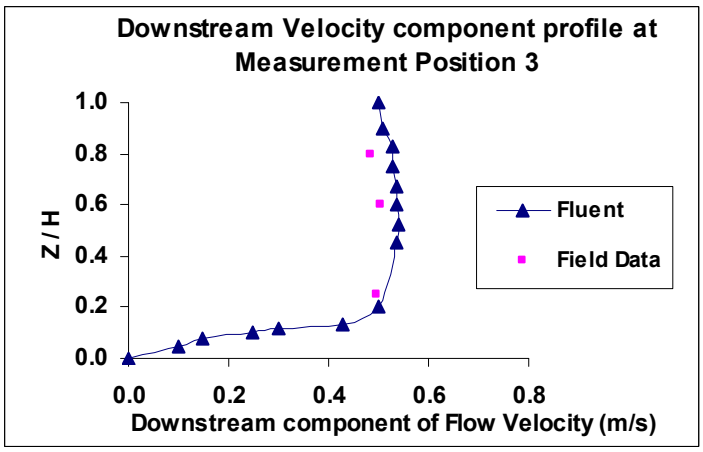

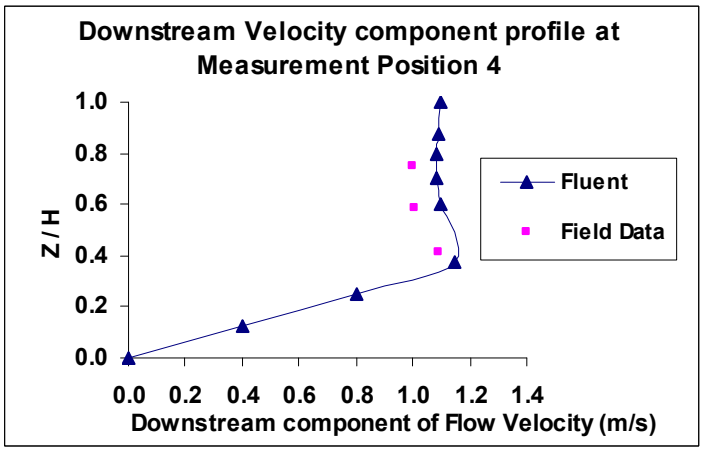

Predicted versus observed downstream flow velocity component at measurement positions 1, 3, and 4.

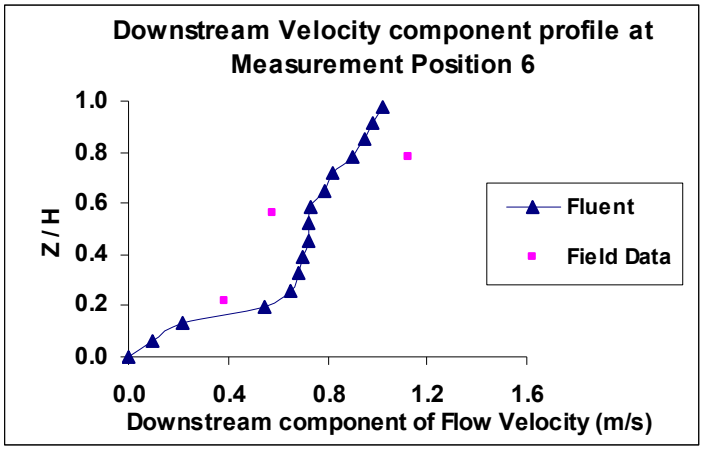

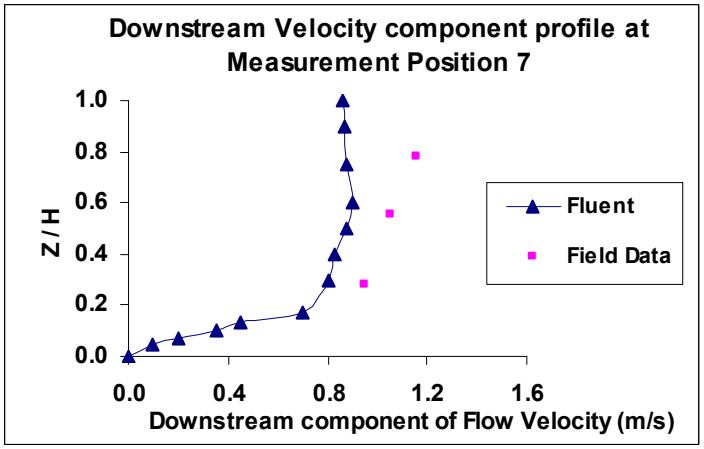

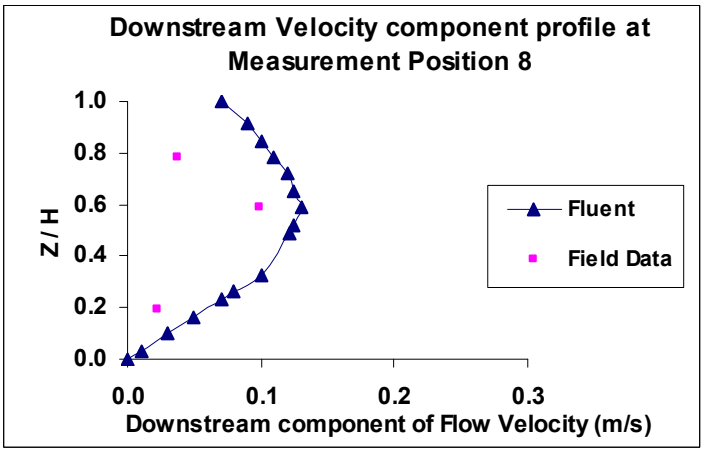

Predicted versus observed downstream flow velocity component at measurement positions 6, 7, and 8.

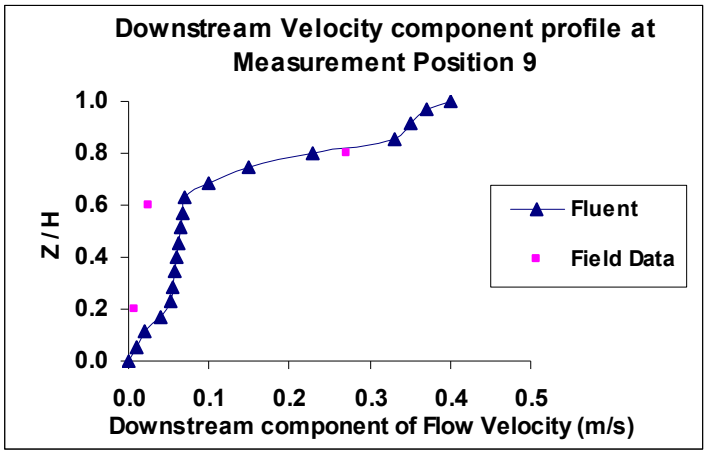

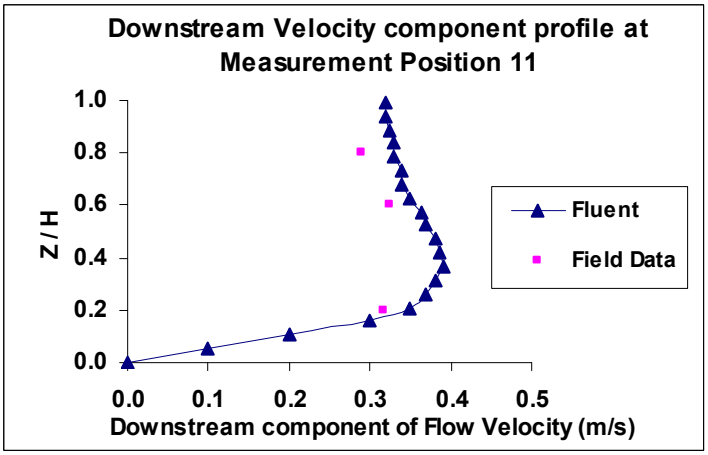

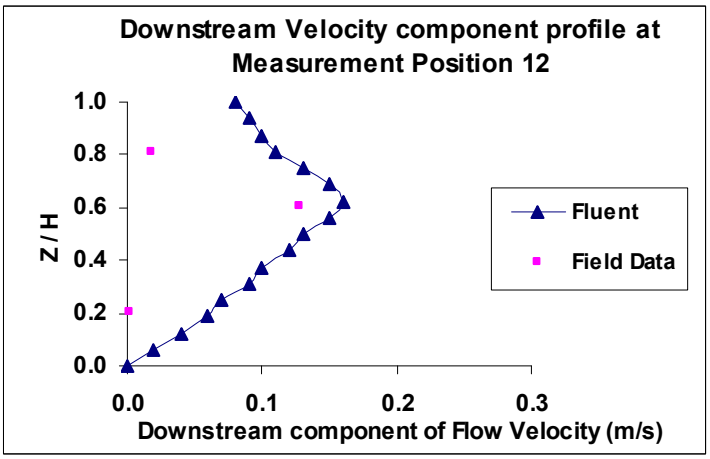

Predicted versus observed downstream flow velocity component at measurement positions 9, 11, and 12.

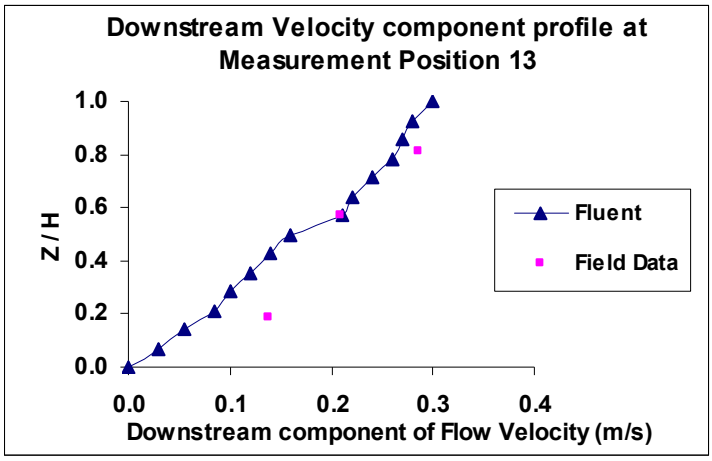

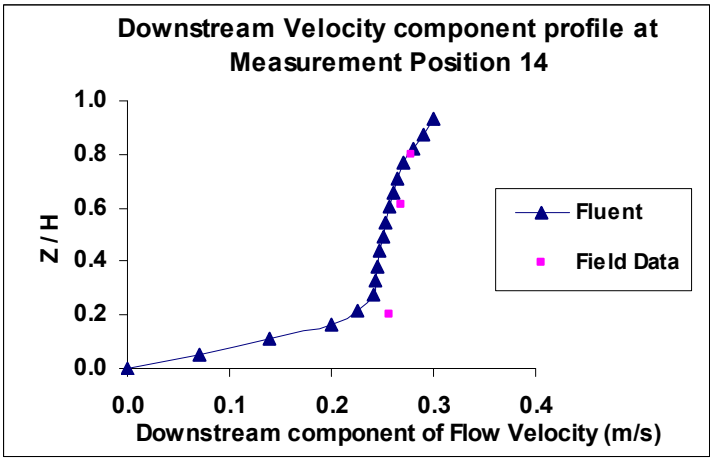

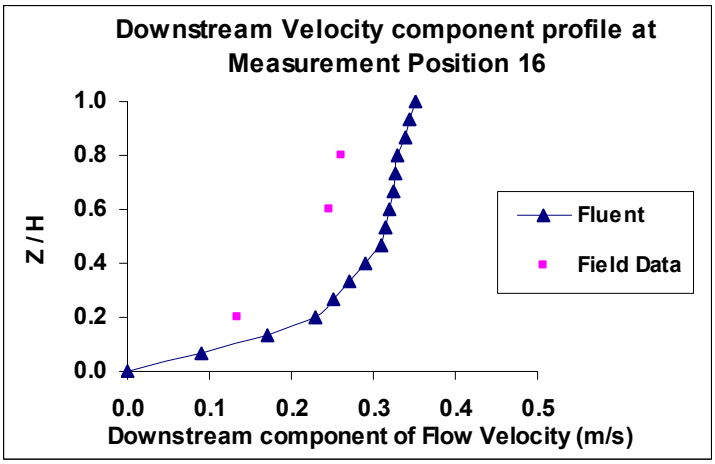

Predicted versus observed downstream flow velocity component at measurement positions 13, 14, and 16.

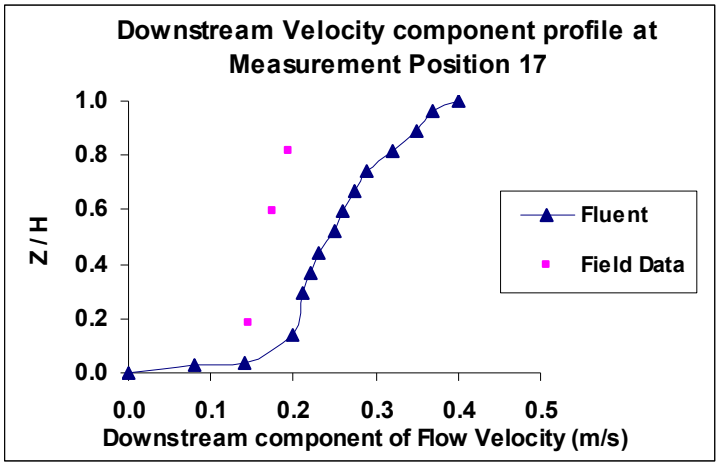

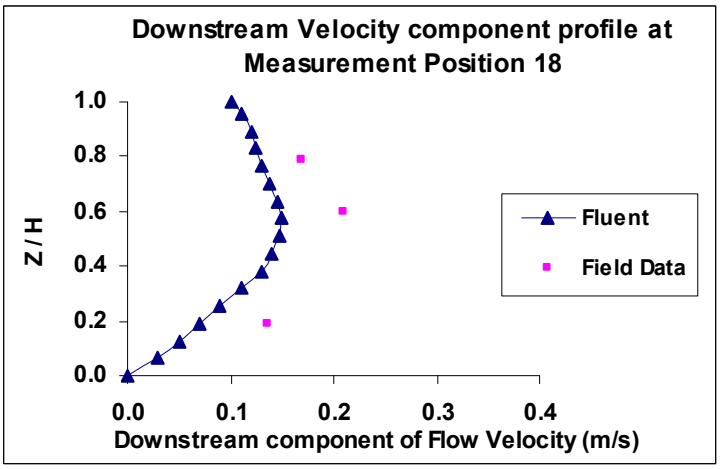

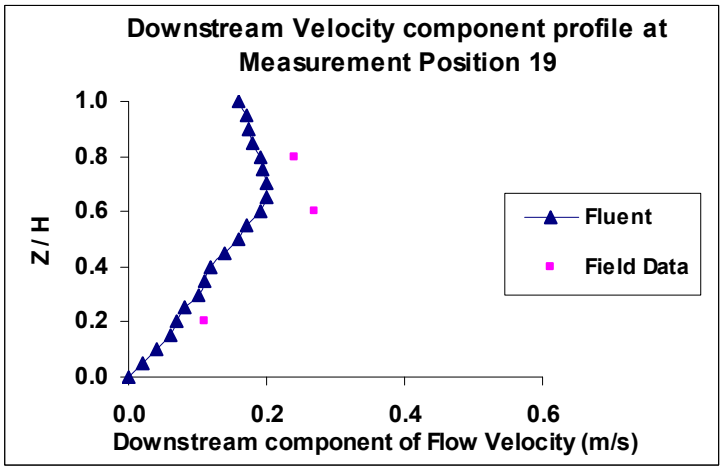

Predicted versus observed downstream flow velocity component at measurement positions 17, 18, and 19.

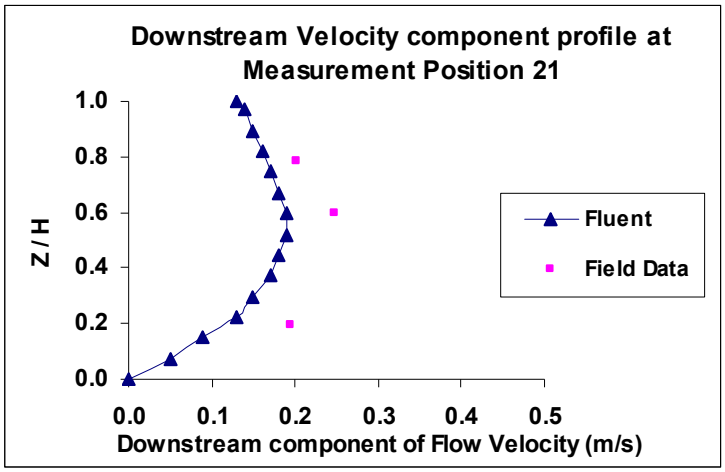

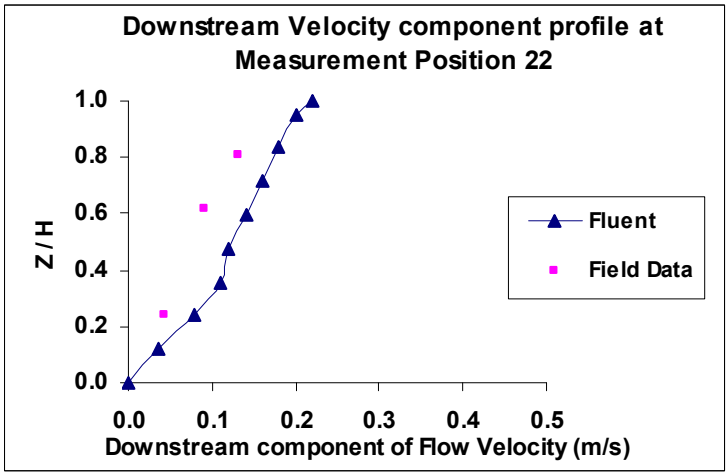

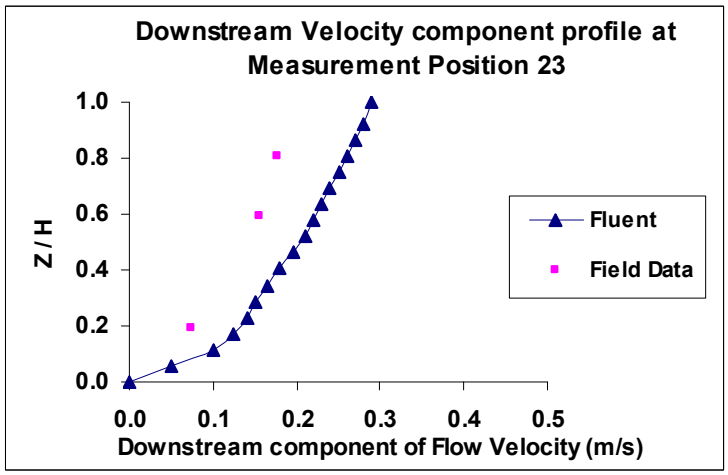

Predicted versus observed downstream flow velocity component at measurement positions 21, 22, and 23.

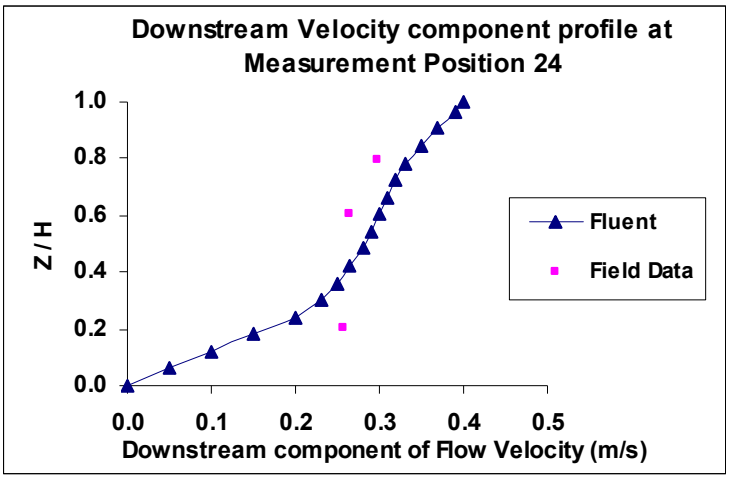

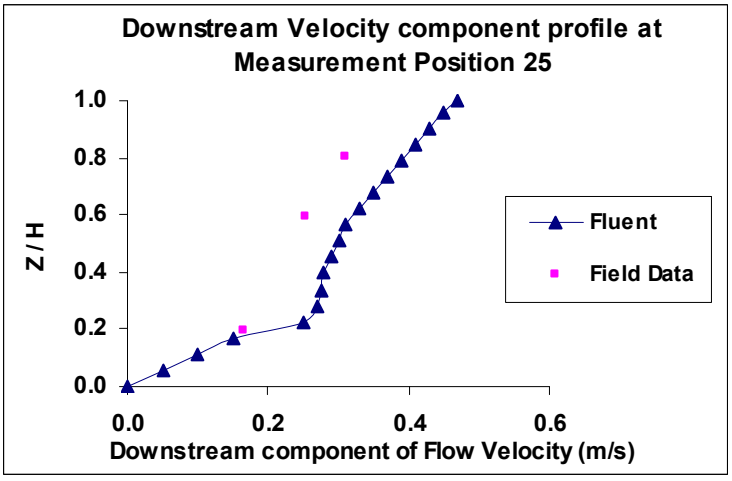

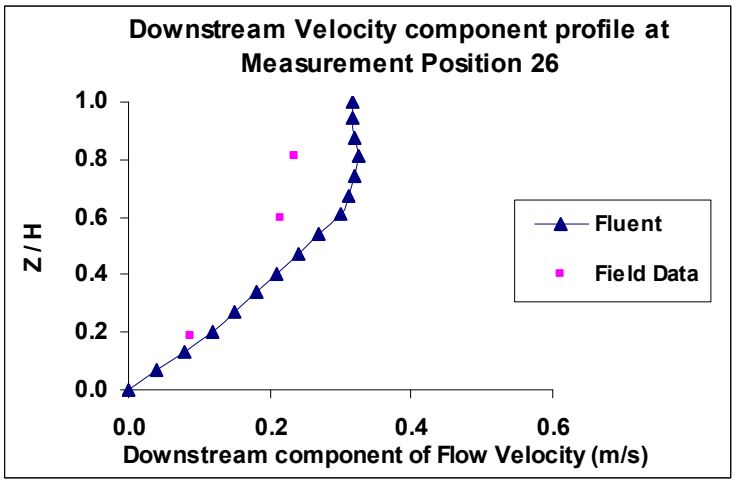

Predicted versus observed downstream flow velocity component at measurement positions 24, 25, and 26.

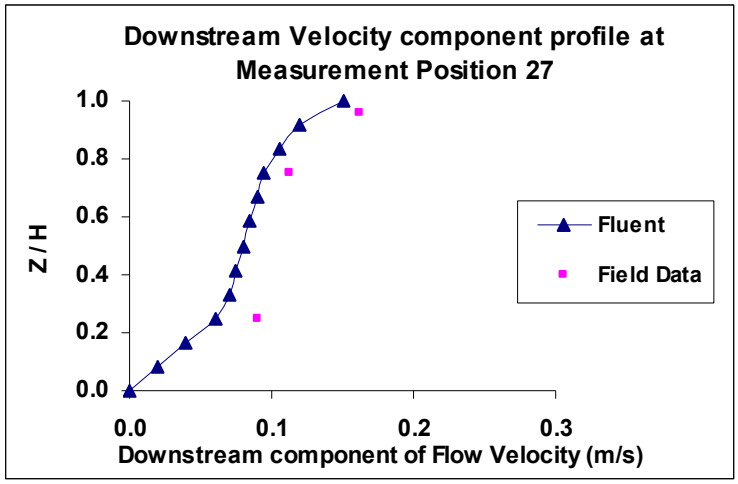

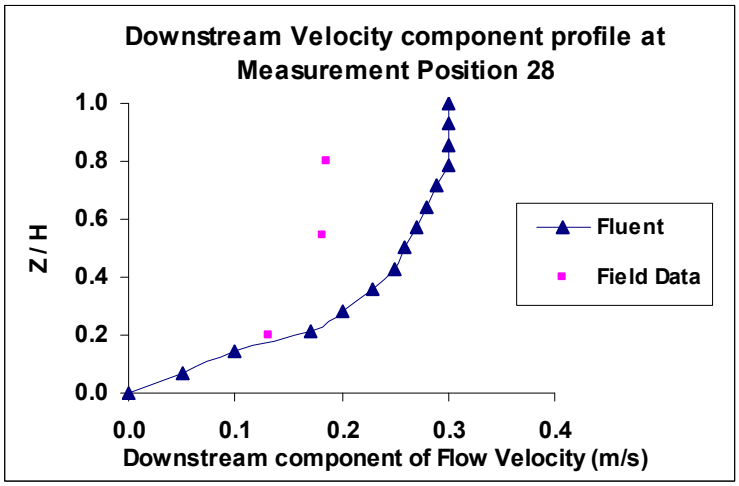

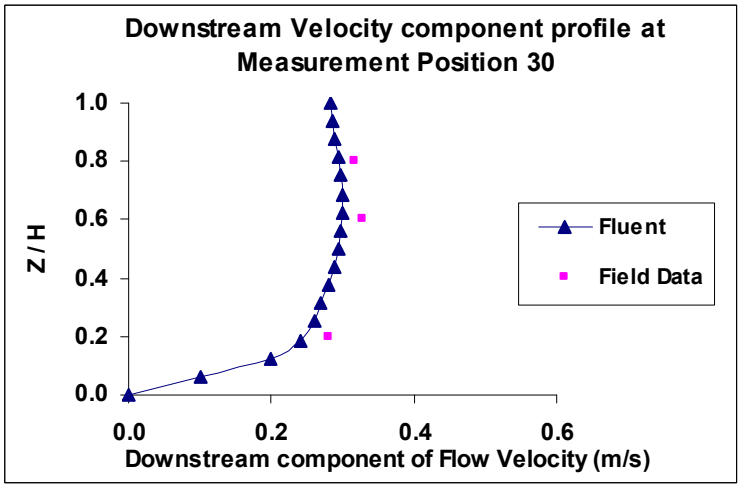

Predicted versus observed downstream flow velocity component at measurement positions 27, 28, and 30.

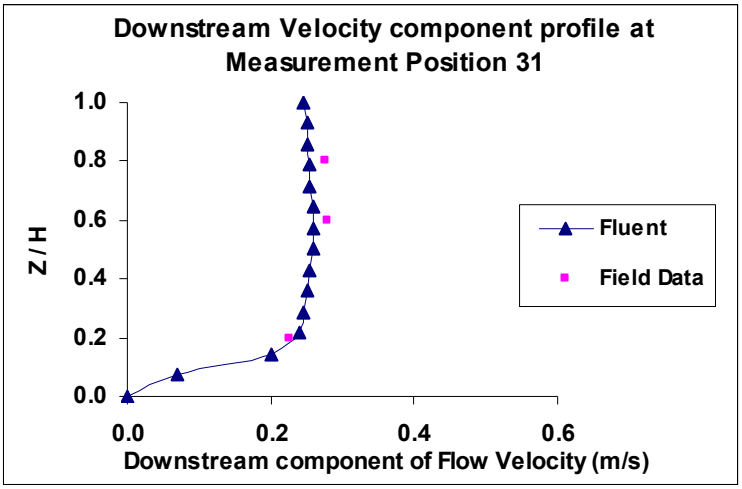

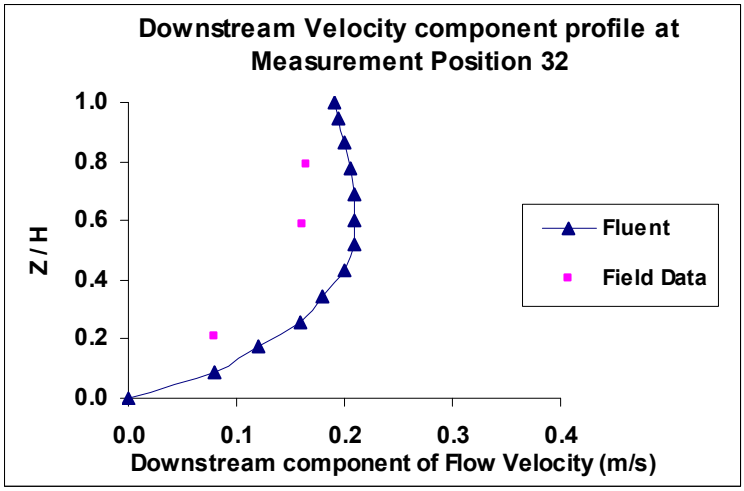

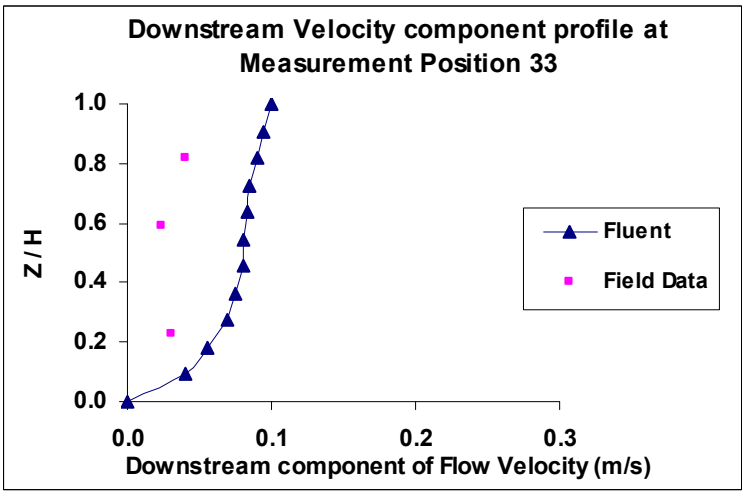

Predicted versus observed downstream flow velocity component at measurement positions 31, 32, and 33.

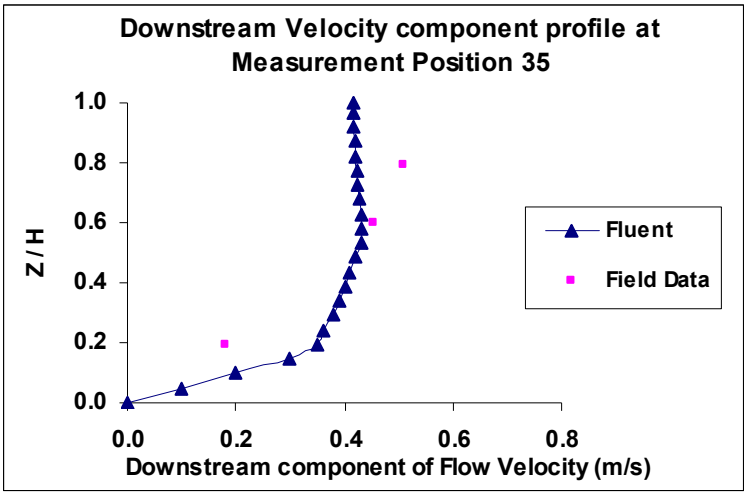

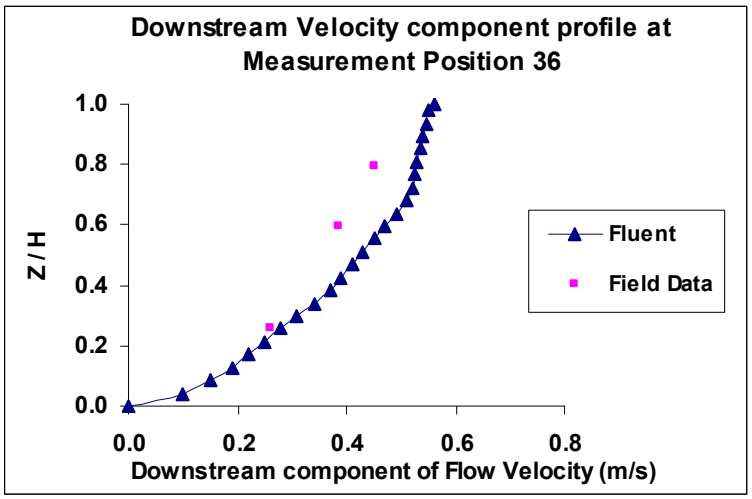

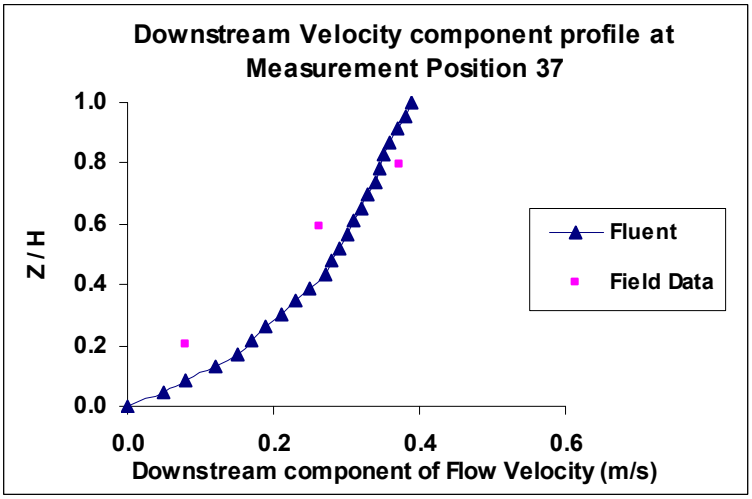

Predicted versus observed downstream flow velocity component at measurement positions 35, 36, and 37.

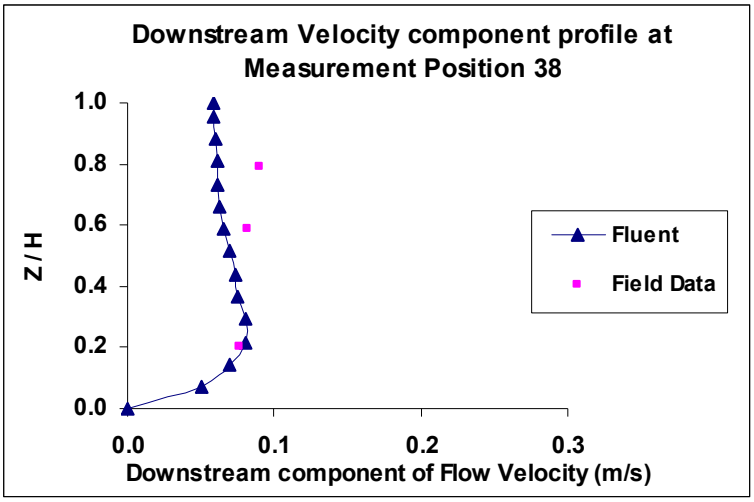

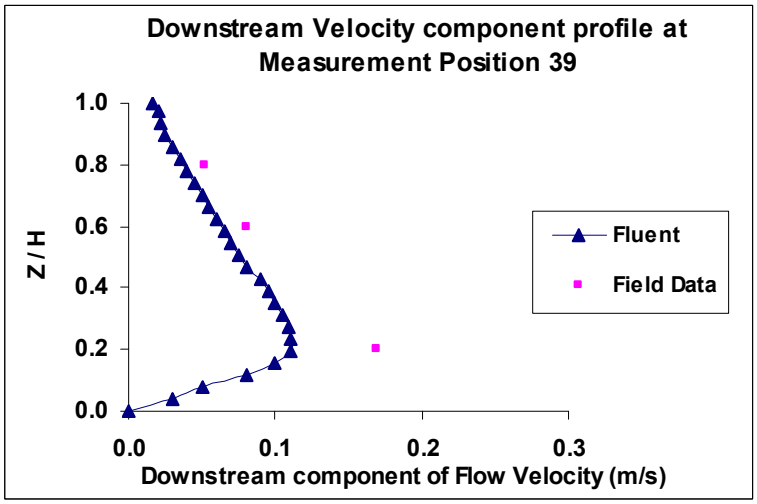

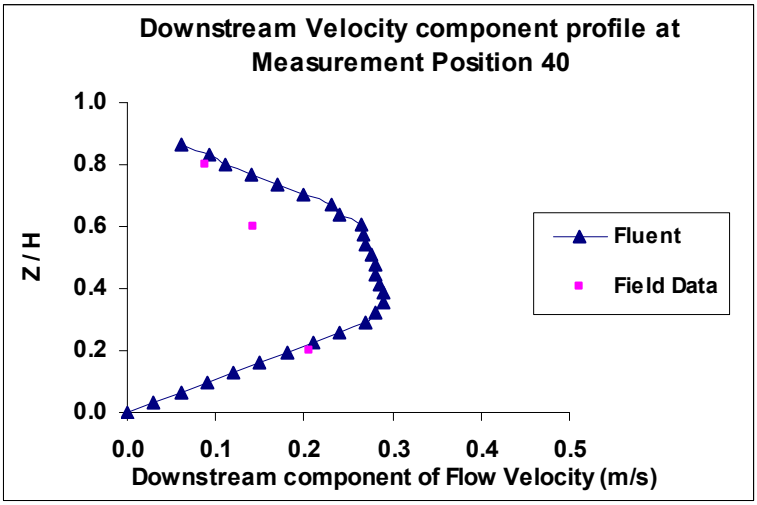

Predicted versus observed downstream flow velocity component at measurement positions 38, 39, and 40.

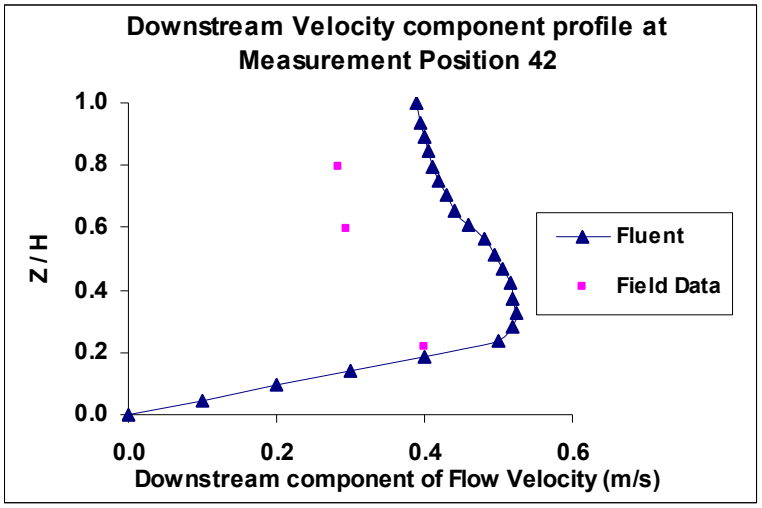

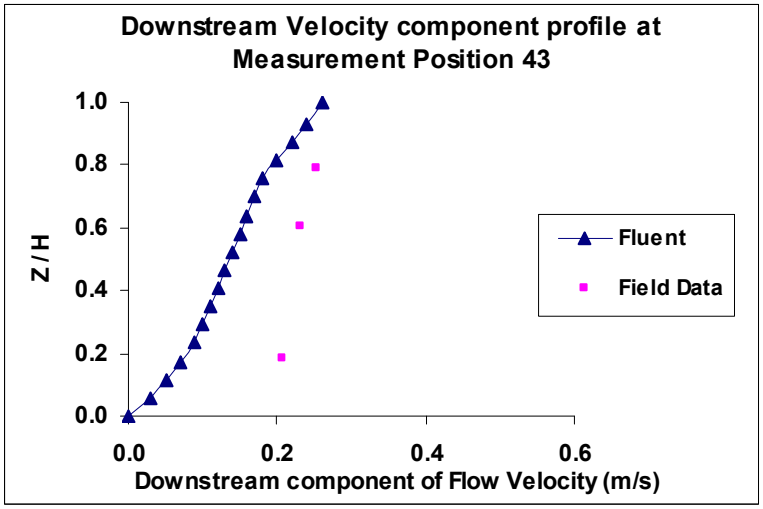

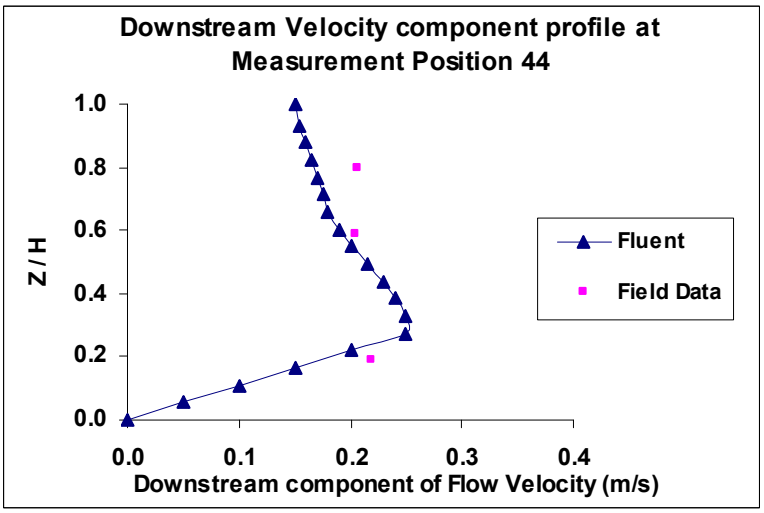

Predicted versus observed downstream flow velocity component at measurement positions 42, 43, and 44.

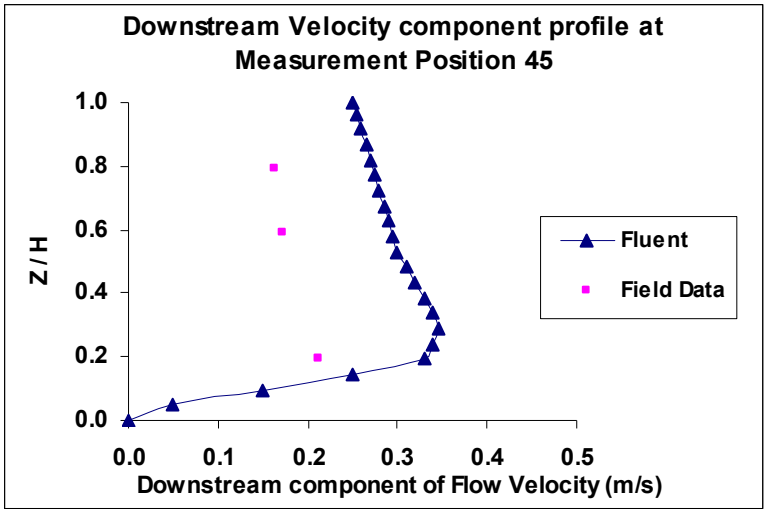

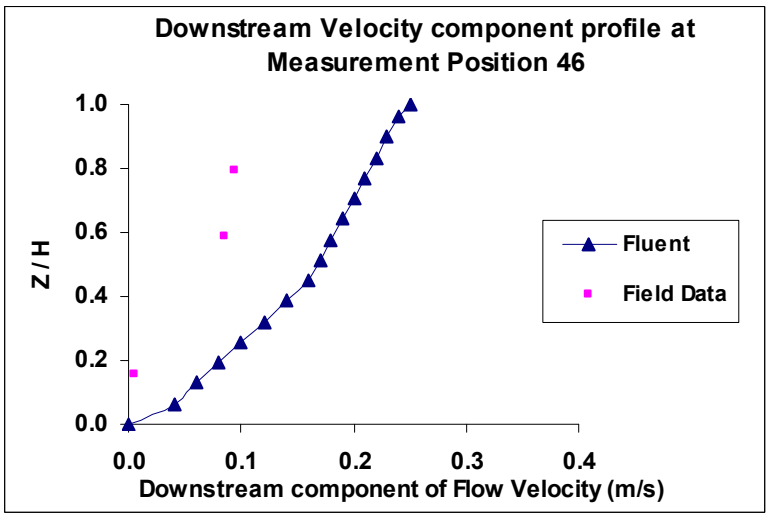

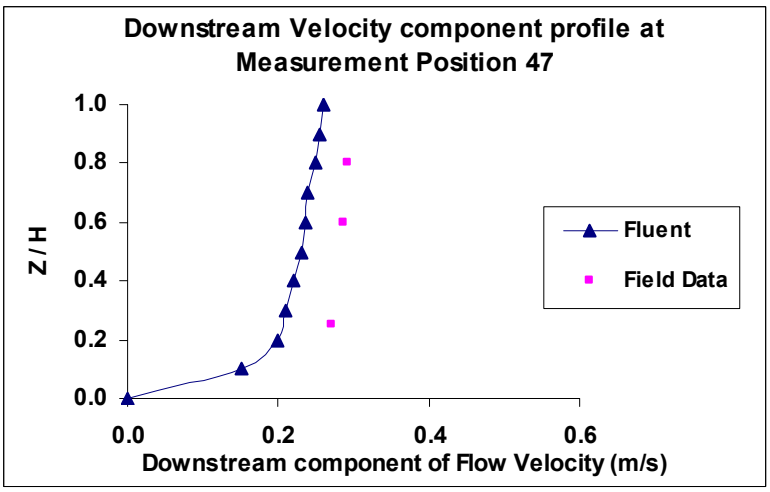

Predicted versus observed downstream flow velocity component at measurement positions 45, 46, and 47.

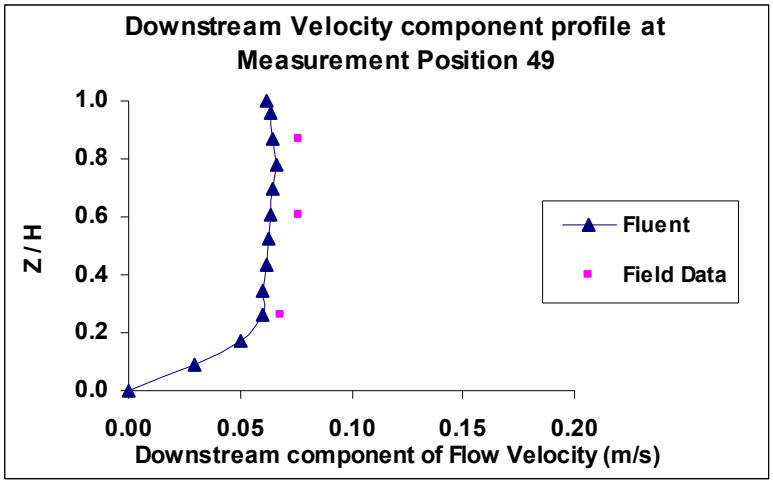

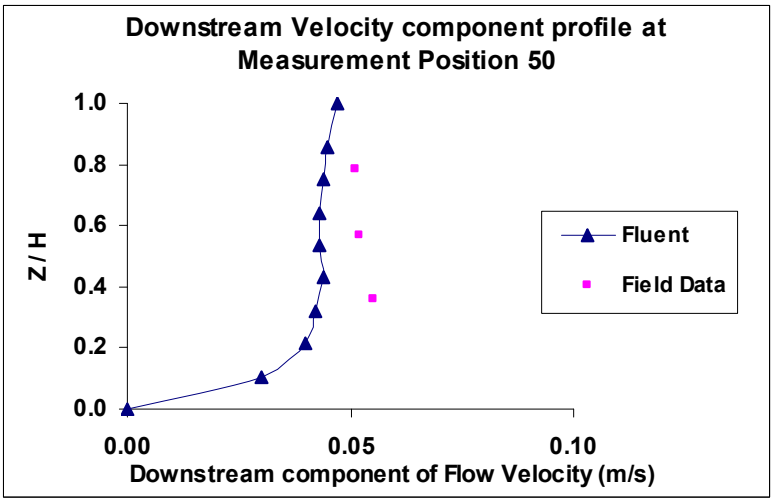

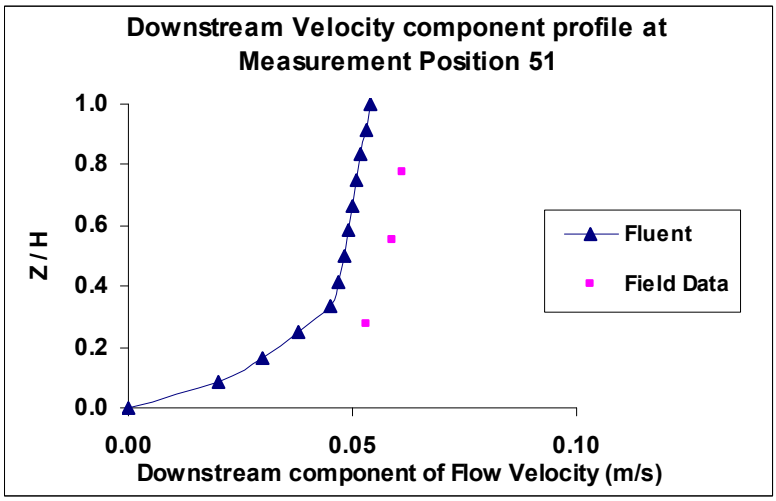

Predicted versus observed downstream flow velocity component at measurement positions 49, 50, and 51.

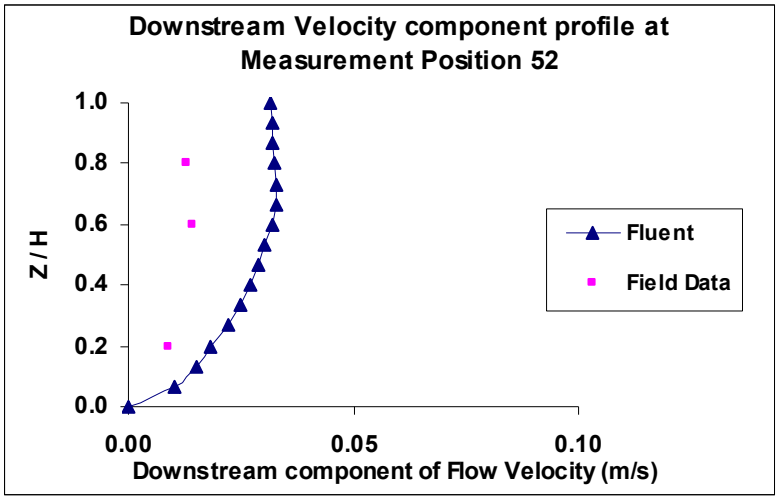

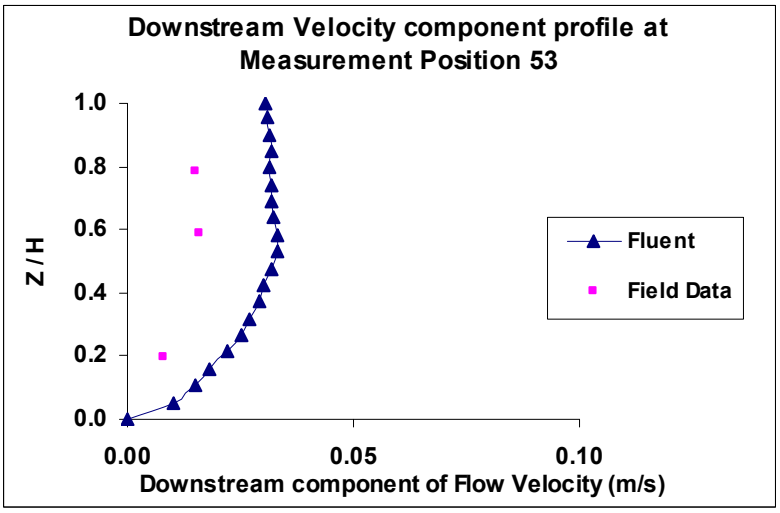

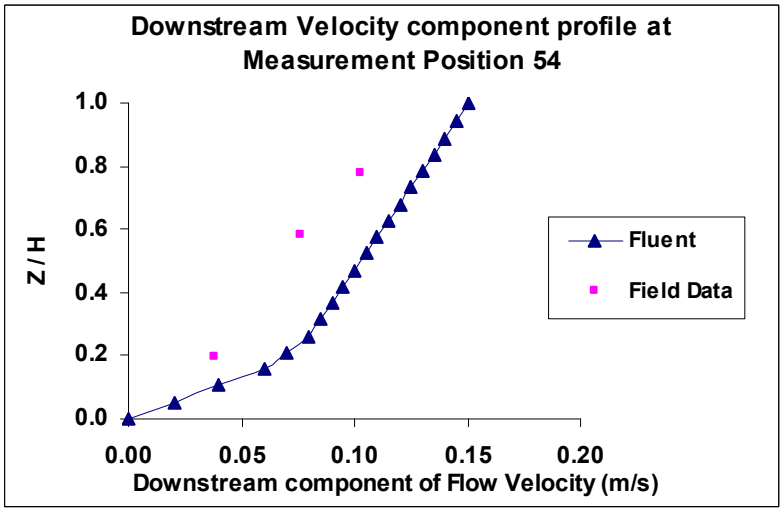

Predicted versus observed downstream flow velocity component at measurement positions 52, 53, and 54.

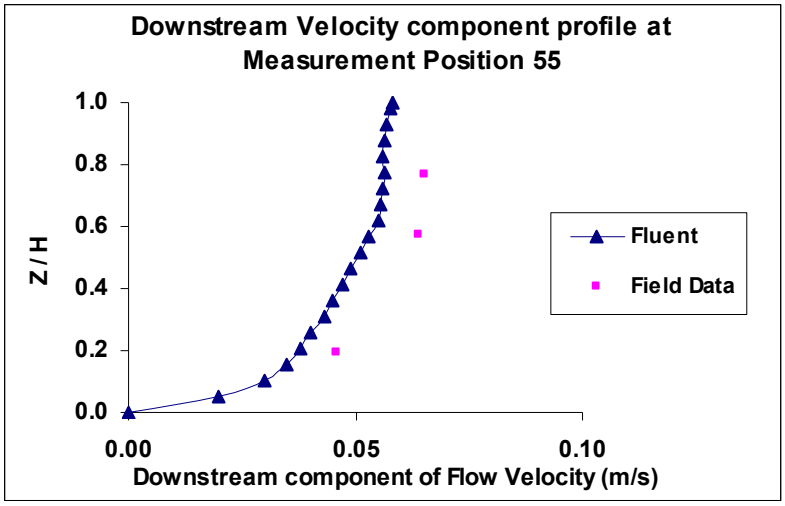

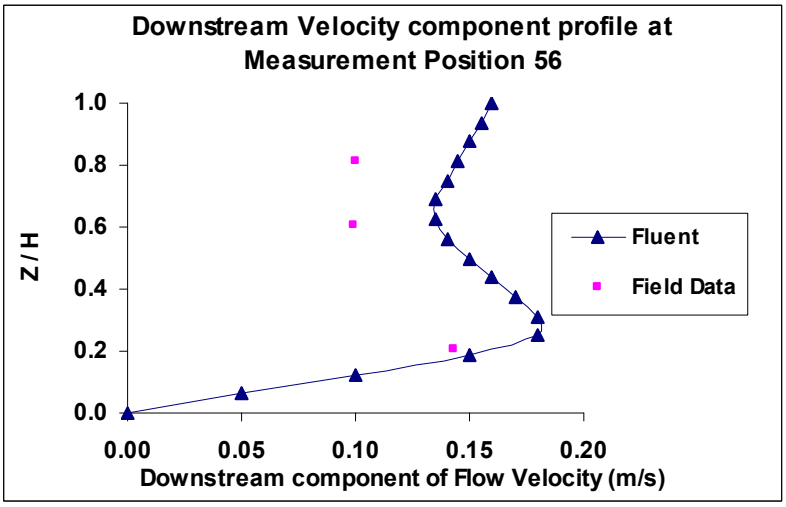

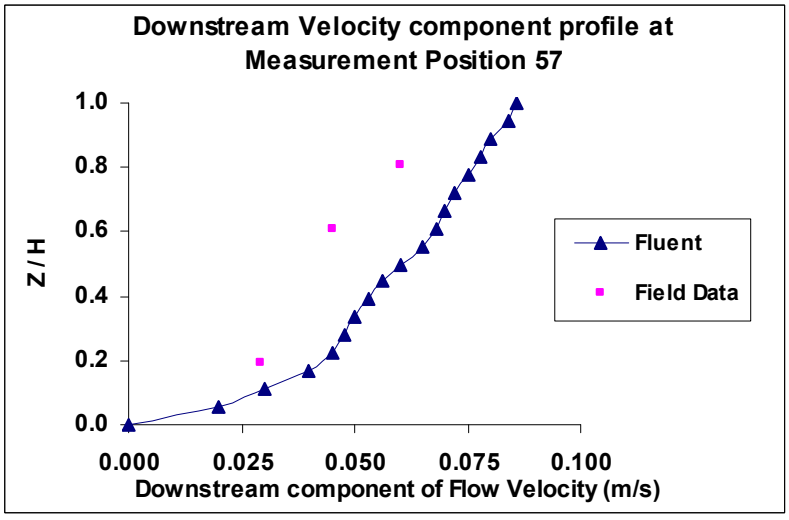

Predicted versus observed downstream flow velocity component at measurement positions 55, 56, and 57.

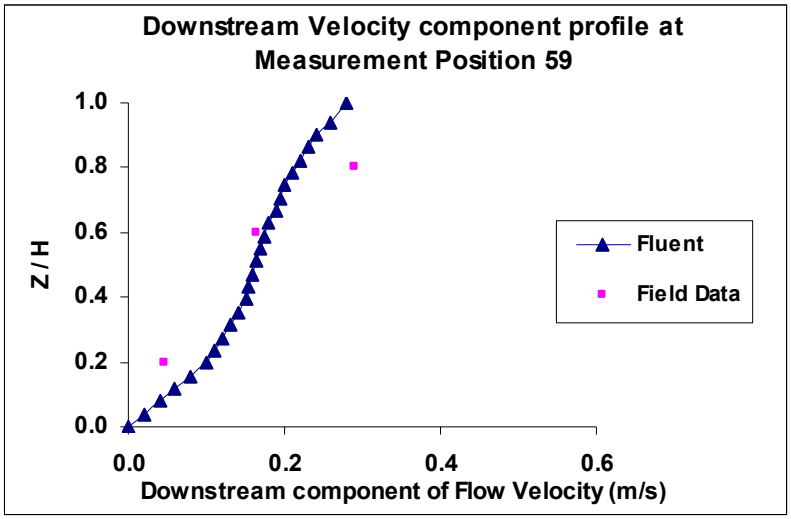

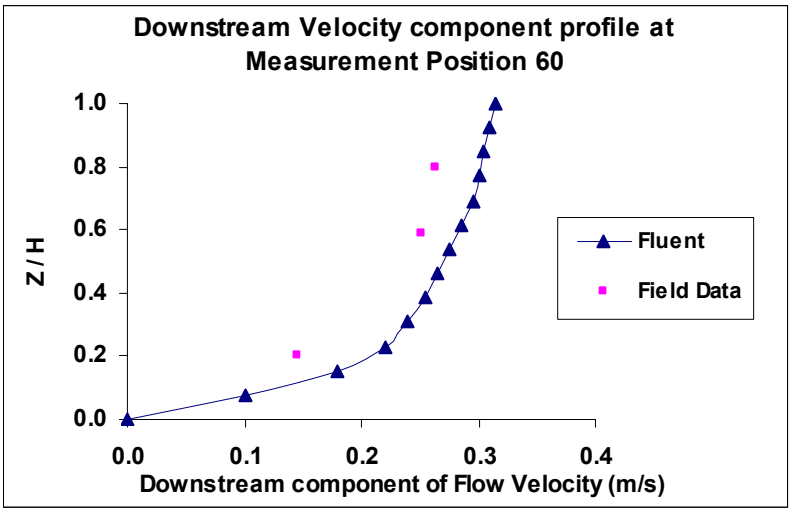

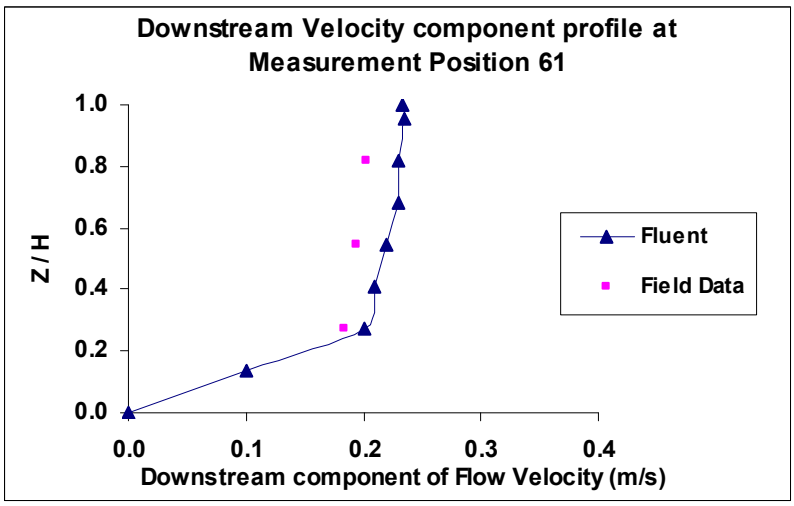

Predicted versus observed downstream flow velocity component at measurement positions 59, 60, and 61.

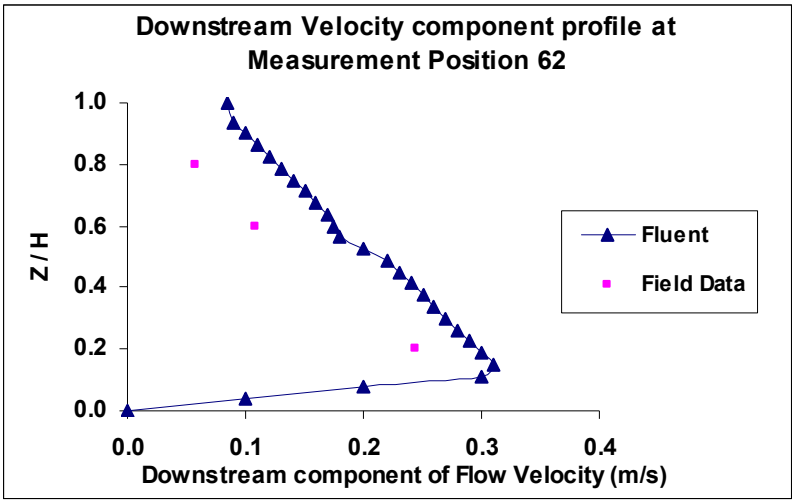

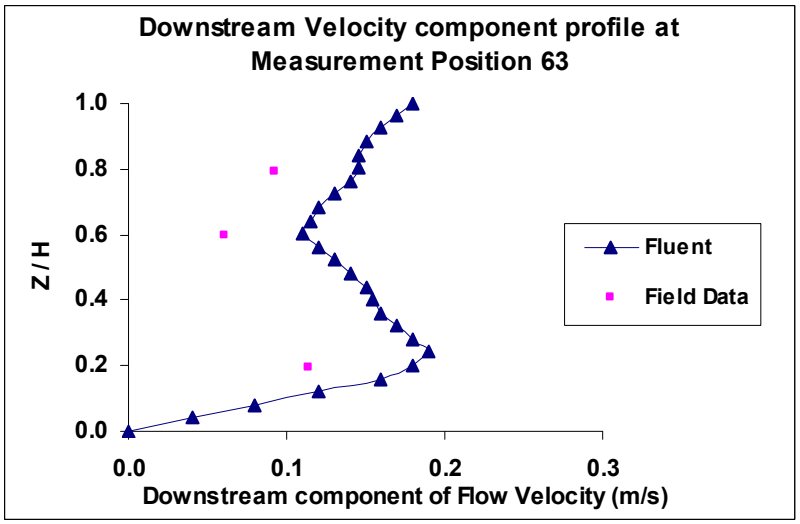

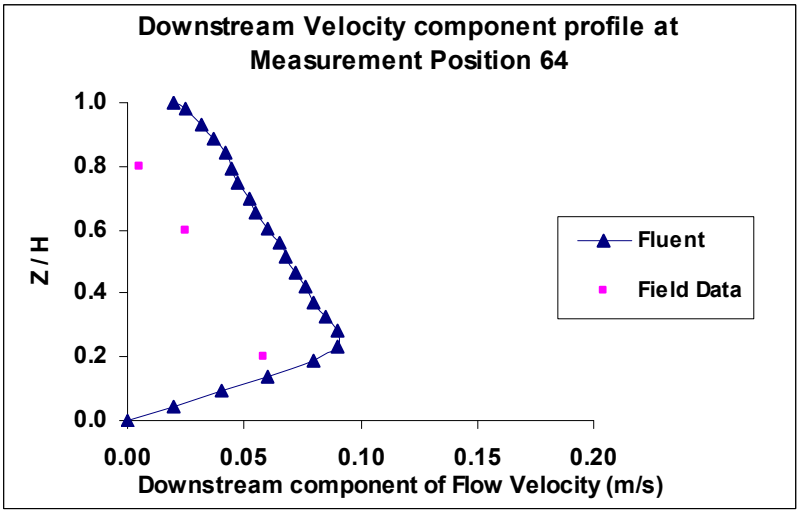

Predicted versus observed downstream flow velocity component at measurement positions 62, 63, and 64.

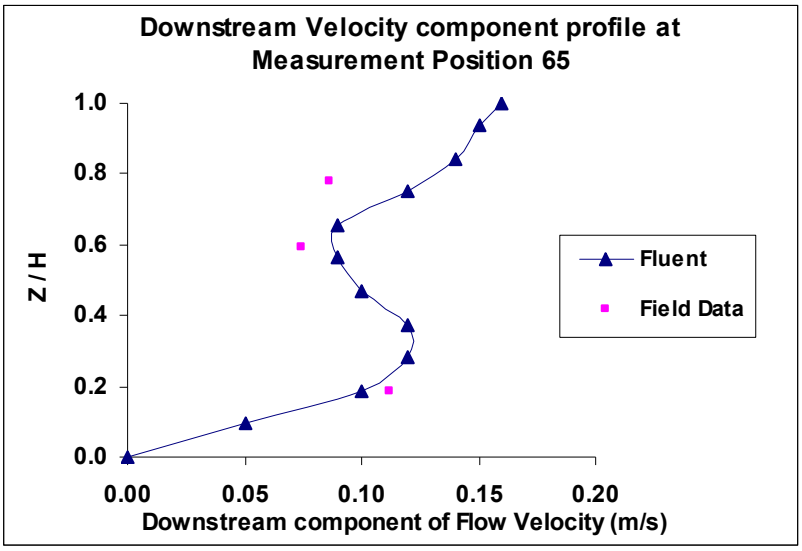

Predicted versus observed downstream flow velocity component at measurement position 65.

Predicted versus Observed Transverse Component of Flow Velocity at all Positions

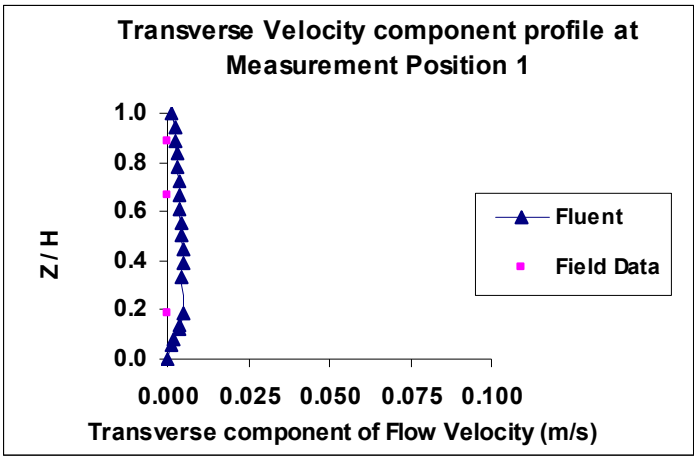

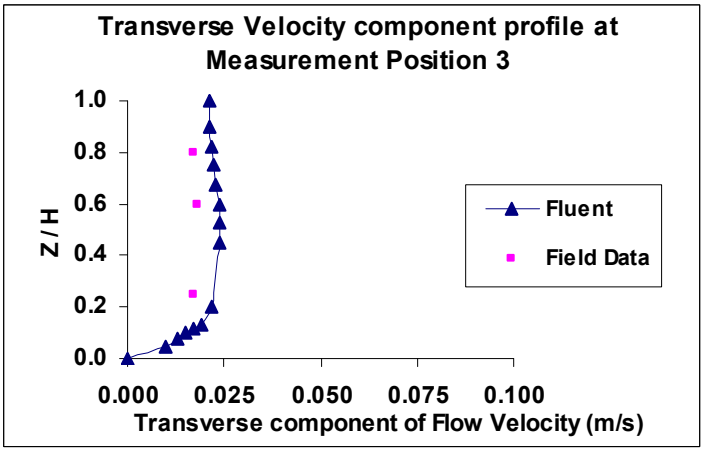

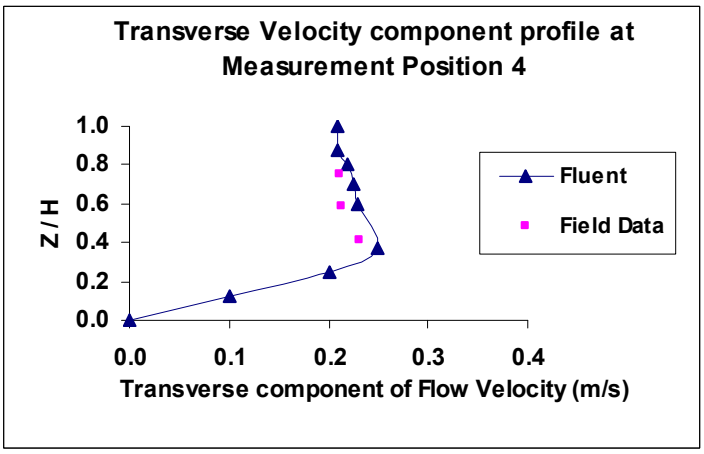

Predicted versus observed transverse flow velocity component at measurement positions 1, 3, and 4.

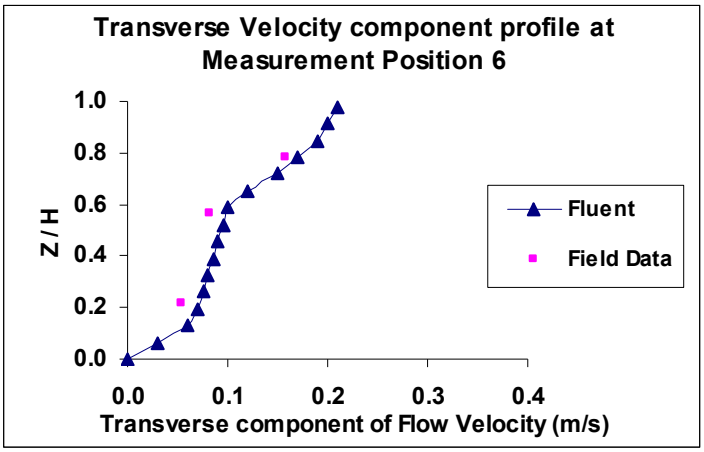

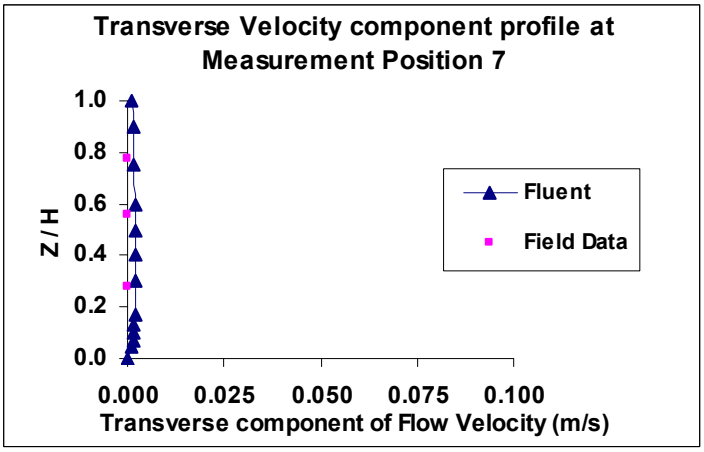

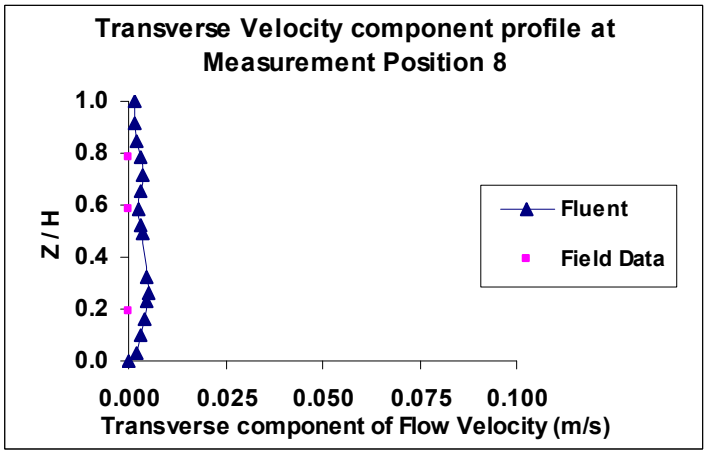

Predicted versus observed transverse flow velocity component at measurement positions 6, 7, and 8.

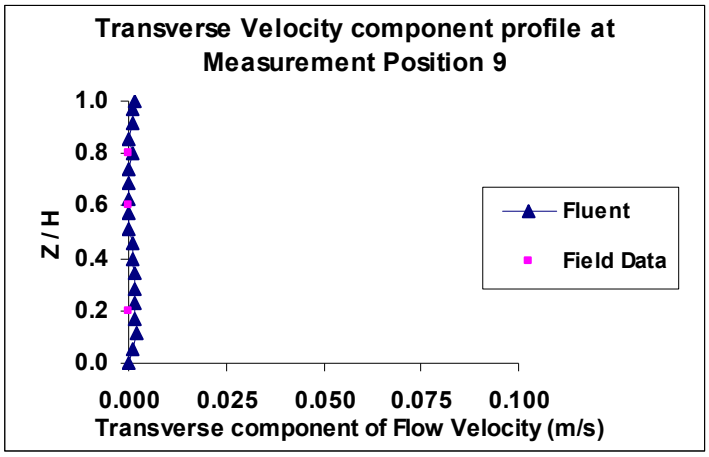

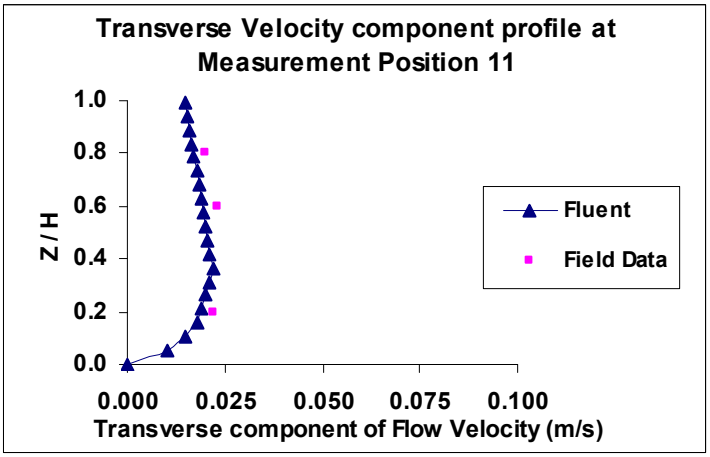

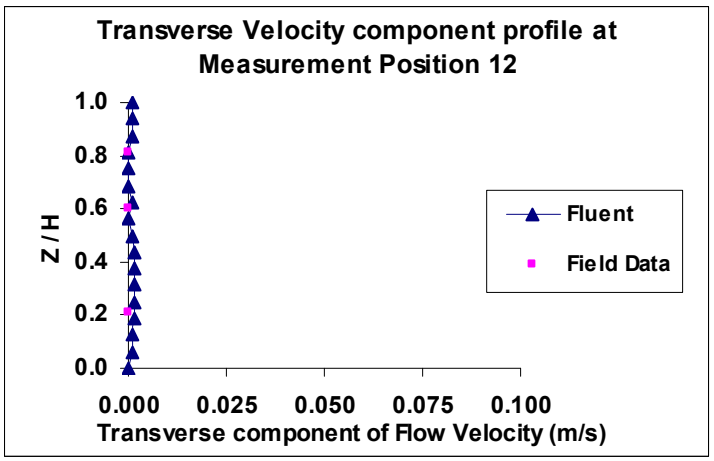

Predicted versus observed transverse flow velocity component at measurement positions 9, 11, and 12.

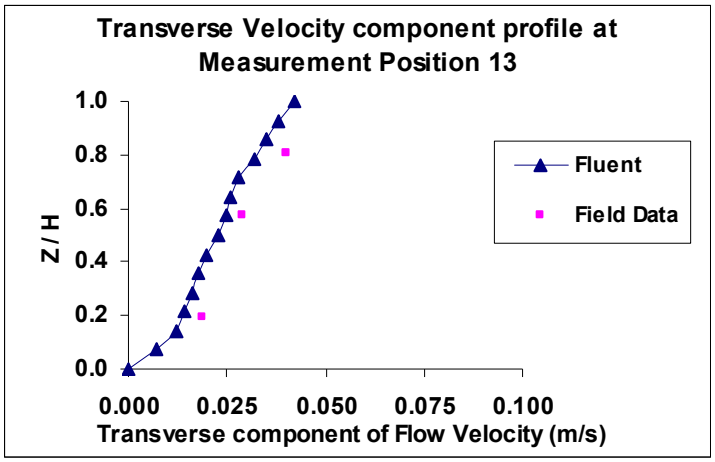

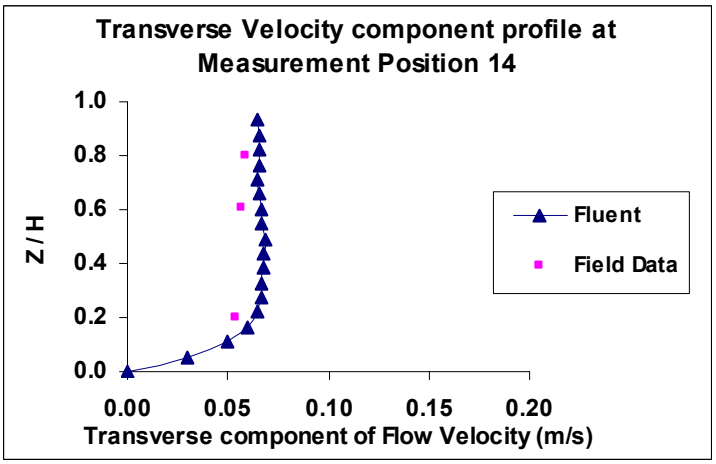

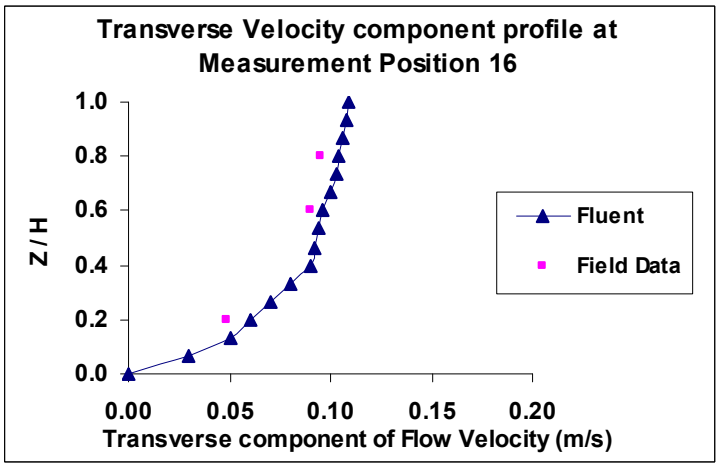

Predicted versus observed transverse flow velocity component at measurement positions 13, 14, and 16.

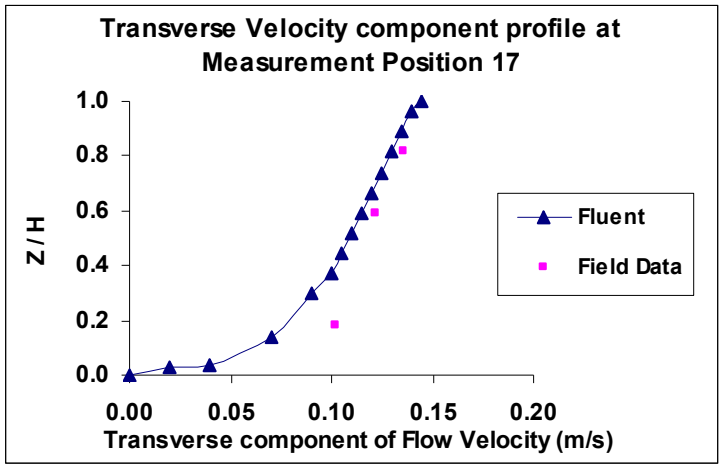

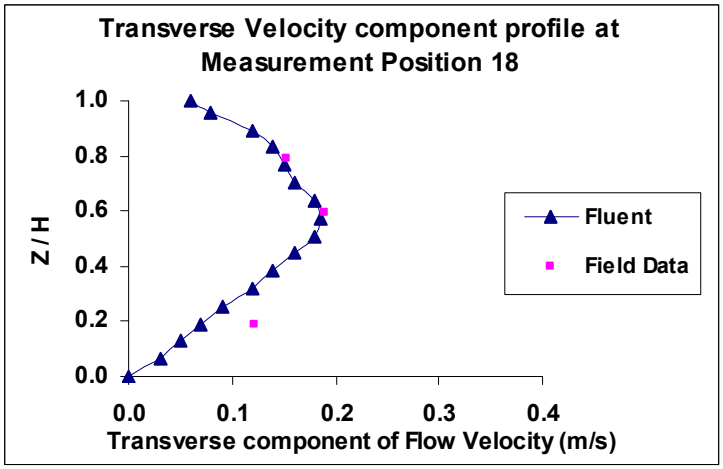

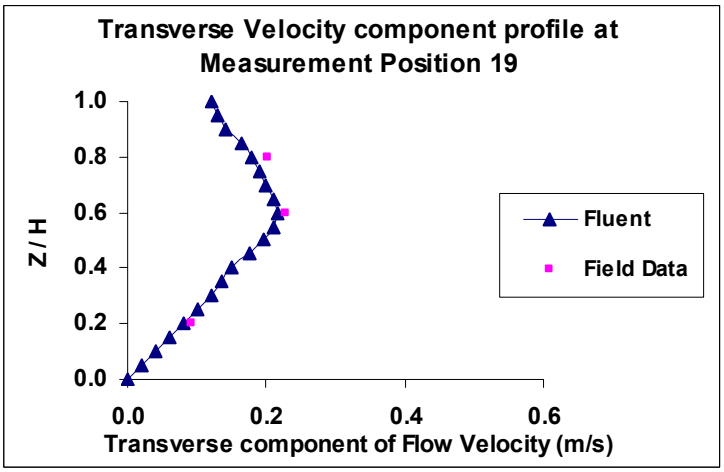

Predicted versus observed transverse flow velocity component at measurement positions 17, 18, and 19.

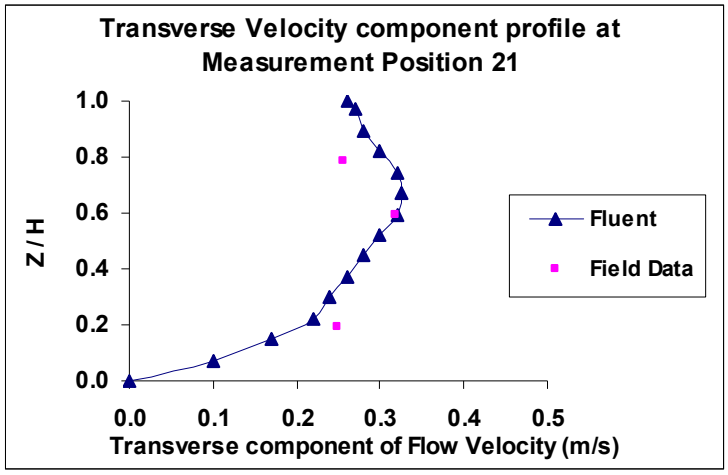

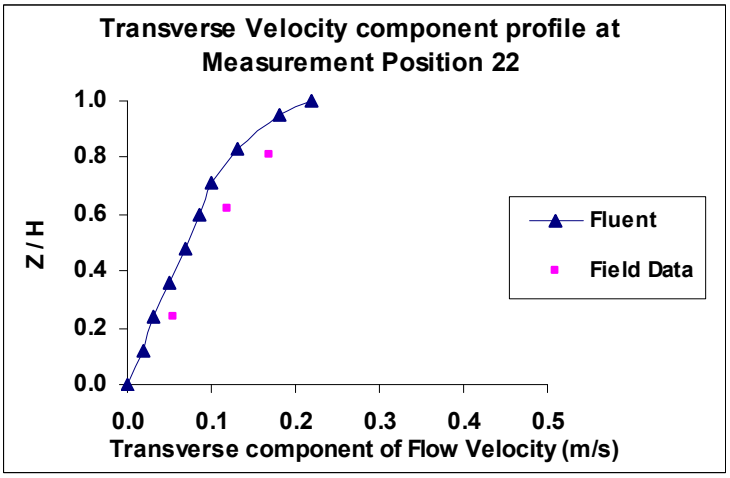

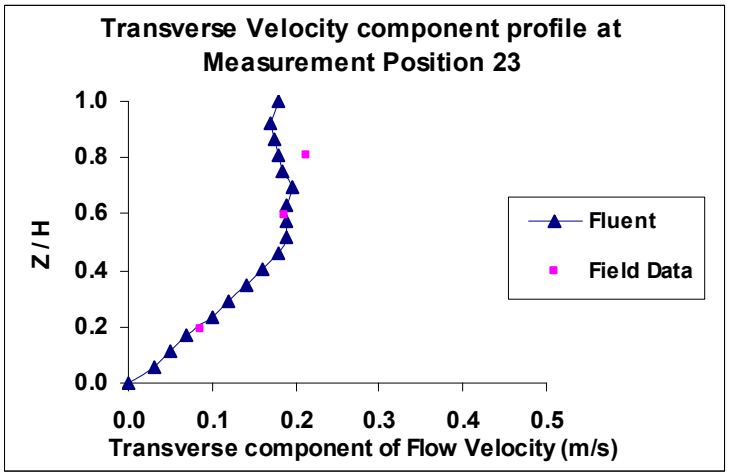

Predicted versus observed transverse flow velocity component at measurement positions 21, 22, and 23.

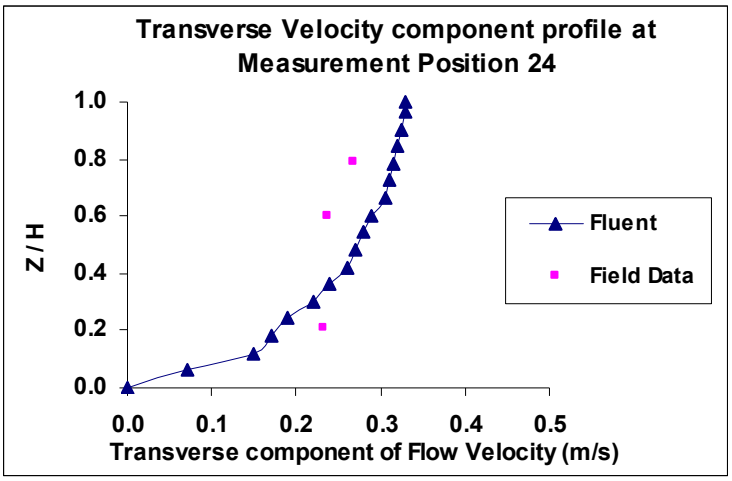

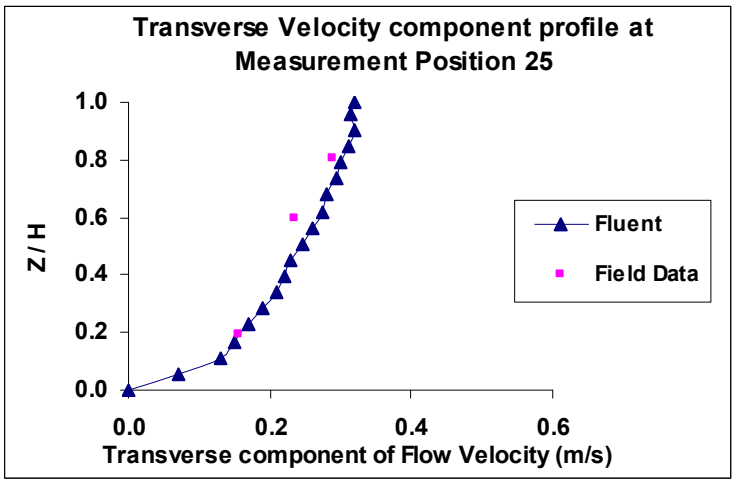

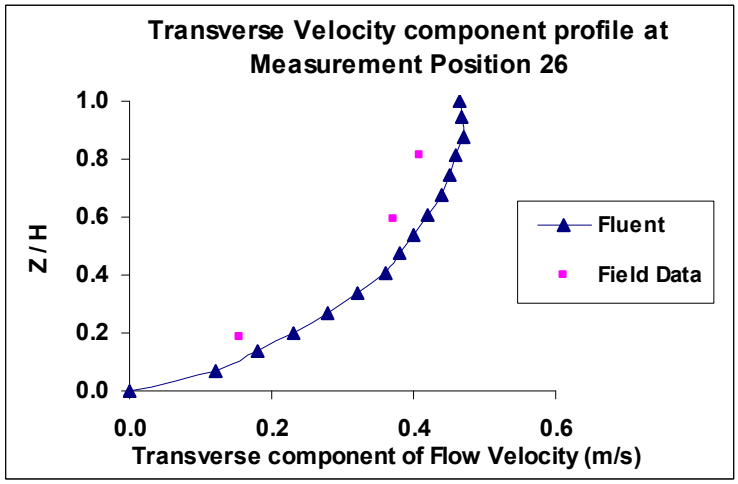

Predicted versus observed transverse flow velocity component at measurement positions 24, 25, and 26.

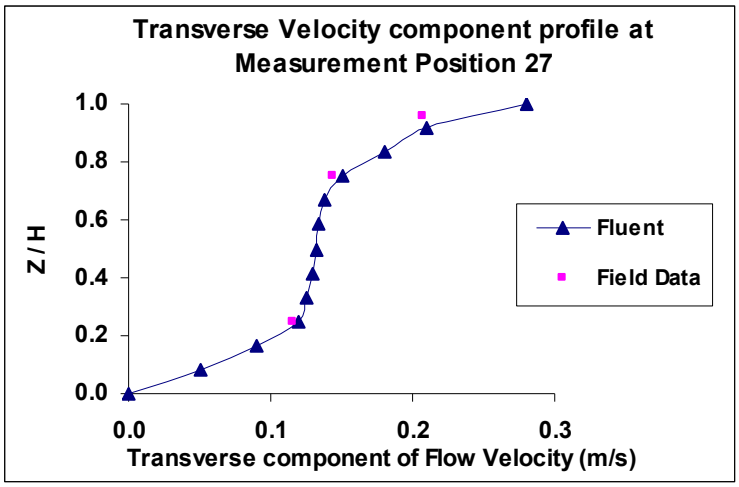

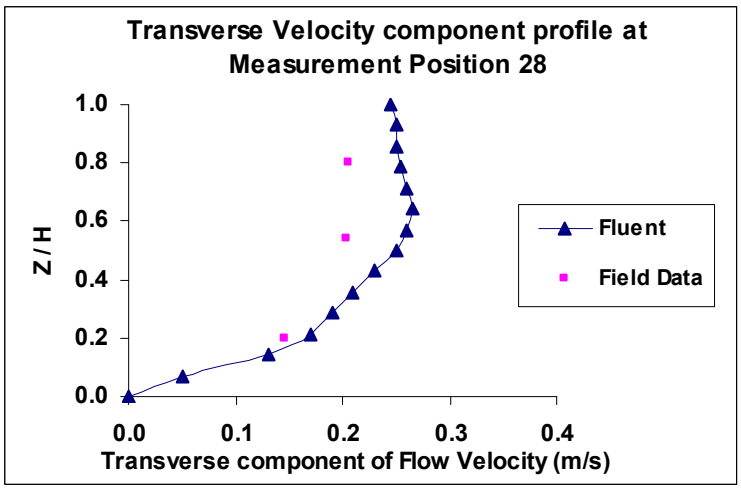

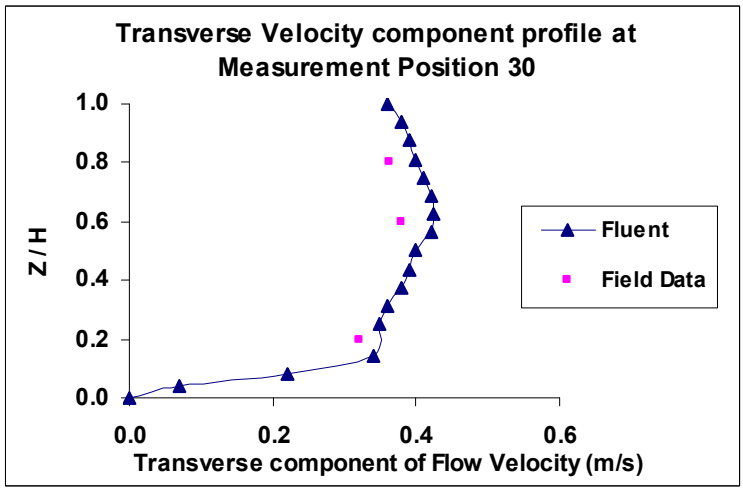

Predicted versus observed transverse flow velocity component at measurement positions 27, 28, and 30.

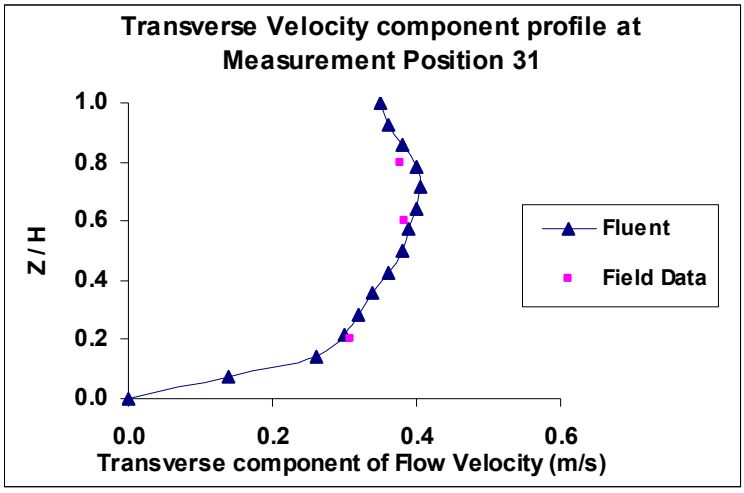

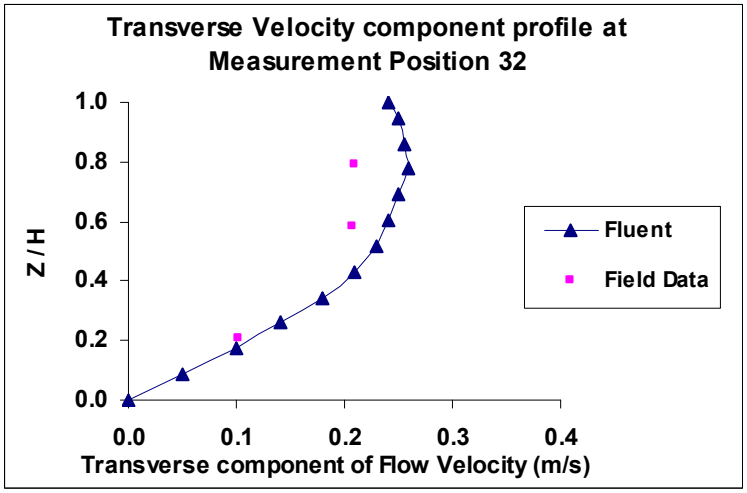

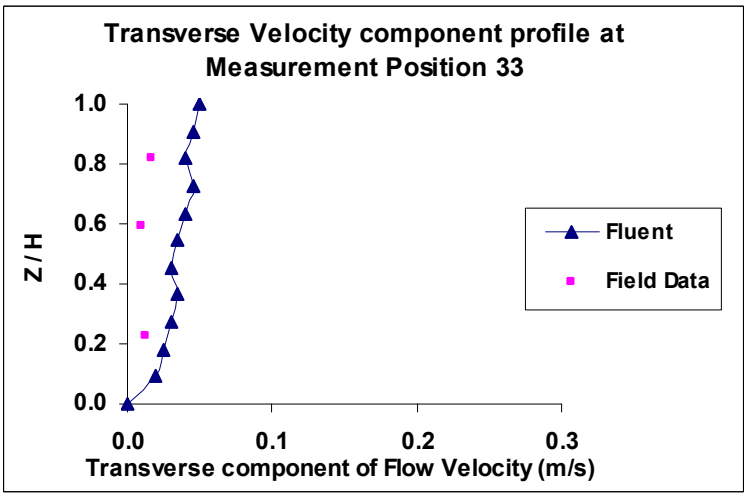

Predicted versus observed transverse flow velocity component at measurement positions 31, 32, and 33.

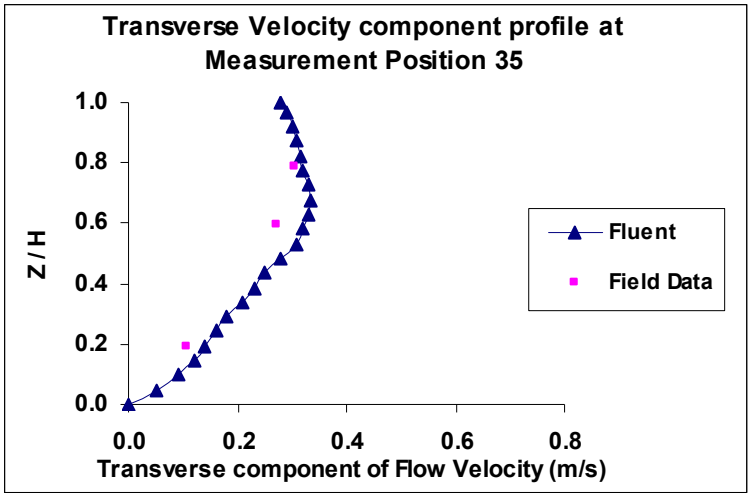

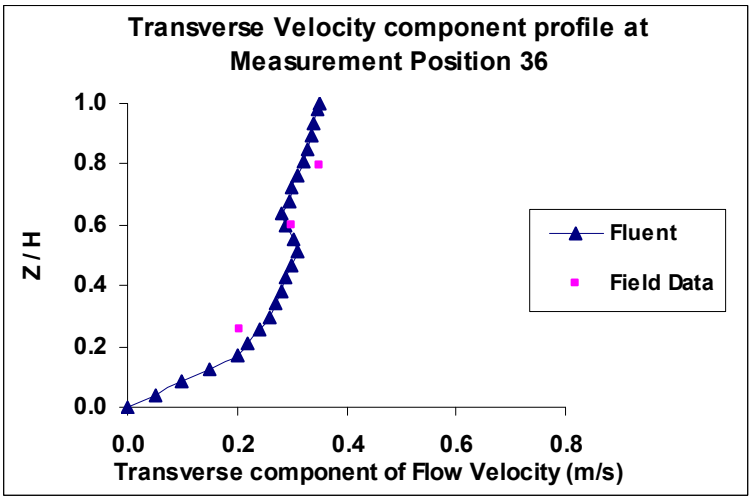

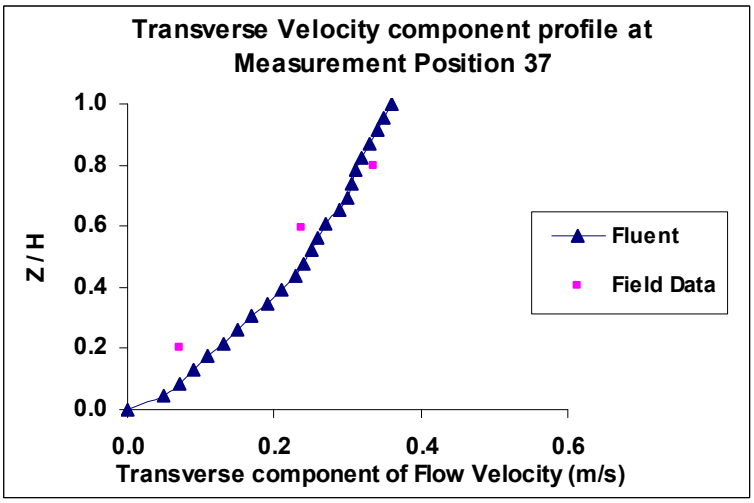

Predicted versus observed transverse flow velocity component at measurement positions 35, 36, and 37.

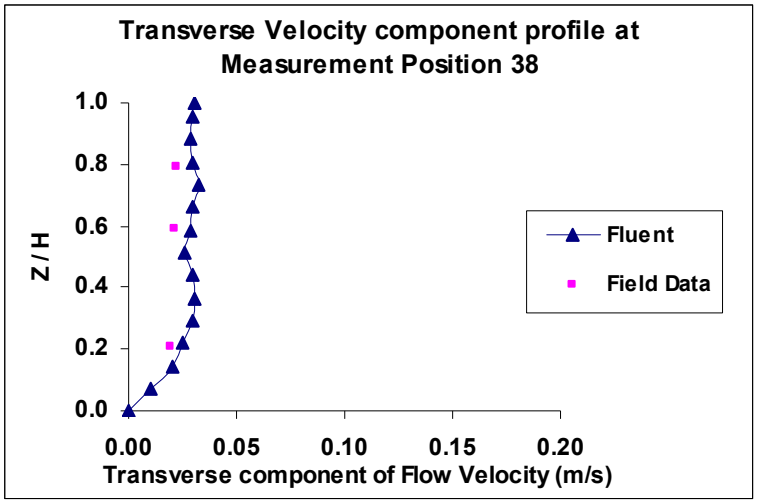

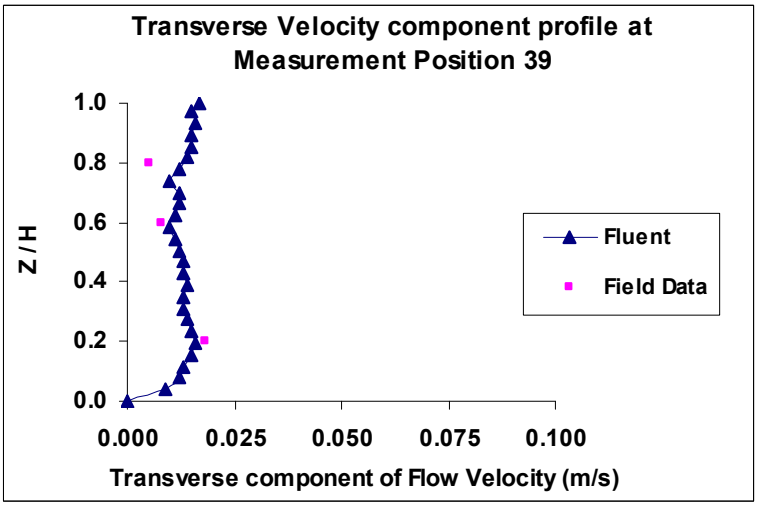

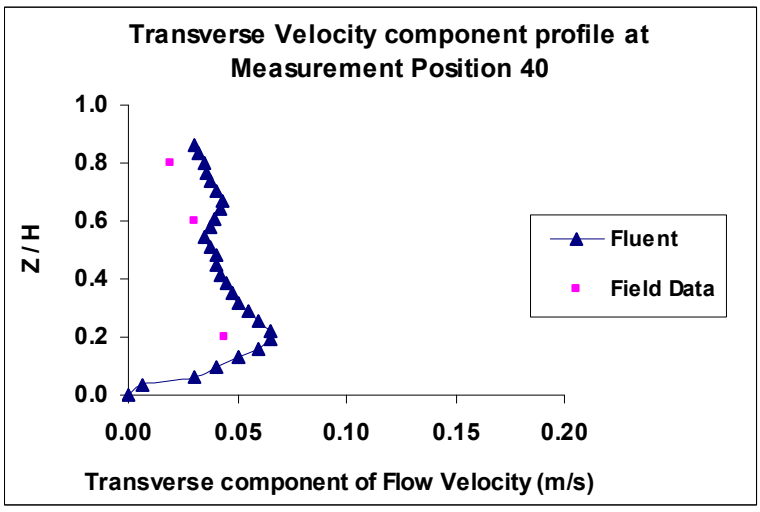

Predicted versus observed transverse flow velocity component at measurement positions 38, 39, and 40.

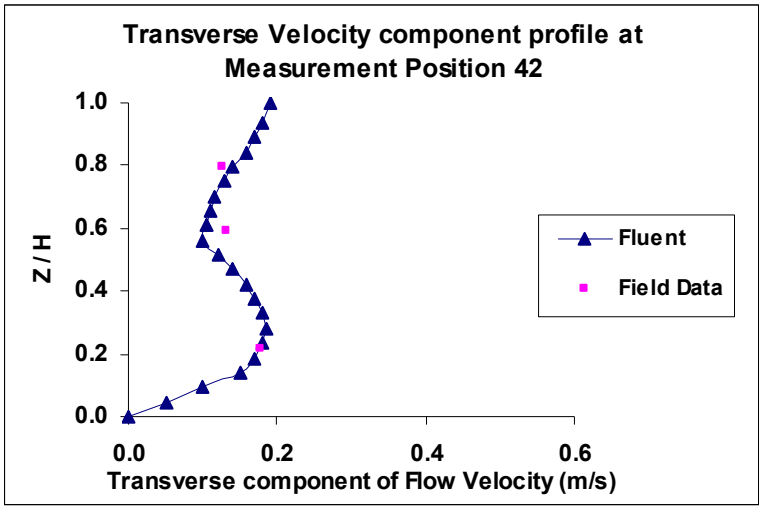

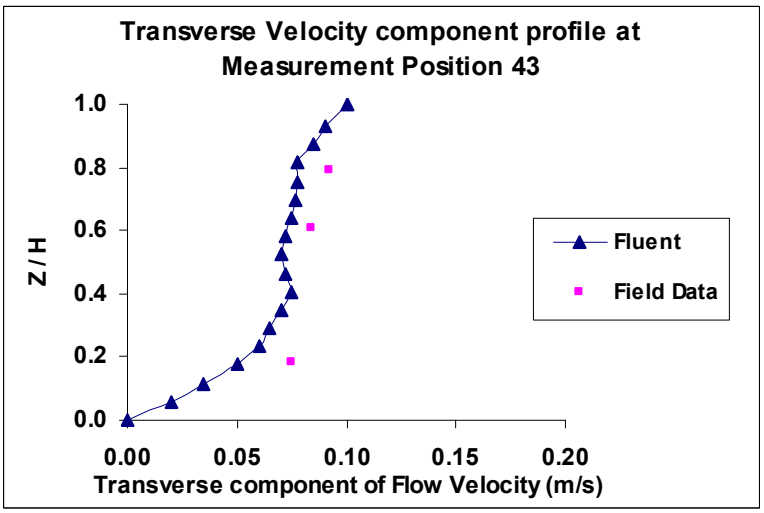

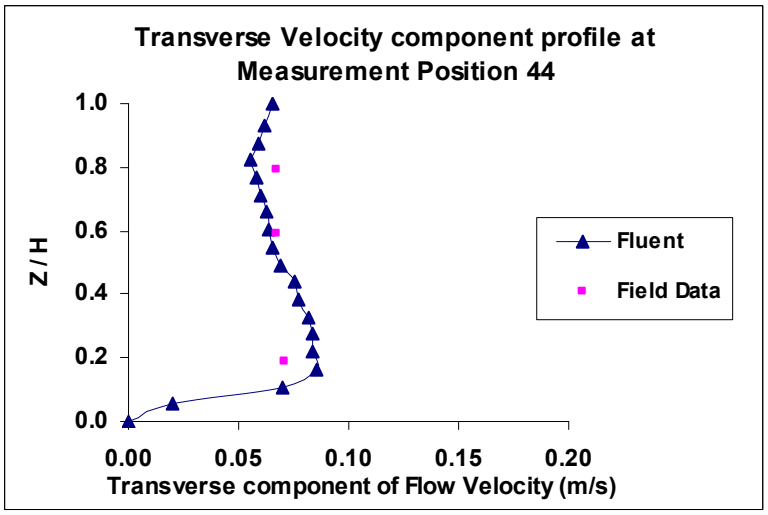

Predicted versus observed transverse flow velocity component at measurement positions 42, 43, and 44.

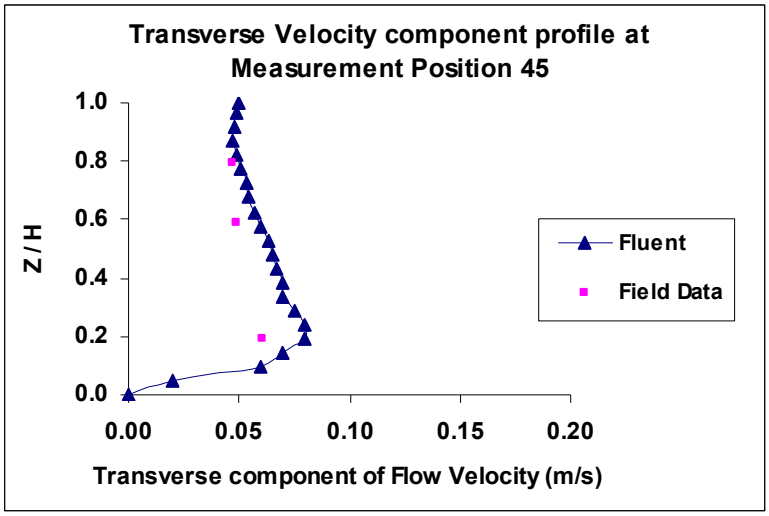

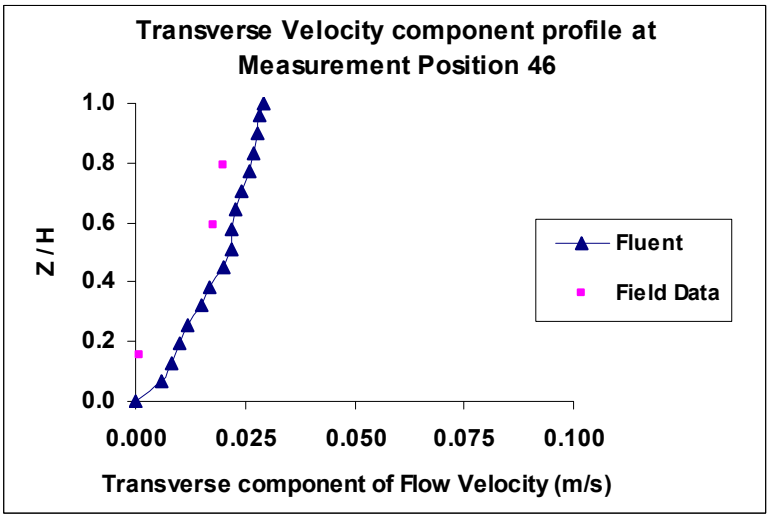

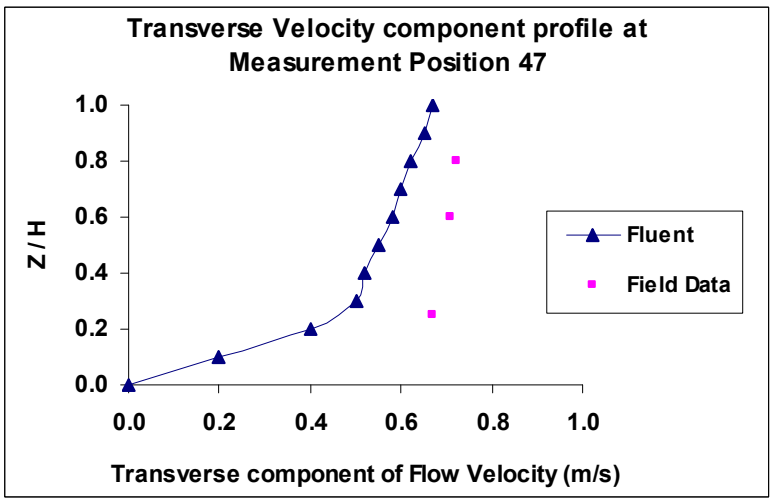

Predicted versus observed transverse flow velocity component at measurement positions 45, 46, and 47.

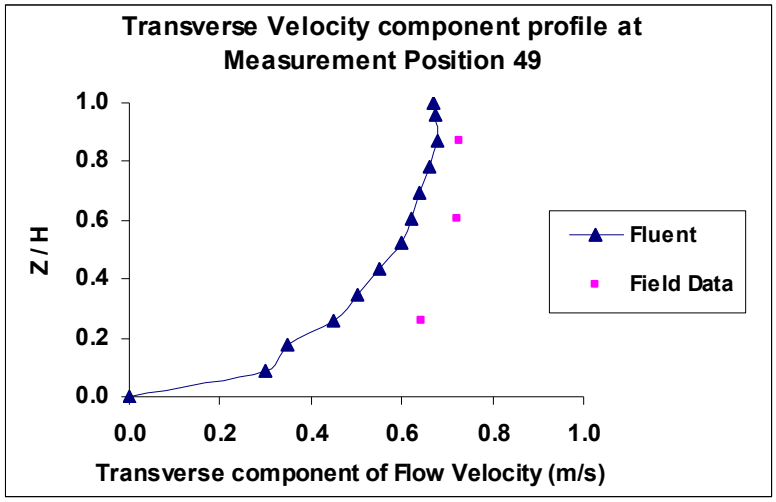

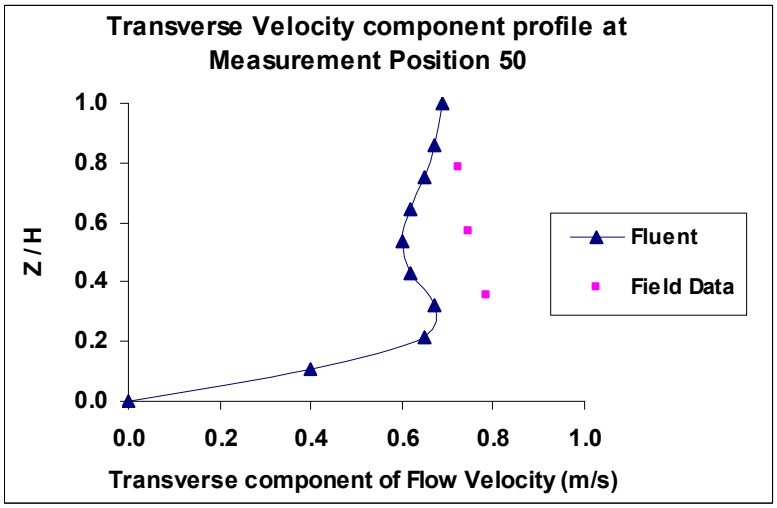

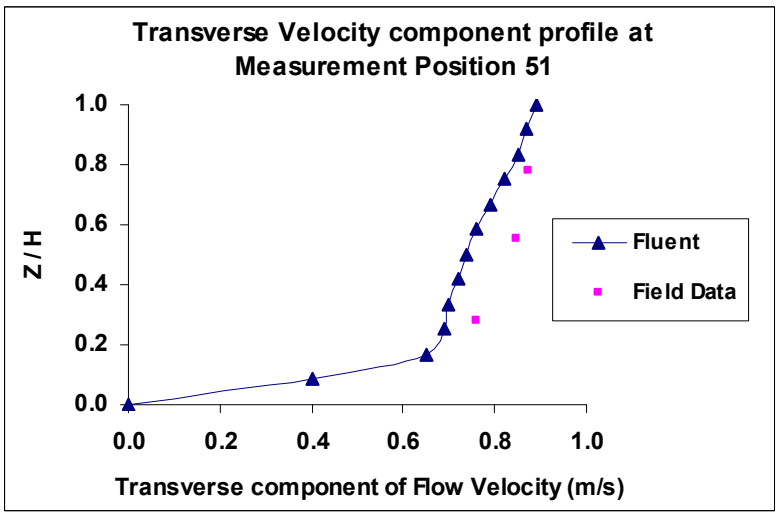

Predicted versus observed transverse flow velocity component at measurement positions 49, 50, and 51.

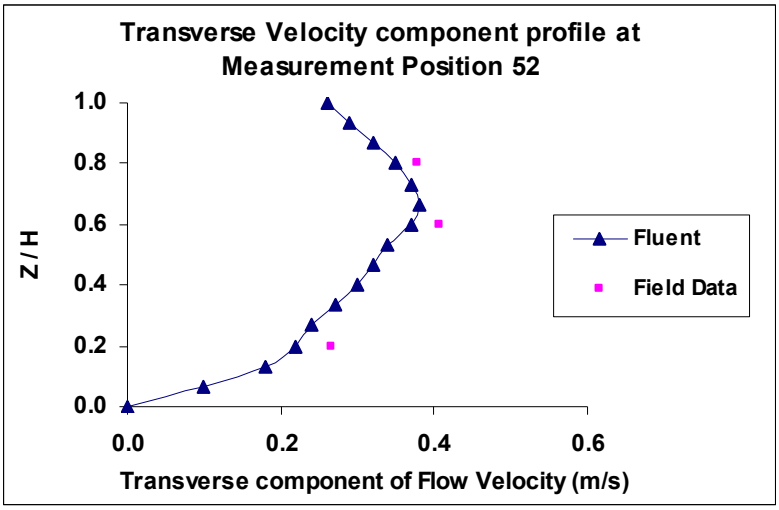

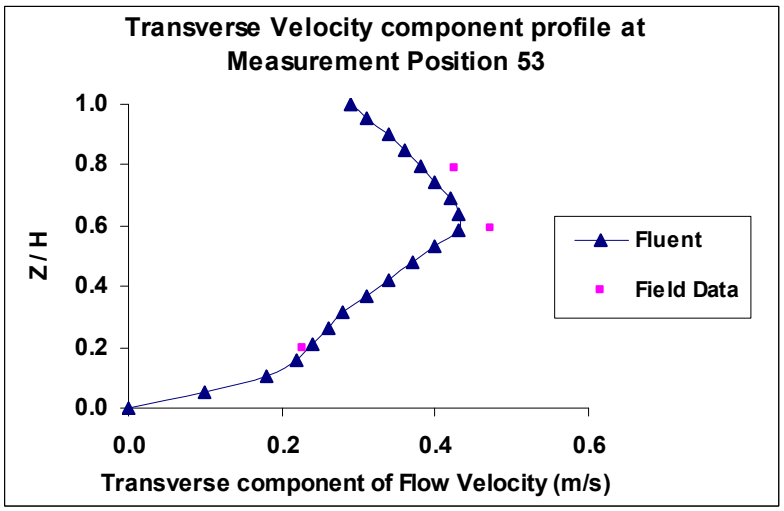

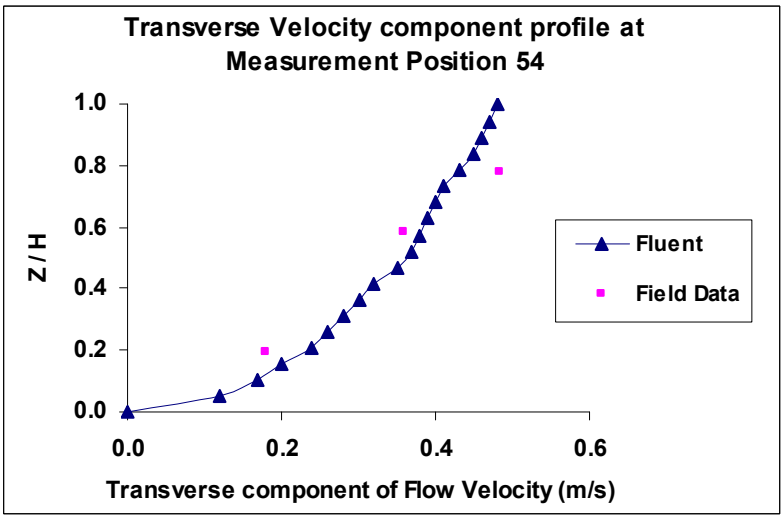

Predicted versus observed transverse flow velocity component at measurement positions 52, 53, and 54.

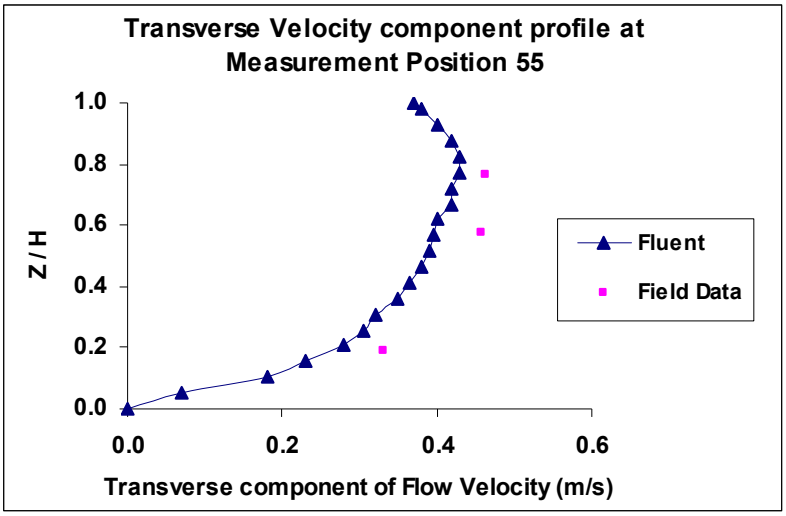

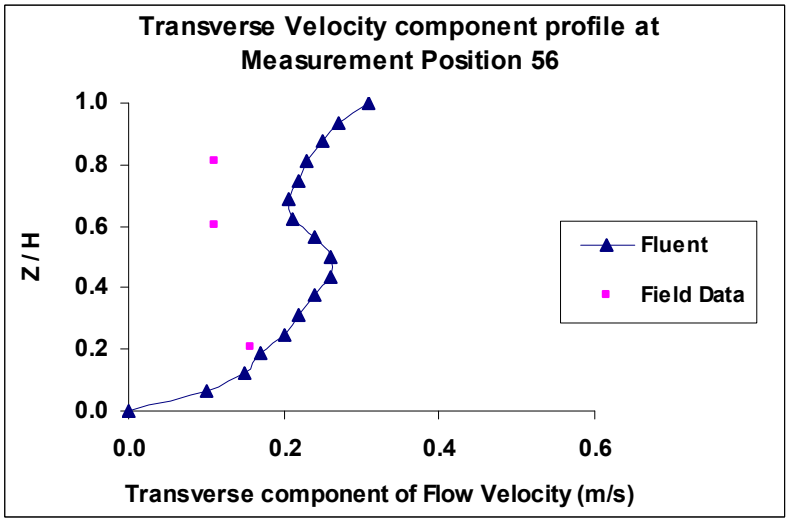

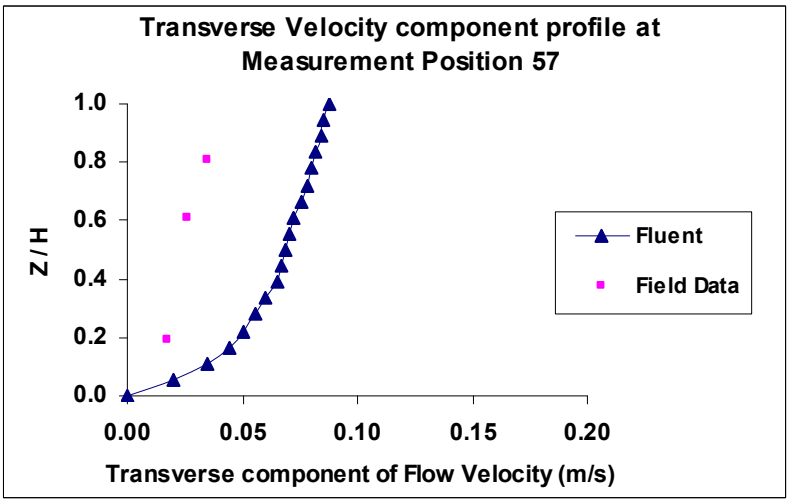

Predicted versus observed transverse flow velocity component at measurement positions 55, 56, and 57.

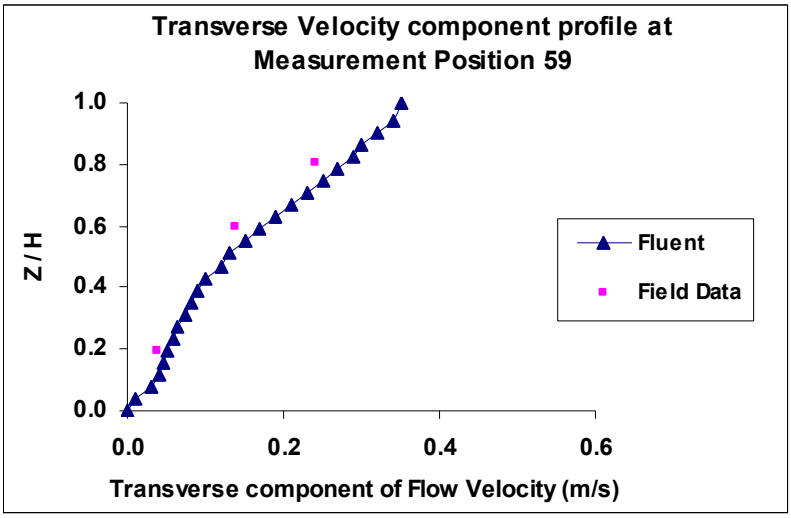

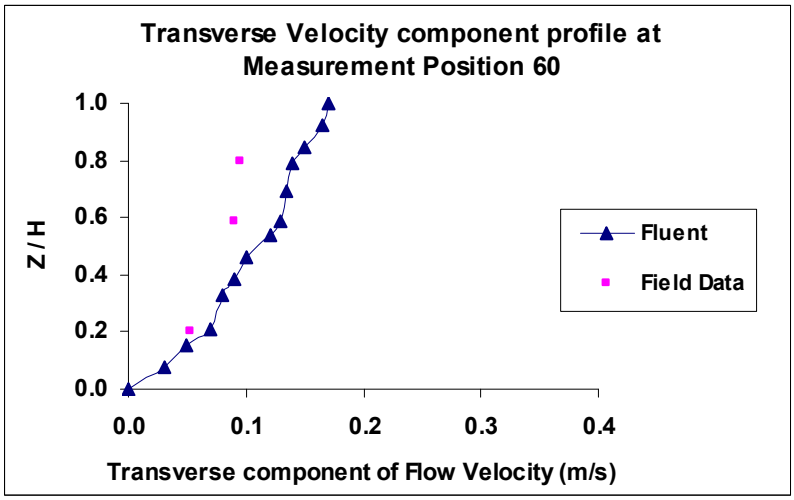

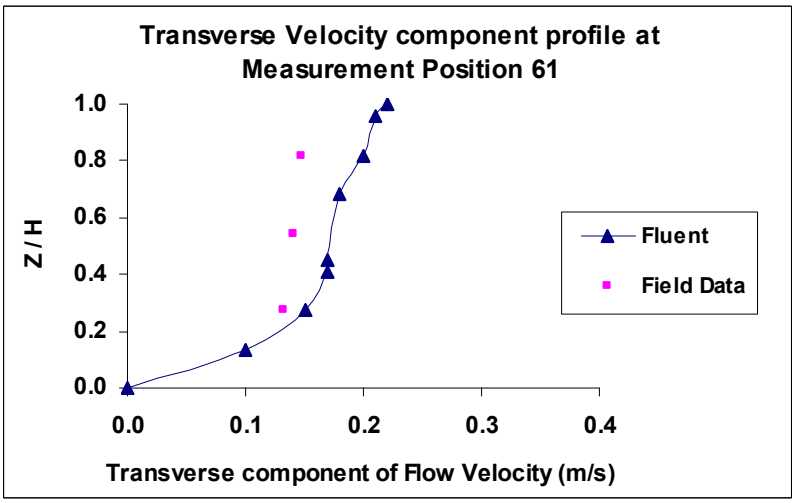

Predicted versus observed transverse flow velocity component at measurement positions 59, 60, and 61.

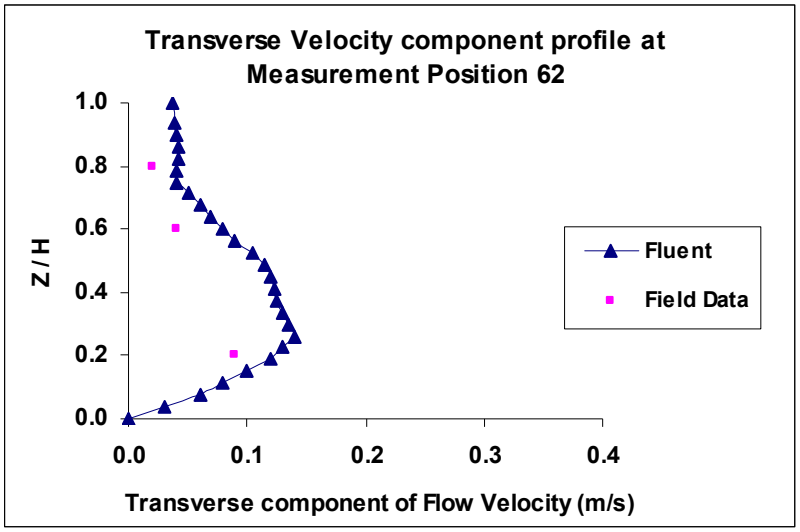

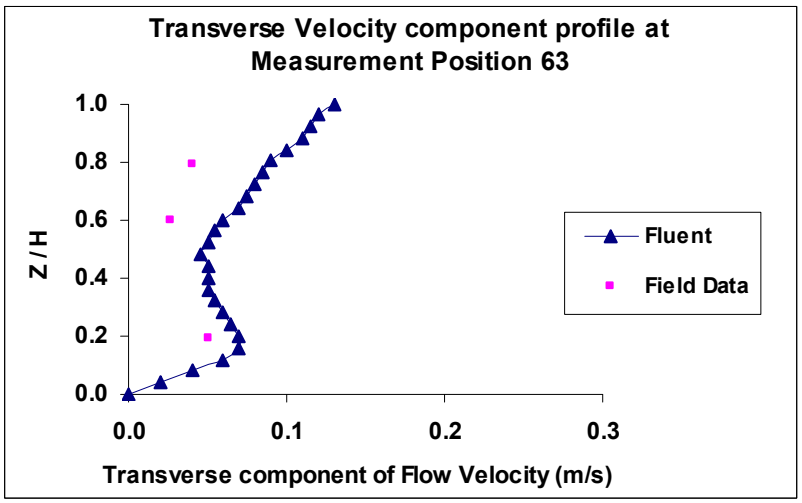

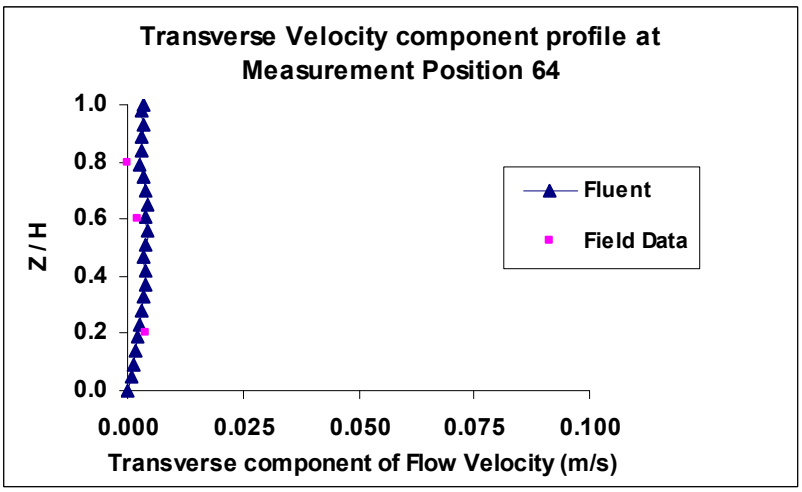

Predicted versus observed transverse flow velocity component at measurement positions 62, 63, and 64.

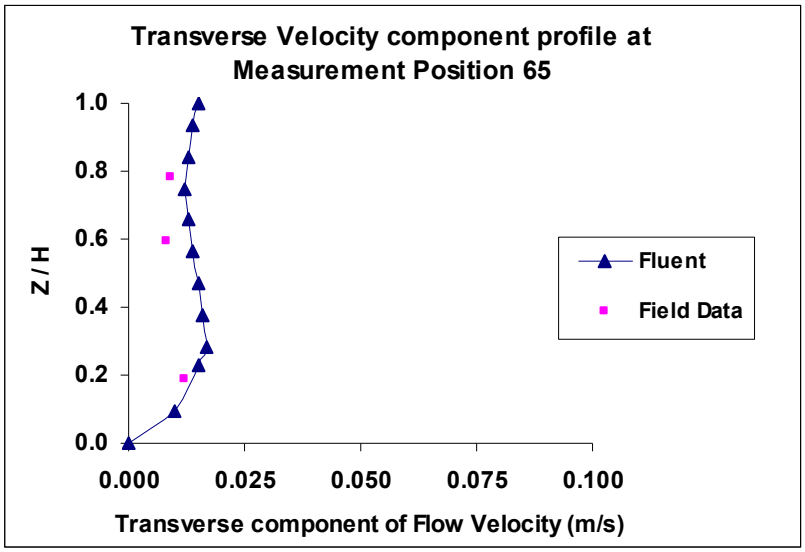

Predicted versus observed transverse flow velocity component at measurement position 65.

References

Abam, T. K. S., (1997). 'Genesis of channel bank overhangs in the Niger Delta and analysis of mechanisms of failure', *Geomorphology*, **18**, 151-164.

Alonso, C. V., and *Combs, S. T.*, (1990). 'Streambank erosion due to bed degradation – A model concept', *Transactions of ASAE*, **33**(4), 1239-1248.

Amoozegar, *A.*, (1989). 'A compact constant-head permeameter for measuring saturated hydraulic conductivity of the vadose zone', *Soil Science Society of American Journal*, **53**, 1356-1361.

Andrews, E. D., (1983). 'Entrainment of gravel from naturally sorted riverbed material', *Geological Society of America Bulletin*, **94**, 1225-1231.

Andrle, *R.*, (1994). 'Flow Structure and Development of Circular Meander Pools', *Geomorphology*, **9**, 261-270.

Apsley, *D.*, and *Hu*, *W.*, (2003). 'CFD simulation of two- and three-dimensional free-surface flow', *International Journal for Numerical Methods in Fluids*, **42**, 465-491.

ASCE Task Committee on Turbulence Models in Hydraulic Computation, (1988). 'Turbulence modelling of surface water flow and transport: Part II', *Journal of Hydraulic Engineering*, **114**(9), 992-1014.

ASCE Task Committee on Hydraulics, Bank Mechanics and Modeling of River Width Adjustment, (1998a). 'River Width Adjustment. I: Processes and mechanisms', *Journal of Hydraulic Engineering*, **124**(9), 881-902.

ASCE Task Committee on Hydraulics, Bank Mechanics and Modeling of River Width Adjustment, (1998b). 'River Width Adjustment. II: Modeling', *Journal of Hydraulic Engineering*, **124**(9), 903-917.

Ashmore, *P. E.*, *Ferguson*, *R. I.*, *Prestegaard*, *K. L.*, *Ashworth*, *P. J.*, and *Paola*, *C.*, (1992). 'Secondary Flow in Anabranch Confluences of a Braided, Gravel-Bed Stream', *Earth Surface Processes and Landforms*, **17**, 299-311.

Ashworth, P. J., and *Ferguson, R. I.*, (1989). 'Size-selective entrainment of bed load in gravel bed streams' *Water Resources Research*, **25**, 627-634.

Ashworth, *P. J.*, *Ferguson, R. I.*, *Ashmore, P. E.*, *Paola, C.*, *Powell, D. M.*, and *Prestegaard, K. L.*, (1992). 'Measurements in a braided river chute and lobe - 2. Sorting of bed load during entrainment, transport, and deposition', *Water Resources Research*, **28**, 1887-1896.

Bates, P., and *Lane, S. N.* (1998). 'Preface: High resolution flow modelling in hydrology and geomorphology', *Hydrological Processes*, **12**, 1129-1130.

Bates, P. D., *Horritt, M.*, and *Hervouet, J. M.*, (1998). 'Investigating two-dimensional, finite element predictions of floodplain inundation using fractal generated topography', *Hydrological Processes*, **12**, 1257-1277.

Bates, P. D., *Marks K. J.*, and *Horritt, M. S.*, (2003). 'Optimal use of high-resolution topographic data in flood inundation models', *Hydrological Processes*, **17**, 537-557.

Bates, P. D., *Lane, S. N.*, and *Ferguson, R. I.*, (2005). 'Computational Fluid Dynamics modeling for environmental flows', in P. D. Bates, S. N. Lane, and R. I. Ferguson (eds), *Computational Fluid Dynamics: Applications in Environmental Hydraulics*, John Wiley, Chichester, 1-16.

Bathurst, *J. C.*, *Thorne*, *C. R.*, and *Hey*, *R. D.*, (1979). 'Secondary flow and shear stress at river bends', *Journal of the Hydraulics Division*, ASCE, **105**, 1277-1295.

Bathurst, *J. C.*, *Thorne*, *C. R.*, and *Hey*, *R. D.*, (1977). 'Direct measurements of secondary currents in river bends', *Nature*, **269**, 504-506.

Berlamont, J., *Ockenden, M.*, *Toorman, E.*, and *Winterwerp, J.*, (1993). 'The characterization of cohesive sediment properties', *Coastal Engineering*, **21**, 105-128.

Beven, K. J., and *Binley, A.*, (1992). 'The future of distributed models: model calibration and uncertainty predictions', *Hydrological Processes*, **6**, 279-298.

Bishop, A. W., (1955). 'The use of the slip circle in the stability analysis of slopes', *Geotechnique*, **5**, 7-17.

Booker, D. J., (2000). 'Monitoring and modelling sediment transport processes in pool-riffle sequences', *PhD Thesis*, Department of Geography, University of Southampton, Southampton, UK.

Booker, D. J., (2003). 'Hydraulic modelling of fish habitat in urban rivers during high flows', *Hydrological Processes*, **17**, 577-599.

Booker, D. J., *Sear, D. A.*, and *Payne, A. J.*, (2001). 'Modelling three-dimensional flow structures and patterns of boundary shear stress in a natural pool-riffle sequence', *Earth Surface Processes and Landforms*, **26**, 553-576.

Boussinesq, J., (1877). 'Essai sur la theorie des eaux courantes', *Mem. Presentes Academie des Sciences*, 23-46.

Bradbrook, K. F., (1999). 'Numerical. Field and Laboratory Studies of Three-Dimensional Flow Structures at River Channel Confluences', *PhD Thesis*, University of Cambridge, UK.

Bradbrook, K. F., *Biron, P. M.*, *Lane, S. N.*, *Richards, K. S.*, and *Roy, A. G.* (1998). 'Investigation of controls on secondary circulation in a simple confluence geometry using a three-dimensional numerical model', *Hydrological Processes*, **12**, 1371-1396.

Bradbrook, K. F., *Lane, S. N.*, *Richards, K. S.*, (2000a). 'Numerical simulation of time-averaged flow structure at river channel confluences', *Water Resources Research*, **36**, 2731-2746.

Bradbrook, K. F., *Lane, S. N.*, *Richards, K. S.*, *Biron, P. M.*, and *Roy, A. G.*, (2000b). 'Large eddy simulation of periodic flow characteristics at river channel confluences', *Journal of Hydraulic Research*, **38**, 207-216.

Bradbrook, K. F., *Lane, S. N.*, *Richards, K. S.*, *Biron, P. M.*, and *Roy, A. G.*, (2001). 'Flow structures and mixing at an asymmetrical open-channel confluence: A numerical study', *Journal of Hydraulic Engineering*, ASCE, **127**, 351-368.

Bray, D. I., (1980); 'Evaluation of effective boundary roughness for gravel-bed rivers', *Canadian Journal of Civil Engineering*, **7**, 392-397.

Bridge, *J. S.*, and *Gabel*, *S. L.*, (1992). 'Flow and sediment dynamics in a low sinuosity braided river – Calamus River, Nebraska Sandhills', *Sedimentology*, **39**, 125-142.

Bridge, *J. S.*, and *Jarvis*, *J.*, (1982). 'The dynamics of a river bend: a study in flow and sedimentary processes', *Sedimentology*, **29**, 499-541.

Bull, L. J., (1997). 'Magnitude and variation in the contribution of bank erosion to the suspended load of the river Severn, UK', *Earth Surface Processes and Landforms*, **22**, 1109-1123.

Caleffi, *V.*, *Valiani*, *A.*, and *Zanni*, *A.*, (2003). 'Finite volume method for simulating extreme flood events in natural channels', *Journal of Hydraulic Research*, **41**, 167-177.

Cao, Z., *Carling, P.*, and *Oakey, R.* (2003). 'Flow reversal over a natural pool-riffle sequence: A computational study', *Earth Surface Processes and Landforms*, **28**, 689-705.

Cao, *Z.*, *Day*, *R.*, and *Liriano*, *S.*, (2003). "Discussion on 'Three-dimensional numerical model for open channels with free-surface variations' (Meselhe, E. A., and Sotiropoulos, F., 2000)", *Journal of Hydraulic Research*, **41**, 110-112.

Carling, P. A., (1987). "Discussion on 'Pivoting analyses of the selective entrainment of sediments by shape and size with application to gravel threshold' (Komar, P. D., and Li, Z., 1986)", *Sedimentology*, **34**, 957-959

Carling, P. A., (1992). "The nature of the fluid boundary-layer and the selection of parameters for benthic ecology', *Freshwater biology*, 28, 0-0.

Carroll, R. W. H., *Warwick, J. J.*, *James, A. I.*, and *Miller, J. R.*, (2004) 'Modelling erosion and overbank deposition during extreme flood conditions on the Carson River, Nevada', *Journal of Hydrology*, **297**, 1-21.

Carson, *M. A.*, and *Lapointe*, *M. F.*, (1983). 'The inherent asymmetry of river meander planform', *Journal of Geology*, **91**, 41-55.

Casagli, N., *Rinaldi, M.*, *Gargini, A.*, and *Curini, A.*, (1999). 'Pore water pressure and streambank stability: Results from a monitoring site on the Sieve River, Italy', *Earth Surface Processes and Landforms*, **24**, 1095-1114.

Chen, Z. Y., and *Morgenstern, N. R.*, (1983). 'Extensions to the generalized method of slices for stability analysis', *Canadian Geotechnical Journal*, **20**, 104-119.

Chen, H. C., and *Patel, V. C.*, (1988). 'Near-Wall Turbulence Models for Complex Flows Including Separation', *AIAA J.*, 26, 641-648.

Choudhury, *D.*, (1993). 'Introduction to the Renormalization Group Method and Turbulence Modelling', *Fluent Inc. Technical Memorandum*, TM-107.

Clifford, N. J., *Robert, A.*, and *Richards, K. S.*, (1992). 'Estimation of flow resistance in gravel-bedded rivers: A physical explanation of the multiplier of roughness length', *Earth Surface Processes and Landforms*, **17**, 111-126.

Cornelius, *C.*, *Volgmann*, *W.*, and *Stoff*, *H.*, (1999). 'Calculation of three-dimensional turbulent flow with a finite volume multigrid method', *International Journal of Numerical Methods in Fluids*, **31**, 703-720.

Couper, P., and *Maddock, I. P.*, (2001). 'Subaerial river bank erosion processes and their interaction with other bank erosion mechanisms on the River Arrow, Warwickshire, UK', *Earth Surface Processes and Landforms*, **26**, 631-646.

Couper, P., (2003). 'Effects of silt-clay content on the susceptibility of river banks to subaerial erosion', *Geomorphology*, **56**, 95-108.

Crosato, A., (1990). 'Simulation of meandering river processes, Communications on Hydraulic and Geotechnical Engineering', *Technical Rep.*, Civil Engineering Dept., Delft University of Technology, Delft, The Netherlands.

Dapporto, S., (2001). 'Non-vertical jet testing of cohesive streambank toe material', School of Geography, University of Nottingham, *in collaboration with* USDA-ARS National Sedimentation Laboratory, Oxford, Mississippi.

Dapporto, S., *Rinaldi, M.*, *Casagli, N.*, and *Vannocci, P*, (2003). 'Mechanisms of riverbank failure along the Arno River, Central Italy', *Earth Surface Processes and Landforms*, **28**, 1303-1323.

Darby, S. E., (1998). 'Modelling width adjustment in straight alluvial channels', *Hydrological Processes*, **12**, 1299-1321.

Darby, S. E., *Alabyan, A. M.*, and *de Wiel, M. J. V.*, (2002). 'Numerical simulation of bank erosion and channel migration in meandering rivers', *Ware Resources Research*, **38**(9), 2.1-2.12.

Darby, S. E., *Gessler, D.*, and *Thorne, C. R.*, (2000). 'Technical communication – Computer program for stability analysis of steep, cohesive riverbanks', *Earth Surface Processes and Landforms*, **25**, 175-190.

Darby, S. E., and *Thorne, C. R.*, (1996a). 'Numerical simulation of widening and bed deformation of straight sand-bed rivers. I: Model development', *Journal of Hydraulic Engineering*, **122**, 184-193.

Darby, S. E., and *Thorne, C. R.*, (1996b). 'Development and testing of riverbank stability analysis', *Journal of Hydraulic Engineering*, **122**(8), 443-454.

Demuren, A. O., (1993). 'A numerical model for flow in meandering channels with a natural bed topography', *Water Resources Research*, **29**, 1269-1277.

Demuren, A. O., and *Rodi, W.*, (1986). 'Calculation of flow and pollutant dispersion in meandering channels', *Journal of Fluid Mechanics*, **172**, 63-92.

De Serres, B., *Roy, A. G.*, *Biron, P. M.*, and *Best, J. L.*, (1999). 'Three-dimensional structure of flow at a confluence of river channels with discordant beds', *Geomorphology*, **26**, 313-335.

Dietrich, *W. E.*, and *Whiting*, *P.*, (1989). 'Boundary shear stress and sediment transport in river meanders of sand and gravel', *River Meandering*, *S. Ikeda* and *G. Parker*, eds Water Resources Monograph No 12, AGU, Washington, D.C., 1-50.

Dietrich, *W. E.*, (1987). 'Mechanics of flow and sediment transport in river bends', In *River channels: environment and process*, ed. *Richards*, *K. S.*, 179-227, Oxford: Blackwell.

Dietrich, *W. E.*, and *Smith*, *J. D.*, (1984). 'Bed-Load Transport in a River Meander', *Water Recourses Research*, **20**, 1355-1380.

Dietrich, *W. E.*, and *Smith*, *J. D.*, (1983). 'Influence of the point bar on flow through curved channels', *Water Recourses Research*, **19**, 1173-1192.

Duan, J. G., (2005). 'Analytical approach to calculate rate of bank erosion', *Journal of Hydraulic Engineering*, **131**(11), 980-990.

Duan, J. G., *Wang, S. S. Y.*, and *Jia, Y.*, (2001). 'The applications of the enhanced CCHE2D model to study the alluvial channel migration processes', *J. Hydraul. Res.*, IAHR, **39**, 469-480.

Duan, J. G., and *Julien, P. Y.*, (2005). 'Numerical simulation of the inception of channel meandering', *Earth Surface Processes and Landforms*, **30**, 1093-1110.

Engelund, *F.*, (1964). 'Flow resistance and hydraulic radius', *ACTA polytechnica Scandinavia, Civ. and Engrg. Series*, **24**, Copenhagen, Denmark, 1-23.

Espinoza, R. D., *Repetto, P. C.*, and *Muhunthan, B.*, (1992). 'General framework for stability analysis of slopes', *Geotechnique*, **42**, 603-615.

Ferguson, R. I., (1994). 'Critical discharge for entrainment of poorly sorted gravel', *Earth Surface processes and Landforms*, **19**, 179-186.

Ferguson, R. I., *Prestegaard, K. L.*, and *Ashworth, P. J.*, (1989). 'Influence of sand on hydraulics and gravel transport in a braided gravel bed river', *Water Resources Research*, **25**, 635-643.

Ferguson, R. I., *Parsons, D. R.*, *Lane, S. N.*, and *Hardy, R. J.*, (2003). 'Flow in meander bends with recirculation at the inner bank', *Water Resources Research*, **39**, 2003WR001965.

Ferguson, R. I., and *Parsons, D. R.*, (2004). 'Flow structures in meander bends with recirculation', in Jirka, G. and Uijttewaal, W. (eds), *Shallow Flows*, Balkema, Leiden, 325-331.

Ferziger, *J. H.*, and *Peric*, *M.*, (1999). '*Computational Methods for Fluid Dynamics*', 2nd edition, Springer, Berlin, 389pp.

Fischer-Antze, T., *Stoesser, T.*, *Bates, P.*, and *Olsen, N. R. B.*, (2001). '3D numerical modelling of open channel flow with submerged vegetation', *Journal of Hydraulic Research*, **39**, 303-310.

Fluent Inc., (2006). 'Fluent 6.2 User's Guide', *Fluent Incorporated*, Lebanon, NH 03766.

Fraser, *T.*, (2003). 'Numerical modelling of an inverted cyclone gasifier', *PhD Thesis*, School of Engineering, University of Wales, Cardiff, UK.

Fredlund, *D. G.*, *Morgenstern*, *N.R*, and *Widger*, *R.A.*, (1978). 'The shear strengths of unsaturated soil', *Canadian Geotechnical Journal*, **15**, 313-321.

Furbish, *D. J.*, (1991). 'Spatial autoregressive structure in meander evolution', *Geological Society of American Bulletin*, **103**, 1576-1589.

Griffin, E. R., *Kean, J. W.*, *Vincent, K. R.*, *Smith, J. D.*, and *Friedman, J. M.*, (2005). 'Modelling effects of bank friction and woody bank vegetation on channel flow and boundary shear stress in the Rio Puerco, New Mexico', *Journal of Geophysical Research*, **110**, F04023, 1-15.

Grissinger, E. H., (1982). 'Bank erosion of cohesive materials', in R. D. Hey, J. C. Bathurst and C. R. Thorne (eds) *Gravel-Bed Rivers*, John Wiley, Chichester, 273-287.

Hagerty, D. J., (1991). 'Piping/Sapping erosion. I: Basic considerations', *Journal of Hydraulic Engineering*, **117**, 991-1008.

Hankin, B. G., *Hardy, R.*, *Kettle, H.*, and *Beven, K. J.*, (2001). 'Using CFD in a glue framework to model the flow and dispersion characteristics of a natural fluvial dead zone', *Earth Surface Processes and Landforms*, **26**, 667-687.

Hanson, G. J., and *Cook, K. R.*, (1997). 'Development of excess shear stress parameters for circular jet testing', ASAE Paper No. 97-2227, *American Society of Agricultural Engineers*, St. Joseph, MI.

Hanson, G. J., and *Simon, A.*, (2001). 'Erodibility of cohesive streambeds in the loess area of the midwestern USA', *Hydrological Processes*, **15**, 23-38.

Hardy, R. J., *Lane, S. N.*, *Ferguson R. I.*, and *Parsons, D. R.*, (2003). 'Assessing the credibility of a series of computational fluid dynamic simulations of open channel flow', *Hydrological Processes*, **17**, 1539-1560.

Hasegawa, K., (1981). 'Bank erosion discharge based on a non-equilibrium theory', *Proc., JSCE*, 316, 37-50.

Hasegawa, K., (1989). 'Universal bank erosion coefficient for meandering rivers', *Journal of Hydraulic Engineering*, **115**, No.6, 744-765.

Hey, R. D., (1979). 'Flow resistance in gravel-bed rivers', *Journal of Hydraulic Division*, ASCE, **105**, 365-379.

Hickin, E. J., and *Nanson, G. C.*, (1984). 'Lateral migration rates of river bends', *Journal of Hydraulic Engineering*, **110**, 1557-1567.

Hickin, E. J., and *Nanson, G. C.*, (1975). 'The character of channel migration on the Beatton River, North East British Columbia, Canada', *Geological Society of American Bulletin*, **86**, 487-494.

Hinze, J., (1975). 'Turbulence', *McGraw Hill Book Co.*, New York.

Hirt, C. W., and *Nichols, B. D.*, (1981). 'Volume of fluid (VOF) method for the dynamics of free boundaries', *Journal of Computational Physics*, **39**, 201-225.

Hodskinson, A., (1996). 'Computational fluid dynamics as a tool for investigating separated flow in river bends', *Earth Surface Processes and Landforms*, **21**, 993-1000.

Hodskinson, A., (1997). 'Flow structure and geomorphology of non-classical meander bends', *PhD Thesis*, University of Sheffield, Sheffield, UK.

Hodskinson, A., and *Ferguson, R. I.* (1998). 'Numerical modelling of separated flow in river bends: Model testing and experimental investigation of geometric controls on the extent of flow separation at the concave bank', *Hydrological Processes*, **12**, 1323-1338.

Hooke, J. M., (1979). 'An analysis of the processes of river bank erosion', *Journal of Hydrology*, **42**, 39-62.

Hooke, J. M., (1980). 'Magnitude and distribution of rates of river bank erosion', *Earth Surface Processes and Landforms*, **5**, 143-157.

Hooke, R. I. B., (1975). 'Distribution of sediment transport and shear stress in a meander bend', *Journal of Geology*, **83**, 543-565.

Hopson, T. M., (1999). 'The form drag of large natural vegetation along the banks of open channels', *M.S. Thesis*, 114, Univ. of Colo., Boulder.

Hsieh, T. Y., and *Yang, J. C.*, (2003). 'Investigation on the suitability of two-dimensional depth-averaged models for bend-flow simulation', *Journal of Hydraulic Engineering*, **129 (8)**, 597-612.

Ikeda, S., *Parker, G.*, and *Sawai, K.*, (1981). 'Bend theory of river meanders, 1, Linear development', *Journal of Fluid Mechanics*, **112**, 363-377.

Ingham, D. B., and *Ma, L.*, (2005). 'Fundamental equations for CFD in river flow simulations', in P. D. Bates, S. N. Lane, and R. I. Ferguson (eds), *Computational Fluid Dynamics: Applications in Environmental Hydraulics*, John Wiley, Chichester, 19-50.

Ingham, D. B., Bloor, *M. I. G.*, *Wen*, *X.*, and *Ma, L.*, (1997). 'Report for the British Gas Research and Technology Centre on Low and High Pressure Modelling of the Uniflow Hydrocyclone Separation Behaviour and Flow Patterns'. *Internal Report*, University of Leeds, Leeds, UK.

Issa, *R. I.*, (1986). 'Solution of the implicitly discretised fluid flow equations by operator splitting', *Journal of Computational Physics*, **62**, 66-82.

Jackson, *R. G.*, (1975). 'Velocity bedform texture patterns of meander bends in the lower Wabash River, Illinois and Indiana', *Geological Society of American Bulletin*, **86**, 1511-1522.

Jang, C.-L., and *Shimizu, Y.*, (2005). 'Numerical simulation of relatively wide, shallow channels with erodible banks', *Journal of Hydraulic Engineering*, **131**(7), 565-575.

Kean, J. W., *Smith, J. D.*, (2004). 'Flow and boundary shear stress in channels with woody bank vegetation', *Riparian Vegetation and Fluvial Geomorphology*, Water Scie. Appl. Ser., **8**, edited by Bennett, S. J., and Simon, A., 237-252, *AGU*, Washington, D.C.

Kean, J. W., *Smith, J. D.*, (2006,I). 'Form drag in rivers due to small-scale natural topographic features: 1. Regular sequences', *Journal of Geophysical Research*, **111**, F04009, 1-13.

Kean, J. W., *Smith, J. D.*, (2006,II). 'Form drag in rivers due to small-scale natural topographic features: 2. Irregular sequences', *Journal of Geophysical Research*, **111**, F04010, 1-15.

Keylock, C. J., *Hardy, R. J.*, *Parsons, D. R.*, *Ferguson*, *R. I.*, *Lane*, *S. N.*, and *Richards*, *K.S*, (2005). 'The theoretical foundations and potential for large-eddy simulation (LES) in fluvial geomorphic and sedimentological research', *Earth-Science Reviews*, **71**, 3-4, 271-304.

Kim, J., *Salgado, R.*, and *Lee, J.*, (2002). 'Stability analysis of complex soil slopes using Limit Analysis', *Journal of Geotechnical and Geoenvironmental Engineering*, **128**, 546-557.

Knight, *D. W.*, *Yuen*, *K. W. H.*, and *Alhamid*, *A. A. I.*, (1994). 'Boundary shear stress distributions in open channel flow', *Physical mechanisms of mixing and transport in the environment*, *K. Beven*, *P. Chatwin*, and *J. Millbank*, eds., John Wiley & Sons, Inc., Chichester, U.K., 51-87.

Knight, *D. W.*, *Samuels*, *P. G.*, and *Shiono*, *K.*, (1990). 'River flow simulation: Research and developments'. *J. Instn. of Water and Envir. Mgmt.*, 4 (**2**), 163-175.

Knight, *D. W.*, *Shiono*, *K.*, and *Pirt*, *J.*, (1989). 'Prediction of depth mean velocity and discharge in natural rivers with over-bank flow', *Proc., Int. Conf. on Hydr. and Envir. Modelling of Coast, Estuarine and River Waters*, *R. A. Falconer*, ed., Gower Technical Press, U.K., 419-428.

Knight, *D. W.*, and *Demetriou*, *J. D.*, (1983). 'Flood plain and main channel flow interaction', *Journal of Hydraulic Engineering*, ASCE, 109 (**8**), 1073-1092.

Kolmogorov, *A. N.*, (1942). 'Equations of Turbulent Motion of an Incompressible Fluid', Izvestia Academy of Sciences, USSR, *Physics*, 6(1, 2), 56-58.

Komar, P. D., and *Li, Z.*, (1986). 'Pivoting analyses of the selective entrainment of sediments by shape and size with application to gravel threshold', *Sedimentology*, **33**, 425-436.

Kovacs, *A.*, and *Parker*, *G.*, (1994). 'A new vectorial bedload formulation and its application to the time evolution of straight river channels', *Journal of Fluid Mech*, 267, 153-183.

Lane, S. N. (1998). 'Hydraulic modelling in hydrology and geomorphology: A review of high resolution approaches', *Hydrological Processes*, **12**, 1131-1150.

Lane, S. N. (1998b). 'The use of digital terrain modeling in the understanding of dynamic river channel systems', *In Landform Monitoring, Modeling and Analysis*, ed. *S. N.*, *Lane*, *K. S.*, *Richards*, *J. H.*, *Chandler*, Chichester: Wiley, 311-342.

Lane, S. N., *Richards, K. S.*, and *Chandler, J. H.*, (1994b). 'Application of Distributed Sensitivity Analysis to a Model of Turbulent Open-Channel Flow in a Natural River Channel', *Proceedings of the Royal Society of London Series a-Mathematical Physical and Engineering Sciences*, **447**, 49-63.

Lane, S. N., *Richards, K. S.*, and *Chandler, J. H.*, (1995). 'Within-reach spatial patterns of process and channel adjustment. In: Hickin, E. J.', *River Geomorphology*, John Wiley, Chichester, 105-130.

Lane, S. N., and *Richards, K. S.* (1998). 'High resolution, two-dimensional spatial modeling of flow processes in a multi-thread channel', *Hydrological Processes*, **12**, 1279-1298.

Lane, S. N., *Biron, P. A.*, *Bradbrook,* K. *F.*, *Butler*, *J. B.*, *Chandler, J. H*, (1998). 'Three dimensional measurement of river channel flow processes using acoustic Doppler velocimetry', *Earth Surface Processes and Landforms*, **23**, 1247-1267.

Lane, S. N., *Bradbrook, K. F.*, *Richards, K. S.*, *Biron, P. A.*, and *Roy, A.G.* (1999a). 'The application of computational fluid dynamics to natural river channels: three-dimensional versus two-dimensional approaches', *Geomorphology*, 29, 1-20.

Lane, S. N., *Bradbrook, K. F.*, *Richards, K. S.*, *Biron, P. A.*, and *Roy, A.G.* (1999b). 'Time-averaged flow structure in the central region of a stream confluence: A discussion', *Earth Surface Processes and Landforms*, **24**, 361-367.

Lane, S. N., and *Richards, K. S.* (2001). 'The validation of hydrodynamic models: some critical perspectives', In *Model Validation: Perspectives in hydrological science*, ed. *M.G. Anderson, P.D. Bates*, 414-438, Chichester, Wiley.

Lane, S. N., *Hardy, R. J.*, *Elliott, L.*, and *Ingham, D. B.*, (2002). 'High-resolution numerical modelling of three-dimensional flows over complex river bed topography', *Hydrological Processes*, **16**, 2261-2272.

Lane, S. N., *Hardy, R. J.*, *Elliott, L.*, and *Ingham, D. B.*, (2004). 'Numerical modelling of flow processes over gravely surfaces using structured grids and a numerical porosity treatment', *Water Resources Research*, **40**, W01302, doi: 10.1029/2002WR001934.

Lane, S. N., and *Ferguson, R. I.*, (2005). 'Modeling reach-scale fluvial flows', in P. D. Bates, S. N. Lane, and R. I. Ferguson (eds), *Computational Fluid Dynamics: Applications in Environmental Hydraulics*, John Wiley, Chichester, 217-270.

Lane, S. N., *Hardy, R. J.*, *Ferguson, R. I.*, and *Parsons, D. R.*, (2005). 'A framework for model verification and validation of CFD schemes in natural open channel flows', in P. D. Bates, S. N. Lane, and R. I. Ferguson (eds), *Computational Fluid Dynamics: Applications in Environmental Hydraulics*, John Wiley, Chichester, 169-192.

Langendoen, E. J., (2000). 'CONCEPTS – Conservational channel evolution and pollutant transport system – Chapter 3: Bank erosion and channel widening', *USDA-ARS National Sedimentation Laboratory*, Research report No.**16**
http://msa.ars.usda.gov/ms/oxford/nsl/agnps/Concepts/manual/StreamBank.html

Laubel, A., *Kronvang, B.*, *Hald, A. B.*, and *Jensen, C.*, (2003). 'Hydromorphological and biological factors influencing sediment and phosphorus loss via bank erosion in small lowland rural streams in Denmark', *Hydrological Processes*, **17**, 3443-3463.

Launder, *B. E.*, and *Spalding*, *D. B.*, (1972). '*Lectures in mathematical models of turbulence*', New York: Academic Press.

Launder, *B. E.*, and *Spalding*, *D. B.*, (1974). 'The numerical computation of turbulent flows', *Computer Methods in Applied Mechanics and Engineering*, **3**, 269-289.

Lawler, D. M., (1986). 'River bank erosion and the influence of frost: a statistical examination', *Transactions of the Institute of British Geographers*, **11**, 227-242.

Lawler, D. M., (1992). 'Process dominance in bank erosion systems', In: *Lowland Floodplain Rivers: Geomorphological Perspectives*, P. A. Carling and G. E. Petts (eds.), John Wiley, Chichester, UK, 117-143.

Lawler, D. M., (1993). 'Needle ice processes and sediment mobilization on river banks: the River Ilston, West Glamorgan, UK', *Journal of Hydrology*, **150**, 81-114.

Lawler, D. M., (1993). 'The measurement of river bank erosion and lateral channel change: A review', *Earth Surface Processes and Landforms*, **18**, 777-821.

Lawler, D. M., (2005b). 'Defining the moment of erosion: the principle of thermal consonance timing', *Earth Surface Processes and Landforms*, **30**, 1597-1615.

Lawler, D. M., *Thorne, C. R*., and *Hooke, J. M*., (1997). 'Bank erosion and instability', in C. R. Thorne, R. D. Hey and M. D. Newson (Eds), *Applied Fluvial Geomorphology for River Engineering and Management*, John Wiley, Chichester, 137-172.

Leonard, A., (1974). 'Energy cascade in large-eddy simulations of turbulent fluid flows', *Advances in Geophysics*, **18A**, 237-248.

Leonard, B. P., (1979). 'A stable and accurate convective modelling procedure based on quadratic upstream interpolation', *Computational Methods in Applied Mechanics and Engineering*, **19**, 59-98.

Leshchinsky, D., (1990). 'Slope stability analysis: Generalized approach', *Journal of Geotechnical Engineering*, **116**, 851-867.

Lien, F. S., and *Leschziner, M. A*., (1994). 'Application of an RNG turbulence model to flow over a backwards-facing step', *Computers and Fluids*, **23**, 983-1004.

Lohner, *R.*, (2001). '*Applied Computational Fluid Dynamics Techniques*', Chichester: John Wiley & Sons Ltd.

Lopez, F., (1997). 'Open-channel flow with roughness elements of different spanwise aspect ratios: Turbulence structure and numerical modeling', *Ph.D. Thesis*, Department of Civil and Environmental Engineering, University of Illinois at Urbana-Champaign.

Lundgren, *H.*, and *Jonsson*, *I. G.*, (1964). 'Shear and velocity distribution in shallow channels', *J. Hydr.Div.*, ASCE, 90 (**1**), 1-21.

Lutenegger, *A. J.*, and *Hallberg*, *G. R.*, (1981). 'Borehole Shear Test in geotechnical investigation', *Special Technical Publ., American Society for Testing and materials*, 740, 566-578.

Ma, L., *Ashworth, P. J.*, *Best, J. L.*, *Elliott, L.*, *Ingham, D. B.*, and *Whitcombe, L. J.*, (2002). 'Computational fluid dynamics and the physical modelling of an upland urban river', *Geomorphology*, **44**, 375-391.

Markham, *A. J.*, and *Thorne*, *C. R.*, (1992). 'Geomorphology of gravel-bed river bends', In *Dynamics of Gravel-bed Rivers*, ed. *Billi*, *P.*, *Hey*, *R. D.*, *Thorne*, *C. R.*, and *Tacconi*, *P.*, 433-450, Chichester: Wiley.

Menter, *F. R.*, (1993). 'Zonal Two Equation k-ω Turbulence Models for Aerodynamic Flows', *24th Fluid Dynamics Conference*, Orlando, Florida, 1-21, July 6-9.

Meselhe, E. A., and *Sotiropoulos, F.*, (2000). 'Three-Dimensional Numerical Model for Open-Channels with Free-Surface Variations', *J. Hydr. Res.*, 38(**2**), 115-121.

Michalowski, R. L., (1995). 'Slope stability analysis: a kinematical approach', *Geotechnique*, **45**, No.2, 283-293.

Millar, R. G., and *Quick, M. C.*, (1993). 'Effect on bank stability on geometry of gravel rivers', *Journal of Hydraulic Engineering*, **119**, 1343-1363.

Mohammadi, B., and *Pironneau, O*., (1994). '*Analysis of the k-epsilon Turbulence model*', Wiley, Chichester.

Morgenstern, N. R., and *Price, V. E*., (1965). 'The analysis of the stability of general slip surfaces', *Geotechnique*, **15**, 79-93.

Mosselman, E., (1998). 'Morphological modelling of rivers with erodible banks', *Hydrological Processes*, **12**, 1357-1370.

Nallasamy, *M.*, (1987). 'Turbulence models and their applications to the prediction of internal flows – A review', *Comput. Fluids*, **15**, 151-194.

Nagata, N., *Hosoda, T*., and *Muramoto, Y*., (2000). 'Numerical analysis of river channel processes with bank erosion', *Journal of Hydraulic Engineering*, **126**, 243-252.

Nece, *R. E.*, and *Smith*, *J.*, (1970). 'Boundary shear stress in rivers and estuaries', *J. Wtrwy., Harb. And Coast. Div.*, ASCE, 96(**2**), 335-358.

Nelson, *J. M.*, and *Smith*, *J. D.*, (1989a). 'Evolution and stability of erodiable channel beds', *In River Meandering, American Geophysical Union water resources monograph 12*, ed. *S.*, *Ikeda*, *G.*, *Parker*, Washington D. C. AGU.

Nelson, *J. M.*, and *Smith*, *J. D.*, (1989b). 'Flow in meandering channels with natural topography', *In River Meandering, American Geophysical Union water resources monograph 12*, ed. *S.*, *Ikeda*, *G.*, *Parker*, Washington D. C. AGU.

Newton, T. M., (1998). 'Rotor-stator interaction in radial flow pumps and fans at shut-off conditions', *PhD Thesis*, University of Newcastle upon Tyne, Newcastle upon Tyne, UK.

Nicholas, A. P., (2001). 'Computational fluid dynamics modelling of boundary roughness in gravel-bed rivers: An investigation of the effects of random variability in bed elevation', *Earth Surface Processes and Landforms*, **26**, 345-362.

Nicholas, A. P., (2003). 'Investigation of spatially distributed braided river flows using a two-dimensional hydraulic model', *Earth Surface Processes and Landforms*, **28**, 655-674.

Nicholas, A. P., (2005). 'Roughness parameterization in CFD modeling of gravel-bed rivers', in P. D. Bates, S. N. Lane, and R. I. Ferguson (eds), *Computational Fluid Dynamics: Applications in Environmental Hydraulics*, John Wiley, Chichester, 329-356.

Nicholas, A. P., and *Sambrook Smith, G. H.*, (1999). 'Numerical simulation of three-dimensional flow hydraulics in a braided channel', *Hydrological Processes*, **13**, 913-929.

Nicholas, A. P., and *Walling, D. E.*, (1998). 'Numerical modelling of floodplain hydraulics and suspended sediment transport and deposition', *Hydrological Processes*, **12**, 1339-1355.

Nikuradse, *J.*, (1952). 'Laws for flows in pipes', *VDI Forschungsheft*, English translation NACA Technical Memorandum, 1292, p 1933.

Odgaard, A. J., (1987). 'Streambank erosion along two rivers in Iowa', *Water Resources Research*, **23**, 1225-1236.

Odgaard, A. J., (1989a). 'River meander model. I: Development', *Journal of Hydraulic Engineering*, **115**(11), 1433-1450.

Odgaard, A. J., (1989b). 'River meander model. II: Applications', *Journal of Hydraulic Engineering*, **115**(11), 1451-1464.

Okagbue, C. O., and *Abam, T. K. S.*, (1986). 'An analysis of stratigraphic control on river bank failure', *Engineering Geology*, **22**, 231-245.

Olsen, N. R. B., (2003). 'Three-dimensional CFD modelling of self-forming meandering channel', *Journal of Hydraulic Engineering*, **129 (5)**, 366-372.

Olsen, N. R. B., and *Kjellesvig, H. M.*, (1998). 'Three-dimensional numerical flow modelling for estimation of maximum local scour depth', *Journal of Hydraulic Research*, **36**, 579-590.

Olsen, N. R. B., and *Skoglund, M.*, (1994). 'Three-dimensional numerical modelling of water and sediment flow in a sand trap', *Journal of Hydraulic Research*, **32**, 571-581.

Olsen, N. R. B., and *Stokseth, S.*, (1995). 'Three-dimensional modelling of water flow in a river with large bed roughness', *Journal of Hydraulic Research*, **33**, 571-581.

Osman, A. M., and *Thorne, C. R.*, (1988). 'Riverbank stability analysis. I: Theory', *Journal of Hydraulic Engineering*, **114**(2), 134-150.

Parsons, D. R., (2002). 'Flow Separation in Meander Bends', *PhD Thesis*, Department of Geography, University of Sheffield, UK.

Partheniades, E., (1965). 'Erosion and deposition of cohesive soils', *Journal of the Hydraulics Division*, Proceedings of the American society of Civil Engineers, **91**, 105-139.

Patankar, S. V., (1980). 'Numerical heat transfer and fluid flow', Hemisphere Publishing Corp., New York.

Patankar, *S. V*., and *Spalding*, *D. B*., (1972). 'A calculation procedure for heat, mass and momentum transfer in three-dimensional parabolic flows', *Int. J. Heat Mass Transfer*, Vol. **15**, p. 1787.

Patel, *V. C.*, *Rodi*, *W.*, and *Scheuerer*, *G.*, (1984). 'Turbulence Models for Near-Wall and Low Reynolds Number Flows: A Review', *AIAA J.*, 23(**9**), 1308-1319.

Pizzuto, J. E., and *Meckelnburg, T. S*., (1989). 'Evaluation of a linear erosion equation', *Water Resources Research*, **25**(5), 1005-1013.

Prandtl, *L.*, (1925). 'Lieber die ausgebildete Turbulenz', *A. Angew. Math. Mech.*, 5: 136-139.

Prosser, I. P., *Hughes, A. O*., and *Rutherfurd, I. D*., (2000). 'Bank erosion of an incised upland channel by subaerial processes: Tasmania, Australia', *Earth Surface Processes and Landforms*, **25**, 1085-1101.

Rameshwaran, *P.*, and *Naden*, *P. S.*, (2003). 'Three-dimensional numerical simulation of compound channel flows', *Journal of Hydraulic Engineering*, **129**, 645-652.

Reid, I., *Bathurst, J. C*., *Carling, P. A*., *Walling, D. E*., and *Webb, B. W*., (1997). 'Sediment erosion, transport and deposition', In: *Applied Fluvial Geomorphology for River Engineering and Management*, Thorne, C. R., Hey, R. D., and Newson, M. D. (eds.), John Wiley, Chichester, UK, 95-135.

Rhoads, B. L., and *Kenworthy, S. T*., (1995). 'Flow structure at an asymmetrical stream confluence', *Geomorphology*, **11**, 273-293.

Rhoads, B. L., and *Kenworthy, S. T*., (1998). 'Time –averaged flow structure in the central region of a stream confluence', *Earth Surface Processes an Landforms*, **23**, 171-191.

Rhoads, B. L., and *Sukhodolov, A.*, (2001). 'Field investigation of three-dimensional flow structure at stream confluences: 1. Thermal mixing and time-averaged velocities', *Water Resources Research*, **37**, 2393-2410.

Rhodes, *D. G.*, and *Knight*, *D. W.*, (1994). 'Distribution of shear force on boundary of smooth rectangular duct', *Journal of Hydraulic Engineering*, **120** (7), 787-807.

Rinaldi, M., and *Casagli, N.*, (1999). 'Stability of streambanks formed in partially saturated soils and effects of negative pore water pressures: the Sieve River, Italy', *Geomorphology*, **26**, 253-277.

Rinaldi, M., *Casagli, N.*, *Dapporto, S.*, and *Gargini, A.*, (2004). 'Monitoring and modelling of pore water pressure changes and riverbank stability during flow events', *Earth Surface Processes and Landforms*, **29**, 237-254.

Roache, P. J., (1997). 'Quantification of uncertainty in computational fluid dynamics', *Annual Review of Fluid Mechanics*, **29**, 123-160.

Roache, P. J., (1998). 'Verification of codes and calculation', *AIAA*, **36**, 696-702.

Rodi, W., (1980). 'Turbulence models and their application in hydraulics', *Int. Assn. for Hydr. Res. (IAHR)*, Delft, The Netherlands, 1-104.

Rodriguez, J. F., *Bombardelli, F. A.*, *Garcia, M. H.*, *Frothingham, K. M.*, *Rhoads, B. L.*, and *Abad, J. D.*, (2004). 'High-resolution numerical simulation of flow through a highly sinuous river reach', *Water Resources Management*, **18**, 177-199.

Sarma, S. K., (1973). 'Stability analysis of embankments and slopes', *Geotechnique*, **23**, No.3, 423-433.

Sarma, J. N., (2005). 'Fluvial process and morphology of the Brahmaputra River in Assam, India', *Geomorphology*, **70**, 226-256.

Schlichting, *H.*, (1955). '*Boundary Layer Theory*', New York: McGraw-Hill.

Schneider, *G. E.*, and *Raw*, *M. J.*, (1987). 'Control-volume finite element method for heat transfer and fluid flow using co-located variables – 1 computational procedure', *Numerical Heat Transfer*, **11**, 363-390.

Schoklitsch, A., (1962). 'Handbuch des Wasserbaues, 3rd edition, Springer, Vienna.

Sellin, *R. H. J.*, *Ervine*, *D. A.*, and *Willetts*, *B. B.*, (1993). 'Behavior of meandering two-stage channels', *Proc., Instn. Civ. Engrs. Water Maritime and Energy*, 101, 99-111.

Sharc Ltd, (2006). 'Harpoon Used Guide', www.sharc.co.uk

Shih, *T. H.*, *Liou*, *W. W.*, *Shabbir*, *A.*, *Yang*, *Z.*, and *Zhu*, *J.*, (1995). 'A New k-ε Eddy-Viscosity model for high Reynolds number Turbulent Flows – Model development and validation', *Computer Fluids*, **24**(3), 227-238.

Simon, A., and *Collison, A. J. C.*, (2001). 'Pore-water pressure effects on the detachment of cohesive streambeds: Seepage forces and matric suction', *Earth Surface Processes and Landforms*, **26**, 1421-1442.

Simon, A., and *Collison, A. J. C.*, (2002). 'Quantifying the mechanical and hydrologic effects of riparian vegetation on streambank stability', *Earth Surface Processes and Landforms*, **27**, 527-546.

Simon, A., *Curini, A.*, *Darby, S. E.*, and *Langendoen, E. J.*, (2000). 'Bank and near-bank processes in an incised channel', *Geomorphology*, **35**, 193-217.

Sinha, *S.*, *Sotiropoulos*, *F.*, and *Odgaard*, *A. J.*, (1998). 'Three-Dimensional Numerical Model for Turbulent Flows through Natural Rivers of Complex Bathymetry', *ASCE Journal of Hydraulic Engineering*, 124(**1**), 13-24.

Smith, *G. D.*, (1978). '*Numerical Solution of Partial Differential Equations: Finite Difference Methods*', Oxford University Press, Oxford, UK.

Smith, *J. S.*, (1998). 'Determination of k-factors of HVAC system components using measurement and CFD modelling', *PhD Thesis*, University of Nottingham, Nottingham, UK.

Sotiropoulos, *F.*, (2005). 'Introduction to statistical turbulence modeling for hydraulic engineering flows', in P. D. Bates, S. N. Lane, and R. I. Ferguson (eds), *Computational Fluid Dynamics: Applications in Environmental Hydraulics*, John Wiley, Chichester, 91-120.

Sotiropoulos, F., and *Patel, V. C.*, (1995b). 'Application of Reynolds-Stress Transport Models to Stern and Wake Flows', *J. Ship Res.*, 39(**4**), 263-283.

Spalart, P., (2000). 'Strategies for turbulence modelling and simulations', *Int. J. Heat Fluid Fl.*, **21**(3), 252-263.

Spalart, *P.*, and *Allmaras*, *S.*, (1992). 'A one-equation turbulence model for aerodynamic flows', *American Institute of Aeronautics and Astronautics*, Technical Report AIAA-92-0439.

Spalding, D. B., (1972). 'A novel finite difference formulation for differential expressions involving both first and second order derivatives', *International Journal of Numerical Methods in Engineering*, **4**, 551-566.

Spalding, D. B., (1985). 'The computation of flow around ships with allowance for free-surface and density-gradient effects', *Proceedings of the First International Maritime Simulation Symposium*, Munich, 101-113.

Spencer, E., (1967). 'A method of analysis of the stability of embankments assuming parallel inter-slice forces', *Geotechnique*, **17**, 11-26.

Stott, T., (1997). 'A comparison of stream bank erosion processes on forested and moorland streams in the Balquhidder catchments, Central Scotland', *Earth Surface Processes and Landforms*, **22**, 383- 399.

Stott, T., *Leeks, G*., *Marks, S*., and *Sawyer, A*., (2001). 'Environmentally sensitive plot-scale timber harvesting: impacts on suspended sediment, bedload and bank erosion dynamics', *Journal of Environmental Management*, **63**, 3-25.

Sukhodolov, A., and *Rhoads, B. L.*, (2001). 'Field investigation of three-dimensional flow structure at stream confluences: 2. Turbulence', *Water Resources Research*, **37**(9), 2411-2424.

Tennekes, H., and *Lumley, J. L*., (1972). 'A first course in turbulence', *The MIT Press*, Cambridge, Massachusetts, London.

Thomas, T. G., and *Williams, J. J. R.*, (1995). 'Large eddy simulation of turbulent flow in an asymmetric compound channel', *Journal of Hydraulic Research*, **33**, 27-41.

Thompson, A., (1986). 'Secondary flows and the pool-riffle unit: a case study of the processes of meander development', *Earth Surface Processes and Landforms*, **11**, 631-641.

Thompson, D. M., *Nelson, J. M*., and *Wohl, E. E*., (1998). 'Interactions between pool geometry and hydraulics', *Water Resources Research*, **34**, 3673-3681.

Thorne, *C. R.*, (1982). 'Processes and mechanisms of river bank erosion', In *Gravel-Bed Rivers*, ed. *Hey*, *R. D.*, *Bathurst*, *J. C.*, and *Thorne*, *C. R.*, 227-271, Chichester: Wiley.

Thorne, *C. R.*, (1992). 'Bend scour and bank erosion on the meandering Red River, Louisiana', In *Lowland Floodplain Rivers – Geomorphologic* Perspectives, ed. *Carling*, *P. A.*, and *Petts*, *G.*, 95-115, Chichester: Wiley.

Thorne, S. D., *Furbish*, *D. J.*, (1995). 'Influences of coarse bank roughness on flow within a sharply curved river bend', *Geomorphology*, **12**, 241-257.

Thorne, C. R., and *Osman, A. M.*, (1988a). 'The influence of bank stability on regime geometry of natural channels', in White, W. R. (Ed) *River Regime*, John Wiley, Chichester, 135-147.

Thorne, C. R., and *Osman, A. M.*, (1988b). 'Riverbank stability analysis. II: Applications' *Journal of Hydraulic Engineering*, **114**(2), 151-172.

Thorne, C. R., and *Tovey, N. K.*, (1981). 'Stability of composite river banks', *Earth Surface Processes and Landforms*, **6**, 469-484.

Ullrich, C. R., *Hagerty, D. J.*, and *Holmberg, R. W.*, (1986). 'Surficial failures of alluvial stream banks', *Canadian Geotechnical Journal*, **23**, 304-316.

Utama, *I. K. A. P.*, (1999). 'Investigation of the viscous resistance components of catamaran forms', *PhD Thesis*, Department of Ship Science, Faculty of Engineering and Applied Science, University of Southampton, Southampton, UK.

Van De Wiel, M. J., (2003). 'Numerical modeling of channel adjustment in alluvial meandering rivers with riparian vegetation', *PhD Thesis*, University of Southampton, Southampton, UK.

Vandoormaal, *J. P.*, and *Raithby*, *D. G.*, (1984). 'Enhancements of the SIMPLE method for predicting incompressible fluid flows', *Numerical Heat Transfer*, **7**, 147-163.

Versteeg, *H. K.*, and *Malalasekera*, *W.*, (1995). '*An Introduction to Computational Fluid Dynamics*', Harlow: Longman.

Wallis, *S. G.*, and *Manson*, *J. R.*, (1997). 'Accurate numerical simulation of advection using large time steps', *International Journal of Numerical Methods in Fluids*, **24**, 127-139.

Wan, *Q.*, *Wan*, *H. T.*, *Zhou*, *C. H.*, and *Wu*, *Y. X.*, (2002). 'Simulating the hydraulic characteristics of the lower Yellow River by the finite-volume technique', *Hydrological Processes*, **16**, 2767-2779.

Waterson, *N. P.*, (1994). 'Validation of convection discretisation schemes', *In VKI Dip. Rep.*, pp 1-33, Rhode-Saint-Genese, Belgium: Von Karmen Institute for Fluid Dynamics.

Weigel, T. A., and *Hagerty, D. J*., (1983). 'Riverbank change – Sixmile Island, Ohio River, USA', *Engineering Geology*, **19**, 119-132.

Whiting, *P. J.*, (1997). 'The effect of stage on flow and components of the local force balance', *Earth Surface Processes and Landforms*, **22**, 517-530.

Wilcox, *D. C*., (1988). 'Reassessment of the Scale Determining Equation for Advanced Turbulence Models', *AIAA J.*, **26**, 1299-1310.

Wilcox, *D. C*., (1998). 'Turbulence Modeling for CFD', *DCW Industries*, Inc., La Canada, California.

Wilson, C. A. M. E., *Boxall, J. B.*, *Guymer, I.*, and *Olsen, N. R. B.*, (2003). 'Validation of a three-dimensional numerical code in the simulation of pseudo-natural meandering flows', *Journal of Hydraulic Engineering*, **129 (10)**, 758-768.

Wright, *N. G.*, (2005). 'Introduction to numerical methods for fluid flow', in P. D. Bates, S. N. Lane, and R. I. Ferguson (eds), *Computational Fluid Dynamics: Applications in Environmental Hydraulics*, John Wiley, Chichester, 147-168.

Wu, W., *Rodi, W.*, and *Wenka, T.*, (2000). '3D Numerical Modelling of Flow and Sediment Transport in Open Channels', *ASCE Journal of Hydraulic Engineering*, 126(**1**), 4-15.

Wynn, T. M., and *Mostaghimi, S.*, (2006). 'Effects of riparian vegetation on stream bank subaerial processes in southwestern Virginia, USA', *Earth Surface Processes and Landforms*, **31**, 399-413.

Yakhot, *V.*, and *Orszag*, *S. A.*, (1986). 'Renormalization group analysis of turbulence', *Journal of Scientific Computing*, **1**, 536-551.

Yakhot, *V.*, *Orszag*, *S. A.*, *Thangham*, *S.*, *Gatshi*, *T. B.*, and *Speziale*, *C. G.*, (1992). 'Development of a turbulence model for shear flow by a double expansion technique, *Physics and Fluids A*, **4**, 1510-1520.

Yoon, J. Y., and *Patel, V. C.*, (1993). 'A Numerical Model of Flow in Channels with Sand-Dune Beds and Ice Covers', *IIHR Report No. 362*, Iowa Institute of Hydraulic Research, University of Iowa, Iowa City, IA.

Younis, B. A., (1992). 'Is turbulence modelling of any use?', *AIRH Conference*, Institute of Civil Engineers, London. (quoted by Lane (1998)).

Zedler, *E. A.*, and *Street*, *R. L.*, (2001). 'Large-Eddy Simulation of Sediment Transport: Currents Over Ripples', *Journal of Hydraulic Engineering*, 127 (**6**), 444-452.

Zienkiewicz, *O.*, and *Cheung*, *Y.*, (1965). 'Finite elements in the solution of field problems', *The Engineer*, pp. 507-510.